

14th Annual Meeting of the Imaging Network of Ontario

March 30th & 31st, 2016

Chestnut Residence,
Toronto, ON

PROCEEDINGS OF THE 14TH ImNO ANNUAL MEETING

(FINAL VERSION)

Table of Contents

| | |
|--|----|
| Welcome Letter | 4 |
| Sponsoring Consortia and Acknowledgements | 5 |
| The Cardiac Arrhythmia Network of Canada (CANet)..... | 6 |
| Development of Novel Therapies for Bone and Joint Diseases (B&J)..... | 6 |
| Heart Failure: Prevention Through Early Detection Using New Imaging Methods (HF) | 6 |
| Imaging for Cardiovascular Device Intervention (ICDI)..... | 6 |
| Medical Imaging Trial Network of Canada (MITNEC)..... | 6 |
| Ontario Consortium for Adaptive Interventions in Radiation Oncology (OCAIRO)..... | 7 |
| Ontario Institute for Cancer Research Imaging Translation Program (ITP)..... | 7 |
| Ontario Institute for Cancer Research Smarter Imaging Program (SIP)..... | 7 |
| Keynote Speaker Biographies..... | 8 |
| Louis Collins, PhD | 8 |
| Daniel Low, PhD, DABMP | 8 |
| Sharmila Majumdar, PhD | 9 |
| Saman Nazarain, MD, PhD | 9 |
| Invited Speaker Biographies | 10 |
| Paula Foster, PhD..... | 10 |
| David Holdsworth, PhD | 10 |
| David Jaffray, PhD | 10 |
| Allan Skanes, MD, FRCPC, FHRS | 11 |
| Jonathan Thiessen, PhD | 11 |
| Symposium Organizing Committees | 12 |
| Scientific Committee..... | 12 |
| Organizing Committee | 12 |
| Abstract Reviewers | 13 |
| Abstract Awards..... | 13 |
| Summa cum Laude | 13 |
| Magna cum Laude | 14 |
| Cum Laude | 15 |
| Presentation Awards | 16 |
| Oral Presentations | 16 |
| Poster Presentations..... | 16 |
| Program at a Glance | 17 |

| | |
|---|-----|
| Wednesday 30 March 2016 | 17 |
| Thursday 31 March 2016 | 21 |
| Oral Session Abstracts | 25 |
| Poster Session Abstracts..... | 94 |
| Image Guided Intervention..... | 94 |
| Image Monitoring of Treatment Response..... | 95 |
| Imaging/Simulation for Therapy Planning | 96 |
| Instrumentation/Devices | 96 |
| Patient-centered Imaging Studies and Trials | 97 |
| Perfusion, Metabolic and Hypoxia Imaging | 97 |
| Preclinical Imaging | 98 |
| Quantitative Imaging | 99 |
| Targeted Probe Development..... | 100 |
| Visualization and Image Analysis | 100 |
| Presenter Index..... | 221 |

30 March 2016

Dear ImNO 2016 Attendees:

Welcome to the Imaging Network Ontario (ImNO) 2016 Meeting. This year marks our 14th annual meeting.

ImNO is an initiative created in response to a request by the Ontario Research Development Challenge Fund for assistance in harmonizing its investments in imaging research. The establishment of ImNO provides a means of harnessing and focusing the intellectual and innovative capabilities at Ontario universities in partnerships with emerging and established medical imaging companies to create a strong and sustainable internationally competitive imaging industry based on scientific excellence in Ontario.

The ImNO meeting since inception in 2003, has welcomed invited presentation for world-class scientists and proffered presentations from Ontario and across the county. Recent years have seen increasing support from Canada-wide sponsoring consortia. This year, I am pleased to welcome the The Cardiac Arrhythmia Network of Canada (CANet) and Medical Imaging Trial Network of Canada (MITNEC) who have joined forces with six Ontario-based programs: Development of Novel Therapies for Bone and Joint Diseases (B&J), Heart Failure: Prevention Through Early Detection Using New Imaging Methods (HF), Imaging for Cardiovascular Device Intervention (ICDI), Ontario Consortium for Adaptive Interventions in Radiation Oncology (OCAIRO), Ontario Institute for Cancer Research (OICR) Imaging Translation Program (ITP), and OICR Smarter Imaging Program (SIP). Without the financial support of these eight consortia, this meeting would not be possible.

For the 2016 meeting, we received a total of 177 submitted abstracts that were reviewed within each consortium by an average of 3 reviewers. The ImNO 2016 Scientific Committee then assembled the final program - 4 plenary speakers, 5 invited and 59 proffered oral presentations, and 118 poster presentations.

In closing I would like to acknowledge the significant contributions made by the members of the Scientific and Organizing Committees. Together they have worked very hard since September 2015 to bring us this year's meeting. During the meeting, I welcome you to approach these individuals and thank them for a job well done!

Sincerely,

A handwritten signature in blue ink, appearing to read 'R. Frayne', is positioned below the word 'Sincerely,'.

Richard Frayne, PhD

Chair, Scientific Committee, 2016 ImNO Meeting

Sponsoring Consortia and Acknowledgements

The Annual Meeting of Imaging Network Ontario (ImNO) promotes Canada's role as a leader in medical imaging innovation by cultivating synergy among consortia and partnerships between Ontario and other Canadian imaging entities.

The 2016 ImNO Symposium is supported financially by eight consortia. These consortia are:

- Cardiac Arrhythmia Network of Canada (CANet)
- Development of Novel Therapies for Bone and Joint Diseases (B&J)
- Heart Failure: Prevention Through Early Detection Using New Imaging Methods (HF)
- Imaging for Cardiovascular Device Intervention (ICDI)
- Medical Imaging Trial Network of Canada (MITNEC)
- Ontario Consortium for Adaptive Interventions in Radiation Oncology (OCAIRO)
- Ontario Institute for Cancer Research Imaging Translation Program (ITP)
- Ontario Institute for Cancer Research Smarter Imaging Program (SIP)

In addition, financial and in-kind support was received from the following:



The ImNO meeting organizers wish to acknowledge and thank all for their support.

The Cardiac Arrhythmia Network of Canada (CANet)

Scientific Director: Dr Anthony Tang

Networks of Centres of Excellence

CANet is a not-for-profit organization dedicated to transforming Canada's arrhythmia health care system through integrated trans-disciplinary research and development.

<http://canet-nce.ca/>

Development of Novel Therapies for Bone and Joint Diseases (B&J)

Program Director: Dr David Holdsworth

Ontario Research Fund

The Development of Novel Therapies for Bone and Joint Diseases group seeks to advance novel therapies for musculoskeletal disorders, which cost the Ontario economy more than \$9 billion dollars annually, based on state-of-the art MRI and x-ray systems.

Heart Failure: Prevention Through Early Detection Using New Imaging Methods (HF)

Program Director: Dr Frank Prato

Ontario Research Fund

The Heart Failure: Prevention Through Early Detection Using New Imaging Methods team seeks to improve methods for early diagnosis and preventive care for heart disease, which affects 10 percent of Ontarians over 60.

Imaging for Cardiovascular Device Intervention (ICDI)

Program Director: Dr Graham Wright

Ontario Research Fund

The Ontario Consortium in Imaging for Cardiovascular Device Intervention (ICDI) transforms the individual efforts of cardiac imaging expertise located at leading cardiac care institutions in London and Toronto into a coordinated program that focuses on critical anatomic and functional information for assessment, treatment planning, and intervention monitoring of heart disease in patients of all ages.

<http://cardiovascularimaging.ca/>

Medical Imaging Trial Network of Canada (MITNEC)

Program Director: Dr Jean-Claude Tardif

CIHR

The central goal of Medical Imaging Trial Network of Canada (MITNEC) is to move innovations in imaging toward their broad application in clinical research and to facilitate the uptake of research outcomes into clinical practice and improved patient care. MITNEC encompasses the three medical disciplines of oncology, cardiology and neurology, and their relevant cross-sectional processes such as immunology and inflammation. The Network's first objective is to reduce our clinical reliance on technetium currently produced by nuclear reactors. Imaging trials will evaluate the clinical use of alternatives to technetium to detect bone metastases, determine response to chemotherapy in women with metastatic breast cancer, detect cardiac blood flow abnormalities and predict cognitive decline.

<http://www.mitnec.org/>

Ontario Consortium for Adaptive Interventions in Radiation Oncology (OCAIRO)

Program Director: Dr David Jaffray

Ontario Research Fund

The Ontario Consortium for Adaptive Interventions in Radiation Oncology sets out to accelerate the development and application of innovative adaptive methods in radiation therapy through focused scientific, technical, and clinical developments in four domains: (1) imaging and instrumentation for adaptive radiation therapy; (2) adaptive radiation therapy (RT) processes; (3) validation of image signal and dose accumulation in adaptive RT; and (4) open source software platforms and databases for the adaptive process.

<http://ocairo.technainstitute.com/>

Ontario Institute for Cancer Research Imaging Translation Program (ITP)

Program Directors: Dr Aaron Fenster/Dr Martin Yaffe

Ontario Institute for Cancer Research

The OICR Imaging Translation Program (OICR ITP) accelerates the translation of research into the development of new imaging innovations for earlier cancer detection and diagnosis and treatment through four major projects; probe development and commercialization, medical imaging instrumentation and software, pathology validation, and imaging for clinical trials. OICR ITP facilitates improved screening and treatment options for cancer patients by streamlining advances of medical imaging through the complex pipeline from discovery through clinical translation and ultimately to clinical use.

<http://www.oicr-itp.ca/>

Ontario Institute for Cancer Research Smarter Imaging Program (SIP)

Program Directors: Dr Martin Yaffe/Dr Aaron Fenster

Ontario Institute for Cancer Research

The goal of the OICR Smarter Imaging Program (OICR SIP) is to increase both the sensitivity (earlier detection) and specificity (more accurate diagnosis) of cancer imaging and to use information from images to help optimize selection of therapy to avoid over- or under-treatment of disease. OICR SIP focuses on diagnosing and effectively treating cancer with imaging technology and probes that target biomarkers representing molecular, physical or functional changes associated with cancer. In conjunction with the Imaging Translation Program, OICR SIP develops and translates tools and techniques for earlier detection and diagnosis of cancer into clinical practices by exploiting recent advances in molecular biology, chemistry and physics.

<http://oicr.on.ca/oicr-programs-and-platforms/innovation-programs/smarter-imaging-program>

Keynote Speaker Biographies



Louis Collins, PhD

Professor, Departments of Neurology and Neurosurgery, and Biomedical Engineering, McGill University, and McConnell Brain Imaging Centre at Montreal Neurological Institute, Montreal, Quebec, Canada

Louis Collins completed his PhD in Biomedical Engineering (1994) at McGill University, and then spent a year in France doing a Postdoctoral Fellowship at Université de Rennes I. He is a Professor of Neurology and Neurosurgery and Biomedical Engineering, and an Associate Member of both the Centre for Intelligent Machines at McGill and the McGill Centre for Studies in Aging. His laboratory develops and uses computerized image processing techniques such as non-linear image registration and model-based segmentation to automatically identify structures within the human brain.



Daniel Low, PhD, DABMP

Professor and Vice Chair Physics, Department of Radiation Oncology, University of California Los Angeles (UCLA), Los Angeles, California, USA

Daniel Low earned his PhD in Physics (1988) from Indiana University and was a postdoctoral fellow for two years in radiation therapy physics at MD Anderson Cancer Center. He moved to Washington University where he eventually became a Professor and Director of Medical Physics. In 2010, he relocated to UCLA to be the Vice Chair and Director of Medical Physics. He is board certified by the American Board of Medical Physics in Therapeutic Medical Physics and by the American Board of Radiology, and is a fellow of the American Association of Physicists in Medicine. His research interests include modeling of human breathing motion, radiation therapy safety, quality assurance methods and image-guided radiation therapy including magnetic resonance-image guided radiation therapy.



Sharmila Majumdar, PhD

Professor and Vice Chair of Research, Department of Radiology
University of California San Francisco (UCSF), San Francisco, California, USA

Sharmila Majumdar obtained her PhD degree in Engineering and Applied Science (1987) from Yale University, where she stayed as a post-doctoral researcher and Assistant Professor. In 1989 she joined UCSF. She currently is a Professor and the Vice Chair of Research in the Department of Radiology and Biomedical Imaging and a Professor in the Departments of Bioengineering and Therapeutic Sciences, Orthopedic Surgery at UCSF and Bioengineering at UC Berkeley. Her research work on imaging, particularly magnetic resonance and micro computed tomography, and development of image processing and analysis tools, has been focused in the areas of osteoporosis, osteo-arthritis and lower back pain. Her research is diverse ranging from technical development to clinical trials. She currently heads an NIH Center of Research Translation focused on Osteoarthritis and Imaging, a joint effort between UCSF and the University of California-Davis.



Saman Nazarian, MD, PhD

Associate Professor, Department of Medicine, Johns Hopkins University
School of Medicine, Baltimore, Maryland, USA

Saman Nazarian is a graduate of Stanford University School of Medicine (MD, 1999) and the Johns Hopkins Bloomberg School of Public Health (PhD, 2012). He received advanced medical training at the Peter Bent Brigham Hospital (Internal Medicine) and Johns Hopkins University (Cardiovascular Medicine and Clinical Cardiac Electrophysiology). He is currently an Associate Professor of Medicine and Epidemiology at the Johns Hopkins University School of Medicine. His interests include the care of patients with atrial and ventricular arrhythmia, cardiomyopathy, and implantable cardiac devices. He performs procedures including implantation of permanent pacemakers and implantable cardioverter defibrillators, and catheter ablation for atrial and ventricular arrhythmias.

Invited Speaker Biographies



Paula Foster, PhD

Professor, Department of Medical Biophysics, University of Western Ontario and Scientist, Robarts Research Institute

Paula Foster completed her PhD at the University of Guelph. She is currently a Professor of Medical Biophysics at Western University, and the leader of the Cellular and Molecular Imaging program at Robarts. She is developing imaging and cell labeling technology that uses ultra-high resolution MRI to detect cells labeled with magnetic nanoparticles. Her laboratory is currently focused on the use of these techniques to track stem cells used for tissue repair and regeneration and to monitor cancer cell metastasis and immune cells used as cancer.



David Holdsworth, PhD

Professor, Departments of Surgery and Medical Biophysics, University of Western Ontario and Scientist, Robarts Research Institute

David Holdsworth has an MSc in Astronomy, and a PhD (1992) in Medical Biophysics from the University of Toronto. He is a Scientist in the Imaging group at the Robarts Research Institute, and a Professor in the Departments of Surgery and Medical Biophysics in the Schulich School of Medicine and Dentistry at Western University. In 2007, he became the Sandy Kirkley Chair in Musculoskeletal Research and has shifted the focus of his research to musculoskeletal disease, with projects ranging from basic skeletal research to clinical therapy.



David Jaffray, PhD

Executive Vice President of Technology and Innovation, University Health Network (UHN)

David Jaffray graduated from the University of Alberta with a BSc in Physics (1988) and completed his PhD in Medical Biophysics at the University of Western Ontario (1994). He is a senior scientist in the Ontario Cancer Institute and a Professor in the Departments of Radiation Oncology, Medical Biophysics, and the Institute for Biomaterials and Biomedical Engineering. He holds the Fidani Chair in Radiation Physics and is a principal in the STTARR Innovation Centre. He is also the Director of the TECHNA Institute and a Senior Scientist within the Ontario Cancer Institute. His current research interests focus on the development of imaging technologies and methods with a focus on image-guided interventions, including radiation therapy and surgery.



Allan Skanes, MD, FRCPC, FHRS

Associate Professor, Department of Medicine, University of Western Ontario

Allan Skanes received his medical degree (1990) from the University of Toronto where he also completed his Internal Medicine training. He completed his Cardiology and Electrophysiology training at the University of Ottawa Heart Institute. He is currently the Director of the Electrophysiology Laboratory at the London Health Sciences Centre, University Hospital, London, Ontario and an Associate Professor of Medicine at Western University. He is an experienced electrophysiologist and clinician scientist with a specific interest in non-pharmacologic therapy for arrhythmia, remote and non-fluoroscopic catheter navigation and catheter ablation of cardiac arrhythmia.



Jonathan Thiessen, PhD

Assistant Professor, Department of Medical Biophysics, University of Western Ontario

Johnathan Thiessen has a PhD in Physics (2012) from the University of Manitoba. He is currently an Assistant Professor of Medical Biophysics at the University of Western Ontario and is interested in technology development for simultaneous PET/MRI systems, applications of PET/MRI to oncology, cardiac and neurological disorders, kinetic modeling and metabolic imaging with PET/MRI, and imaging correlates of tissue pathology.

Symposium Organizing Committees

Scientific Committee

Jerry Battista, OCAIRO
Maria Drangova, CANet
Aaron Fenster, ITP
Gabor Fichtinger, OCAIRO
Richard Frayne, MITNEC (Chair)
David Holdsworth, B&J

Kevin O'Neil, CANet
Frank Prato, HF
Giles Santyr
Aaron Ward, ITP
Graham Wright, ICDI
Martin Yaffe, SIP

Organizing Committee

Linda Andersen, MITNEC
Johanne Langford, Robarts
Carol Richardson, ITP
Jean Rookwood, ICDI

Janette Wallace, Robarts (Chair)
Pamela Wilkinson, University of Calgary
Mary Wong, OCAIRO
Yulia Yerofeyeva, SIP

Abstract Reviewers

Special thank you to the 28 reviewers drawn from the sponsoring consortia membership.

Stephen Breen

Tim Burkhart

Juan Chen

Catherine Coolen

Rob deKemp

Mamadou Diop

Maria Drangova

Stewart Gaede

Therese Heinonen

Tyna Hope

Farzad Khalvati

Ali Khan

Emily Lalone

Louis Lauzon

Cheryl McCreary

Michael Noseworthy

Meagan O'Reilly

Mihaela Pop

Tim Scholl

Navneet Singh

William Song

Matthew Teeter

Jonathan Thiessen

Rebecca Thornhill

Marie-Claude Villeneuve

Aaron Ward

Martin Yaffe

Ivan Yeung

Note for purposes of review the CANet, HF and ICDI consortia were combined.

Abstract Awards

Congratulations to all of our abstract award winners.

Summa cum Laude

Awarded to Highest-rated Abstract by Consortia.



Sachi Elkerton (SIP) – Differentiation of arterioles from venules in mouse histology images using machine learning

Jeff Gaudet (SIP) – Tracking the rejection of 19F-labeled stem cells through signal quenching resulting from infiltrating iron-labeled immune cells

Adam Gribble (SIP) – Mueller matrix polarimetry imaging using four photoelastic

modulators for rapid wide-field analysis of biological tissues

Margaret Hess (OCAIRO) – Virtual design of patient specific neuroendoscopic tools for pineal region masses

Amani Ibrahim (B&J) – Image Processing Software for Designing Custom Craniofacial Implants

Marta Overchuk (ITP) – HDL-like Nanoparticles for Dual-Wavelength Cancer Imaging and Image-Guided Therapy

Mohammad Tavallaei (ICDI) – MRI-Compatible Remote Catheter Navigation System with 3-Degrees-of-Freedom

Adrian Tsang (MITNEC) – Changes in white matter structural connectivity and cortical functional connectivity over the healthy adult lifespan

Tamas Ungi (ITP) – Breast lumpectomy navigation using an open-source clinical application

Magna cum Laude

Awarded to Top-rated Abstracts by Consortia.



Yonathan Araya (SIP) – Spin-Lattice Relaxation Dispersion using Fast Field-Cycling Magnetic Resonance Relaxometry

Stephen Arnott (MITNEC) – Web-based dashboards and other tools for quality assurance and quality control monitoring of multisite neuroimaging studies

Audrey Chuong (SIP) – Discovery Radiomics via Layered Random Projection (LaRP) Sequencers for Prostate Cancer Classification

Kimberly Desmond (SIP) – Chemical Exchange Saturation Transfer metrics for assessing early response to stereotactic radiosurgery in human brain metastases

Armin Eilaghi (SIP) – Radiomics Features Analysis for Tumor Characterization in Pancreatic Ductal Adenocarcinoma

Esmail Enjilela (MITNEC) – Sparse-view quantitative CT perfusion imaging of liver

Vinyas Harish (ITP) – Monitoring electromagnetic tracking error in computer-navigated breast cancer surgery

Patricia Johnson (MITNEC) – Retrospective motion correction in MRI using spherical navigator echoes

Lewis Joo (MITNEC) – Characterization of Microvascular Function in Transgenic Rat Model of Alzheimer's Disease

Philippa Krahn (ICDI) – Intrinsic MRI visualizes RF lesions within minutes after MR-guided ablation

Elodie Lugez (OCAIRO) – Enhanced electromagnetic catheter tracking with application in high-dose-rate brachytherapy

Sarah Mattonen (ITP) – Detection of local cancer recurrence after stereotactic ablative radiotherapy (SABR) for lung cancer: physician performance versus radiomic assessment

Evan McNabb (MITNEC) – Localizing Fiducial Markers using Undersampled co-RASOR MRI for Radiation Therapy Planning

Mihaela Pop (CANet) – Analysis of activation-recovery intervals from intracardiac electrograms in porcine hearts

Amy Schranz (MITNEC) – Reduced Brain Glutamine in Female Varsity Rugby Athletes after Concussion

Noor Shaikh (ICDI) – Guidewire puncture forces related to magnetic resonance imaging signatures for peripheral arterial disease plaque types

Shawn Stapleton (ITP) – Modulating Nanoparticle Drug Delivery using Radiation and Heat

Justin Tse (B&J) – Dual-Energy Micro-Computed Tomography in a Rat Hindlimb Model of Osteoarthritis

Dan Wang (SIP) – The Application of a Novel Multiplexing Staining Technology in the Breast Cancer Research

Ilma Xhaferllari (OCAIRO) – Validating internal and external correlation during respiratory gated VMAT using on-board kV imaging

Cum Laude

Awarded to Top-rated Poster Abstracts by Consortia.



Rudy Baronette (B&J) – Performance evaluation of a peripheral cone-beam computed tomography scanner

Alexandra Blokker (B&J) – Micro-CT Compatible Load-Controlled Knee Motion Simulator

Marcus Couch (MITNEC) – Assessing the Effects of Inflammation and Fibrosis using Inert Fluorinated Gas MRI

Donna Goldhawk (HF) – MagA-derived MR Contrast Persists Despite Cellular Differences in Iron Metabolism

Shahid Haider (SIP) - Single-click lung nodule contouring method using hierarchical conditional random fields

Matthew Holden (SIP) - Central Venous Catheterization Curriculum Development via Objective Performance Metrics

David Holdsworth (B&J) – Geometric calibration phantom for MRI and CT

Jessica Kishimoto (ITP) – Cranial ultrasound in 2D and 3D to guide treatment in preterm neonates with posthemorrhagic ventricular dilatation

Daniel Lorusso (B&J) – Development and validation of a system for high-frequency

vibration of live cells during real-time microscopy

Matthew MacDonald (ICDI) – A Simple MRI Scanner Control Technique for Device Localization During MRI-Guided Percutaneous Procedures

Raanan Marants (MITNEC) – Clearance of Indocyanine Green by the Liver during Hemodialysis as a Measure of Hepatic Function

Donna Murrell (SIP) - Investigating cancer cell dormancy with cellular MRI

Eranga Ukwatta (CANet) – Virtual electrophysiological study using T1 mapping techniques improves sensitivity in predicting adverse arrhythmic events in post-infarction patients

Joseph Umoh (B&J) – Micro-CT Validation of 3D-Printed Patient-Specific Components

Jason Vickress (OCAIRO) - Prediction of the spatial distribution of deformable image registration error in lung 4DCT's

Brandon Zanette (SIP) - Gas Exchange Quantification using Hyperpolarized ¹²⁹Xe and a Clinical MRI System

Presentation Awards

Prizes will be awarded to the top oral and poster presentations.

Oral Presentations

Thank you to our oral presentation judges.

Jerry Battista, OCAIRO

Frank Prato, HF

Maria Drangova, CANet

Giles Santyr

Gabor Fichtinger, OCAIRO

Aaron Ward, ITP

David Gobbi, MITNEC

Graham Wright, ICDI (Chair)

David Holdsworth, B&J

Martin Yaffe, SIP

Poster Presentations

Posters will be judged within their consortia by faculty selected from each consortium. Judging will occur during the Poster Session and Cash Bar Reception during the evening of Wednesday 30 March 2016. All presenters - Please ensure that you are available and near your poster during this time.

Program at a Glance

Wednesday 30 March 2016

- 7:00 – 8:00 Registration (Colony Grande Foyer)
- 8:00 – 8:40 Poster Set-Up Time (Colony Grande (West), Giovanni and Armoury Rooms)
- 8:40 – 8:50 Opening Remarks (Colony Grande (Centre and East) Room)
Richard Frayne, PhD, University of Calgary
ImNO 2016 Scientific Committee Chair
- 8:50 – 10:40 Keynote Session 1 (Colony Grande (Centre and East) Room)
Chairs: Jerry Battista, David Holdsworth
- Advances in MR-Guided IMRT*
Daniel Low, PhD
Department of Radiation Oncology, University of California Los Angeles, Los Angeles, California, USA
- Quantitative Imaging of Osteoarthritis and its Relation to Function and Pain*
Sharmila Majumdar, PhD
Department of Radiology, University of California San Francisco, San Francisco, California, USA
- 10:40 – 11:00 Poster Session & Coffee Break (Colony Grande (West), Giovanni and Armoury Rooms)

| | |
|--|---|
| <p>11:00 – 12:15 Oral Session 1 (Colony Grande (Centre) Room)</p> <p>IMAGE GUIDED INTERVENTION - CANCER</p> <p>Chairs: Tom Purdie, John Schreiner</p> <p>1.1–Invited Talk – Image Guidance and Intervention in Precision Radiotherapy - David Jaffray (OCAIRO)</p> <p>1.2–Monitoring electromagnetic tracking error in computer-navigated breast cancer surgery - Vinyas Harish (ITP)</p> <p>1.3–Breast lumpectomy navigation using an open-source clinical application - Tamas Ungi (ITP)</p> <p>1.4–3D Ultrasound Guided Liver Ablation Therapy: Development Of Real-time Motion Compensation- Derek Gillies (ITP)</p> <p>1.5–Automatic Registration Error Maps in Intraoperative CT-based Navigation - Michelle Arkhangorodsky (SIP)</p> | <p>11:00 – 12:15 Oral Session 2 (Colony Grande (East) Room)</p> <p>NEW IMAGING APPROACHES</p> <p>Chairs: Navneet Singh, Martin Yaffe</p> <p>2.1–Standardization Framework to Correct the Variability Between FLAIR Images in Large-Scale Studies - Brittany Reiche (MITNEC)</p> <p>2.2–Optimization Methods in MR-Guided Transcranial Focused Ultrasound - Alec Hughes (MITNEC)</p> <p>2.3–Optimized Correlated Diffusion Imaging for Prostate Cancer Detection - Farzad Khalvati (SIP)</p> <p>2.4–Improving Fluorescence Tomography using Imaging Priors from Intraoperative Cone-Beam CT - Michael Daly (SIP)</p> <p>2.5–⁸⁹Zr-Trastuzumab-DM1: A Novel Probe for Positron-Emission Tomography (PET) Imaging of the Delivery of T-DM1 (Kadcyla) to HER2-Positive Breast Cancer - Noor Alsaden (SIP)</p> |
|--|---|

12:15 – 1:15 Lunch (Colony Grande (West) Room)

| | |
|--|---|
| <p>1:15 – 2:45 Oral Session 3 (Colony Grande (Centre) Room)</p> <p>IMAGING BIOMARKERS AND PATIENT-CENTERED STUDIES AND TRIALS</p> <p>Chairs: Robert deKemp , Paula Foster</p> <p>3.1–Invited Talk - Fluorine-19 Labeling of Peripheral Blood Mononuclear Cells for Clinical Cell Tracking - Paula Foster (SIP)</p> <p>3.2–The Application of a Novel Multiplexing Staining Technology in the Breast Cancer Research - Dan Wang (SIP)</p> <p>3.3–Modulating Nanoparticle Drug Delivery using Radiation and Heat - Shawn Stapleton (ITP)</p> <p>3.4–Reduced Brain Glutamine in Female Varsity Rugby Athletes after Concussion - Amy Schranz (MITNEC)</p> <p>3.5–Web-based dashboards and other tools for quality assurance and quality control monitoring of multisite neuroimaging studies - Stephen Arnott (MITNEC)</p> <p>3.6–Inflammation Imaged with [18F]-FDG PET/CTA is Related to the 3D Ultrasound Volumetric Phenotype of High-Risk Carotid Plaque: Sub-study of the Canadian Atherosclerosis Imaging Network (CAIN-2) - Myra Cocker (MITNEC)</p> | <p>1:15 – 2:45 Oral Session 4 (Colony Grande (East) Room)</p> <p>PERFUSION, METABOLISM, HYPOXIA AND NEW PROBES</p> <p>Chairs: Ting Lee, Frank Prato</p> <p>4.1–Characterization of Microvascular Function in Transgenic Rat Model of Alzheimer's Disease - Lewis Joo (MITNEC)</p> <p>4.2–Effects of exercise on human calf muscle in vivo sodium single and triple Quantum filtered magnetic resonance spectroscopy - Alireza Akbari (MITNEC)</p> <p>4.3–Associations of hemodynamic load with impaired myocardial flow reserve: role of sex and hypertension - Robert deKemp (HF)</p> <p>4.4–Gadolinium-Free Blood Pool Magnetic Resonance Imaging Contrast Agents for High Clinical Field at 3 Tesla: Comparative Studies of Two Manganese (III) Porphyrin Dimers - Hanlin Liu (SIP)</p> <p>4.5–Sparse-view quantitative CT perfusion imaging of liver - Esmaeil Enjilela (MITNEC)</p> <p>4.6–Developing a combined contrast kinetic model for assessment of post-infarction inflammation using hybrid PET/MRI - Benjamin Wilk (HF)</p> |
|--|---|

2:45 – 3:30 Poster Session & Coffee Break (Colony Grande (West), Giovanni and Armoury Rooms)

| | |
|--|---|
| <p>3:30 – 5:00 Oral Session 5 (Colony Grande (Centre) Room)</p> <p>PRE-CLINICAL IMAGING STUDIES</p> <p>Chairs: Giles Santyr, Michael Noseworthy</p> <p>5.1–Dual-Energy Micro-Computed Tomography in a Rat Hindlimb Model of Osteoarthritis - Justin Tse (B&J)</p> <p>5.2–Vascular contrast agent for preclinical dual energy computed tomography - Charmainne Cruje (B&J)</p> <p>5.3–A micro-CT-integrated radiolucent treadmill for fluoroscopic gait assessment in small-animal models - Adam Paish (B&J)</p> <p>5.4– HDL-like Nanoparticles for Dual-Wavelength Cancer Imaging and Image-Guided Therapy - Marta Overchuk (ITP)</p> <p>5.5–High-content imaged-based screening of patient derived leukemia cells to identify novel treatments and to personalize therapy for chronic lymphocytic leukemia - Sina Oppermann (ITP)</p> <p>5.6–Tracking the rejection of ¹⁹F-labeled stem cells through signal quenching resulting from infiltrating iron-labeled immune cells - Jeff Gaudet (SIP)</p> | <p>3:30 – 5:00 Oral Session 6 (Colony Grande (East) Room)</p> <p>QUANTITATIVE IMAGING</p> <p>Chairs: Mihaela Pop, Eranga Ukwatta</p> <p>6.1–Changes in white matter structural connectivity and cortical functional connectivity over the healthy adult lifespan - Adrian Tsang (MITNEC)</p> <p>6.2–The Effect of T1 Signal Decay on Ventilation Mapping using Hyperpolarized Gas MRI during Multiple Breath Wash-out - Felipe Morgado (ITP)</p> <p>6.3– Mueller matrix polarimetry imaging using four photoelastic modulators for rapid wide-field analysis of biological tissues - Adam Gribble (SIP)</p> <p>6.4–Spin-Lattice Relaxation Dispersion using Fast Field-Cycling Magnetic Resonance Relaxometry - Yonathan Araya (SIP)</p> <p>6.5–Interleaved multi-frequency excitation for robust spectrally-selective ¹³C echo planar imaging- Justin Lau (SIP)</p> <p>6.6–Myocardial local frequency shift mapping - Junmin Liu (HF)</p> |
|--|---|

5:00 – 7:00 Poster Session and Cash Bar Reception (Colony Grande (West), Giovanni and Armoury Rooms)

Posters will be judged within their consortia. Judging will occur during this Poster Session and Reception. All Poster Presenters: Please ensure that you are available by your poster during this time.

Thursday 31 March 2016

7:00 – 8:00 Registration (Colony Grande Foyer)

8:00 – 8:50 Poster Session (Colony Grande (West), Giovanni and Armoury Rooms)

8:50 – 10:40 Keynote Session 2 (Colony Grande (Centre and East) Room)
Chairs: Richard Frayne, Graham Wright

Brain Structures, Anatomical Variability and an Application in Multiple Sclerosis

Louis Collins, PhD

Departments of Neurology and Neurosurgery and Biomedical Engineering, McGill University, and McConnell Brain Imaging Centre at Montreal Neurological Institute

Imaging the Anatomic Substrate for Reentrant Arrhythmia

Saman Nazarian, MD, PhD

Department of Medicine, Johns Hopkins University School of Medicine, Baltimore, Maryland, USA

10:40 – 11:00 Poster Session & Coffee Break (Colony Grande (West), Giovanni and Armoury Rooms)

| | |
|---|---|
| <p>11:00 – 12:15 Oral Session 7 (Colony Grande (Centre) Room)</p> <p>IMAGE GUIDED INTERVENTION - CARDIAC</p> <p>Chairs: Maria Drangova, Rebecca Thornhill</p> <p>7.1–Invited Talk – Cardiac Arrhythmia Network of Canada (CANet): Mission, Goals and Imaging Research Opportunities - Allan Skanes (CANet)</p> <p>7.2–Analysis of activation-recovery intervals from intracardiac electrograms in porcine hearts - Mihaela Pop (CANet)</p> <p>7.3–Guidewire puncture forces related to magnetic resonance imaging signatures for peripheral arterial disease plaque types - Noor Shaikh (ICDI)</p> <p>7.4–Intrinsic MRI visualizes RF lesions within minutes after MR-guided ablation - Philippa Krahn (ICDI)</p> <p>7.5– Automated Segmentation of Scoliotic Lumbar Spine using Statistical Shape Models - Sinthu Sivanesan (B&J)</p> | <p>11:00 – 12:15 Oral Session 8 (Colony Grande (East) Room)</p> <p>IMAGE MONITORING OF TREATMENT RESPONSE</p> <p>Chairs: Stuart Gaede, Ivan Yeung</p> <p>8.1–Detection of local cancer recurrence after stereotactic ablative radiotherapy (SABR) for lung cancer: physician performance versus radiomic assessment - Sarah Mattonen (ITP)</p> <p>8.2–Focused ultrasound hyperthermia mediated drug delivery using thermosensitive liposomes and visualized with in vivo two-photon microscopy - Marc Santos (ITP)</p> <p>8.3–Development of a predictive radiomics signature for response to immune checkpoint inhibitors (ICIs) in patients with recurrent or metastatic squamous cell carcinoma of the head and neck (RM-SCCHN) - Paul Dufort (ITP)</p> <p>8.4–A generalized approach towards multi-parametric response mapping using principal component analysis - Anthony Lausch (OCAIRO)</p> <p>8.5–Chemical Exchange Saturation Transfer metrics for assessing early response to stereotactic radiosurgery in human brain metastases - Kimberly Desmond (SIP)</p> |
|---|---|

12:15 – 1:15 LUNCH (Colony Grande (West) Room)

| | |
|--|---|
| <p>1:15 – 2:30 Oral Session 9 (Colony Grande (Centre) Room)</p> <p>VISUALIZATION AND IMAGE ANALYSIS I</p> <p>Chairs: David Holdsworth, Emily Lalone</p> <p>9.1–Invited Talk – Biomedical Imaging within a Transdisciplinary Musculoskeletal Research Program - David Holdsworth (B&J)</p> <p>9.2– Simulating Heat Transfer in Bone During Magnetic Resonance Image-guided Focused Ultrasound Therapy - Alexander Chisholm (B&J)</p> <p>9.3– Image Processing Software for Designing Custom Craniofacial Implants - Amani Ibrahim (B&J)</p> <p>9.4– Left Atrial Wall Segmentation using Hierarchical Max-Flow - Jiro Inoue (CANet)</p> <p>9.5– Augmented Reality for Improved Ultrasound Guidance in Central Venous Access- Golafsoun Ameri (ICDI)</p> | <p>1:15 - 2:30 Oral Session 10 (Colony Grande (East) Room)</p> <p>IMAGING/SIMULATION FOR THERAPY PLANNING</p> <p>Chairs: Jerry Battista, Aaron Ward</p> <p>10.1– Standardized interpretation of Tc-99m-SPECT perfusion images in a multi-center study of MITNEC (Medical Imaging Trials Network of Canada) - Jennifer Renaud (MITNEC)</p> <p>10.2– Semi-automatic segmentation of high-dose-rate prostate brachytherapy needles using 3D ultrasound - William Hrinivich (ITP)</p> <p>10.3–Localizing Fiducial Markers using Undersampled co-RASOR MRI for Radiation Therapy Planning - Evan McNabb (MITNEC)</p> <p>10.4–Development of a CZT-Based Gamma Camera for Simultaneous Molecular and MR Breast Imaging - Ashley Tao (MITNEC)</p> <p>10.5–Validating internal and external correlation during respiratory gated VMAT using on-board kV imaging - Ilma Xhaferllari (OCAIRO)</p> |
|--|---|

2:30 – 3:30 Poster Session & Coffee Break (Colony Grande (West), Giovanni and Armoury Rooms)

| | |
|---|---|
| <p>3:30 – 4:45 Oral Session 11 (Colony Grande (Centre) Room)</p> <p>INSTRUMENTATION AND DEVICES</p> <p>Chairs: Johanthan Thiessen, Tamas Ungi</p> <p>11.1–Invited Talk - Simultaneous PET/MRI with Clinical and Preclinical Systems - Jonathan Thiessen (HF)</p> <p>11.2–Enhanced electromagnetic catheter tracking with application in high-dose-rate brachytherapy - Elodie Lugez (OCAIRO)</p> <p>11.3–Development of improved gel dosimeter vessels for low stray light optical CT scanners - Kurtis Dekker (OCAIRO)</p> <p>11.4–Whole-Slide Digital Pathology via Lens-free Spectral Light-field Fusion Microscopy - Farnoud Kazemzadeh (SIP)</p> <p>11.5–MRI-Compatible Remote Catheter Navigation System with 3-Degrees-of-Freedom - Mohammad Tavallaei (ICDI)</p> | <p>3:30 – 4:45 Oral Session 12 (Colony Grande (East) Room)</p> <p>VISUALIZATION AND IMAGE ANALYSIS II</p> <p>Chairs: David Gobbi, Terry Peters</p> <p>12.1–Differentiation of arterioles from venules in mouse histology images using machine learning - Sachi Elkerton (SIP)</p> <p>12.2–Retrospective motion correction in MRI using spherical navigator echoes - Patricia Johnson (MITNEC)</p> <p>12.3–Discovery Radiomics via Layered Random Projection (LaRP) Sequencers for Prostate Cancer Classification - Audrey Chuung (SIP)</p> <p>12.4–Dynamic management of segmented structures in 3D Slicer - Csaba Pinter (OCAIRO)</p> <p>12.5–An Image Analysis Pipeline for Machine Learning applied to Pathologist Annotations of Prostate and Pancreatic Cancer Specimens - Trevor McKee (OCAIRO)</p> |
|---|---|

4:45 – 5:00 Award Presentation and Closing Remarks (Colony Grande (Centre) Room)
Chairs: Aaron Fenster, Richard Frayne, Graham Wright

5:00 – 5:30 Poster Take Down (Colony Grande (West), Giovanni and Armoury Rooms)

Oral Session Abstracts

Listed by first author last name. Abstracts are provided in session-talk order starting on page 30.

| | |
|---|----|
| 4.2–Effects of exercise on human calf muscle in vivo sodium single and triple Quantum filtered magnetic resonance spectroscopy Alireza Akbari (MITNEC) | 47 |
| 2.5– ⁸⁹ Zr-Trastuzumab-DM1: A Novel Probe for Positron-Emission Tomography (PET) Imaging of the Delivery of T-DM1 (Kadcyla) to HER2-Positive Breast Cancer Noor Alsaden (SIP)..... | 39 |
| 9.5–Augmented Reality for Improved Ultrasound Guidance in Central Venous Access Golafsoun Ameri (ICDI)..... | 78 |
| 6.4–Spin-Lattice Relaxation Dispersion using Fast Field-Cycling Magnetic Resonance Relaxometry Yonathan Araya (SIP)..... | 61 |
| 1.5–Automatic Registration Error Maps in Intraoperative CT-based Navigation Michelle Arkhangorodsky (SIP) | 34 |
| 3.5–Web-based dashboards and other tools for quality assurance and quality control monitoring of multisite neuroimaging studies Stephen Arnott (MITNEC)..... | 44 |
| 9.2–Simulating Heat Transfer in Bone During Magnetic Resonance Image-guided Focused Ultrasound Therapy Alexander Chisholm (B&J) | 75 |
| 12.3–Discovery Radiomics via Layered Random Projection (LaRP) Sequencers for Prostate Cancer Classification Audrey Chung (SIP)..... | 91 |
| 3.6–Inflammation Imaged with [¹⁸ F]-FDG PET/CTA is Related to the 3D Ultrasound Volumetric Phenotype of High-Risk Carotid Plaque: Sub-study of the Canadian Atherosclerosis Imaging Network (CAIN-2) Myra Cocker (MITNEC)..... | 45 |
| 5.2–Vascular contrast agent for preclinical dual energy computed tomography Charmaine Cruje (B&J) | 53 |
| 2.4–Improving Fluorescence Tomography using Imaging Priors from Intraoperative Cone-Beam CT Michael Daly (SIP)..... | 38 |
| 4.3–Associations of hemodynamic load with impaired myocardial flow reserve: role of sex and hypertension Robert deKemp (HF)..... | 48 |
| 11.3–Development of improved gel dosimeter vessels for low stray light optical CT scanners Kurtis Dekker (OCAIRO)..... | 86 |

| | |
|---|----|
| 8.5–Chemical Exchange Saturation Transfer metrics for assessing early response to stereotactic radiosurgery in human brain metastases Kimberly Desmond (SIP) | 73 |
| 8.3–Development of a predictive radiomics signature for response to immune checkpoint inhibitors (ICIs) in patients with recurrent or metastatic squamous cell carcinoma of the head and neck (RM-SCCHN) Paul Dufort (ITP) | 71 |
| 12.1–Differentiation of arterioles from venules in mouse histology images using machine learning Sachi Elkerton (SIP) | 89 |
| 4.5–Sparse-view quantitative CT perfusion imaging of liver Esmail Enjilela (MITNEC) | 50 |
| 3.1– Fluorine-19 Labeling of Peripheral Blood Mononuclear Cells for Clinical Cell Tracking (Invited) Paula Foster (SIP) | 40 |
| 5.6–Tracking the rejection of 19F-labeled stem cells through signal quenching resulting from infiltrating iron-labeled immune cells Jeff Gaudet (SIP) | 57 |
| 1.4–3D Ultrasound Guided Liver Ablation Therapy: Development Of Real-time Motion Compensation Derek Gillies (ITP) | 33 |
| 6.3–Mueller matrix polarimetry imaging using four photoelastic modulators for rapid wide-field analysis of biological tissues Adam Gribble (SIP) | 60 |
| 1.2–Monitoring electromagnetic tracking error in computer-navigated breast cancer surgery Vinyas Harish (ITP) | 31 |
| 9.1–Biomedical Imaging within a Transdisciplinary Musculoskeletal Research Program (Invited) David Holdsworth (B&J) | 74 |
| 10.2–Semi-automatic segmentation of high-dose-rate prostate brachytherapy needles using 3D ultrasound William Hrinivich (ITP) | 80 |
| 2.2–Optimization Methods in MR-Guided Transcranial Focused Ultrasound Alec Hughes (MITNEC) | 36 |
| 9.3–Image Processing Software for Designing Custom Craniofacial Implants Amani Ibrahim (B&J) | 76 |
| 9.4–Left Atrial Wall Segmentation using Hierarchical Max-Flow Jiro Inoue (CANet) | 77 |
| 1.1–Image Guidance and Intervention in Precision Radiotherapy (Invited) David Jaffray (OCAIRO) | 30 |
| 12.2–Retrospective motion correction in MRI using spherical navigator echoes Patricia Johnson (MITNEC) | 90 |

| | |
|--|----|
| 4.1–Characterization of Microvascular Function in Transgenic Rat Model of Alzheimer's Disease Lewis Joo (MITNEC) | 46 |
| 11.4–Whole-Slide Digital Pathology via Lens-free Spectral Light-field Fusion Microscopy Farnoud Kazemzadeh (SIP) | 87 |
| 2.3–Optimized Correlated Diffusion Imaging for Prostate Cancer Detection Farzad Khalvati (SIP) | 37 |
| 7.4–Intrinsic MRI visualizes RF lesions within minutes after MR-guided ablation Philippa Krahn (ICDI) | 67 |
| 6.5–Interleaved multi-frequency excitation for robust spectrally-selective 13C echo planar imaging Justin Lau (SIP)..... | 62 |
| 8.4–A generalized approach towards multi-parametric response mapping using principal component analysis Anthony Lausch (OCAIRO) | 72 |
| 4.4–Gadolinium-Free Blood Pool Magnetic Resonance Imaging Contrast Agents for High Clinical Field at 3 Tesla: Comparative Studies of Two Manganese (III) Porphyrin Dimers Hanlin Liu (SIP) | 49 |
| 6.6–Myocardial local frequency shift mapping Junmin Liu (Heart Failure) | 63 |
| 11.2–Enhanced electromagnetic catheter tracking with application in high-dose-rate brachytherapy Elodie Lugez (OCAIRO) | 85 |
| 8.1–Detection of local cancer recurrence after stereotactic ablative radiotherapy (SABR) for lung cancer: physician performance versus radiomic assessment Sarah Mattonen (ITP) | 69 |
| 12.5–An Image Analysis Pipeline for Machine Learning applied to Pathologist Annotations of Prostate and Pancreatic Cancer Specimens Trevor McKee (OCAIRO) | 93 |
| 10.3–Localizing Fiducial Markers using Undersampled co-RASOR MRI for Radiation Therapy Planning Evan McNabb (MITNEC) | 81 |
| 6.2–The Effect of T1 Signal Decay on Ventilation Mapping using Hyperpolarized Gas MRI during Multiple Breath Wash-out Felipe Morgado (ITP)..... | 59 |
| 5.5–High-content imaged-based screening of patient derived leukemia cells to identify novel treatments and to personalize therapy for chronic lymphocytic leukemia Sina Oppermann (ITP) | 56 |
| 5.4–HDL-like Nanoparticles for Dual-Wavelength Cancer Imaging and Image-Guided Therapy Marta Overchuk (ITP) | 55 |

| | |
|--|----|
| 5.3–A micro-CT-integrated radiolucent treadmill for fluoroscopic gait assessment in small-animal models Adam Paish (B&J) | 54 |
| 12.4–Dynamic management of segmented structures in 3D Slicer Csaba Pinter (OCAIRO) | 92 |
| 7.2–Analysis of activation-recovery intervals from intracardiac electrograms in porcine hearts Mihaela Pop (CANet)..... | 65 |
| 2.1–Standardization Framework to Correct the Variability Between FLAIR Images in Large-Scale Studies Brittany Reiche (MITNEC)..... | 35 |
| 10.1–Standardized interpretation of Tc-99m-SPECT perfusion images in a multi-center study of MITNEC (Medical Imaging Trials Network of Canada) Jennifer Renaud (MITNEC) | 79 |
| 8.2–Focused ultrasound hyperthermia mediated drug delivery using thermosensitive liposomes and visualized with in vivo two-photon microscopy Marc Santos (ITP) | 70 |
| 3.4–Reduced Brain Glutamine in Female Varsity Rugby Athletes after Concussion Amy Schranz (MITNEC)..... | 43 |
| 7.3–Guidewire puncture forces related to magnetic resonance imaging signatures for peripheral arterial disease plaque types Noor Shaikh (ICDI) | 66 |
| 7.5–Automated Segmentation of Scoliotic Lumbar Spine using Statistical Shape Models Sinthu Sivanesan (B&J)..... | 68 |
| 7.1– Cardiac Arrhythmia Network of Canada (CANet): Mission, Goals and Imaging Research (Invited) Allan Skanes (CANet)..... | 64 |
| 3.3–Modulating Nanoparticle Drug Delivery using Radiation and Heat Shawn Stapleton (ITP) | 42 |
| 10.4–Development of a CZT-Based Gamma Camera for Simultaneous Molecular and MR Breast Imaging Ashley Tao (MITNEC)..... | 82 |
| 11.5–MRI-Compatible Remote Catheter Navigation System with 3-Degrees-of-Freedom Mohammad Tavallaei (ICDI) | 88 |
| 11.1–Simultaneous PET/MRI with Clinical and Preclinical Systems (Invited) Jonathan Thiessen (HF) | 84 |
| 6.1–Changes in white matter structural connectivity and cortical functional connectivity over the healthy adult lifespan Adrian Tsang (MITNEC) | 58 |
| 5.1–Dual-Energy Micro-Computed Tomography in a Rat Hindlimb Model of Osteoarthritis Justin Tse (B&J)..... | 52 |

| | |
|--|----|
| 1.3–Breast lumpectomy navigation using an open-source clinical application Tamas Ungi (ITP) | 32 |
| 3.2–The Application of a Novel Multiplexing Staining Technology in the Breast Cancer Research Dan Wang (SIP)..... | 41 |
| 4.6–Developing a combined contrast kinetic model for assessment of post-infarction inflammation using hybrid PET/MRI Benjamin Wilk (HF)..... | 51 |
| 10.5–Validating internal and external correlation during respiratory gated VMAT using on-board kV imaging Ilma Xhaferllari (OCAIRO)..... | 83 |

Image Guidance and Intervention in Precision Radiotherapy Dr. David Jaffray

Since 2010, the OCAIRO has brought together Ontario's radiation oncology research community and best-in-class industrial collaborators to accelerate the development and application of innovative adaptive methods in radiation therapy through focused scientific, technical, and clinical advancements.

The quantitative yield of the project over the years is evident and substantial. This includes the training and coordination of over 390 highly qualified personnel (HQP) in the field of radiation therapy and imaging who are continuing to contribute to innovation and healthcare system performance. The academic yield of the investigators and their trainees is another important metric and this is demonstrated by a total of 91 peer-reviewed publications, with an additional 20 submitted to high impact journals. Many of these publications describe novel technologies that are being patented for commercial development. To date, the OCAIRO has produced 12 patent applications and 21 technologies are in licensing discussions or fully licensed. These licensing deals are an outstanding reflection of the collaborations in adaptive radiotherapy processes and methods emerging across the province with leadership from investigators involved in the OCAIRO.

The commercialization of the technologies developed under the OCAIRO continues to strengthen with several examples. The AQUA product has now been licensed to Elekta through the Ontario-based start-up (Acumyn Inc.) and is being distributed with multiple sales pending worldwide. The integrated quality monitor (IQM) system has now reached CE clearance and has multiple sales around the world through our partner (iRT Systems, Koblenz, Germany). The image-guided Perfexion development was released at the 2015 ESTRO meeting in Barcelona and achieved FDA clearance in summer of 2015. The recently patented automatic beam modelling software (ABMOS) was licensed to a commercial partner. The automatic treatment planning and MORFEUS technologies have now reached the market through the sale of Raystation systems by Raysearch Laboratories. Each of these technologies supports the advancement of adaptive radiation therapy techniques and is enabling the transition from research platform to clinical application. Moreover, revenues are now returning to Ontario and further research funding has been negotiated to extend the validation processes that are key to clinical uptake.

The work being performed by the OCAIRO is exciting and relevant to a worldwide network of biomedical commercial entities and the commercial uptake thus far is a key milestone towards the overarching objective of the OCAIRO mission, which is to bring adaptive radiation therapy to a clinical reality.

Monitoring electromagnetic tracking error in computer-navigated breast cancer surgery

Vinyas Harish^{*1}, Aidan Baksh¹, Tamas Ungi^{1,2}, Andras Lasso¹, Zachary Baum¹, Gabrielle Gauvin², Jay Engel², John Rudan^{1,2}, Gabor Fichtinger^{1,2}

¹Laboratory for Percutaneous Surgery, Queen's University, Kingston, ON, Canada

²Department of Surgery, Queen's University, Kingston, ON, Canada

Consortium: Other

Introduction. Lumpectomy, or breast conserving surgery, is done to remove cancerous tissue from the breast. Computer navigation using electromagnetic (EM) tracking can ensure that all cancerous tissue is excised¹, however electromagnetic tracking is error-prone. Ferromagnetic objects and the position of the electromagnetic field generator can lead to tracking error and the possibility of an incomplete resection. Therefore, it is crucial to monitor tracking error in clinical environments, not just in navigated lumpectomy procedures but in all image-guided interventions using EM tracking. Our goal was to develop and test a system to monitor electromagnetic tracking error for computer-navigated interventions in an accessible and open-source fashion.

Methods. A pointer tool was designed for simultaneous electromagnetic and optical tracking. Optical tracking can be used to estimate positional and rotational electromagnetic tracking error since it is unaffected by ferromagnetic objects. The PLUS software toolkit's² PlusServer application sent tracking data to 3D Slicer. Software modules were developed for automatic calibration of the measurement system, real-time error visualization, and analysis as an extension for 3D Slicer. In order to measure EM tracking error, a measurement tool, software module, and optical tracker were added to the navigation system (Figure 1, Left). In an operating room environment, we tested for field distortion in a computer-navigated lumpectomy set-up.

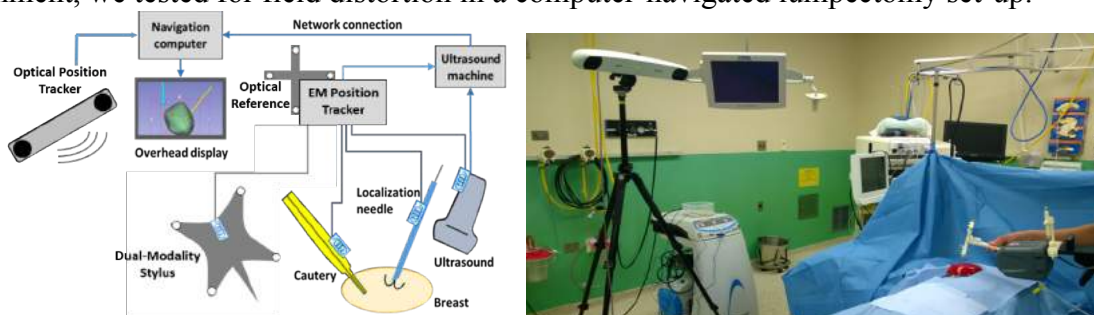


Figure 1. Hardware configuration diagram of the breast surgery navigation system augmented with EM tracking measurement tools (Left). The system as it appears in the operating room (Right).

Results. Setup and deployment of our system is quick and easy. In only a few minutes, users can calibrate our system and obtain quantitative values for tracking error or qualitative depictions of tracking error within a region of interest using 3D Slicer's Transform Visualizer (Figure 2)³. Tracking error in a clean field without any surgical equipment was approximately 0.90 mm (positional) and 0.31° (rotational). The presence of an electrosurgical cautery, a surgical table, and anesthesia machine caused negligible increases in error. Both the positional and rotational error only increased by a few tenths of a millimeter or few tenths of a degree in these cases.

Conclusion. Our open-source system is available as an extension for 3D Slicer. CAD files for our designed hardware tools are also available on the PLUS Model Catalog. As demonstrated in a computer-navigated lumpectomy set-up, our system can be used to quantify electromagnetic tracking error in the operating room.

References. [1] Ungi *et al.*, Real Time Navigation in Breast Tumor Surgery, *International Journal of Computer-Assisted Radiology and Surgery*, vol. 10, no. 3, pp. 253-62, 2015. [2] Lasso *et al.*, PLUS: open-source toolkit for ultrasound-guided intervention systems. *IEEE Trans Biomed Eng.*, vol. 61, no. 10, pp. 2527-37, 2014. [3] King *et al.*, A tool for intraoperative visualization of registration transformations. Proc. SPIE 9036, Medical Imaging 2014: Image-Guided Procedures, Robotic Interventions and Modeling, 90362A (March 14, 2014).

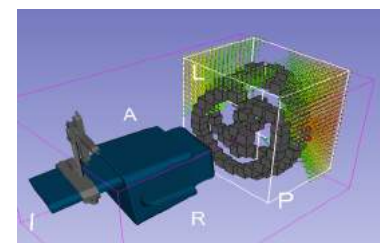


Figure 2. Real-time display of electromagnetic tracking error.

Breast lumpectomy navigation using an open-source clinical application

Tamas Ungi^{1,2}, Gabrielle Gauvin², Andras Lasso¹, Thomas Vaughan¹, C. Jay Engel²,
John Rudan², and Gabor Fichtinger^{1,2}

¹Laboratory for Percutaneous Surgery, School of Computing, Queen's University, Kingston, ON, Canada

²Department of Surgery, Queen's University, Kingston, ON, Canada

Introduction. The most common surgical treatment for early stage breast cancer is called lumpectomy. It is the excision of the tumor from the breast, while sparing most of the healthy tissue. The long term survival of lumpectomy is similar to that of mastectomy, but the cosmetic outcomes are more favorable in lumpectomy. However, lumpectomy often fails to remove the entire tumor in the first attempt. When histological examination reveals cancer at the resection margins, these patients need to undergo another surgery to extend the excision. The rate of these cancer-positive margins is reported between 15% and 50%. Although a number of technologies have been developed to reduce the rate of positive margins, none of them have been adopted in the routine clinical practice, either due to limited effectiveness, or significant additional cost.

Methods. We propose to reduce the positive margin rate of lumpectomies using electromagnetic tracking and navigation of the cautery (surgical cutting device). The key to our surgical navigation method is to show the position of the cautery with respect to the radiologically defined tumor margins. This is achieved in the mobile breast tissue using a tumor localization needle. A needle with wire hooks at its end is deployed in the tumor under ultrasound guidance, and an electromagnetic position tracker is fixed to the needle. The tumor margins are marked by a radiologist, and 3-dimensional margins are saved with respect to the tracked needle. We can show the marked tumor position in real time during surgery, under the assumption that the tracked needle moves with the tumor. The surgical cautery is also tracked by an electromagnetic sensor. Tracked tools are shown along with the tumor in two 3-dimensional virtual reality views during the operation.

Position tracking data and ultrasound images are acquired and synchronized in real time by the PLUS toolkit [1]. Disposable tracking fixtures for intraoperative sterile devices can be downloaded and replicated by a 3D printer. Editable design files are shared publicly (www.plustoolkit.org). Both hardware and software components of the system can be used and modified without any restrictions. The navigation application software is written as an extension of the 3D Slicer application (www.slicer.org). Its source code can be obtained from a public repository (<https://github.com/SlicerIGT/LumpNav>).

Results. The navigation system has been tested in phantom models, and was found to improve surgical outcomes both by reduced positive margin rate, and by less healthy tissue removed. Clinical safety and feasibility has been tested in ten palpable tumor patients undergoing lumpectomy. No breach of sterility, or interference with the normal flow of operation were reported. The method is currently under clinical investigation in non-palpable tumor patients (Figure 1).

Conclusions. Lumpectomy can be improved by electromagnetic navigation. All hardware and software components of the navigation application are open-source, and ready to be used in lumpectomy, or similar surgical applications.

References. [1] Lasso A, *et al.* PLUS: open-source toolkit for ultrasound-guided intervention systems. *IEEE Trans Biomed Eng.* 2014 Oct;61(10):2527-37.

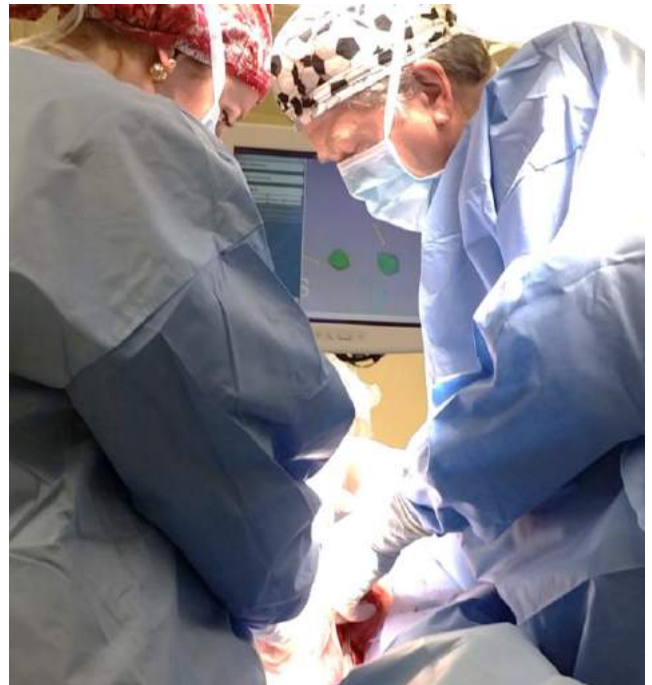


Figure 1. The surgical navigation display shows the real-time position of the cautery relative to the tumor margins during a lumpectomy procedure.

3D Ultrasound Guided Liver Ablation Therapy: Development Of Real-time Motion Compensation

Derek J Gillies^{1,2}, Ren Zhao³, Lori Gardi^{1,2}

Research Supervisor: Aaron Fenster^{1,2,3}

¹Department of Medical Biophysics, Western University, London, Ontario, Canada; ²Robarts Research Institute, Western University, London, Ontario, Canada; ³Centre for Imaging Technology Commercialization, London, Ontario, Canada;

Consortia: Ontario Institute for Cancer Research - Imaging Translation Program

Introduction: Minimally invasive percutaneous techniques, such as radiofrequency ablation, have recently become an alternative and accepted therapy for early-stage liver cancer. This approach is now considered a first-line therapy option for some patients with feasibility similar to partial hepatectomy. To perform liver ablation techniques, the current standard of care uses computed tomography or magnetic resonance images for planning and 2D ultrasound (US) for intra-operative guidance of the ablation applicator(s) into the tumour. Due to low complication rates and shorter recovery times, the popularity of minimally invasive focal ablation procedures are increasing but these procedures have greater local recurrence rates than surgery because of insufficient or inaccurate local ablation. Poor ablation coverage is caused by inexperience of the operators with 2D US imaging and liver motion due to patient breathing. We are developing 3D US imaging methods and motion compensation software to increase the accuracy of focal liver ablation and reduce the high recurrence rates.

Methods: To provide registration with real-time capabilities, rigid registration was performed using an intensity based normalized cross-correlation algorithm with Powell's method as the optimizer. The developed algorithm was implemented into a clinical Ultrasonix Sonixtouch US system with a C5-2 curvilinear transducer and a custom built stabilizing arm. 3D images typically had a matrix size of $820 \times 570 \times 130$ pixels with pixel dimensions of 0.27 mm. Initial tests were completed on a rigid CIRS abdominal phantom that was manually moved to simulate respiratory motion, resulting in a 3D image and 2D live image sequence. Three unique features per image were used as fiducials to compute target registration errors (TRE), which included simulated vasculature and calcifications. The 2nd stage of testing was completed on 7 healthy volunteers with written informed consent, producing 25 3D images and corresponding 2D image streams under breath-hold. Five images per breath-hold were then analyzed to compute a mean TRE in a similar manner as the phantom.

Results: Registrations were computed at approximately twenty frames per second when imaging the phantom and volunteers. Seventeen random live images with the phantom 3D image were analyzed, resulting in a mean TRE of 3.6 ± 2.9 mm (Figure 1). The average TRE for the twenty-five healthy volunteer 3D images was 5.7 ± 3.6 mm. Using 5 mm as a guideline for a clinically acceptable tolerance, 12 of the 25 scans had ideal image quality and below this target with an average TRE of 2.5 ± 0.7 mm.

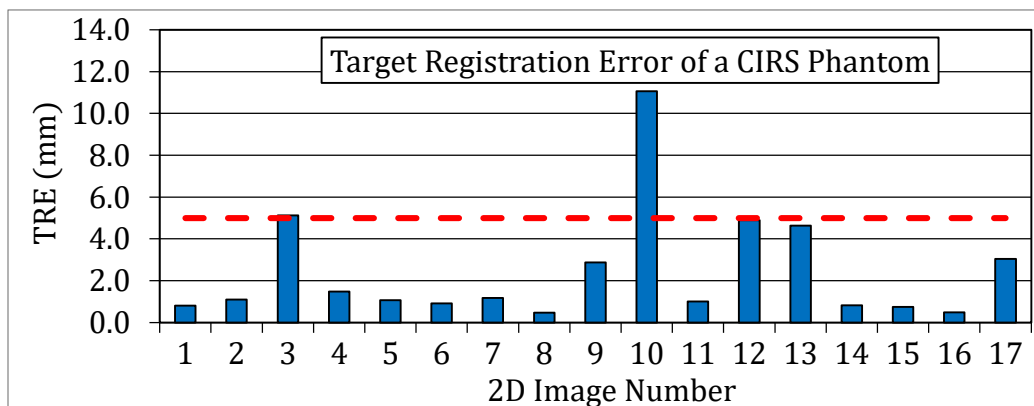


Figure 1 - Registration errors for an abdominal phantom with a target error of less than 5 mm.

Conclusion: With minimal shadowing, good transducer skin contact, and good image contrast, registration errors were less than 5 mm. The algorithm processed US images at 20 frames per second, which is a significant step towards useful intra-operative guidance. Future work will be motivated by the need to choose an efficient region-of-interest to deal with shadowing. Also, applications for other anatomy will be investigated such as motion compensation needed during prostate biopsies.

Automatic Registration Error Maps in Intraoperative CT-based Navigation

Michelle Arkhangorodsky,¹ Jimmy Qiu,¹ Michael Daly,¹ Prakash Nayak^{1,2}, Harley Chan,¹ Robert Weersink,¹ David Jaffray,¹ Jonathan Irish,¹ Peter Ferguson,² Jay Wunder²

¹Guided Therapeutics (GTx) Program, Princess Margaret Cancer Centre

²Division of Musculoskeletal Oncology, Mount Sinai Hospital

Introduction. In the workflow of image-guided surgery, registration can be a time-consuming and frustrating experience for the surgeon. Choosing anatomical points in relevant regions can force exposure of more bone surface than otherwise necessary to perform the surgery. These challenges motivated the development of an anatomy-agnostic registration technique which leverages on optical tracker technology and intraoperative cone-beam CT imaging. The purpose of this clinical study is to validate an automatic registration technique against anatomical point-based registration using target registration error (TRE) maps.

Methods. To automatically register the patient for navigation, custom metal-free sensors with spherical markers are positioned on the patient's skin surface above the lesion prior to intraoperative cone-beam CT imaging. An NDI Polaris tracker obtains the 3D-coordinates of the markers, which eliminates the need for surgeons to manually localize each fiducial point. The corresponding tracker landmarks are captured using an NDI Polaris infrared camera, eliminating the need for surgeons to manually localize fiducial points. For comparison, anatomic point-based registration was also obtained. Two principal measures of error from both marker-based and anatomic-based registrations were obtained: fiducial registration error (FRE) and TRE. FRE is a single value which measures how well fiducials align, while TRE is a set of values that measure the uncertainty calculated at every point in the image. As shown in Fig. 1(b), accurate registration enables the navigation system to precisely track and visualize surgical instruments in real-time.

Results. To date, four patients with lower-extremity bone tumors have been included in the study (3 distal femur, 1 distal tibia/fibula). The mean FRE value over four patient registrations using the metal-free reference markers was 0.97 ± 0.23 [standard deviation] mm. Representative examples of the TRE distribution across the bone volume are shown in Fig. 2, for both marker-based [Fig. 2(a)] and anatomy-based [Fig. 2(b)] paired-point registrations. The mean TRE calculated over the entire bone surface within the image was 0.99 ± 0.28 mm for marker-based registration, compared to 2.54 ± 1.54 mm for anatomy-based. The percentage of surface area encompassed by the 1 mm TRE zone was 60.0% for marker-based, compared to 32.1% for anatomy-based. The time required to perform the complete process of intraoperative CBCT imaging and tracker registration is currently ~5-10 minutes, with further streamlining in progress.

Conclusions. We have used intraoperative CBCT imaging with automatic registration in the OR with four patients and achieved consistently reliable tracking in each case. Initial results demonstrate that TRE distributions obtained from marker-based registration provide better coverage over a surgical region of interest when compared to anatomical point-based registration, with further investigations focused on optimal marker geometry. Provided that intraoperative scanning is available, the automatic registration technique is feasible to integrate into the surgical OR. We will continue to investigate this registration technique for surgical navigation in 15 more extremity patients, and future studies involving pelvic sarcoma tumor resection.

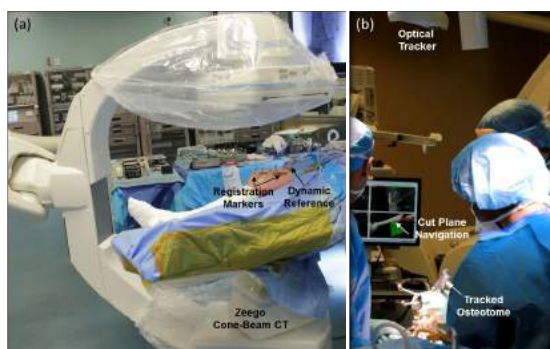


Figure 1. (a) Intraoperative cone-beam CT imaging (Artis Zeego, Siemens Healthcare) during extremity bone tumor surgery using custom metal-free registration markers. (b) In-house surgical navigation system using optical tracking for real-time resection guidance.

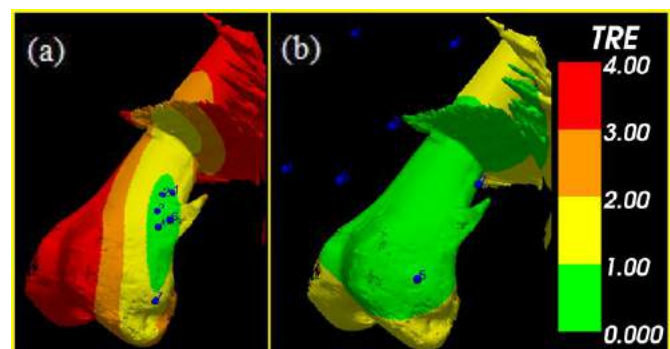


Figure 2. Colormap representations of target registration error (TRE) distributions [mm], where blue points represent fiducial landmarks using anatomical landmarks (a) and using intraoperative registration markers (b).

Standardization Framework to Reduce Variability between FLAIR Images in Large-Scale Studies

Brittany Reiche*, Alan R. Moody**, April Khademi*

Canadian Atherosclerosis Imaging Network (CAIN)

*Image Analysis in Medicine Laboratory (IAMLAB), School of Engineering, University of Guelph, **Department of Medical Imaging, University of Toronto

Introduction. FLAIR MR images are used by physicians to identify and analyze white matter lesions (WML) in the brain to determine the prognosis of patients that are at-risk for stroke [1]. To better understand the relationship between disease and WML, images from large patient cohorts must be analyzed. Manual analyses of this data is laborious and subject to observer variability; automated analysis is a better alternative, as algorithms can perform analyses objectively, accurately, and efficiently [2]. A pre-processing step for analyses often includes brain extraction for robustness. However, images acquired for multi-centre studies are subject to multiple sources of variability, including varying scanner parameters, acquisition noise, intensity inhomogeneity, lack of intensity standardization, and patient motion. This paper proposes a robust standardization pipeline that account for these variations, and presents a novel brain extraction tool developed solely for the FLAIR modality.

Methods. To minimize sources of variability in MRI, we used a novel standardization framework that consisted of denoising with a bilateral filter, bias field correction by filtering low frequency artifacts, intensity standardization using histogram matching [3]. Additionally, images were registered to an atlas using affine registration to correct for patient motion. The metrics used to optimize standardization included: Coefficient of Variation (CoV) to measure bias field effects, Difference of Modes (DoM) and correlation to quantify the quality of histogram-matching, and Mean Squared Error (MSE) to measure the accuracy of registration. For brain extraction, a Random Forest Classifier was constructed using straightforward features, such as intensity, spatial location and texture. Following classification, a false positive reduction scheme was applied. The results of segmentation were evaluated using quantitative metrics, such as Dice Similarity Coefficient which evaluates overlap between manual and automatic brain segmentations, Extra Fraction which quantifies oversegmentation, and Hausdorff Distance, which quantifies the difference in distance between outlines. To show the utility of standardization, the same experiments were also conducted on unstandardized data and compared to the results of the standardized images.

Results. A total of 468 FLAIR MRI (CAIN) were used, where 70% were used for training, and 30% for testing. Table 1 shows improvement in metrics following standardization, were decreases in CoV, DoM, and MSE show that the effects of bias field, intensity non-standardness, and patient motion were reduced, and increased correlation shows that the intensity distributions were better aligned following histogram-matching. Table 2 shows the results of the metrics used to quantify the accuracy of segmentation and Figure 1 shows the results of brain segmentation, on both original and standardized data [4]. These results, visually and quantitatively indicate that the standardized version provides better segmentation results.

Conclusions. This work demonstrates that a thorough standardization framework can significantly improve the classification accuracy of a Random Forest when applied to FLAIR MRI. This allows for the efficient and accurate processing of large-scale data sets by reducing the effects of variability. This work also presents one of the first approaches to automatic brain extraction of FLAIR images.

References. [1] M. Essig *et al.* "Fast fluid-attenuated inversion-recovery (FLAIR) MRI in the

assessment of intraaxial brain tumors," *J. Magn. Reson. Imaging*, vol. 8, no. 4, pp. 789–798, 1998. [2] Khademi *et al.* "Robust White Matter Lesion Segmentation in FLAIR MRI," *IEEE Trans. Biomed.*

Eng., vol. 59, no. 3, pp. 860–871, Mar. 2012 [3] Reinhard *et al.* "Color transfer between images," *IEEE Comput. Graph. Appl.*, vol. 21, no. 5, pp. 34–41, 2001. [4] B. Reiche *et al.* "Effect of Image Standardization on FLAIR MRI for Brain Extraction," *Signal Image Video Process.*, vol. 9, no. 9, Dec. 2015.

Table 1 Average standardization performance metrics with and without standardization

| | ADNI | CAIN |
|--------------------------|---------|---------|
| CoV original | 44.2150 | 39.3128 |
| CoV standardized | 6.6107 | 3.9596 |
| Correlation original | 0.9792 | 0.9799 |
| Correlation standardized | 0.9934 | 0.9840 |
| DoM original | 0.4633 | 0.5134 |
| DoM standardized | 0.0542 | 0.0348 |
| MSE original | 0.2641 | 0.2483 |
| MSE standardized | 0.2311 | 0.1759 |

Table 2 Summary of classifier performance metrics

| | Original data | Standardized data |
|--------------------|---------------|-------------------|
| Dice similarity | 0.6569 | 0.8281 |
| Extra fraction | 12.0854 | 0.1751 |
| Hausdorff distance | 9.6761 | 5.3791 |

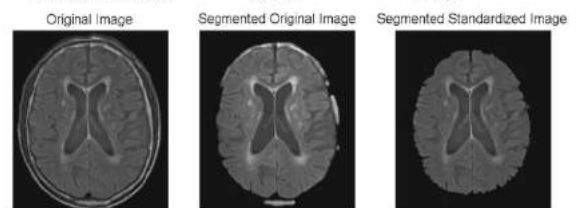


Figure 1 Sample Segmentation Using Original and Standardized Data

Optimization Methods in MR-Guided Transcranial Focused Ultrasound

MITNEC

Alec Hughes* and Kullervo Hynynen

Sunnybrook Research Institute and Department of Medical Biophysics, University of Toronto

Introduction. MR-Guided Transcranial Focused Ultrasound is a growing field with many applications for neurosurgery and neurology. By using a phased array consisting of hundreds or thousands of individual ultrasound elements, it has been shown to be possible to create a sharp focus non-invasively in the brain. Recent clinical successes have occurred in treating essential tremor (Lipsman *et al*, 2013), neuropathic pain (Jeanmonod *et al*, 2012), and brain tumors (McDannold *et al*, 2010). Even more recently, the blood-brain barrier was opened for drug delivery using focused ultrasound, allowing for a range of potential future therapies. As the list of postulated treatments grows and transcranial focused ultrasound becomes a more widely-accepted modality, it becomes necessary to optimize the treatments based on patient safety and treatment efficacy.

Two main ideas will be emphasized here. First, it will be shown that by using a Tikhonov regularization parameter, α , it is possible to rotate a focus. Second, it will be shown that a Tikhonov regularization scheme can also be used to reduce extraneous heating in bone for improved patient safety. These two concepts give additional degrees of freedom to the treatment planning.

Methods. CT data was obtained from patients from a clinical trial of MR-guided focused ultrasound for the treatment of essential tremor. A hemispherical array consisting of 1024 elements was constructed, as in Figure 1. Two methods for control of the treatment are introduced: control over the focus and control over extraneous heating. In order to achieve both, Tikhonov regularization will be used to optimize the ill-posed inverse problem. To rotate the focus in the brain, by sampling points away from the target focus location, it is possible to solve the inverse problem for the desired rotated focus. To Numerical simulations demonstrate the implementation of these novel phased array controls to a planar phased array. By setting up an inverse problem for phasing, it is possible to reduce heating at the base of the skull using the concept of the anti-focus (Pulkkinen *et al*, 2011), while maintaining therapeutic levels of heating at the focus.

Results. It is shown in Figure 2 that it is possible to rotate a focus using Tikhonov regularization for a suitable regularization parameter. In addition, Figure 3 shows the reduction in temperature at a point of the skull base when using conventional phasing (solid line), and full-wave (dashed line) and hybrid (dotted line) models.

Conclusions. Conventional focusing of ultrasound phased arrays consider the target location as an infinitesimal point in space. We argue that there are benefits to considering the spatial manifestation of the focus and its extraneous acoustic field. Novel techniques for focusing ultrasound phased arrays are introduced.

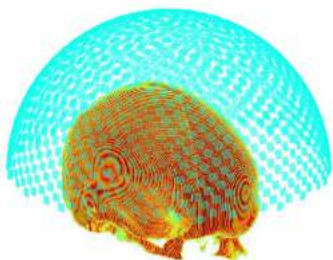


Figure 1. The hemispherical phased array of transducer elements around the segmented CT image of the skull.

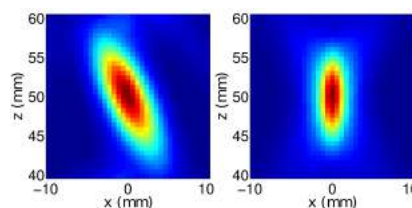


Figure 2. The original focus (right) and the rotated focus (left).

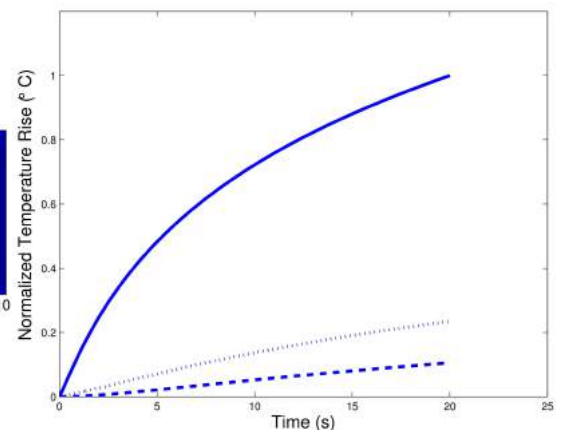


Figure 3. The normalized temperature rise at a point of the skull base.

Optimized Correlated Diffusion Imaging for Prostate Cancer Detection

Junjie Zhang¹, Armin Eilaghi¹, Masoom A. Haider¹, Alexander Wong², Farzad Khalvati¹

¹Medical Imaging, University of Toronto, Sunnybrook Research Institute, Toronto, ON, Canada

²Systems Design Engineering, University of Waterloo, Waterloo, ON, Canada

Introduction: Diffusion magnetic resonance imaging (dMRI) is increasingly becoming the standard of care for detection and diagnosis of prostate cancer. Correlated Diffusion Imaging (CDI) is a new dMRI technique that exploits joint correlation of diffusion attenuations across different gradient strengths, durations, and timings to enhance delineation of healthy and cancerous tissues [1,2,3]. In this study, we introduce an optimized CDI (oCDI) technique, in which the contribution of diffusion attenuation at different gradient strengths, durations, and timings are optimized to further enhance the delineation between healthy and cancerous tissues.

Methods: dMRI is a promising imaging modality in which the sensitivity of tissue to Brownian motion of water molecules is measured by applying pairs of magnetic field gradient pulses with opposite phases, where the signal loss due to spin dephase is controlled by b (Eqn. 1), which among other factors consists of gradient strength and duration, and the time between the two pulses [4]. The dMRI signal (S) is formulated as: Eqn. 1 $S = S_0 e^{-bD}$ where S_0 is the signal intensity without diffusion and D represents the diffusion strength or velocity. In the proposed oCDI technique, a sequence of dMRI signal acquisitions are performed at different b values (b_i), and the following weighted signal mixing is performed to obtain the final CDI image signal:

$$\text{Eqn. 2 } oCDI(x) = \int \dots \int_{b_i}^{b_j} S_i(x)^{\alpha_i} \dots S_j(x)^{\alpha_j} P(S_i(x), \dots, S_j(x) | V(x)) \times dS_i(x) \dots dS_j(x)$$

where P is the conditional joint probability density function and $V(x)$ is a local subvolume around x . To determine the optimal values for α_i to α_j in the weighted signal mixing function, a training dataset is used where the tumour regions have been contoured by a radiologist. A grid search is performed to determine a set of parameters that yield the maximum area under ROC curve (AUC) via a leave-one-patient-out cross-validation approach.

Results: The performance of the proposed oCDI was evaluated using clinical dMRI data of 17 patients with cancer acquired using a Philips Achieva 3.0T machine at Sunnybrook Health Sciences Centre, Toronto, ON, Canada. All data was obtained retrospectively under the local institutional research ethics board. The images obtained using oCDI were compared with apparent diffusion coefficient (ADC) maps as well as those obtained using the original CDI technique [1] for delineation of healthy and cancerous tissue for prostate, as shown in Figure 1. The AUC of the proposed oCDI technique was also compared against that of ADC map and the original CDI technique. The results are shown in Table 1.

Conclusion: Optimized CDI significantly improved the separability of cancerous and healthy tissues in prostate dMRI and hence, it is a promising technique for prostate cancer screening.

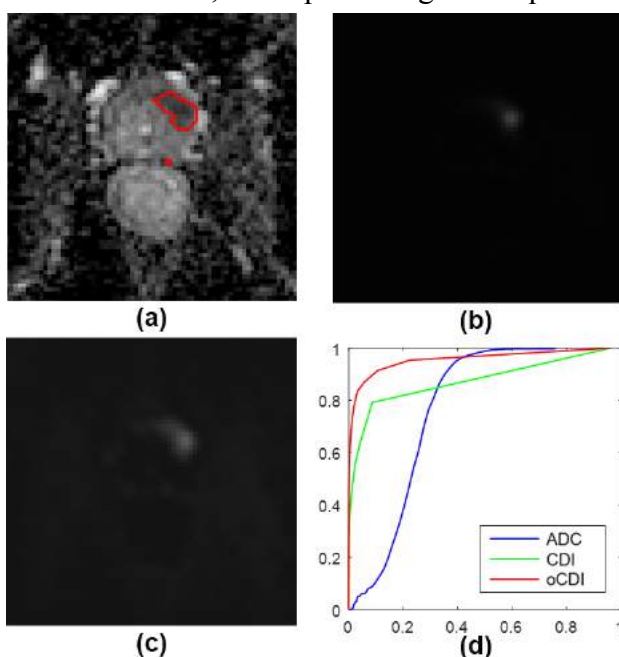


Table 1. AUC results of ADC map, original CDI and the proposed optimized CDI (oCDI)

| | ADC | CDI | oCDI |
|-----|--------|--------|--------|
| AUC | 0.5346 | 0.8462 | 0.9184 |

References:

- [1] Wong et al. "Correlated Diffusion Imaging", BMC Medical Imaging, 13:26, 2013.
- [2] A. Wong, F. Khalvati, M. Haider, "Dual-Stage Correlated Diffusion Imaging", ISBI, 75–78, 2015.
- [3] Khalvati et al. "Automated prostate cancer detection via comprehensive multi-parametric magnetic resonance imaging texture feature models", BMC Medical Imaging, 15-27, 2015.
- [4] D. M. Koh, A. R. Padhani, "Diffusion-weighted MRI: a new functional clinical technique for tumour imaging". Br J Radiol. 79:633–5, 2006.

Acknowledgement: This research has been supported by CCO-CINO, OICR, and NSERC.

Figure 1. (a) ADC map (tumour contoured in red), (b) CDI, (c) oCDI, (d) ROC curves for all 17 cases for detection of prostate cancer. Tumour is shown as a brighter nodule in the proposed oCDI (c) compared to original CDI (b).

Improving Fluorescence Tomography using Imaging Priors from Intraoperative Cone-Beam CT

Michael J. Daly,^{1,2} Nidal Muhanna,³ Harley Chan,² Jimmy Qiu,² Robert Weersink,²
Brian C. Wilson,^{2,4} Jonathan C. Irish,^{3,4} and David. A. Jaffray^{1,2,4,5}

¹Institute of Medical Science, University of Toronto, Toronto ON

²TECHNA Institute, University Health Network, Toronto ON

³Department of Surgical Oncology, Princess Margaret Cancer Centre, Toronto ON

⁴Ontario Cancer Institute, Princess Margaret Cancer Centre, Toronto ON

⁵Department of Radiation Physics, Princess Margaret Cancer Centre, Toronto ON

A multi-modality intraoperative imaging system has been developed for hybrid cone-beam computed tomography (CBCT) and fluorescence diffuse optical tomography (FDOT). The fluorescence imaging system is configured for use with indocyanine green (ICG) using a collimated 760 nm laser diode and a 14-bit near infrared (NIR) camera. Freehand image collection in a non-contact geometry is achieved using a stereoscopic optical camera for real-time localization of the laser source and camera. Intraoperative CBCT images with sub-mm spatial resolution are acquired with a flat-panel C-Arm. FDOT is implemented using a finite element method for diffuse tissue optics (NIRFAST), with structural information from CBCT used directly in the optical reconstruction algorithm using Laplacian-type regularization (“soft priors”). The light rays from the laser source and camera pixels are geometrically projected onto the boundary elements of the tissue mesh using algorithms for ray-triangle intersection and camera lens distortion. Registration errors between real and projected boundary points are <2 mm for typical acquisition geometries. Surface flux is converted from CCD photon counts using free-space radiometry models and camera photon transport calibrations (e.g., filter transmittance, camera quantum gain, sensor noise). Experiments with ICG inclusions embedded in liquid phantoms demonstrate that the use of CBCT spatial priors improves the quantitative performance ($<15\%$ error, a reduction of 50% relative to no priors) in the tomographic reconstruction of fluorescence yield at depths <1 cm. This translational research system is under investigation for clinical applications in head and neck surgery including oral cavity tumor resection, lymph node mapping, and free-flap perforator assessment.

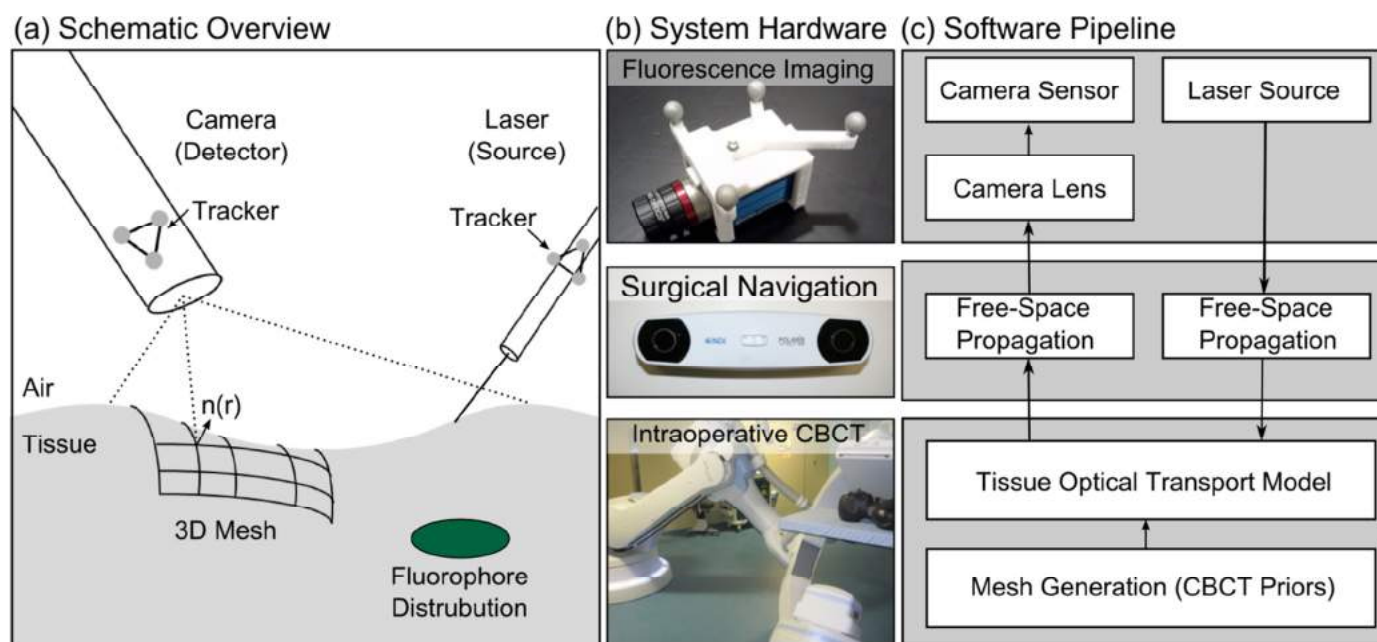


Figure 1. (a) Schematic of a surgical navigation system for CBCT-guided fluorescence tomography. Volumetric mesh segmentations are generated from intraoperative CBCT images. Laser source and camera detector positions relative to the tissue surface are obtained in real-time from an optical tracking system. (b) System hardware components include a NIR CCD camera (PCO Pixelfly USB) and lens (Edmund Optics), a stereoscopic optical tracking system (NDI Polaris Vicra), and a flat-panel cone-beam CT C-Arm. (c) Software pipeline for non-contact fluorescence tomography. Registered fluorescence CCD images are used in a finite element diffuse optics model to generate 3D reconstructions of sub-surface fluorescence inclusions (e.g., tumours, lymph nodes, blood vessels) that are fused with intraoperative CBCT.

Title: ^{89}Zr -Trastuzumab-DM1: A Novel Probe for Positron-Emission Tomography (PET) Imaging of the Delivery of T-DM1 (Kadcyla) to HER2-Positive Breast Cancer

Noor Al-saden¹, Conrad Chan¹, Raymond M. Reilly^{1,2,3,4}

Departments of ¹ Pharmaceutical Sciences and ² Medical Imaging, University of Toronto and ³ Joint Department of Medical Imaging and ⁴ Toronto General Research Institute, University Health Network, Toronto, ON, Canada

Background: Our aim was to construct a novel molecular imaging probe (^{89}Zr -labeled T-DM1) to visualize the delivery of trastuzumab-DM1 (T-DM1; Kadcyla, Roche) to HER2-positive breast cancer (BC) by positron-emission tomography (PET). T-DM1 is an antibody-drug immunoconjugate (ADC) approved for treatment of trastuzumab-resistant HER2-positive BC.

Methods: T-DM1 was modified with desferrioxamine (DFO) for chelating ^{89}Zr by reaction with a 14-fold excess of p-NCS-Bz-DFO for 30 min at 37°C. The number of DFO per T-DM1 molecule was quantified spectrophotometrically at 430 nm following reaction with FeCl_3 . Purity and homogeneity were assessed by SDS-PAGE and size-exclusion (SE)-HPLC. ^{89}Zr labeling was performed at a specific activity of $2\mu\text{Ci}/\mu\text{g}$ in 2 M sodium carbonate/0.5 M HEPES buffer, pH 7.0 at RT for 60-90 mins. Radiochemical purity was determined by instant thin layer-silica gel chromatography (ITLC-SG) and SE-HPLC. HER2 immunoreactivity was measured in a saturation binding assay using SK-BR-3 human BC cells.

Results: T-DM1 was modified with 3.0 ± 0.2 DFO chelators. SDS-PAGE and SE-HPLC revealed a pure and homogeneous immunoconjugate. The labeling efficiency with ^{89}Zr was $>95\%$. ^{89}Zr -p-NCS-Bz-DFO-T-DM1 exhibited preserved HER2 immunoreactivity with high affinity binding ($K_d = 4.9 \pm 0.4$ nM).

Conclusions/implications: A novel ^{89}Zr -labeled probe of T-DM1 was produced that exhibited high affinity binding to HER2 on human BC cells. This agent has application for PET imaging of the delivery of T-DM1 to tumours in patients with HER2-positive BC. Imaging may inform on those patients likely to benefit from T-DM1 treatment. Supported by the Ontario Institute for Cancer Research (OICR) Smarter Imaging Research Program.

Fluorine-19 Labeling of Peripheral Blood Mononuclear Cells for Clinical Cell Tracking

OICR – Smarter Imaging Program

Paula J Foster

¹*Imaging Research Laboratories, Robarts Research Institute,* ²*Medical Biophysics, Western University,*

Cancer vaccine-based therapies are an area of expanding research. In 2010, the first FDA approved cell therapy was released to target metastatic castration-resistant prostate cancer. This therapy uses antigen-presenting peripheral blood mononuclear cells (PBMC) in order to prime the immune system to target a tumor. The efficient delivery of PBMC to lymph nodes remains one of the most significant barriers to the success, and widespread use, of cancer immunotherapy. Our long-term goal is to be able to track cell-based immunotherapies in human cancer patients to determine (1) the number of injected cells reaching the intended target and (2) how long the therapeutic cells remain in place. Cellular magnetic resonance imaging (MRI) can provide this information when a suitable cell labeling agent is employed. Fluorine-19 (¹⁹F) –based cell tracking with MRI has advantages over the more commonly used iron-based cell tracking methods. Specifically, ¹⁹F-MRI provides unambiguous detection, with a signal that is linearly dependent on the number of cells/voxel.

Over the last seven years we have developed *in vivo* cell-tracking methodologies using superparamagnetic iron oxide nanoparticles (SPIO) and [¹⁹F]-fluorine-based perfluorocarbon nano-emulsion cell labeling agents in conjunction with magnetic resonance imaging (MRI). We have developed extensive experience labeling many immune cell types that have clinical relevance including monocyte/macrophages, dendritic cells, NK cells, T cells and B cells as isolated populations or within mixed leukocyte populations such as peripheral blood mononuclear cells. We have developed and optimized the MRI hardware and software needed to obtain optimal MRI results with high sensitivity and specificity. We are the only ones in Canada conducting this type of research and only one of 6 laboratories worldwide. There is increasing interest in the [¹⁹F]-fluorine-based perfluorocarbon nano-emulsion cell labeling agent from several of the U.S.-based laboratories producing CAR-T cell immunotherapies in the United States and dendritic cell-based immunotherapies in Europe.

Although the majority of our most recent research has focused on pre-clinical models of immunotherapy, we are now poised to move forward with a human study. This study will be in labeling peripheral blood mononuclear cells (PBMC) with the [¹⁹F]-fluorine-based perfluorocarbon nano-emulsion cell labeling agent to demonstrate its safety in humans in order to get Health Canada permission to use it in other clinical trials. The PBMC tracking study is being supported by current OICR funding via the Smarter Imaging Program. We are also working to determine whether it is feasible to use the [¹⁹F]-fluorine-based perfluorocarbon nano-emulsion cell labeling agent, known as Cell Sense, to monitor sipuleucel-T (Provenge, Dendreon Pharmaceuticals Inc., Seattle, WA)-immunotherapy in humans.

In this talk I will review the steps we have taken to develop the technology to perform *in vivo* ¹⁹F cell tracking on a preclinical 9.4T MR system and on a clinical 3T MRI system. This work has been performed in collaboration with Dr. Greg Dekaban (PI, Robarts Research Institute), Jeff Gaudet (PhD candidate, Robarts), Corby Fink (PhD candidate, Robarts) and Dr. Matthew Fox (PDF, Robarts).

The Application of a Novel Multiplexing Staining Technology in the Breast Cancer Research

Dan Wang¹, Tyna Hope¹, Kela Liu¹, Sharon Nofech-Mozes², Sireesha Kaanumalle⁴, Yousef Al-Kohafi⁴, Kashan Shaikh⁴, Robert Filkins⁴, and Martin Yaffe^{1,3}

¹Physical Sciences, Sunnybrook Research Institute, Toronto, Canada

²Department of Anatomy Pathology, Sunnybrook Health Science Centre, Toronto, Canada

³Department of Medical Biophysics, University of Toronto, Toronto, Canada

⁴GE Global Research Center, Niskayuna, USA

The visualization of multiple biomarkers within a single tissue section may assist in our understanding of the complex cell interactions within the tumour microenvironment. The development of multiplexing staining technology allows reporting the presence of multiple biomarkers that can provide insight into the status of complex pathways or interplay of proteins in tumour formation, growth and metastasis. In our work we are utilizing a novel technology, developed by GE Global Research Center in the US. This consists of an automated staining system for sequential immunofluorescence-labeling, multiplexing, imaging and analysis of onco-proteins in fixed tissues. This multiplexing platform enables the study of multiple biomarker expressions on a single tissue section at subcellular level (i.e. nuclear, membrane, and cytoplasmic). Utilizing the GE automated staining system, the pilot experiment on a triple (estrogen receptor (ER), progesterone receptor (PgR), and human epidermal growth factor receptor 2 (HER2)) positive breast cancer section was aimed to: 1) validate the novel multiplexing technique by comparing to traditional immunohistochemistry; 2) visualize an extended panel of breast tumour markers, including ER, PgR, HER2, Ki-67, a proliferation marker, Cytokeratin (CK), an epithelial marker, and additional nuclear and membrane markers important for image processing. The automated sequential stain-image-bleach (SSB) technology incorporates a microfluidic flow cell realizing the following sequence [1]: staining with dye (Cy3 or Cy5) -conjugated antibodies, imaging using corresponding filters, bleaching the signal and re-imaging, and then repeating with the next conjugated antibodies. Images acquired in each staining round were registered, background noise removed, and cell compartments segmented. Biomarker expressions at subcellular compartments of a single cell were quantified and analyzed with Cran R.

The immunofluorescence measurements correspond to the positivity of the ER/PgR/HER2 as evaluated by conventional DAB single staining. The individual channel images HER2, ER, PgR, Ki67, and CK, as well as the overlapping images are shown in pseudo-color images in Fig. 1. The matrix plot of HER2, ER, PgR, and Ki67 biomarkers is shown in Fig. 2. The good correlation ($r=0.75$) between PgR and ER in multiplexing staining corresponds to the clinical findings that most ER positive cases were also positive for PgR. The clusters in the Ki67 and ER/PgR plots may suggest that the proliferative cells (high Ki67 expression) have reduced ER and PgR expression in nuclei.

Our experiments to date suggest that SSB multiplexing technology is a useful research tool for studying coexpression of biomarkers involved in complex cellular activities and may be a viable alternative to multi-gene assays. The system provides objective quantitative measurements and allows visualizing either a single marker or any panel combination digitally. It overcomes the practical limitation of sparse tissue samples. Such multiplex assays may facilitate the use of biomarker panels for assessment and precision therapy in individual cancer patients.

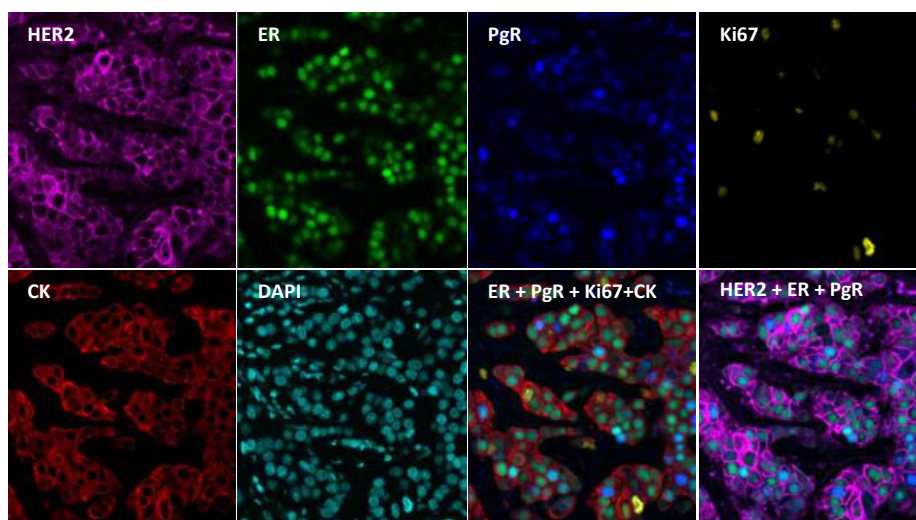


Fig. 1 Multiplexing of HER2 (purple), ER (green), PgR (blue), Ki67 (yellow), CK (red) and overlay images on a triple positive breast cancer patient.

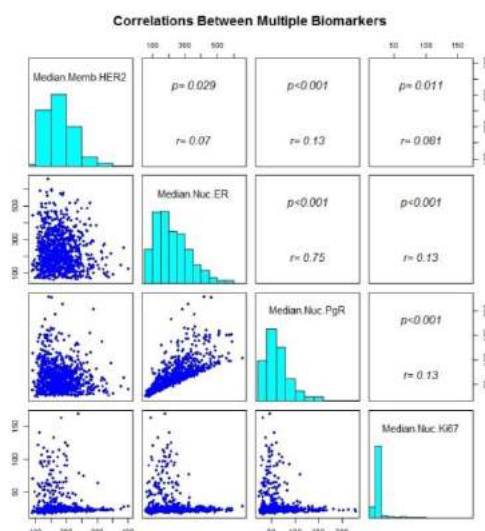


Fig. 2 Matrix plot to show correlations between 4 biomarkers.

[1] Gina C et al. A novel, automated technology for multiplex biomarker imaging and application to breast cancer. *Histopathology*. 2014;64(2):242-255

Modulating Nanoparticle Drug Delivery using Radiation and Heat

Shawn Stapleton¹, Ali Vedadi¹, Michael Dunne², Michael Milosevic¹, Christine Allen² and David Jaffray¹

¹Radiation Medicine Program, Princess Margaret Hospital, Toronto, Canada

²Pharmaceutical Sciences, University of Toronto, Toronto, Canada

Introduction. Nanomedicine drug delivery systems assists in delivering large doses of drugs specifically to cancer, however only a modest increase in anti-tumor efficacy relative to the standard of care has been observed. The intra-tumoral distribution of drug is a critical determinant of efficacy [1, 2]. High-resolution pre-clinical imaging has confirmed that the intra-tumoral distribution of a clinically relevant liposome drug delivery system is heterogeneous throughout the tumor volume [3]. Considerable effort has been made to develop methods to modify and/or improve the intra-tumoral distribution and efficacious use of nanomedicine in the clinical setting. In this study, we investigate the ability for radiation (RT) and heat (HT) to improve the intra-tumoral distribution of liposomes. Furthermore, we investigate the effects of RT and HT on the tumor microenvironment to elucidate the mechanisms that drive the improved intra-tumoral transport.

Methods. Measurements of the intra-tumoral distribution of liposome were made by micro-CT imaging of a nanoparticle liposome computed tomography (CT) contrast agent (CT-liposome). Measurements were performed in a MDA-MB-231 metastatic breast adenocarcinoma tumor model implanted orthotopically. Tumors were pre-treated with 15 Gy of radiation (n=5) 24 hrs in advance, pre-treated with mild-hyperthermia (42°C) 10 min in advance (n=5), or untreated in advance (n=5) of CT-liposome administration. Images were acquired pre- and 5 min, 8 h, 24 h, and then every 24 h up to 168 h post-administration. The bulk accumulation and intra-tumoral distribution (i.e. fraction of enhanced tumor volume and changes in radial distribution) were quantified. To investigate mechanism, interstitial fluid pressure (IFP) was measured using a probe based fluid pressure measurement system. Additionally, perfusion, vascular permeability, vascular volume fraction and interstitial volume fraction were measured using dynamics contrast enhanced CT (DCE-CT). Measurements were made following pre-treatment with RT, HT, or no pre-treatment.

Results. Pre-treatment of tumors with RT and HT resulted in a 1.6 and a 1.9 fold increased in bulk CT-liposome accumulation 72 h post-injection (time of peak enhancement). The rate of CT-liposome accumulation was substantially faster and persisted longer for HT compared to RT and untreated tumors. The enhanced fraction of tumor volume increasing from 55% in untreated tumors to 70% with RT and 75% with HT. Furthermore, RT and HT increased CT-liposome enhancement in the central tumor regions compared to untreated tumors (Figure 1). Both RT and HT significantly decreased IFP, which explains the increased accumulation of CT-liposomes in the central tumor region. RT had a modest effect on decreasing perfusion and vascular volume. HT caused an increase in perfusion and the vascular volume. No changes to permeability or interstitial volume was observed.

Conclusions.

The results of this study demonstrate that RT and HT improve the bulk accumulation and intra-tumoral distribution of liposomes. RT and HT cause a significant drop in IFP, which likely contributes to improve trans-vascular pressure gradients, resulting in the observation of improved accumulation of liposomes in the central tumor region. The substantial increase in perfusion and vascular volume following HT, also appears to contribute to the increase bulk accumulation and intra-tumoral distribution of liposomes compared the RT and untreated tumors. Overall, RT and HT are viable strategies to improve the accumulation of liposomes in solid tumors, which should result in increased delivery of drug and improvements on treatment outcome.

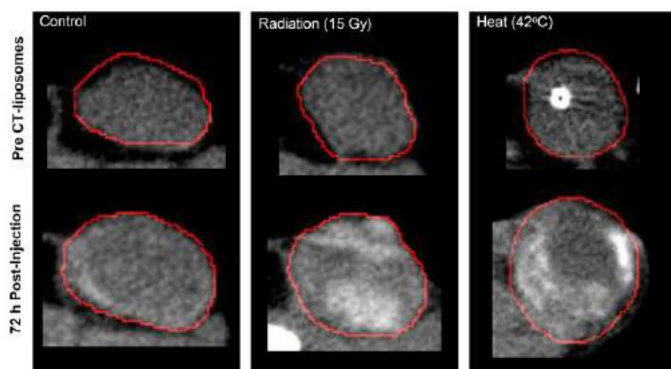


Figure 1. Representative micro-CT images of MDA-MB-231 tumors pre- and 72 h post-injection of CT-liposomes. Control (no pre-treatment) tumors had modest intra-tumoral enhancement of CT-liposomes. Both RT and HT resulted in substantial improvements to the intra-tumoral distribution of CT-liposomes.

References: [1] Simpson-Herren et al., *Cancer Chemoth Pharm* 1988 22(2). [2] Tannock et al. *Clin Cancer Res*. 2002, 8(3). [3] Stapleton et al. *J Controlled Release*, 2013. 172 (1)

Reduced Brain Glutamine in Female Varsity Rugby Athletes after Concussion

Amy Schranz*, BSc¹, Kevin Blackney, BSc¹, Arthur Brown, PhD¹, Lisa Fischer, MD², Kathryn Y. Manning, MSc¹, Ravi S. Menon, PhD¹, Christy Barreira, BSc¹, Tim Doherty, MD, PhD³, Douglas Fraser, MD, PhD⁴, Gregory A. Dekaban, PhD¹, and Robert Bartha, PhD¹

¹Robarts Research Institute, The University of Western Ontario, ²Primary Care Sport Medicine, Fowler Kennedy Sport Medicine, ³Physical Medicine and Rehabilitation, University of Western Ontario, ⁴Paediatrics Critical Care Medicine, London Health Sciences Centre, London, Ontario, Canada

Introduction. A concussion is a brain injury caused by a blow to the head or another part of the body that can result in disturbances in brain function [1]; including ionic shifts, massive neurotransmitter release, mitochondrial dysfunction, and inflammation [2]. Due to the lack of proper diagnosis and prognosis of a concussion, athletes often return to play before the concussion has fully resolved, which puts them at an increased risk of more serious injury [3]. Biomarkers must be found that identify concussion as well as recovery. Non-invasive imaging biomarkers in particular could be used to directly measure brain changes following concussion. The objective of this study was to quantify changes in brain metabolite levels in female athletes over the course of a rugby season. It was hypothesized that metabolite levels would change after concussion.

Methods. This study followed a women's varsity rugby team (ages 18-22) over three seasons. Players were subdivided into two groups; those that were diagnosed with a single concussion (n=6) and players that were not concussed (n=46). Each athlete was evaluated at the beginning of each season, and followed up at the end of each season. Concussed athletes were additionally evaluated 24-72 hours post-concussion. An evaluation consisted of clinical tests (SCAT3 and ImPACT), hematology, and an MRI scan. Magnetic resonance spectroscopy (MRS) was acquired from the prefrontal white matter using single voxel point-resolved spectroscopy (PRESS: TE/TR=135/2000ms, voxel=2x2x1.5 cm³, 192 averages). Spectra were post-processed using in-house software to measure absolute *N*-acetyl aspartate, choline, creatine, glutamate, glutamine, and myo-inositol. Paired t-tests were performed between time points, within groups.

Results. In the concussed group, a 42% reduction in glutamine was found post-concussion compared to baseline (Figure 1). Interestingly, in the unconcussed group a 22% reduction in glutamine was found at the end of the season, compared to baseline (Figure 2). No other metabolite changes were observed in either group.

Discussion. Reduced glutamine may occur in non-concussed athletes due to repetitive sub-concussive hits over the course of a season leading to a shift in the glutamate-glutamine cycle. This shift could cause excess glutamate to preferentially be converted to α -ketoglutarate and not glutamine [4]. A future study is needed to rule out an exercise effect.

References. [1] McCrory et al. *Journal of Athletic Training*, 48(4), 554–75, 2012. [2] Giza et al. *Journal of Athletic Training*, 36(3), 228–235, 2001. [3] Bey et al. *The Western Journal of Emergency Medicine*, 10(1), 6–10, 2009. [4] Frigerio et al. *Biochimica et Biophysica acta*, 1777 (7-8) p. 965-72, 2008.

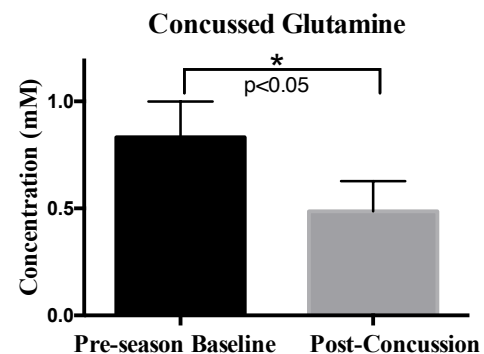


Figure 1. Mean absolute concentration of glutamine in the concussed rugby group at Baseline and 24-72 hours after obtaining a concussion (Post-Concussion)

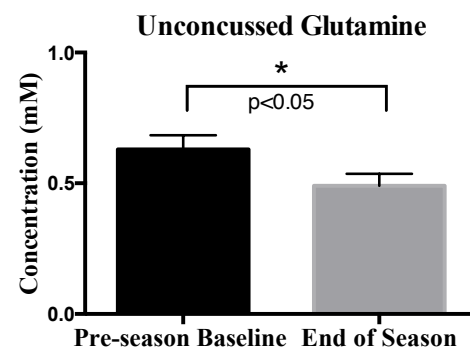


Figure 2. Mean absolute concentration of glutamine in the unconcussed rugby group

Web-based dashboards and other tools for quality assurance and quality control monitoring of multisite neuroimaging studies

Stephen R. Arnott*¹, Aditi Chemparathy¹, Fan Dong¹, Shuai Liang¹, Mojdeh Zamyadi¹, Mojib Javadi², Moyez Dharsee², Tom Gee¹, Robert Bartha^{3,4}, Christopher Scott⁵, Igor Solovey³, Sandra Black⁵, Sean Symons⁵, the ONDRI investigators, Glenda MacQueen⁶, Jacqueline Harris⁶, Andrew Davis⁷, Geoffrey Hall⁷, Stefanie Hassel⁸, Neshah Mathikcantan¹, Abiramy Uthirakumar¹, Tanya Schmah⁹, Sofia Chavez^{10,11}, Stephen C. Strother^{1,12}

¹Rotman Research Institute, Baycrest, Toronto, Canada, ²Indoc Research, Toronto, Canada, ³Robarts Research Institute, London, Canada, ⁴Department of Medical Biophysics, Western University, London, Canada, ⁵Sunnybrook Research Institute, Toronto, Canada, ⁶University of Calgary, Calgary, Canada, ⁷McMaster University, Hamilton, Canada, ⁸Aston University, Birmingham, UK, ⁹University of Ottawa, Ottawa, Canada, ¹⁰Centre for Addiction and Mental Health, Toronto, Canada, ¹¹Department of Psychiatry, University of Toronto, Toronto, Canada, ¹²Medical Biophysics Department, University of Toronto, Toronto, Canada

Introduction. To monitor and troubleshoot the performance of magnetic resonance (MR) scanners participating in multisite Integrated Discovery Programs (IDPs) funded by the Ontario Brain Institute (OBI), the advanced data informatics and analytics platform of Brain-CODE (Centre for Ontario Data Exploration) has created Quality Assurance (QA) and Quality Control (QC) tools and procedures that include web-based dashboards.

Methods. Monthly scans of fBIRN (functional Biomedical Informatics Research Network) phantoms are performed at each scanner using the ONDRI (Ontario Neurodegenerative Disease Research Initiative) MR protocol, and these data are uploaded to Brain-CODE's Stroke Patient Recovery Research Database (SPReD). Within 24-hours of upload, resting state functional scans are automatically processed with fBIRN's Phantom Processing Script(1) and a summary HTML file is created. Nightly pipelines extract key summary variables from each report and aggregate those data into a text file that automatically updates libraries populating interactive web-based dashboards (e.g., Figure A) created with TIBCO® Spotfire® software. Both cross-sectional and longitudinal displays are available, and human

QC summary data can also be displayed in addition to phantom QA data. Spotfire's analytical capabilities enable statistical thresholds to be set that, when exceeded, prompt site notifications as well as consultation with relevant IDP neuroimaging leads.

Results. To date, these dashboards have been useful for highlighting scanner manufacturer (e.g., Siemens versus General Electric) as a major source of between-site MR signal variance; alerting, monitoring and resolving problematic MR ghosting issues at several sites; and normalizing image resolution across sites.

Conclusions. Web-based dashboards and other tools are important QA/QC components of multisite imaging studies.

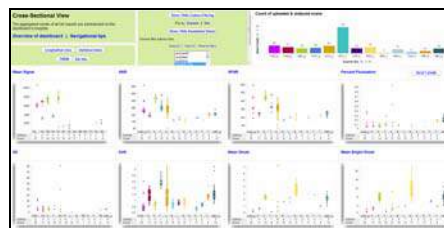


Figure A

1Friedman L, Glover GH. Report on a multicenter fMRI quality assurance protocol. *J Magn Reson Imaging* 2006;23(6):827-839.

Inflammation Imaged with [18F]-FDG PET/CTA is Related to the 3D Ultrasound Volumetric Phenotype of High-Risk Carotid Plaque: Sub-study of the Canadian Atherosclerosis Imaging Network (CAIN-2)

Myra S Cocker Ph.D.*, Aaron Fenster Ph.D. FCCPM†, Robert Hammond M.D.‡, Robert A. deKemp Ph.D.*, Cheemun Lum M.D.¶, Andrew Hill M.D.††, Sudhir Nagpal M.D.††, Grant Stotts M.D.‡‡, Linda Garrard RN*, Jean DaSilva Ph.D.*, Jean-Claude Tardif M.D.§§, Rob S.B. Beanlands M.D.*¶¶#, J. David Spence M.D.¶¶

*Molecular Function and Imaging Program and the National Cardiac PET Centre, Division of Cardiology, Department of Medicine, Univ. of Ottawa Heart Institute, Ottawa, Ontario

†Imaging Research Laboratories, Robarts Research Institute, Western Univ., London, Ontario

‡Dept. of Pathology, Western Univ., London, Ontario

¶Dept. of Radiology, Univ. of Ottawa and The Ottawa Hospital, Ottawa, Ontario

†† Div. of Vascular Surgery, Dept of Surgery, Univ. of Ottawa and The Ottawa Hospital, Ottawa, Ontario

‡‡ Div. of Neurology, Dept of Medicine, Univ. of Ottawa and The Ottawa Hospital, Ottawa, Ontario

§§ Division of Cardiology, Montreal Heart Institute, Univ. of Montreal, Montreal, Quebec

¶¶ Stroke Prev. & Atherosclerosis Research Centre, Robarts Research Institute, Western Univ., London, Ontario

Consortium Affiliation - MITNEC; Supervisor - Dr. Rob Beanlands

Background:

Inflammation may contribute towards plaque instability. [18F]-fluorodeoxyglucose (FDG) uptake imaged with positron emission tomography (PET) and computed tomography (CT) may serve as a biomarker of plaque inflammation.

3-dimensional ultrasound (U/S)-derived total plaque volume (TPV) and vessel wall volume (VWV) are measures of plaque volume and vessel wall thickness that are used for monitoring carotid plaque progression and regression. The progression of TPV has been related to cardiovascular events.

Morphological volumetric assessment of plaque and the extent of inflammatory burden within plaque may independently predict plaque vulnerability. However, the interrelationship between FDG uptake and measures of TPV and VWV remains poorly understood.

We hypothesized that FDG uptake in high-risk carotid plaque is related to TPV and VWV.

Methods:

Thirty-seven patients (67±9 years, 9 female) scheduled for carotid endarterectomy were prospectively recruited for 3D U/S and FDG PET/CT imaging of the left and right internal carotid arteries.

Maximum FDG uptake normalized to blood (tissue to blood ratio - TBR) was measured for bilateral carotid plaque. Manual planimetry was used to measure bilateral TPV and VWV. Each 3-D image was sliced transverse to the vessel axis, with an increment of 1mm, moving from the bifurcation down the common carotid 2cm, and from the bifurcation up the internal and external carotid artery for 1.5cm. Plaque boundaries were manually traced.

Results:

U/S imaging was not feasible in 3 patients.

Maximum FDG uptake correlated with TPV ($r=0.42$, $p<0.001$) and VWV ($r=0.30$, $p=0.015$) (Figure 1). FDG uptake was greater in plaque scheduled for endarterectomy (TBR = 3.6 ± 1.3 endarterectomy vs. 3.0 ± 1.2 contralateral plaque, $p=0.049$). There was also a trend for greater TPV at the side of endarterectomy: $799 \pm 390 \text{ mm}^3$ endarterectomy vs. $672 \pm 150 \text{ mm}^3$ contralateral ($p=0.088$).

Conclusion:

FDG uptake in high-risk carotid plaque is related to TPV and VWV. The burden of inflammation and volumetric phenotype of plaque may synergistically provide a more robust evaluation of plaque vulnerability. Longitudinal follow-up for the assessment of plaque progression in this study cohort is currently underway.

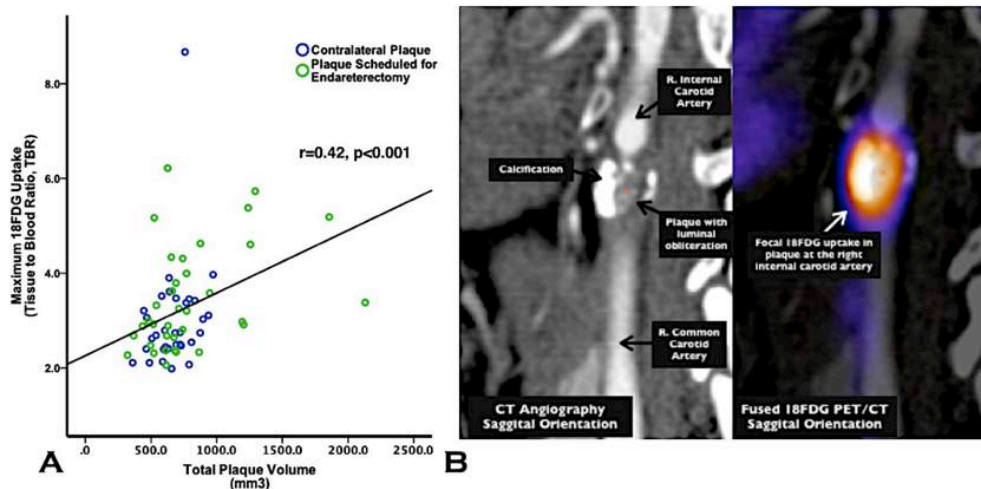


Figure 1. In patients with high-risk lesions, inflammation imaged with [18F]-fluorodeoxyglucose (18FDG) hybrid PET/CT correlates with 3-dimensional total plaque volume measured on ultrasound ($r=0.42$, $p<0.001$), (Panel A). Panel B: CT angiography (sagittal plane) fused with 18FDG PET in a 60-year old patient with a symptomatic right internal carotid artery plaque (arrow). From the PET/CT images, there is significant narrowing of the right internal carotid artery and luminal obliteration.

Characterization of Microvascular Function in Transgenic Rat Model of Alzheimer's Disease

Lewis I. Joo*, Adrienne Dorr, Margaret M. Koletar, Lysie A. M. Thomason, Bojana Stefanovic

Medical Biophysics, University of Toronto, Toronto, Ontario, Canada

Introduction The most common cause of dementia, Alzheimer's disease (AD) is clinically characterized by progressive decline of cognitive functions with pathological hallmarks of amyloid- β ($A\beta$) deposition, neurofibrillary tangle formation and neurodegeneration¹. Recent findings in AD progression through transgenic mice model showed the morphological and functional changes in cerebral microvascular network which seems to precede the onset of clinical symptoms^{2,3}. Application of this presymptomatic alterations in cerebral microvasculature to early detection of AD onset can be advanced through investigation using animal model that affords wider range of neuropsychological tests to assess cognitive decline observed with AD and enhanced recapitulation of AD pathologies. We here set out to examine the mechanism behind the functional changes in cerebral microvascular network in response to vasodilatory stimulation in a rat model that replicates wider spectrum of human AD pathologies and progressive cognitive decline compared to mice model previously used in our lab.

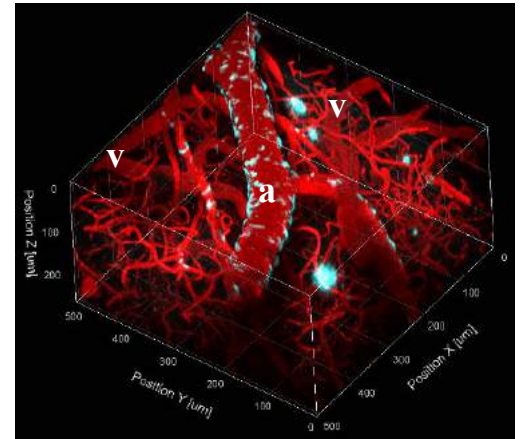


Figure 1: 3D image of cortical microvasculature (red) of transgenic rat model of AD. Cerebral amyloid angiopathy (CAA) around the arteriolar vessels and tissue plaques (cyan) stained with Methoxy-X04. a: arterioles. v: venules.

Methods Two-photon fluorescence microscopy was employed to image the microvessels of the non-transgenic (nTg) and transgenic (Tg) rat's primary somatosensory cortex in vivo while eliciting global vasodilation through CO₂ challenge. In addition to the craniotomy to remove skull and dura, the rats were tracheostomized and mechanically ventilated, with inspired CO₂ concentration profiles prescribed via digitally programmable gas mixer. The blood flow through microvessels were quantified as time-to-peak (TTP), time interval between the injection of fluorescent dye and occurrence of peak intensity in select microvessels through 1D-over-time imaging of bolus passage, during periodic triggered injection of 70kDa Texas Red dextran into tail vein. The TTP data from arterioles, capillaries, and venules were collected during normal air breathing and 10% CO₂ breathing. The morphology of transgenic rat's cortical microvasculature was acquired with Methoxy-X04 staining to show perivascular and parenchymal deposition of $A\beta$.

Results The cortical microvasculature with $A\beta$ deposition is shown in Figure 1. The reduction of TTP shortening due to CO₂ challenge from nTg to Tg, representing reduced increase in flow from CO₂ challenge in Tg was evident in arterioles and venules ($p < 0.05$). The dispersion of TTP got tighter with CO₂ challenge ($p < 0.01$) in arterioles and capillaries of nTg whereas it remained the same or wider in all vessel types of Tg. The tightening of TTP dispersion from CO₂ challenge compared to air breathing in nTg resulted in linear regression with fitted line slope close to 0.5, meaning 100% increase in flow as opposed to no change in relative flow in Tg.

Conclusions This work shows reduced cerebrovascular reactivity to global vasodilatory probe in rats with AD pathology along with morphological addition of $A\beta$ to the cortical microvasculature. Using the transgenic rat model of AD, more clinically applicable investigation of the functional changes in cerebral microvasculature can be obtained that could go toward explaining the mechanism behind the functional changes seen in brain with AD and eventually identifying early indicators of AD prior to the onset of clinical symptoms.

1. Querfurth HW, LaFerla FM. Alzheimer's disease. *New England Journal of Medicine* 2010; 362: 329–44.
2. Dorr A, Sahota B, et al. Amyloid- β -dependent compromise of microvascular structure and function in a model of Alzheimer's disease. *Brain* 2012; 135: 3039-50.
3. Lai AY, Dorr A, et al. Venular Degeneration leads to vascular dysfunction in a transgenic model of Alzheimer's disease. *Brain* 2015; 138: 1046-58.

Effects of exercise on human calf muscle in vivo sodium single and triple Quantum filtered magnetic resonance spectroscopy

Alireza Akbari MEng^{1,4}, Dinesh A. Kumbhare MD, MSc, FRCPC^{1,2} and Michael D. Noseworthy PhD PEng^{1,3,4}

¹McMaster School of Biomedical Engineering, McMaster University, Hamilton;

²Toronto Rehabilitation Institute, Faculty of Medicine, University of Toronto, Toronto;

³Electrical and Computer Engineering, McMaster University, Hamilton; ⁴Imaging Research Centre, St Joseph's Healthcare, Hamilton

Introduction Sodium plays a pivotal role in carrying out cellular processes during muscle contraction. A number of studies have used sodium MRI to study the effects of exercise on total sodium concentration (TSC) [1-3]. However, the knowledge of how the intracellular sodium content is affected by exercise would provide a better understanding of how myocyte physiology is altered in normal and diseased skeletal muscle at the cellular level. Triple quantum filtered (TQF) sodium MRI would be able to spatially map out the intracellular content of skeletal muscle. However, it requires long imaging times that makes it very hard to study acute changes in muscle physiology. Contrary to TQF sodium MRI, QF sodium MR spectroscopy would be sensitive to acute effects of exercise due to its high temporal resolution. The purpose of this work was to demonstrate how exercise affects the QF sodium spectrum in human calf muscle.

METHODS MRI experiments were performed using a GE MR750 3T (General Electric Healthcare, Milwaukee WI) and a home-built 6-inch diameter transmit/receive sodium surface coil. An in-house-made MRI compatible ergometer was used to carry out ankle plantar flexion exercise in the bore of the magnet concurrent with spectroscopy scans. A total of nine healthy normal subjects (7 male and 2 female, mean age = 26.3 ± 4.5 years) were recruited. For a point-to-point comparison between SQF and TQF data across time, the same acquisition parameters were used for both SQF and TQF sequences (i.e. TR = 166.7ms, number of complex points = 1024, and spectral bandwidth = 15.625kHz, hard pulse width = $500 \mu\text{s}$, flip angle = 90° , number of averages = 6, Total scan time = 14min). The subject started performing ankle plantar flexion two minutes into the scan for a period of 2 minutes at a frequency of 0.5 Hz pushing against a load of 30% of maximum voluntary contraction (MVC). Sodium SQF and TQF peak intensities at each time point were calculated.

RESULTS Figure 1 demonstrates how sodium TQF signal time signal is affected by exercise in comparison to the rest period. The results demonstrated in figure 2 indicate that SQF signal intensity tends to increase and overshoot the resting period level and slowly recover back to baseline after exercise. However, the TQF decreased during exercise and almost immediately recovered back to baseline after exercise cessation.

CONCLUSIONS Our results demonstrate how exercise affects SQF and TQF sodium spectroscopy in skeletal muscle. The post-exercise slow recovery of the SQF signal is expected and is lower than reported value (i.e. a 30-minute half-life) reported by the previous TSC MRI studies done on exercising calf muscle [1-3]. The increase in the SQF intensity could be well due to increase in T_2 relaxation time of the sodium in the exercising muscle as a result of alteration in water content of the muscle, which is also suggested by other studies [4,5]. During exercise, the intracellular fraction of restricted water molecules decreases [6] and hence intracellular space becomes more, so to speak, diluted leading to decrease in the sodium macromolecular interactions and in TQF signal. This could explain why the TQF levels decrease during exercise. As the exercise terminates, cellular homeostasis will restore the cell back to resting state and the TQF signal goes back up. QF MRS offers a very high temporal resolution for studying exercise acute effects in the skeletal muscle that could help study muscle diseases.

REFERENCES [1] Constantinides CD, et al. Radiology. 2000;216(2):559–68. [2] Bansal N, et al. J Magn Reson Imaging. 2000;11(5):532–8. [3] Chang G, Wang L, et al. Eur Radiol. 2010;20(8):2039–46. [4] Fleckenstein JL, et al. AJR Am J Roentgenol. 1988;151(2):231–7. [5] Fullerton GD, Potter JL, et al. Magn Reson Imaging. 1982;1(4):209–26. [6] Bratton CB, et al. Science. 1965;147(3659):738–9.

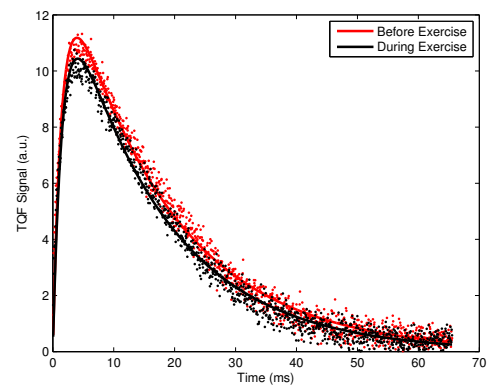
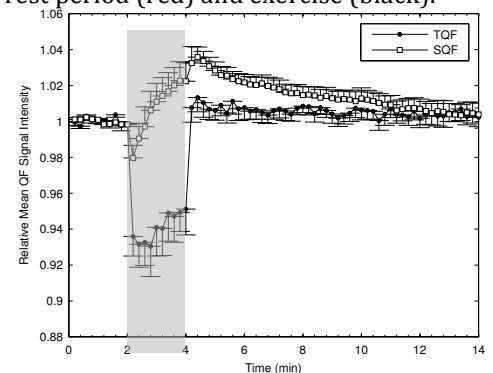


FIG. 1. Sodium TQF free induction decay acquired from human calf muscle during rest period (red) and exercise (black).



Mean \pm SE obtained from 9 individuals' relative SQF and TQF ^{23}Na signal intensities. The shaded area represents exercise regime at 30% subjects' MVC.

T. Coutinho, K. Srivaratharajah, R. Beanlands, L. Mielniczuk, R. deKemp

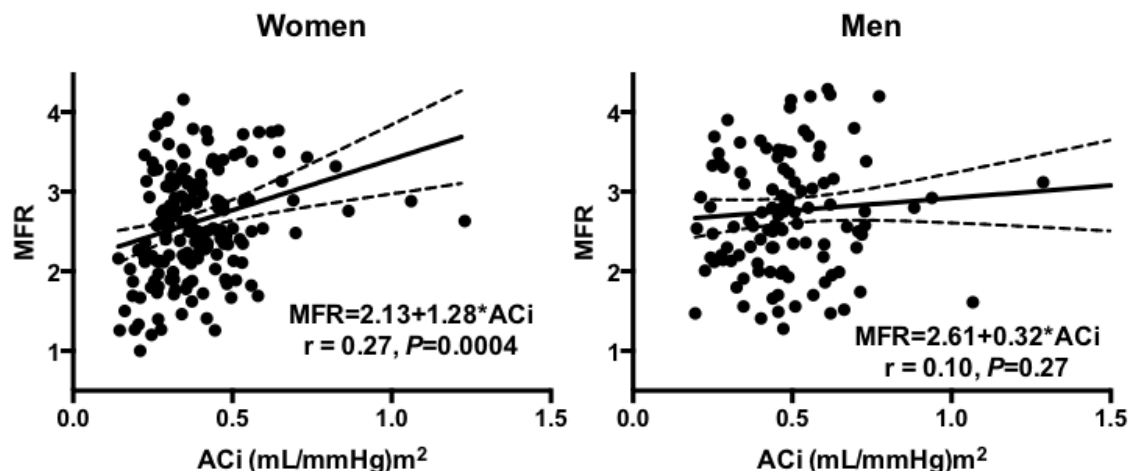
University of Ottawa Heart Institute, Cardiology, Ottawa, Canada

Background: Heart failure with preserved ejection fraction (HFpEF) predominantly affects hypertensive women, with coronary micro-vascular dysfunction and rarefaction recently described as novel arterial abnormalities. To determine alterations in ventricular-arterial interactions that may predispose to HFpEF, we evaluated sex-specific associations of hemodynamic load with micro-vascular coronary artery function in subjects without heart failure.

Methods: Subjects with a cardiac ^{82}Rb positron-emission tomography between 2010 and 2013, ejection fraction $\geq 50\%$, no heart failure, dyspnea, coronary artery disease or regional perfusion defects were eligible. Left ventricular microvascular reactivity was assessed by myocardial flow reserve (MFR = peak hyperemic stress/rest myocardial blood flow). “Low MFR” was defined as the lowest sex-specific quartile. Steady and pulsatile components of load were estimated by systemic vascular resistance index [SVRI = $(80 \times \text{mean arterial pressure} / \text{cardiac output}) \times \text{BSA}$] and indexed aortic compliance [AoCi = $(\text{stroke volume} / \text{pulse pressure}) / \text{BSA}$], respectively. Multivariable linear and logistic regression evaluated associations of SVRI and AoCi with MFR and “low MFR”, adjusting for age, heart rate, hypertension, diabetes, dyslipidemia, smoking, use of aspirin, statins and anti-hypertensives. Interaction terms for sex and hypertension with load measures were included.

Results: 297 subjects (61% women, age: 61.3 ± 11.0 yrs) were eligible. Risk factors, medications and MFR did not differ, but SVRI was higher [5348 ± 1676 vs. 4616 ± 1514 (dyn-s/cm 5) m 2] and AoCi was lower [0.40 ± 0.16 vs. 0.52 ± 0.28 (mL/mmHg)/m 2] in women ($P < 0.0001$), confirming greater arterial load in women. Interaction analyses showed that associations of SVRI and AoCi with MFR were only present in hypertensive women ($\beta \pm \text{SE}$: 0.24 ± 0.09 , $P = 0.008$ and 0.21 ± 0.08 , $P = 0.01$, respectively). Findings persisted after adjusting for rest flow. Each 1SD decrease in SVRI and AoC was associated with 2.24 (95% CI: 1.12–4.98, $P = 0.02$) and 1.95 (1.06–4.70, $P = 0.03$) greater odds of having “low MFR”, respectively, in hypertensive women. SVRI and AoCi interacted in the prediction of MFR ($P = 0.01$).

Conclusions: In subjects at highest risk for HFpEF (hypertensive women), but not in men or normotensive women, lower steady and higher pulsatile arterial load were associated with worse MFR. Since coronary perfusion is related directly to diastolic and inversely to systolic aortic pressure, a combination of lower SVR and higher aortic stiffness (lower AoCi) in hypertensive women may adversely affect the coronary microvasculature, a mechanism that could predispose to HFpEF.



Gadolinium-Free Blood Pool MRI Contrast Agents for High Clinical Field at 3 T: Comparative Studies of Two Mn(III) Porphyrin Dimers

Hanlin Liu^{a,b}, Weiran Cheng^{a,b}, Shili Dong^b, Feng Xu^b, and Xiao-An Zhang^{a,b,c*}

^aDepartment of Chemistry, University of Toronto. ^bDepartment of Physical and Environmental Sciences,

^cDepartment of Biological Sciences, University of Toronto Scarborough

Background: Magnetic resonance angiography (MRA) provides high resolution anatomical and functional information of the vascular system without exposure to ionizing radiation. MRA signals can be improved using blood pool agents (BPAs), a class of special MRI contrast agents (CAs) that have prolonged vascular retention and thus selective contrast enhancement in blood vessels. Currently, the only FDA approved BPA is Gadofosveset, which is a Gd-based CA (GBCA). Gadofosveset binds non-covalently to human serum albumin (HSA) to avoid rapid extravasation and to achieve long blood circulation. Its extended retention, however, will increase the risk of Gd-release *in vivo*, which is the confirmed cause of nephrogenic systemic fibrosis (NSF), a life-threatening side effect of GBCAs occurring mainly in patients with renal dysfunction. Moreover, the sensitivity of Gadofosveset-HSA complexes (measured as T_1 relaxivity or r_1) sharply decreases at high clinical fields. To combat these issues, we recently developed MnP2 as the first Gd-free BPA based on the manganese (III) porphyrin (MnP) platform.^{1,2} MnPs reduce the risk of toxic side effects since they are highly stable against metal release and unlike Gd, Mn is a micronutrient. Moreover, certain MnPs exhibit high r_1 at magnetic fields up to 3 T, making them superior candidates for high-field MRA. Herein, we report the development of the second generation MnP-based BPA, *m*-MnP2, and investigate the relaxivity and HSA binding of both constitutional isomers with different biphenyl linkers (Fig1), which are highly involved in HSA binding.

Methods: Both MnP2 and *m*-MnP2 were synthesized through similar pathways involving four steps. The field-dependent r_1 (NMRD profiles) was obtained with a fast field cycling NMR relaxometer (SMARTracer™) coupled with a cryogen-free superconducting magnet (HTS-110), covering magnetic fields from 0 to 3 tesla. HSA binding interactions of both MnPs and their metal-free analogs were monitored with optical methods including UV-vis absorption, circular dichroism (CD) and fluorescence spectra.

Results and Discussion: Both MnP dimers were successfully synthesized. The products and their synthetic

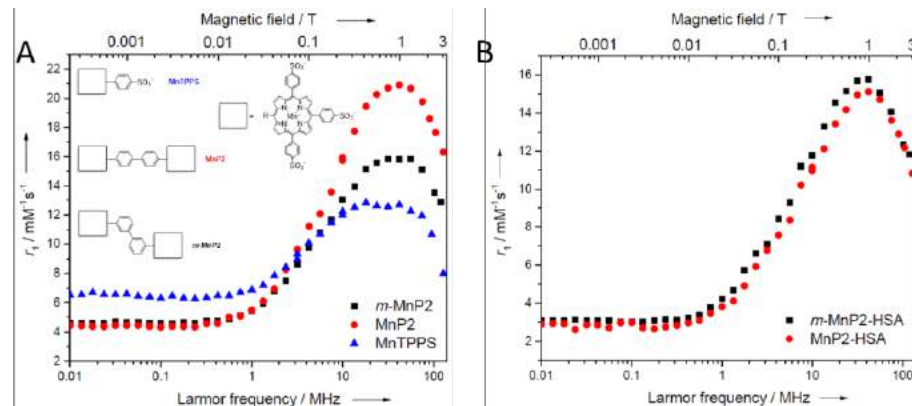


Figure 1. NMRD profiles of free or HSA-bound MnPs from 0.01-128 MHz at 25 °C (A) free MnP2, *m*-MnP2, and MnTPPS (B) MnP2-HSA and *m*-MnP2-HSA.

intermediates were purified and structurally characterized by HPLC, MS, NMR and UV-vis spectroscopy. Both MnP dimers exhibit higher relaxivities in comparison to MnTPPS, the monomeric MnP building-block, and Gd-DTPA (a GBCA), especially at high magnetic fields. The fully extended MnP2 has the highest r_1 while the r_1 curve of conformationally twisted *m*-MnP2 is somewhere between the MnTPPS monomer and extended dimeric MnP2 (Fig. 1a). This r_1 trend is consistent with the predicted hydrodynamic sizes, indicating that decreases in molecular tumbling rate of MnPs enhance the r_1 . MnP2 forms a high affinity complex with HSA with a K_d of $0.55 \pm 0.26 \mu\text{M}$, while *m*-MnP2 has a K_d of $16.5 \pm 1.5 \mu\text{M}$, as monitored by UV-vis and CD spectroscopic titration. In comparison, the affinity of Gadofosveset to HSA is considerably lower ($K_d = 90 \mu\text{M}$). Upon HSA binding, MnP2 and *m*-MnP2 exhibit similar NMRD profiles (Fig 1b). At the high clinical field of 3 T, the HSA complexes of both MnP dimers exhibit a molar relaxivity above $20 \text{ mM}^{-1} \text{ s}^{-1}$ due to the dimer-construction, twice the sensitivity of Gadofosveset.

Conclusion: We demonstrated that the biphenyl linker of MnP dimers has a direct impact on molecular geometry, and thus the relaxivity and HSA binding, providing a rational approach for tuning the sensitivity and potentially the pharmacokinetics of MnP-based BPAs. Both MnP dimers exhibit higher r_1 at 3 T and higher affinities to HSA in contrast to Gadofosveset, making them suitable candidates for high-field vascular imaging.

References: ¹ *J. Med. Chem.* **2014**, *57*, 516-520. ² *J. Biol. Inorg. Chem.* **2014**, *19*, 229-235.

Sparse-view quantitative CT perfusion imaging of liver

¹Esmail Enjilela, ^{1,2}Ting-Yim Lee, ³Jiang Hsieh, ^{1,2}Errol Stewart, ¹Mark Dekaban, ¹Feng Su, and ^{1,2}Aaron So

¹Imaging, Robarts Research Institute, London, Ontario, Canada

²Imaging, Lawson Health Research Institute, London, Ontario, Canada

³CT Engineering, GE Healthcare, Waukesha, Wisconsin, United States

Introduction. Radiation dose of a quantitative CT liver perfusion study can be potentially reduced by acquiring less number of projections in dynamic contrast enhanced (DCE) scanning. We investigated the effectiveness of sparse-view DCE image reconstruction with filtered backprojection (FBP) and compressed sensing (CS) for CT perfusion imaging of the liver.

Method. DCE liver images were acquired from a 68 kg patient after intravenous contrast injection (Isovue 370) at 4 mL/s and 0.7 mL/kg of dosage with a 64-slice GE Healthcare CT750 HD scanner. A 75 mm section of the liver was scanned dynamically at 120 kVp, 70 mA and 0.4s gantry period, using an axial shuttle mode in which the scanner table joggled between two adjacent 40 mm sections for 42 times. The duration of dynamic acquisition was 2.1 minutes and the patient was free breathing throughout.

The measured projections were corrected for beam hardening prior to image reconstruction with FBP and CS. DCE liver images were reconstructed from all 984 projections using FBP, and 1/3 and 1/4 of full projections (328 and 246 respectively), evenly distributed over 360° using both FBP and CS. Each set of 5 mm thick DCE liver images were manually registered with the Analyse 10.0 software before analyzed with the CT Perfusion software (GE Healthcare) to generate hepatic arterial blood flow (HABF) maps. HABF values measured from the sparse-view protocols (246 and 328 views with FBP and CS) were compared against that from the full-view FBP protocol.

Results. Figure 1 compares a DCE liver image acquired from 984-view FBP (A) to those from different sparse-view protocols: 328-view FBP (B), 246-view FBP (C), 328-view CS (D) and 246-view CS (E). The corresponding HABF maps are shown in Fig. 2. HABF measured from full-view FBP was not different from those from 328-view FBP and 328-view CS: 60.6 versus 63.1 and 62.2 mL/min/100g in the liver tumor (red arrows in Fig. 2), and 27.7 versus 25.6 and 23.4 mL/min/100g in the adjacent normal liver tissue (yellow arrows in Fig. 2), respectively. The findings suggested that hepatic arterial liver perfusion can be measured from only 1/3 of full projections that is conventionally used. In the extremely sparse condition where the number of projection was reduced to 246, FBP failed to minimize streaks in the reconstructed DCE images (Fig. 1C), leading to large discrepancy in HABF measurement from the standard full-view FBP method: 37.0 vs. 27.7 mL/min/100g in tumor (-25% difference), and 70.5 vs. 60.6 mL/min/100g (16.3% difference) in normal tissue, respectively. By contrast, DCE images generated from the same number of projections (246) with CS was without streaks (Fig. 1E) and the HABF derived from these images with CT Perfusion was in good agreement with the full-view FBP method: 29.8 versus 27.7 (-7.6% difference) in tumor, and 55.1 versus 60.6 mL/min/100g (-9.1% difference) in normal tissue, respectively.

Conclusions. Our preliminary results suggest that only 1/3 of full projections are needed in CT liver perfusion measurement, as HABF maps generated from FBP DCE liver images do not require high spatial resolution. CS may be more reliable than conventional FBP in preserving image quality and accuracy of liver perfusion measurement in attempt to achieve maximal dose reduction by further reducing the number of projection measurement in DCE acquisition.

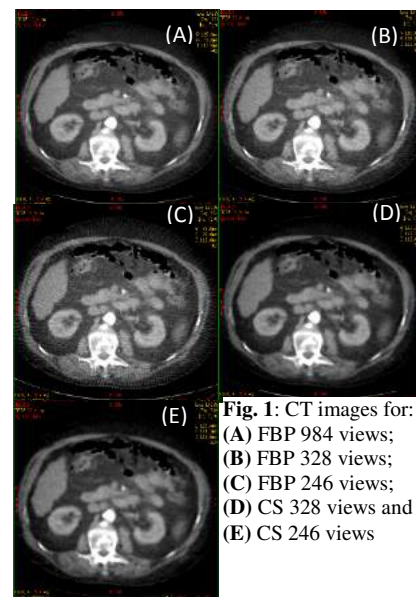


Fig. 1: CT images for: (A) FBP 984 views; (B) FBP 328 views; (C) FBP 246 views; (D) CS 328 views and (E) CS 246 views

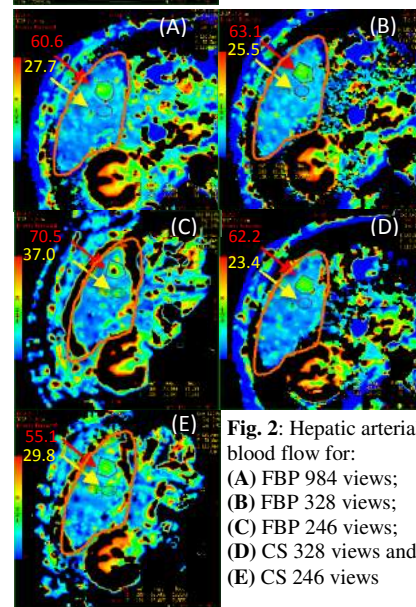


Fig. 2: Hepatic arterial blood flow for: (A) FBP 984 views; (B) FBP 328 views; (C) FBP 246 views; (D) CS 328 views and (E) CS 246 views

Developing a combined contrast kinetic model for assessment of post-infarction inflammation using hybrid PET/MRI

Primary: Benjamin Wilk¹, Supervisor: Jonathan D. Thiessen², Jane Sykes², Gerald Wisenberg², John Butler², Michael Kovacs², Robert T. Thompson², Supervisor: Frank S. Prato²

¹Western University, ²The Lawson Health Research Institute

Introduction: The remodeling process after myocardial infarction (MI) involves a complicated interplay of reperfusion and inflammatory processes which leads to the development of a cardiac patch [1]. However, the remodeling process may also have adverse effects that can ultimately result in heart failure [2]. More than 500,000 Canadians are affected by heart failure and this number is steadily increasing [3]. A kinetic model for combined contrast with a constant infusion of Gd-DTPA and ¹⁸F-FDG might help determine the extent of fibrosis and inflammation in the heart after myocardial infarction (a major determinant of heart failure), and overcome the lack of penetration of tracer following bolus injection into zones of severely compromised flow. We followed the progression of inflammation after MI from baseline to 40+ days in a well-characterized canine model wherein ¹⁸F-FDG uptake by macrophages serves as a surrogate marker of inflammation [4, 5]. Previous attempts by other groups, to model both Gd-DTPA and ¹⁸F-FDG have been limited to either separate acquisitions [6] or static analysis [7] of late gadolinium enhancement and ¹⁸F-FDG uptake in MI.

Methods: To study the early stages of infarction, the left anterior descending coronary artery was permanently occluded in four bred-for-research hounds. Using a 20% lipid infusion, the normal myocardial uptake of ¹⁸F-FDG was suppressed. The animals were imaged at 3, 8, 15, 22 and 43 days following surgery and PET/MRI data were collected before, during and after a 60 minute constant infusion of ¹⁸F-FDG (0.17 MBq·min⁻¹·kg⁻¹) and Gd-DTPA (0.004 mmol·min⁻¹·kg⁻¹). PET data was collected in list-mode and reconstructed into 3 minute frames. MRI data was collected at 10 minute intervals. T1 maps were used to derive Gd-DTPA concentration maps [8]. The extracellular/extravascular volume (ECV) is defined as the Gd-DTPA concentration in the tissue divided by the plasma concentration and corrected for the hematocrit. Using the resulting maps, regions of the myocardium which were remote, infarcted but without MR evidence of microvascular obstruction (I), and infarcted with microvascular obstruction (MO) could be identified. Due to the suppression of myocardial uptake by the lipid infusion, this uptake of FDG in the heart is primarily from macrophages, and tracks the inflammatory response. Initial approaches to modeling the data include the extended Tofts [9] and the Patlak [10] models. Both models describe a transfer constant (K_{trans} and K_i , respectively) and a plasma volume fraction (V_p). The metabolic rate of glucose is given by the K_i value multiplied by the measured plasma glucose level and divided by the lumped constant (assumed to be 1.1 for dogs [11]).

Results: It was found that, while the rate of increase of the concentration of Gd-DTPA and FDG in the plasma initially was rapid, it slowed down as the infusion progressed. The concentration in both the I and MO regions increased linearly with time during the entire constant infusion time. Once the constant infusion ended, the concentration in the blood pool rapidly declined while it continued to increase linearly, and had a positive slope in both the I and MO regions, although at a reduced rate. However, no visible MO was found on day 43 in any of the animals. During the infusions, the ECV quickly reached an equilibrium point of 0.25 in the remote myocardium. However, in both the I and MO regions, this value continued to rise beyond the end of the infusion. Early attempts at modeling the data have shown a high metabolic rate of glucose in the infarcted region describing the inflammatory response with an increased ECV.

Conclusions: Using gadolinium enhanced MRI allows us to identify I and MO regions which would not be possible using PET alone. Dynamic Gd-DTPA and ¹⁸F-FDG concentrations were acquired simultaneously, allowing us to measure the ECV and perfusion rates into the infarcted region using both tracers, which can then be compared and ultimately assembled into a combined contrast kinetic model of glucose metabolism of the macrophage cells. This research represents a unified kinetic model using simultaneous PET/MRI that will give exciting new insights into the remodeling process after a myocardial infarction.

References: 1. Sutton *et al.* 2015, *Clin Cardiol: New Frontiers*, 2981–2988 2. Frangogiannis *et al.* 2014, *Nat Rev Cardiol*. 11(5), 255–65 3. Ross *et al.* 2006, *Can J Cardiol*, 22(9), 749–754 4. Prato *et al.* 2015 *J Nuc Med*, 56(2), 299–304 5. Lee *et al.* 2012, *J Am Coll Cardiol*, 59(2), 153–163 6. Poulin *et al.* 2014, *Magn Reson Med*, 748, 740–748 7. Rischpler *et al.* 2015, *Eur Heart J Cardiovasc Imag*, 16(6), 661–9. 8. Gerber 2008, *J Cardiovasc Mag Res*, 10:18 9. Tofts 2010, *MAGNETOM Flash*, 1–5 10. Patlak 1983, *J Cerebr Blood F Met*, 3(1), 1–7 11. Kofoed *et al.* 2000, *Cardiovasc Res*, 45(2), 321–329

Dual-Energy Micro-Computed Tomography in a Rat Hindlimb Model of Osteoarthritis

Justin J. Tse,^{1,3} Vasek Pitelka,² Joy Dunmore-Buyze,^{1,3} Maria Drangova,^{1,3} and David W. Holdsworth^{1,3,4}

Development of Novel Therapies for Bone and Joint Diseases Consortium

¹Robarts Research Institute, ²Department of Physiology and Pharmacology, ³Department of Medical Biophysics, ⁴Department of Surgery
Western University, London, Ontario, Canada

Introduction: The ability to routinely image and quantify the vasculature near and within bone is important for understanding joint diseases such as osteoarthritis (OA). The small size of the vasculature (*i.e.* <10 μm), lack of inherent x-ray contrast, and proximity to dense local environments has made these studies challenging with current imaging techniques. A recent advancement in dual-energy micro-computed tomography (DECT)¹ demonstrated the ability to resolve perfused vasculature from bone, but required high energies (140 kVp). We describe a DECT technique that is applicable to a large installed base of micro-CT scanners, which operate up to 90 kVp. Our technique combines a novel *ex-vivo* Erbium-based vascular perfusion contrast agent, Erbium-based x-ray filter, DECT protocols, image co-registration, and decomposition. Combined with a rat hindlimb model of OA², our technique facilitates the visualization and quantification of vessels and bone. This will provide new information regarding vascular changes during the initiation and progression of OA.

Methods: Our novel *ex-vivo* vascular perfusion contrast agent was based on a silicone rubber (MV-132, Microfil) with added Er powder (14 wt%), providing sufficient contrast and an optimal K-edge energy (57.5 keV). Dual-energy scans were performed on a micro-CT scanner (Vision120, GE HealthCare). Low-energy scans were performed at 70 kVp and 50 mA, with an additional custom cylindrical resin filter with added Er powder (0.19 g/ml) and a total pathlength of 6 mm. High-energy scans were acquired at 90 kVp and 40 mA, with a 480 μm Cu filter. Each scan was 3 hrs, 1200 projections, 0.3° increments, 160 ms per view, and an isotropic resolution of 50 μm . Ten Teflon beads (1.58 mm) along the sample allowed for sub-voxel rigid-body fiducial registration. Decompositions were performed as previously described.¹ To study vascular changes due to OA, male Sprague-Dawley rats (N=54) were separated into two groups (N=6) as controls or those with surgically induced OA, and studied at five time points (T=0,1,2,4,8 weeks).

Results: Our novel contrast agent provided substantial contrast enhancement of the perfused vasculature (3576 \pm 138 HU at low energy, 4328 \pm 182 HU at high energy), with background noise of 28 HU. In addition, sufficient vascular perfusion was observed, as judged by the filling of the popliteal artery and vein (Fig. 1 arrow), a major blood supply for the femoral-tibial joint. Downsampled reconstructions (*i.e.* 100 μm resolution) provided sufficient resolution to separate soft tissue, bone (Fig. 1c), and vasculature (Fig. 1d), with <5% cross-contamination between components. This allowed for the visualization of the small and dense vascular network around and within bone (Fig. 1ef).

Conclusions: We successfully demonstrated our technique by decomposing sub-voxel co-registered images into soft tissue, bone, and perfused vasculature. This technique will be implemented in a surgically induced rat hindlimb model of OA to observe the vascular changes that may occur during the initiation and progression of OA.

References: **1.** Granton PV, et al. Implementation of dual- and triple-energy cone-beam micro-CT for postreconstruction material decomposition. *Med Phys* 2008;35:5030-5042. **2.** McErlain DD, et al. Study of subchondral bone adaptations in a rodent surgical model of OA using in vivo micro-computed tomography. *Osteoarthr Cartil* 2008;16:458-469.

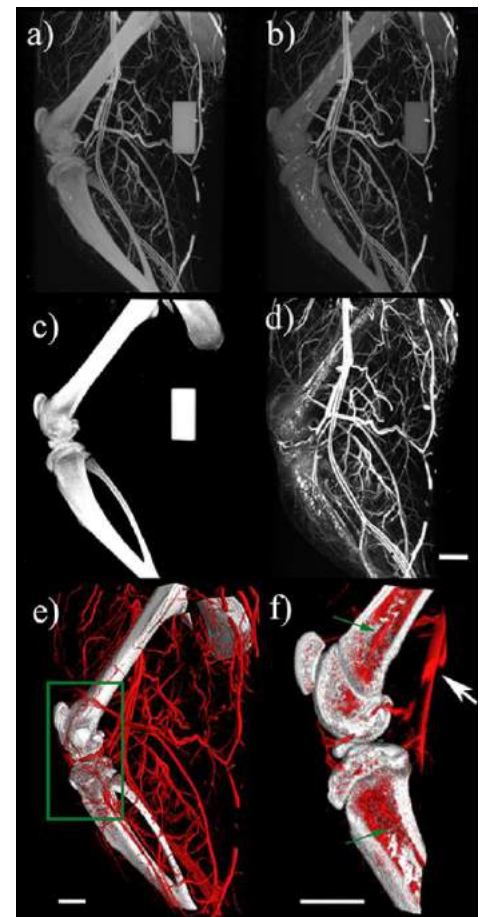


Fig. 1: Results of a perfused rat hindlimb (a) low energy; (b) high energy; (c) bone; (d) vasculature; (e) 3D visualization of bone (white) and vessel (red) interaction; and (f) interior view of the green box in (e). Scale bars represent 5 mm.

Vascular contrast agent for preclinical dual energy computed tomography

Charmaine Cruje,^{1,3} Olivier Nguon,² Elizabeth Gillies,² and Maria Drangova^{1,3}

¹Department of Medical Biophysics, ²Department of Chemistry, ³Robarts Research Institute
The University of Western Ontario, London, Ontario, Canada

Supervisors: M. Drangova and E. Gillies

Consortium: Development of Novel Therapies for Bone and Joint Diseases

Introduction. Dual energy computed tomography (DECT) has been introduced clinically and in preclinical studies. For *in vivo* vascular studies, a contrast agent is required to distinguish between the blood pool and soft tissues. While vascular contrast agents with long circulation times exist for preclinical imaging, they use iodine as the contrast material; iodine has a low k-edge (33.2 keV), which is not optimal for DECT. An optimized contrast agent for vascular DECT must contain an element with a k-edge in the range of approximately 50-65 keV and remain in the bloodstream in sufficient quantities during imaging, which can be on the order of 5-10 minutes. To remain in the blood pool over several minutes, the contrast agent must be composed of particles that are at least 10 nm in size. All lanthanides have k-edges in the required range, with Gadolinium (Gd) having a k-edge of 50.2 keV. While used clinically as MRI contrast agents, the Gd compounds do not have sufficiently high concentrations of Gd and have rapid clearing times (with molecular sizes less than 1 nm). Therefore, the aim of this study is to synthesize a contrast agent containing Gd with particle sizes exceeding 10 nm and sufficient Gd loading to provide contrast in preclinical vascular micro CT.

Methods. Spherical nanoparticles (*seeds* and *particles*) were synthesized following a method reported by Bridot et al.¹ Gd trichloride was exposed to thermal and chemical treatments using diethylene glycol and sodium hydroxide so that Gd oxide *seeds* under 5 nm in size were formed. These were used to make Gd oxide *particles* by subjecting the *seeds* to further thermal and chemical treatments, and additional Gd trichloride. The samples were observed by transmission electron microscopy (TEM) using a Philips CM10 microscope. Nanoparticle sizes were evaluated using ImageJ, where each nanoparticle was treated as a circle. Hydrodynamic diameters were measured by dynamic light scattering (DLS) using a Malvern Zetasizer Nano ZS instrument.

Results and Discussion. TEM images of the Gd oxide *seeds* are shown in Figure 1. In the selected image, the average dimension of Gd *seeds* was 4.1 ± 1.1 nm. As shown in Figure 2, the average hydrodynamic diameter of the seeds was 2.5 nm with a polydispersity index of 0.2, indicating a moderately polydisperse size distribution. Initial attempts have suggested that it is possible to grow the *seeds* into *particles* by resubjecting them to treatment with Gd trichloride and sodium hydroxide in diethylene glycol. Further development and characterization of nanoparticles are underway to obtain desired diameters and ensure sufficient Gd loading. Surface modification may also be done to promote circulation times as well as to ensure biocompatibility.

References. [1] Bridot, J.L., et al. J Am Chem Soc 2007; 129(16): 5076-5084.

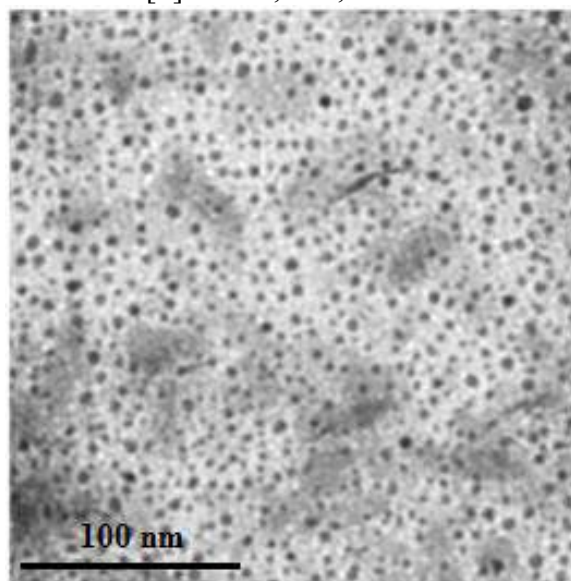


Figure 1. TEM image of Gd oxide *seeds*.

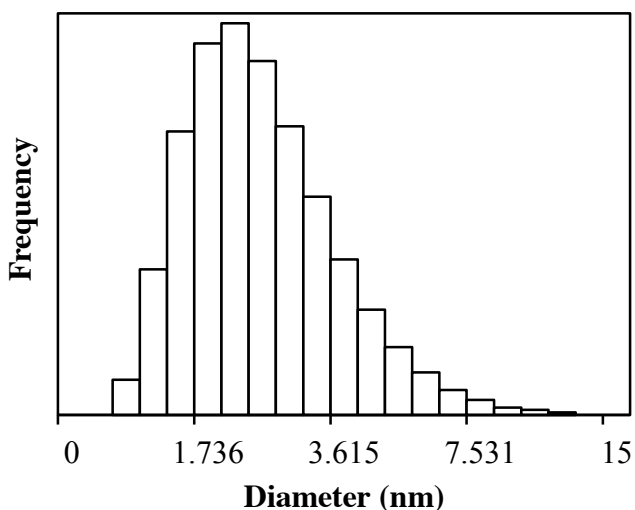


Figure 2. Hydrodynamic diameters of Gd oxide *seeds*.

A micro-CT-integrated radiolucent treadmill for fluoroscopic gait assessment in small-animal models

Adam D.M. Paish^{1,3}, Tomacz Chmiel¹, Steven I. Pollmann¹, David W. Holdworth^{1,2,3} (Supervisor)

Development of Novel Therapies for Bone and Joint Diseases Consortium

¹Robarts Research Institute, ²Department of Surgery, ³Department of Medical Biophysics, Schulich School of Medicine and Dentistry, Bone and Joint Institute, Western University, London, Ontario, Canada

Introduction: Small animal models serve as valuable platforms for research into novel therapies for bone and joint diseases, including osteoarthritis¹ and joint replacement studies^{2,3}. As changes in functional mobility are central to musculoskeletal diseases, imaging functional movement pre- and post-intervention is invaluable when assessing treatment efficacies¹. Systems for kinematic analysis of skeletal structures utilizing x-ray fluoroscopy to image joints as they experience cyclic motion exist, however these systems are built for human and large-animal models. We describe the development of a radiolucent treadmill for small-animal gait studies that can be integrated with a commercially available micro-CT system with fluoroscopic capacity. Our objective is to visualize rat skeletal gait during locomotion with distinguishable bone boundaries uninhibited by artifacts from the treadmill.

Methods: Carbon fibre tubing was used to support an acrylic enclosure that houses the treadmill. Air holes were drilled into either end of the enclosure to ensure adequate ventilation. A commercially available rat treadmill belt (90x10 cm, Harvard Apparatus) was mounted between two plastic rollers 3.8 cm in diameter attached to low-friction plastic bearings. Deterrent rails were placed in close proximity to the rear roller to prevent the animal from falling below the treadmill. A stepper motor was rigged to a rubber drive belt to power the unit, controllable by a laptop. The completed unit (51.0 x 15.8 x 13.3 cm) was then integrated with a commercially available micro-CT scanner (eXplore Ultra, GE Medical), which has been modified to provide high-resolution fluoroscopy at 60 Hz. After the treadmill was tested numerous times at speeds between 0 and 125 cm•s⁻¹, an unanaesthetized male Sprague Dawley rat (660g) was placed inside the treadmill and allowed to acclimatize to running on the unit at speeds between 12 and 25 cm•s⁻¹. N=6 fluoroscopy trials were conducted in total; imaging in both the dorsal-ventral plane and the medial-lateral plane at belt speeds of 12 cm•s⁻¹ and 25 cm•s⁻¹ (80 kVp, 50 mA, 16 seconds) and trials in each view plane at 12 cm•s⁻¹ with different x-ray exposure parameters (120kVp, 20mA, 16 seconds).

Results: We successfully acquired and analyzed fluoroscopic video of the rat running at speeds of 12 cm•s⁻¹ and 25 cm•s⁻¹. Hind-limb anatomy was visualized satisfactorily over multiple consecutive gait cycles during each of the n=6 trials. Clear visualization of the bone boundaries was achieved (Fig 1b, 1c) with both sets of x-ray parameters. Although some blurring was observed during peak limb swing velocities, no confounding artifacts from the treadmill were observed overlaying the skeletal anatomy.

Conclusions: We have demonstrated that x-ray fluoroscopy in the bore of a commercially available small-animal scanner is possible for visualizing locomotion in rats. This device is the first of its kind and will provide a new tool to investigate kinematics in small-animal models. Subsequent iterations of our device will include a self-pacing mechanism to increase the efficacy of hind-limb visualization during the entire scan duration.

References: 1. McErlain et al. An in vivo investigation of the initiation and progression of subchondral cysts in a rodent model of secondary osteoarthritis *Arthritis Research and Therapy*. 2012; Feb 3;14(1):R26. 2. Paish et al. Image-based design of a rat hip prosthesis. *CSHRF National Competition*. 2015-06-02. 3. Powers et al. The rat as an animal model for total hip replacement arthroplasty. *J Invest Surg*. 1995; Sep-Oct 8(5): 349-62.

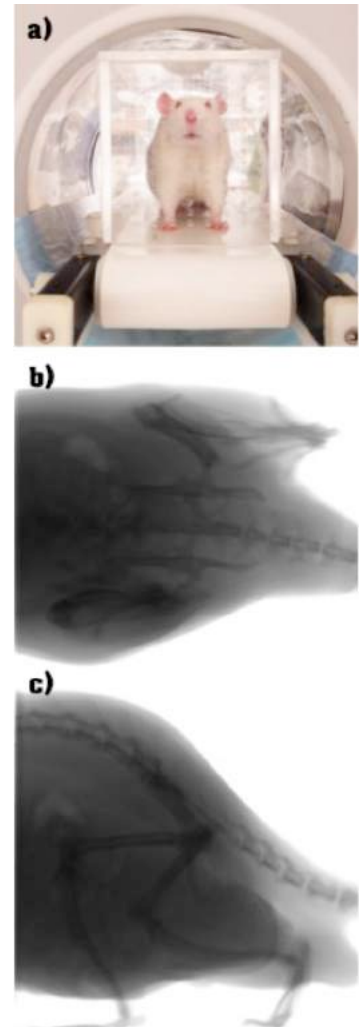


Fig. 1: (a) A radiolucent treadmill integrated into a micro-CT scanner housing a rat. Fluoroscopic still frames of a rat during locomotion in (b) ventral-dorsal and (c) medial-lateral views.

HDL-like Nanoparticles for Dual-Wavelength Cancer Imaging and Image-Guided Therapy

Marta Overchuk^{1,2}, Juan Chen², Gang Zheng²

¹Institute of Biomaterials and Biomedical Engineering, University of Toronto; ²Princess Margaret Cancer Centre and Techna Institute, University Health Network, Toronto, ON, Canada and Department of Medical Biophysics, University of Toronto, Toronto, ON, Canada.

Introduction. Timely, effective and non-invasive cancer detection is a prerequisite for successful personalized treatment. Near infrared (NIR) fluorescence imaging is one of the most promising strategies for cancer visualization due to its excellent sensitivity and high potential for combination with other imaging and therapeutic modalities. High density lipoprotein-mimicking nanoparticles (HPPS) provide an ideal platform for delivery of various imaging agents and drugs due to their incredibly small size (~12 nm) and strong selective uptake by scavenger receptor class B type 1 (SRB1)-expressing tumors (such as prostate). In current study we designed BP-HPPS, an HDL-mimetic nanoparticle, containing bacteriopheophorbide (Bchl)-lipid conjugate in its amphiphilic shell and pyropheophorbide (Pyro)-oleate in the hydrophobic core. These two NIR fluorophores possess strong photosensitizing properties, which makes them ideal multimodal agents for cancer image-guided photodynamic therapy.

Methods. BP-HPPS were synthesized by previously described method (5 mol% Bchl-lipid, 0.3 μ mol Pyro-oleate) [1]. BP-HPPS were characterized by ultraviolet-visible and fluorescence spectroscopy. Cellular uptake specificity was confirmed by incubating BP-HPPS with mSRBI (SRB1⁺) and ldlA7 (SRB1⁻) cells and evaluating nanoparticle binding and uptake using fluorescence microscopy. *In vivo* tumor accumulation of BP-HPPS was monitored by CRI Maestro *in vivo* imaging system in PC3-Luc orthotopic prostate cancer mice.

Results. BP-HPPS are selectively taken up by SRB1 overexpressing cells *in vitro* and orthotopic prostate tumor *in vivo*. Having two NIR fluorophores with distinguishable fluorescence spectra (maximum emission - 667 nm for Pyro-oleate and 763 nm for Bchl-lipid) – allows us to monitor nanoparticle *in vivo* integrity and biodistribution, which will enable a clinical scenario, where two NIR wavelengths are used for tumor margins visualization and image-guided surgical resection.

Conclusions. This research demonstrates that BP-HPPS is an excellent theranostic agent for highly selective delivery of NIR fluorescent photosensitizers for cancer imaging and phototherapy.

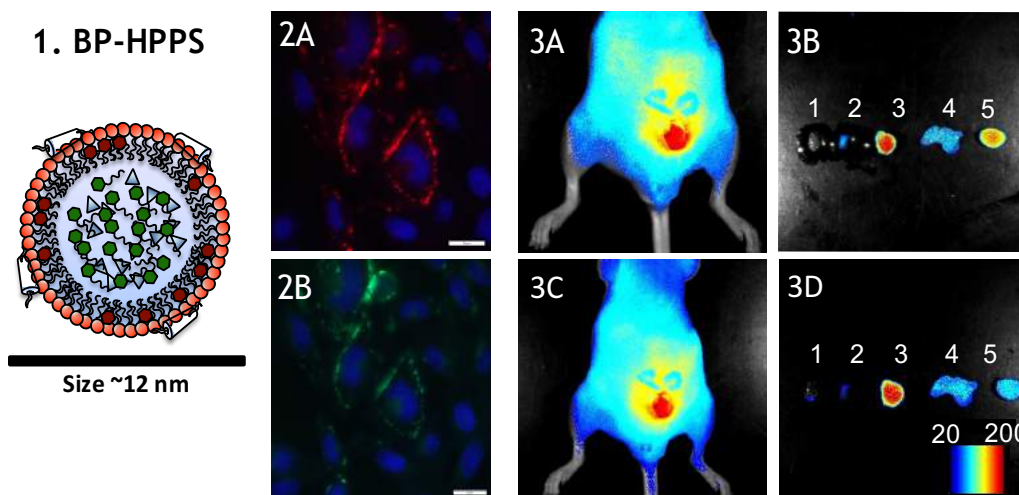


Figure 1. Schematics of BP-HPPS structure; 2. BP-HPPS binding to SRB1-expressing cells: 2A) Pyro channel and 2B) Bchl channel; 3. Selective tumor accumulation of BP-HPPS in orthotopic prostate cancer mouse model: 3A-B) Pyro channel (Ex: 616 – 661 nm, Em: 675 long pass.) 3C-D) Bchl channel (Ex: 616 – 661 nm, Em: 675 long pass). 1 - prostate; 2 - rectal wall; 3- tumor; 4- seminal vesicle; 5- testes. Exposure time=500ms.

Reference: [1] Zhang, Z., Chen, J., Ding, L., Jin, H., Lovell, J. F., Corbin, I. R., Zheng, G. (2010). HDL-mimicking peptide-lipid nanoparticles with improved tumor targeting. *Small*, 6(3), 430–437.

High-content imaged-based screening of patient derived leukemia cells to identify novel treatments and to personalize therapy for chronic lymphocytic leukemia

Sina Oppermann¹, Jarkko Ylanko¹, Yonghong Shi¹, Santosh Hariharan¹, Brian Leber², David E. Spaner¹ and David W. Andrews¹

¹ Biology Platform, Sunnybrook Research Institute, University of Toronto, ON, Canada;

² Department of Medicine, McMaster University, Hamilton, ON, Canada;

Supervisors: Drs David E. Spaner and David W. Spaner

Introduction. Chronic lymphocytic leukemia (CLL) exists in blood and in proliferation centers in spleen, bone marrow and lymph nodes. Multiagent chemoimmunotherapy is a common strategy for disease management but available drugs predominantly target circulating tumor cells, which are often highly chemosensitive, whereas proliferating cells protected by the microenvironment are more chemoresistant and may mediate disease recurrence.¹ Moreover, patient responses to current treatment regimes are variable and temporary. High-throughput screens have been used to identify new indications in CLL for bioactives and FDA-approved drugs, but the ability of such screens to identify leads for patient therapy has been limited by a general focus on single agent effects, use of non-proliferative tumor cells as disease model, and assays for cytotoxicity that preclude insights at the level of the cell. We are instead using a high-content image-based screening technique and machine-learning analysis methods to identify the most effective drug combinations in individual patients by particularly screening combinations of the Bcl-2 inhibitor Venetoclax with small molecules in primary patient cells that have been stimulated to recapitulate their proliferative state in the solid tumor microenvironment.

Methods. Using primary CLL cells, we developed an *in vitro* microenvironment model that could be incorporated into an automated high-content microscopy-based screening system. With this automated methodology resistance in patient derived cells was assayed and the effectiveness of combining Venetoclax with any one of 320 kinase inhibitors (KIs) was tested to improve therapy in a personalized manner. To assay cell responses to drug treatments cells were stained with three fluorescence dyes, Annexin V, Tetramethylrhodamine ethyl ester and DRAQ5 to measure loss of lipid asymmetry at the plasma membrane as a characteristic of apoptosis, mitochondrial transmembrane potential and nuclear condensation, respectively and images were acquired 72 h after drug treatment using an automated microscope. Draq5 fluorescence was used as a marker for cell detection and segmentation in each micrograph. Quantitative analysis of cell death was performed by either establishing thresholds of fluorescence intensity (AnnexinV, TMRE) and nuclei area (Draq5) per cell for single assay analysis, or by extracting a set of 8 features measuring AnnexinV, TMRE and Draq5 intensity (mean and standard deviation); nuclei area; plus TMRE and AnnexinV colocalization (by Pearsons R) for multiparametric image analysis using a multiparametric classifier generated by automated machine learning techniques.

Results. The results confirm the striking effectiveness of Venetoclax in circulating CLL cells but resistance in cells stimulated by microenvironmental signals. While a marked inter-patient variability was noted for which KIs were effective, Sunitinib was identified as the most common, clinically available KI that was effective to improve the therapeutic efficacy of Venetoclax.

Conclusion. We show that our automated high-content methods for analysis of image-based multiplexed fluorescence-based drug screening allows to identify and to explore the patient-specific effects of cytotoxic drug combinations under relevant physiological conditions, and suggest that this method could be used in clinical practice as a tool to personalize treatment plans and to monitor treatment outcomes in a timely manner.

References. Crystal AS, Shaw AT, Sequist LV et al. Patient-derived models of acquired resistance can identify effective drug combinations for cancer. *Science*. 2014;346(6216):1480-1486.

Tracking the rejection of ^{19}F -labeled stem cells through signal quenching resulting from infiltrating iron-labeled immune cells

OICR – Smarter Imaging Program

Jeff M Gaudet^{1,2}, Amanda M Hamilton¹, Matthew S Fox^{1,2}, and Paula J Foster^{1,2}

¹Imaging Research Laboratories, Robarts Research Institute, London, Ontario, Canada, ²Medical Biophysics, Western University, London, Ontario, Canada

Background: Regenerative stem cell therapy is anticipated to revolutionize modern medicine. Mesenchymal stem cells (MSC) are a leading candidate for clinical trials due to their multipotent properties and presence in adult tissue. However, before treatment can progress to the clinic there are still many questions that must be answered concerning the immune rejection of transplantations. Cellular MRI offers a tool to non-invasively track the fate of stem cells and improve treatment outcomes. In this study we use multiple cellular MRI techniques to monitor two distinct cell populations: (i) MSC, labeled *in vitro* with ^{19}F prior to implantation and, (ii) phagocytic immune cells, labeled *in situ* through administration of intravenous (IV) iron.

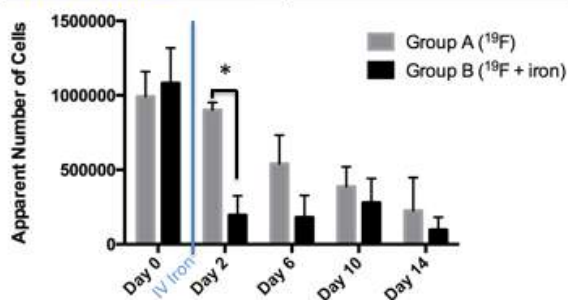
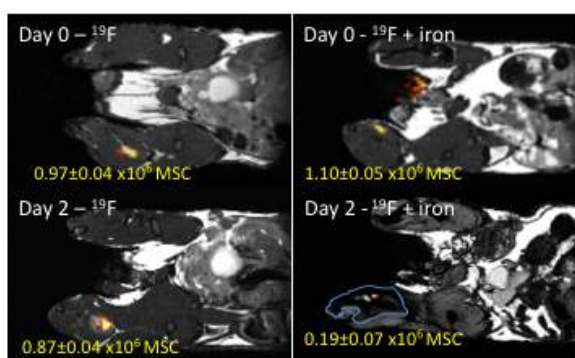
Methods: Immune competent, C57Bl/6 mice (n=14) were implanted intramuscularly with 1×10^6 human MSC (hMSC) labeled with a red fluorescent perfluorocarbon emulsion (day 0). This model was chosen to produce a hyperacute immune response. 24 hours after hMSC implantation (day 1), half of the mice received an IV tail vein injection of ultra-small iron oxide nanoparticles (USPIO) at a dose of 0.5mmol/kg. Proton (^1H) and ^{19}F images were acquired at 9.4T with a dual-tuned $^1\text{H}/^{19}\text{F}$ mouse body coil using a 3D-balanced steady state free precession (bSSFP) sequence. Total scan time was under 60 minutes. Mice were anaesthetized with isoflurane and imaged five times, on days 0, 2, 6, 10, and 14. NMR was performed using 2×10^6 ^{19}F -labeled hMSC in order to determine the intracellular loading. Quantification of the ^{19}F -labeled cells was performed by measuring the signal in the region of interest and in a reference of known concentration using Voxel Tracker software. Following imaging, mice were sacrificed and tissues removed for immunohistochemistry (IHC).

Results/Discussion: On the day of implantation (day 0) the ^{19}F -labeled hMSC were visible in all mice and *in vivo* ^{19}F -MRI quantification agreed strongly with the number of implanted cells (Fig 1A). The ^{19}F signal gradually decreased between days 0 and 14 (Fig. 1B). Proton images obtained on day 2, 24 hours after the IV injection of USPIO, showed a large region of signal void at the transplantation site. Coincident with this was a significant drop in the ^{19}F signal at the transplant site. The observation of signal loss in proton images after IV USPIO is consistent with the infiltration and accumulation of iron-labeled macrophages at the implant site. Many studies have proven the utility of IV iron for macrophage tracking. The transplant model we used would be expected to cause a hyperacute cellular inflammatory response; host macrophages migrate into transplants in

response to cell death and inflammation. IHC confirms the presence of hMSC and macrophages in tissue. On day 2 large numbers of macrophages were visible throughout the tissue. By day 14, macrophages were only found within the initial stem cell track.

Significance: In this study, we have shown that it is possible to non-invasively monitor implanted stem cells with ^{19}F -MRI, while simultaneously monitoring the influx of iron-labeled immune cells. Ultimately, this technique could be used as an early, non-invasive marker of stem cell rejection.

References: 1. Hitchens TK, Liu L, Foley LM, Simplaceanu V, Ahrens ET, Ho C. Combining perfluorocarbon and superparamagnetic iron-oxide cell labeling for improved and expanded applications of cellular MRI. *Magnetic Resonance in Medicine*. 2014.



Changes in white matter structural connectivity and cortical functional connectivity over the healthy adult lifespan

Adrian Tsang^{1,2,3,5}, Catherine Lebel^{1,4,5}, Signe Bray^{1,4,5}, Brad Goodyear^{1,2,3,5}, Roberto Sotero Diaz^{1,5}, Cheryl R McCreary^{1,3,5}, Richard Frayne^{1,2,3,5} (Supervisor)

¹Department of Radiology, ²Hotchkiss Brain Institute, ³Seaman Family MR Research Centre, ⁴Child and Adolescent Imaging Research Program (Alberta Children's Hospital Research Institute), ⁵University of Calgary, Calgary, Canada

Introduction: Structural connectivity (SC) of white matter (WM) and functional connectivity (FC) of cortical regions undergo changes in normal aging. It has been shown that resting-state networks (RSNs) reflect the underlying SC architecture,^[1] thus simultaneous analysis of diffusion tensor imaging (DTI) and resting-state functional MRI (rs-fMRI) data from healthy subjects over the adult lifespan would provide a more comprehensive understanding on SC and FC changes, respectively, with age than using individual methods alone. Previous studies had explored the relationship between SC and FC and demonstrated strong FC was consistently observed between pairs of cortical regions with direct structural link via WM tracts, and also between some pairs of regions with indirect links.^[2,3] The objective of this work was to investigate SC and FC changes with age, and to explore their relationship across the healthy adult lifespan.

Methods: Healthy participants (n=216; male/female=86/130; aged 18–87 years) were imaged on a 3T GE Discovery MR750 scanner. DTI acquisition used a single-shot spin-echo echo-planar imaging (EPI) sequence with $b=1000\text{s/mm}^2$ (applied in 31 directions) and 4 $b=0$ volumes. rs-fMRI acquisition used a single-shot gradient-echo EPI sequence to acquire 150 whole brain volumes. Forty cortical regions across both hemispheres belonging to 7 template-defined RSNs^[4] were transformed to each subject's native space using an in-house automated pipeline for analysis. Whole brain WM tracts were delineated using deterministic tractography. Subsequently, masks were generated in each network for WM tracts that either begin or end at each of the cortical regions (O), and at pairs of regions (P). The pairs of regions in (P) were connected with direct WM pathways, and the remaining pairs of regions in the network were connected indirectly. Masks of WM tracts associated with indirect connected regions were generated from the subtraction of (O) and (P). Mean, radial, and axial diffusivity (MD, RD, AD) and fractional anisotropy (FA) of WM tracts were computed as measures of SC. Pearson correlations of average BOLD signal time series between pairs of regions within each RSN were computed as a measure of FC. A linear model was used to fit the average SC and FC measures versus age, as well as SC versus FC, for directly and indirectly connected pairs of regions in each network.

Results: FC for the direct regions was significantly negatively correlated (*i.e.* $p < 0.05$) with age in all networks except in the Visual and Dorsal Attention (DA) networks. Similarly, decreased FC for the indirect regions was significant in all networks except in the Limbic (L) network. On the other hand, the age-correlations in FA, MD, and RD were all significant for WM tracts of direct or indirect regions in all networks. AD showed a significant effect of age in most networks except in WM tracts associated with direct regions of Somato-motor (SM), DA, and Ventral Attention (VA) networks. In general, SC measures were not correlated with FC. For the direct regions, MD and RD were significantly correlated with FC only in the L and DM networks. FA was significantly correlated with FC in VA and L networks. For the indirect regions, AD, MD and RD were significantly correlated with FC in the SM and DM networks. Furthermore, SC was not correlated with FC in all networks after controlling for the effect of age.

Conclusions: The observed changes in both SC and FC with age among all 7 networks are consistent with independent DTI^[5-7] and rs-fMRI^[8,9] human brain aging studies, as well as a recent multi-modal study^[10] that demonstrated decreased FC and FA with age in healthy subjects. In this study, SC was correlated with FC only in specific networks as described above across the healthy adult lifespan, reflecting a complex relationship between SC and FC. Future longitudinal studies may elucidate possible causality of SC and FC changes in normal aging.

References: [1] van den Heuvel, et al. Human Brain Map (2009); [2] Koch, et al. Neuroimage 2002; [3] Honey, et al. Proc Natl Acad Sci USA (2009); [4] Yeo, et al. J Neurophysiol 2011; [5] Westlye, et al. Cereb Cortex 2010; [6] Lebel, et al. Neuroimage 2012; [7] Chen, et al. Neurobiol Aging 2013; [8] Cao, et al. Dev Cogn Neurosci 2014; [9] Fjell, et al. Neurobiol Aging 2015; [10] Betzel, et al. Neuroimage 2014.

The Effect of T₁ Signal Decay on Ventilation Mapping using Hyperpolarized Gas MRI during Multiple Breath Wash-out

Felipe Morgado*^{1,2}, Marcus Couch², Giles Santyr^{1,2}

¹Department of Medical Biophysics, University of Toronto, Toronto, Ontario, Canada

²Peter Gilgan Centre for Research and Learning, The Hospital for Sick Children, Toronto, Ontario, Canada

INTRODUCTION: Functional lung imaging may provide a useful approach for diagnosing and monitoring treatment response in diseases such as cystic fibrosis, including exacerbations. Hyperpolarized (HP) gas magnetic resonance imaging (MRI) is promising in this regard as it allows mapping of ventilation (r), defined as the per-voxel ratio of the volume of fresh gas to total gas on multiple breath wash-out (MBW) (1). However, MBW MRI with HP gases is confounded by several signal loss effects unrelated to r , including radiofrequency (RF) depolarization and oxygen-induced T₁ relaxation (2). While the former can be corrected by appropriate flip angle calibration, the latter is more problematic as the alveolar partial pressure of oxygen, p_AO₂, will change as a function of breath number. In this work, a theoretical error propagation model for MBW ¹²⁹Xe lung imaging is presented which estimates r by incorporating a realistic T₁, based on the changing p_AO₂ as a function of wash-out breath number for a rat. Results are presented comparing the relative bias in r between this model (r_{real}) and a conventional model where T₁ is assumed to be constant (r_{conv}).

METHODS: T₁ values were obtained using the relationship $T_{1,O_2} = \zeta/p_{A}O_2$ ($\zeta = 2.68$ bar·s) for ¹²⁹Xe (3), where p_AO₂ was calculated using the law of partial pressures and an iterative method to calculate the volume of O₂ in the lungs as a function of breath number under the following ventilation conditions (typical of a rat): tidal volume = 3 mL, lung volume = 8 mL and endotracheal tube dead space = 1 mL. Signal as a function of wash-out breath number was evaluated based on the following equation:

$$S_j = S_0 \left[e^{-\frac{(N \cdot TR + \tau)}{T_1(j)}} \cdot (1 - r) \right]^{j-1} \quad [1]$$

where j is the image number out of J total images, N is the number of phase-encoding lines in k-space ($N = 64$), $N \cdot TR = 0.903$ s, τ is the inter-image delay ($\tau = 1$ s) and r is as defined above. Flip angle dependence was ignored by assuming a variable flip angle (VFA) scheme. All parameter values were obtained from preliminary experiments with Sprague-Dawley rats (not described here). r was obtained for each wash-out signal curve through least-squares fitting using equation 1. The r value bias introduced by T₁ was calculated as follows:

$$\Delta r(\%) = \frac{r_{real} - r_{conv}}{r_{conv}} * 100\% \quad [2]$$

RESULTS AND DISCUSSION: As expected, the signal decay for the fixed T₁ case was less pronounced than the variable T₁ case, since T₁ decreases with each exhalation due to the subsequent inhalation of more oxygen. Δr was determined to be 12.5%, demonstrating the existence of bias when a fixed T₁ assumption is made. Previous studies under similar conditions have shown that ventilation maps for Sprague-Dawley rats tend to have a coefficient of variation of approximately 0.2 (2). Therefore, the relative biases predicted in this work would have a considerable impact on the accuracy of the r values measured in ventilation mapping that did not explicitly account for variable T₁ and will be confirmed experimentally in future. Although this study was performed with parameters for rat ventilation, the model presented here is applicable to humans, where we would expect τ to be greater than 1 s for subjects undergoing regular tidal breathing which would increase the bias. Further simulations utilizing typical ventilation parameters from clinical studies will be discussed.

CONCLUSION: This theoretical study predicts that the increasing rate of T₁ signal loss in an MBW imaging scheme significantly influences ventilation measurement accuracy and thus MBW analysis should explicitly include the variation of T₁ with breath number.

Acknowledgments: This research was funded by The Hospital for Sick Children through the Cystic Fibrosis Research Catalyst Grant and the Research Training Competition (Restrcomp) Award.

References: [1] Horn et al., J Appl Physiol. 2014;116(2):129-139. [2] Couch et al., Mag Reson Med. 2012;68(5):1623-1631. [3] Jameson et al. J Chem Phys. 1988;89:4074.

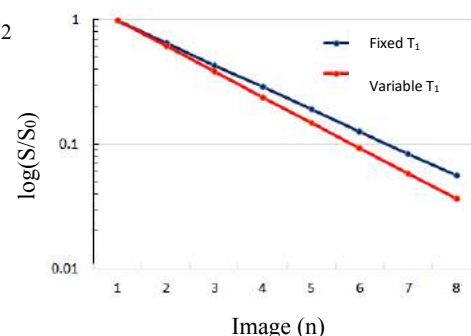


Fig. 1 Theoretical signal decay as a function of breath number for a MBW imaging scheme.

Mueller matrix polarimetry imaging using four photoelastic modulators for rapid wide-field analysis of biological tissues

Adam Gribble^{1,*}, Sanaz Alali², and I. Alex Vitkin^{1,3,4}

Ontario Institute for Cancer Research – Smarter Imaging Program

¹Department of Medical Biophysics, University of Toronto, Toronto, Ontario, Canada

²Senior Design Engineer, Optical Sensor and Metrology, ASML, Wilton, Connecticut, USA

³Department of Radiation Oncology, University of Toronto, Toronto, Ontario, Canada

⁴Division of Biophysics and Bioimaging, Princess Margaret Cancer Centre, Toronto Ontario, Canada

Introduction: A promising method to probe tissue structural arrangement non-invasively is using polarized light. Tissue polarization properties are contained in its Mueller matrix, a complete mathematical description of its interaction with polarized light. To derive this 4x4 matrix it is necessary to observe how a tissue interacts with different polarizations, requiring measurements under at least 16 unique orientations of static polarization optics. However, mechanical rotation of optical components is slow, can lead to errors, and prevents real-time monitoring. Further, the turbid nature of biological tissues increases light scattering and depolarization. Thus, it is imperative to isolate the weakly remaining, polarized signal with high accuracy and SNR.

A well-suited approach for tissue polarimetry is to replace static optical components with photoelastic modulators (PEMs), which dynamically modulate the polarization of light. When combined with synchronous signal detection, PEMs allow for fast, accurate measurement of weak polarization signals, with improved SNR, and without moving parts. However, rapid PEM modulations (10s of kHz) are difficult to resolve using conventional imaging detectors (i.e. CCD cameras), and thus are confined to point detection systems. Given the spatial heterogeneity of biological tissues, a PEM-based imaging method is needed for realistic biomedical applications. To extend the rapid, high SNR, PEM-based polarimetry techniques to the imaging regime, we used a field-programmable gate array (FPGA) to synchronize CCD camera acquisition times to four PEMs.

Methods: The imaging system consisted of a laser for illumination, a polarizer followed by two PEMs to modulate polarization incident on the sample, two PEMs followed by a polarizer to analyze output polarization after sample interaction, a CCD camera, and an FPGA. Dynamic birefringence of the PEMs resulted in a time-varying intensity signal reaching the CCD. CCD image acquisition was synchronized to PEM reference frequencies using the FPGA, enabling precise image acquisition over the entire four-PEM modulation period.

Images of known calibration samples were acquired over the entire modulation period. An evolutionary algorithm was then used to determine the PEM relative phases. Once the PEM phases were known, unknown samples were imaged at 50 time points, which were used to calculate the unknown Mueller matrices.

Results: The four-PEM imaging system was used to image the Mueller matrices of a blank sample, as well as polarizers and quarter-wave plates at multiple orientations, with an average Mueller matrix element error of <0.025 , and total imaging time of ~ 1 s per sample. Representative images are shown in Fig. 1. To demonstrate the ability of the system to analyze thick turbid samples, a polyacrylamide phantom with known scattering and birefringence was imaged. The four-PEM imaging system was used to image this phantom, and extract the correct birefringence. Thus, the system shows potential for turbid, biological sample analysis [1].

Conclusions: A PEM-based wide-field Mueller matrix imaging system with high SNR has been developed, which is capable of rapidly imaging any turbid sample with no moving parts and large field of view. Future work will extend the platform to biological tissue analysis and applications.

References: [1] S. Alali, A. Gribble, and I. Alex Vitkin, *Opt. Lett.*, doc. ID 252483 (16 Dec 2015, accepted).

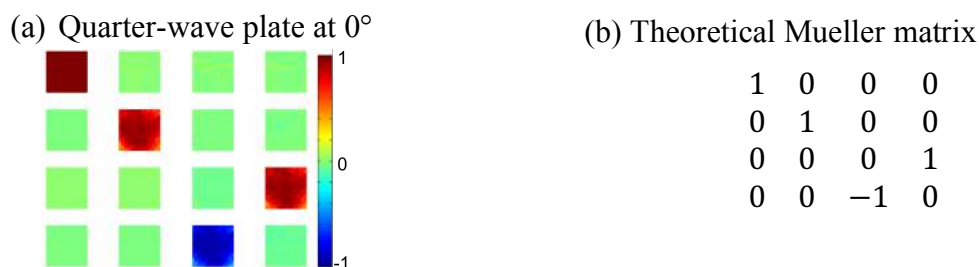


Fig. 1. (a) Mueller matrix image of a quarter-wave plate at 0° , as found with the 4-PEM Mueller matrix imaging system, and (b) its theoretical form. Excellent agreement was observed.

Spin-Lattice Relaxation Dispersion using Fast Field-Cycling Magnetic Resonance Relaxometry

Yonathan Araya^{1,2}, Francisco Martínez-Santesteban^{1,2}, William Handler³,
Blaine Chronik^{1,2,3}, and Timothy Scholl^{1,2,4}¹Department of Medical Biophysics, ²Imaging Research Laboratories, Robarts Research Institute,³Department of Physics and Astronomy, Western University, London, ON Canada, ⁴Ontario Institute for Cancer Research

Introduction: The ability to exploit the native proton spin-lattice relaxation rates (R_1) and their associated dispersion over a range of magnetic field shifts (ΔB_0) using fast field-cycling magnetic resonance imaging (FFC-MRI), is a potential tool to differentiate between normal and atypical tissues. This study quantified the R_1 -dispersion of rodent tissues using two FFC-MRI relaxometry methods from 0.23 mT to 1.74 T.

Method 1: Adult mice tissues were excised for *ex vivo* R_1 -dispersion analysis at 37°C for variable magnetic field strengths below 1 T. All tissues were stored at 4 °C until measured, with a maximum delay of 8 hours from sacrifice to first measurement. R_1 -dispersion profiles were acquired using nuclear magnetic resonance dispersion (NMRD) data for magnetic field strengths ranging from 0.23 mT to 1.0 T, using a SpinMaster FFC2000 1 T C/DC (Stelar s.r.l., Italy) FFC nuclear magnetic resonance relaxometer.

Method 2: Imaging was performed on a 1.5T GE CVMR system outfitted with a fast field-cycling insert magnet to dynamically control B_0 prior to imaging. Five images, (1.26, 1.39, 1.50, 1.61, 1.74 T), were acquired using a field-cycling T_1 -weighted fast spin-echo inversion recovery pulse sequence, where ΔB_0 was modulated for a duration of relaxation times prior to imaging (50, 89.7, 161.1, 289.1, 518.9, 931.3, 1671.5, 3000, 5000, and 8000 ms). Prior to each magnetic field shift, the sample was allowed to polarize for 2000 ms at 1.5 T followed by an 180° inversion RF pulse, after which the magnetic field shift was applied (ramp time=10 ms, 6 ms delay before imaging). The remaining sequence parameters were as described (TE=12.4 ms, NEX=1, matrix=256x256, FOV=12.0x4.8 mm², slice thickness 2.0 mm, 4 echoes). The repetition time was maintained as the sum of the polarization, relaxation and imaging times over the course of imaging. Mice were anesthetized and placed on a heated bed (37°C) in a Tx/Rx birdcage RF coil within the field-cycling magnet for imaging.

Results R_1 -dispersion profiles are composed of *ex vivo* tissue relaxometry measurements below 1 T (Fig. A-E), and *in vivo* FFC-MRI at 1.5 T (Fig. F&H). *In vivo* whole-body spin-lattice relaxation rates (R_1) and dispersion maps (Fig. H) of protons for mice tissues have been quantified for a magnetic field of shift of ± 0.235 T about 1.5 T. R_1 -maps were produced for 1.26, 1.39, 1.50, 1.61, and 1.74 T using a 4-parameter non-linear fit for spin-lattice relaxation on a pixel-by-pixel basis. ROI analysis (Fig. G) of the tissues showed little dispersion, $\Delta R_1/\Delta B_0$, within a field shift of ± 0.235 T about 1.5 T (Table 1).

Conclusions These findings emphasize the inherent weak R_1 magnetic field dependence of healthy tissues. These are important data as we study atypical or cancerous tissues, which may have a significantly greater field dispersion or may be highlighted by a targeted contrast agent that increases their dispersion.

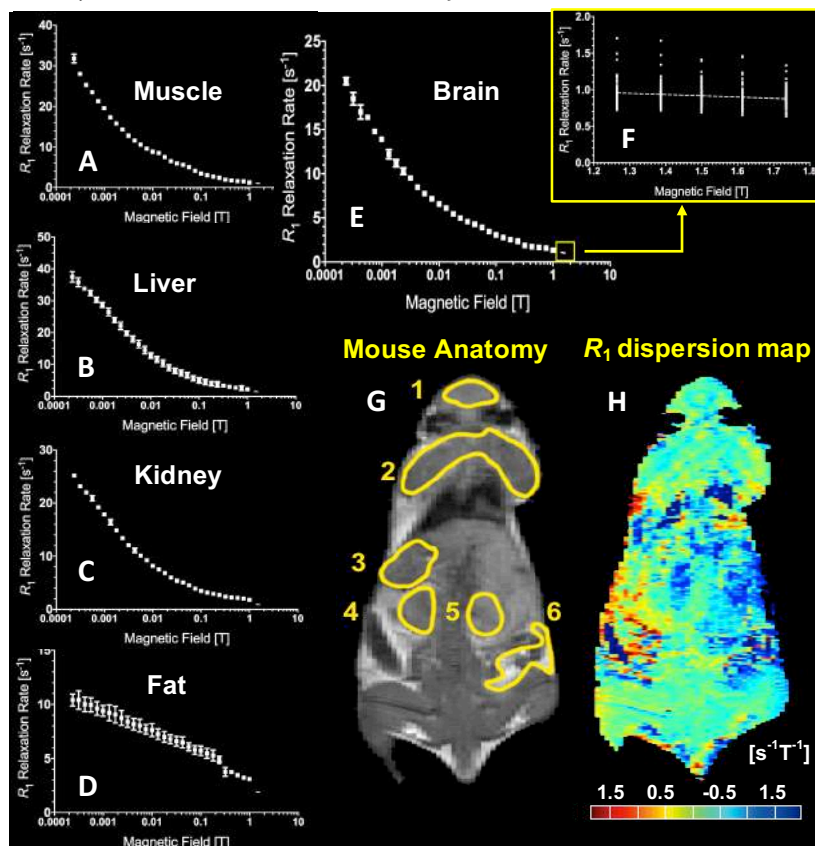


Figure 1. Anatomical T_1 -weighted MRI highlighting ROIs of selected tissues and R_1 -dispersion FFC-MRI map, $\Delta R_1/\Delta B_0$, [$s^{-1}T^{-1}$] at 1.5 T. The associated R_1 -dispersion profiles of tissues ranging from 0.23 mT to 1.74 T.

| Tissue Type | R_1 dispersion slope, $\Delta R_1/\Delta B_0 \pm SE$ | | |
|-------------|--|------------------|------------------|
| | Mouse 1 | Mouse 2 | Mouse 3 |
| 1 Brain | -0.29 ± 0.05 | -0.09 ± 0.04 | -0.17 ± 0.03 |
| 2 Muscle | -0.19 ± 0.03 | -0.32 ± 0.04 | -0.22 ± 0.05 |
| 3 Liver | -0.55 ± 0.10 | -0.52 ± 0.07 | -0.42 ± 0.03 |
| 4&5 Kidneys | -0.52 ± 0.07 | -0.20 ± 0.04 | -0.55 ± 0.10 |
| 6 Fat | -0.17 ± 0.28 | -0.59 ± 0.07 | -0.65 ± 0.12 |
| TUMOUR | - | - | -0.17 ± 0.01 |

Table 1. ROI analysis of selected tissues for R_1 -dispersion. The dispersion slope ($\Delta R_1/\Delta B_0$) \pm standard error [$s^{-1}T^{-1}$] was determined by linear regression (Fig. F). MDA-MB-231 tumour (30-days post-Sx) was measured for mouse 3.

Interleaved multi-frequency excitation for robust spectrally-selective ^{13}C echo planar imaging

Justin Y. C. Lau^{1,2,*}, Benjamin J. Geraghty^{1,2}, Albert P. Chen³, Charles H. Cunningham^{1,2}

Ontario Institute for Cancer Research Smarter Imaging Program; ¹Physical Sciences, Sunnybrook Research Institute, Toronto, ²Medical Biophysics, University of Toronto, ³GE Healthcare, Toronto, ON, Canada

Introduction: Incorrect prescription of frequency offsets in frequency-selective ^{13}C imaging^[1] can result in loss of signal due to incomplete excitation of magnetization. An interleaved multi-frequency excitation scheme with juxtaposed blip reversal^[2] is proposed as an approach for robust spectrally-selective ^{13}C echo planar imaging.

Methods: The pulse sequence consisted of an 18.7 ms spectral-spatial pulse with 120 Hz passbands followed by 3D echo-planar readout. Three frequencies 150 Hz apart were prescribed for each of pyruvate and lactate, as shown in Figure 1, for a total of 12 interleaves in 10 s. The scanner centre frequency was purposely offset by 50 Hz to simulate a realistic case of incorrect frequency prescription. $[1-^{13}\text{C}]$ Pyruvic acid with 15 mM OX63 was polarized using a 5T SPINlab DNP Polarizer (GE Healthcare). A Sprague-Dawley rat was administered 2.5 mL of 80 mM pre-polarized pyruvate over 12 s via the tail vein. Measurements were performed at 3T using a GE MR750 scanner with a dual-tuned $^1\text{H}/^{13}\text{C}$ rat coil (GE Healthcare). Mutual information off-resonance spatial shift correction based on blip-reversal was applied.

Results: In Figure 2, the lactate resonance was straddled between interleaves (a) and (b) each applying 25% of the intended excitation. There is signal contamination in interleaf (a) by pyruvate hydrate, as evidenced by opposing shifts under blip reversal. The pyruvate resonance was excited by both interleaves (d) and (e) with approximately 15% and 50% of the intended excitation, respectively. By shifting the images in interleaves (a) and (d) by the corresponding spatial offset for 150 Hz, lactate and pyruvate signals can be added with images in interleaves (b) and (e) to form combined images with higher signal. In Figure 3, a comparison of the SNR in a ROI containing the left kidney gave higher SNR in the combined images, with a maximum SNR increase of 23% for lactate and 40% for pyruvate.

Conclusion: Using a multi-frequency excitation scheme with juxtaposed blip reversal, it was possible to recover some of the lactate and pyruvate signal that would otherwise have not been excited due to incorrect frequency prescription.

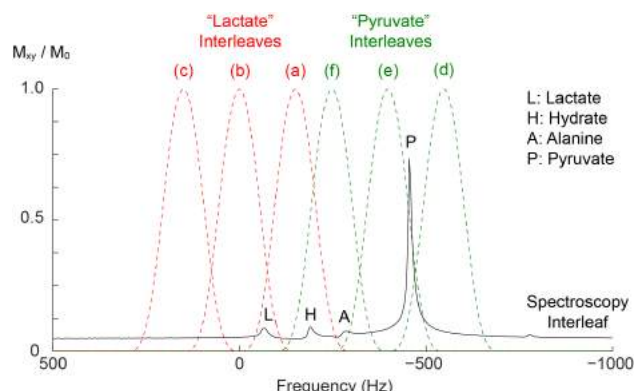


Fig 1. Excitation profiles of each pair of blip-reversed interleaves, applied from (a) to (f).

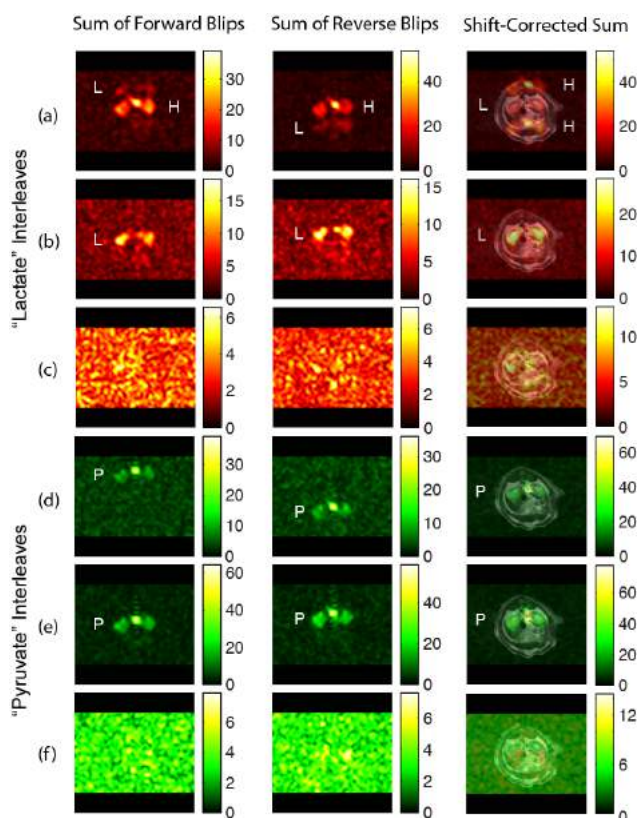


Fig 2. Area under the curve images from each interleaf (a-f) acquired with forward and reverse blipping. Pyruvate, lactate, and pyruvate hydrate are labeled P, L, and H.

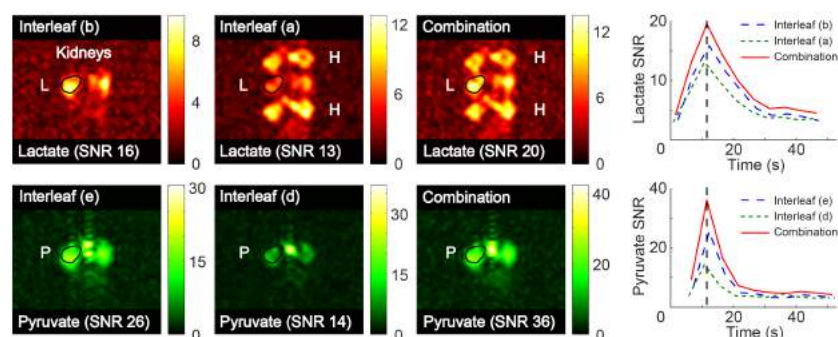


Fig 3. Images from the time point of maximum SNR (dashed vertical line) are shown with measured SNR values.

References: [1] Lau *et al.* (2011) *NMR in Biomed* 24(8): 988. [2] Cunningham *et al.* (2014) *NMR in Biomed* 27(2): 212.

Myocardial local frequency shift mapping

Junmin Liu,¹ James W. Goldfarb,³ and Maria Drangova^{1,3}

¹Imaging Research Laboratories, Robarts Research Institute, ²Department of Medical Biophysics
Schulich School of Medicine & Dentistry, Western University, London, Ontario, Canada

³Dept. of Research and Education, St. Francis Hospital, Roslyn; SUNY Stony Brook, Stony Brook, NY, USA

Consortium: Heart Failure: prevention through early detection; **Supervisor:** Maria Drangova

Introduction: Local frequency shift (LFS) mapping techniques have shown potential for visualizing white matter microstructure (1). Extending these techniques to the heart may provide important information about the integrity and organization of myofibers. We present a method to extract myocardial LFS maps by explicitly removing the B0 inhomogeneity (ΔB_0) and the chemical-shift (CS) related components from multi-echo data (B0CS-LFS).

Method: Data acquisition: Data were acquired at 1.5 T with a dark blood double inversion recovery gradient echo sequence (1 slice per breath-hold, repetition time 20 ms; 12 echo times, 2.4 – 15.5 ms (1.2 ms spacing); flip angle 20°; bandwidth 1860 Hz/pixel; in-plane resolution $2.3 \times 1.7 \text{ mm}^2$, slice thickness 8 mm; flow compensation in read and slice directions). The bipolar multi-echo data were split into odd- and even-echo data sets; the first echo was excluded from the odd-echo group because of significant image corruption caused by eddy currents. **The B0CS-LFS approach** comprises three steps. First, a field (Δf_{b0}) map and fat-fraction (FF) map are generated from the even- and odd-echo groups separately. For this purpose, we used the unwrapping-based B0 mapping technique B0-NICE (2), which also estimates a T2* map from all echoes. To mitigate issues related to the presence of local field information in the B0 map, we performed low-pass filtering of the B0 complex image, which is the Hermitian product between the sixth and the second echoes (even-echo) or the seventh and the third echoes (odd-echo). The second step is to remove the unwanted constant, B0, and CS phase components. To remove the constant phase term, the Hermitian products between echoes were calculated. The LFS at each individual echo (f_j) were estimated by removing the B0- and CS-related phase terms:

$$f_j = \text{angle}(I_{j, hp} \times e^{-\varphi_{b0,j}} \times e^{-\varphi_{CS,j}}) / (2 \times \pi \times \Delta TE_j), j > 3,$$

where $\varphi_{b0,j}$ is equal to $2\pi \times \Delta f_{b0} \times \Delta TE_j$; $\varphi_{CS,j}$ is calculated using the six-peak fat model and FF map determined from step 1; ΔTE_j is equal to $(TE_j - TE_2)$ and $(TE_j - TE_3)$ for the even and odd echoes, respectively. The third step is to calculate the LFS map, defined as the mean over all included echoes on a pixel-by-pixel basis.

Results: Successful Δf_{b0} and FF maps were generated (Fig. 1), as demonstrated by the lack of fat-water swaps in the heart. More importantly, the circled region in the T2* map matches well with an infarct identified in a corresponding LGE image (detail described in a reference (3)), while the field map in the region remains smooth. A decrease in LFS values is also observed in the infarct region (Fig. 1d). Interestingly, spatial LFS gradients of approximately 4 Hz are observed across the myocardium in the vertical long axis (VLA) plane (Fig. 2), but are not observed in the short axis (SA) or horizontal long axis (HLA) planes (detail not shown).

Conclusion: Myocardial LFS mapping can identify hemorrhagic infarct zones and has potential to depict myofiber orientation.

References: 1. Wharton and Bowtell, MRM 2015;73(3):1258-1269.
2. Liu and Drangova, MRM 2015;74(4):1177-1188.
3. Goldfarb et. al., MRM 2014;71(3):1210-1120.

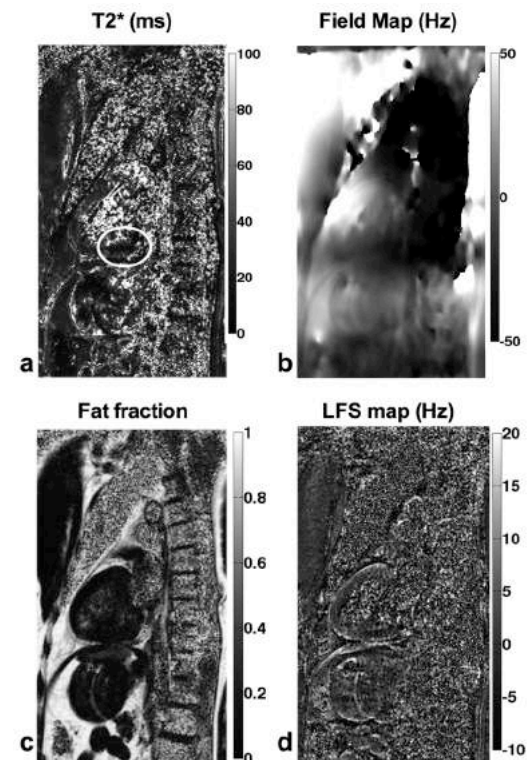


Fig. 1 B0-NICE results in the VLA plane: (a), (b), (c) and (d) are the T2*, even-echo B0, even-echo FF and LFS maps, respectively. The ellipse in (a) indicates an acute hemorrhagic infarct. The odd-echo results (not shown) are similar.

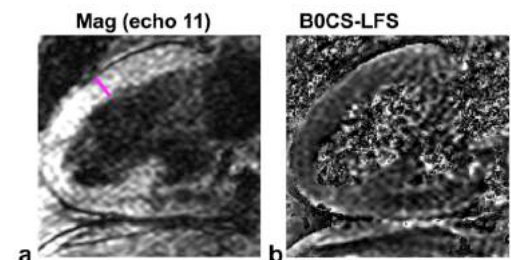


Fig. 2 Magnitude (a) and B0CS-LFS (b); the line profiles along the line-segment in (a) are plotted in (c). An epi- to endo-myocardium gradient is observed in LFS, which facilitates delineation of the tissue boundary (myocardium shaded in grey).

Cardiac Arrhythmia Network of Canada (CANet): Mission, Goals and Imaging Research Opportunities

Allan Skanes

As one of Canada's leading causes of death, cardiac heart rhythm disorders (arrhythmia) kill 40,000 Canadians a year and profoundly effects the quality of life of millions more. The Cardiac Arrhythmia Network of Canada (CANet) is a national research network established in December, 2014 through the Networks of Centres of Excellence (NCE) to address this national health problem, specifically in the areas of atrial fibrillation, sudden cardiac death and syncope. CANet brings together health care professionals, academia, government, industry, not-for-profit, and patients to support new ideas and ground-breaking research. Ultimately, CANet will provide innovative therapies and solutions to reduce premature deaths and suffering caused by heart rhythm disturbances. CANet is committed to developing effective practical solutions that address unmet needs, and promote their use in personal, healthcare, and business applications. Our approach is to put the right tools in the right hands at the right time, to empower patients to manage their own health, caregivers to improve patient care at the bedside and in the community and healthcare providers to give timely, effective, and efficient services.

Imaging research has much to offer the scientific community at CANet. Many serious rhythm disorders are associated with scarring of the heart or abnormal autonomic innervation resulting in structural abnormalities, disordered electrical impulse formation and propagation. Translation of mechanistic insights gained from cardiac imaging including late gadolinium enhanced MRI (LGE MRI) and PET, as well as others may be leveraged into better, higher quality care for patients with or at high risk for cardiac rhythm disorders.

Analysis of activation-recovery intervals from intracardiac electrograms in porcine hearts

-- Cardiac Arrhythmia Network of Canada --

Danielle Denisko¹, Sudip Ghate², Samuel Oduneye^{1,2}, Ilan Lashevsky³, Graham Wright^{1,2}, Mihaela Pop^{1,2}
¹Medical Biophysics, Univ. of Toronto, ²Sunnybrook Research Institute, ³Sunnybrook-Arrhythmia Services, Toronto, CA

Introduction: Catheter-based mapping of intracardiac electrical signals can help identify the foci of abnormal heart rhythms associated with myocardial infarction, a major cause of death [1]. We recently showed that these foci reside in the 'border zone' (BZ) between healthy tissue and collagenous scar, and can be structurally identified using MRI [2]. The purpose of this work was to better understand the electrical characteristics of tissue in the BZ area. Specifically, we focused on the features of intracardiac electrical signals in the BZ area, by studying the *activation-recovery interval* (ARI), an important clinical surrogate of action potential duration.

Methods: Activation maps and bipolar voltages were recorded *in vivo* from 8 pigs at ~5 weeks following infarction and 7 control pigs, as in [3]. Endocardial and epicardial bipolar maps were obtained during normal sinus rhythm and/or pacing conditions, via an X-ray guided catheter-based electro-anatomical CARTO-XP mapping system (Biosense, Webster). Clinical threshold was used to categorize tissue into: healthy (>1.5mV), scar (<0.5mV) and BZ (between 0.5 and 1.5mV) (Fig 1a). Depolarization and repolarization maps were derived through manual annotation of ecg waves, where the peak of the QRS wave marked the time of depolarization and the peak of the T wave marked the recovery time using Wyatt method as in [4], (Fig 1b). Finally, at each recording point, activation-recovery intervals (ARI) were found by subtracting activation times from repolarization times (Fig 1c). Mean ARIs were compared between: BZ and healthy areas, in sinus rhythm and paced conditions, and between endo- and epicardium. Statistically significant differences were defined by $p < 0.05$.

Results: First, we observed a dispersion of repolarization near the scar region, with a spatial pattern of ARI being similar to that of late repolarization times. Second, we obtained a weak negative correlation between the activation times and ARI values in both sinus rhythm and paced conditions, suggesting a coupling of these variables. There were statistically significant differences between mean ARI from LV-endo and epicardium in healthy tissue ($p=0.020$) and BZ ($p=0.024$), (see Fig. 1d). Finally, we also observed that ARI values in the BZ have recovered from the acute stage of infarction and were somewhat close to ARI values in normal tissue. Notably, although the ARI values were different between BZ and healthy areas per each animal (up to 30ms), the ARI values averaged per all pigs were not significant ($p < 0.5$). This result suggested that parameterization of computer models from ARI maps (an important step in our future work) should be performed on an individual heart basis rather than using averaged or literature values, to ensure accurate predictions.

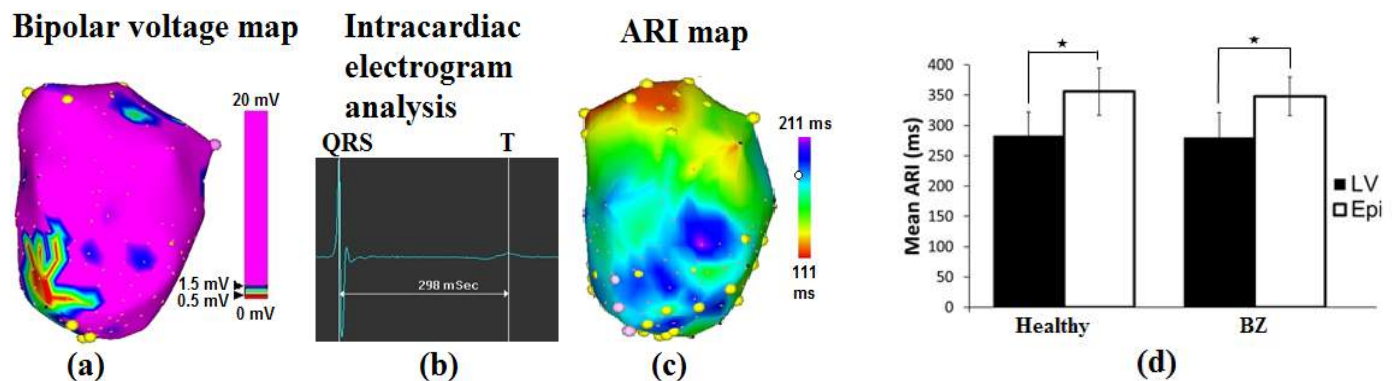


Fig 1. Example result from an infarcted pig heart: (a) endocardial bipolar voltage map; (b) depolarization and repolarization times determined from the peaks in QRS and T waves; (c) ARI map calculated by subtracting activation times from repolarization times; and (d) comparison between mean ARIs between endo and epi areas. Error bars represent standard deviations and * means $p < 0.05$.

Conclusion: We successfully developed an analysis framework to quantify features of electrical signals in an animal model of chronic infarction. Future work will focus on translating this work to patient data and personalizing our 3D MRI-based computer models [3,5] per individual heart from *in vivo* electrical maps, enabling more accurate predictions of cardiac wave propagation and simulation of scar-related arrhythmia.

References: [1] Stevenson W - Trans Am Clin Climatol Assoc, 2009; [2] Pop M *et al* Physics in Med Biol, 2013; [3] Pop M *et al* IEEE TBME, 2011; [4] Gepstein L *et al* Circulation, 1997 [5] Pop M *et al* Medical Image Analysis, 2012.

Guidewire puncture forces related to MRI signatures for peripheral arterial disease plaque types

N. Shaikh¹, T. Roy^{1,2}, G. Liu¹, K. Anderson¹, N. Yak¹, A. Dueck^{1,2}, and G. Wright^{1,3}

¹Schulich Heart Program and the Sunnybrook Research Institute, Sunnybrook Health Sciences Centre, Toronto, ON, Canada, ²Division of Vascular Surgery, University of Toronto, Toronto, Canada, ³Department of Medical Biophysics, University of Toronto, Toronto, Canada

Introduction: Percutaneous vascular interventions (PVI) for peripheral arterial disease (PAD) have high immediate technical failure rates (20%), and high re-intervention rates (~30%)¹. PVI is done under X-ray fluoroscopy, which does not visualize vessel walls and lacks soft tissue contrast for accurate plaque characterization². We hypothesize that MRI can characterize PAD plaque components and their associated mechanical properties. This information could assist physicians in predicting PVI success and wire/device selection according to plaque type. We hypothesize that MRI signatures of PAD lesions associated with “hard” lesions (e.g. fibrocalcific plaque) will require higher puncture forces to cross with a guidewire compared to “soft” lesions (e.g. fibroatheroma and lipid rich).

Methods: 21 excised human PAD lesions from 3 lower-limb amputation patients were tested. All samples were chronic total occlusions (CTOs). The samples were imaged with high-resolution MRI at 7 Tesla using T2-weighted (T2W) and ultrashort echo time sequences (UTE). The following MR imaging signatures have been previously validated with microCT and histology: lumen (T2W, UTE) = (\emptyset, \emptyset), fat (+, \approx), thrombus (\emptyset , +), loose fibrous tissue (\approx , \approx), dense fibrous tissue/collagen (\emptyset, \approx), and calcium ($\emptyset, -$), where \emptyset means no signal, and -, \approx , + mean hypo-, iso-, an hyper-intense versus muscle respectively (Figure 1). An independent image reviewer classified lesions into: calcified, hard or soft regions based on their imaging signatures. CTOs with imaging signatures corresponding to fat, thrombus, or microchannels were classified as “soft”. CTOs with loose fibrous tissue imaging signatures were classified as “intermediate”. CTOs with dense fibrous tissue/collagen signatures were classified as “hard”. Guidewires could not cross CTOs with dense calcified nodules in preliminary testing and were excluded. Samples were tested with an industry-grade catheter test station. The back-end of an Amplatz Super Stiff wire was driven through the CTO at a fixed displacement rate of 0.05mm/s by a 2kg motorized load cell. Puncture forces required to cross the CTOs were measured (Figure 3).

Results: MRI signatures for “hard”, “intermediate” and “soft” CTOs correlated with guide wire force-displacement testing. Non-calcified hard CTOs (n=6) required a puncture force of $1.74\text{N} \pm 0.58$; intermediate CTOs (n=11) required a puncture force of $0.45\text{N} \pm 0.33$; soft CTOs (n=4) required a puncture force of $0.07\text{N} \pm 0.02$. There was a statistically significant difference between groups as determined by one-way ANOVA ($P < .05$).

Conclusion: PVI is a minimally invasive option for treating PAD patients. Certain plaque types are amenable to PVI, whereas others are more ideal for bypass surgery. Surgery is currently recommended for densely calcified lesions due to high failure and complication rates with PVI^{3,4}. Non-calcified/minimally-calcified lesions also impact procedural success⁵, but predicting PVI failure is difficult because current imaging modalities can only effectively characterize calcium. In this study it was found that significantly higher puncture forces were required to cross non-calcified “hard” CTOs compared to “intermediate” and “soft” CTOs as defined by MRI signatures. This demonstrates the feasibility of using MRI to differentiate densely calcified plaques and non-calcified hard plaques from intermediate and soft plaques, which are more amenable to PVI.

Acknowledgements: This study was supported by funds from the Canadian Institutes of Health Research.

References: ¹ *J. Vasc. Surg.* 2010; 51(5):18S-31S, ² *BMJ* 2007; 334(7606): 1257-2007, ³ *Catheter. Cardiovasc. Interv.* 2014; 83(1): 115-122, ⁴ *Circulation* 2012; 125(3): 522-8, ⁵ *J. Endovasc. Ther.* 2015; 22(5): 663-677

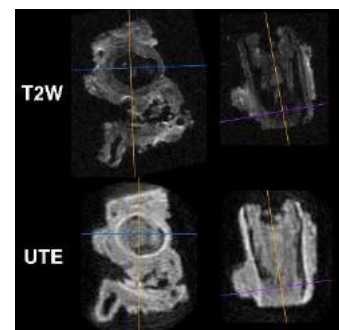


Figure 1: MRI biomarkers of peroneal artery non-calcified hard CTO. T2W images do not show dense collagen due to short T2. UTE images show dense collagen as isointense using smooth muscle as the reference intensity.

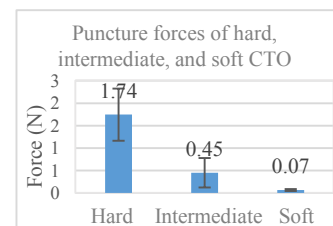


Figure 2: Puncture forces of CTO types

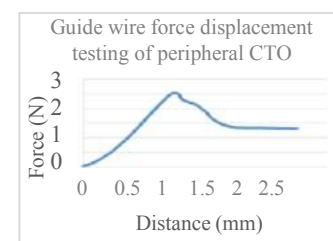


Figure 3: Force-displacement curve of the hard CTO

Intrinsic MRI visualization of RF lesions within minutes after MR-guided ablation

Philippa Krahn^{1,2}; Venkat Ramanan¹; Labonny Biswas¹; Jennifer Barry¹; Nicolas Yak¹; Robert Xu^{1,2}; Kevan Anderson^{1,2}; Mihaela Pop^{1,2}; Graham A. Wright^{1,2}

¹Physical Sciences, Sunnybrook Research Institute, ²Medical Biophysics, University of Toronto

Imaging for Cardiovascular Device Intervention

Introduction: RF ablation is currently the only curative therapy for structural arrhythmias such as ventricular tachycardia; however, arrhythmia recurrence rates are high even after successful procedures^[1]. To understand the cause of these recurrences, intrinsic-contrast MRI may reveal the features of ablation lesions likely to prevent arrhythmia in the long term. Here we used MRI to visualize regions of ablation-induced necrosis and inflammation during a time frame relevant to a clinical ablation procedure.

Methods: MR-guided interventional catheter procedures were performed in 5 healthy pigs to create 6 RF lesions. An MRI-enabled catheter (Imricor Medical Systems, Burnsville, MN) was navigated using real-time active tracking feedback^[2] into the left ventricle, where endocardial ablation was performed by applying 30W with irrigation for 45-90s. The resulting lesions were visualized using two primary MR sequences: an IR-prepared b-SSFP sequence for T₁-based contrast, and a T₂-prepared b-SSFP sequence for T₂ mapping. All imaging was performed on a GE 1.5T system (Optima MR450W) using a 4-channel cardiac anterior array. T₂ maps were generated from 4 images at TE= 3-188ms, fitted using a 3-parameter model. From the visualization of lesion extent over time, linear regression analysis was performed where p<0.05 is considered significant.

Results: Ablation-induced inflammatory edema was detected as regions with T₂ above 55ms (Fig 1A), approximately 3SD above the remote T₂ (consistent with a previous approach in T₂-weighted images^[3]). The mean T₂ in remote and edematous tissue was 41ms and 61ms, respectively. Ablation-induced edema grew in size substantially over the post-ablation imaging period, with the exception of one lesion remaining at approximately the same size. A mild ablation injury may cause a smaller amount of edema to develop, stabilizing more rapidly than the edema in more severely injured tissue. The RF lesion necrotic cores were evident in IR-SSFP images as regions of shortened T₁^[4] (Fig 2A). Linear regression demonstrated that the edema area increased significantly (slope=1.03, p=0.005) while the lesion necrosis remained at a stable size (slope=-0.001, p=0.5) during the 1-2 hour period post-ablation imaging period. The non-zero intercept (at a time immediately after ablation) reflects the rapid lesion development that occurs during ablation.

Conclusions: We successfully visualized RF lesions within minutes of ablation, specifically identifying areas believed to be irreversible and reversible zones of thermal injury. Future work will focus on understanding the time course of lesion evolution and accompanying alterations to myocardial excitability.

References: [1] Tanner et al.: J Cardiovasc Electrophysiol 2010, 21: 47-53. [2] Dumoulin et al.: MRM 1993, 29:411-415. [3] Knowles et al.: IEEE TBME 2010, 57:1467-1475. [4] Celik et al.: Circ EP 2014, 7:718-727.

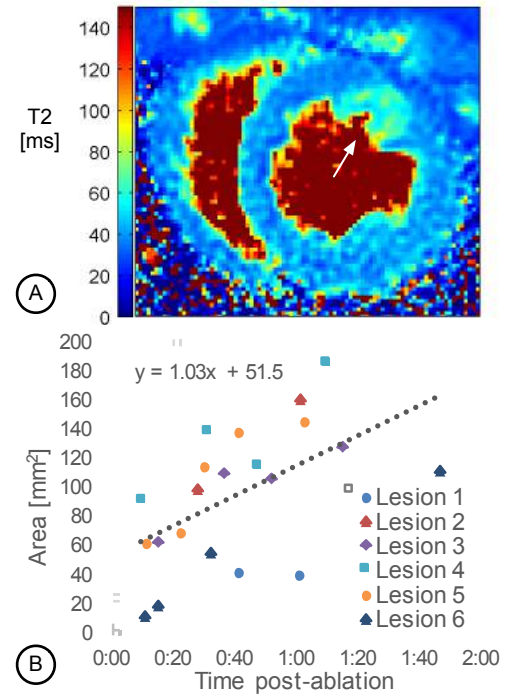


Fig 1 (A) T₂ map depicting edema from lesion 3 at 35min post-ablation (resolution=1.5x1.5x6mm). (B) Area of edema (delineated semi-automatically) from 6 lesions with time after ablation.

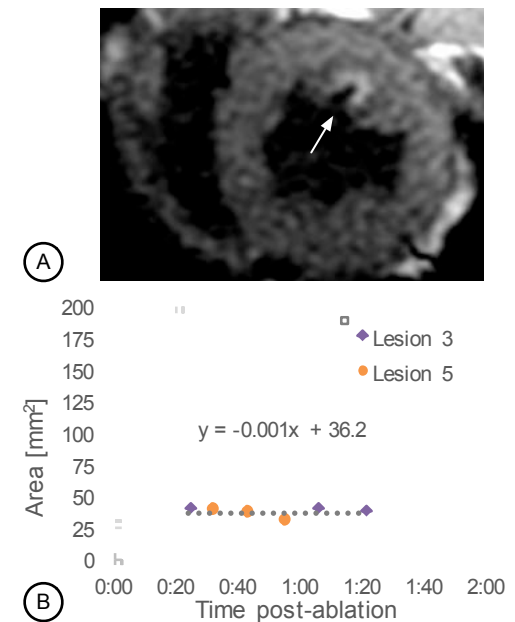


Fig 2 (A) IR-SSFP visualization of lesion 3 at 24min after ablation (resolution= 1.5x1.25x6mm, and TI=875ms – yielding high contrast between the lesion and surrounding myocardium^[3]). (B) Area of the necrotic cores (delineated manually) from 2 lesions with time after ablation.

Automated Segmentation of Scoliotic Lumbar Spine using Statistical Shape Models

Sinthu Sivanesan¹, Purang Abolmaesumi², Abtin Rasoulilian², Alexander Seitel², Robert Rohling², and Parvin Mousavi¹

¹School of Computing, Queen's University, Kingston, ON, CA

²Department of Electrical and Computer Engineering, University of British Columbia, Vancouver, BC, CA

Introduction: Spinal needle interventions are routinely used in analgesia and for epidural anaesthesia. Currently, these procedures are conducted using palpation, fluoroscopic imaging or ultrasound imaging. However, anatomical models such as those from segmented pre-operative CT can be combined with ultrasound imaging to provide 3D guidance and reduce the rate of complications. CT imaging normally provides effective visualization of bony structures. Vertebrae are highly variable between subjects and provide as a complex problem as edges in several regions such as intervertebral disk, and facet joints are not immediately visible. Rasoulilian et al. [1] proposed statistical shape and pose model(SSM) of the lumbar vertebrae for automated segmentation of CT of normal spines. SSMs are mathematical entities that capture the statistical information, including the mean and variation of a group of objects. In purpose of this study is to extend and evaluate the previously built SSM to automatically segment the lumbar spine of subjects with scoliosis and bone degeneration. Scoliosis is a condition where there is a lateral spinal curvature in straight standing position. Approximately 2-4% of the population is affected by some degree of scoliosis, and 10% of these need medical attention.

Materials and Methods: We used data from CT images of 62 patients. Of these, 40 cases are normal (32 from [1]), 16 are scoliotic and 6 have bone degeneration. We performed manual segmentation on the lumbar spine for all cases using MITK software to create the gold standard. We used 47 cases for training and 15 cases for test. The training set consisted of 36 normal, 8 scoliotic and 3 bone degeneration cases, respectively. The test set had 8 scoliotic, 3 bone degeneration, and 4 normal cases. The SSM was built with the training set using the exact approach detailed in Rasoulilian et al. [1]. The model captures two important properties: (1) shape - the variations of the shapes in the training population is calculated; (2) pose - the variations of the individual vertebrae in orientation and translation with respect to the mean shape are calculated. The constructed model is then evaluated on the CT images of the test set. Segmentation results are compared with the manual reference segmentation of each respective cases using the Dice Similarity Coefficient(DSC) [2].

Results: Two examples of automated segmentation on the CT images using the trained SSM are shown for normal and scoliotic patients in Figures 1 and 2, respectively. The average DSCs over all available vertebrae in the CT for each test subject are shown in Figure 3. As can be seen in this figure, the DSC is higher for scoliotic cases compared to normal and bone degeneration. As the DSC value gets closer to 1, it indicates higher similarity between the automated and the manually segmentation CTs.

Conclusion: We built a SSM of the lumbar spine using a combination of spinal abnormalities along with the normal cases. In 15 CTs from test subjects, we demonstrated that the generated model results in efficient segmentation of the CT and coherently works well for all studied clinical classes. Among the studied cases, the scoliotic class shows the best results compared to other classes.

References: [1] Rasoulilian et al. SPIE Medical Imaging 2013. [2] Sorensen. Kongelige Danske Videnskabernes Selskab 1948;4:1-34.

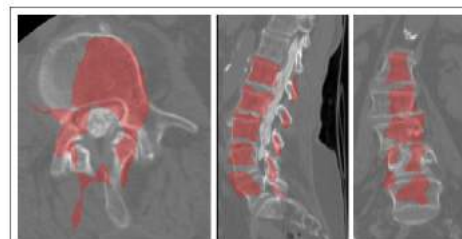


Figure 1: Normal Spine

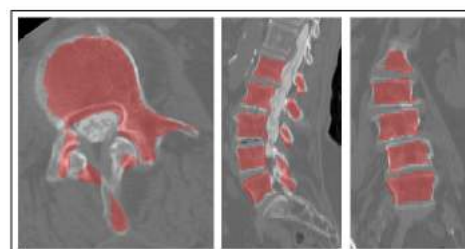


Figure 2: Scoliotic Spine

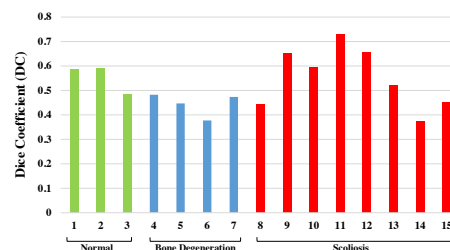


Figure 3: Segmentation Performance

Detection of local cancer recurrence after stereotactic ablative radiotherapy (SABR) for lung cancer: physician performance versus radiomic assessment

Sarah A. Mattonen^{1,2}, David A. Palma¹⁻³, Carol Johnson², Alexander V. Louie³, Mark Landis⁴, George Rodrigues³, Ian Chan⁴, Roya Etemad-Rezai⁴, Timothy P.C. Yeung^{1,2}, Suresh Senan⁵ and Aaron D. Ward¹⁻³

¹Department of Medical Biophysics, The University of Western Ontario, London, Ontario, Canada

²Baines Imaging Research Laboratory, London Regional Cancer Program, London, Ontario, Canada

³Department of Oncology, The University of Western Ontario, London, Ontario, Canada

⁴Department of Medical Imaging, The University of Western Ontario, London, Ontario, Canada

⁵Department of Radiation Oncology, VU University Medical Center, Amsterdam, Netherlands

OICR Imaging Translation Program; Research Supervisors: Aaron D. Ward & David A. Palma

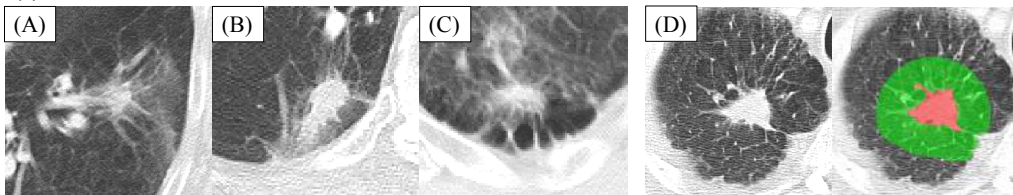
Introduction: Stereotactic ablative radiotherapy (SABR) is a guideline-specified treatment option for early-stage lung cancer. However, significant post-treatment fibrosis can occur and confound the detection of local recurrence. The goal of this study was to assess physician ability to detect timely local recurrence on computed tomography (CT) imaging, and compare physician performance with that of a radiomics tool.

Methods: CT scans (n=182) of 45 patients (15 with proven local recurrence matched to 30 with no local recurrence) were used to measure physician and radiomic performance in assessing response. Scans were individually scored by three thoracic radiation oncologists and three thoracic radiologists, all of whom were blinded to clinical outcomes. Radiomic features (first-order, second-order grey-level co-occurrence matrix, and size- and shape-based) were extracted from the same images in two semi-automatically generated regions of interest intended to sample regions of post-SABR changes; consolidative and peri-consolidative (Figure 1). Performance of the physician assessors and the radiomics signatures were compared.

Results: When taking into account all CT scans during the entire follow-up period (median imaging follow-up of 20 months), median sensitivity for physician assessment of local recurrence was 83% (range 67–100%) and specificity was 75% (range 67–87%), with only moderate inter-observer agreement ($\kappa=0.54$). The median time to detection of recurrence across all observers was 15.5 months. When predicting recurrence using images acquired <6 months post-SABR, physicians assessed the majority of images as no recurrence, with a mean error of 35%, false positive rate (FPR) of 1%, and false negative rate (FNR) of 99%. At the same time point, a radiomic signature consisting of five image appearance features in the consolidative and surrounding peri-consolidative regions demonstrated excellent discrimination, with an area under the receiver operating characteristic curve of 0.85, leave-one-out cross-validation classification error of 24%, FPR of 24%, and FNR of 23%. As seen in Figure 1, patients with recurrence tend to have increased presence of ground-glass opacity surrounding consolidative changes compared to patients with benign injury at this early follow-up time point.

Conclusions: These results suggest that radiomics can detect early changes associated with local recurrence that are not typically considered by physicians. These appearances detected by radiomics may be early indicators of the promotion and progression to local recurrence; our ongoing studies include using correlative histology to determine their composition. This has the potential to lead to a clinically useful computer aided decision support tool based on routinely acquired CT imaging, which could lead to earlier life-saving salvage opportunities for patients with recurrence and fewer unnecessary invasive investigations of patients with only benign injury.

(1) Local recurrence



(2) Benign radiation induced lung injury

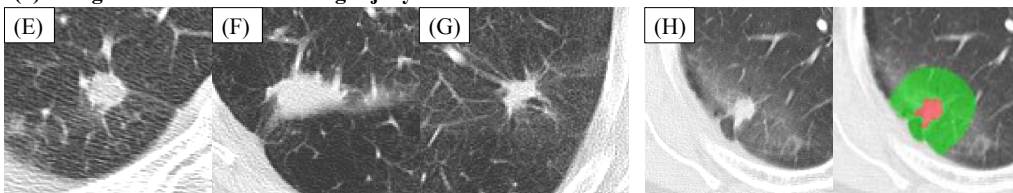


Figure 1: Example 2–5 month post-SABR scans for four patients who developed local recurrence (A–D) and four who developed only benign injury (E–H). Correctly classified recurrence (A–C) and injury patients (E–G) in leave-one-out cross-validation by the radiomic signature are shown. A false negative (D) and false positive (H) patient are also shown. An example of the corresponding semi-automated consolidative (red) and peri-consolidative (green) segmentations are also shown.

Focused ultrasound hyperthermia mediated drug delivery using thermosensitive liposomes and visualized with *in vivo* two-photon microscopy

Ontario Institute for Cancer Research – Imaging Translation Program

Marc A. Santos[†], Kullervo Hynynen and David E. Goertz

Sunnybrook Research Institute, University of Toronto, Toronto, ON, Canada

Introduction: Preclinical studies have shown that MRI-guided focused ultrasound (MRIgFUS) can achieve spatially localized thermal exposures in the range of 41-43°C. It has been demonstrated through histology that MRIgFUS is capable of inducing the targeted uptake and release of doxorubicin (DOX) from thermosensitive liposomes (ThermoDox®, Celsion Corporation) in tumour models, and that this gives rise to potent antitumour effects [1]. To enable the treatment of a broad spectrum of tumour types, improved heating approaches must be developed to overcome issues relating to respiratory motion, bone shielding, and large blood vessel cooling during MRIgFUS. To facilitate this process, it is important to gain insight into the microscale spatiotemporal release patterns induced by ultrasound mediated hyperthermia. Window chamber microscopy is well established as a method for investigating thermosensitive drug delivery, but to date it has generally employed resistive coil heating and water bath heating to control temperature [2]. Here we describe the first integration of ultrasound mediated hyperthermia into a two-photon microscopy (2PM) setting, and report initial results with this approach.

Methods: GFP-tagged FaDu tumours were initiated in dorsal skinfold window chambers in nude mice 10-14 days before imaging. On experiment day, two thermocouples were implanted to allow real-time temperature monitoring. A ‘ring’ transducer (1.2 MHz) was attached to the window chamber such that the ultrasound beam was directed into the tissue in a region that was co-incident with the optical field-of-view. Tumour cells were located using 2PM at 900nm as shown in Figure 1(a). Temperature based control of the acoustic power was used to maintain the tissue temperature at 41°C or 42°C for 20 minutes. Serial 3D vascular and DOX images were acquired before, during and after the FUS hyperthermia exposure in the presence of ThermoDox® at 810nm as shown in Figure 1(b)-(c).

Results: ThermoDox® drug release was successfully visualized with 2PM during FUS hyperthermia. The intra- and extravascular DOX signals were observed for up to 60 minutes following the initiation of treatments. The temperature controller was able to achieve a temperature response with variable rise time and maximum temperature to allow the investigation of different heating schemes.

Conclusions: We have developed the use of 2PM to image the release of DOX from ThermoDox® in real-time under FUS hyperthermia in mouse tumours. This capability will enable the evaluation of different FUS schemes (stand alone or cavitation enhanced) for hyperthermia-mediated drug delivery with the goal of overcoming limitations on clinical MRIgFUS hyperthermia.

References: [1] Staruch *et al.*, *Int J Hyperthermia*, 2015;31:118-133, [2] Manzoor *et al.*, *Cancer Res*, 2012;72:5566-5575

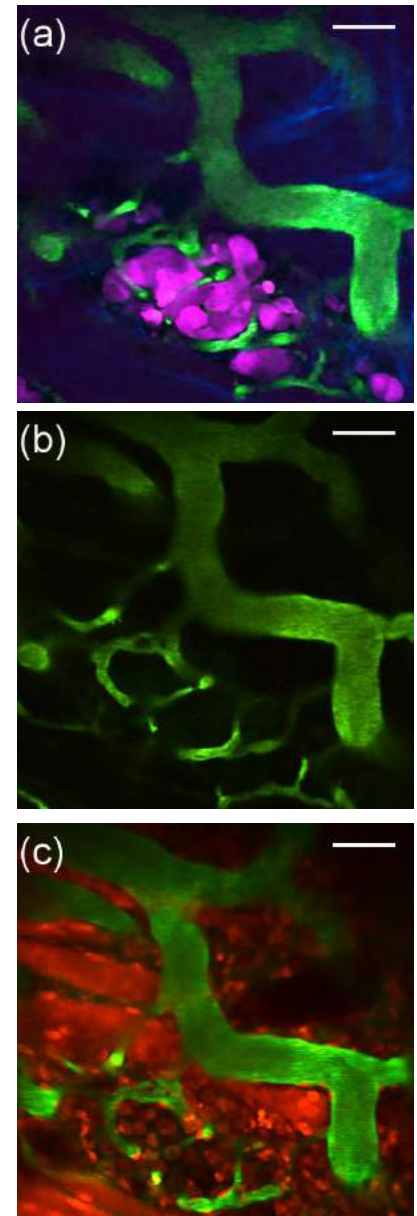


Figure 1: Pre-treatment image where tumour cells expressing GFP are false-coloured magenta and collagen is in blue (a), tumour vasculature before ThermoDox® injection (b), and following injection and FUS hyperthermia at 42°C for 20 minutes where the DOX signal is in red (c), FITC-labelled vasculature is green in all images, scale bar = 50µm

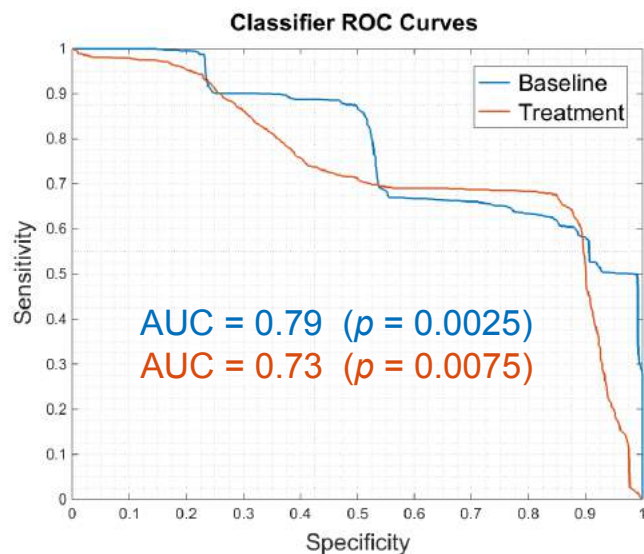
Development of a predictive radiomics signature for response to immune checkpoint inhibitors (ICIs) in patients with recurrent or metastatic squamous cell carcinoma of the head and neck (RM-SCCHN)

Dufort P², Prawira A¹, Halankar J², Paravasthu DM², Hansen AR¹, Spreafico A¹, Abdul Razak AR¹, Chen EX¹, Jang RW¹, Metser U², Siu LL¹

¹ Division of Medical Oncology and Hematology, Princess Margaret Cancer Centre / University of Toronto, Canada; ² Joint Department of Medical Imaging, University Health Network, Princess Margaret Cancer Centre / Mount Sinai Hospital / Women's College Hospital, Canada

INTRODUCTION: The nascent field of cancer radiomics is predicated on the hypothesis that medical images contain patterns difficult to discern with the naked eye, yet prognostic for response to therapy or disease states of clinical interest. In a typical application, a large set of quantitative texture and geometric features are extracted from tumor ROIs in study images, and are then subjected to a machine learning protocol to train a classifier to predict outcomes of interest based only on the image information. We employed this approach to the pursuit of a predictive radiomics signature of response to ICIs for RM-SCCHN patients from pre- and post-treatment CT-images. Early phase clinical trials of ICIs in RM-SCCHN have shown promising results, but there is no validated predictive marker of response to date.

METHODS: We conducted a retrospective analysis of clinical data and pre- and post-treatment CT-images from prospectively enrolled cohorts of RM-SCCHN patients treated with ICIs at the Princess Margaret Cancer Centre. A total of 25 tumor lesions spanning 9 patients were contoured from both baseline and post-treatment CT scans, each cross-checked by two experienced radiology fellows: 3 at primary head and neck sites, 11 metastases in lung, 5 in liver, 5 in lymph nodes, and 1 skin nodule. Following discretization of CT densities into 32 bins, a standard battery of 152 texture metrics was computed from the grey-level co-occurrence¹, neighborhood grey-tone difference², grey level run-length³, and grey level size zone⁴ matrices extracted from each ROI at multiple resolutions. The gold standard classification was defined by an analysis of lesion trajectories based on temporal evolution of the RECIST criteria, identifying 17 responders and 8 non-responders.



A radial basis function support vector machine was employed for machine learning, implemented in the LibSVM package⁵. Two nested levels of resampling were applied for training, hyperparameter tuning, and testing, with 10-fold cross-validation employed to tune hyper-parameters in the inner loop, and 1,088 random 3/22 test/train splits to assess accuracy and produce data for ROC analysis in the outer loop.

RESULTS: The classifier trained on the pre-treatment baseline data achieved an overall accuracy of 82.6% (50% sensitivity, 98% specificity) with an area under the ROC curve of 0.79 (see figure). A permutation test of the classifier yielded a statistical significance of $p = 0.0025$ for the area under the ROC curve under label randomization. For the classifier trained on the post-treatment data, an accuracy of 79.8% was achieved (64% sensitivity, 87% specificity) with an area under the ROC curve of 0.73 and a significance of $p = 0.0075$.

CONCLUSION: This pilot study showed early promising results given the low number of subjects and the heterogeneity of tumor sites. Patient accrual is ongoing, and further improvement in the accuracy of the developed algorithm is expected with increasing numbers.

REFERENCES: 1: Haralick, M.H. et al. (1973) IEEE Trans Systems, Man, Cyber, 3:610-621. 2: Amadasun, M. et al. (1989) IEEE Trans Systems, Man, Cyber, 19:1264-1274. 3: Loh, H.H. et al. (1988) IEEE Trans Industrial Electron, 35:323-328. 4: Thibault, G. et al. (2009) Patt Recog Info Proc (PRIP), 140-145. 5: Chang, C. C. et al. (2011) ACM Trans Intel Systems Technol, 2:1-27.

A GENERALIZED APPROACH TOWARDS MULTI-PARAMETRIC RESPONSE MAPPING USING PRINCIPAL COMPONENT ANALYSIS

Anthony Lausch^{1,*}, Timothy Pok-Chi Yeung¹, Jeff Chen¹, Elton Law², Yong Wang², Enrico Fainardi³, Ting-Yim Lee^{1,3} and Eugene Wong¹

Consortium Affiliation: Ontario Consortium for Adaptive Interventions in Radiation Oncology

¹Dept. of Medical Biophysics, University of Western Ontario, London, Ontario, Canada

²Robarts Research Institute, London, Ontario, Canada

³Dept. of Neurosciences and Rehabilitation, Azienda Ospedaliero-Universitaria Arcispedale S. Anna, Italy

*Primary author

INTRODUCTION: Development of image-based treatment response biomarkers is an important step towards guidance of adaptive radiotherapy (RT) strategies such as sub-volume boosting. Parametric response mapping (PRM) is a promising voxel-wise image analysis technique previously shown to be predictive of early treatment response [1]. PRM may be ideal for guiding these novel RT strategies however to date it has been almost exclusively applied to longitudinally acquired pairs of single-parameter functional image data. Our goal was to develop a generalized multi-parametric response map method (MPRM) to enable improved treatment response prediction via analysis of multi-parametric image data.

METHODS: MRI-derived apparent diffusion coefficient (ADC) and relative cerebral blood volume (rCBV) images acquired from patients treated for glioma at 1 and 3 months post-RT were used to develop the MPRM algorithm ($N = 4$ images/patient). Images were rigidly registered to enable voxel-wise analysis. The three major steps in the MPRM algorithm are; **Step 1**) principal component analysis (PCA) of image data within a normal tissue region of interest (ROI), **Step 2**) classification of image data within a tumour ROI and **Step 3**) response map construction. The output of step 1 is four principal component vectors (PCs) which characterize the typical multi-parametric variability in normal tissue ADC and rCBV values. The first PC describes the most variance and is similar to a line of best fit through a 4D plot of the normal tissue image intensity values. PCs 2-4 then describe the typical variability of these image intensity values about the line of best fit (i.e. about the linear model). In step 2, the data within the tumour ROI is plotted within the same 4D space and is orthogonally projected onto the i -th ($i \neq 1$) normal tissue PC. Each tumour voxel is then classified according to its distance from the normal tissue multi-parametric mean and with respect to the normal tissue variability in the direction of the PC. For example, if a tumour voxel is further away from the mean than 95% of all normal tissue voxels then it is classified by the value 95 (or if it is further away than only 50% it would be classified by 50). In step 3, MPRMs are constructed directly from the voxel-wise classifications from step 2.

RESULTS: An MPRM is an image of the tumour which visualizes the voxel-wise classification values. Each voxel intensity value summarizes how abnormal the voxel is with respect to normal tissue. This could facilitate localization of abnormal tumour regions which are driving treatment response or progression and subsequently provide targets for sub-volume boosts. Peri-tumoural regions could also be analyzed for signs of progression.

CONCLUSIONS: A generalized MPRM algorithm was developed which enables analysis of an arbitrary number of multi-parametric images via PCA. Next steps will involve investigation of predictive efficacy.

[1] Galban CJ et al. Nat. Med. 2009;15(5):572-6

CEST METRICS FOR ASSESSING EARLY RESPONSE TO STEREOTACTIC RADIOSURGERY IN HUMAN BRAIN METASTASES

K. L. Desmond^{1,2}, H. Mehrabian^{1,2}, S. Chavez³, A. Saghal^{1,4}, H. Soliman^{1,4}, G. J. Stanisz^{1,2}

Ontario Institute for Cancer Research Smarter Imaging Program

1. Physical Sciences, Sunnybrook Research Institute, Toronto, ON, Canada 2. Medical Biophysics, University of Toronto, Toronto, ON, Canada
3. Research Imaging Centre, Center for Addiction and Mental Health, Toronto, ON, Canada 4. Radiation Oncology, Sunnybrook Health Sciences Centre, Toronto, ON, Canada

Introduction: Stereotactic radiosurgery (SRS) is common for the management of brain metastases. Chemical exchange saturation transfer (CEST) is a MRI contrast mechanism which is sensitive to mobile protons in biomolecules which exchange with tissue water. CEST shows great promise for improving the characterization of brain tumours and their response to therapy¹⁻⁵. This study explores if CEST changes correlate with the change in tumour volume following therapy, and if CEST imaging at early time-points is predictive of future growth or regression of the tumour.

Methods: The CEST spectrum was approximated by five pools: "magnetization transfer" (0 ppm), "bulk water" (0 ppm), "amide" (3.5ppm), "amine" (2ppm), and "NOE" (-3.5ppm). Two groups of CEST metrics were considered for each CEST peak: the magnetization transfer ratio (MTR) evaluated at the frequency of the pool (Eq. 1) and the peak amplitude of each CEST effect (with amplitude "A", width "w", and offset frequency " Δ_0 ") from a Lorentzian decomposition of the CEST spectrum (Eq. 2). 14 patients with brain metastases were scanned on at 3T at three time-points: pre-treatment, one week and one month post-therapy. Image acquisition: 2D, single-shot gradient echo EPI (FE-EPI), TR:1532ms, effTE:30ms, resolution: 2.5mm, slice thickness: 3mm. Saturation scheme: 750ms block pulse, 0.52 μ T, preceding EPI. Offset frequencies: -750 to 750 Hz with reference at 100,000 Hz. Averages: 5, Total Scan Time: 12 minutes. ROIs were drawn in enhancing tumour and ipsilateral normal-appearing white matter (iNAWM). Mean MTR was calculated over the ROI at three different offset frequencies: amide, amine and NOE peak offsets. CEST peakfit metrics were determined for each voxel, then averaged over the ROI with a partial-volume correction⁶.

Results: MTR metrics offered the best discrimination between tumour and adjacent white matter at the pre-treatment time-point (example maps in Fig. 1). Tumour volume change 1 month post-therapy was correlated with Amide MTR in tumour ($p=0.085$) and NOE peak amplitude in iNAWM ($p=0.0048$) 1 wk post-therapy. It was also correlated with baseline values of NOE amplitude ($p=0.0180$), amide width ($p=0.042$) and NOE MTR ($p=0.08$) in the iNAWM. Interestingly, the correlation was greater in the iNAWM than within the tumour, likely a consequence of it having a more consistent baseline upon which to assess altered metabolism⁷.

Conclusion: Early CEST metric increases in either tumour or the surrounding iNAWM following SRS correlated with future tumour expansion. At the pre-treatment stage, low MT amplitude in tumour, or low NOE amplitude or MTR in iNAWM correlated with worse outcome at one month. CEST metrics have potential as biomarkers for response to SRS.

References: 1. Sagiya et al., Proc. Natl. Acad. Sci., 2014. **111**(12). 2. Dula et al., Magn. Reson. Med., 2013. **70**(1). 3. Paech et al., PLoS ONE, 2014. **10**(3). 4. Togao et al., Neuro-oncol., 2014. **16**(3). 5. Wen et al., Neuroimage, 2010. **51**(2). 6. Hofheinz et al., EJNMMI research, 2012. **2**(1). 7. Steeg et al., Nature Reviews Cancer, 2011. **11**(5).

$$\text{Eq. 1: } \text{MTR}(\Delta) = \frac{S_{\text{ref}} - S(\Delta)}{S_{\text{ref}}}$$

$$\text{Eq. 2: } S(\Delta) = 1 - \sum_{i=1}^5 A_i \left(1 + \left(\frac{\Delta - \Delta_{0i}}{0.5 * w_i} \right)^2 \right)^{-1}$$

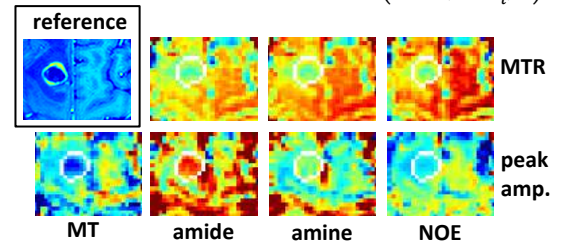


Figure 1. Example CEST metric maps: MTR and peakfit.

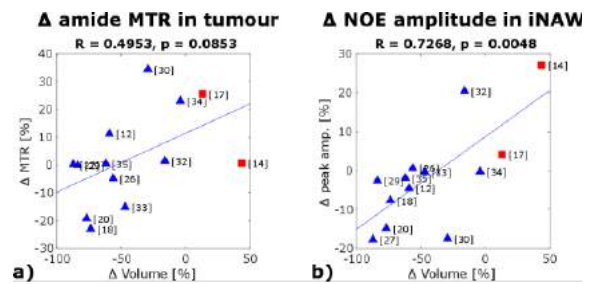


Figure 2. Scatter plots detailing correlations uncovered between changes in CEST metrics between pre-treatment and the 1 week time-point and volume changes at 1 month time-point. [Patient ID], blue triangle for responder and stable disease, red square for non-responder.

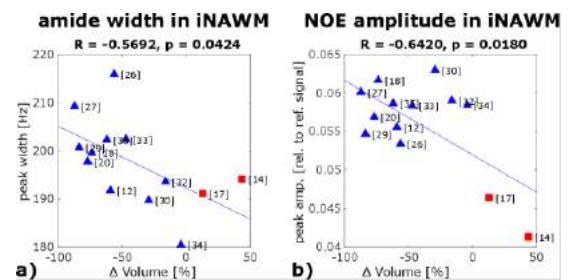


Figure 3. Scatter plots detailing correlations between CEST metrics at the pre-treatment time-point, and volume changes at one month post-treatment. [Patient ID], blue triangle for responder and stable disease, red square for non-responder.

Biomedical Imaging within a Transdisciplinary Musculoskeletal Research Program

David W. Holdsworth
Bone and Joint Institute
Western University, London ON

We depend on pain-free movement of our joints for our work, recreation, and daily activities. Unfortunately, the normal functioning of joints is often reduced as a result of: osteoarthritis, osteoporosis, sports injury, or traumatic accident. We have developed an integrated program of scientists and physicians to develop new therapies and assessment tools to reduce the impact of bone and joint diseases in Ontario, and across Canada. Biomedical imaging plays a key role within this program, with applications ranging from cellular microscopy and small-animal imaging to clinical imaging. This presentation will provide an overview of our current research activities, with an emphasis on areas for potential future collaboration. With funding from the Ontario Research Fund, we are developing advanced orthopaedic components, using image-based design and additive manufacturing in metal alloys. Advanced MRI and CT-based imaging techniques are being developed to provide quantitative 3D models for “virtual surgery” and patient-specific surgical guides. We are also developing unique facilities for dynamic 3D imaging of moving joints, under normal physiological loads. These techniques will allow us to prescribe the best therapies and monitor interventions, optimizing care for bone and joint conditions, with a long-term goal of maintaining lifelong mobility.

Simulating Heat Transfer in Bone During Magnetic Resonance Image-guided Focused Ultrasound Therapy

Alexander Chisholm¹, Thomas Looi¹, Samuel Pichardo², Adam C. Waspe¹, James M Drake¹,
Dionne Aleman³

¹Center for Image Guided Innovation and Therapeutic Intervention, Hospital for Sick Children

²Department of Electrical Engineering, Lakehead University

³Department of Mechanical and Industrial Engineering, University of Toronto

Introduction

High Intensity Focused Ultrasound (HIFU) is a non-invasive tumour treatment, alternative to surgery and radiotherapy. HIFU waves are localized at the tumour location in order to generate sufficient heat to ablate the tumour with minimal damage to neighboring tissue. HIFU treatment is often used in conjunction with magnetic resonance (MR) imaging for image guidance and temperature feedback during treatment. The limitation of HIFU treatment is the lack of pre-treatment planning.

Methods

Simulating heat transfer within bone can be used as a pre-treatment planning tool for MR guided HIFU (MRgHIFU) therapy. A computer simulator model was developed and has three main components. First, the simulator uploads and segments MRI scans. An automatic segmentation tool is developed to accurately segment bone as an alternative to the more time consuming method, manual segmentation. Next, the simulator uses the segmented data to simulate acoustic propagation to the target tissue, in order to calculate the acoustic velocity distribution. Finally the velocity distribution is converted to a heat distribution. A heat transfer model then simulates the change in the temperature distribution. Thermal simulations were performed on clinical trial patients and volunteers. Automatic segmentation was performed on clinical trial data, volunteers and a femur phantom.

Results

First, automatically segmented femurs were validated against the manually segmented ones. The average volume overlap difference and sensitivity between automatic and manual segmentation were 12.82 % and 93.94% respectively. The same validation metrics performed on volunteers were 7.37% and 94.4% respectively. Second, the exact volume of a femur phantom was compared with the automatically segmented volume. The total volume error was determined to be 1.7%. Third, the thermal simulations performed with manual segmentation were compared with simulations using automatically segmented data. The average ratio of ablated tissue and ablation centroid distance were determined to be .78 and .2mm respectively. Finally, the thermal simulations are validated with MRI thermometry data. The same metrics were determined to be .43 and 3.19mm respectively.

Conclusions

The manual and automatic segmentation validation metrics suggest the automatic segmentation performs well under ideal conditions. Factors such as poor image resolution can affect the automatic segmentation. This can explain the higher 12.82% volume overlap difference. The thermal validation metrics suggest that the simulator can reasonably predict where and how much ablation occurs at the focus. Lack of MR thermometry signal and thermal parameter estimation can affect the thermal prediction accuracy. This can explain the higher 3.19mm ablation centroid distance. If this MRgHIFU simulator is implemented as a pre-treatment planning tool, this will lead to improved safety, accuracy, patient throughput, and outcomes.

Image Processing Software for Designing Custom Craniofacial Implants

Amani Ibrahim¹, Michael Hardisty², Andras Lasso¹, Gabor Fichtinger¹, James Mainprize³, Cari Whyne²
 Laboratory for Percutaneous Surgery, School of Computing, Queen's University, Kingston, Canada¹
 Orthopaedic Biomechanics Laboratory, Sunnybrook Research Institute, Toronto, Ontario, Canada²
 Calavera Surgical Design, Toronto, Ontario, Canada³
 Consortium: Cancer Care Ontario (CINO); Consortium member: Gabor Fichtinger

Introduction. Craniofacial implants attempt to restore the cranial and facial skeletal anatomy which has been compromised due to accidental or natural defects. In general, using manually-shaped implants to carry out reconstruction of the craniofacial skeleton is challenging due to the skull's complex anatomy and the uniqueness of each defect.^[1] Custom craniofacial implants have gained importance due to their ability to achieve better performance over their manually-shaped counterparts.^[1,2] Using custom implants can yield better fitting implants which leads to improved cosmetic and functional output. Additionally, performing a surgery using custom implants leads to reduced surgery time since the design process of the implant mould, which is used to shape the implant, is carried out preoperatively.^[2] The preoperative time taken to create the implant design varies, and relies heavily on the expert designer, as well as the complexity and location of the defected area. If the defect area consists of thin bone structures, it is particularly difficult to automate the design process, making the task very time-consuming for the user. Our goal was to target these difficulties, and create specialized software for the efficient and accurate design of custom craniofacial implants, with a focus on improving the resolution of areas of thin bone, commonly occurring around the orbit.

Methods. We created tools to enhance the appearance of thin bone within computed tomography (CT) volumes, and the resolution of their associated 3D models, using the 3D Slicer platform.^[3] Restoration is carried out in two phases. The first phase focuses on restoring the quality of the CT volume by using Richardson-Lucy deconvolution and unsharp masking algorithms. The second phase focuses on enhancing the quality of the 3D skull model by filling in any remaining holes using Delaunay triangulation. Once skull geometry is restored, the undamaged region of the skull is mirrored, and used to dictate the implant shape of the damaged region.

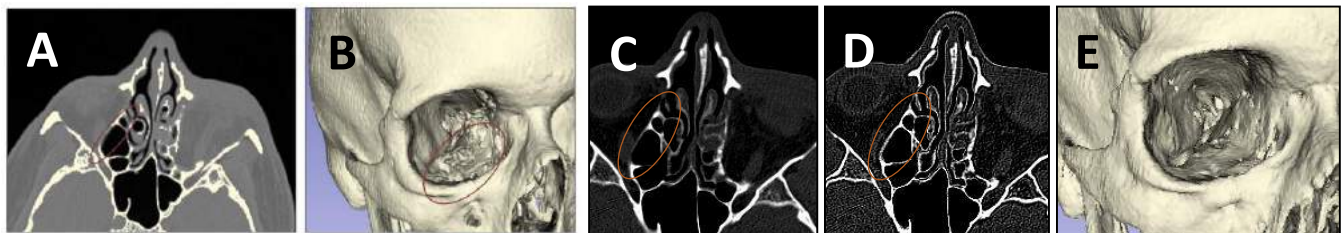


Fig. 1. A: Example of CT data used in design process, where thin bone around orbital (red) is difficult to resolve. B: Model generated using A. C: CT data prior to application of Richardson-Lucy Deconvolution algorithm. D: CT data after application of Richardson-Lucy Deconvolution algorithm. E: Model with restored geometry generated from D.

Results. The symmetry of the 3D models was evaluated on 4 patients. For each patient, the implant plan was registered to the undamaged orbital, and the average distance between the two surfaces was computed. The distances were $0.32 \text{ mm} \pm 0.35 \text{ mm}$ and $0.33 \text{ mm} \pm 0.21$ for the surfaces generated by manually segmenting CT data and by using the proposed automated method (Fig. 1), respectively.

Conclusions. We developed a computer assisted workflow for the design of custom facial implants that specifically addresses the problems of the design process for thin bone structures. The method described decreases design time and has been demonstrated to be of similar accuracy to previous, more time-intensive methods.

[1] Parthasarathy, J. (2014). 3D modeling, custom implants and its future perspectives in craniofacial surgery. *Annals of maxillofacial surgery*, 4(1), 9.

[2] Connell H, Statham P, Collie D, Walker F, Moos K. Use of a template for custom cranioplasty. *Phidias - EC Funded Network Project on Rapid Prototyping in Medicine*. 1999;2:7-8.

[3] Fedorov, Andriy, et al. "3D Slicer as an image computing platform for the Quantitative Imaging Network." *Magnetic resonance imaging* 30.9 (2012): 1323-1341.

Left Atrial Wall Segmentation using Hierarchical Max-Flow

J. Inoue, J. S. H. Baxter, and M. Drangova

Robarts Research Institute, Western University, London, Ontario, Canada
Consortium: CANet, Supervisor: M. Drangova

Introduction. Atrial fibrillation (AF) is the most common cardiac arrhythmia and a major cause of ischemic stroke. It is characterized by irregular electrical activity in the upper chambers of the heart. Radiofrequency (RF) ablation can be an effective, minimally invasive, image-guided intervention for AF, but often fails, possibly due to insufficient detail in modeling the left atrial (LA) geometry. In particular, the current clinical workflow does not include a LA wall thickness measurement as part of ablation dose planning. Segmenting the wall from preoperative, contrast-enhanced CT is a first step in providing this measurement to clinicians, but this is a challenging task – the atrial wall and surrounding muscular tissue have similar image intensity values, and the wall itself is thin in comparison to the image resolution. A method that incorporates anatomical knowledge is needed to successfully segment the atrial wall.

Methods. Hierarchical max-flow (HMF)¹ is a mathematical optimization-based segmentation method that uses probability distributions (estimated through direct sampling of each anatomy of interest) to determine image intensity characteristics of tissues, and a user-defined class-hierarchy to further constrain regularization. HMF was incorporated into a two-stage segmentation pipeline using the hierarchies shown in Figure 1. Blood was first segmented as a single class using HMF and manually separated into *atrial blood* and *other blood* classes. A hierarchy separating *atrial blood/myocardium* from *other blood/myocardium* was used with the segmented *atrial/other blood* in order to allow the previously segmented blood to anchor the two myocardium labels and distinguish between them. The method was validated on ten gated, contrast-enhanced cardiac CT images of RF ablation patients with AF. For the reference standard, one observer manually segmented the LA walls in all images in 3D, using the pre-computed blood pool segmentation as a guide to regions that were in-scope.

Results. An example of the resulting segmentation is shown in Figure 2. The overlap, by mean Dice similarity coefficient, was 0.79, and the mean root-mean-squared-error of the atrial wall segmentation (epicardial side only) was 0.86 mm. On average, the proposed segmentation pipeline generated segmentations that were 13% larger than manual segmentation. The LA wall was successfully differentiated from aortic wall, and esophagus. The right atrium was largely differentiated as well, but segmentation in this region was less accurate.

Conclusions. Using HMF to leverage information provided by the blood in other structures allows the LA wall to be distinguished from nearby muscular structures. This alleviates the need for much of the manual correction required by methods that do not bring this context into the final segmentation. Segmentation accuracy is comparable to the variation between experts² and in similar work on ventricles³ despite the lack of manual correction and minimal interaction.

References. ¹Baxter et al. *arXiv:1404.0336*, 2014. ²Koppert et al. *Proc. IEEE ISBI*, pp. 480 - 483, 2010. ³Rajchl et al. *Proc. IEEE ISBI*, pp. 1409 - 1412, 2012.

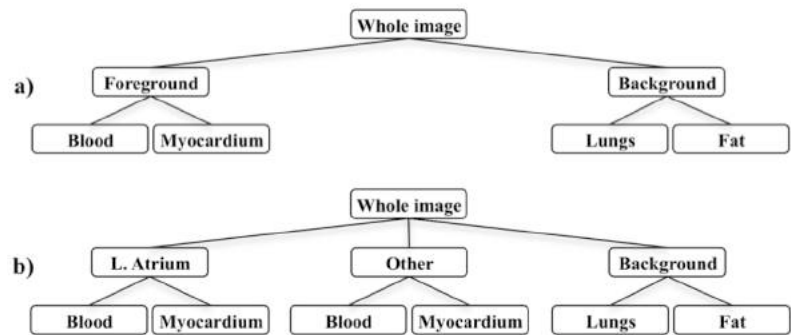


Fig. 1. a) Hierarchy for first segmentation. b) Hierarchy for second segmentation.

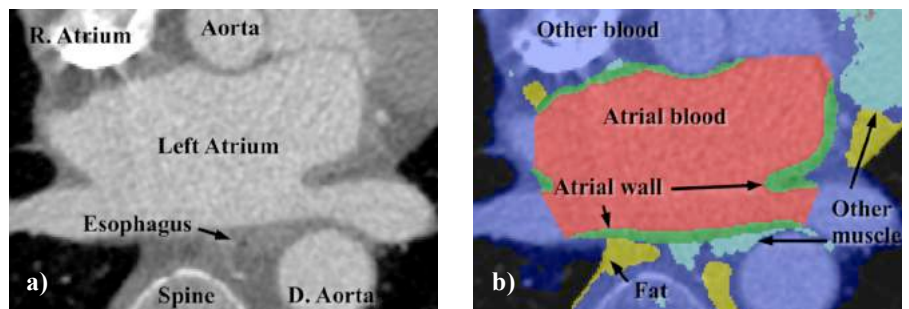


Fig. 2. a) Original axial slice image of left atrium. b) Segmented image of left atrium. The central red label is *left atrial blood*. The *other blood* label leaks into neighbouring areas due to classification of most blood as *other blood*, but the strong *left atrial blood* label forces nearby muscle tissue to be classified as *atrial wall*.

Augmented Reality for Improved Ultrasound Guidance in Central Venous Access

Golafsoun Ameri*, John SH Baxter, Jonathan McLeod, Elvis CS Chen, and Terry M Peters
Robarts Research Institute, Western University, London, Ontario, Canada

Introduction: Cannulation of the internal jugular vein (IJV) is widely performed to access the central venous system for a large number of applications including hemodynamic monitoring, drug delivery, and endomyocardial biopsy¹. Over five million central venous catheters are inserted annually in the USA alone². Traditionally, the IJV is identified using external anatomical landmarks, which are not always reliable due to anatomical variation¹. Consequently, Carotid artery (CA) puncture sometimes occurs³, which could lead to severe complications including hemorrhage, stroke, or death⁴. The rate of CA puncture during IJV cannulation is as high as 9.7%⁵. Real-time ultrasound (US) guidance has been shown to decrease the rate of CA puncture⁶ but complications still arise, mainly because of uncertainties regarding the position of the needle tip with respect to the target due to the difficulty in distinguishing the needle shaft from needle tip in US⁴. The purpose of this work is to develop a novel guidance system to facilitate needle placement in the IJV and improve the overall safety of this procedure. This guidance system, which has been approved for clinical evaluation, integrates an augmented reality (AR) environment and real-time US to improve needle tip visualization.

Methods: An AR guidance platform was developed, which allowed tracked real-time US images and a virtual representation of a tracked needle to be displayed simultaneously in the same environment (Fig. 1). The performance of this guidance system was compared against traditional US-only guidance in a preliminary user study. Eighteen novice participants went through a brief training phase. After training, they performed two sets of central line procedures in a phantom under both AR guidance and US only guidance in a randomized order. For each procedure, procedure time and needle path tortuosity were recorded.

Results: The results were processed using two-way ANOVA with the guidance system type and the trial number as factors. The Holm-Bonferroni correction was used with a combined significance of $p < 0.05$. No significant interaction between factors was observed. The results showed a significant improvement with AR guidance comparing to US-only guidance. The 95% confidence interval on the average improvement in terms of time and needle path tortuosity for AR was 3.51 ± 1.44 s, and $150 \pm 40\%$, respectively. In addition, AR showed more performance consistency across participants. A significant training effect was also detected in our analysis.

Conclusion: In this work, we propose and perform preliminary validation on an augmented reality (AR) guidance system tailored for the central line procedure. This system has been shown to significantly reduce procedure time and path tortuosity, improving the safety of the procedure. This system has received regulatory approval and is scheduled for clinical trials.

References: [1] Denys, Critical Care Medicine, 1991, [2] McGee, New England J. of Medicine, 2003, [3] Odasso, Anesthesiology, 1996, [4] Bowdle, Journal of cardiothoracic and vascular anesthesia, 2014, [5] Martin, Critical care medicine, 1990, [6] Schmidt, Intensive care medicine, 2015.

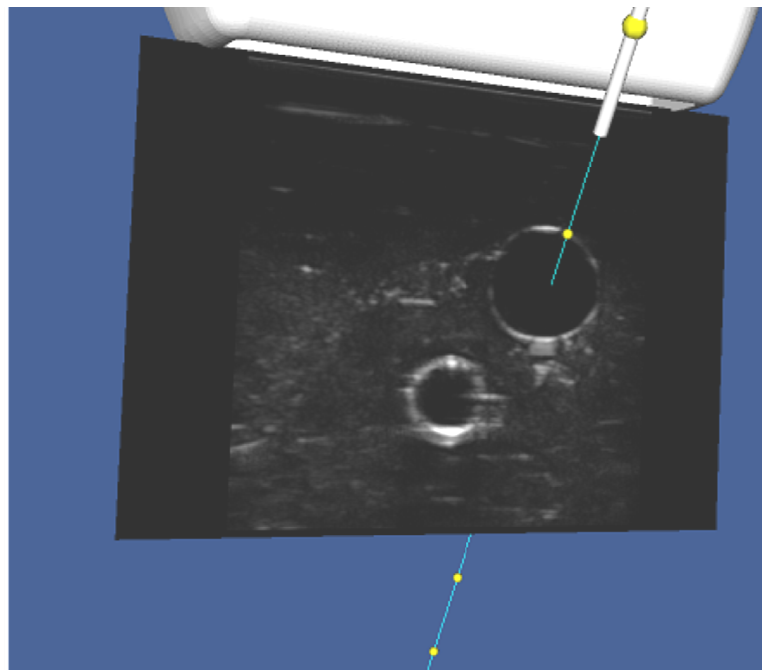


Figure 1: The AR guidance system.

Standardized interpretation of Tc-99m-SPECT perfusion images in a multi-center study of MITNEC (Medical Imaging Trials Network of Canada)

Jennifer Renaud¹, Francois Harel², Manuja Premaratne¹, Marie-Claude Villeneuve², Vincent Finnerty², Therese Heinonen², Jean-Claude Tardif², Terrence Ruddy¹, Robert deKemp¹

¹University of Ottawa Heart Institute, Ottawa ON, Canada

²Montreal Heart Institute, Montreal QC, Canada

Consortium affiliation: MITNEC

Introduction: Accuracy of Tc-99m SPECT is under evaluation vs. non-nuclear imaging modalities in patients at high risk of multi-vessel disease in one of the MITNEC studies. Consistent interpretation methods are essential for analysis of pooled data from multiple centers, thus standardized scoring techniques between the 2 core labs were implemented and evaluated.

Methods: Rest-stress Tc-99m patient scans were acquired at 2 centers on cameras previously qualified via phantom scans confirming thresholds for ischemia. Ten scans from each site were read by an expert reviewer at both core labs. Defects were scored in 17 segments using visual interpretation of sum stress (SSS) and difference scores (SDS) using a 10-step color-map, with SDS reflecting the combined extent and severity of ischemia. $SSS \geq 4$ indicated flow-limiting disease and $SDS \geq 2$ indicated ischemia. Cases with scoring differences >3 between core labs, or discordant clinical interpretations (norm/abnormal) underwent consensus review. Variability of scoring, interpretation and image quality assessment between core labs was assessed.

Results: Excellent agreement was found for SSS using the intraclass correlation coefficient: $r = 0.96$. SDS agreement was lower: $r = 0.78$. 90% of SSS and 85% of SDS values had differences ≤ 3 between core labs. Clinical interpretations were found to be in 90% agreement. Following consensus review, scoring agreement improved to $r = 0.99$ (SSS) and 0.93 (SDS), and clinical interpretation agreement was 100%, $p < 0.05$. Agreement of abnormal ($SSS \geq 4$) and ischemic ($SDS \geq 2$) scans was excellent ($r = 0.95$ and 1.00). All images were ranked as good or fair quality, resulting in 70% agreement in image quality between core labs.

Conclusion: With effective standardization, repeatable scoring and interpretation are achievable across core labs. This consistency is critical to combine multi-site data for evaluation of the accuracy of Tc-99m SPECT perfusion imaging.

Semi-automatic segmentation of high-dose-rate prostate brachytherapy needles using 3D ultrasound

W. Thomas Hrinivich^{1,2}, Douglas Hoover^{1,3,4}, Kathleen Surry^{1,3,4}, David D’Souza^{3,4}, Aaron Fenster^{1,2,4,5*}, Eugene Wong^{1,3,4,5*}

1 Dept. of Medical Biophysics, Western University; 2 Robarts Imaging Research Laboratories; 3 London Regional Cancer Program; 4 Dept. of Oncology, Western University; 5 Dept. of Physics and Astronomy, Western University, London ON; Consortium: OICR Imaging Translation Program; *Trainee Supervisors

Introduction: High-dose-rate brachytherapy (HDR-BT) is a prostate cancer treatment option involving the insertion of 10-18 hollow needles into the prostate through the perineum using a labelled template, allowing the temporary delivery of a radioactive source. HDR-BT dose distributions depend critically on the relative positions of the needles, prostate, and surrounding organs at risk. 3D ultrasound imaging is effective for needle localization; however, manual segmentation must be performed intra-operatively adding time to the procedure. The purpose of this study is to present a semi-automatic needle segmentation algorithm designed for HDR-BT, specifically capable of 1) segmenting multiple needles with ~5 mm inter-needle spacing and 2) assisting the user in labelling each needle with the corresponding template hole for treatment delivery. **Materials and Methods:** The algorithm was implemented in MATLAB 2015b (Mathworks, Natick MA) using a modified version of the randomized Hough transform with additional regularization steps, followed by interactive template registration. For algorithm validation, 12 prostate cancer patients underwent HDR-BT during which 3D ultrasound images were acquired. Needles present in each of the 12 images were segmented by a single user using the algorithm, and manually by a medical physicist using BrachyVision (Varian Medical Systems, Palo Alto CA) providing a gold-standard for comparison. Tip errors were defined as the 3D Euclidean distance between needle tips, and trajectory error was defined as the mean 3D Euclidean distance between trajectories along 5 cm of their length beginning at the image entry point. Clinically-relevant error thresholds of 3 mm and 5 mm were used to stratify segmentations. **Results:** In total, 188 needles were investigated. Mean execution time of the algorithm was 22 s per patient plus 64 s per patient for interactive template registration. Example template registration and needle segmentations are provided in Figure 1a-b. Results are summarized in Table 1 and Figure 1c. Tip errors tended to be largest in the superior/inferior direction, which is the direction of needle insertion. **Conclusions:** To the authors’ knowledge, this is the first needle segmentation algorithm designed to segment and label multiple nearby needles in 3D ultrasound images. In a previous study we found that manual needle segmentations provided superior/inferior tip errors ≤ 3 mm and ≤ 5 mm for 83% and 92% of needles respectively (Hrinivich *et al. Brachytherapy. In Press*), suggesting an upper bound on potential accuracy. The algorithm shows promise for trajectory localization, which could be used to provide the user with a cross-sectional view of each needle for manual tip identification.

Table 1. Subsets of needles with semi-automatic segmentation errors within thresholds.

| | All needles | Tip error ≤ 3 mm | Tip error ≤ 5 mm | Mean trajectory error ≤ 3 mm | Mean trajectory error ≤ 5 mm |
|---------------------------|-------------|-----------------------|-----------------------|-----------------------------------|-----------------------------------|
| # of needles (% of total) | 188 (100) | 134 (71) | 152 (81) | 171 (91) | 174 (93) |

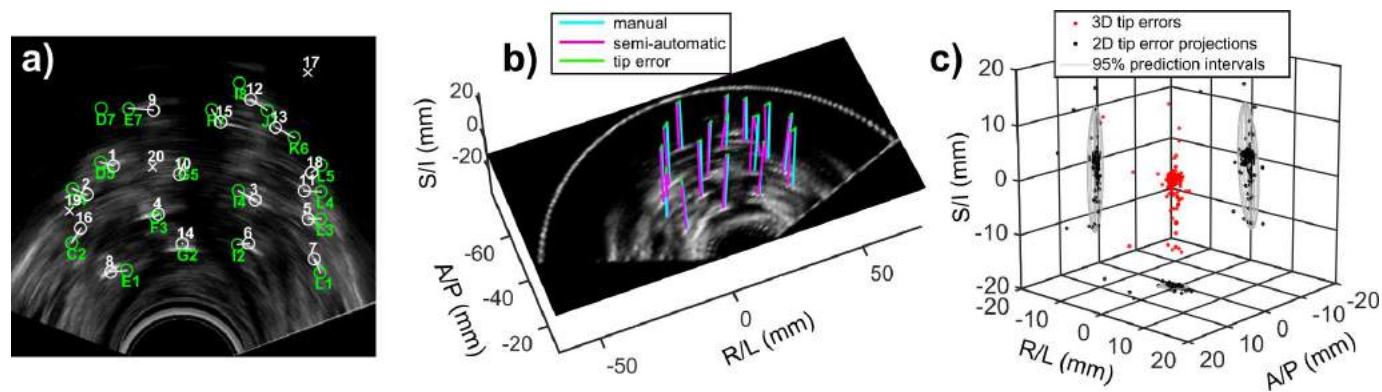


Figure 1a) Screenshot from the interactive template registration tool. Template hole labels (green circles) are registered to a 2D axial projection of the auto-segmented needles (white circles). Anchor points may be added by the user to update the registration. **b)** Example manual and semi-automatic segmentations for a single patient intersecting an axial slice of the 3D image. **c)** Plot of needle tip errors for all needles. *8 needles had superior/inferior errors beyond -20 mm so are cropped from the plot.

Localizing Fiducial Markers using Undersampled co-RASOR MRI for Radiation Therapy PlanningEvan McNabb¹, Raimond Wong², Michael D. Noseworthy^{1,3}¹*School of Biomedical Engineering, McMaster University, Hamilton, ON;* ²*Juravinski Cancer Centre, Hamilton;* ³*Department of Electrical and Computer Engineering, McMaster University.*

Purpose: Metallic fiducial markers, implanted inter/intra-tumour due to their low migration are used for Computer Tomography (CT) Electron Beam Radiation Therapy of prostatic and bladder lesions. Magnetic Resonance (MR) imaging has been used for planning since CT images can overestimate volumes with larger interobserver variability¹, and lead to higher radiation to adjacent regions². However, fiducials cause image artifacts in MR leading to hypointense signal voids. Hyper-intense contrast from paramagnetic brachytherapy seeds was demonstrated using centre-out Radial Acquisition using Off-Resonance Reception (co-RASOR)³ by radially rewinding signal pile-ups around the edges of field perturbers. Radial readouts have additional benefits of oversampling the centre of k-space and can be reconstructed from undersampled data using multi-channel coils and variation penalties⁴. This work aims to demonstrate that undersampled co-RASOR can be used to localize implanted fiducials to accelerate abdominal imaging to avoid motion artifacts and reduce clinical scan times.

Methods: Platinum seed fiducial markers (ISI Medical Products) were placed in agarose gel phantom at angles of 0, 55, and 90 degrees with respect to the B₀-field. CT scans were performed using a Siemens Biograph-16 PET/CT (512x512; FOV = 384 mm²; 50 mA; 80 keV) as an imaging reference for the metallic fiducials. MR imaging was performed using a GE MR Discovery 750 3T and a 32-channel head coil. An in-house sequence was developed, modifying a 2D Fast Gradient Echo sequence, acquiring full echo, radial readouts over 360° following the co-RASOR method⁴. Undersampled (R=8) axial images of fiducials lying parallel and perpendicular to the B₀-field, and one coronal image showing two in-plane fiducials using co-RASOR were acquired (TE = 5.5 ms; FOV = 20.0 cm; thickness = 1.0 mm; 256 readout points). Fully sampled MR data used non-uniform DFT (NUFFT), and undersampled data used the Total Generalized Variation penalty to inverse Fourier Transform MR data and reconstruct the images.

Results: Varying frequency offsets (-4 kHz to +4 kHz) were performed on fully sampled co-RASOR coronal images with the optimal offset chosen by visual inspection at to create an image

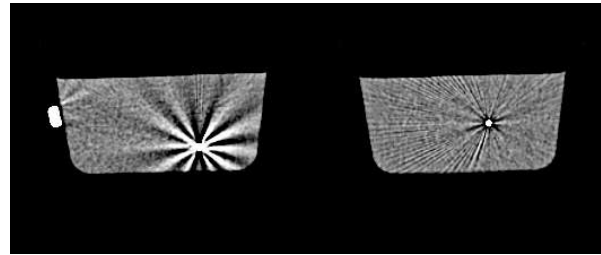


Figure 1: Reference CT showing axial slices of fiducials perpendicular to each other.

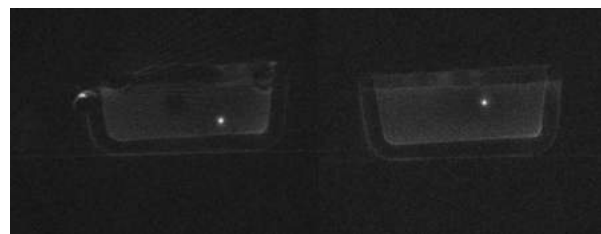


Figure 2: Axial views of undersampled (R=8) co-RASOR images for fiducials perpendicular and parallel to the B₀-field respectively were reconstructed using a regridding Kaiser-Bessel interpolation kernel showing the radial streaking and blurring artifacts expected when the number of readouts is well below the Nyquist limit.

for all other slices. When reconstructed using variation penalties, masked co-RASOR images showed hyper-intense signals for fiducial markers regardless of its orientation with respect to B₀.

Discussion: This work demonstrated that accelerated radial imaging together with off-resonance reconstruction techniques was able to quickly and accurately locate paramagnetic fiducial markers. Scan time was reduced by a factor of approximately 8 by limiting the number of readouts from 804 down to 101 (256 readout points) for a scan time of 2.02s per slice. Deviations from the original co-RASOR method included using a 2D slice-selective sequence rather than a 3D non-selective excitation sequence resulting in a narrower excitation bandwidth to achieve slice thickness, resulting in fewer off-resonant protons achieving excitation around the edges of fiducial markers.

References:

- [1]: Parker *et al.* (2003) J Radiol Oncol; 66: 217
 [2]: Debois *et al.* (1999) Int J Radiat Oncol; 45: 857
 [3]: Seevinck *et al.* (2011) MRM; 65: 146
 [4]: Knoll *et al.* (2011) MRM; 67: 34

Development of a CZT-Based Gamma Camera for Simultaneous Molecular and MR Breast Imaging

Ashley T. Tao^{1*}, Michael D. Noseworthy^{1,2}, Troy H. Farncombe^{1,3}

Medical Imaging Trial Network of Canada

¹Department of Medical Physics, McMaster University, Hamilton, Ontario

²School of Biomedical Engineering, McMaster University, Hamilton, Ontario

³Department of Nuclear Medicine, Hamilton Health Sciences, Hamilton, Ontario

Introduction - Breast MRI has been shown to provide high sensitivity for detection of breast cancer, however it may result in a high number of false positives due to lower specificity [1]. Molecular breast imaging (MBI) on the other hand, provides functional information through the uptake of Tc-99m and offers high specificity with good sensitivity [2]. A recent study by Golan [3], indicated that using MBI with breast MRI improved lesion scoring as compared to MRI alone. Recent advances in semiconductor technology have led to the ability to build develop MR compatible imaging systems. A solid-state gamma camera has been designed with the goal of performing simultaneous MBI and MR in order to improve sensitivity and specificity in breast cancer imaging.

Method - The CZT based gamma camera consists of four CZT detector modules arranged into a 32x32 array with a pixel pitch of 2.46 mm. A custom digital readout board was designed to communicate with the modules. The array was encased within a lead-lined carbon fiber box and a parallel hole collimator affixed to the detector surface. The gamma camera was positioned in the isocentre of a 3T MRI (GE Discovery MR750) and imaging performance measured. Gamma camera performance was characterized by measuring the energy resolution, uniformity and spatial resolution outside the MRI and again when placed inside the MR bore using Tc-99m (γ energy = 140 keV). Initial tests were performed in the main magnetic field only. Influence of the gamma camera on MRI image quality was assessed using a 2D T1-weighted gradient echo sequence (TR = 500ms, TE = 5/8ms, flip angle = 45° FOV = 12cm, slice thickness = 3mm) to measure the B0 field homogeneity, SNR and geometric accuracy, when used with a Sentinelle 16-channel breast coil.

Results - The measured energy resolution at 140 keV was 7.2% and 7.0% when the gamma camera was positioned inside and outside the MRI, respectively. The integral uniformity for both imaging conditions were 4.6% and the differential uniformity was 1.5% and 1.9% outside and inside the B0 field. The spatial resolution of the system approached the intrinsic resolution given by the pixel size and was unaffected by the B0 field.

A uniform breast-like phantom was used to assess the influence of the gamma camera on MRI image quality. B0 inhomogeneity was measured with a maximal shift of 8 ppm in the area closest to the camera. This field distortion resulted in a 10% decrease in SNR. However, negligible geometric distortion was observed in the magnitude images.

Two lines sources filled with Tc-99m were inserted into the breast phantom and imaged sequentially with MR. The planar image from the gamma camera was fused manually with the MRI image in Fig. 1 to show the feasibility of registering the two images together.

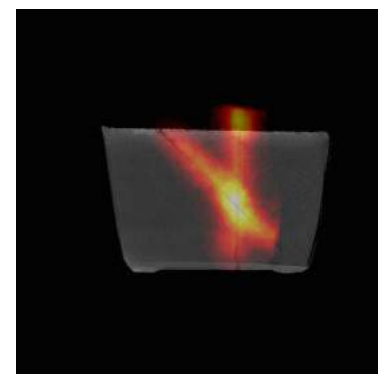


Fig. 1. Co-registered of magnitude image from MRI to the projection image from the gamma camera.

Conclusion – Preliminary results indicate negligible effect from the main magnetic field on gamma camera performance. In addition, while the magnetic field homogeneity was affected by the presence of the gamma camera, overall MR performance of the geometric accuracy and overall SNR was minimally affected. Future results will include gamma camera performance during simultaneous acquisition with an MRI sequence. Upon successful simultaneous testing, this design could be scaled to a larger area for future use in combined breast MR/MBI.

References

- [1] Leach, M. et al. "Screening with Magnetic Resonance Imaging and Mammography of a UK Population at High Familial Risk of Breast Cancer: A Prospective Multicentre Cohort Study (MARIBS)" *Lancet*. 2005; 365: 1769-1778.
- [2] Rhodes, D. et al. "Molecular Breast Imaging at Reduced Radiation Dose for Supplemental Screening in Mammographically Dense Breasts" *Am. J. Roentgenol*. 2015; 204(2): 241-251.
- [3] Golan, O. et al. "Molecular Breast Imaging(MBI). Does It Have a Complementary Role to breast MRI" *J. Nucl. Med*. 2012; 53(S1): 1290.

Validating internal and external correlation during respiratory gated VMAT using on-board kV imagingIlma Xhaferllari*, Omar El-Sherif, Stewart Gaede
Department of Medical Biophysics, Western University

Introduction: A main uncertainty in using an external surrogate for respiratory gated treatment delivery, lies in the motion of the surrogate to accurately predict the motion of the tumour. Respiratory gated treatment is vulnerable to variability in intrafractional tumour motion especially when the motion is exhibiting baseline shifts. This can lead to discrepancies in the delivered dose, with some target volumes nearing under-dosage¹. The combination of respiratory gating with volumetric modulated arc therapy (VMAT) in high dose rate delivery, further enhances this uncertainty. In this phantom study, internal and external correlation motion during VMAT delivery was retrospectively validated using on-board kV imaging for free-breathing, phase- and amplitude-gating deliveries. Also, the ability to accurately quantify known baseline phase shifts is investigated.

Methods: The Quasar respiratory motion phantom (Modus Medical Devices, London, ON) is utilized to trace a 3-cm delrin sphere embedded in a moving cedar insert as the motion of the internal target. The motion of the external surrogate, the respiratory gating box is acquired from the on-board kV projections during treatment plan using TrueBeam Research mode v.2.0 (Varian Medical Systems, Palo Alto, CA). Free-breathing treatment delivery using sinusoidal motion with four second period and 2-cm peak-to-peak amplitude, and retrospective real-patient breathing (RPB) motion waveform was programmed to the phantom to investigate internal and external correlation. Respiratory-gated treatment deliveries (30-60% gating window) on five retrospective RPB waveforms were performed to further investigate gating window verification. To investigate the capability of during treatment kV imaging to detect phase shifts, a second Quasar respiratory phantom was programmed to trigger respiratory gating. Controlled phase shifts in intervals of 0.4 seconds were added to the sinusoidal motion in both directions, totalling for eight shifts. Pearson linear correlation coefficient statistical test was performed to determine correlation. To validate the programmed baseline phase shift, the external waveform was shifted, in time, until the Pearson linear correlation coefficient was maximized.

Results: In the full motion encompassed treatment delivery, a high correlation (sinusoidal $R^2=0.993$ and RPB $R^2=0.990$) was obtained demonstrating that the kV projections can accurately be used as a tool despite the various angle projections, other structure obstructions, and MV beam degradation artifacts. In the 30% gating window deliveries, a high Pearson linear correlation coefficient ($R^2=0.986-0.996$) was observed in five real patient breathing waveforms indicating that dose delivery occurred while the target was in correct position; Figure 1 displays an example. Figure 2 indicates the kV projections were able to accurately account for any phase shifts in phase respiratory gating. The programmed and actual shift obtained no significant differences ($p=0.899$) and R-squared is 0.997.

Conclusion: During treatment kV imaging has the capability to verify intrafractional anatomical position. It can be accurately used as a tool to verify internal and external correlation, and phase shifts within the gating window, and ultimately, accuracy of respiratory-gating treatment delivery.

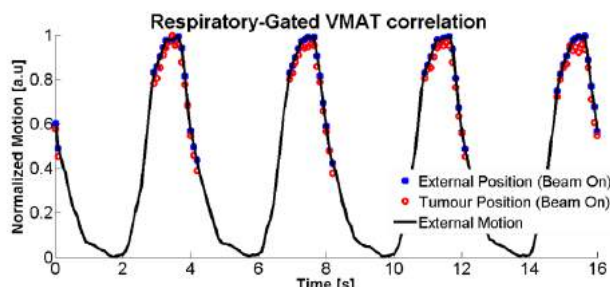


Figure 1: Gating window verification for using a real-patient breathing waveform. Pearson linear correlation coefficient within gating window, $R^2=0.996$.

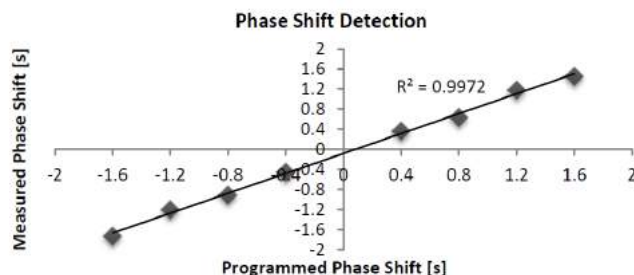


Figure 2: Comparing the phase shift programmed to shift required to maximize Pearson linear correlation coefficient.

References: ¹Bo Z., Yang Y., Li T., et al. 2012. "Dosimetric Effect of Intrafraction Tumor Motion in Phase Gated Lung Stereotactic Body Radiotherapy." *Medical Physics* 39 (11): 6629–37.

Simultaneous PET/MRI with Clinical and Preclinical Systems

Jonathan D. Thiessen

Imaging Program, Lawson Health Research Institute
Department of Medical Biophysics, University of Western Ontario

When imaging patients and large animal models with a simultaneous clinical 3T PET/MRI (Siemens Biograph mMR), we have seen several inherent advantages beyond improved anatomical information. In the heart, for example, new insight can be gained when fusing cine, gadolinium-enhanced, and relaxation time mapping MRI with PET tracers sensitive to glycolysis (^{18}F -FDG), perfusion (^{13}N -ammonia), or sympathetic innervation (^{11}C -HED). Simultaneous PET/MRI with combined contrast infusions of both MRI and PET tracers may help improve pharmacokinetic modeling in tissue. Simultaneity can also be used to retrospectively correct PET data for motion and partial volume effects based on information derived from the MRI. Efforts at Lawson to improve the quantitative accuracy of clinical PET/MRI have also included improvements to MR-based attenuation corrections, multi-site phantom measurements, and implementation of novel, PET-compatible, 32-channel RF coils designed specifically for the Siemens Biograph mMR.

Although the installed base of clinical PET/MRI systems continues to grow, the number of simultaneous preclinical PET/MRI systems world-wide can be counted on one hand. Ultimately, there are countless mouse and rat models of disease that are unavailable and/or too expensive in larger animals. For PET images, the Biograph mMR has a resolution of 4.3 mm in the centre of its field-of-view with a peak sensitivity of 1.5%, whereas a small animal PET system can, in theory, achieve <1 mm resolution with $>5\%$ peak sensitivity. The entire brain of an adult mouse is ~ 400 μL in volume. Quantification of small structures in mice and rats with PET and MRI demands sub-millimetre spatial resolution and increased sensitivity that can only be produced by a dedicated preclinical PET/MRI system. Applications for a preclinical PET/MRI include:

- Development and translation of new tracers that require biodistribution studies, pharmacokinetics, and toxicity prior to more expensive large animal models and human studies.
- Concurrent use of tracers being tested in both human and non-human studies, where human imaging protocols can be informed by preclinical imaging that includes histopathological correlations and longitudinal monitoring of potential treatments.
- Development of new PET/MRI methods that require testing in both control and disease models. This might include complementary PET/MRI acquisition methods (e.g. simultaneous measurements of perfusion and glucose metabolism) or cross-validation of PET and MRI methods intended to measure the same thing (e.g. blood flow, metabolic brain activity, etc.)

In order to develop methods and perform imaging studies on small animals that are comparable to our clinical 3T PET/MRI, a truly simultaneous, small animal PET/MRI system is required. In recognition of this clear need, we have been working with industry and academic partners, led by Dr. Andrew Goertzen at the University of Manitoba, to develop a high-resolution PET insert designed to operate in a preclinical MRI. This technology has been licensed by a Canadian company (Cubresa, Winnipeg) who will deliver the first commercially available, preclinical PET/MRI insert to Lawson in the first half of 2016. Although it will initially be installed in our clinical 3T PET/MRI, this system is small enough (113 mm outer diameter) to operate simultaneously in most high-field preclinical MRI systems. The design and initial results from this system will be presented.

Acknowledgements: NSERC, ORF, Mitacs, Siemens Canada, Cubresa, MMI, and the Lawson Internal Research Fund.

Enhanced electromagnetic catheter tracking with application in high-dose-rate brachytherapy

Elodie Lugez^{*1}, Hossein Sadjadi¹, Chandra P. Joshi², Selim G. Akl³, and Gabor Fichtinger¹

Ontario Consortium for Adaptive Interventions in Radiation Oncology

¹Laboratory for Percutaneous Surgery, Queen's University, Kingston, ON, Canada

²Cancer Centre of Southeastern Ontario, Kingston General Hospital, Kingston, ON, Canada

³School of Computing, Queen's University, Kingston, ON, Canada

Introduction. Catheter path reconstruction is a necessary step in many interventional procedures, such as cardiovascular interventions and high-dose-rate brachytherapy. To overcome shortcomings in standard imaging modalities, electromagnetic (EM) tracking has been employed to reconstruct catheter paths^[1]. However, EM tracking is prone to measurement errors which can compromise the outcome of the procedure. While several error minimization techniques have been proposed, the tracking error still poses a challenge in accurate path reconstruction. Minimizing these errors is therefore paramount. We address this challenge by means of a specialized filtering technique for catheter tracking.

Methods. EM tracking of catheter paths was improved by means of an extended Kalman filter (EKF), combining both the position and orientation measurements of an EM sensor with the nonlinear kinematic constraints of that EM sensor inside the catheter. The performance of our proposed approach was experimentally evaluated using an Ascension trakSTAR electromagnetic tracker. A 3D printed calibration phantom, illustrated on Figure 1(a), firmly held ten HDR catheters into predefined ground truth paths with mean curvatures varying from 0 m^{-1} to 6.6 m^{-1} . The experimental setup was placed in an HDR brachytherapy suite, pictured on Figure 1(b). The EM sensor measurements were recorded while the sensor was retracted into the paths at various speeds ranging from 8.8 to $25.2 \text{ mm}\cdot\text{s}^{-1}$. We collected raw measurement data and applied our method to improve the tracking performance. Results were compared with the filtered data provided by the manufacturer. Finally, the sensitivity of our nonholonomic EKF method to sensor velocity and path curvature was determined.

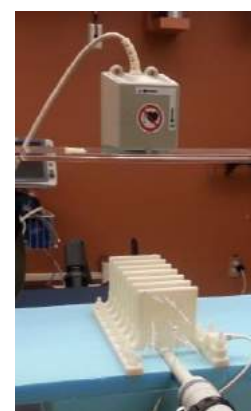
Results. Errors in path reconstruction were reduced from 3.5 to 1.9 mm using the advanced nonholonomic EKF, which outperformed the manufacturer's filters efficacy to reduce errors by 21% . Although path curvature and sensor velocity did not yield a clinically significant trend on the reconstruction performance, the position of the EM field transmitter predominantly impacted path reconstruction accuracies.

Table 1. Path reconstruction results

| | Raw measurements | Standard manufacturer filter | Nonholonomic EKF |
|------------------|------------------|------------------------------|------------------|
| Accuracy | 3.5 mm | 2.4 mm | 1.9 mm |
| Precision | 1.7 mm | 1.0 mm | 0.8 mm |
| 95% CI | 6.2 mm | 3.9 mm | 3.1 mm |

Conclusions. The nonholonomic EKF has the advantage of exploiting the additional orientation measurements and the sensor kinematic constraints in its formulation. Combined with the position measurements, the advanced filter can successfully improve the accuracy of path reconstruction. In conclusion, filtering using a nonholonomic model is promising for tracking catheters and seems applicable to a plurality of procedures.

Reference. [1] Bharat *et al.*, Electromagnetic tracking for catheter reconstruction in ultrasound-guided high-dose-rate brachytherapy of the prostate. *Brachytherapy*, 13(6):640-650, 2014.



(a)



(b)

Figure 1. (a) Ground truth phantom firmly holding ten catheters in a predefined path. (b) Experimental setup in the HDR suite.

Development of improved gel dosimeter vessels for low stray light optical CT scanners

Kevin J. Jordan^{1,2*}, Kurtis H. Dekker¹, Jerry J. Battista^{1,2}

¹Department of Medical Biophysics, Western University, London, Ontario, Canada

²London Regional Cancer Program, London Health Sciences Centre, London, Ontario, Canada

Introduction: Recently, we modified a cone beam optical CT scanner for gel dosimetry (Vista™, Modus Medical Devices Inc., London, Canada) by replacing the original diffuse illumination source with a convergent-cone light source (Fresnel lens), which greatly reduces stray light in the system. This substantially improves the accuracy of the scanner's attenuation measurement[1]. However, the new low stray light design is sensitive to optical features in gel vessels, which create artifacts in reconstructions (Figure 1). Therefore, vessels of higher optical quality are now required.

Methods: To investigate the performance of a new vessel, a uniform attenuating solution[2] was imaged with the modified scanner. The refractive index of the optical CT aquarium liquid was tuned on a per-vessel basis to achieve the least amount of missing projection data. We acquired 512 projections of 640x480 pixels, spanning 360° of rotation. Reconstructions were performed on a 512³ voxel grid (0.25mm voxels) with both filtered backprojection (FBP) and an iterative algorithm, OSC-TV, which has recently been studied for optical cone beam CT[3]. Projections and reconstructions were examined for the presence of artifacts and noise in several vessel constructions: standard PETE gel dosimetry vessels (0.5mm walls), 2L PETE pop bottles (0.25mm walls), and custom cylinders made from 0.2mm or 0.1mm thick polyester sheets.

Results: Figures 1 and 2 compare projection images and central reconstruction slices obtained with the original 0.5mm wall vessel and a custom 0.1mm wall vessel, respectively. As seen in the projection images (Figures 1a, 2a), custom vessels display significantly fewer optical features than the original jars, and thus result in reconstructions (Figures 1b, 2b) with reduced noise and fewer streak artifacts. In general, thinner vessel walls allow better refractive index optimization and therefore more of the volume can be uniformly reconstructed[4]. 0.25mm wall thickness pop bottles are an improvement over the standard jars, but show considerably more optical imperfections than the custom vessels. Custom vessels also have a single seam, rather than two, reducing the largest streak artifact source by half. Finally, OSC-TV reconstruction can suppress noise and streak artifacts even further compared to FBP (Figure 2b).

Conclusions: High optical quality jars can be manufactured from thin sheets of plastic. These custom-made, thin-walled vessels provide significantly better optical CT data when using a low stray light scanner. Future work will involve verifying that the new vessels are chemically compatible with our hydrogel dosimeter formulations.

References:

- [1] K. Dekker *et al.*, (submitted manuscript) 2015.
- [2] K. Jordan and J. Battista, *J. Phys. Conf. Ser.*, vol. 164, no. 1, p. 012045, 2009.
- [3] D. Matenine *et al.*, *Med. Phys.*, vol. 42, no. 11, pp. 6376–6386, 2015.
- [4] K. Jordan *et al.*, *Proc. World. Congress on Medical Physics and Biomedical Engineering (Chicago)*, 2000.

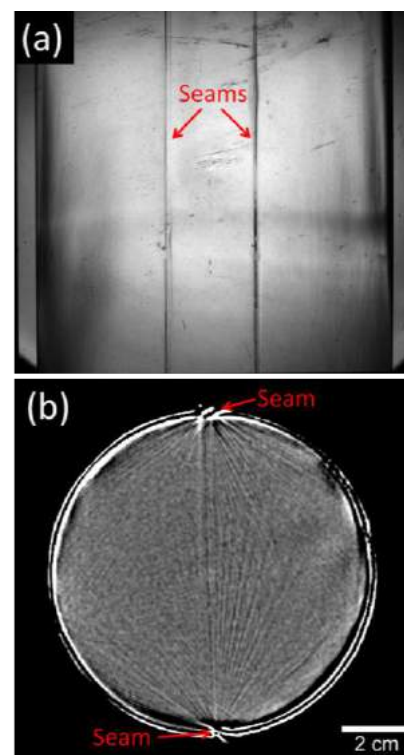


Figure 1. Projection (a) and FBP reconstruction (b) of standard 0.5mm wall vessel.

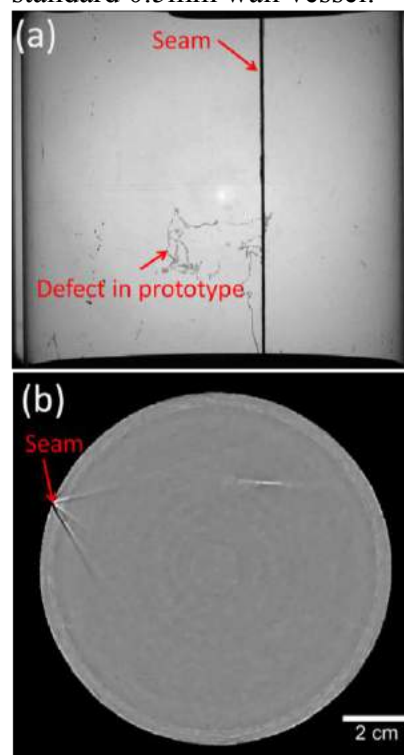


Figure 2. Projection (a) and OSC-TV reconstruction (b) of custom 0.1mm wall vessel.

Whole-Slide Digital Pathology via Lens-free Spectral Light-field Fusion Microscopy

Farnoud Kazemzadeh* and Alexander Wong*

Ontario Institute for Cancer research – Smarter Imaging Program

*Department of Systems Design Engineering, University of Waterloo, Waterloo, ON, Canada

Introduction. Digital pathology is becoming more widely used for cancer diagnostics and personalized cancer therapy, and is slowly replacing the practice of examinations under a traditional optical microscope. An advantage of digital pathology is that the entire sample slide can be scanned using whole-slide scanners and stored and examined with a large virtual field-of-view in digital form. The process of scanning the entire slide at high magnifications, and then stitching the sub-images together to create the whole-slide image is time consuming, and post processing often lead to artifacts and color and intensity inhomogeneity that degrade image quality and may adversely affect diagnostic accuracy. Motivated by this, we propose a method for whole-slide digital pathology via lens-free spectral light-field fusion microscopy [1] that allows for fast, high-resolution, high-contrast, ultra-wide field-of-view, three-dimensional imaging of pathology slides without the need for numerous piecewise scans, thus greatly mitigating artifacts associated with combining many sub-images as is done with current whole-slide scanners, and can aid in more rapid and accurate cancer diagnostics.

Method. In the lens-free spectral light-field fusion microscopy instrument developed in this study for whole-slide pathology, a three-channel (RGB) coherent light source sequentially pulses at the three wavelengths to illuminate the pathology slide and the detector through a single-mode optical fiber. The interaction of the light at each wavelength with the tissue on the slide is observed as unique interferometric light-field encodings on the detector, which are then computationally fused to reconstruct the pathology image [1, 2]. The absence of any optical elements in this instrument allows for the placement of the pathology slide directly onto the detector's active area, which allows for the field-of-view of the instrument to be as large as the detector being used, which in the developed instrument is 116 times larger than a traditional optical microscope would be capable of imaging at the same lateral resolution.

Results. For illustrative purposes, a bovine lung sample showing inflammation (Figure 1) and a prostate sample (Figure 2) was imaged using the developed instrument. The pathology sample has been prepared with a stain, with an area of $\sim 29 \text{ mm}^2$. The instrument was capable of imaging the entire sample in a single acquisition without the need for any lateral scanning. The resolution of the image captured is comparable to the microscopy techniques currently used for whole-slide pathology. Unlike other whole-slide scanners, there are no stitching artifacts or color inhomogeneity caused by sub-image scanning.

Conclusion. The developed lens-free spectral light-field fusion microscopy instrument enables highly compact, highly cost-effective digital pathology given the lack of optical elements, which can have strong potential impact on cancer diagnostics in developing countries, while delivering high-resolution, high-contrast, three-dimensional color imaging for improved diagnostic accuracy.

Acknowledgements. This work was supported by NSERC, Canada Research Chairs Program, and the Ontario Ministry of Research and Innovation. We also thank Lumalytics Inc. for their continued support of this project.

References. [1] Kazemzadeh et al. "Lens-free spectral light-field fusion microscopy for contrast- and resolution-enhanced imaging of biological specimens," *Opt. Lett.* 40, 3862-3865 (2015).

[2] Wong et al., "Bayesian-based aberration correction and numerical diffraction for improved lensfree on-chip microscopy of biological specimens," *Opt. Lett.* 40, 2233-2236 (2015).

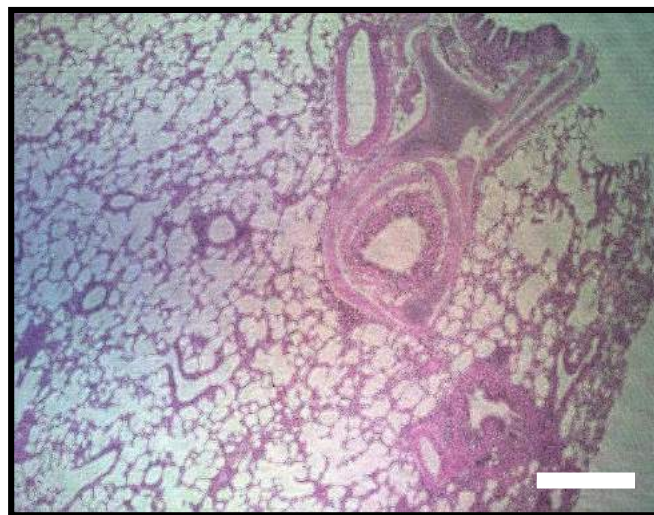


Figure 1. A sample of inflamed bovine lung. The size of the captured microscopy image is $6.4 \times 4.5 \text{ mm}$. The scale bar denotes 1 mm.

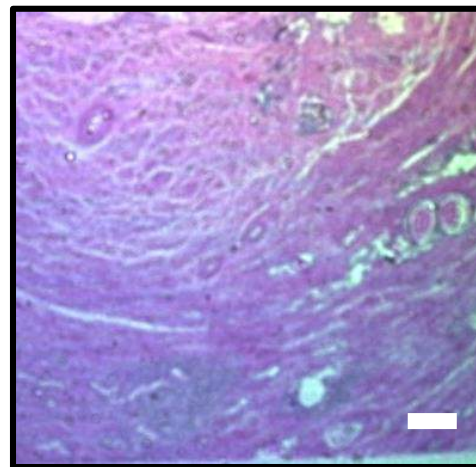


Figure 2. A sample of healthy prostate. The scale bar denotes $100 \mu\text{m}$.

MRI-Compatible Remote Catheter Navigation System with 3-Degrees-of-Freedom

M. A. Tavallaei,^{1,2,3} M. K. , Lavdas,¹ D. Gelman,¹ and M. Drangova^{1,3}

¹Robarts Research Institute; ²Western Medical Innovation Fellowship Program; ³Department of Medical Biophysics, Schulich School of Medicine & Dentistry, Western University, Canada

Consortium: Imaging for Cardiovascular Device Intervention; **Supervisor:** M. Drangova

Introduction: Conventionally, cardiac catheterization is guided with x-ray fluoroscopic imaging and more recently, with MRI. Fluoroscopic x-ray imaging only provides 2D projection images with low anatomical soft tissue contrast and exposes the staff and interventionalists through scattered on a daily basis. In contrast, MRI allows 3D visualization and localization and provides very high soft tissue contrast, while removing the radiation risk. However, the closed bore of conventional MRI scanners limits patient access and hinders catheter manipulation by the interventionalist. To overcome this limitation, we have developed an MRI-compatible remote catheter navigation system that enables remote manipulation of steerable catheters with 3-degrees-of-freedom (DOF) during real-time MR imaging guidance.

Methods: A non-magnetic robot was designed and developed that enables manipulation of steerable catheters of various gauges with 3 DOF. The robot consists of a handle manipulator (HM), which enables actuation of the catheter handle's plunger (for steerable catheters) and a catheter manipulator (CM), which rotates and translates the catheter [1]. The robot is remotely manipulated using an intuitive user interface that takes advantage of the interventionalist's dexterous skills in catheter manipulation. The master unit consists a catheter sensor (CS) and a plunger sensor (PS). The robot is actuated with non-magnetic ultrasonic motors (USM) that are controlled using a custom USM servomechanism [2]. The servomechanism measures the position of the motors as well as the interventionalist's applied input motion, on the master unit. The servomechanism then controls the USMs such that the user's input motion is replicated by the robot on the patient catheter. The performance of the developed robotic system was evaluated in terms of MRI compatibility (SNR and artifact), feasibility of remote navigation under real-time MRI guidance, and motion replication accuracy. All experiments were performed in a 3T GE magnet. For MRI guided navigation, and accuracy evaluation, a custom designed phantom was used that allowed for visualization of the angle and position of the catheter tip with respect to plastic landmarks that were visualized using signal void. For real-time MRI guidance a 16-channel cardiac coil was used to acquire 2D Fiesta Cine images (FOV 18cm, slice thickness 3mm TR/TE=4.3/1.7 ms, flip angle 45°, matrix 128×128) with a temporal resolution of ~85ms, with a spatial resolution of 1.4 mm. The effect of the robot on the image SNR drop and image artifacts were evaluated based on the NEMA[3] and ASTM [4] protocols, correspondingly.

Results and discussion: Real-time MRI experiments demonstrated that the catheter was successfully navigated remotely to desired target references in all 3-DOF. The system had an absolute value error of <1 mm in axial catheter motion replication over 30mm of travel and $3^\circ \pm 2^\circ$ for radial catheter motion replication over 180° (N=10). The worst case SNR drop was observed to be less than 3%; the robot did not introduce any artifacts in the MR images. The proposed RCNS is fully MRI compatible and facilitates the navigation of steerable catheters with 3-DOF in conventional closed bore scanners without compromising image quality or system performance.

References: [1] M. A. Tavallaei *et al.*, *IJMRCAS*, 2015. [2] M. A. Tavallaei *et al.*, *IEEE Trans. Indust. Elect.*, 2015. [3] NEMA, Standard, 2008 [4] ASTM, Standard, 2006.

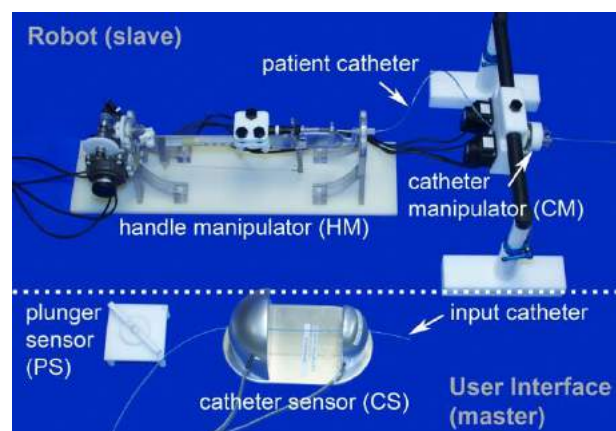


Fig. 1. The master and slave units are shown

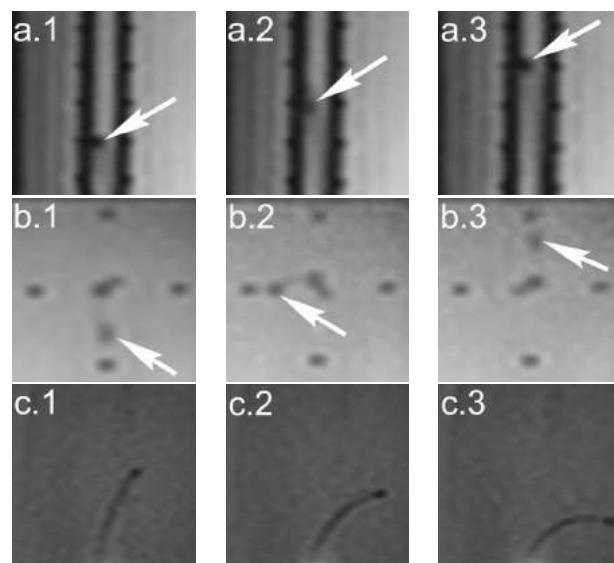


Fig. 2. Selected frames from the real-time image streams in each degree-of-freedom. a.1-3: the catheter's axial position with 1 cm of axial motion between figures; the arrows point to the catheter's tip. b.1-3 catheter's radial angle with 90° of counterclockwise catheter rotation between the presented consecutive figures; arrow points to the tip of the indicator dial connected to the catheter. c. 1-3 bending of the catheter's distal end at 3 bending states.

Differentiation of arterioles from venules in mouse histology images using machine learning

J. Sachi Elkerton^{1,3}, Yiwen Xu^{1,2,3}, J. Geoffrey Pickering^{1,2}, Aaron D. Ward^{1,3}

¹Dept. of Medical Biophysics, Western University; ²Robarts Research Institute; ³Baines Imaging Research Laboratory, London Regional Cancer Program.
OICR Smarter Imaging; Research Supervisor: Aaron D. Ward

Introduction: Measurement of microvessel structure and network organization is essential to our understanding of multiple disease scenarios. The arteriolar and venular networks vary in their function, where arteries and arterioles control the blood flow of the system and the venous side is responsible for proper drainage. Currently however, histologic analysis of microvasculature carries a substantial risk of not reliably distinguishing arterioles from venules as they are on a similar scale, which leads to confounded data. Thus, it is critical to our understanding of disease to be able to analyze and compare arterioles and venules separately. Manual detection and measurement of vessels in tissue requires a prohibitive amount of time and an automatic system would eliminate the need for the laborious and observer-dependent manual classification.

Materials and Methods: The experiments were conducted on tissue of the tibialis anterior hind limb muscle from 10 wild type C57BL/6 mice (1 tissue section per mouse). In 5 of the 10 mice, tissue was collected two weeks post hind limb ischemia. The tissue was immunostained for smooth muscle α -actin using 3,3'-Diaminobenzidine (DAB) and counter stained with hematoxylin for nuclei (Fig. 1a). Each vessel was manually classified by 2 observers for a total of 202 arterioles and 133 venules. After automatic vessel detection and segmentation [1], texture feature computation was performed within each vessel on 10 colour channels separately: 3 RGB, 3 HSV, 3 Lab, and a DAB stain channel extracted by color deconvolution [2]. 22 first-order textures, 22 second-order textures and 14 morphological features were computed for a total of 454

features for each vessel. To choose the best combination of 3 features, forward feature selection was implemented and evaluated using PRTTools 5.2.1 (Delft Pattern Recognition Research, Delft, The Netherlands). We tested the performance of three different machine learning classifiers: a support vector machine (SVM), a random forest classifier (RFC), and a logistic linear classifier (LOGLC). Each classifier was tested using leave-one-mouse-out cross-validation. Feature selection was performed on the training set during each iteration and the selected features were used to train the classifiers.

Results: The classification performance metrics are provided in Table 1. All three classifiers performed similarly, with AUCs between 0.88 and 0.90. The frequency of selection of each feature is shown in the histogram in Figure 2, showing 10 different sets of three features.

Table 1. Performance metrics from cross validation (mean \pm SD)

| | LOGLC | SVM | RFC |
|----------------------|-----------------|-----------------|-----------------|
| Classification Error | 0.17 \pm 0.11 | 0.18 \pm 0.12 | 0.16 \pm 0.09 |
| False Negative Rate | 0.18 \pm 0.22 | 0.20 \pm 0.27 | 0.18 \pm 0.23 |
| False Positive Rate | 0.22 \pm 0.31 | 0.22 \pm 0.27 | 0.20 \pm 0.24 |
| AUC | 0.90 \pm 0.00 | 0.89 \pm 0.00 | 0.88 \pm 0.00 |

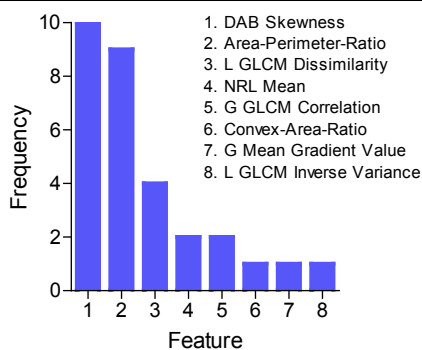


Figure 2. Histogram of the features chosen over the 10 cross-validations.

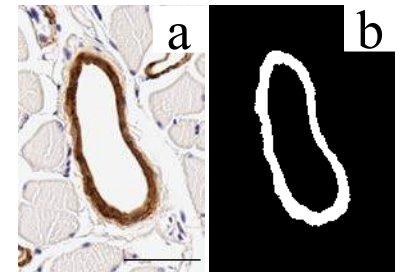


Figure 1. Arteriole with the DAB stain (a), and the binary mask (b) output from the automated segmentation. Scale bar is 50 μ m.

Conclusion: Our software system based on supervised machine learning provided excellent classification accuracy for differentiation of arterioles and venules on histology images of the mouse hind limb, achieving an area under the receiver operating characteristic curve of 0.90. Feature selection was consistent across cross-validation iterations, and a small set of three features was required to achieve the reported performance. This system will enable scientists to conduct high-throughput studies of animal models, measuring and comparing arteriolar and venular networks to deepen our understanding of human disease.

[1] Xu, Y., et al., Proc. SPIE 9420, 942003-7 (2015).

[2] Ruifrok, A.C. et al., Analytical and Quantitative Cytology and Histology/The International Academy of Cytology, 23(4), 291-299 (2001).

Retrospective motion correction in MRI using spherical navigator echoes

P.M. Johnson, J. Liu, T. Wade and M. Drangova (research supervisor)

Imaging Research Laboratories, Robarts Research Institute, Western University, London, Ontario, Canada

Introduction: Patient motion during magnetic resonance imaging (MRI) can corrupt image data and severely degrade image quality. 3D motion is a significant problem that remains unsolved; it is a limiting factor in many MRI applications such as clinical cardiac and neuro imaging. If the motion of the subject is known, the raw image data can be adjusted to compensate for the motion. Image space navigators, navigator echoes, and optical tracking are common techniques used to measure subject motion. Navigator echoes, acquired in the Fourier domain of the image (k-space), can be acquired more quickly than image space navigators¹ and unlike optical tracking, do not require additional external hardware. Spherical Navigator Echoes (SNAV) can measure full 3D rigid-body motion.^{2,3} The objective of this work is to develop a navigated spoiled gradient echo sequence (SPGR-SNAV) and retrospectively correct brain images to improve image quality.

Methods: SPGR-SNAV imaging sequence. We developed a modified SPGR sequence in which SNAVs are acquired after every four Cartesian image lines. The built-in SNAV has a radius of 0.40 cm^{-1} and 2508 sample points.

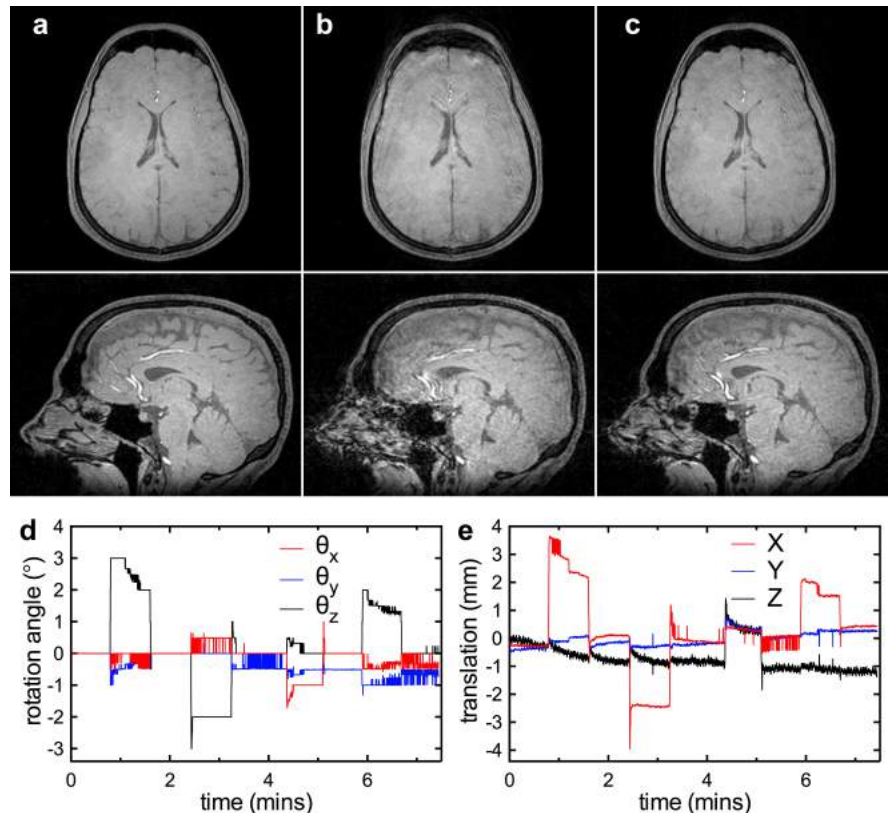
Data acquisition. Three volunteers were scanned using the required 2.5s baseline sequence followed by the SPGR-SNAV sequence. The volunteers performed step-wise motion; they were instructed to move approximately every 50 s of the 7.5 min scan and perform head rotations in both the θ_x and θ_z directions (nodding and axial). An additional no-motion reference image was acquired after all motion trials. The sequence parameters used were as follows: matrix size = $256 \times 160 \times 124$, TE/TR = 3.9/15 ms; image bandwidth = 62.5 kHz, SNAV bandwidth = 125 kHz, flip angle = 8° ; field of view = $24 \times 24 \times 18.6 \text{ cm}$.

Motion correction. All 6 rigid-body motion parameters were extracted from 4960 interleaved navigators. Phase shifts were first applied to the data to correct for the measured translations; next, the coordinates of the phase-corrected data were rotated based on the measured rotation. K-space data were then interpolated at the transformed coordinates.

Results: Representative results of retrospective motion correction are shown in the figure, which compares a reference (no motion) image (a) to a motion-corrupted image (b) and retrospectively motion-corrected images (c). The measured motion agrees well with the intended motion; step-like rotations about X and Z with accompanying translations are observed at the time-points of directed motion. The uncorrected image acquired during motion has severe artifacts particularly in the ventricles and frontal region. Excellent correction of these artifacts is observed in the corrected image (c). The measured rotations and translations are shown (d) and (e) respectively.

Discussion & Conclusions: SPGR-SNAV is able to track 3D rigid brain motion during image acquisition. The SNAV data was successfully used to improve image quality. SNAV measurement and processing times are very short ($<30 \text{ ms}$), making this technique feasible for prospective motion correction in the future. For the first time, we have demonstrated that spherical navigators can be used for intra-image motion correction. Our results demonstrate that an SNAV technique may be used for real-time motion correction in brain and cardiac MRI.

REFERENCES (1) Maclaren, et al., MRM 69:621-36, 2013 (2) Welch, et al., MRM 47:32-41, 2002. (3) Liu et al., MRM 65:506-14, 2010.



Axial and sagittal slices from the 3d reference image (a) uncorrected image acquired with intended rotation (b) and motion corrected image (c). The measured rotations and translations are shown in (d) and (e)

Discovery Radiomics via Layered Random Projection (LaRP) Sequencers for Prostate Cancer Classification

Audrey G. Chung¹, Mohammad Javad Shafiee¹, Devinder Kumar¹, Farzad Khalvati², Masoom A. Haider², and Alexander Wong¹

¹ Vision and Image Processing Research Group, University of Waterloo, Waterloo, ON, Canada

² Medical Imaging, University of Toronto and Sunnybrook Research Institute, Toronto, ON, Canada

Introduction: Prostate cancer is the most diagnosed form of cancer in Canadian men, and is the third leading cause of cancer death. The use of magnetic resonance imaging (MRI) has recently grown in popularity as a non-invasive imaging-based prostate cancer screening method. Automatic computer-aided prostate cancer classification or radiomics-driven methods based on MR images for prostate cancer classification have been developed to help streamline the diagnostic process and increase diagnostic consistency. Current radiomics-driven methods for prostate cancer classification typically employ a set of predefined, hand-crafted quantitative features extracted from multi-parametric MR images. We introduce discovery radiomics via a Layered Random Projection (LaRP) sequencer, where we forgo the notion of predefined feature models by discovering customized radiomic feature models directly from the wealth of readily available medical imaging data.

Methods: To realize the concept of discovery radiomics, we propose a novel discovery radiomics framework via a LaRP sequencer for discovering a customized sequencer that can generate radiomic sequences of abstract imaging-based features tailored for prostate cancer classification. The LaRP sequencer comprises of alternating layers of: i) linear, localized random projection ensembles (LRPE), and ii) non-saturating, global nonlinearities (NONL) to facilitate complex, nonlinear random projections. Using a projection matrix support of 25, the LaRP sequencer consists of three sequencing layers of 256, 512, and 2000 projections, respectively, and is discovered using past patient multi-parametric MRI data, i.e., T2w, ADC (using 0, 100, 400, 1000s/mm²), high-b DWI (2000s/mm²), and correlated diffusion imaging. Given the limited amount of available data, data augmentation is performed via the rotation of each tumour candidate at 45° intervals, resulting in 1280 cancerous regions and 1280 healthy regions that can be used as tumour candidates for training the proposed LaRP radiomic sequencer.

Results: The discovered LaRP radiomic sequencer was evaluated against two state-of-the-art hand-crafted radiomic sequencers proposed by Peng *et al.* [1] and Khalvati *et al.* [2] for classifying tumour candidates as either healthy or cancerous using a feedforward neural network classifier with a single hidden layer of 100 nodes. Sensitivity, specificity, and accuracy were calculated via leave-one-patient-out cross-validation with the collected dataset. The LaRP sequencer produced a sensitivity, specificity, and accuracy of 0.6400, 0.8248, and 0.7365, respectively, and has noticeably more consistent performance relative to [1] and [2].

Conclusion: Unlike conventional radiomics-driven methods that use hand-crafted radiomic features, the discovered LaRP radiomic sequencer can generate radiomic sequences that are specifically tailored for quantifying and differentiating healthy and cancerous prostate tissue, demonstrating the potential of discovery radiomics for building custom radiomic sequences for cancer classification.

Acknowledgements: This research has been supported by the Ontario Institute of Cancer Research (OICR), Canada Research Chairs programs, Natural Sciences and Engineering Research Council of Canada (NSERC), and the Ministry of Research and Innovation of Ontario. The authors also thank Nvidia for the GPU hardware used in this study through the Nvidia Hardware Grant Program.

References

- [1] Y. Peng *et al.*, *SPIE Medical Imaging*, pp. 86 701H–86 701H, 2013.
- [2] F. Khalvati *et al.*, *BMC medical imaging*, vol. 15, no. 1, p. 27, 2015.

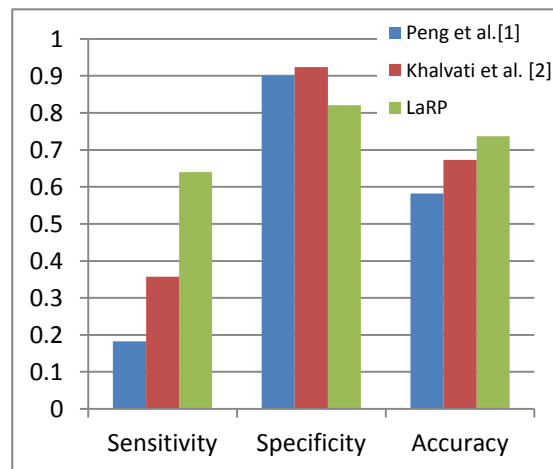


Fig. 1. Sensitivity, specificity, and accuracy metrics for proposed LaRP, Peng *et al.* [1], and Khalvati *et al.* [2].

Dynamic management of segmented structures in 3D Slicer

Csaba Pinter, Andras Lasso, Gabor Fichtinger

Laboratory for Percutaneous Surgery, School of Computing, Queen's University, Kingston, ON, Canada

Introduction: Image segmentation, i.e. delineation of anatomical structures of interest in images is a common operation in medical image computing. One of the many applications is in radiation therapy, where a segmented set of structures is used to determine the delivered dose to the target and the organs at risk in order to evaluate treatment plans. These segmented structures can be stored in various representations (Fig. 1), each optimal for a certain purpose. Planar contours come naturally for contouring on CT slices and are simple to store, closed surface models are optimal for 3D visualization, binary volumetric images (labelmaps) are the input format for most processing algorithms, and ribbon models are a quick way to visualize planar contours in 3D. Many other representations exist, such as fractional labelmaps, parametric functions, etc. Conversion between these representations is needed in nearly every case, however, it is a complex operation: (a) the structures (segments) that belong together must be converted together to preserve coherence, (b) when a segment representation changes, the others must follow so that no outdated data is used, and (c) relationships between the converted objects need to be preserved to be able to determine their origin and identity. The described method aims to address the above problems, and many more issues arising in the topics of visualization, transformation, and persistent and in-memory storage.

Methods: We propose a software infrastructure for dynamic management of segmentation results and conveniently perform conversions between representations. A storage object contains and manages segments and conversion parameters. It defines a *master* representation type that contains the spatial information in a lossless way as it was created: (a) all conversions use it as source, (b) when changed all other representations are invalidated, and (c) it is the representation that is saved to disk. Each segment contains all available representations. Representation types can be defined by registering conversion algorithms (rules) that specify their source and target representations, and an estimated cost metric. These converter rules constitute the edges of a conversion graph, where the nodes are the available representation types. This graph offers a dynamic way to define new representations and new converters. Conversions are automatically performed if a representation is requested that does not yet exist. The automatic conversion uses the cheapest path in the graph between the master representation and the requested one, calculated by summing the cost metrics for each rule. The user can override the default conversion parameters from the user interface.

Results: The Segmentations infrastructure has been implemented as a C++ module and library in the SlicerRT [1] (<http://slicerrt.org>) extension for the 3D Slicer medical image visualization and analysis platform [2]. The implementation contains an easy-to-use user interface for handling segments and representations, a base library with the objects and logic explained in methods including default conversion rules between the four basic representations, display managers allowing simultaneous visualization of multiple representations, and storage capabilities supporting various modalities in the DICOM standard and research file formats. Advanced features include the ability to apply rigid or deformable transformations on the segmented structure set at once with real-time visualization, efficient memory storage for labelmaps allocating only the effective image extent, custom conversion paths and parameters exposed to the user, and automatic calculation of segment opacity for optimal 3D visualization.

Conclusions: The Segmentations mechanism enables convenient, dynamic, deterministic, and generic management of segmentation results in a user-friendly way that is efficient both in terms of workflow and computational resources.

Acknowledgement: This work was in part funded by Cancer Care Ontario through Applied Cancer Research Unit and Research Chair in Cancer Imaging grants, and the Ontario Consortium for Adaptive Invention in Radiation Oncology.

[1] C. Pinter, et al. "SlicerRT: Radiation therapy research toolkit for 3D Slicer", Med. Phys. 39(10), 6332/7 (2012)

[2] A. Fedorov, et al. "3D Slicer as an image computing platform for the Quantitative Imaging Network." Magnetic resonance imaging 30.9 (2012): 1323-1341.

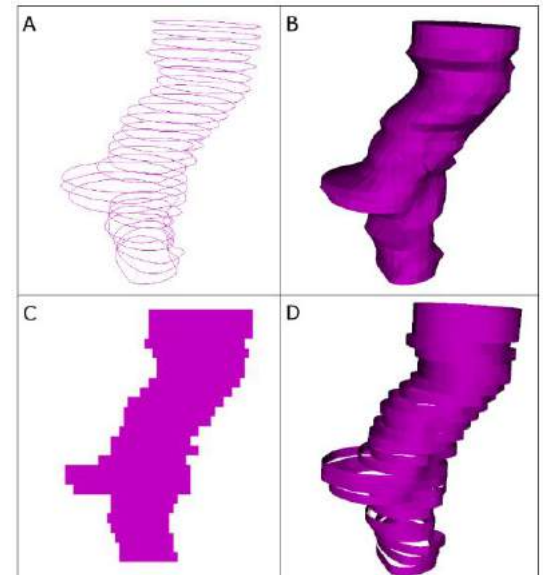


Fig. 1: Different representations of the same brain stem structure. A: Planar contours, B: Closed surface, C: Binary labelmap, D: Ribbon model

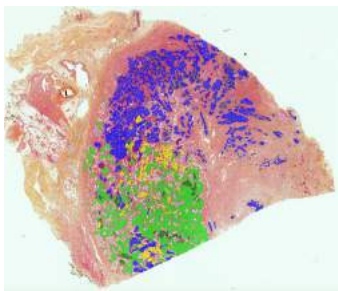
Title: An Image Analysis Pipeline for Machine Learning applied to Pathologist Annotations of Prostate and Pancreatic Cancer Specimens.

Authors: Trevor D. McKee¹, Jade Bilkey¹, Iram Siddiqui^{2,3}, Mehdi Masoomian², David Hedley², Aaron Ward⁴, Theodorus van der Kwast², David A. Jaffray^{1,2,5}.

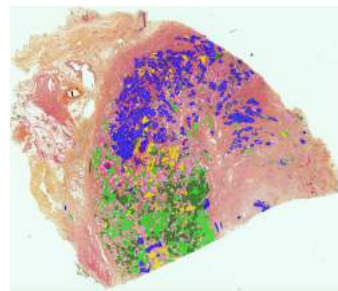
Affiliations: 1) STTARR Innovation Program, Princess Margaret Cancer Centre, Toronto, ON. 2) Princess Margaret Cancer Centre, University Health Network, Toronto, ON, 3) Hospital for Sick Children, Toronto, ON, 4) Robarts Research Institute, University of Western Ontario, London, ON, 5) Techna Institute for the Advancement of Technology for Health, University Health Network, Toronto ON.

Consortia: Ontario Consortium for Adaptive Interventions in Radiation Oncology (OCAIRO)

The advent of digital pathology has resulting in the availability of high resolution image pyramids of pathological samples from cancer specimens in digital format. However, in most cases the gold standard for annotation of these tissue sections remains manual scoring by a pathologist of microscopic images, which in some cases can limit the type and amount of image-derived features that can be extracted from such specimens, and can lack consistency and reproducibility. Machine-Learning aided image analysis offers some advantages for learning from pathologist-guided annotations, in order to extract relevant features on a set of training data. The set of features identified by this technique can then be applied to generate robust classifiers to identify and count cell types, and gland subclasses, that can serve to play a role in high-throughput quantification of cellular staining intensity, proportion of glands of particular subtype, or other useful metrics. Such supervised machine learning algorithms can be particularly effective when desiring to correlate histologic features from surgical biopsies or specimens with 3D medical images generated in the same patient prior to surgery. Here, we describe a pipeline for integrating pathologist oversight and training of gold standard annotations into an image analysis workflow. We use this pipeline to perform image segmentation on two separate sets of clinical pathology specimens: First, distinct prostate cancer gland subtypes are identified using a training dataset, in order to classify the proportion of individual glands in particular regions of prostate cancer sections. Second, we train on whole mount pancreatic ductal adenocarcinoma samples, in order to identify the fraction of hypoxic cells stained with a hypoxia marker, pimonidazole, in distinct cellular subtypes within the tumor. An example of an initial trained annotation is shown in the figure below. These tissue-specific analysis algorithms form the basis of a pathology analysis pipeline within the STTARR Image Analysis Core Facility, with the ultimate goal of high-throughput image segmentation, for registration with medical imaging data, and for application to quantitative analysis of hypoxia, proliferation, and other important biological readouts.



Pathologist Gold Standard Annotations



Initial Machine-Learning Classifier Annotations

Poster Session Abstracts

Listed by first author last name. Abstracts are listed by poster order starting on page 103.

Posters P1-P43 are located in the Colony Grande-West Room. Posters P44-P103 are located in the Giovanni Room. Posters P104-P118 are located in the Armoury Room.

Image Guided Intervention

Found in Colony Grande-West Room.

| | |
|---|-----|
| P1–Functional Medical Software David Adair (MITNEC)..... | 103 |
| P2–On-Demand Dynamic Updating of the Temporal Resolution of Interleaved PRFS and T2 Temperature Mapping Methods for MR-HIFU Steven Engler (SIP) | 104 |
| P3–In Situ Ultrasound Calibration Azharhosein Faraz (ICDI) | 105 |
| P4–An inexpensive system for competency-based pericardiocentesis training Vinyas Harish (MITNEC)..... | 106 |
| P5–Central Venous Catheterization Curriculum Development via Objective Performance Metrics Matthew Holden (SIP) | 107 |
| P6–Simultaneous Estimation of Feature Correspondence and Stereo Object Pose with Application to Ultrasound-Augmented Robotic Laparoscopy Uditha Jayarathne (MITNEC) | 108 |
| P7–A Robust Method for Tracking Lung Tumors during External Beam Radiation Therapy Elham Karami (ITP) | 109 |
| P8–Cranial ultrasound in 2D and 3D to guide treatment in preterm neonates with posthemorrhagic ventricular dilatation Jessica Kishimoto (ITP) | 110 |
| P9–A Simple MRI Scanner Control Technique for Device Localization During MRI-Guided Percutaneous Procedures Matthew MacDonald (ICDI) | 111 |
| P10–Hands-Free Dynamic Contrast Control for MRI-Guided Percutaneous Procedures Matthew MacDonald (ICDI) | 112 |
| P11–System for objectively evaluating colonoscopy procedural skills using motion analysis Kyle MacNeil (ITP) | 113 |
| P12–How does prostate biopsy guidance error impact pathologic cancer risk assessment? Peter Martin (SIP)..... | 114 |
| P13–Development of a Three Dimensional Ultrasound System for Guidance of Permanent Breast Seed Implantation In the Treatment of Breast Cancer Justin Michael (ITP) | 115 |

| | |
|---|-----|
| P14–Hidden Markov Models for Characterization of Temporal Ultrasound Data in Prostate Cancer Layan Nahlawi (ITP) | 116 |
| P15–Minimally invasive mitral valve repair using tracked 3D ultrasound navigation Adam Rankin (ICDI) | 117 |
| P16–3D Transrectal Ultrasound Needle Guidance System for High-Dose-Rate Interstitial Gynaecological Brachytherapy Jessica Rodgers (ITP) | 118 |
| P17–Electromagnetically-guided catheter insertions in breast phantoms for brachytherapy Thomas Vaughan (OCAIRO)..... | 119 |
| P18–Mouse brain developmental outcomes after whole brain vs focal irradiation Kiran Beera (ITP)..... | 120 |

Image Monitoring of Treatment Response

Found in Colony Grande-West Room

| | |
|---|-----|
| P19–Early Detection of Tumour Response using volumetric DCE CT and DCE-MRI in Metastatic Brain Patients Treated with Radiosurgery Catherine Coolens (ITP)..... | 121 |
| P20–Hybrid PET-MRI Imaging of Acute Radiation Induced Cardiac Toxicity Omar El-Sherif (ITP)..... | 122 |
| P21–Developing 19F-MRI for Clinical Cell Tracking Jeff Gaudet (SIP) | 123 |
| P22–The Effect of the Chemotherapy Agent Methotrexate on the Developing Brain Leigh Spencer Noakes (ITP) | 124 |
| P23–Vertebral landmark visualization with portable ultrasound imaging in scoliosis monitoring Christina Yan (B&J)..... | 125 |
| P24–In-vivo Detection of Acute Intracellular Acidification in Glioblastoma Multiforme Following a Single Dose of Cariporide Mohammed Albatany (SIP) | 126 |
| P25–Dichloroacetate Induced Intracellular Acidification in Brain Tumor: In-Vivo Detection Using AACID-CEST MRI at 9.4Tesla Mohammed Albatany (SIP) | 127 |
| P26–Prediction of Intracerebral Hemorrhage Secondary to Acute Ischemic Stroke: Multi- Parametric CT Perfusion is Optimal Connor Batchelor (MITNEC) | 128 |
| P27–In Vivo MRI Detection of Cucurbit[6]uril Xenon Cage HyperCEST Effect in Rat Abdomen Tao Li (MITNEC)..... | 129 |
| P28–Diminished image resolution lead to reduced sensitivity in infarct mass determined by T1 mapping for stratifying patient risk for ventricular arrhythmias Eranga Ukwatta (ICDI) | 130 |

| | |
|--|-----|
| P29—Measurement of tumor hypoxia in patients with advanced pancreatic cancer based on 18F-fluoroazomyin arabinoside (18F-FAZA) uptake Ivan Yeung (ITP)..... | 131 |
|--|-----|

Imaging/Simulation for Therapy Planning

Found in Colony Grande-West Room

| | |
|--|-----|
| P30—Real-time self-calibration of a handheld augmented reality overlay system Zachary Baum (SIP)..... | 132 |
| P31—Can intratreatment PET CT based adaptive radiotherapy reduce treatment margins in Head and Neck Cancers? Georges Farha (OCAIRO) | 133 |
| P32—4D Monte Carlo simulation for verification of dose delivered to a moving anatomy Sara Gholampourkashi (OCAIRO) | 134 |
| P33—Evaluating Electron Density Measurements and Dosimetry Surrounding Metallic Implants using Co-60 Computed Tomography Christopher Jechel (OCAIRO)..... | 135 |
| P34—Is it possible to use simultaneous MRI (scar) and PET (sympathetic innervation) to select patients for Radio-Frequency Ablation of Atrial Fibrillation? Ali K Saeid (CANet) | 136 |
| P35—Patient-specific calibration of Cone-Beam Computed Tomographic Images for radiotherapy plan adaptation Michael MacFarlane (OCAIRO)..... | 137 |
| P36—Analysis of dose volume histogram deviations using different voxelization parameters Kyle Sunderland (OCAIRO) | 138 |

Instrumentation/Devices

Found in Colony Grande-West Room (P37-P43) and Giovanni Room (P44-45)

| | |
|---|-----|
| P37—Micro-CT Compatible Load-Controlled Knee Motion Simulator Alexandra Blokker (B&J)..... | 139 |
| P38—Quantifying clinical detector performance to ensure lower patient exposures Terenz Escartin (ITP)..... | 140 |
| P39—Control of Rewarming Rate following Rapid Selective Brain Cooling Mohammad Fazel Bakhsheshi (ICDI)..... | 141 |
| P40—Novel flexible polarimetric probe for enhanced urologic cystoscopy Sarah Forward (SIP)..... | 142 |
| P41—In Vitro Evaluation of a Novel Catheter Contact-Force Controller for Cardiac Ablation Therapy Daniel Gelman (ICDI) | 143 |
| P42—Virtual design of patient specific neuroendoscopic tools for pineal region masses Margaret Hess (OCAIRO)..... | 144 |

| | |
|---|-----|
| P43–Geometric calibration phantom for MRI and CT David Holdsworth (B&J) | 145 |
| P44–Development and validation of a system for high-frequency vibration of live cells during real-time microscopy Daniel Lorusso (B&J)..... | 146 |
| P45–Designing and testing a perfusion phantom for validating cerebral blood-flow measurements made with deconvolution techniques Eric Wright (MITNEC) | 147 |

Patient-centered Imaging Studies and Trials

Found in the Giovanni Room

| | |
|---|-----|
| P46–An Update from the Quantitative Imaging for Personalized Cancer Medicine (QIPCM) Initiative Brandon Driscoll (ITP)..... | 148 |
|---|-----|

Perfusion, Metabolic and Hypoxia Imaging

Found in the Giovanni Room

| | |
|---|-----|
| P47–Novel Dual-Echo Planar Imaging Sequence for Hyperpolarized Carbon-13 Magnetic Resonance Imaging Distortion Correction Benjamin Geraghty (SIP) | 149 |
| P48–Towards assessing therapeutic response of glioblastoma in a rat model of cancer using novel multi-modality imaging Trung Le (SIP) | 150 |
| P49–Estimating Ex Vivo Total and ¹³ C-Lactate Concentration in Rat Tumour using NMR Spectroscopy Casey Lee (SIP)..... | 151 |
| P50–Tracer kinetics of histone deacetylase and its metabolites in epigenetic tumors Fiona Li (SIP) | 152 |
| P51–Monitoring changes in pH gradient using two different magnetic resonance imaging techniques Patrick Lim (SIP)..... | 153 |
| P52–Clearance of Indocyanine Green by the Liver during Hemodialysis as a Measure of Hepatic Function Raanan Marants (MITNEC)..... | 154 |
| P53–Numerical Optimization Accuracy & Performance of a Perfusion Kinetic Modeling Algorithm using Volumetric DCE CT Igor Svistoun (ITP) | 155 |
| P54–Optimal strategy for quantifying hypoxia from static PET imaging Edward Taylor (ITP) | 156 |
| P55–Effects of respiratory gated ¹⁸ F-FAZA PET-CT on hypoxic fraction in patients and phantom Douglass Vines (ITP) | 157 |

| | |
|---|-----|
| P56–Evaluating the non-small cell lung cancer between pre- and post- radiation therapy Dae-Myoung Yang (SIP) | 158 |
|---|-----|

Preclinical Imaging

Found in the Giovanni Room

| | |
|--|-----|
| P57–Effects of the acquisition window length on articular cartilage sodium MR image quality Alireza Akbari (MITNEC) | 159 |
| P58–In vivo sodium (²³ Na) magnetic resonance imaging of human knee using a pseudo-random k-space sampling scheme Alireza Akbari (MITNEC) | 160 |
| P59–Assessing the Effects of Inflammation and Fibrosis using Inert Fluorinated Gas MRI Marcus Couch (MITNEC) | 161 |
| P60–Dependence of Signal-to-Noise Ratio on Radiofrequency Coil and Static Magnetic Field Strength for Preclinical Hyperpolarized ¹²⁹ Xe Gas MRI of the Brain Yonni Friedlander (MITNEC) | 162 |
| P61–Characterizing the role of stress and Neuropeptide Y in breast cancer metastasis Jenna Kara (SIP) | 163 |
| P62–Detecting Hippocampal Changes in Mice on a Diet of 2'-Fucosyllactose Using Chemical Exchange Saturation Transfer Magnetic Resonance Imaging Wilfred Lam (SIP) | 164 |
| P63–Dependence of Hyperpolarized ¹²⁹ Xe Lung MRI Morphometry on Diffusion Time, Pressure and Gas Composition Andras Lindenmaier (SIP) | 165 |
| P64–Diffusion Tensor Imaging in a Rodent Model of Amyotrophic Lateral Sclerosis – Patrick McCunn (MITNEC) | 166 |
| P65–Interrogation of neurovascular coupling in an optogenetic mouse model using electrophysiology and two-photon fluorescence microscopy James Mester (MITNEC) | 167 |
| P66–Investigating cancer cell dormancy with cellular MRI Donna Murrell (SIP) | 168 |
| P67–The development of a multimodality imaging model to monitor breast cancer metastasis Katie Parkins (SIP) | 169 |
| P68–Micro-CT Validation of 3D-Printed Patient-Specific Components Joseph Umoh (B&J) | 170 |
| P69–Gas Exchange Quantification using Hyperpolarized ¹²⁹ Xe and a Clinical MRI System Brandon Zanette (SIP) | 171 |

Quantitative Imaging

Found in the Giovanni Room

| | |
|---|-----|
| P70—Performance evaluation of a peripheral cone-beam computed tomography scanner Rudy Baronette (B&J)..... | 172 |
| P71—A novel energy-dependent subtraction method for cardiac imaging: signal and noise analysis Christiane Burton (HF)..... | 173 |
| P72—Fractal Analysis of the brain blood oxygenation level dependent (BOLD) signal of mild traumatic brain injury (mTBI) patients Olga Dona (MITNEC)..... | 174 |
| P73—Radiomics Features Analysis for Tumor Characterization in Pancreatic Ductal Adenocarcinoma Armin Eilaghi (SIP) | 175 |
| P74—Performance of reduced dose compressed sensing-based sparse view CT myocardial perfusion imaging – a simulation study Esmail Enjilela (MITNEC) | 176 |
| P75— ¹⁹ Fluorine cellular magnetic resonance imaging to monitor in vivo therapeutic cell migration Corby Fink (SIP) | 177 |
| P76—Quantitative Evaluation of Tumour Associated Macrophages in Breast Cancer Using Fluorine-19 and Iron Based MRI Cell Tracking Ashley Makela (SIP) | 178 |
| P77—Deformable Registration of Dynamic Contrast Enhanced Breast MRI: The Influence of Sampling Percent on Enhancement Curves and Computation Time Matthew Mouawad (ITP) | 179 |
| P78—In vivo Quantitative Fluorescence Imaging Enabled by Spatial Frequency Domain Imaging for Enhanced Resection of Brain Tumors Mira Sibai (SIP) | 180 |
| P79—Clinical Workflow for Spinal Curvature Measurement with Portable Ultrasound Reza Tabanfar (B&J) | 181 |
| P80—Quantification of Vertebral Trabecular Bone Strain Via Feature Based Image Registration Hoi-Ki Tong (B&J)..... | 182 |
| P81—Carotid Atherosclerosis Imaging with Quantitative Susceptibility Mapping Chaoyue Wang (MITNEC)..... | 183 |
| P82—Radiomics Feature Clusters and Prognostic Signatures Specific for Lung Cancer Yucheng Zhang (SIP)..... | 184 |

Targeted Probe Development

Found in the Giovanni Room

| | |
|---|-----|
| P83—MagA-derived MR Contrast Persists Despite Cellular Differences in Iron Metabolism Donna Goldhawk (HF) | 185 |
| P84—Formulation of a GMP Quality Kit for the Preparation of ¹¹¹ In-DTPA-NLS-Trastuzumab Injection: An Auger Electron-Emitting Theranostic Agent for HER2-Positive Breast Cancer Vanessa Prozzo (ITP) | 186 |
| P85—Improving the Relaxivity of Non-Gadolinium Magnetic Resonance Imaging Contrast Agents: Tuning the Electron Spin of Manganese(III) Porphyrin Henry Tieu (SIP) | 187 |

Visualization and Image Analysis

Found in the Giovanni Room (P86-P103) and Armoury Room (P104-P118)

| | |
|--|-----|
| P86—Contrast Optimization for Prostate Cancer Tumours in vivo at 3T Christopher Abraham (SIP) | 188 |
| P87—Validation of 3D Slicer Based Gel Dosimetry Analysis Kevin Alexander (OCAIRO) | 189 |
| P88—Coded Hemodynamic Imaging for Non-Contact Detection of Abnormal Blood Pulse Waveforms Robert Amelard (CANet) | 190 |
| P89—Cyclic Continuous Max-Flow for MRI Phase Processing John Baxter (MITNEC) | 191 |
| P90—A Unified Reconstruction Framework for Compensated Magnetic Resonance Imaging Ameneh Boroomand (SIP) | 192 |
| P91—Accuracy of Melanoma Classification using Dermal Radiomic Sequences Daniel Cho (SIP) | 193 |
| P92—In vitro study of the effects of vessel stiffening on carotid artery hemodynamics using particle image velocimetry Amanda DiCarlo (MITNEC) | 194 |
| P93—Subject-Specific Patched-Based Denoising for Contrast-Enhanced Cardiac MR Images Mehran Ebrahimi (HF) | 195 |
| P94—Single-click lung nodule contouring method using hierarchical conditional random fields Shahid Haider (SIP) | 196 |
| P95—Automatic Prostate Cancer Mapping on Digital Histopathology Imaging Wenchao Han (SIP) | 197 |
| P96—Large scale segmentation free analysis of 3D microscopy data Santosh Hariharan (SIP) | 198 |
| P97—Preservation of fine details in 7 T phase images by processing channel phase data prior to combination Zahra Hosseini (MITNEC) | 199 |

| | |
|--|-----|
| P98–Seamless Reconstruction of Preview Images in Digital Pathology Mahdi Hosseini (MITNEC)..... | 200 |
| P99–Quality Assessment in Digital Pathology Images Keyvan Kasiri (ITP) | 201 |
| P100–Cross Modality Label Fusion in Multi-Atlas Segmentation of Brain MRI Keyvan Kasiri (ITP) | 202 |
| P101–Noise in parallel MRI: how to determine whether single-coil assumptions still hold (they don't) Jesse Knight (MITNEC)..... | 203 |
| P102–Discovery Radiomics for Lung Cancer Classification Devinder Kumar (SIP) | 204 |
| P103–Toward breast cancer histopathology image diagnosis using local color binary pattern Xingyu Li (SIP) | 205 |
| P104–Imaging scar with two-point bipolar Dixon MRI Junmin Liu (CANet)..... | 206 |
| P105–Web-application Based Ultrasound Bone Segmentation Evaluation Matt Loughheed (SIP)..... | 207 |
| P106–Automatic pipeline of lesion classification on breast 3D MRI data YingLi Lu (SIP) | 208 |
| P107–Apodized Aperture Pixel design: A novel x-ray detector with increased detective quantum efficiency and reduced aliasing Tomi Nano (ITP)..... | 209 |
| P108–Single Slice US-MRI Registration for Neurosurgical MRI-Guided US Utsav Pardasani (MITNEC)..... | 210 |
| P109–Method for global thresholding in Metal Artifact Reduction (MAR) Ivailo Petrov (ICDI)..... | 211 |
| P110–Validation of the prostate segmentation on MRI: manual vs computer-assisted methods Maysam Shahedi (SIP) | 212 |
| P111–Scattering Wavelet Representation of fMRI BOLD data Saurabh Shaw (MITNEC)..... | 213 |
| P112–Cartan frames for characterizing myofiber geometry in pig hearts from diffusion tensor imaging (DTI) Kaleem Siddiqi (HF) | 214 |
| P113-Computer-Assisted Prostate Cancer Characterization on Multi-Parametric MRI Derek Soetemans (SIP) | 215 |
| P114–Max-tree\Watershed Combination for Medical Image Segmentation Roberto Souza (MITNEC)..... | 216 |
| P115–Virtual electrophysiological study using T1 mapping techniques improves sensitivity in predicting adverse arrhythmic events in post-infarction patients Eranga Ukwatta (CANet) | 217 |

P116–Prediction of the spatial distribution of deformable image registration error in lung
4DCT’s
Jason Vickress (OCAIRO)..... 218

P117–Automated 3D morphometry of the vasculature derived from whole-slide digital histology
Yiwen Xu (SIP)..... 219

P118–Evaluating rigid and deformable registration of brain images before and after temporal
lobectomy
Yujun Zeng (MITNEC) 220

Functional Medical Software

David Adair*, David G Gobbi, Richard Frayne

Medical Imaging Trial Network of Canada

Biomedical Engineering, Radiology, and Hotchkiss Brain Institute, University of Calgary, Calgary, Alberta
Calgary Image Processing and Analysis Centre, Foothills Medical Centre, Calgary, Alberta, Canada

Introduction: Medical software should be held to a high standard of software development, as this software, whether directly or indirectly, influences patient safety and treatment efficacy. As computer architectures trend to more and more processing cores [1], the shared-memory model of imperative programming (IP) increases the complexity of software needed to take full advantage of the available computational power. The complexity arises from the need to explicitly control concurrent access to shared mutable data structures, a process which may reduce the robustness and correctness of software through the introduction of data races and deadlocks. Even if done correctly, explicit synchronization of shared mutable data access increases the cognitive demand required of programmers to understand the programs they write or maintain, which may introduce bugs in the software. Functional programming (FP) is a programming paradigm that promises a reduction in software complexity, bugs, and size, and provides a more robust form of concurrency through the use of immutable data structures and functional purity [2]. FP, however, is not without its shortcomings: namely, a reputation for slow performance per computational unit [3]. We propose that modern hardware has evolved to enable FP to supplant IP in the creation of robust, correct, and performant medical software. We discuss the results of a literature review done to support this proposition, and present our current research directions.

Methods: We conducted iterative searches of the University of Calgary research library catalogue over November 2015-January 2016 to retrieve articles, reports, and textbooks related to the evaluation of FP in the creation of soft real-time medical software, particularly in the domain of surgical image guidance. Search terms included “functional programming”, “medical systems”, “real-time”, “high performance”, “Haskell”, and “LISP”. We excluded 1) articles which relied on subjective discussion, rather than objective experimentation and evaluation, and 2) articles evaluating FP in industries other than medicine, as performance is an ambiguous term and connotations are specific to requirements in the problem domain. Using FP, we propose the creation of a novel image guidance system for endoscopic procedures, as this domain requires robust, correct, and low-latency software. The system will be implemented redundantly in both imperative and functional languages (C++ and Scheme, a functional LISP), and the performance and development characteristics of the implementations will be evaluated. External developers will be asked to review code in both implementations to reduce potential bias.

Results: We were unable to find articles with objective evaluation of FP for high-performance medical software. While excluded from evaluation, the use of FP in other domains, such as video games, virtual reality (VR), and robotics [4]–[7] encourages further evaluation and experimentation. Purely functional VR systems are encouraging as they have similar requirements as image guidance. However, FP in VR has, so far, been limited to scripting [7], where a small FP system provides a thin interface around an imperative core. Scripting is undesirable because the imperative core limits the robustness and correctness desirable in medical systems.

Conclusions: FP promises the reduction of software complexity, bugs, and size, but has historically been criticized for its slow performance [3]. The crossroads of modern central processing unit architectures, with shifts towards an increasing number of processing cores [1], and the safety and simplicity of developing concurrent programs in functional languages [2] inspires the further evaluation of FP for developing robust medical systems. We have chosen to perform this evaluation by creating a novel image guidance system in both imperative and functional languages, where we will be able to compare and contrast the implementations for their development and performance characteristics. The implementations will be open-source and available for extension by the medical software community.

References: [1] Parkhurst et al, *Proc. ICCAD*, 2006. [2] Hinsien, *Comput. Sci. Eng.*, 2009. [3] Verna, *Int. J. Comput. Sci.*, 2006. [4] Wan, *PhD Dissertation, Yale University*, 2000. [5] Cheong, *BEng thesis, Univ. New South Wales*, 2005. [6] Petersen, et al, *Proc. Int. Conf. Funct. Program*, 2013. [7] Marvin, *Software Development Times*, 2015. [Online].

On-Demand Dynamic Updating of the Temporal Resolution of Interleaved PRFS and T2 Temperature Mapping Methods for MR-HIFU

Steven Engler^{1,2,*}, Charles Mougenot³, Jochen Keupp⁴, Steffen Weiss⁴, Edwin Heijman⁵, Samuel Pichardo^{1,6,†}

¹Thunder Bay Regional Research Institute, Thunder Bay, Canada; ²Lakehead University, Computer Science, Thunder Bay, Canada; ³Philips Healthcare, Toronto, Canada; ⁴Philips Research, Hamburg, Germany; ⁵Philips Research, Eindhoven, Netherlands; ⁶Lakehead University, Electrical Engineering, Thunder Bay, Canada

*:primary author, †:supervisor

Introduction: Temperature monitoring is used during MR-guided High-Intensity Focused Ultrasound (MR-HIFU) induced hyperthermia to ensure controlled thermal uptake. Temperature change in non-adipose tissue can be calculated from the water-proton resonance frequency shift (PRFS), while absolute temperature in adipose tissue can be calculated from an apparent T2 map¹. Interleaved scanning has been previously demonstrated as a means to simultaneously acquire PRFS and apparent T2 maps during sonication². The temporal resolution of temperature measurements at the ultrasound focus should be high during rapid heating, but can be lowered while maintaining hyperthermia or during cooling. The objective of this study was to demonstrate the feasibility of dynamically controlling the temporal resolution of both interleaved scans in response to temperature changes.

Methods: Experiments were performed using a Sonalleve V2 MR-HIFU system (Philips Healthcare, Best, The Netherlands). A Python script acquired images and controlled the interleaved scanning using a modified version of the MatMRI³ toolbox with dynamic control of MR parameters, which uses the Philips eXTernal Control⁴ scanner interface. The HIFU system was controlled using MatHIFU³. A degassed *ex vivo* porcine leg muscle with a subcutaneous fat layer was used as the HIFU target.

An interleaved scanning protocol was configured with single-slice gradient-echo (TR/TE = 25/16 ms; EPI Factor = 11) and dual fast spin-echo (TR/TE₁/TE₂ = 3000/38/180 ms; TSE Factor = 40) dynamic sequences for PRFS and apparent T2 MR-thermometry methods, respectively. The PRFS and T2 slices were positioned at the focal point and in the near-field subcutaneous fat, respectively. Three PRFS dynamics were interleaved with one T2 kernel. Maximum and mean temperatures were calculated within a 16 mm region for T2 temperature maps, and a 10 mm region for PRFS temperature maps.

The MR-HIFU hyperthermia protocol began with an acoustic power of 40 Watts for rapid heating until reaching a target temperature change of 8 degrees. The power was then reduced to 12 W to sustain the target temperature. To demonstrate the on-demand feature, apparent T2 acquisition was disabled during the rapid heating phase to accelerate PRFS acquisition, then re-enabled while maintaining hyperthermia and during the subsequent cooling.

Results: The temporal resolution of the interleaved scans was successfully modified in real-time during MR-HIFU induced hyperthermia. As can be seen in Figure 1, the apparent T2 scan was disabled and the temporal resolution of the PRFS scan increased when the initial rapid heating began. After obtaining the target temperature, the T2 scan was re-enabled resulting in decreased temporal resolution of the PRFS scan.

To determine any potential mutual signal influences of the interleaved scans, the same HIFU protocol was used in two separate non-interleaved PRFS and apparent T2 experiments. There was no noticeable difference between the interleaved and non-interleaved PRFS temperature results. The greater heating observed in the subcutaneous fat compared to the ultrasound focus may be due to the closeness of the ultrasound focus to the fat.

Conclusion: In this study, we demonstrated the feasibility of dynamically modifying the temporal resolutions of interleaved scans on-demand. This new approach is very promising for achieving better control of near field heating in adipose tissue for different MR-HIFU applications and for general MRI interventional applications.

References: [1] Baron et al. *Mag Res Med*. 2014; 72(4):105764. [2] Keupp et al. *Proc ISMRM*. 2015; abstract 4061. [3] Zaporzan, et al. *J Therap Ultras*. 2013; (4):1-7. [4] Smink, et al. *Proc ISMRM*. 2011; abstract 1755.

Acknowledgements: Authors acknowledge support from the Discovery and Undergraduate Student Research Awards programs of the Natural Sciences and Engineering Research Council of Canada and Philips Healthcare. Charles Mougenot, Jochen Keupp, Steffen Weiss, and Edwin Heijman are employees of Philips.

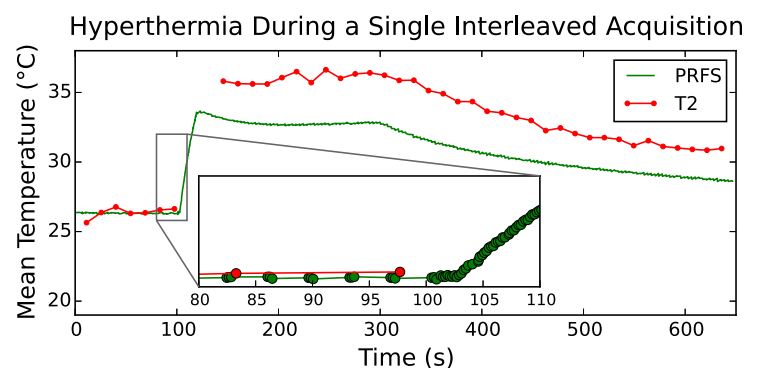


Figure 1: Temperature values from interleaved PRFS and apparent T2 thermometry within the muscle and subcutaneous fat tissue, respectively. The inset window shows the precise timing when the T2 scan was disabled during rapid heating to increase the PRFS temporal resolution.

In Situ Ultrasound Calibration

Azhar H. Faraz^{1,2}, Terry M. Peters^{1,2,3} and Elvis C. S. Chen^{1,2,3}

¹Biomedical Engineering Program, Western University, London ON Canada

²Imaging Laboratories, Robarts Research Institute, London ON Canada

³Department of Medical Biophysics, Western University, London ON Canada

INTRODUCTION: Accurate Ultrasound (US) calibration is essential for the navigated transapical mitral valve (MV) repair surgery. In the navigated MV repair, a transesophageal echocardiography (TEE) US is used to guide the transapical surgical tool, using the bi-plane and real-time 3D US imaging modes. The TEE probe and the surgical tool are tracked by magnetic spatial positioning system, enabling an Augmented Reality (AR) technique to be used as a guidance environment. Relationship between the US image and the tracking system, known as US calibration, is often achieved pre-operatively, using specialized phantoms with known geometry. In these calibrations, speed-of-sound (SOS) usually assumed to be $1540 \text{ m}\cdot\text{s}^{-1}$ (average SOS in human tissue) which often is a mismatch compared to the SOS at the target site of surgery. We propose an in situ US calibration, using the bi-plane US images and the surgical tool as a phantom, to be performed during surgery. We also determined the intrinsic relationship between the TEE bi-plane and the 3D US, to obtain an accurate 3D calibration from high-quality bi-plane calibration.

METHODS: Our paradigm is the adaptation of the phantom-less¹ calibration, with extension to use the surgical tool and to operate based on bi-plane images. The calibration parameters are: anisotropic scales, followed by rotation and translation. The Philips 3D TEE probe (X7-2t), capable to provide 2D bi-plane and real-time 3D US, was used. A transapical surgical tool (NeoChord DS1000) was used as a calibration phantom. A 6DOF magnetic tracking sensor (Aurora, NDI Canada) was attached to each of the TEE probe and calibration phantom. A left ventricle (LV) phantom was used to simulate the surgical scene within a laboratory setup (Fig. 1). An automatic segmentation was implemented to detect US reflection of the surgical tool, using a custom randomize Hough transform². The calibration transform was derived based on the tool's US reflections and the corresponding orientation from the tracking system. The intrinsic relationship between the bi-plane and 3D US imaging mode was determined from the internal coordinate system. Accuracy of individual calibration parameter was evaluated through different validation metrics. A grid-line phantom was scanned by a calibrated bi-plane US to assess scaling parameters. Volume Reconstruction (VR) was used to validate the overall performance of scaling parameters, in which a table-tennis ball was scanned by the calibrated US and the resultant volume was compared against the 'true' volume. Finally, Point Reconstruction (PR) was used to assess the calibration parameters as a whole: the tip of a tracked stylus was imaged and used as the basis for Target Registration Error (TRE) metric.

RESULTS: Our calibration was performed within a limited range of movement: $\pm 16^\circ$ rotation and ± 19 , ± 36 , ± 22 mm of translation in x, y and z directions, respectively. The accuracy of scale in the in-plane direction was $0.09 \pm 0.57\%$ and out-of-plane was $0.46 \pm 0.42\%$. The VR accuracy was $0.36 \pm 0.67\%$ and our system achieved the TRE of 0.9 ± 0.29 mm. The calibration can be obtained within 60-90 sec, thus has minimal impact on the surgical workflow. The reproducibility of the system was confirmed by performing the experiments at different setup/time. Fig. 2 demonstrates the qualitative validation.

CONCLUSIONS: We developed a fast and accurate in situ US calibration using a surgical tool for the trans-apical MV repair surgery. The system demonstrated accurate calibration in a simulated surgical environment and compensates for the correct SOS of a target medium.

REFERENCES: [1] Khamene A, *et al.* MICCAI2005, [2] Lu, Wei, *et al.* *Pattern Recog.* 41.4 (2008)

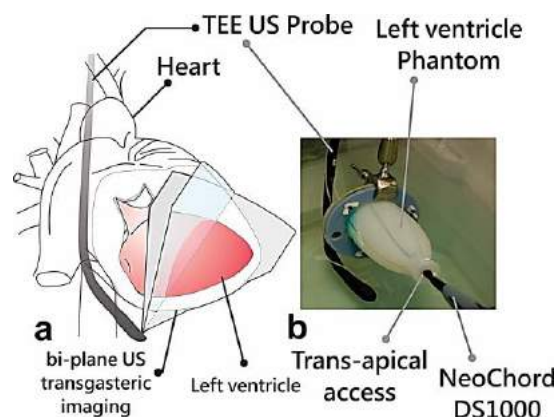


Figure 1. (a) Schematic diagram, representing the position of the TEE probe with respect to the LV. (b) simulated surgical scene in a laboratory setup.

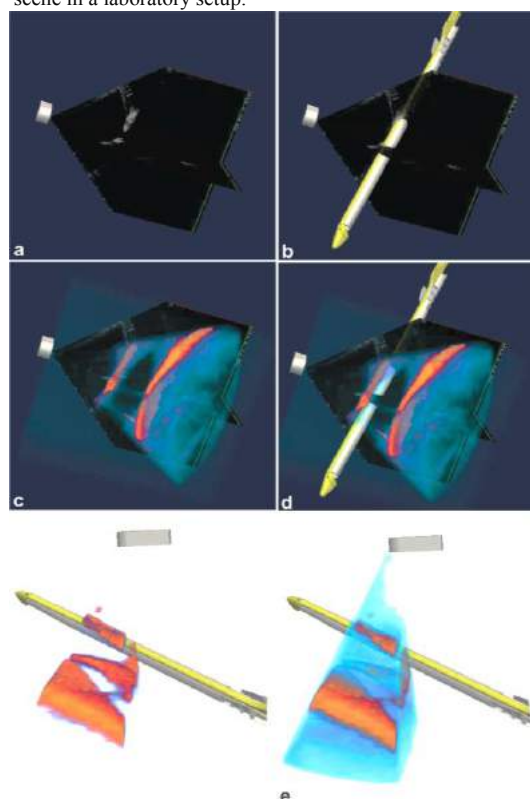


Figure 2. Qualitative validation. Overlay of the tracked surgical tool with the calibrated bi-plane and 3D US images.

An inexpensive system for competency-based pericardiocentesis training

A. Baksh^{1*}, V. Harish^{1*}, T. Ungi¹, R. Pal², G. Fichtinger¹

¹ Laboratory for Percutaneous Surgery, Queen's University, Kingston, Canada

² Department of Cardiology, Queen's University, Kingston, Canada

Consortium: Other

Introduction. Competency-Based Medical Education (CBME) involves practicing procedures in a simulated environment before they are performed on real patients to improve patient safety and trainee comfort. Pericardiocentesis is a high-risk procedure involving the aspiration of fluid from the pericardial cavity to relieve compression of the heart. Ultrasound imaging is used to provide real-time feedback of the needle tip's position relative to surrounding organs. Commercially available pericardiocentesis phantoms are prohibitively expensive, costing over ten thousand dollars. Less expensive phantoms lack realistic physiological features and anatomical landmarks [1]. Our goal was to create a realistic, low-cost phantom to be used in conjunction with an open-source software platform for image-guided pericardiocentesis intervention training.

Methods. Our phantom consists of a model heart inside a gelatin-filled plastic container. To construct the heart model, a balloon is placed around a second balloon. Rubber pneumatic tubing runs out from the inner balloon and is connected to a 60 cc syringe to simulate pumping. The inner and outer balloons are filled with water of different colors. Plastic cutting board, cut to resemble the ribs and sternum, is placed on top of the gelatin. Silicon skin is then laid over the ribs. The cost to make a phantom is under \$10, with a preparation time of roughly 15 minutes excluding the time needed for the gelatin to set. To test the phantom, an ultrasound machine and electromagnetic tracking system were used (Figure 1). A reference sensor was fixed underneath the phantom and a tracked needle was used to drain the effusion. A computer running the PlusServer application (www.assembla.com/spaces/plus/wiki) was connected to the electromagnetic tracker, and all tracking and image data was relayed to 3D Slicer (www.slicer.org/). In the SlicerIGT extension (www.slicerigt.org/wp/), a model representing the needle was created and visualized in 3D relative to the ultrasound image plane. The needle tip was marked with a sphere, to clearly distinguish the needle tip from the needle shaft (Figure 2).

Results. Our system allows for low-cost practice of ultrasound-navigated pericardiocentesis. Our phantoms appear anatomically and sonographically realistic. A beating effect of 30 beats per minute can be achieved by manually pumping the syringe. The volume of water in both balloons can be varied easily to simulate different patients. Realistic anatomical landmarks are provided by synthetic ribs and skin. The pericardium, myocardium, and myocardial decompression are clearly visible in the ultrasound. The use of different colours of water in each balloon allows users to easily determine if they punctured the pericardium or heart. Five phantoms were created, all appearing identical except for the amount of water put in the outer balloon, to simulate different degrees of difficulty for the procedure. No mechanical failure was observed during needle insertion trials; however, the phantoms are single use.

Conclusion. Using inexpensive materials, we have created a pericardiocentesis training phantom and demonstrated it with an open-source navigation software. The phantom is easily reproducible due to its limited cost and manufacturing simplicity, and it is expected to be a viable tool for training medical residents to perform pericardiocentesis in a simulated environment.

Reference. [1] Zerth, M., *et al.* (2012, Dec). An Inexpensive, Easily Constructed, Reusable Task Trainer for Simulating Ultrasound-Guided Pericardiocentesis. *The Journal of Emergency Medicine*, 43(6), 1066-1069.

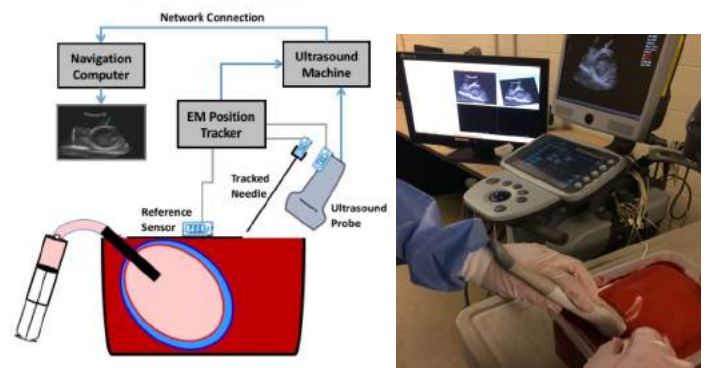


Figure 1. Schematic diagram of the setup (left) and photograph (right) for performing ultrasound-guided pericardiocentesis with our phantom.



Figure 2. Ultrasound image of unfilled inner balloon showing use of SlicerIGT to visualize the needle during insertion.

Central Venous Catheterization Curriculum Development via Objective Performance Metrics

Matthew S. Holden¹, Mark Woodcroft², Tim Chaplin², Louise Rang², Melanie Jaeger³, Nici Rocca², Robert C. McGraw², Gabor Fichtinger¹, Tamas Ungi¹

¹School of Computing; ²Department of Emergency Medicine; ³Department of Anaesthesiology
Queen's University, Kingston, Canada

Consortium: Cancer Care Ontario (CINO); Research Supervisor: Gabor Fichtinger

INTRODUCTION: Ultrasound-guided (USG) central venous catheterization (CVC) is an invasive procedure with significant potential for complications. Thus, it is ideally mastered in a simulated setting before attempted on patients. In the past, training curricula for CVC and other USG needle interventions have been developed using subjective measures of competence. In this work, we have used objective performance metrics to follow novice learning curves to determine the amount of practice required to reach expert procedural competency in CVC.

METHODS: Over the course of six weeks, eight PGY2 emergency medicine and anaesthesiology residents each engaged in three dedicated CVC training sessions. Training sessions were performed on simulation phantoms and were closely monitored by CVC experts, who provided specific guidance, feedback, and drills for each resident (Fig. 1). Before and after each training session, each resident performed one CVC insertion that was tracked for the purposes of hand motion analysis (HMA) and objective performance metric computation using the Perk Tutor software (www.perktutor.org). Specifically, the number of discrete motions associated with each hand, as well as total procedure time were captured [1]. Resident learning curves were established by comparing, over time, their motion efficiency metrics with expert benchmarks.

RESULTS: At baseline, all metrics were significantly different between the novice and expert groups. After three training sessions (approximately 85 procedure attempts), residents' learning curves for total number of hand motions approached or surpassed the expert baseline (Fig. 2), and therefore simulated training was considered complete. Learning curves were similar for total procedure time. Direct expert observation revealed that residents had the most difficulty with needle tip visualization and were thus assigned specific drills to reinforce this skill.

CONCLUSIONS: We have shown that objective performance metrics are a valuable tool that can be incorporated into a procedural task curriculum. Our study was able to reliably identify the quantity of training required to reach competency in CVC: 85 simulated procedure attempts over three training sessions. Although the precise amount of required training will vary between trainees and be influenced by the simulation setup, these values can serve as a guideline for medical educators designing competency-based curricula.

ACKNOWLEDGEMENTS: This work was in part funded by Cancer Care Ontario through Applied Cancer Research Unit and Research Chair in Cancer Imaging grants.



Figure 1: Photograph of novice performing an ultrasound-guided CVC with hand tracking setup.

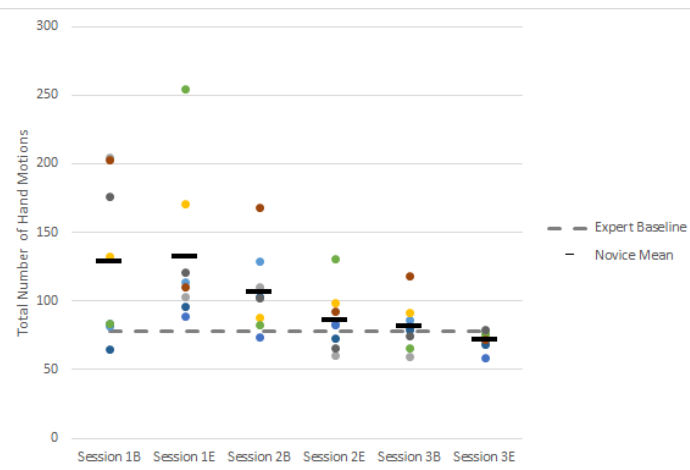


Figure 2: Novice learning curves for total number of hand motions versus session number (B = beginning; E = end).

[1] D. Clinkard, *et al.*, "The Development and Validation of Hand Motion Analysis to Evaluate Competency in Central Line Catheterization," *Academic Emergency Medicine*, vol. 22, no. 2, pp. 212-218, 2015.

Simultaneous Estimation of Feature Correspondence and Stereo Object Pose with Application to Ultrasound-Augmented Robotic Laparoscopy

Uditha L. Jayarathne^{1,2}, Xiongbiao Luo², Elvis C.S. Chen^{1,2}, and Terry M. Peters^{1,2}

¹Biomedical Engineering Graduate Program, Western University, London, Canada

²Robarts Research Institute, London, Canada

Background: In-situ visualization of ultrasound in robot-assisted surgery requires robust, real-time computation of the pose of the intra-corporeal ultrasound (US) probe with respect to the stereo-laparoscopic camera. Image based, intrinsic methods of computing this relative pose need to overcome challenges such as irregular illumination, partial feature occlusion and clutter that are unavoidable in practical robotic-laparoscopy. In this work, we extend a state-of-the-art simultaneous monocular pose and correspondence estimation framework to a stereo imaging model. The method is robust to partial feature occlusion and clutter, and does not require explicit feature matching.

Methods: The state-of-the-art monocular pose tracking method^[1] was extended to a stereo imaging model using Unscented Kalman Filtering (UKF)^[2] framework to jointly solve for feature correspondence and object pose. Once initialized, the algorithm robustly tracks a fiducial pattern attached to a curved back surface of a clinical US probe (Fig. 1a) in 6 degrees of freedom (6DoF).

Tracking performance of the proposed method was compared to the state-of-the-art monocular camera-based method^[1] and to the conventional stereo-triangulation-based method^[3], with Optical tracking system (Spectra, NDI, Canada) providing ground truth measurements. A mock-probe (Fig. 1b) rigidly attached to an optically tracked jig was moved freely in front of a stereo laparoscopic camera while it was tracked by the optical tracking system. Robustly-determined calibration transform between the optically tracked dynamic reference body (DRB) and the fiducial pattern attached to the US probe allowed transformation of measurements from different tracking algorithms (MONO: monocular image-based method^[1], STEREO: stereo image-based method proposed here, TR: conventional stereo triangulation-based method^[4]) to a common coordinate system for comparison.

Results: Over a total of 650 laparoscopic camera frames, the root mean square (RMS) translational error was 2.0 ± 1.4 mm, 2.4 ± 1.3 mm and 1.6 ± 0.9 mm for MONO, TR and STEREO methods respectively. The results are summarized in Fig 2. The average computation time for the monocular image-based method was 15.7ms, while that for the proposed method was 38.3ms per frame. These results suggest that in terms of accuracy, the proposed method outperforms the conventional stereo pose estimation approach and the state-of-the-art monocular camera-based still maintaining real-time performance.

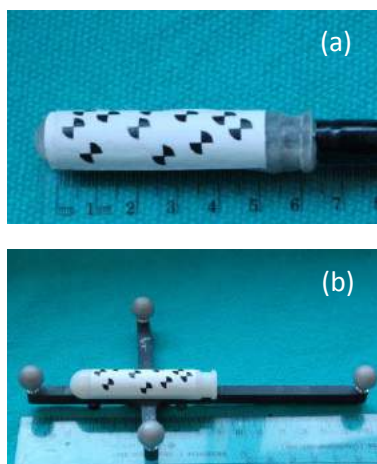


Fig. 1. (a) Fiducial pattern attached to the back surface of an intracorporeal US probe. (b) Optically tracked validation tool with a mock-probe rigidly placed in the middle

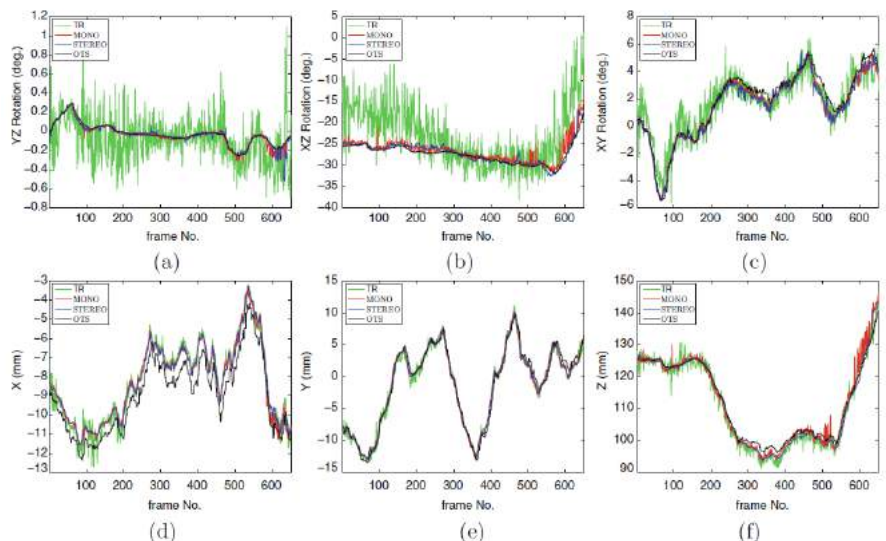


Fig. 2. Estimates computed by MONO (in red), STEREO (in blue) and TR (in green) while the ground truth measurements are in black.

References:

- [1] Jayarathne et. al, "Robust Intraoperative US Probe Tracking Using a Monocular Endoscopic Camera", MICCAI, 2013
- [2] Wan et. al., "The Unscented Kalman Filter for Nonlinear Estimation", IEEE Adaptive Systems for Signal Processing, Communications, and Control, 2003
- [3] Choi et. al, "Real-time 3D object pose estimation and tracking for natural landmark-based Visual Servo", IEEE Intelligent Robots and Systems, 2008

A Robust Method for Tracking Lung Tumors during External Beam Radiation Therapy

Elham Karami^{1,2}, Stewart Gaede^{1,3,4}, Ting-Yim Lee^{1,2,5,6}, Abbas Samani^{1,2,7,8}

¹Department of Medical Biophysics, Western University; ²Imaging Research Laboratories, Robarts Research Institute; ³Department of Physics and Engineering, London Regional Cancer Program; ⁴Department of Oncology, Western University; ⁵Imaging Program, Lawson Health Research Institute; ⁶Department of Medical Imaging, Western University; ⁷Department of Electrical and Computer Engineering, Western University; Biomedical Engineering Graduate Program, Western University, London, Ontario, Canada

Abstract

Despite recent advances in its treatment, lung cancer still remains the most common cause of cancer related death in both men and women. External Beam Radiation Therapy (EBRT) is one of the primary treatment methods of lung cancer which is extremely challenging due to respiration induced tumor motion. Various methods have been proposed for respiratory motion compensation, among which real-time tumor tracking is known to be the optimal solution. Tumor tracking methods usually use either mathematical or biomechanical motion models to estimate tumor motion from a surrogate signal. One popular approach is to use chest surface motion as a surrogate to tumor motion. However, recent studies show that the correlation coefficient between tumor and chest motion signals obtained from a single chest marker is not necessarily strong as it is dependent on several factors such as the marker and tumor locations. As such, it has been suggested by several groups to use a combined chest surface motion signal obtained from several chest markers to predict tumor motion. While the combined chest motion signal has been demonstrated to have stronger correlation with tumor motion, none of the studies provide a robust method for determining the optimal location and number of markers.

In this paper, we demonstrate that location data of patient's individual ribs can be used to find the optimal number and location of external chest markers. The rationale behind this is that the motion of ribs is one of the primary causes of lung tissue deformation and tumor motion. To obtain the raw data, the individual ribs as well as the tumor were segmented automatically in five 4D-CT data sets. Next, the tumor centroid was found in each image while rigid registration was used to track each individual rib during breathing. Figures 1(a) and (b) represent the displacement data for one rib point and the tumor centroid, respectively. Motion signals obtained from 6 rib points in x, y and z directions (18 signals) were used to find the location of tumor. For this purpose, all 18 chest motion signals were used in a Partial Least Squares (PLS) regression algorithm to find the correlation coefficients between the principle components of the chest motion signals and the tumor motion. As shown in Fig.1(c), at least 6 PLS components were required for accurate prediction of tumor motion and this was the case for all the patients. Preliminary results indicate that when motion signals are obtained from tracking the ribs while PLS is used to find the principal components of motion signals, the correlation between the combined chest motion signal and tumor motion is robust and reliable for tumor motion prediction. For future, we aim to change the number and

location of rib points systematically to find optimal set of points that lead to maximum correlation with tumor motion.

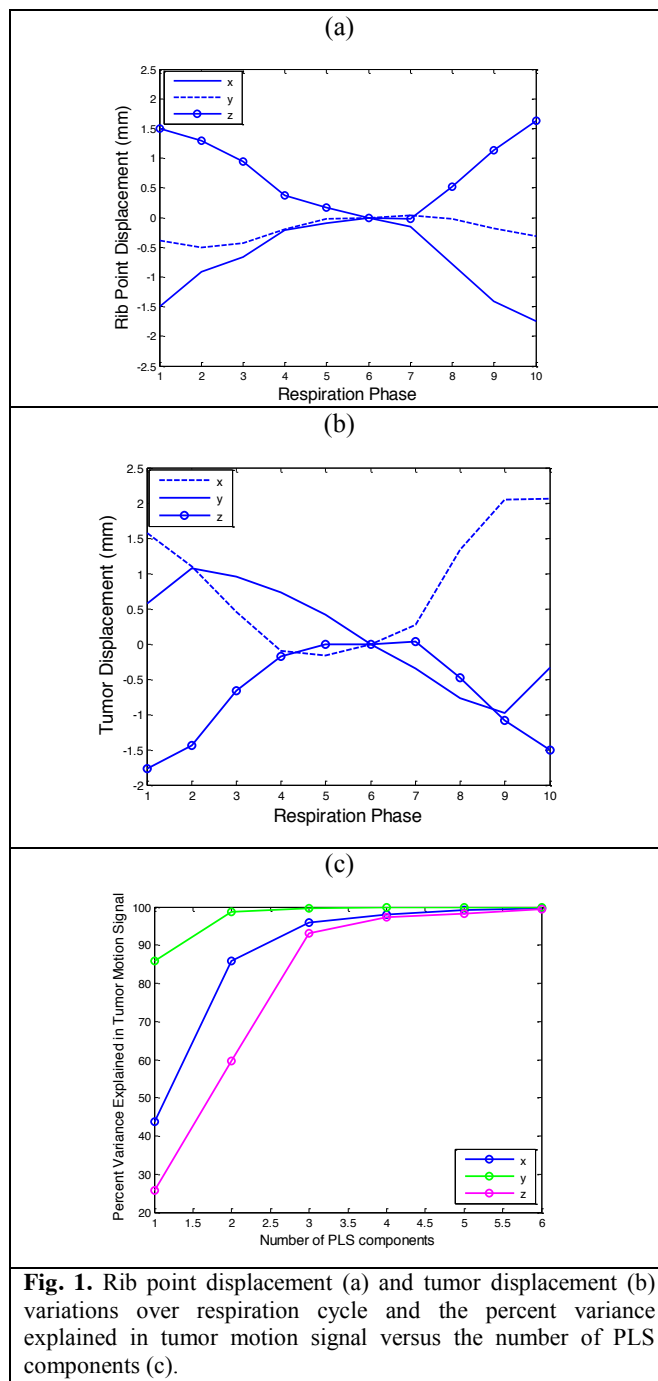


Fig. 1. Rib point displacement (a) and tumor displacement (b) variations over respiration cycle and the percent variance explained in tumor motion signal versus the number of PLS components (c).

Cranial ultrasound in 2D and 3D to guide treatment in preterm neonates with posthemorrhagic ventricular dilatation

J Kishimoto^{1,2}, D.S.C Lee⁴, F. Salehi^{2,3}, W. Romano, A Fenster^{1,2}, S. de Ribaupierre^{1,4,5}

¹Department of Medical Biophysics, University of Western Ontario; ²Robarts Imaging, University, Western Ontario; ³Department of Neonatology, University of Western Ontario, London Health Sciences Centre; ⁴Department of Clinical Neurological Sciences, University of Western Ontario, London Health Sciences Centre: London, Ontario, Canada
Consortia: Ontario Institute for Cancer Research - Imaging Translation Program

Research Supervisors: Sandrine de Ribaupierre and Keith St. Lawrence

Introduction Preterm neonates with intraventricular hemorrhage (IVH) often acquire post hemorrhagic ventricle dilation (PHVD), which, when severe, can lead to neurological impairment. Cranial 2D ultrasound (US) images are used for the diagnosis and monitoring of PHVD; however, there is no consensus on the use of 2D US images to guide treatment. This can lead to delays in interventions, and the potential for brain injury. We have developed a 3D US system that has been shown to accurately detect changes ventricle volumes (VV).

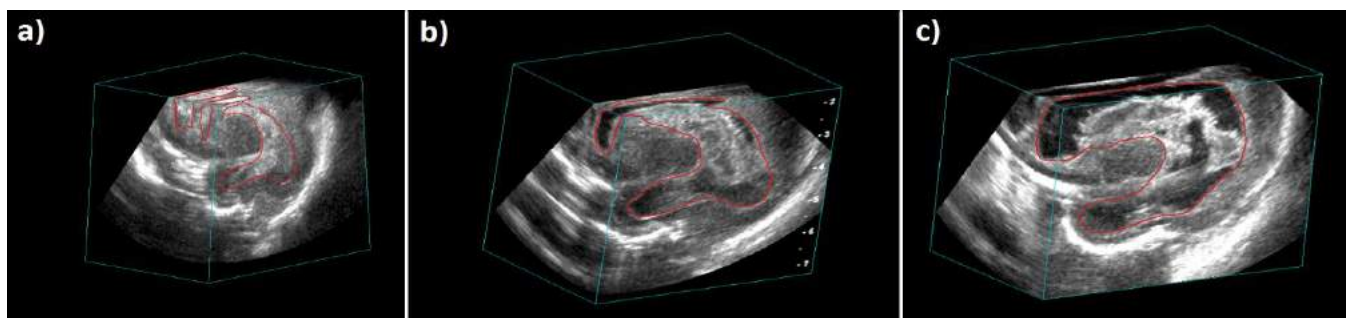


Figure 1 - The dilation of the left lateral ventricle in a neonatal patient with grade III IVH during the a) first week of life, b) second week of life, and c) third week of life (taken immediately prior to the first interventional ventricle tap). Manual contours shown on each image.

Methods Neonates were imaged twice weekly in accordance to a protocol approved by the research ethics board. 3D US images were manually segmented to obtain VV. 2D measurements included ventricle index, anterior horn widths, third ventricle width, and largest thalamo-occipital distance. The rate of change for each measurement was calculated. Decisions to perform ventricular taps (VTs) to relieve intracranial pressure were made independently by neurosurgeons who were blinded to study images. Receiver operator curves (ROC) were generated using the sensitivity and specificity of the rates of change of sonographic parameters in predicting the need for VT. For each parameter optimal threshold for intervention was estimated by the area under ROC; and positive and negative predictive values (PPV, NPV) were calculated. Additionally, we investigated whether US measurements predicted the need for multiple interventions.

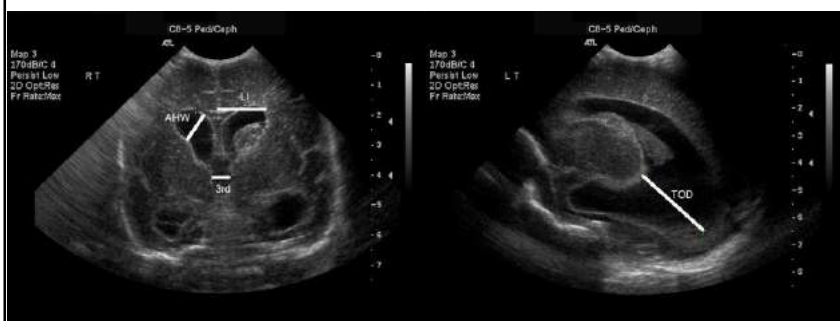


Figure 2 - The dilatation of the lateral ventricles in a neonatal patient with grade II IVH. 2D US measurements indicated in the coronal slice (left image) AHW – anterior horn width, LI – Levene's index and 3rd – third ventricle width and in the sagittal slice (right image) TOD – thalamo-occipital distance.

Results 23 neonates with PHVD were enrolled, 8 required interventions. The best predictor to determine initial intervention was the rate of change in VV when a threshold of $>2.04 \text{ cm}^3/\text{day}$ was used within the first three weeks of life (NPV and PPV of 1) and, this measurement was able to determine if then a patient would require further interventions when a threshold of $-0.04 \text{ cm}^3/\text{day}$ was used looking at imaging time points after the first intervention (NPV and PPV of 1). 2D measurements were less sensitive and/or less specific (sensitivity of 88-57%, specificity of 100-79%, PPV of 0.88-0.57 and NPV of 0.93-0.79).

Conclusions 3D US VV can predict the requirement for interventional ventricular tap in neonates with IVH, and can identify patients that have resolving PHVD following initial intervention, with higher sensitivity and specificity than 2D US measurements. These findings show promise for early classification of neonates using 3D US for prediction of interventional therapy, potentially aiding in timely management of these patients.

A Simple MRI Scanner Control Technique for Device Localization during MRI-Guided Interventions (Imaging for Cardiovascular Device Intervention)

Matthew MacDonald^{*1,2}, Adam C. Waspe^{3,4}, Joao Amaral^{3,4}, Samuel Pichardo^{**1,2}

¹Thunder Bay Regional Research Institute, Thunder Bay, ON, Canada, ²Lakehead University, Electrical Engineering, Thunder Bay, ON, Canada, ³University of Toronto, Medical Imaging, Toronto, ON, Canada,

⁴Hospital for Sick Children, Toronto, ON, Canada, *Primary Author, **Research Supervisor

Introduction: MRI guided percutaneous interventions performed inside closed-bore MRI scanners can be performed with freehand device placement methods, which are conducted in real time during rapid image acquisition[1]. Here, we demonstrate how a clinician operator can simultaneously align multiple dynamic scan planes to an interventional device. This is done using foot pedal inputs to highlight device/axial plane intersection points that define a virtual line of best fit about which auxiliary dynamic scan planes are automatically oriented.

Methods: Ex-vivo trials were conducted with the experimental setup illustrated in Figure 1 using a 3T Philips Achieva MRI, an 11 gauge titanium biopsy needle, a porcine hind limb specimen, and an MR safe projector unit (MRA Inc., Washington, PA). Operator input was collected using foot-pedal optical switches constructed with plastic and brass to interrupt a 5mw 650nm multi-mode fiber-optic circuit interfaced with an external control PC. A GUI application was written in the Python computer language to control the scanner according to operator input using the MatMRI software toolbox[2]. This application was also used to display a visualization of the procedure inside the scanner room using the connected projector. MR parameters for the dynamic images were: FOV = 300×300mm² resolution = 3×3×7mm³, TE/TR = 2.1ms/78ms, flip angle = 70°, acquisition matrix = 100×99, ETL = 11, reconstruction matrix = 112, NEX = 1, dynamic time = 701ms. Volunteer operators (N=3) manually guided the biopsy needle tip from an externally marked entry site at the anterior leg to a target planted within the anterior thigh marked with a 1ml vial of gadoteridol (0.32mmol/L). Final needle tip distance from the target and scan plane alignment was verified using a T1-weighted 3D acquisition, FOV = 300×300×338mm³, resolution = 2.5×2.5×5mm³, TE/TR = 2.3ms/3.3ms, flip angle = 7°, acquisition matrix = 120×120, reconstruction matrix = 480, ETL = 1, NEX = 4.

Results: Needle tip contact with the target occurred in two out of three trials for an average tip to target distance of 4.73mm. Average plane misalignment was 5.36° between horizontal and vertical axes. The average completion time was 11 minutes and 58 seconds. Figure 2 shows an example screen-shot of real time dynamic image display. A device/axial plane intersection point is highlighted within the GUI in the primary (left) view and also shown are the automatically aligned views (center and right) showing the needle tip contacting the contrast enhanced target.

Conclusions: This set-up offers efficient interactive image plane control capabilities accessible with an array of only four input foot switches. Future study will focus on expanding this method to incorporate device motion information and further simplify operator input. Figure 3 shows a volunteer operator successfully aligning scan planes to an instrument using the proposed hands-free technique without having to deviate sight from inside the scanner bore.

[1]Kaye, Elena A., et al. "Closed-Bore Interventional MRI: Percutaneous Biopsies and Ablations." *American Journal of Roentgenology* 205.4 (2015): W400-W410. [2] Zaporzan, Benjamin, et al. "MatMRI and MatHIFU: software toolboxes for real-time monitoring and control of MR-guided HIFU." *Journal of therapeutic ultrasound* 1.1 (2013): 1-12.

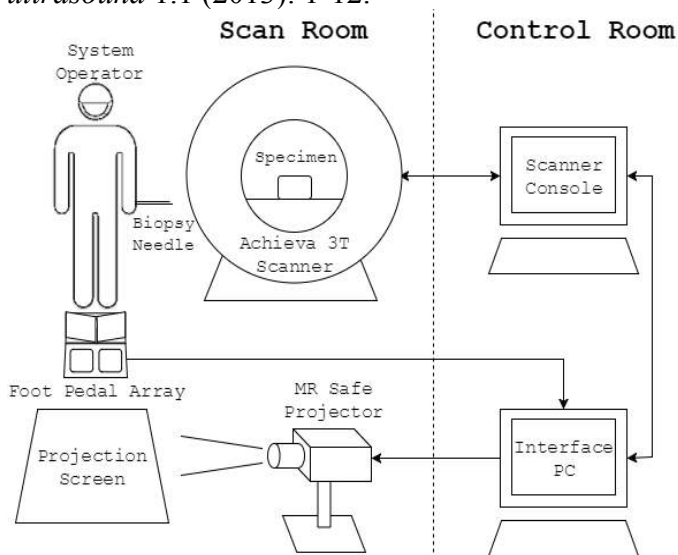


Fig 1. Diagram of the experimental set-up

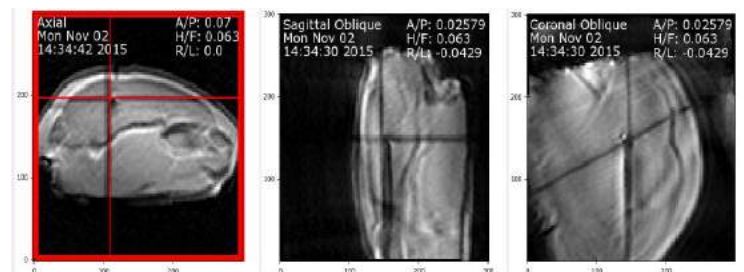


Fig 2. Example screen-shot of real time dynamic image display showing auxiliary views (centre, right) aligned to the biopsy needle according to points highlighted in primary view (left).



Fig 3. A volunteer operator performing the experimental procedure with a projector screen mounted inside the scanner bore.

Hands-Free Dynamic Contrast Control for MRI-Guided Percutaneous Procedures (Imaging for Cardiovascular Device Intervention)

Matthew MacDonald^{*1,2}, Steven Engler^{1,3}, Adam C. Waspe^{4,5}, Joao Amaral^{4,5}, Samuel Pichardo^{**1,2}

¹Thunder Bay Regional Research Institute, Thunder Bay, ON, Canada ²Lakehead University, Electrical Engineering, Thunder Bay, ON, Canada ³Lakehead University Computer Science, Thunder Bay, ON, Canada

⁴University of Toronto, Medical Imaging, Toronto, ON, Canada, ⁵Hospital for Sick Children, Toronto, ON, Canada, *Primary Author, **Research Supervisor

Introduction: MRI guided biopsies can be performed with freehand device placement methods, which are conducted in real time during rapid image acquisition using multiple sets of contrast parameters[1]. Here, we demonstrate how a clinician operator can interactively select contrast parameters for dynamic images using a foot pedal input to adjust the number of repetitions assigned to co-aligned interleaved scans.

Methods: Ex vivo trials were conducted with the experimental setup illustrated in Figure 1 using a 3T Philips Achieva MRI, an 11 gauge titanium biopsy needle, a porcine hind limb specimen, and an MR safe projector unit (MRA Inc., Washington, PA). A time-interleaved scan protocol[2] was developed as shown in Figure 2.

Repetition settings for the T1-weighted (T1w) and T2-weighted (T2w) dynamic scans were adjusted at the operator's command to interactively toggle the protocol between the two configurations shown. Operator input was collected using a foot-pedal optical interrupter switch constructed with plastic and brass to interrupt a 5mW 650nm multi-mode fiber-optic circuit interfaced with an external control PC. A GUI application was written in the Python computer language for scanner communication using the MatMRI software toolbox[3]. This application was also used to display a visualization of the procedure inside the scanner room using the connected projector. MR parameters for (A) T1w and (B) T2w dynamic images were: (A) FOV = 300x300mm, resolution = 3x3x7mm, TE/TR = 2.1ms/78ms, flip angle = 70°, acquisition matrix = 100x99, ETL = 11, reconstruction matrix = 112, NEX = 1, image frame time = 701ms for three stacks; and (B) FOV = 300x300mm, resolution = 3x3x7mm, TE/TR = 10ms/100ms, flip angle = 12°, acquisition matrix = 100x99, ETL = 11, reconstruction matrix = 112, NEX = 1, image frame time = 900ms for three stacks. Volunteer operators (N=3) evaluated the system's contrast switching capabilities as they manually guided the biopsy needle tip from an externally marked entry site at the anterior leg to a target planted within the anterior thigh marked with a 1ml vial of gadoteridol (0.32mmol/L).

Results: It was discovered that when using 'configuration A' (alternating between T1w and T2w scans), repeated excitations in voxels along plane intersections caused cross contamination between image frames and lower signal-to-noise (SNR) as shown in Figure 3. A solution was devised to automatically offset the T1w scan plane geometry outside the field of view while 'configuration A' was selected for an SNR improvement of 6.4dB in T2w images. This solution allowed an operator to effectively switch between acquisitions of T1w images at a rate of 701ms per image frame or T2w images at a rate of 1601ms (the combined acquisition time of both scans.)

Conclusions: This set-up offers efficient interactive image contrast control capabilities accessible with a single input foot switch. Future studies will focus on expanding interactive capabilities for interleaved scans to allow cycling between multiple scan locations along a parameterized interventional device trajectory.

[1]Kaye, Elena A., et al. "Closed-Bore Interventional MRI: Percutaneous Biopsies and Ablations." *American Journal of Roentgenology* 205.4 (2015): W400-W410. [2] Keupp et al. ISMRM 23rd Annual Meeting & Exhibition, Toronto, ON, Canada.2015; abstract 4061. [3] Zaporzan, Benjamin, et al. "MatMRI and MathIFU: software toolboxes for real-time monitoring and control of MR-guided HIFU." *Journal of therapeutic ultrasound* 1.1 (2013): 1-12.

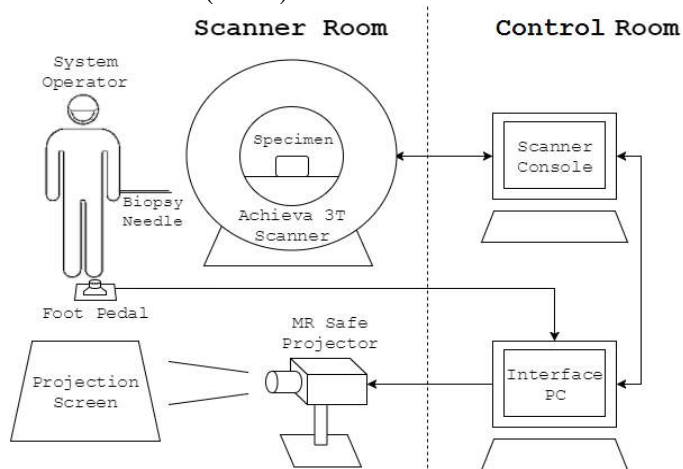


Fig 1. Diagram of the experimental set-up

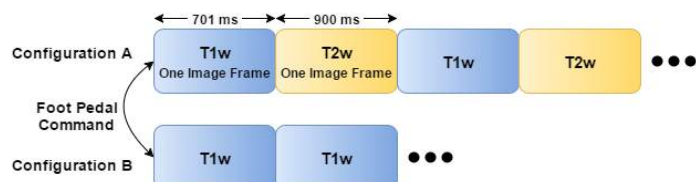


Fig 2.(above) Interleaved sequence timing diagram



Fig 3.(left) T2w image degraded by cross contamination due to collocation of interleaved scanning planes.

System for objectively evaluating colonoscopy procedural skills using motion analysis

Kyle MacNeil^{1*}, Chang (Nancy) Wang², Matthew S. Holden¹, Tamas Ungi¹, Gabor Fichtinger¹, Lawrence Hookey³

¹Laboratory for Percutaneous Surgery, School of Computing, Queen's University

²Department of Medicine, Queen's University

³Division of Gastroenterology, Department of Medicine, Queen's University

*Corresponding Author: 11km94@queensu.ca

Introduction: In recent years, there has been a shift away from a “time-based” model of medical education to competency-based medical education. In the area of colonoscopy, psychomotor skills associated with the procedure are generally acquired through practice on live patients. Recently, hand motion analysis has been studied as a means for measuring proficiency and ranges of motion [1]. The objective of this work is to demonstrate validity of a motion analysis setup for evaluating colonoscopy skill by comparing novice baseline performance to an expert baseline.

Methods: First, hand motion baseline data was collected from experienced gastroenterologists (at least 5 years of experience and at least 200 procedures/year). Subsequently, baseline data was collected from novices (medical trainees) who had no previous experience in the simulated and/or clinical setting. The simulated colonoscopy procedures were completed using a previously developed wooden bench-top model [2], and an Olympus/Pentax colonoscope (Fig. 1). Participants' left and right hands, forearms, and upper arms were each tracked relative to the bench-top model. Motion data was collected using the PLUS software library [3] and analyzed using the Perk Tutor extension [4] for 3D Slicer (www.slicer.org). Range of motion analysis was performed for both wrists and elbows using the protocol outlined by Mohankumar *et al.* [1].

Results: An expert baseline for proportion of time spent outside normal ranges of motion was generated for the right and left hands and the novice baseline was compared to it. Preliminary results show that novices spend on average 31% more time outside normal ranges of motion than experts, for both the right and left hands (Fig 2.). The difference was found to be statistically significant for both the right ($p=0.0093$) and left ($p=0.030$) hands. Average total procedure time was also included in preliminary results and showed that on average experts complete the procedures 50% faster.

Conclusion: We have developed a method for objectively evaluating colonoscopy procedural skills using motion analysis. A preliminary study has demonstrated the feasibility of the proposed setup, determined expert benchmarks, and shown evidence of metric validity for evaluation of competence. A study of the novice learning curves is ongoing.

Acknowledgement: G. Fichtinger (research supervisor) is supported as a Cancer Care Ontario Research Chair.
 [1] Mohankumar *et al.*, Characterization of right wrist posture during simulated colonoscopy: an application of kinematic analysis to the study of endoscopic maneuvers. *Gastrointest. Endosc.* 79, 480–489, 2014.
 [2] Walsh *et al.*, Concurrent Versus Terminal Feedback: It May Be Better to Wait. *Acad. Med.* 84, S54-7, 2009.
 [3] Lasso *et al.*, PLUS: Open-Source Toolkit for Ultrasound-Guided Intervention Systems. *IEEE Trans. Biomed. Eng.* 61, 2527–2537, 2014.
 [4] Ungi *et al.*, Perk Tutor: An Open-Source Training Platform for Ultrasound-Guided Needle Insertions. *IEEE Trans. Biomed. Eng.* 59, 3475–3481, 2012.



Figure 1. Experimental user setup, with exposed model.

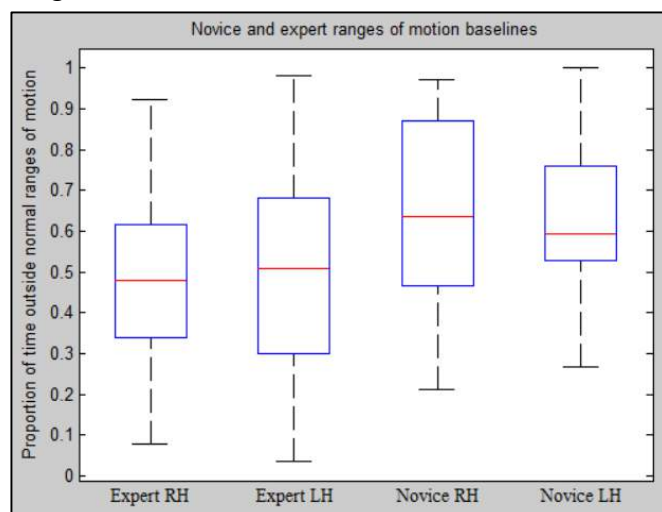


Figure 2. Proportion of time spent outside normal ranges of motion for both the expert (n=4) and novice (n=1) groups.

How does prostate biopsy guidance error impact pathologic cancer risk assessment?

Peter R. Martin¹, Mena Gaed^{2,6}, José A. Gómez², Madeleine Moussa², Eli Gibson^{6,7,8},

Derek W. Cool^{3,6}, Joseph L. Chin^{4,5}, Stephen Pautler^{4,5}, Aaron Fenster^{3,6}, and Aaron D. Ward^{1,5}

Departments of ¹Medical Biophysics, ²Pathology, ³Medical Imaging, ⁴Surgery, ⁵Oncology, ⁶Robarts Research Institute; Western University, Canada. ⁷Centre for Medical Image Computing, University College London, UK.

⁸Department of Radiology, Radboud University Medical Centre, Netherlands.

Ontario Institute for Cancer Research – Smarter Imaging Program, Research supervisor: Aaron D. Ward

Introduction: Magnetic resonance imaging (MRI)-targeted, 3D transrectal ultrasound (TRUS)-guided prostate biopsy aims to reduce the 21–47% false negative rate [1] of clinical 2D TRUS-guided sextant biopsy, but still has a substantial false negative rate. This could be improved via biopsy needle target optimization, accounting for uncertainties due to guidance system errors, image registration errors, and irregular tumour shapes. As an initial step toward the broader goal of optimized prostate biopsy targeting, we elucidated the impact of biopsy needle delivery error on the probability of obtaining a tumour sample and on the core involvement, for lesions of all Gleason grades and intermediate/high-grade lesions.

Methods: 4 μm thick histology sections were cut from the midgland of 18 prostate specimens after radical prostatectomy, and digitized at a 0.5 μm pixel size. Cancer was contoured by a physician trained in prostate cancer morphology (Fig. 1) with all contours verified by a genitourinary pathologist. This yielded 99 foci of all Gleason grades (\geq Gleason 3), including 10 intermediate/high grade foci (\geq Gleason 4+3). We modeled the biopsy system's root mean squared needle delivery error (RMSE) using an isotropic 2D Gaussian distribution with no bias. The magnitude of standard deviation modeled the error in delivering the centre of the needle core to a target. We performed simulations wherein the centroid of the tumour was the biopsy target and the needle was oriented posteroanteriorly (approximating a transrectal approach). The contents of the 18 mm long biopsy core were recorded for 1000 simulations per tumour. We investigated how RMSE impacts the core involvement, and the probability of obtaining a cancer-negative biopsy core, when targeting lesions of all Gleason grade, and intermediate/high grade only. We subtracted the 5th percentile core length from the 95th percentile core length to obtain a nonparametric measure of variability in core length across the 1000 simulated biopsies.

Results: From Fig. 2, we observe no significant difference in core involvement variability or probability of missing the tumour when targeting intermediate/high grade lesions compared to lesions of all grades. This suggests that by preferentially targeting lesions of intermediate/high grade (analogous to targeting regions of low apparent diffusion magnitude on MRI [2]), the probability of missing targeted tumours may not be more likely than when targeting lesions of all grades. At an RMSE = 4 mm (as has been observed in practice [3]), we observed a median core involvement variability of 6.5 mm (Figure 2A). This range of variability constitutes more than 1/3 of a full core. This amount of variability is large enough to influence treatment decision.

Conclusions: For expected needle guidance errors, repeated biopsies of the same tumour target can yield core involvement measures with sufficient variability to influence the decision between active surveillance and treatment. However, this may be mitigated by >1 biopsy attempt at selected tumour targets.

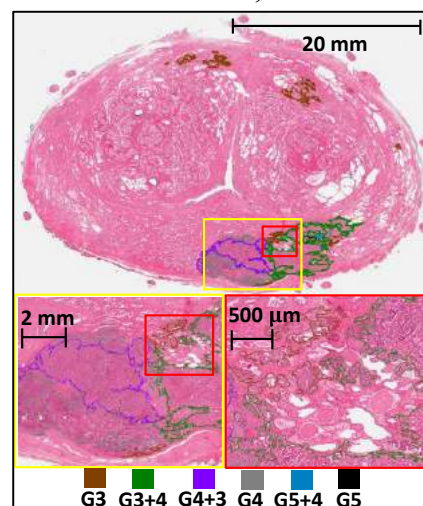


Figure 1: Illustrating the level of detail used for histopathology contours in this study.

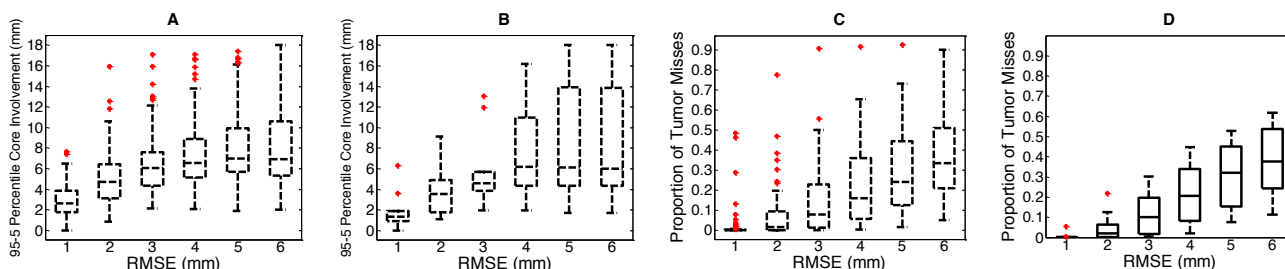


Figure 2: 95-5 percentile core involvement range values, for RMSE = 1 to 6 mm, calculated for (A) targeting all Gleason grade and (B) targeting high-grade lesions. (C-D) The proportion of tumour misses per 1000 simulations calculated for (C) targeting all Gleason grade and (D) targeting high-grade lesions. Whiskers give the largest and smallest values within $1.5 \times$ inter-quartile range.

[1] Rabbani, F., J Urol 159(4), 1998

[2] Hambrock, T., Radiology 259(2), 2011

[3] Martin, P., Med Phys 41(7), 2014

*Development of a Three Dimensional Ultrasound System for Guidance of Permanent Breast Seed Implantation
In the Treatment of Breast Cancer*

Michael, Justin^{1,2}, Fenster, Aaron^{1,2,3}

¹Imaging Research Laboratories, Robarts Research Institute, Western University; ²Biomedical Engineering Graduate Program, Western University; ³Department of Medical Biophysics, Western University; Consortia: Ontario Institute for Cancer Research - Imaging Translation Program

Research Supervisor: Aaron Fenster

Introduction Permanent breast seed implantation (PBSI) is a type of low dose-rate brachytherapy used in breast conserving therapy of early stage breast cancer to reduce radiation treatment time to a single day¹. PBSI uses needles to implant ‘seeds’ of radioactive Pd-103 under 2D ultrasound guidance. A limiting factor to wider adoption of PBSI is operator dependence, caused primarily by limitations of 2D ultrasound. Our goal is to develop a 3D ultrasound guidance system to reduce operator dependence, increase the accuracy of seed implantation and reduce the procedure time.

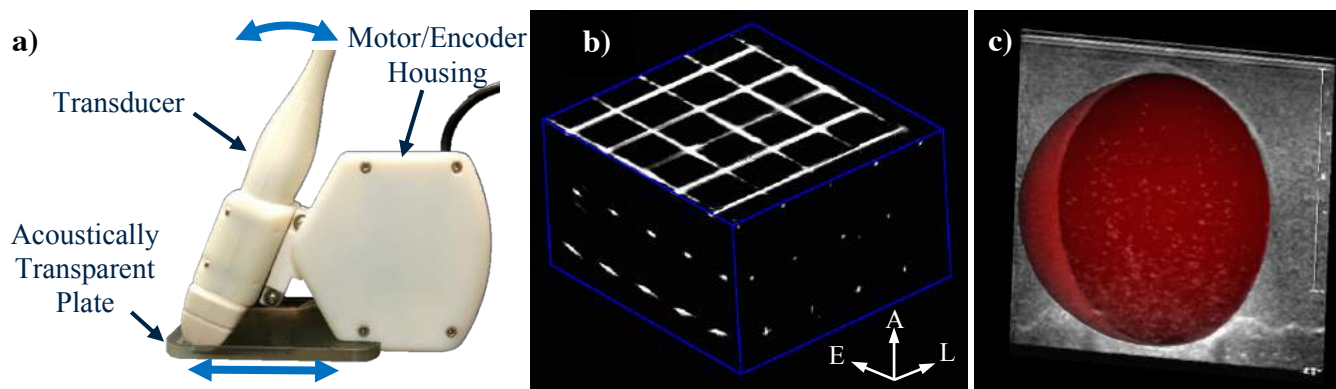


Figure 1 a) 3D US scanner. Blue arrows indicate directions of transducer motion. b) 3D US image of string phantom; axial, lateral and elevational directions as indicated (A, L, E). c) Volumetric phantom with manual segmentation (red) overlaid onto central slice.

Methods A 3D ultrasound (3D US) system was constructed consisting of a conventional linear, 2D ultrasound transducer connected to motors and encoders capable of moving and tracking the probe (Figure 1a). A thin plate of acoustically transparent TPX plastic is used to prevent deformation of the tissue by the transducer during the scan. Images are captured using a laptop and commercial screen-grabber and reconstructed into a 3D image in a hybrid geometry (combined translational and rotational movement) as the images are acquired. The scan time is 20s and the 3D image is available immediately after the scan. 3D reconstruction was validated, 1) geometrically, using distance measurements of strings placed 10mm apart in each direction, and 2) volumetrically, using an embedded spherical phantom molded in agar to volume displacement measurements. Distance and volume measurements were analyzed using one-sample and two-sample t-tests, respectively.

Results No significant differences from expected ($p > 0.05$) were found in any direction of geometric validation nor in volumetric validation (Tables 1 & 2). Example images from each test shown in Figure 1 b) and c), respectively.

Table 1 Results of geometric validation

| Direction | N | Mean (mm) | St. dev. (mm) | 95% CI (mm) |
|-------------|----|-----------|---------------|--------------|
| Lateral | 70 | 9.96 | 0.42 | 9.86 – 10.06 |
| Axial | 40 | 10.08 | 0.30 | 9.98 – 10.17 |
| Elevational | 75 | 9.99 | 0.40 | 9.90- 10.08 |

Table 2 Results of volumetric validation

| Measurement Method | N | Mean (cm ³) | St. dev. (cm ³) |
|---------------------|---|-------------------------|-----------------------------|
| Volume Displacement | 3 | 21.51 | 0.25 |
| 3DUS Segmentation | 3 | 21.11 | 0.15 |

Conclusions A 3D US scanner tailored to the needs of PBSI has been developed and validated to demonstrate geometric and volumetric accuracy. Future work includes a pilot study with healthy women to verify suitability in a clinical environment as well as phantom studies to develop needle segmentation techniques.

¹ J.P. Pignol, B. Keller, E. Rakovitch, R. Sankreacha, H. Easton, and W. Que, Int. J. Radiat. Oncol. Biol. Phys. **64**, 176 (2006).

Hidden Markov Models for Characterization of Temporal Ultrasound Data in Prostate Cancer

Layan Nahlawi¹, Farhad Imani², Mena Gaed³, Jose A. Gomez⁴, Madeleine Moussa⁴, Eli Gibson⁵, Aaron Fenster⁶, Aaron D. Ward⁶, Purang Abolmaesumi², Hagit Shatkay⁷, and Parvin Mousavi¹

¹School of Computing, Queen's University, ² Dept. of Electrical and Computer Engineering, University of British Columbia, ³ Robarts Research Institute, ⁴ Dept. of Pathology, Schulich School of Medicine and Dentistry, Western University, ⁵ Centre for Medical Image Computing, University College London, ⁶ Dept. of Medical Biophysics, Western University, ⁷ Dept. of Computer and Information Sciences, University of Delaware

Introduction: Prostate cancer is an immediate health concern world wide [1]. The current diagnosis practice involves core needle biopsy using Trans-Rectal UltraSound (TRUS). TRUS cannot accurately guide biopsies due to the low sensitivity and specificity of standard ultrasound imaging in characterization of cancerous versus normal tissue in the prostate. Current research aims to improve the accuracy of biopsy either by adding tissue specific information obtained from ultrasound signals or by fusing ultrasound data with pre-operative Magnetic Resonance Imaging (MRI). Temporal sequences of ultrasound data have also been shown to carry tissue characterizing information, resulting in improved differentiation of tissue types [2].

Temporal ultrasound sequences are a series of ultrasound frames captured from a specific location in the tissue, over a short period of time, without moving the transducer or the tissue [2]. This data relays tissue response to repetitive ultrasound sonication. Hidden Markov Models (HMMs) have been traditionally used to capture patterns in time series, and as such we use to model the ultrasonic sequences [3]. These models capture temporal relations that are typically not represented in existing work. Utilizing the framework of HMMS, we build a probabilistic model of cancerous versus normal prostate tissues.

Methods: We use the temporal ultrasound data from 10 patients that have undergone radical prostatectomy. The ultrasound images of the prostates were co-registered with annotations obtained from histopathology analysis to be used as a gold standard.

Each ultrasound frame is divided into Regions of interest (ROIs) representing an area of approximately 1.7x1.7 mm². Figure 1 shows an example of temporal ultrasound data of one subject along with a grid dividing each image into ROIs, and the respective pathology annotations. Each ROI is represented by the mean intensity of all the spatial values in that ROI. Two types of HMM models are built, one trained and tested on the temporal ultrasound data of all normal ROIs and the other on the data obtained from all cancerous ROIs. A 5-fold cross-validation scheme is used for training and testing. We calculate the probability of each test ROIs under each of the learned HMMs. If the HMM that models the cancerous tissue generates a higher probability for the test ROI, the ROI is labeled as *cancerous*, otherwise it is labeled as *normal*.

Results and Conclusions: We calculated the accuracy, sensitivity and specificity for all the predicted labels. The average accuracy is 80%. Our preliminary results suggest that HMMs have the potential to model the differences in the temporal responses to ultrasound sonication between the normal and the cancerous prostate tissue.

References:

- [1] R. L. Siegel, K. D. Miller, and A. Jemal, "Cancer statistics, 2015," *CA: a cancer journal for clinicians*, vol. 65, no. 1, pp. 5–29, 2015.
- [2] M. Moradi, P. Mousavi, P. A. Isotalo, D. R. Siemens, E. E. Sauerbrei, and P. Abolmaesumi, "A new approach to analysis of RF ultrasound echo signals for tissue characterization: animal studies," in *Medical Imaging*. International Society for Optics and Photonics, 2007, pp. 65 130P–65 130P–10.
- [3] L. Rabiner and B.-H. Juang, "An introduction to hidden markov models," *ASSP Magazine, IEEE*, vol. 3, no. 1, pp. 4–16, 1986.

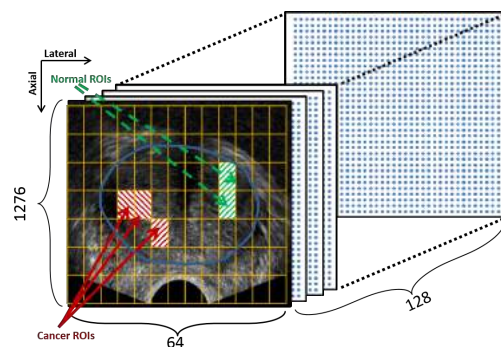


Figure 1: Temporal ultrasound data; the prostate is encircled and cancerous and normal ROIs are labeled.

Minimally invasive mitral valve repair using tracked 3D ultrasound navigation

*Adam Rankin^a, John Moore^a, Daniel Bainbridge MD^b, and Terry M. Peters^a

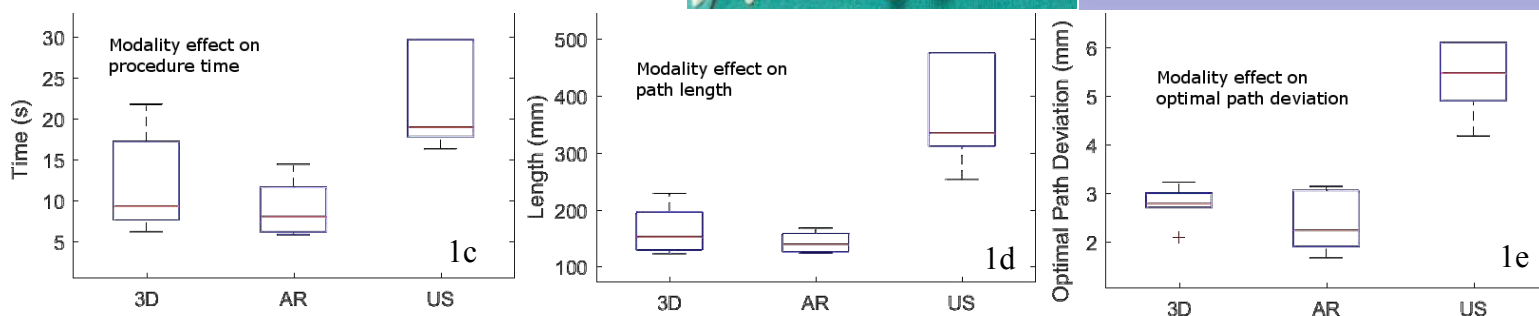
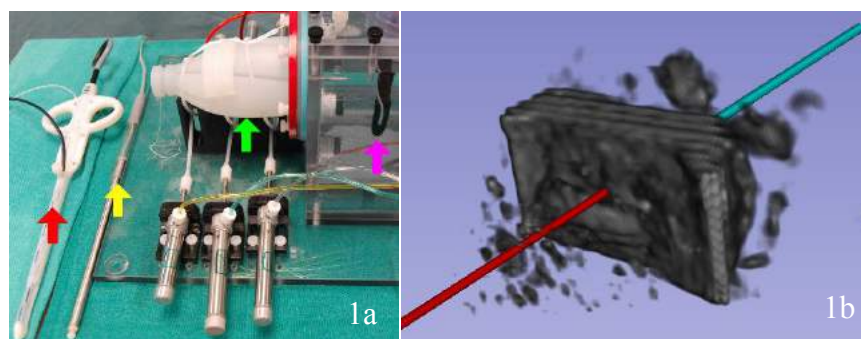
^aRobarts Research Institute, Ontario, Canada; ^bLondon Health Sciences Centre, Ontario, Canada

INTRODUCTION: Degenerative mitral regurgitation is a consequence of chordae rupture of the mitral valve. The NeoChord DS1000 (NeoChord Inc., Minnetonka, MN) is a device shown to be effective at treating mitral insufficiency by attaching neochordae under off-pump beating heart conditions [1]. The current standard of care for image guidance during neochordae attachment is bi-plane ultrasound. We propose a novel system that uses magnetically tracked 3D TEE ultrasound in an augmented reality interface to provide navigation guidance.

METHODS: The experiment comprised a modified iE33 xMATRIX ultrasound machine with a X7-2t TEE probe (Philips Healthcare, Andover, MA), a modified NeoChord DS1000, a custom calibration stylus, a beating heart phantom (Archetype Medical, ON, Canada), and an Aurora tabletop magnetic tracking system (NDI, ON, Canada). The beating heart phantom was configured to produce rhythmic left ventricular contractions at 60bpm (Fig. 1a). A mixed reality environment was developed to enable navigation of the NeoChord DS1000 from the entry point in the apex of the heart phantom through the mitral annulus. The virtual scene was configured such that users were presented with a perspective view of the scene at an oblique angle to the surgical elements (Fig. 1b). A counterbalanced repeated measures study was performed to validate the effectiveness of the proposed guidance system. Image and tracking information for the DS1000 was recorded and considered for analysis. This process was repeated with conventional bi-plane ultrasound (US), augmented reality tracked 3D ultrasound (3D) and augmented reality tracked 2D bi-plane (AR).

RESULTS: Duration, path length and optimal path deviation of a feasibility trial are reported. Three novice users performed 6 observations each. Results are presented in figures 1c, 1d and 1e. The mean durations for 3D, AR and US were 11.85s±6.19, 8.95s±3.37, and 26.06s±14.89 respectively. The mean path lengths were 163.73mm±41.13, 142.35mm±18.69, and 427.21mm±221.61. Mean optimal path deviations were 2.77mm±0.38, 2.37mm±0.60, and 6.05mm±2.14.

CONCLUSIONS: A system was developed that reduced the operational workflow complexity. By using magnetically tracked 3D TEE, the system is able to present an intuitive navigation interface to the user, thus providing constant guidance towards the target. Experiments performed with this system showed guidance capabilities equivalent to previously presented augmented reality bi-plane guidance and demonstrated that a less complex workflow is feasible with magnetically tracked 3D TEE imaging.



[1] Rucinskas, K., Janusauskas, V., Zakarkaite, D., Aidietiene, S., Samalavicius, R., Speziali, G., and Aidietis, A., "Off-pump transapical implantation of artificial chordae to correct mitral regurgitation: Early results of a single-center experience," *The Journal of Thoracic and Cardiovascular Surgery* **147**(1), 95 – 99 (2014).

3D Transrectal Ultrasound Needle Guidance System for High-Dose-Rate Interstitial Gynaecological Brachytherapy

J Rodgers^{1,2}, D Tessier², D D'Souza³, E Leung⁴, G Hajdok³, K Surry³, A Fenster^{1,2}

¹Biomedical Engineering, The University of Western Ontario, London, Ontario, Canada; ²Robarts Imaging Research Lab, London, Ontario, Canada; ³London Regional Cancer Program, London, Ontario, Canada; ⁴Odette Cancer Centre, Toronto, Ontario, Canada
Consortia: Ontario Institute for Cancer Research Imaging Translation Program

Research Supervisor: Aaron Fenster

Introduction Gynaecological cancers are one of the most prevalent in females and the number of gynaecological malignancies are expected to increase by 16% in Ontario between 2011 and 2018.¹ High-dose-rate (HDR) interstitial brachytherapy is a treatment for these cancers where needles are inserted into the tumour area through a perineal template. There is no standard real-time imaging modality to guide the needle placement in this procedure and, given the proximity to critical organs, serious complications can arise. Guidance systems have been proposed based on both x-ray computed tomography (CT)² and magnetic resonance imaging (MRI)³; however, these systems have limited translatability. While two-dimensional (2D) ultrasound (US) can be used for real-time needle guidance, visualization of needle placement and depth is difficult and subject to variability and inaccuracy in 2D images. We propose improving needle positioning and verification during HDR interstitial gynaecological brachytherapy using a three-dimensional (3D) transrectal ultrasound (TRUS) system.

Methods The 3D TRUS system acquires 300 2D US images during a tilt scan using a clinical 2D TRUS side-fire transducer and reconstructs these into a 3D image as they are collected. The geometry of the 3D US images was previously validated using phantoms. As a proof-of-concept, a 3D US image and a CT scan were acquired following needle insertion for two patients undergoing HDR interstitial gynaecological brachytherapy. Manual rigid registration was performed between the modalities based on the vaginal cylinder of the perineal template. For both modalities the tip of each visible needle and a second point on the needle path were selected to determine the needle trajectories and calculate the distance between corresponding needle tips and the angular trajectory difference.

Results Figure 1 shows a view of a 3D US image from a patient and the corresponding view in the registered CT image. Fourteen needles were placed for both patients and the differences in identified needle tips and trajectories between modalities is summarized in Table 1.

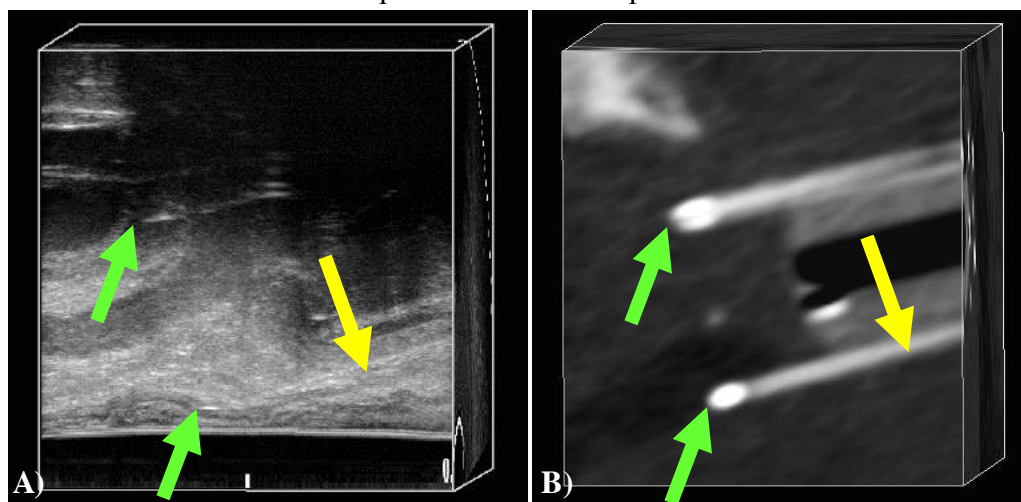


Figure 1: A) Sagittal view of a 3D TRUS patient scan with two needle tips indicated by green arrows and the bottom edge of the vaginal cylinder indicated by the yellow arrow. B) Corresponding slice in the registered CT scan, with needle tips and cylinder also indicated.

Table 1: Differences in needle trajectory and tip positions for visible needles between 3D US and CT

| | Case 1 | Case 2 |
|---|-----------------|-----------------|
| Number of visible needles | 14 | 13 |
| Mean Trajectory Difference (degrees) | 2.15 ± 1.28 | 3.89 ± 1.86 |
| Mean Difference in Needle Tip Position (mm) | 3.90 ± 2.08 | 4.28 ± 1.90 |

Conclusions Based on the preliminary results, comparison of the 3D US images to post-insertion CT images has shown that 3D TRUS is a feasible technique for correctly visualizing needles, providing the potential for needle guidance during HDR interstitial gynaecological brachytherapy. Improved needle placement could allow for more tailored treatment, leading to improved dose distributions with potentially fewer needles inserted and fewer complications.

References [1] Fung-Kee-Fung et al., Cancer Care Ontario "Organizational Guideline for Gynecologic Oncology Services in Ontario" (2013). [2] Lee et al. Brachytherapy **12**(4), 303–310 (2013). [3] Viswanathan et al. Brachytherapy **12**(3), 240–247 (2013).

Electromagnetically-guided catheter insertions in breast phantoms for brachytherapy

T Vaughan¹, H Brastianos², A Lasso¹, M Westerland², T Ungi¹, CB Falkson², G Fichtinger¹

¹School of Computing, Queen's University, Kingston, Ontario, Canada

²Department of Radiation Oncology, Kingston General Hospital, Kingston, Ontario, Canada

Consortium Affiliation: OCAIRO

INTRODUCTION: One in nine Canadian women will be diagnosed with breast cancer in their lifetime. Interstitial high dose rate brachytherapy is a method of delivering radiation therapy. In this procedure, hollow needles are inserted through the tumour bed, and flexible plastic catheters are pulled through each needle. The needles are removed, leaving only the plastic catheter inside the breast. Radioactive seeds are guided through the catheters to apply the treatment. Ideally the catheters should be inserted to cover the entire tumour bed and be evenly-spaced apart, but this is complicated by the fact that the breast is a deformable organ, and it is difficult to maintain a sense of the tumour bed's position relative to the catheters. We propose to apply electromagnetic (EM) guidance [1] to address this challenge.

METHODS: In our system, a tracked localization needle is inserted under ultrasound guidance into the tumour bed, which establishes a locally rigid coordinate system for the tumour bed (Figure (a)). The tumour bed is segmented on tracked ultrasound to create a model of the tumour bed in a virtual view (Figure (b)). A tracked needle guide (Figure (c)) is pointed at the tumour bed under EM guidance, and then a catheter needle is inserted through the guide and the tissue. Additional parallel catheter paths are planned and drawn on the virtual view based on this first insertion. The radiation oncologist aligns the needle guide with a planned catheter path before each subsequent insertion. Our software uses the 3D Slicer (www.slicer.org) [2] and PLUS (www.plustoolkit.org) [3] platforms. A phantom experiment was conducted to evaluate our system.

RESULTS: A radiation oncology resident inserted a row of four catheter needles under only ultrasound guidance on two phantoms, and under both EM and ultrasound guidance on two phantoms. The goal was to insert all catheters through the tumour bed with even spacing. CT scans were obtained to verify the placement of the catheter needles. Seven out of eight catheter needles passed through the tumour bed when using only ultrasound guidance. All eight catheter needles passed through the tumour bed when using both EM and ultrasound guidance. We did not observe improvement in catheter spacing in this study.

CONCLUSIONS: We have shown in this phantom study that EM guidance can help target catheter needles into the tumour bed. Further study is warranted. Other applications for EM guidance, such as real-time catheter tracking [4] and catheter path reconstruction, are being investigated.

ACKNOWLEDGEMENTS: Thomas Vaughan is funded by an Alexander Graham Bell Canada Graduate Scholarship (Doctoral Program). Gabor Fichtinger is funded as a Cancer Care Ontario Research Chair.

REFERENCES: [1] Ungi *et al.* Navigated breast tumor excision using electromagnetically tracked ultrasound and surgical instruments. IEEE TBME. 2015. Available online. [2] Pieper S, *et al.* 3D Slicer. In IEEE ISBI 2004 Apr 15 (pp. 632-635). IEEE. [3] Lasso *et al.* PLUS: open-source toolkit for ultrasound-guided intervention systems. IEEE TBME. 2014. 61(10):2527-37. [4] Lugez *et al.* Improved electromagnetic tracking for catheter path reconstruction in high-dose-rate brachytherapy. Med Phys. 2016. Accepted conditionally.

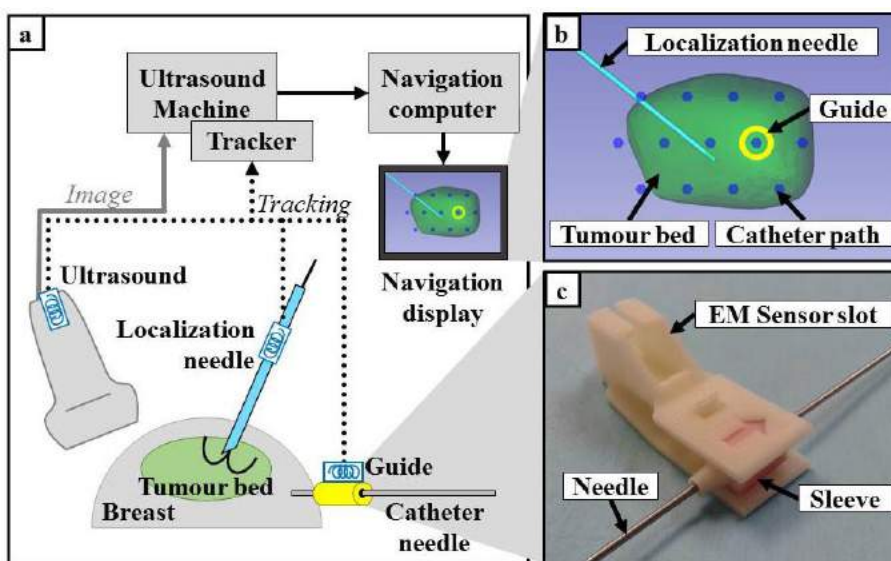


Figure. EM guided breast brachytherapy. (a) Overview schematic of EM guided HDR breast brachytherapy. (b) The virtual view in our software. (c) The tracked needle guide in this study.

Mouse brain developmental outcomes after whole brain vs focal irradiation

Kiran Beera*, Jun Dazai, David Jaffray, Brian Nieman;

University of Toronto, Toronto, Canada; Hospital for Sick Children, Toronto, Canada

Introduction

Radiation therapy is a critical component of pediatric brain tumour treatments. In cases such as medulloblastoma, the current standard of care includes surgical resection at the primary tumour site, systemic chemotherapy, and craniospinal radiotherapy--a treatment in which the whole brain and spinal cord are exposed to radiation doses from 20 to 40 Gy. Although this can result in an 80% 5-year survival for average risk patients, 75% of the survivors experience late effects--cognitive and behavioral deficits--that appear months to years after treatment. Childhood cancer survivors that received whole-brain irradiation also tend to exhibit decreased brain structure volumes, where white matter volume is significantly affected. Because the brain is highly interconnected and development of structures is interdependent, some of the observed volume decreases may result from damage to other brain regions, such as those containing neuronal connections or neurogenic niches. One neurogenic niche is localized on the walls of the lateral ventricles (LV), and is termed the subventricular zone (SVZ). From the SVZ, neural stem cells (NSCs) differentiate and travel surprisingly long distances via the rostral migratory stream (RMS) in order to continuously replenish interneuron populations in the olfactory bulbs (OB). In early stages, NSCs and their progeny may be especially critical to sustain normal growth. In addition, the anterior commissure (AC) is a major white matter tract that includes OB connections. We have previously shown widespread volume deficits in mice after cranial irradiation in infancy. In this study, we compare brain development results after radiation to the whole-brain (WB) and after focal radiation to the OB, AC or LV.

Methods

Dose distribution plans were generated using a preclinical treatment planning software for all regions of interest. Radiation was delivered to infant 2.5 week-old mice, and neuroanatomy was characterized using ex-vivo magnetic resonance imaging (MRI) at an adult-equivalent age of 9 weeks using a T2-weighted FSE sequence. A single 8 Gy dose was delivered to the WB, OB, AC or LV using a high-precision image-guided small-animal focal irradiator using a 15 mm, 5 mm or 2.5 mm circular collimator.

Results

In the WB irradiation cohort, we observed a pattern of volume deficits consistent with our previous work. In the OB irradiation cohort, the OB were found to be reduced in volume but only 50% as severely as in the WB irradiation cohort. After thresholding at 5% false discovery rate (FDR), several unirradiated brain regions were significantly reduced in volume, including the visual and somatosensory cortices and the AC. Surprisingly, irradiation of the AC did not result in any significant AC volume loss as was seen after WB irradiation. Lastly, irradiation of the LV and surrounding area had a significant effect on the growth of the AC and the OB. The degree of volume change attributable to direct irradiation and indirect developmental change was comparable in the case of OB and LV irradiations.

Conclusions

These results demonstrate that even focal irradiation to the brain may have widespread off-target effects on subsequent development, and show that these effects can be quite significant, particularly in WM regions such as the AC.

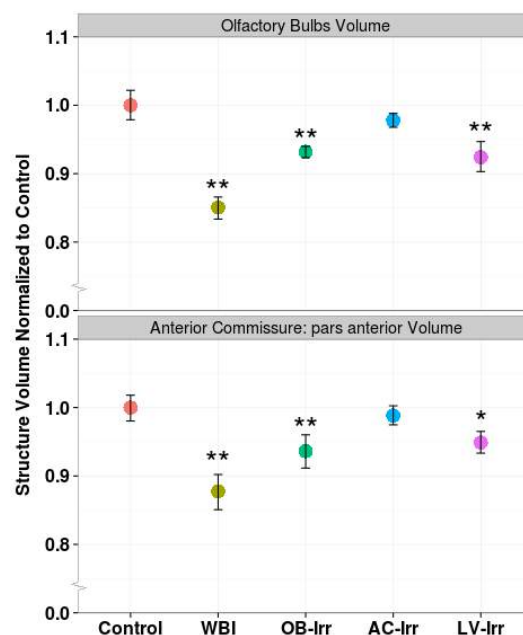


Figure 1 - Volumetric analysis of treatment groups; OB and AC volumes normalized to control group; *, 5% FDR; **, 1% FDR; error bars are 95% CIs

Early Detection of Tumour Response using volumetric DCE CT and DCE-MRI in Metastatic Brain Patients Treated with Radiosurgery

Coolens C.^{1,2,3}, Driscoll B.¹, Foltz W.^{1,2}, Chung C.^{1,2}

Ontario Institute for Cancer Research Imaging Translation Program

¹ Princess Margaret Cancer Center and University Health Network, Toronto, Canada;

²Department of Radiation Oncology, University of Toronto, Canada;

³Department of Biomaterials and Biomedical Engineering, University of Toronto, Canada

Objectives: Early change in tumour perfusion following stereotactic radiosurgery (SRS) is a potential biomarker of response. Efforts for quantitative model-based measures of dynamic contrast enhanced (DCE) MRI parameters have shown variable findings to-date. As DCE-CT is considered a gold standard for tracer-kinetic validation given its signal linearity, we compared tumour perfusion measurements from DCE-MRI and DCE-CT done at the same time points at baseline and following SRS for brain metastases using a recently developed 4D temporal dynamic analysis (TDA) method.

Methods and Materials: Patients with brain metastases treated with SRS underwent volumetric DCE-CT (Toshiba, Aquilion ONE) and DCE-MRI (IMRIS 3T Verio) scans at baseline then 7 and 21 days post-SRS. Tumours were defined with a semi-automated approach using post-contrast T1-weighted MRI at each time point and were co-registered to the corresponding DCE-CT and DCE-MRI. Individual arterial input functions (AIF) were selected in the internal carotid artery for DCE-CT whilst a population-based AIF was used for DCE-MRI. Voxel-based whole brain TDA was performed on all data using in-house software producing the following DCE metrics: Area under enhancement curve (AUC), K_{trans} , K_{ep} , and V_b (using the Modified Tofts model with static $T_{10} = 2400ms$) for each tumour at every time point. Linear regression of temporal changes in parameters was compared to baseline with tumour response based on tumor volume changes.

Results: Fourteen tumours in 9 patients were evaluated. At day 20, 1 tumour had grown, 5 were stable and 8 had decreased in volume (mean of 53.6 +/- 31%). Stable and shrinking (responding) tumors continued to remain stable or shrank further by 3 and 6 months.

DCE-CT: At day 7 post-SRS, 3 responding tumours had a K_{trans} reduction of 47.6 +/- 36.6% while at day 21, 10 of 13 responding tumours had a reduction in K_{trans} of 26.0 +/- 16.6%. The non-responding tumour showed an increase in K_{trans} at day 7 and 21. **DCE-MRI:** At day 7 post SRS, 7 responding tumours had a K_{trans} reduction of 16.7 +/- 16.7% while at day 21 post SRS, 10 of 13 responding tumours had a K_{trans} reduction of 48.7 +/- 36.5%. The non-responding tumour showed a decrease in K_{trans} at day 7 and day 21. AUC reduction was seen in both responding and non-responding tumours. Pearson correlation between DCE-CT and DCE-MRI for the magnitude of change in K_{trans} was low ($R^2 = -0.25$) but the relative change in K_{trans} over time was similar between CT & MR in 6/12 (Day 7) and 10/14 (Day 21).

Conclusions: Preliminary results suggest early K_{trans} reduction at 20 days following SRS may be a promising response biomarker. There was good correlation in predicting response using DCE-MRI or DCE-CT when the same TDA method was applied. Further efforts to improve quantitative analysis of DCE-MRI metrics, including T_{10} quantification and robust AIF selection, may alleviate such discrepancies.

Hybrid PET-MRI Imaging of Acute Radiation Induced Cardiac Toxicity

Omar El-Sherif^{1,2}, I. Xhaferllari^{1,2}, J. Sykes³, J. Butler³, G. Wisenberg^{1,3}, F. Prato^{1,3}, S. Gaede^{1,2}

¹Western University, London, ON, ²London Regional Cancer Program, London, ON,

³Lawson Health Research Institute, London, ON

Consortia: Ontario Institute for Cancer Research - Imaging Translation Program

Purpose: To identify the presence of *low-dose radiation induced cardiac toxicity* in a canine model using hybrid positron emission tomography (PET) and magnetic resonance imaging (MRI).

Methods: Research ethics board approval was obtained for a longitudinal imaging study of 5 canines after cardiac irradiation. Animals were imaged at baseline, 1 week post cardiac irradiation, and 1 month post cardiac irradiation using a hybrid PET-MRI system (Biograph mMR, Siemens Healthcare). The imaging protocol was designed to assess acute changes in myocardial perfusion and inflammation. Myocardial perfusion imaging was performed using N¹³-ammonia tracer followed by a dynamic PET acquisition scan. A compartmental tracer kinetic model was used for absolute perfusion quantification. Myocardial inflammation imaging was performed using F¹⁸-fluorodeoxyglucose (FDG) tracer. The standard uptake value (SUV) over a region encompassing the whole heart was used to compare FDG scans. All animals received a simulation CT scan (GE Medical Systems) for radiation treatment planning. Radiation treatment plans were created using the Pinnacle³ treatment planning system (Philips Radiation Oncology Systems) and designed to resemble the typical cardiac exposure during left-sided breast cancer radiotherapy. Cardiac irradiations were performed in a single fraction using a TrueBeam linear accelerator (Varian Medical Systems).

Results: The delivered dose (mean \pm standard deviation) to heart was 1.8 \pm 0.2 Gy. Reductions in myocardial stress perfusion relative to baseline were observed in 2 of the 5 animals 1 month post radiation. A global inflammatory response 1 month post radiation was observed in 4 of the 5 animals. The calculated SUV at 1 month post radiation was significantly higher ($p=0.05$) than the baseline SUV.

Conclusion: Low doses of cardiac irradiation (< 2 Gy) may lead to myocardial perfusion defects and a global inflammatory response that can be detectable as early as 1 month post irradiation using hybrid PET-MRI imaging techniques.

Developing ^{19}F -MRI for Clinical Cell Tracking

OICR – Smarter Imaging Program

Jeff M Gaudet^{1,2}, Corby Fink^{3,4}, Matthew S Fox^{1,2}, Gregory A Dekaban^{3,4}, and Paula J Foster^{1,2}

¹Imaging Research Laboratories, Robarts Research Institute, ²Medical Biophysics, Western University,

³Molecular Medicine, Robarts Research Institute, ⁴Immunology and Cell Biology, Western University

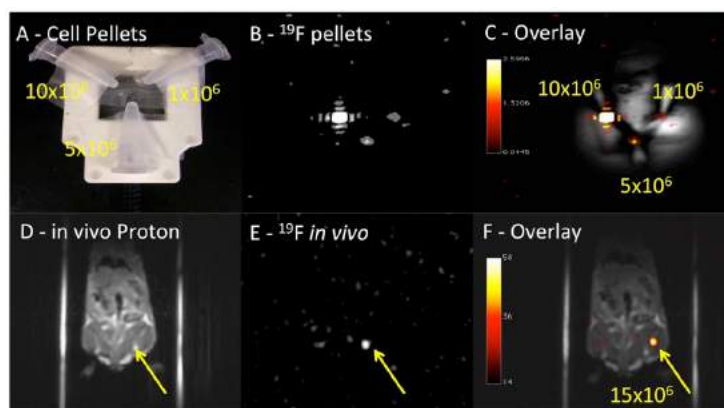
Background: Cancer vaccine-based therapies are an area of expanding research. In 2010, the first FDA approved cell therapy was released to target metastatic castration-resistant prostate cancer¹. This therapy uses antigen-presenting peripheral blood mononuclear cells (PBMC) in order to prime the immune system to target a tumor. Despite this progress, clinical results have been varied and inconsistent. Patient outcome is strongly dependent on *in vivo* behavior of these cells after administration. Antigen containing PBMC must migrate to a nearby draining lymph node to exert their therapeutic effect. Fluorine-19 (^{19}F) cellular MRI offers a tool to non-invasively track the fate and quantify migration of these cells. ^{19}F -MRI provides unambiguous detection, with a signal that is linearly dependent on the number of cells/voxel. In this study we: (i) optimized ^{19}F imaging on a clinical 3T MRI system, (ii) verified quantification accuracy using PBMC cell pellets containing a known number of cells.

Methods: Human PBMC donated from prostate cancer patients were labeled with a commercial, FDA approved, perfluorocarbon agent. NMR was performed on a known number of labeled cells to determine the average PBMC ^{19}F uptake. Imaging performed on a 3T system with a dual-tuned surface coil designed and approved for human use. A balanced steady state free precession (bSSFP) sequence was used at a resolution of $0.5 \times 0.5 \times 1 \text{cm}^3$ and a scan time of 15min for ^{19}F imaging. ^{19}F -bSSFP images were acquired of three PBMC cell pellets ranging from $1\text{-}10 \times 10^6$ cells. *In vivo* imaging was performed in a mouse following injection of 15×10^6 PBMC into the mouse hindlimb muscle using the same imaging parameters. Quantification was performed by measuring the ^{19}F signal in regions of interest and in a reference tube of known ^{19}F concentration.

Results/Discussion: With the human approved surface coil, all cell pellets (ranging from 1-10 million PBMC) were detectable within the 15min scan session [Figure 1A-C]. Proton images were acquired for pellet localization [A], followed by ^{19}F -MRI [B]. Analysis was performed by overlaying ^{19}F images onto the corresponding proton image [C]. In the smallest pellet, as few as 4×10^{17} ^{19}F /spins were detectable, the highest sensitivity reported in the literature with a clinical 3T system thus far.¹ Using the same dual-tuned coil, *in vivo* proton imaging was performed following injection of 15million PBMC into the hindlimb muscle of a mouse [D]. Once again, ^{19}F -MRI clearly shows the site of injection [E], which is given anatomical context when overlaid on the corresponding proton image [F].

Significance: This study is the first to report on clinical-strength MR imaging of PBMC. Here we have shown the highest reported sensitivity thus far for fluorine labeled cells using a clinical protocol. Based upon these results, we anticipate translation of ^{19}F -MRI into the clinic is feasible and foresee application of the technique in the near future for tracking PBMC in cancer patients.

References: 1. Ahrens E et al. (2014) Clinical cell therapy imaging using a perfluorocarbon tracer and fluorine-19 MRI. *Magnetic Resonance in Medicine*.



The Effect of the Chemotherapy Agent Methotrexate on the Developing Brain

Leigh Spencer Noakes¹, Ellen van der Plas³, Shoshana Spring¹, Russell Schachar³, Brian Nieman^{1,2}

¹Mouse Imaging Centre, Hospital for Sick Children, Toronto, ON, Canada; ²Medical Biophysics, University of Toronto; ³Psychiatry, University of Toronto

Introduction. Methotrexate (MTX) is one of the chemotherapy drugs commonly used to treat acute lymphocytic leukemia (ALL), the most common form of childhood cancer. Typically, a cocktail of chemotherapy agents is used to treat ALL, and recent advances in the treatment protocol have resulted in a 90% survival rate. Sadly, 50 % of ALL survivors are left with “late effects”, which impair cognitive ability. Late effects are accompanied by changes in brain structure volume.¹ It has been hypothesized that common genetic variants, such as in the MTHFR gene, contribute to MTX sensitivity. Here, we have used a mouse model to determine if treatment with MTX at an infant stage has consequences for brain development, and furthermore if these consequences are related to the Mthfr genotype.

Methods. C57Bl/6 mice and mice heterozygous for Mthfr gene (Mthfr +/-) were treated with a cumulative dose of 30 mg/kg of MTX, or saline, by intravenous (IV) injection at postnatal day (P) 17 and 19. Mice were imaged *in vivo* before and after treatment at days P14, P24, P42 and P63. A T1-weighted gradient echo sequence was used with parameters: k-space dimensions 224x224x854, isotropic resolution of 90 μ m, excitation flip angle of 37°, TR of 26 ms, effective echo time of 5.37 ms, 5 averages, and total scan time of ~ 1 h 45 min. Images were registered together nonlinearly through a series of iterative steps to produce an unbiased average.² Volumetric changes were computed by registering a structural atlas with 159 structures to the average. The volume of each structure was fit with a linear model, including an intercept, categorical treatment group (MTX or saline) and genotype (WT or Mthfr +/-).

Results. Many brain regions were affected by treatment with MTX. Affected areas showed a smaller volume in controls with increased impairment immediately after treatment. For these regions we observed an almost complete recovery after treatment, such that MTX-treated mice were equivalent to their saline-treated counterparts at the end of the study. Additionally, we observed that the WT mice exhibited greater volume deficits than the Mthfr +/- mice.

Conclusion. With MRI we have detected changes in the brain that result from early treatment with MTX. Many of the deficits seen after treatment recover by P63. Interestingly, the Mthfr +/- mice were less susceptible to the effects of MTX treatment, suggesting there may be a protective mechanism in place.

References. (1) Zeller, B. *et al. J. Clin. Oncol.*, **2013**, *31*, 2078-2086. (2) Lerch, J. P. *et al. Methods Mol. Biol.*, **2011**, *711*, 349-361.

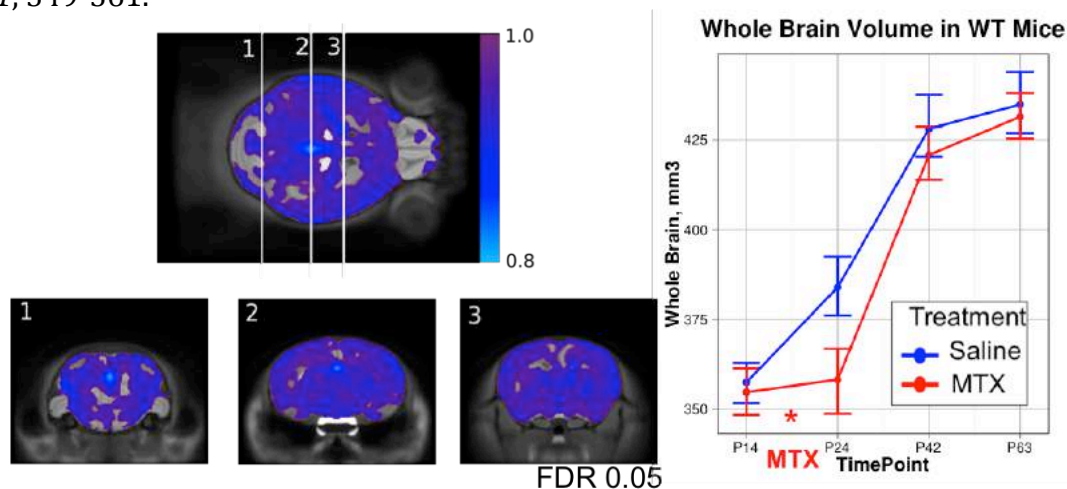


Figure 1. Voxel-wise volume differences in the mouse brain after treatment with MTX. Many brain regions are affected, resulting in a significant volume deficit after treatment, which is recovered at time point P63. The colours in the image represent the ratio of volume changes in MTX-treated mice to those in saline-treated mice.

Vertebral landmark visualization with portable ultrasound imaging in scoliosis monitoring

Christina Yan^{1*}, Reza Tabanfar^{1,2}, Michael Kempston², Daniel Borschneck², Tamas Ungi¹, Gabor Fichtinger¹

¹Laboratory for Percutaneous Surgery, School of Computing, Queen's University, Kingston, Canada

²Department of Surgery, Queen's University, Kingston, Ontario, Canada

Consortium: Other

Introduction. In scoliosis monitoring, X-ray imaging is traditionally used to visualize the spinal column of the patient to assess spinal curvature progression. Frequent screening is necessary to determine if spinal curvature has progressed such that bracing becomes necessary, as conservative treatments are preferred to avoid the need for corrective surgery later on. However, cumulative radiation exposure increases the risk of tumor development, and discourages frequent curve monitoring. Tracked ultrasound is a safe imaging alternative that relies on the precise identification of vertebral landmarks, but bones have reduced visibility in ultrasound imaging and high quality ultrasound machines are often expensive and stationary. In this work, we offer quantitative confirmation of equivalency between the Telemed MicrUs EXT-1H (Vilnius, Lithuania, EU), a portable USB ultrasound costing \$4,000, and the standard \$80,000 Sonix Touch (Analogic Corp., Peabody, MA, USA) in visualizing transverse processes for the measurement of transverse process angles (TxA), which can be used for spinal curvature measurement.

Methods. Two ultrasound machines were tested on three human subjects, using the Ascension 3D trakSTAR (NDI, Waterloo, ON, Canada) electromagnetic tracking system and 3D Slicer software. Spinal curves were measured in the same reference coordinate system for both ultrasound machines in 3D Slicer's Scoliosis module. Transverse process angles (TxA), were defined as lines connecting the left and right transverse process on the same vertebrae (1). Spinal curvature was then obtained from the angle between two such TxA-s, which were projected onto the coronal plane. Three experienced observers localized transverse processes as skeletal landmarks and obtained TxA measurements in images obtained from both ultrasound machines.

Results. 94% of transverse processes visualized in the Sonix Touch were also visible in the Telemed. The average difference per TxA measured with images obtained from the Telemed in comparison with the Sonix Touch was $3.0 \pm 2.1^\circ$. Inter-observer error was also calculated from the mean range of all observer's TxA measurement per vertebrae in all subjects, and was 4.5° in the Telemed and 4.3° in the Sonix Touch. Results indicate the Telemed is able to offer equivalent visualization of skeletal landmarks that can be used in TxA measurement, which may be used to obtain spinal curvature measurements.

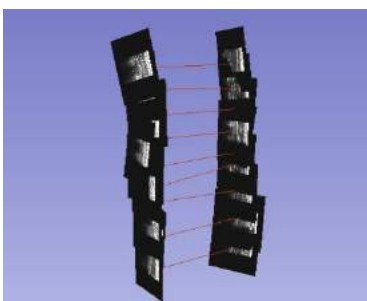


Fig. 1. Marked TxA-s of a full spinal column

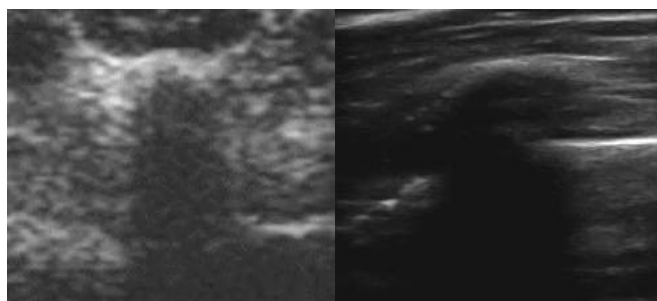


Fig. 2. Visualization of a single transverse process by the Telemed (left) and Sonix Touch (right)

Conclusion. Price and convenience suggest the Telemed to be a viable alternative for scoliosis monitoring. However, before implementing the Telemed in the clinical setting, a reduction in image noise is needed to further enhance landmark visibility. With improved image quality, the Telemed will be a suitable tool for safe and convenient scoliosis screening.

References. [1] Ungi *et al.* Ultrasound in medicine and biology 2(40), 447-454 (2014).

In-vivo Detection of Acute Intracellular Acidification in Glioblastoma Multiforme Following a Single Dose of Cariporide

Mohammed Albatany¹, Alex Li², Miranda Bellyou², Susan Meakin³, and Robert Bartha^{1,2}

¹Department of Medical Biophysics,

²Centre of Functional and Metabolic Mapping, ³Molecular Medicine Group, Roberts Research Institute, Western University, London, Ontario, Canada

Purpose: Glioblastoma Multiforme remains one of the most lethal cancers with a mean survival of 12-18 months. Clear identification of tumour boundaries is challenging due to the infiltrative nature of the cancer. In this work we explore the use of a physiological challenge to detect cancer cells. Specifically, the goal of this study is to determine whether chemical exchange saturation transfer (CEST) MRI measurement of tumour intracellular pH (pHi) is sensitive to tumour acidification after cariporide injection. Cariporide is a Na⁺/H⁺ pump inhibitor. We hypothesized decreased tumour pHi within 2 hours.

Methods: CEST is a novel MRI contrast mechanism that is dependent on pHi. Amine and amide concentration-independent detection (AACID)¹ is a recently developed CEST contrast that is sensitive to pHi. AACID is the ratio of the amine CEST effect at chemical shift 2.75 ppm and the amide effect at 3.5ppm. Using a 9.4T MRI scanner, full CEST spectra (3averages) were acquired in six mice approximately 14 days after implanting 10⁵ U87 human glioblastoma multiforme cells in the brain, before and after administration of cariporide (dose: 6 mg/kg)². Cariporide was dissolved in DMSO and diluted with saline then injected intraperitoneal (i.p.) over 2 min until the dose was achieved. The MR imaging protocol included standard anatomical imaging (T₁-, T₂-, diffusion-weighted imaging), and pre-injection B₀, B₁, and AACID-CEST images. AACID-CEST images were reacquired ~2 hours following cariporide injection. pH was estimated in all mice in manually defined regions of interest (ROIs) containing tumor and contralateral tissue. All animals were sacrificed post imaging.

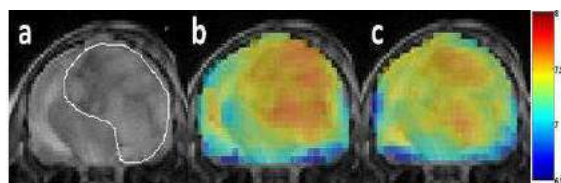


Figure1. Mouse brain with GBM tumor: a) T₂-weighted image b) pH map prior to cariporide injection c) pH map ~2 hours post cariporide (6mg/kg) i.p. injection.

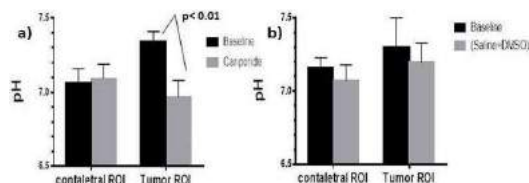


Figure2. Average pHi in tumor and contralateral ROIs: a) pre and post cariporide 6mg/kg intraperitoneal injection (N=6), b) pre and post saline+DMSO injection as control N=3.

Results: Figure 1a shows a T₂-weighted image of the mouse brain tumour. Figures 1b and 1c show pH maps prior to and after cariporide injection respectively. Figure 2a shows the changes in pHi for the six mice (N=6). In the tumour ROI the pHi significantly decreased after cariporide injection by 0.37±0.03 (p<0.05), but there was no change in pHi within the contralateral ROI. There was no significant change in pHi for three mice (N=3) injected with (saline+DMSO) only (control, Figure 2b).

Discussion: In this experiment we used cariporide to induce an acute metabolic change detectable by endogenous MRI CEST³ contrast. The observed decrease in pHi within the tumour may be due to the blockage of Na⁺/H⁺ exchange by cariporide in the cancer cells. Cariporide is approved in humans. The physiological change induced by cariporide could help localize brain cancer and monitor tumour response to chemotherapy. This unique approach to cancer detection does not require injection of an imaging contrast agent.

References: 1. McVicar, Nevin, et al. "Imaging chemical exchange saturation transfer (CEST) effects following tumor-selective acidification using lonidamine." *NMR in Biomedicine* (2015). 2. Harguindey, Salvador, et al. "Cariporide and other new and powerful NHE1 inhibitors as potentially selective anticancer drugs an integral molecular/biochemical/metabolic/clinical approach after one hundred years of cancer research." *Journal of translational medicine* 11.1 (2013): 282. 3. Sagiya, Koji, et al. "In vivo chemical exchange saturation transfer imaging allows early detection of a therapeutic response in glioblastoma." *Proceedings of the National Academy of Sciences* 111.12 (2014): 4542-4547. **Funding provided by Ontario Institute of Cancer Research (OICR).**

Dichloroacetate Induced Intracellular Acidification in Brain Tumor: In-Vivo Detection Using AACID-CEST MRI at 9.4Tesla

Mohammed Albatany¹, Alex Li², Miranda Bellyou², Susan Meakin³, and Robert Bartha^{1,2}

¹Department of Medical Biophysics, ²Centre of Functional and Metabolic Mapping, ³Molecular Medicine Group, Robarts Research Institute, Western University, London, Ontario, Canada

Purpose: Glioblastoma Multiforme remains one of the most lethal cancers with a mean survival of 12-18 months. Clear identification of tumour boundaries is challenging due to the infiltrative nature of the cancer. In this work we explore the use of a physiological challenge to detect cancer cells. Specifically, the goal of this study is to determine whether chemical exchange saturation transfer (CEST) MRI measurement of tumour intracellular pH (pH_i) is sensitive to tumour acidification after dichloroacetate (DCA) injection. DCA reduces expression of monocarboxylate transporters (MCT) and vacuolar H^+ -ATPases. We hypothesized lower tumour pH_i after 1 hour.

Methods: CEST is a novel MRI contrast mechanism that is dependent on pH_i . Amine and amide concentration-independent detection (AACID)¹ is a recently developed CEST contrast that is sensitive to pH_i . AACID is the ratio of the amine CEST effect at chemical shift 2.75 ppm and the amide effect at 3.5ppm. Using a 9.4T MRI scanner, full CEST spectra (3 averages) were acquired in six mice approximately 14 days after implanting 10^5 U87 human glioblastoma multiforme cells in the brain, before and after administration of DCA (dose: 200 mg/kg).² Dichloroacetate (DCA) was dissolved in pure saline and injected intravenously (i.v.) over 1 min until the dose was achieved. The MR imaging protocol included standard anatomical imaging (T_1 -, T_2 -, diffusion-weighted imaging), and pre-injection B_0 , B_1 , and AACID-CEST imaging. AACID-CEST imaging was repeated 50 minutes following DCA injection. pH_i was estimated in all mice in manually defined regions of interest (ROIs) containing tumor and contralateral tissue. All animals were sacrificed post imaging.

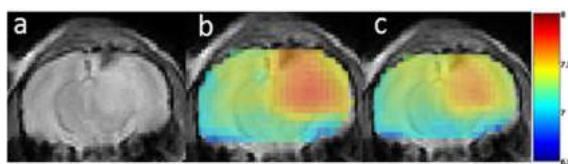


Figure1. Mouse brain with GBM tumor: a) T_2 -weighted image b) pH map prior to DCA injection c) pH map ~50 minutes post DCA (200mg/kg) intravenous injection.

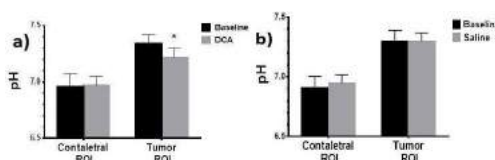


Figure2. Average pH_i in tumor and contralateral ROIs: a) pre and post DCA 200mg/kg intravenous injection N=6. b) pre and post intravenous saline (control) injection as control N=3.

Results: Figure 1a shows a T_2 -weighted image of the mouse brain tumour. Figures 1b and 1c show pH maps from before and after DCA injection respectively. Figure 2a shows the changes in pH_i for the six mice (N=6). In the tumour ROI the pH_i significantly decreased after DCA injection by 0.12 ± 0.03 ($p < 0.05$), but there was no change in pH_i within the contralateral ROI. There was no change in pH_i for three mice (N=3) injected with saline only (control, Figure 2b).

Discussion: In this study we used DCA to induce an acute metabolic change detectable by endogenous MRI CEST³ contrast. The observed decrease in pH_i within the tumour may be due to the effect of DCA on decreasing the expression of V-ATPases and MCTs in cancer but not in normal tissue. DCA also inhibits pyruvate dehydrogenase kinase and increases oxidative phosphorylation. The physiological change induced by DCA could help localize brain cancer and monitor tumour response to chemotherapy. This unique approach to cancer detection does not require injection of an imaging contrast agent.

References: 1. McVicar, Nevin, et al. "Imaging chemical exchange saturation transfer (CEST) effects following tumor-selective acidification using lonidamine." *NMR in Biomedicine* (2015). 2. Park, Jae Mo, et al. "Metabolic response of glioma to dichloroacetate measured in vivo by hyperpolarized ^{13}C magnetic resonance spectroscopic imaging." *Neuro-oncology* (2013): nos319. 3. Sagiya, Koji, et al. "In vivo chemical exchange saturation transfer imaging allows early detection of a therapeutic response in glioblastoma." *Proceedings of the National Academy of Sciences* 111.12 (2014): 4542-4547. **Funding provided by Ontario Institute of Cancer Research (OICR).**

Prediction of Intracerebral Hemorrhage Secondary to Acute Ischemic Stroke: Multi-parameter CT Perfusion is Optimal

C. Batchelor^{1,2}, C.D. d'Este^{2,3,4}, P. Pordeli^{1,5}, C. McDougall^{2,6}, M. Boesen⁷, M. Najm⁶, T.Y. Lee^{4,9}, A.M. Demchuk^{1,2,3}, M. Goyal^{1,2,3,4}, B.K. Menon^{1,2,3,4,8}.

¹Hotchkiss Brain Institute- University of Calgary- Alberta, Clinical Neurosciences, Calgary, Canada., ²Seaman Family MR Centre- Alberta, Neuroscience, Calgary, Canada., ³Calgary Stroke Program- Department of Clinical Neurosciences- University of Calgary- AB, Clinical Neurosciences, Calgary, Canada., ⁴Department of Radiology- University of Calgary- Alberta, Clinical Neurosciences, Calgary, Canada., ⁵University of Calgary, Department of Community Health Sciences- University of Calgary, Calgary, Canada. ⁶University of Calgary, Clinical Neurosciences, Calgary, Canada., ⁷QuiKFloHealth Inc.- Alberta, Clinical Neurosciences, Calgary, Canada., ⁸Department of Community Health Sciences- University of Calgary- Alberta, Health Sciences, Calgary, Canada., ⁹Lawson Health Research Institute and Robarts Research Institute- Ontario, Clinical Neurosciences, London, Canada.

Background: Intra-cerebral hemorrhage (ICH) after acute ischemic stroke (AIS) therapy is a major complication. We sought to investigate for any association between various CT perfusion (CTP) parameters and post stroke ICH.

Methods: 291 AIS patients (113 excluded for no tPA) underwent CTP (150s) imaging within 12hrs of onset. CTP software (GE Healthcare) was used to calculate CBF, CBV, Tmax, and permeability surface-area product (PS) functional maps. Ipsilateral hemisphere volumes (mL), normalized to z-axis coverage, were obtained for: 1) regions of very low CBV (lower 10th, 5th, and 2.5th percentiles) of the contralateral hemisphere (vICBV_{10th, 5th, 2.5th}), 2) CBF $\leq 7 \text{ml}\cdot\text{min}^{-1}\cdot(100\text{g})^{-1}$ (vCBF _{≤ 7}), and 3) Tmax $\geq 16\text{s}$ (vTmax_{16s}). Mean values were obtained for: 1) PS within a Tmax $\geq 8\text{s}$ (PS_{Tmax}), 2) PS within the total ipsilateral hemisphere (PS_{Ipsi}), and 3) Tmax within vTmax_{16s}. The interaction parameter vICBV_{10th} x PS_{Tmax} was also calculated. ICH was determined using ECASS II criteria and assessed on 24-48 hr MRI/CT. Random forest analysis (RFA) was used to rank each parameter in order of importance for hemorrhage prediction.

Results: Figure 1 shows results for RFA and ROC analysis in 104 evaluable out of 178 AIS patients (43 hemorrhage, 61 no hemorrhage). PS within vICBV and PS within Tmax $\geq 16\text{s}$ parameters are most important for hemorrhage prediction in WM and GM respectively.

Conclusion: Combining multiple CTP parameters is necessary for robust hemorrhage prediction.

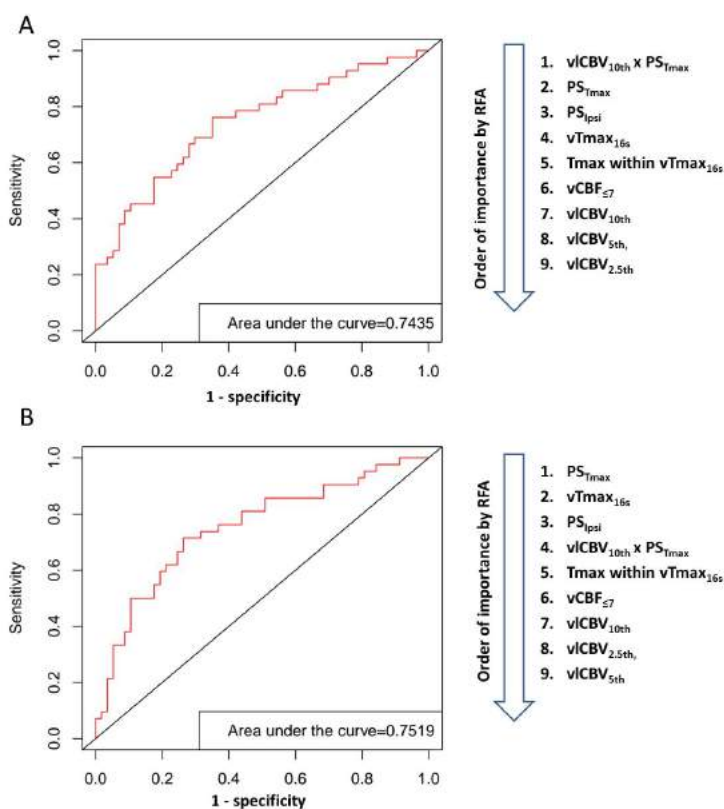


Figure 1. White (A) and Gray (B) matter RFA and ROC results.

In Vivo MRI Detection of Cucurbit[6]uril Xenon Cage HyperCEST Effect in Rat Abdomen

Francis Hane^{1,2}, Tao Li¹, Peter Smylie¹, Jennifer Plata^{1,2}, Raiili Pellizzari¹, Brenton Deboef³, Boguslaw Tomanek², Mitchell Albert^{1,2}

(1) Lakehead University Department of Chemistry, Thunder Bay, Canada.

(2) Thunder Bay Regional Research Institute, Thunder Bay, Canada.

(3) University of Rhode Island, Kingston, RI, U.S.A

Introduction: Hyperpolarized Chemical Exchange Saturation Transfer (HyperCEST) (1) is a technique combining Hyperpolarized (HP) ¹²⁹Xe MRI (2) and Chemical Exchange Saturation Transfer (CEST) (3), each capable of enhancing the signal from biosensors by several orders. This technology potentially has the sensitivity to provide molecular imaging ability to conventional MRI. Cucurbit[6]uril has been reported to be an ultra-sensitive ¹²⁹Xe NMR contrast agent (4). In this work we present *in vivo* HyperCEST MR images of the cucurbit[6]uril (CB6) HyperCEST agent in a rat.

Methods: A 400g male Sprague-Dawley rat was anesthetized and prepared for intraperitoneal (IP) injection. Xenon-129 gas (83.6% isotopically enriched) was hyperpolarized to 30% polarization using a Xemed XeBox polarizer (Durham, NH). Before each injection, 5 mL HP ¹²⁹Xe was introduced into a syringe containing 5mL 5.0mM CB6 solution in PBS solvent. The syringe was shaken for 12 seconds in order for xenon gas to sufficiently dissolve, and excess xenon gas was then removed from the syringe. Then 3mL CB6 solution was injected intraperitoneally into the rat. All ¹²⁹Xe and ¹H images were acquired on a Philips Achieva 3.0T clinical scanner, using a custom-made, four-end ring birdcage RF coil dual-tuned to the Larmor frequency of ¹²⁹Xe (35.33 MHz) and ¹H (127.74 MHz) at 3 T. The saturation pulse sequence was designed to comprise sixteen 3-lobe Sinc pulses of 6 ms pulse length and 3 ms pulse interval. This saturation pulse was applied at the CB6-Xe resonance frequency (+124.3 ppm) to create a HyperCEST effect, and at the opposite position with respect to dissolve phase peak (+260 ppm) as a control. 2D Fast Field Echo (FFE) MR images were acquired with control pulses and saturation pulses applied, respectively, using the parameters of 150 mm x 150 mm FOV, 64x64 voxels, 300 mm slice thickness, TR=197 ms, TE=1.57 ms, and a bandwidth of 200Hz/pixel. We also acquired multi-slice T2-weighted ¹H spin echo localization images with a slice thickness of 2mm for anatomical information.

Results: After both HyperCEST image and control images were acquired, the HyperCEST image was subtracted from the control image and then divided by the control image on a pixel-by-pixel basis to create an HyperCEST map. Figure 1 shows the HyperCEST saturation map overlaid on the centre slice ¹H image. Figure 1 clearly shows that the HyperCEST signal is localized to the intraperitoneal space.

Conclusion: Presented data are among the first reports of *in vivo* applications of a HP ¹²⁹Xe HyperCEST biosensor. The result is a clear demonstration of the ultra-sensitivity of the HyperCEST effect from low concentration CB6 contrast agent in a live animal, and its potential to provide pathological molecular images using MRI.

References: [1] Schroeder L, et al. Science. 2006; 314:446-440 [2] Albert M, et al. Nature. 1994; 370:199-201. [3] Ward K, et al. J Magn Reson 2000; 143: 79–87[4] Wang Y, et al. Chem. Comm. 2015; 51:8982–8985.

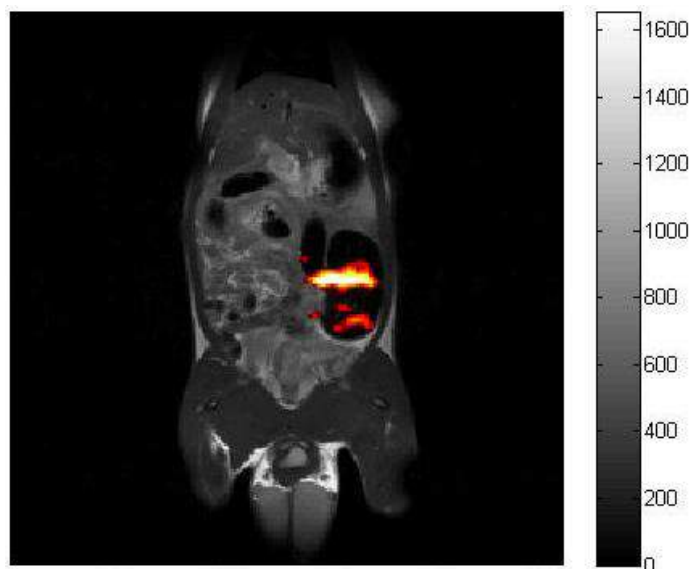


Figure 1: A ¹H MRI of the abdomen of a Sprague-Dawley rat overlaid with a HyperCEST saturation map showing a HyperCEST signal from 5 mL of 5 mM CB6 solution injected into the rat intraperitoneally.

Diminished image resolution lead to reduced sensitivity in infarct mass determined by T1 mapping for stratifying patient risk for ventricular arrhythmias

Eranga Ukwatta^{1,2}, Venkat Ramanan¹, Tasnim Vira¹, Graham Wright^{1,2}

¹Sunnybrook Research Institute, Sunnybrook Health Sciences Centre, Toronto, ON, Canada

²Department of Medical Biophysics, University of Toronto, Toronto, ON, Canada

Background: Indices based on myocardial infarct (MI) have been shown to be sensitive in predicting adverse arrhythmic events. In comparison to conventional late enhancement MRI, T1 mapping techniques, such as multi-contrast late-enhancement (MCLE), yield more reproducible estimate of MI. Spatial image resolution (IM-res) is one of the limiting factors in T1 mapping images, which is often limited by the imaging hardware and patient's inability to hold breath for longer. The aim of this study was to investigate the effect of diminished IM-res to the sensitivity of MI mass in predicting appropriate ICD therapy.

Methods: Twenty five patients (age 61 ± 11 yrs, 84% men, average LVEF $26.7 \pm 10.6\%$) with chronic MI underwent MCLE post gadolinium injection prior to ICD implantation and were followed up for 6-46 months. The acquired in-plane IM-res was 1.37×1.37 mm². The T1* and steady-state maps were generated from the MCLE images using a curve fitting approach, and the MI dense core (DC) and border zone (BZ) were segmented using a clustering approach. The MCLE images were then downsampled to a coarser IM-res of 2.74×2.74 mm² and recomputed the MI masses.

Results: Thirteen patients had at least one ICD therapy for ventricular arrhythmias at the follow-up. The MI masses determined by downsampled MCLE were significantly higher than those of regular MCLE. Comparing regular and downsample MCLE, the MI masses determined by the latter were less distinguishable between the patients with and without ICD therapy (Table 1).

Conclusions: Similar to recent observations in ex-vivo animal studies, this study demonstrated that diminished IM-res of clinical images lead to overestimation of the MI mass due to partial volume averaging. Further, this study also showed that the diminished IM-res lead to reduced sensitivity in MI mass in predicting ventricular arrhythmic events.

| | Entire sample (n = 25) | | | With ICD therapy (n = 13) | | Without ICD therapy (n = 12) | | P value | |
|---------------------------------|---------------------------|---------------------|------------------|------------------------------|---------------------|---------------------------------|---------------------|-----------------|---------------------|
| | Regular MCLE | Downsampled MCLE | P value | Regular MCLE | Downsampled MCLE | Regular MCLE | Downsampled MCLE | Regular MCLE | Downsampled MCLE |
| Core MI/LVM (%) | 26.4 | 32.78 | <0.001 | 29.77 | 36.39 | 22.56 | 29.17 | 0.098 | 0.158 |
| BZ MI/LVM (%) | 15.15 | 20.41 | 0.0015 | 17.36 | 22.77 | 12.95 | 17.73 | 0.055 | 0.26 |
| Total MI/LVM (%) | 41.55 | 53.19 | 0.045 | 47.13 | 59.16 | 35.51 | 46.9 | 0.072 | 0.252 |

Measurement of tumor hypoxia in patients with advanced pancreatic cancer based on ^{18}F -fluoroazomyin arabinoside (^{18}F -FAZA) uptake

I Yeung^{1,5}, C Metran-Nascente², D Vines¹, U Metser^{3,5}, N Dhani², D Green^{1,5}, M Milosevic⁴,
D Jaffray^{1,5}, D Hedley²

¹ Radiation Medicine Program, Princess Margaret Cancer Centre, UHN, Toronto, ON

² Department of Medical Oncology, Princess Margaret Cancer Centre, UHN, Toronto, ON

³ Joint Department of Medical Imaging, UHN, Toronto, ON

⁴ Department of Radiation Oncology, Princess Margaret Cancer Centre, UHN, Toronto, ON

⁵ QIPCM Program, Techna Institute, UHN, Toronto, ON

Introduction: Pancreatic cancers are thought to be unusually hypoxic, which might sensitize them to drugs that are activated under hypoxic conditions. In order to develop this idea in the clinic, a minimally-invasive technique for measuring the oxygenation status of pancreatic cancers is needed.

Methods: We tested the potential for minimally-invasive imaging of hypoxia in pancreatic cancer patients, using the 2-nitroimidazole positron-emission tomography (PET) tracer ^{18}F -fluoroazomyin arabinoside (FAZA). Dynamic as well as static scans were made in 20 patients with either locally advanced or metastatic disease. Perfusion was evaluated with a 2 compartment model using the dynamic data of early time. The hypoxic fraction (HF) was determined in the 2h static scans as the percentage of voxels with SUV values more than three standard deviations from the mean values obtained for skeletal muscle (Mortensen et al., Radiother Oncol 2012;105:14-20).

Results: Hypoxia was detected in 15/20 evaluable patients. Figure 1 shows an example with patients with high and low uptake. The range of HF was found to be from <5% to >50% (Figure 2) Compartmental analysis of the dynamic scans acquired after tracer injection allowed us to approximate the tumor perfusion as ml/min/g of tissue; a value that is independent of the extent of hypoxia derived from tracer uptake in the 2hr static scan. There was no significant correlation between tumor perfusion and hypoxia; nor did we see an association between tumor volume and hypoxia.

Conclusions: Although pancreatic cancers can be highly hypoxic, a substantial proportion appears to be well-oxygenated. Therefore we suggest that a minimally-invasive technique such as the one described in the present paper is used for patient stratification in future clinical trials of hypoxia-targeting agents treating pancreatic cancer.

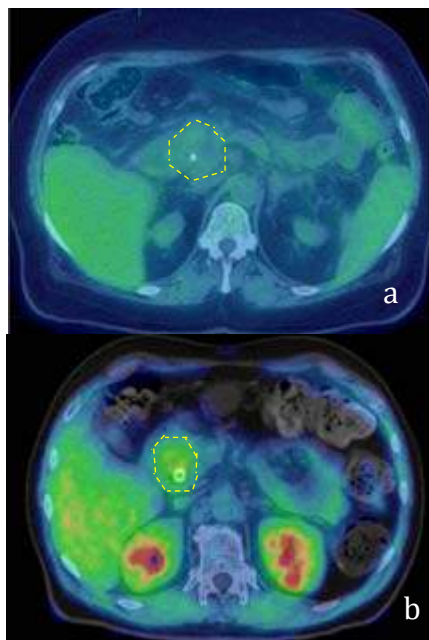


Figure 1: (a) and (b) are examples of PET images of patients with low and high ^{18}F -FAZA uptake respectively.

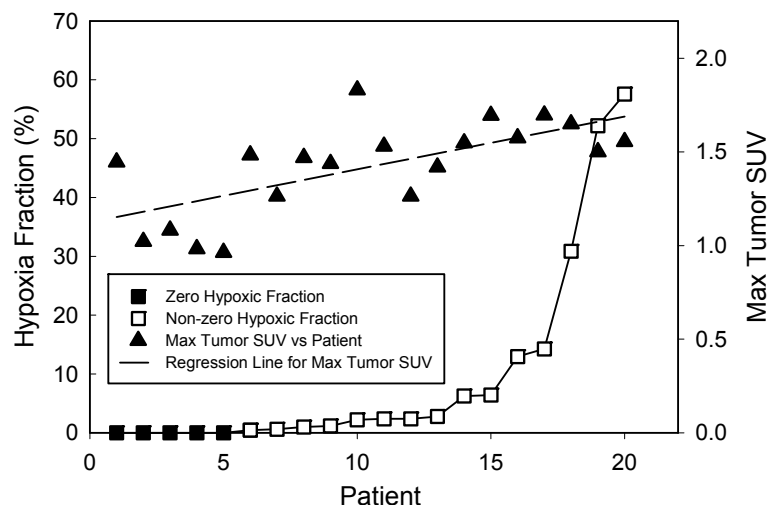


Figure 2: Results for tumor SUV_{max} and HF obtained from 20 patients with static scans, arranged in rank order of HF.

Real-time self-calibration of a handheld augmented reality overlay system

Zachary Baum*, Andras Lasso, Tamas Ungi, Gabor Fichtinger

Laboratory for Percutaneous Surgery, Queen's University, Kingston, Canada

INTRODUCTION: Augmented reality systems have been designed for image-guided needle interventions but they have not become widely translated into clinical practice. This lack of use stems from their limited portability, low display refresh rates, and tedious calibration procedures. Our proposed mobile image overlay system allows self-calibration without the use of any temporary tracked markers to achieve a consistent and precise calibration workflow. Using an adaptable modular design also allows for different tablet computers to be used interchangeably.

METHODS: A modular, handheld augmented reality viewbox was constructed from a tablet computer and a semi-transparent mirror. A consistent and precise self-calibration method, without the use of any temporary markers, was designed in order to achieve an accurate calibration of the system. Markers attached to the viewbox and patient are simultaneously tracked using an optical pose tracker to report the position of the patient with respect to a displayed image plane that is visualized in real-time (Figure 1). The software was built using the open-source 3D Slicer^[1] application platform's SlicerIGT extension and the PLUS toolkit^[2].

RESULTS: The accuracy of the image overlay with image-guided needle interventions yielded a mean absolute position error of 0.99 mm (95th percentile 1.93 mm) in-plane of the overlay and a mean absolute position error of 0.61 mm (95th percentile 1.19 mm) out-of-plane. The differences between the in-plane and out-of-plane distances are attributed to the tracking error resulting from the optical pose tracking system.

CONCLUSION: A self-calibration method was developed and evaluated for a tracked augmented reality display. The image overlay system could be used to guide a tool with accuracy that is suitable for facet joint injections or other musculoskeletal needle placements.

REFERENCES: [1] Fedorov *et al.*, "3D Slicer as an image computing platform for the quantitative imaging network," *Magnetic Resonance Imaging*. 30(9), 1323-1341 (2012). [2] Lasso *et al.*, "PLUS: open-source toolkit for ultrasound-guided intervention systems," *Biomedical engineering, IEEE Transactions on*, vol. 61, no. 10, pp. 2527-37, 2014.

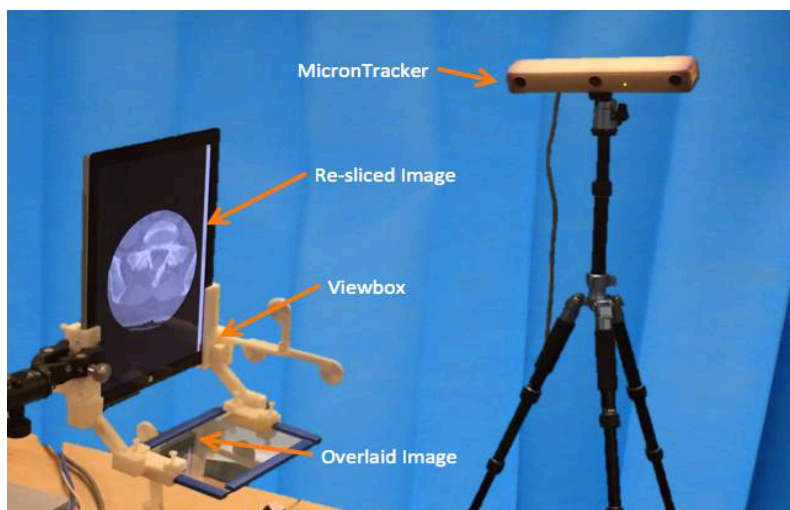


Figure 1: Setup of the system and MicronTracker optical tracking device.

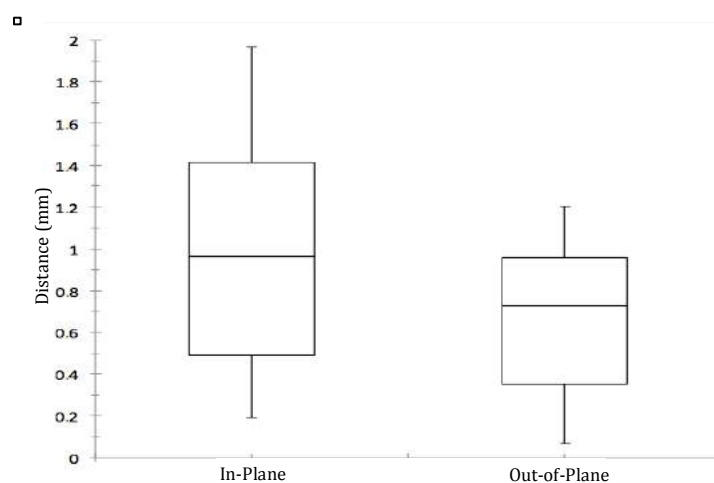


Figure 2: Box and Whisker Plot of in-plane and out-of-plane distances.

Can intratreatment PET CT based adaptive radiotherapy reduce treatment margins in Head and Neck Cancers?

Georges Farha*^{1,2}, Lee Chin³, Amanpreet Dhillon³, Stephanie Lim-Reinders³, Jidney Cifuentes Gaitan³, Tatiana Conrad², Drew Brotherston¹, Curtis Caldwell⁴, Justin Lee^{1,2}, Irene Karam^{1,2}, Ian Poon^{1,2}

¹Department of Radiation Oncology, Sunnybrook Health Sciences Center, ²Department of Radiation Oncology, University of Toronto, ³Department of Medical Physics, Sunnybrook Health Sciences Center, ⁴Department of Medical Imaging, Sunnybrook Health Sciences Center

Introduction. Modern radiation therapy (RT) techniques offer precise delivery to the defined targets in head and neck cancer (HNC) while respecting surrounding critical organ tolerances. This is due in part to the enhanced ability to define the gross tumor volume (GTV) with supplemental imaging such as MRI and PET scans. As a standard, a high dose clinical target volume (CTV) of 5 mm is added to the GTV to further ensure complete coverage of gross disease. However, HN tumors often shrink during RT, which suggests that the high dose CTV margin (expanded in normal surrounding tissue) during treatment may be greater than the original 5 mm, thus leading to overdosage of normal tissues. This study intends to quantify the potential gain of an adaptive technique that maintains the CTV to a changing gross tumour volumes in a series of HNC patients treated with chemoradiotherapy. **Methods.** A prospective study in 2009 enrolled advanced HNC patients undergoing curative IMRT (70 Gy in 33 fractions, with or without chemotherapy) to receive a dynamic pre-treatment fluorodeoxyglucose (FDG) PET-CT simulator scan (with mask), which was also repeated intratreatment (IT) between the 10th and 15th fraction. 53 patients were evaluated. Two radiation oncologists separately contoured GTVs in the pre- and intra-treatment scans to account for inter-observer variability. Rigid fusion of the planning CT to pre- and intra- treatment PET-CT scans was performed. Margin expansions ranging from 1-25 mm were performed on the pre-treatment GTV to volumetrically match the original clinical target volume (CTV) (as defined by the treating radiation oncologist), based on optimal Dice Similarity Indices (DSI). An identical process took place with the IT PET CT scan, where the intra-treatment GTV margins were expanded to the original treatment CTV.

Results. 53 patients were evaluated with a total of 152 targets (50 primaries and 102 LNs). Volume matching given by DSI showed that the pre-treatment GTV needed an average 7.22 ± 4.75 mm expansion to optimally match the clinical CTV while the IT GTV required a margin of 8.27 ± 4.18 mm. On average, the radial size of the primary CTV decreased by 1.05 ± 3.59 mm between pre- and IT scans but 17 patients (26.4%) had a shrinkage at 2 weeks over 5 mm and 6 patients (11.3%) had tumor growth of more than 5 mm. 19 patients had a paradoxical response between the primary and the LNs; 14 patients had smaller primary with larger LNs and 5 patients had larger primary with smaller LNs. In total, primaries and LNs had similar outcome with a mean of 1.14 ± 3.99 mm and 0.67 ± 3.63 mm respectively ($p=0.54$).

Conclusions. Our results show that HNC tumor shrinkage during RT is highly variable. A subset of patients is highly responsive to treatment where an adaptive approach to reduce treatment margins (CTV) may reduce normal tissue toxicities. Further analysis to define these groups, particularly association with potential factors (HPV, stage) is ongoing.

4D Monte Carlo simulation for verification of dose delivered to a moving anatomy

Sara Gholampourkashi^{1,2}, Miro Vujicic², Jason Belec², Joanna E. Cygler^{1,2}, Emily Heath¹

¹Department of Physics, Carleton University, Ottawa, Canada

²Department of Medical Physics, The Ottawa Hospital Cancer Centre, Ottawa, Canada

Introduction: The impact of respiratory motion on the delivered dose is of high concerns in radiotherapy. Respiratory motion can cause a deviation between the dose received by the target volume and the prescribed dose and this augments the importance of accurate dose calculations in presence of such motions. The long-term goal of this work is to develop a Monte Carlo-based dose reconstruction tool to estimate the dose delivered to a patient, accounting for their respiratory motion. The goal of the current work is to validate a 4DMC simulation method to calculate the dose delivered by an Elekta Agility linear accelerator to a moving phantom.

Methods: A Quasar respiratory motion programmable phantom (Modus Medical) with a lung insert containing a 3 cm diameter tumour was used for dose measurements. Measurements were performed on an Elekta Agility linac with the phantom in stationary and moving (sinusoidal motion, 1.8 cm respiratory amplitude) states. Dose to the centre of tumor was measured using calibrated EBT3 film and the RADPOS 4D dosimetry system¹. RADPOS position tracker recorded the phantom motion with time steps of 100 ms. Static and 4DCT scans of the Quasar phantom were acquired using a helical CT scanner (Brilliance CT Big Bore). A single 6 MV 4x4 cm² square field and a VMAT field, both covering the tumour were planned on the static CT scans using the Elekta XiO V.4.7 and Monaco V.5.10.02 Treatment Planning Systems (TPS) respectively. A previously validated BEAMnrc model of our Elekta Agility linac was used for all simulations². The DOSXYZnrc and defDOSXYZnrc³ user codes were used respectively for static and moving anatomy dose simulations with 500,000,000 number of histories to achieve a statistical uncertainty of 0.5%. The defDOSXYZnrc code was modified to sample a new geometry for each incident particle, thereby simulating the continuous phantom motion. A dose grid resolution of 0.125x0.125x0.1 cm³ was used for all simulations. The treatment plan was exported from TPS as DICOM format and a Python script was used to extract the data and generate input files for MC simulations. For 4D simulations, deformation vectors that exactly modelled the rigid translation of the lung insert were generated as input to the defDOSXYZnrc code as well as the phantom motion trace measured with RADPOS. Only stationary phantom was used for the VMAT plan and MC simulations using the linac log files recorded during measurements were performed too. Log file data was extracted using Python scripts to generate MC input files.

Results: Table 1 shows the calculated and measured tumor doses and their uncertainties for the 4x4 cm² square field and figure 1 shows corresponding dose profiles.

| Phantom | Dose (cGy) | | | | %Ratio | | | | | |
|------------|------------|-------------|-------------|-------------|--------|----------|------------|---------|-----------|-------------|
| | XiO | MC | Measured | | MC/XiO | Film/XiO | RADPOS/XiO | MC/Film | MC/RADPOS | Film/RADPOS |
| | | | Film | RADPOS | | | | | | |
| Stationary | 80.5 | 79.9 ± 0.5% | 79.2 ± 2.3% | 79.0 ± 1.4% | -0.75% | -1.61% | -1.89% | 0.88% | 1.13% | 0.25% |
| Moving | - | 76.3 ± 0.5% | 76.0 ± 2.3% | 77.3 ± 1.4% | - | - | - | 0.39% | -1.31% | -1.71% |

Table 1. Calculated and measured tumor doses for the 4x4 cm² square field.

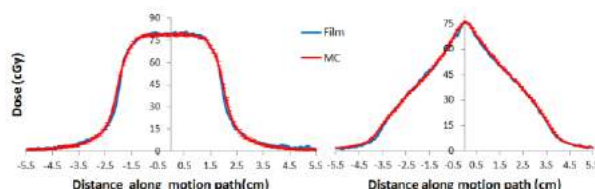


Fig1. Simulated and measured (Film) dose profiles for static (left) and moving (right) states.

Table 2 and figure 2 show similar information for the VMAT field.

| Phantom | Dose (cGy) | | | | %Ratio | | | | | | | | | |
|------------|-------------|-------------|-------------|-------------|-------------|-----------------|-------------------|-------------|---------------|---------------|-----------------|-----------------|-------------------|-------------|
| | Monaco | MC-DICOM | MC-Logfile | Measured | | MC-DICOM/Monaco | MC-Logfile/Monaco | Film/Monaco | RADPOS/Monaco | MC-DICOM/Film | MC-Logfile/Film | MC-DICOM/RADPOS | MC-Logfile/RADPOS | Film/RADPOS |
| | | | | Film | RADPOS | | | | | | | | | |
| Stationary | 61.9 ± 1.0% | 61.0 ± 0.5% | 61.9 ± 0.5% | 60.9 ± 2.3% | 60.3 ± 1.4% | -0.75% | 0.00% | -1.61% | -2.56% | 0.16% | 1.64% | 1.16% | 2.61% | 0.99% |

Table 2. Calculated and measured tumor doses for the VMAT field.

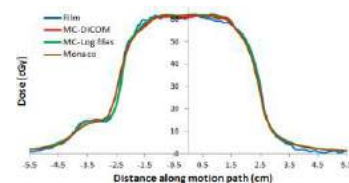


Fig2. Simulated, measured (Film) and Monaco dose profiles.

Conclusion: The level of agreement between MC Simulation results and measurements is within 2%. This makes our 4D Monte Carlo simulations using the defDOSXYZnrc code an accurate and reliable method to calculate dose delivered to a moving anatomy. Future work will focus on validation of VMAT delivery on a moving phantom and establishing the accuracy of our method in a deforming anatomy.

Reference: [1] A. Cherpak *et al.*, Med. Phys. 36 (5), 2009. [2] M. Vujicic *et al.*, Radiotherapy & Oncology, Vol. 115, 2015, p.792 (abstract). [3] Heath *et al.*, Med. Phys. 33 (2), 2006, pp. 434-445.

Evaluating Electron Density Measurements and Dosimetry Surrounding Metallic Implants using Co-60 Computed Tomography

Christopher Jechel¹, Greg Salomons^{1,2} and L. John Schreiner^{1,2}

Ontario Consortium for Adaptive Interventions in Radiation Oncology

¹Queen's University Department of Physics & ²Cancer Centre of South-Eastern Ontario, Kingston, ON

Abstract:

Introduction: The streaking artifacts found in kilovoltage CT (kVCT) images of metallic objects are a common issue in radiation therapy planning. Accurate treatment planning requires an estimate of the electron density (ED) distribution within the patient's body which is determined from CT images. Metal artifacts degrade CT image quality and can therefore affect the accuracy of dose calculations. In this work we investigate the importance of these effects in treatment planning.

Methods: Our group has developed a benchtop cone-beam CT system to investigate the potential for patient alignment on a cobalt-60 teletherapy unit. The high energy (~1.25 MeV) and nearly monoenergetic gamma ray spectrum of cobalt-60 reduces metal-induced artifacts, suggesting cobalt-60 CT (CoCT) may be useful for evaluating ED information derived from kVCT images acquired in the presence of metal objects. Homogeneous phantoms housing metal rods of varied ED and atomic number were imaged using CoCT and conventional kVCT including images reconstructed using a commercial metal artifact reduction (MAR) algorithm known as O-MAR (Philips Healthcare Systems, Cleveland, OH). The presence of mild metal artifacts in CoCT images also led to the implementation of a MAR tool for the CoCT system. Dose profiles in a water phantom containing metal rods were measured in a large field (6 MV, 25x25 cm²) with an ion chamber and compared to treatment planning system calculations based on kVCT and CoCT images as well as artificial images representing the exact phantom geometry and composition.

Results: Comparing the known phantom ED distribution to CT images converted from HU to ED allowed the severity of image artifacts to be quantified (Figure 1 a-d). The O-MAR algorithm was found to greatly diminish artifacts surrounding metal implants but significant ED discrepancies remained within the metals themselves due to the truncated range of HU values available in 12-bit kVCT images. Reduced artifacts in regions surrounding metal objects and the lack of a limit on CT number range enable a more faithful representation of electron density information with CoCT. The CoCT MAR system was found to improve the qualitative appearance of metal artifacts as well as the accuracy of ED estimates adjacent to metal cylinders. Point dose measurements 5 cm downstream of a stainless steel cylinder were compared to dose calculations based on kVCT images with and without MAR corrections yielding overestimates of dose of 27% and 26% respectively. The same comparison using calculations based on CoCT images with and without MAR corrections produced dose errors of only 4.4% and 5.8%. The abbreviated CT number range limits the range of ED values that can be faithfully represented, causing the density of the steel to be drastically underestimated, an issue not found in the CoCT images.

Conclusions: CoCT imaging has enabled the evaluation of metal artifact perturbations in planning kVCT images while the CoCT MAR tool notably reduced the metal artifacts found in CoCT images. The application of a commercial MAR tool improved image quality, however, the accuracy of dose calculations did not appreciably improve as dose discrepancies were found to be primarily caused by CT number truncation.

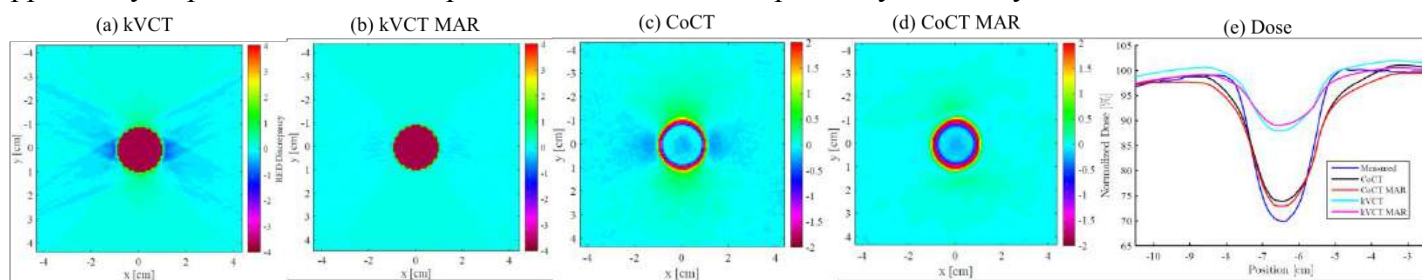


Figure 1: Discrepancies between measured and true electron density (normalized to the ED of water) surrounding a stainless steel cylinder for kilovoltage and cobalt-60 CT images reconstructed with standard (a,c) and metal artifact reduction (b,d) algorithms. Dose profiles calculated using the image data in (a-d) are compared to measured dose in (e) approximately 5 cm downstream of the steel cylinder in a large 6 MV field.

Acknowledgements: Support for this work from OCAIRO is acknowledged and appreciated.

Is it possible to use simultaneous MRI (scar) and PET (sympathetic innervation) to select patients for Radio-Frequency Ablation of Atrial Fibrillation?

Ali K Saeid¹, Allan Skanes¹, Jonathan Thiessen², Justin Hicks², Jane Sykes², John Butler², Frank S. Prato²

¹London Health Sciences Centre, ²Lawson Health Research Institute

Introduction: Atrial fibrillation (AF) is the most common sustained arrhythmia and is associated with explicit structural and electrical remodeling. It is initiated mainly by myo-electrical triggers from cardiothoracic veins and perpetuates through scar formation in atrial myocardium. In patients with longstanding AF, recurrence rate after radio-frequency ablation (RFA) remains unacceptably high [(50%-60% in persistent AF and less than 40% in longstanding AF (1)]. As scarred atrium and abnormal sympathetic innervations (SI) are major factors of this failure we are investigating the use of hybrid PET/MRI as a predictor of outcome of RFA. Evidence from both canine models and patients indicates that AF recurrence after RFA is dependent on amount of fibrosis and SI in left atrium. According to our experience and some published data, more than 8% of fibrosis (determined from histology) is predictive of AF recurrence after RFA. Comparison of percent fibrosis by histology and the distribution volume of the MRI contrast agent Gd-DTPA suggest that MRI could be used to detect this extent of atrial fibrosis (3). Recent MRI studies done in patients partially support this claim. Canine studies using ¹¹C HED to investigate the predictive value of the pattern of sympathetic innervation remain equivocal. We aim to investigate the potential of hybrid PET/MRI using a well-characterized canine model of AF (2).

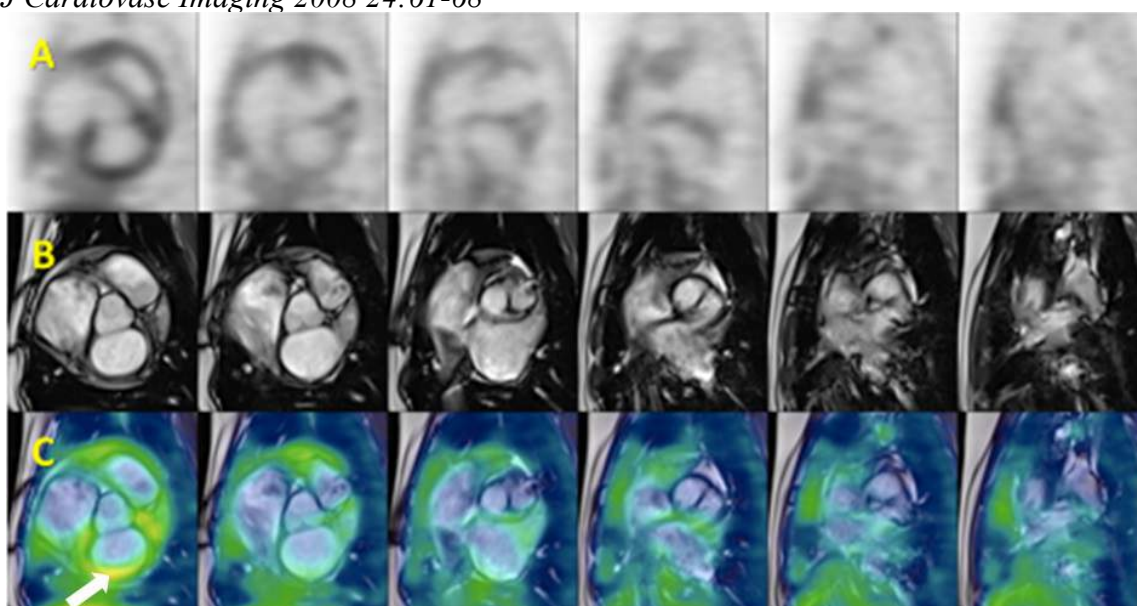
Approach: With recent funding from CANet we will induce AF in 14 canines. We will PET/MRI image the dogs as the condition develops and compare this to voltage measurement of the myocardium. On the last imaging session we will euthanize the dog while in the PET/MRI scanner to evaluate the quality of motion correction of the in-vivo images. We will then excise the heart and perform high resolution PET and MRI imaging followed by tissue sectioning for immuno-histology. Following the outcome of this canine study patients will be investigated using MRI only in Calgary (Dr White), PET and MRI in Ottawa (Drs Dekemp, Thornhill, Nery and Beanlands) and in London (Drs Skanes and Drangova).

Results: In a pilot PET/MRI study in one normal dog performed using a hybrid PET/MRI scanner (see figure) we have shown that imaging of the sympathetic innervation of the LA may be possible.

Conclusions: We anticipate that quantitation of atrial fibrosis and sympathetic innervation in patients with longstanding AF can be achieved using a hybrid combination of LGE-CMR and ¹¹C HED-PET. Our goal is to generate a quantitative syntheses of the extensiveness of LA damage that can be used to predict the outcome for the individual patient of this high risk, time-consuming and expensive AF ablation procedures.

Acknowledgements: Pilot study funded in part by Thames Valley Veterinarian Services; Full canine study funded in part by CANet, Bayer, Medtronic, and Lawson Health Research Institute.

References: 1. Calkins H. *Circulation* 2012;125:1439-45; 2.Saeid AK Presented at AHA 2014.; 3. Kehr E, et al. *Int J Cardiovasc Imaging* 2008 24:61-68



¹¹C-HED PET images of the atria registered to simultaneously acquired MRI images in a control dog demonstrating proof-of-principle. (A) Short-axis PET images spanning the atria (left = closest to ventricles, right = furthest) were reconstructed with cardiac gating (B) True fast imaging with steady state precession (TrueFISP) short-axis MR cine images. (C) Fused PET/MR images with matching gate times show ¹¹C-HED uptake in left atrial wall (LA).

Patient-specific calibration of Cone-Beam Computed Tomographic Images for radiotherapy plan adaptation

Michael MacFarlane*, Daniel Wong, Carol Johnson, Karl Bzdusek, Jerry Battista, Jeff Chen
Ontario Consortium for Adaptive Interventions in Radiation Oncology
London Regional Cancer Program, University of Western Ontario, London ON, Canada

Introduction: Radiotherapy quality may be degraded by changes in patient weight and tumor volume, as these factors alter the dose distribution delivered to a patient. To ensure that the planned dose distribution is delivered over a treatment course of several weeks, an efficient dose tracking and adaptation method needs to be established. Currently, this is done by monitoring anatomical changes with daily on-board kilovoltage cone-beam computed tomographic (CBCT) imaging. If the changes observed in the CBCT are deemed significant, a new treatment plan is generated using an off-line diagnostic “planning” CT with superior CT number calibration and tissue density information.

Alternatively, many groups have proposed the direct use of CBCTs for dose calculation and plan adaptation, as these image sets are already acquired daily for beam guidance and patient monitoring. In order to do this, corrections need to be made to the CBCT data sets to ensure accurate CT numbers for correct dose calculations. Previously investigated methods include CT calibration using plastic phantoms with known tissue-equivalent densities (1), or by utilizing deformable image registration (DIR) to link the CBCT pixel data to the original planning CT pixels (2). Both of these techniques, however, have their limitations, either due to sensitivity to the errors introduced by DIR, or depending on the scanning conditions of phantom calibration being different from the CBCT scanning condition for a patient. The purpose of this work is to evaluate two alternative methods for computing delivered dose distributions directly on daily CBCT using patient-specific calibration.

Methods: The first proposed approach is a “density override” technique that uses the CBCT to segment specific regions on the planning CT where weight loss or the passage of air cavities has occurred. Dose calculations can then be re-performed using the planning CT data, with the density values of these altered regions overridden. The second approach is a patient-specific calibration method that uses DIR to generate a mutual linear correlation between the CBCT pixel data and the planning CT image values. A model is generated and applied to *each* slice of the CBCT, since x-ray scattering conditions vary between slices of the CBCT. The calibrated CBCT image set is then merged with the patient’s original planning CT for dose calculations.

To evaluate these techniques, 15 head-and-neck patients requiring plan adaptation were arbitrarily selected from our institution. The re-planning CT was acquired within 48 hours of the CBCT in order to ensure comparable anatomy. The original plan was then computed on the re-planning CT as gold standard, along with the data sets of each proposed CBCT method. Clinically relevant dose metrics were then compared for each patient and analyzed statistically using Friedman omnibus tests, followed by post-hoc Wilcoxon signed rank tests when applicable.

Results: Compared to the repeated planning CT as gold standard, our density-overridden and patient-specific calibrated CBCT methods displayed promising results with accuracies within 3%. The other techniques demonstrated higher disparity compared to the results from re-planning CT.

Conclusion: The density-overridden and patient-specific calibrated CBCT methods were shown capable of accurately computing delivered doses at the time of treatment. This could potentially allow for on-line dose tracking and plan adaption, without the need of a diagnostic re-planning CT.

References: [1] Richter *et al.* Radiat. Oncol. 2008; 3(1):42. [2] Veiga *et al.* Med. Phys.2014; 41(3):031703.

Analysis of dose volume histogram deviations using different voxelization parameters

Kyle Sunderland, Csaba Pinter, Andras Lasso, Gabor Fichtinger

Laboratory for Percutaneous Surgery, School of Computing, Queen's University, Kingston, Canada

Consortium: Ontario Consortium for Adaptive Interventions in Radiation Oncology (OCAIRO)

Introduction. In radiotherapy treatment planning systems, structures of interest such as targets and organs at risk are stored as 2D contours on evenly spaced planes. In order to be used in various different algorithms, the contours must first be converted into binary "labelmap" volumes through voxelization. The process of voxelization results in a loss of information, which has a small effect on the volume of structures which are large relative to voxel size, but can have a significant impact on small structures, which may only contain a few voxels. The accuracy of these segmented structures can affect metrics such as dose volume histograms (DVH), which are used for treatment planning. Our goal is to evaluate the effect that varying voxel size has on the accuracy of DVH for each structure.

Methods. We implemented tools for analysis as modules in the SlicerRT toolkit [1] based on the 3D Slicer platform [2]. Within the modules, a series of implicit functions are created that represent simulated physiological structures (Fig. 1.). These structures are then sampled at varying resolutions, and are compared to a labelmap with a high sub-millimeter resolution, in order to calculate Hausdorff distance and Dice similarity coefficient between the labelmaps. Both labelmaps and dose volumes are used to generate DVH, and evaluate voxelization error for the same structures at different resolutions by calculating the agreement acceptance percentage between the DVH.

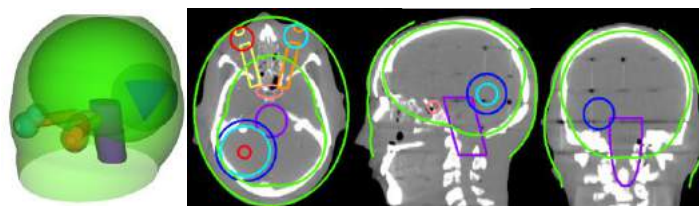


Fig. 1. Models representing the implicit functions that are used as the ground truth structures for the head and neck phantom in our experiments, and CT images showing the phantom that is being approximated.

Results. We found that while there were small differences in the DVH for large structures, a much larger difference was found for smaller structures such as optic lenses and nerves. The DVH differences were also amplified if the structure was located in a high dose gradient region. This caused several types of artifacts to appear in the DVH for small structures, such as a staircase-like effect, as well as consistent differences between the low resolution and high resolution DVH (Fig. 2).

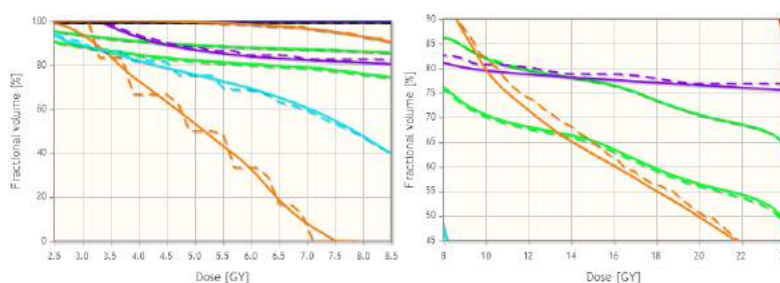


Fig. 2: DVH the high resolution (solid) and low resolution (dashed) labelmaps showing the staircase effect of voxelization (left) and consistent differences between DVH (right).

Conclusion. Labelmap and dose volume voxel size was found to be an important factor in DVH accuracy, especially for plans which include small structures or in regions with a high dose gradient. It is possible that these effects can potentially cause high errors in the DVH V and D metrics, which are calculated from the dose and volume levels, and are used in treatment planning to assess the quality of a plan. If these errors were large enough, they could potentially cause a suboptimal plan to be accepted. This problem might not be noticed by the physician since the DVH values would support the results, however the problem could be caused by errors in the DVH itself.

[1] Pinter, C., et al., "SlicerRT: radiation therapy research toolkit for 3D Slicer," Med. Phys. 39(10), 6332-6337 (2012).

[2] Fedorov, Andriy, et al. "3D Slicer as an image computing platform for the Quantitative Imaging Network." Magnetic resonance imaging 30(9), 1323-1341 (2012).

Micro-CT Compatible Load-Controlled Knee Motion Simulator

Alexandra Blokker^{a,c}, Timothy A. Burkhart, PhD^{a,b}, Alan Getgood, MD^b, David W. Holdsworth, PhD^c

Development of Novel Therapies for Bone and Joint Diseases Consortium

a. Department of Biomedical Engineering, University of Western Ontario

b. Fowler Kennedy Sports Medicine Clinic, University of Western Ontario

c. Robarts Research Institute, University of Western Ontario

Introduction. More than 100,000 anterior cruciate ligament reconstructions (ACLR) are performed annually in the United States (1) and despite significant advancements in ACLR methods, upwards of 14% fail (2). The primary causes of failure are non-anatomic graft placement, impingement, and failure of graft incorporation (2). Furthermore, persistent rotational instability following traditional ACLR occurs in 30% of patients (3,4). To date, there is no experimental method capable of imaging and non-invasively measuring the mechanical properties of the ACL and graft under varying fixations and physiological loading protocols; this has contributed to sub-optimal reconstruction methods. Therefore, the purpose of this research was to develop a novel, micro-CT compatible knee joint motion simulator to quantify the mechanical behaviour of the ACL and reconstruction grafts in response to physiologically accurate loading.

Methods. The joint simulator consists of a standalone frame with an actuating platform that subsequently fixes the tibia to a 6 degree-of-freedom load cell while a flexion jig (rigidly mounted to the CT-scanner bed) immobilizes the femur (Figure 1). This set-up centres the knee joint in the scanner's 15cm (transverse) by 10cm (axial) field of view. All motions and load patterns are controlled by a custom LabView program on a cRIO controller system (National Instruments, cRIO 9014). With this design, 30° of passive flexion can be achieved in addition to active control over 134N anterior translation, 5Nm internal rotation, 10Nm valgus rotation, and 500N of axial compression to human cadaveric knee joints. These motions can be combined to simulate a pivot shift (an important clinical test). To test the CT-compatibility of this innovative system, a composite knee-joint phantom (Sawbone) was tested using a standard imaging protocol (16s anatomical scan at 120 kVp, 20mA).

Results. Preliminary data suggests that the robot was capable of successfully loading the composite knee joint to 5Nm of internal rotation and maintaining the pre-set load. All micro-CT images were qualitatively free of artefacts and captured the relevant structures within the joint capsule, with isotropic resolution of 0.15 mm (Figure 2).

Conclusions. The novel five degree-of-freedom knee joint simulator presented here accurately loaded the composite knee while high-resolution micro-CT images were acquired. Independent actuation of motion axes facilitates a wide range of potential loading patterns while the 6 DOF load cell captures joint reaction loads along all axes. By placing Teflon™ tracking beads (which appear with high contrast in micro-CT images) into the tissues, this system will allow for the accurate mechanical property quantification of the ACL, reconstructed ACL, and surrounding bone as a function of graft fixation method. The outcomes of this research will result in novel, interdisciplinary approaches aimed at improving the outcome of ACL injuries. This work has the potential to improve treatment of these injuries, thus reducing the costs associated with treatment and improving an individual's quality of life.

References. [1] Darcy *et al.* J Biomech. 2006;39(13):2371–7. [2] van Eck *et al.* Am J Sports Med. 2012 Apr;40(4):800–7. [3] Mohtadi *et al.* Cochrane Database Syst Rev. 2011;(9):CD005960. [4] Prodromos *et al.* Arthrosc J Arthrosc Relat Surg 2005 Oct;21(10):1202.



Figure 1. CAD model rendering of joint simulator from the (a) table side, and (b) back side of micro-CT scanner.

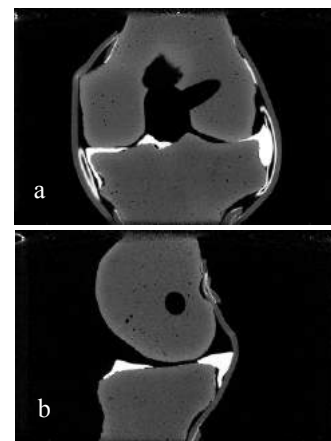


Figure 2. (a) Coronal, and (b) sagittal plane images of an unloaded composite knee-joint mounted in the simulator.

Detective Quantum Efficiency: Quantifying clinical detector performance to ensure lower patient exposures

Department of Medical Biophysics and Robarts Research Inst., University of Western Ontario, London, Canada

Primary Author: Terenz Escartin

Consortium Affiliation: Ontario Institute for Cancer Research – Imaging Translational Program

Research Supervisor: Dr. Ian Cunningham

Introduction: The detective quantum efficiency (DQE) of an x-ray detector, expressed as a function of spatial frequency, describes the ability to produce high signal-to-noise ratio (SNR) images relative to an ideal detector. While regulatory and scientific communities have used the DQE as a primary metric for optimizing detector design, the DQE is rarely used by end users to ensure high-performance is maintained and patients receive the health benefits of high-quality images and low exposures throughout the life of the system. The reasons for this include: limited access to DQE expertise and instrumentation in most facilities; restricted access to imaging systems for the purpose of testing; and limited understanding of how great the difference in DQE values can be from one system to another, and what that difference means for image quality.

Methods: We have conducted a survey of DQE measurements in a clinical setting using a prototype DQE-testing instrument. Following laboratory validation, it is shown the instrument could be used to measure the DQE in all clinical radiographic systems tested. Accurate DQE assessments required careful linearization of image data and normalization of the MTF. An RQA-5 spectrum was used to obtain DQE values from a CR system and four different DR systems that are all currently in clinical use.

Results: The zero-frequency DQE value ranges from 0.3 to 0.75 and varies by a factor of two at 1 mR detector exposure. Of greater concern is how quickly the high-frequency DQE drops on some systems (Figure 1). It is also proposed that the DQE integral (area under the DQE curve) is a meaningful single-value metric for simple monitoring of system performance over time, ranging from 0.31 to 2.5 cycles/mm in the systems tested. The DQE integral varies by a factor of eight, from 0.31 (DR1) to 2.5 (DR4) cycles/mm. For some systems (DR2), the DQE drops quickly with decreasing exposure, causing a further degradation in image quality in parts of an image corresponding to increase tissue density.

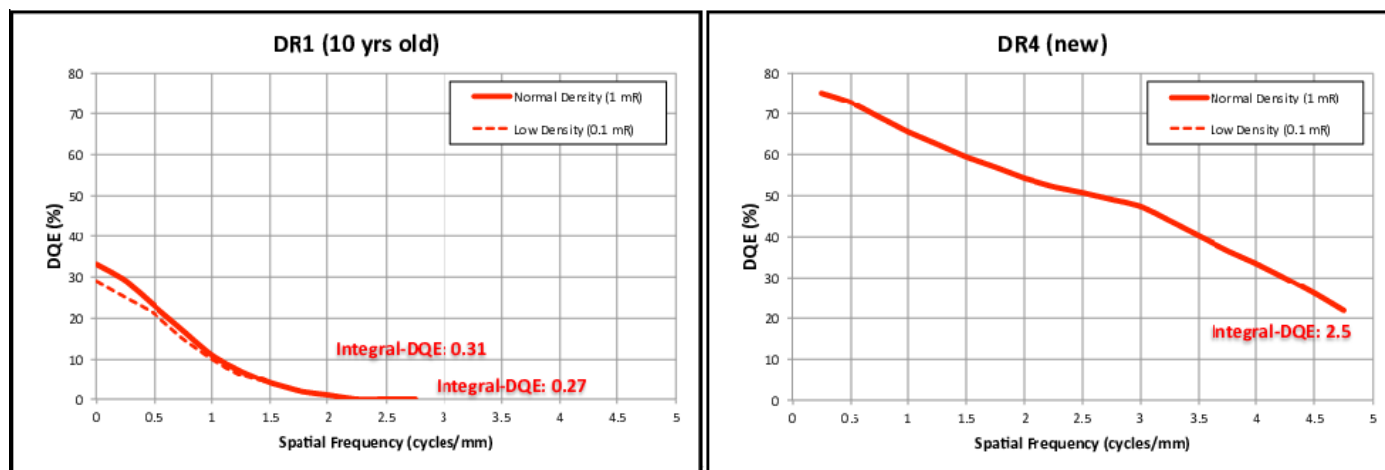


Figure 1: the DQE at 2 cycles/mm varying from 0.01 (DR1) to 0.55 (DR4), a factor of 50x

Conclusion: It is concluded that DQE specifications in purchasing decisions, combined with periodic DQE testing, are important factors to ensure patients get the benefits of high-quality images for low x-ray exposures.

Control of Rewarming Rate following Rapid Selective Brain Cooling

Mohammad Fazel Bakhsheshi, PhD^{1,2}, Laura Morrison, RVT¹, Lynn Keenlside¹, Ting-Yim Lee, PhD, FCCPM^{1,2,3}

¹Imaging Program, Lawson Health Research Institute, London, Ontario, Canada, ²Imaging Research Laboratories, Robarts Research Institute, London, Ontario, Canada.

³Department of Medical Imaging and Biophysics, Western University, London, Ontario, Canada,

INTRODUCTION: There are 40,000 cardiac arrests each year in Canada. Mild hypothermia has been shown to improve survival and neurologic recovery after cardiac arrest [1]; however, current cooling methods are far from optimal. The most critical gap is the absence of a suitable Selective Brain Cooling (SBC) method that rapidly cools down brain to the therapeutic range of 32-34°C and maintains the hypothermia up to 12 or 24 hours before gradually return to baseline temperature with a rewarming rate of 0.25°C/hr [2]. Rewarming is a delicate phase of therapeutic hypothermia. Adverse consequences of rapid rewarming may lead to secondary injury seriously limiting the protective effects of hypothermia [3]. Therefore, rewarming after cooling and maintenance phases should be done slowly and in a controlled manner. Recently, we developed a novel method of SBC and demonstrated its safety and efficacy to selectively reduce and maintain brain temperature over 6 hours in a juvenile pig model. The method was based on spraying cold air, generated by a vortex tube, into the nostrils at different flow rates using a feedback controller to automatically generate cold air at temperatures and flow rates that can be selected. The primary focus of the current study was to evaluate the ability of this approach to tightly control the rewarming rate to be not more than 0.25°C per hour on juvenile pigs.

METHODS: Experiments were conducted on four juvenile pigs, approximately 2-3 months old with an average weight of 28 ± 2kg. The surgical procedure has been presented in detail elsewhere [4]. Body temperature was measured continuously using an esophageal and a rectal temperature probe attached to a Surgivet monitor. Brain temperature was also measured continuously and invasively with a thermocouple probe. A 5-mm burr hole was made in the skull with a Dremel tool. The needle thermocouple probe was inserted laterally through the skull into the brain to a depth of 2 cm vertical from the brain surface and 1.5 cm posterior to the bregma. A custom-made catheter (made from Polyvinyl Chloride), coated with 2% lidocaine gel for anaesthesia and better contact with turbinate in the nasal cavity, was inserted 4-5 cm into each nostril. The nasal catheter comprises a tubular body defining a lumen and an open end in continuous fluid communication with the cold air outlet of the vortex tube and first and second tubular nasal prongs extend from the tubular body. Intranasal brain cooling was initiated by setting the controller to the desired air temperature of -5°C and flow rate of 50 L/min for 60 minutes using medical air cylinders. After one hour, the source of compressed air was switched to the hospital medical air to continue the intranasal cooling. Once the brain temperature stabilized at the target temperature of 33 ± 1°C as measured by the intracranial thermocouple, the flow rate was decreased to 35-45 L/min and air temperature increased to 5 ± 1°C to maintain the target temperature while core body temperature were maintained above 37°C. After 4 hours of cooling, the brain temperature was allowed to gradually return to the baseline temperature in 6 hours by increasing the air temperature gradually and adjusting the flow rate. Each experiment was completed within 13-14 hours and the animal was sacrificed with intravenous potassium chloride (1-2 ml/kg, 2 mEq/mL) infusion. Fig 1 shows the schematic of the experimental setup.

RESULTS: Changes in rectal, esophageal and brain temperatures are shown in Figure 2. During 30-40 minutes of baseline monitoring, mean brain and core body temperatures did not change more than 0.1 ± 0.1°C. Following baseline, brain temperature decreased biexponentially, dropping rapidly from 37.9 ± 0.3°C to 35.0 ± 0.8°C within 30 minutes and then decreased more slowly and stabilized at 33.5 ± 0.5°C within the two hour of brain cooling, corresponding to a brain-body temperature gradient of 3.5 ± 1°C. Following four hours of cooling, the brain was then allowed to gradually rewarm from 33.2 ± 0.2°C to the temperature of 35.1 ± 0.5°C in 6 hours corresponding to rewarming rates of 0.3 ± 0.1°C/h.

CONCLUSIONS: We have shown that our method is able to tightly control the rewarming rate within 0.3 ± 0.1°C per hour. This study was the first step in developing a fully automatic controller during rewarming for future studies. For the next step, we will upgrade our controller to automatically adjust the flow rate and temperature of cold air according to the tympanic (ear drum) temperature measured by a near infrared sensor in the ear canal as surrogate of the brain temperature.

REFERENCES: 1-Bernard S et al, N Engl J Med, 2002. 2-Peberdy, M.A., et al., Circulation, 2010. 3- Thompson, H.J., et al., J Trauma Nurs, 2010. 4-Fazel Bakhsheshi, M., et al., Neurocrit Care, 2015.

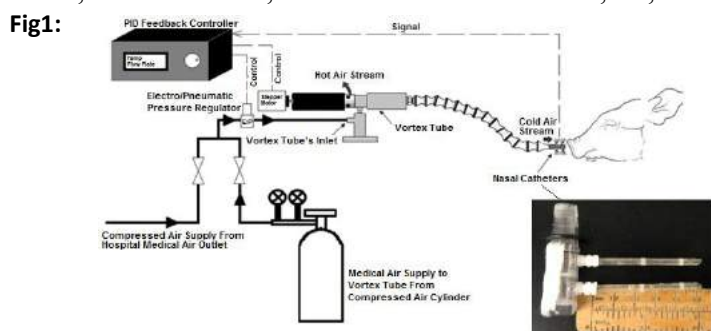


Fig 1. Schematic drawing of the cooling circuit used for intranasal brain cooling.

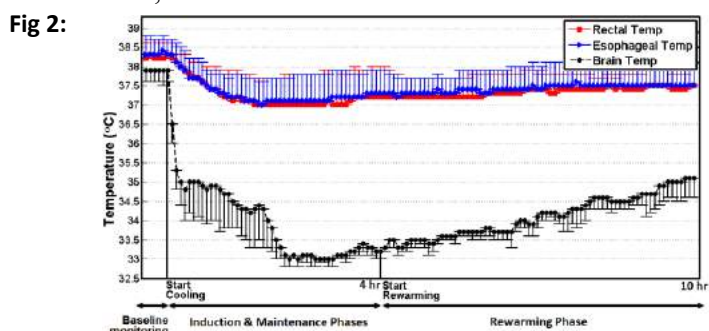


Fig 2. Measured brain, rectal and esophageal temperature over time during baseline, cooling and rewarming phase. (N=4)

Novel flexible polarimetric probe for enhanced urologic cystoscopy

Author: Sarah Forward*, Supervisor: Alex Vitkin*, Ontario Institute for Cancer Research - Smarter Imaging Program

*University of Toronto dept. of Medical Biophysics

Introduction: in Canada alone, the total cost of genitourinary disease exceeds 2.5 billion dollars annually¹, with bladder cancer being the **most expensive** cancer to treat per patient². As is common in urology, its surveillance is usually conducted by white light cystoscopy where biopsies can be taken, but this is rather inaccurate and invasive (e.g. 22% of the recurrences of the disease are missed³). Several other urological diseases and procedures (e.g. defects in urethral openings⁴ (“*hypospadias*”), bladder regeneration procedures) are also in need of a more accurate, precise, and minimally invasive alternative to white light cystoscopy with enhanced information content, to enable more informed and thus improved management of bladder cancer and related pathologies.

Methods: a promising method to non-invasively probe the biophysical properties of tissue is **polarimetry**, a method to measure tissue properties up to 4 mm in depth using polarized light. For example, polarimetry reveals the presence of tissue **asymmetry** (perhaps linked to extracellular matrix (**ECM**) alignment), its optical activity (associated with concentration of chiral molecules e.g. glucose), and its depolarization (linked to micro-morphological differences between normal and pathologic tissues⁵). Polarimetry is thus a useful tool since the ECM has been shown to organise cellular behaviour where in cancer, for example, the ECM plays a critical role in its pathogenesis⁷.

Results/Work to date: Previous collaborative work between the biophotonics lab of Dr. Alex Vitkin (Princess Margaret Cancer Centre, Toronto) and the urology lab of Dr. Darius Bägli (Hospital for Sick Children, Toronto) has shown that changes in bladder wall morphology arising from bladder outlet obstruction can be accurately characterized with polarimetry⁵. For example, polarimetry-derived metric of linear retardance measured in specific areas of the bladder indicates regions of distending bladder obstruction, a cause of bladder dysfunction⁵. However, this work was done in *ex-vivo* preclinical bladder disease models. Thus, the next logical translational step is to engineer a flexible polarimetric probe suitable for *in-vivo* clinical deployment.

Hypothesis: *Minimally invasive in-vivo bladder pathology with polarimetric cystoscopy can extract previously unavailable and informative biophysical tissue metrics to monitor bladder cancer and to aid in the characterization of poorly managed urethral corrective procedures, thus overcoming inadequacies associated with the current gold-standard of white light cystoscopy.*

The corresponding work plan will consist of:

- 1) **Development of Probe:** The difficulty with a fiber-optic based flexible polarization probe is that the polarization state of light is not only affected by the tissue (“*signal*”), but is also altered by the fiber probe itself (“*noise*”). A previous PhD student in Dr. Vitkin’s lab has developed a patented novel methodology to account for this probe artefact effect, and demonstrated a proof-of-concept alpha-prototype⁶. Resources available at the University of Toronto will enable my further work in rapid fabrication of the next prototype, which involves producing the necessary micron-scale optical components, 3D printed parts, and fibre optical hardware, and then performance characterization of the resultant device in control phantom media with tissue-like properties.
- 2) ***in vivo* studies in bladder cancer:** In collaboration with Dr. Darius Bägli and with my previous experience with bladder cancer research under Dr. Lothar Lilge at Theralase Technologies Inc., Toronto (awkward sentence but want to include expertise/experience), the refined probe will be implemented first pre-clinically in rabbits or dogs using models developed by the Bägli lab and further deployed in humans after sterilization logistics that maintain the integrity of the optical components is negotiated.

Conclusions: the over-arching goal of my research is to develop and implement a refined *in vivo* tissue polarimetry technology for a rapid, minimally invasive information-rich assessment of urological pathology and treatment monitoring. The development of a new polarization-based methodology specifically targeted at costly, complex, and poorly managed urological diseases will offer previously unavailable tissue polarimetry metrics and provide a clear translational path for *in vivo* clinical deployment in the bladder, extendable to other hollow organs.

In Vitro Evaluation of a Novel Catheter Contact-Force Controller for Cardiac Ablation Therapy

D. Gelman,¹ A. C. Skanes,² M. A. Tavallaei,¹ M. Drangova^{1,3}

¹Robarts Research Institute and the Biomedical Engineering Graduate Program, Western University, Canada;

²Division of Cardiology, Schulich School of Medicine & Dentistry, Western University, Canada;

³Department of Medical Biophysics, Schulich School of Medicine & Dentistry, Western University, Canada

Consortium: Imaging for Cardiovascular Device Intervention **Supervisor:** M. Drangova

Introduction. To treat cardiac arrhythmia – an irregular heart rhythm – ablation catheters are introduced into the heart and manipulated until the distal tip contacts the targeted myocardium. Radiofrequency power is then delivered to form ablation lesions that isolate the heart from electrical pathways responsible for the arrhythmia. Monitoring delivery time and catheter-tip-to-tissue contact force (CF) of the lesion can predict lesion volume, conventionally termed as the force-time integral (FTI). However, varying CF due to inherent cardiac and respiratory motion, as well as catheter instability, make it difficult to clinically assess FTI during treatment. The solution to this problem would be to maintain a prescribed CF level, enabling the interventionalist to deliver a lesion under predetermined parameters as guided by the FTI model. To facilitate CF regulation, we developed a catheter contact force controller (CCFC) and the objective of this work is to evaluate its performance. The CCFC is a handheld, electromechanical device that monitors changes in CF due to tissue motion and compensates by autonomously adjusting the position of a force-sensing ablation catheter within a steerable sheath in real-time.

Methods. To evaluate the CCFC, a custom-built linear motion phantom was used to impart a series of physiological motion profiles on an experimental catheter, illustrated in Figure 1. Sixteen motion profiles, corresponding to CF profiles recorded during clinical ablation using a SMARTTOUCH™ catheter, were tested. The CCFC was programmed to deliver prescribed force of 15, 25, and 40 g on the moving target; CCFC-controlled and uncontrolled profiles were compared. FTI values of 500, 1000, and 1500 gs delivered at CF of 25 and 40 g were also prescribed. The CCFC retracted the catheter once the target FTI was reached. Delivery times were recorded and compared with the theoretical duration.

Results. Consistent, narrow CF distributions centered on the prescribed force levels were achieved for all motion profiles, depicted in Figure 2. Prescribed CF of 15, 25, and 40 g resulted in mean (\pm SD of 16 means) of 15.3 ± 0.1 , 25.4 ± 0.1 , 40.4 ± 0.1 g, with root mean squared errors of 3.2 ± 0.6 , 3.4 ± 0.7 , and 3.9 ± 0.8 g, respectively. During the prescribed FTI experiments, the lesion delivery times recorded were within $1.2 \pm 0.6\%$ of the theoretical duration, confirming accurate and effective force control throughout the delivery.

Conclusion. The CCFC has the ability to maintain CF at a specified level with repeatable deviation despite clinically relevant motion experienced during cardiac ablation, as well as the ability to deliver a predefined FTI.

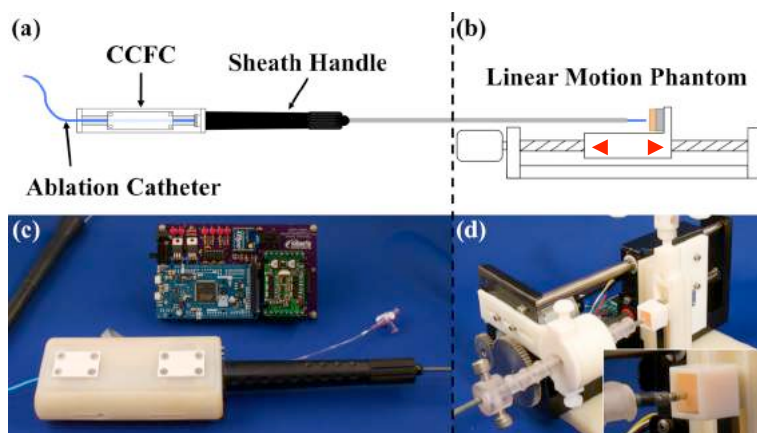


Figure 1. Experimental setup to used to evaluate the performance of the CCFC. (a) line drawing (not to scale) showing the CCFC, sheath and catheter mounted with the linear motion phantom (b); photographs of the CCFC (c) and motion phantom (d) are also shown.

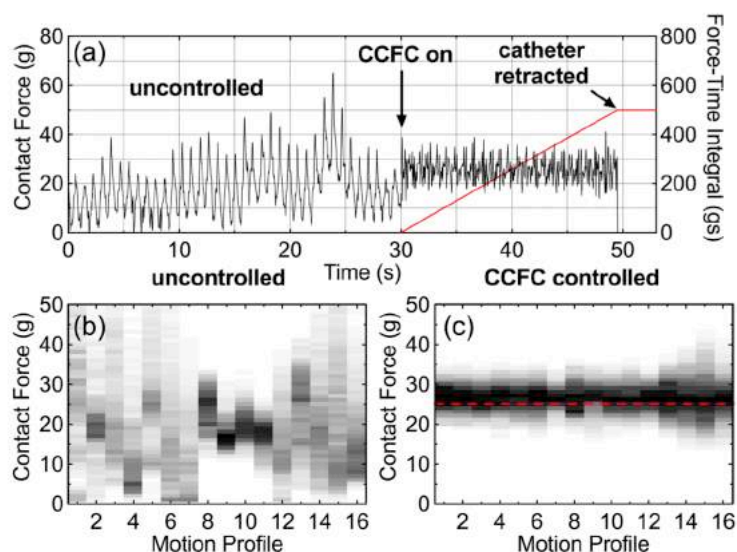


Figure 2. (a) Interval 0-30 s, the catheter was in contact with the phantom while the CCFC was disabled. Interval 30-49.5 s, the CCFC was engaged to deliver 500 gs at 25 g. Interval 49.5-53 s, the tip of the catheter retracted into the sheath once the desired FTI (red) had been reached. Histograms of uncontrolled (b) and CCFC-controlled (c) interventions, represented as grey scale values, show significant difference in CF distribution for all 16 motion profiles. The uncontrolled CF profile in (a) corresponds to profile #2 in (b) and (c).

Virtual design of patient specific neuroendoscopic tools for pineal region masses

Maggie Hess^{1,2}, Kyle Eastwood², Bence Linder¹, Vivek Bodani², Andras Lasso¹, Thomas Looi², Gabor Fichtinger¹, James Drake²

¹Laboratory for Percutaneous Surgery, Queen's University, Kingston, CA

²Centre for Image Guided Innovation and Therapeutic Intervention, Hospital for Sick Children, Toronto, CA

Consortium: Other

Introduction. Pineal region masses are a very common neurological finding, and can cause pressure in the brain ventricles. In order to relieve ventricular pressure and obtain histological diagnosis, neurosurgeons perform an endoscopic third ventriculostomy (ETV) and endoscopic tumor biopsy (ETB). The ETV fenestrates the floor of the third ventricle to allow CSF drainage, and the ETB targets the pineal mass. Currently, this occurs through a single entry point with a rigid trocar that passes through a channel in the ventricles. As the trocar is manipulated to reach the two targets, this channel is displaced laterally, and can cause memory impairment. To address this problem, continuum tools made from multiple pre-curved tubes are under development to create highly dexterous instruments, that are patient specific. Designing these devices is not trivial and relies heavily upon surgeon input. Thus, a user-friendly design process is essential.

Methods. We propose a method to design patient and procedure specific continuum tools through simulation, allowing visual verification. Our software allows for input and visualization of pre-operative scans and patient models. Burr-hole location and target locations can be placed through interaction with the 2D and 3D viewers. The burr-hole position can also be set automatically based on the targets' positions. A trocar with multiple continuum tools can be modeled in this virtual patient environment by inputting design parameters for the tools, such as segment number. Tool parameters are specified in the user interface. The user can then interactively change the position and direction of the trocar. The user can also reshape and reconfigure the continuum tools by dragging points along the tool models curve, automatically updating the tool shape. Anatomical boundaries can be set, constraining the tool position. Violations of these bounds are displayed visually to the user through collision detection. The tool shape and entry points can then be optimized.



Figure 1. Virtual neuroendoscope with three continuum tools being designed.

Results. Pre-operative data was collected from a patient requiring an ETV/ETB procedure. Two neurosurgeons were given basic instruction on the GUI workflow and then used the interface to design a tool while testing for usability. The burr-hole was placed automatically, and fell within the clinically defined range. The design consisted of one tool with three segments. In both tool to target configurations the tool body did not collide with the ventricle walls. Unlike the current procedure, the trocar position remained constant eliminating the damage from a moving trocar. The entire design process took 5.3 mins and 3.8 mins were spent on tool manipulation to design configurations to reach the target sites.

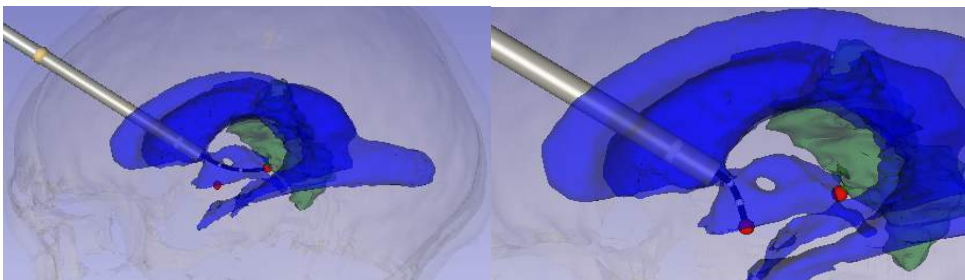


Figure 2. The two configurations of the single tool to reach the pineal mass, and ETV target location.

Conclusion. Our open source simulation-based solution enables user-friendly visual design and verification of continuum tool geometries to reach patient specific target sites in ETV/ETB procedures.

Geometric Calibration Phantom for MRI and CT

David W Holdsworth,^{1,2,3} Gregory Hong,^{2,3} Matthew G Teeter,^{1,2,3} Jaques S Milner,² Steven I Pollmann,² and Maria Drangova^{2,3}

Development of Novel Therapies for Bone and Joint Diseases Consortium

¹Department of Surgery, Western University, ²Robarts Research Institute, ³Department of Medical Biophysics, Western University, London, Ontario, Canada

Introduction: The capability for routine and accurate characterization – and correction – of geometric distortion is becoming increasingly important for MRI and CT applications, such as image-guided radiotherapy,¹ quantitative brain imaging, and for the preparation of patient-specific positioning guides in orthopaedic surgery.² In order to correct for inherent geometric distortion, a variety of fiducial grids and sheets have been proposed, typically based on regularly structured 3D grids³ or 3D distributions of glass marker beads. Recent advances in rapid prototyping – or “3D printing” – have made it possible to create accurate plastic structures of any desired 3D shape, facilitating an entirely new design of geometric distortion phantom.⁴ We describe such a 3D grid phantom, comprised of beads supported by thin walls at known spacing. The phantom provides images that facilitate automated segmentation and analysis of the 3D distortion field within an image.

Methods: The phantom consists of 4.5 mm diameter spheres, supported on 0.8 mm thick walls, with nominal 13 mm spacing. The phantom fits within an 11.4 cm diameter cylinder, with axial extent of 14 cm, providing a matrix of 580 fiducial markers. The device was fabricated by fused-deposition printing in polylactic acid (PLA) plastic, using a commercial 3D printer (Dremel® Idea Builder). For MRI imaging, the device is immersed in a solution of copper sulphate (7.8 mmol) in saline. To evaluate the geometric accuracy of the device, it was scanned in a calibrated micro-CT scanner (eXplore Ultra, GE Medical), at 120 kVp and 320 mAs with isotropic resolution of 0.15 mm. To isolate individual fiducial locations within the grid, a segmented (binary) image was morphologically eroded (1.2 mm kernel) to remove the thin walls, while retaining the beads at each intersection and thereby produce a 3D point-cloud of fiducial centroids.

Results: The accuracy of the printed construct was verified with a measuring microscope (STM-6, Olympus), which showed that the printed marker spacing was 12.97 mm (*i.e.* within 0.2% of the nominal spacing). Analysis of micro-CT image data showed centroid deviations with mean magnitude of 0.104 mm \pm 0.003 mm over a 760 cm³ volume. The grid phantom exhibited a low volumetric packing fraction within the background liquid, displacing less than 11% of the imaging volume, thereby minimizing susceptibility artifacts in derived MRI vector-displacement maps.

Conclusions: 3D printing in plastic resin has been used to fabricate and evaluate a geometric distortion phantom for MRI and CT imaging. The grid structure provides a rigid and accurate phantom, which produces images that are amenable to fully automated quantitative analysis. This approach will be useful in routine quality assurance, or as a component of future distortion correction utilities.

References: 1. Crijsns SP, et al. Towards inherently distortion-free MR images for image-guided radiotherapy on an MRI accelerator. *Phys Med Biol.* 2012; 57:1349-1358; 2. Krishnan SP, et al. A review of rapid prototyped surgical guides for patient-specific total knee replacement. *J Bone Joint Surg Br.* 2012; 94:1457-1461; 3. Baldwin LN, et al. Characterization, prediction, and correction of geometric distortion in 3 T MR images. *Med Phys.* 2007; 34:388-399; 4. Holdsworth DW, et al. Method and apparatus for measuring 3D geometric distortion in MRI and CT images, United States Patent Application 20150309149, Apr. 23, 2015.

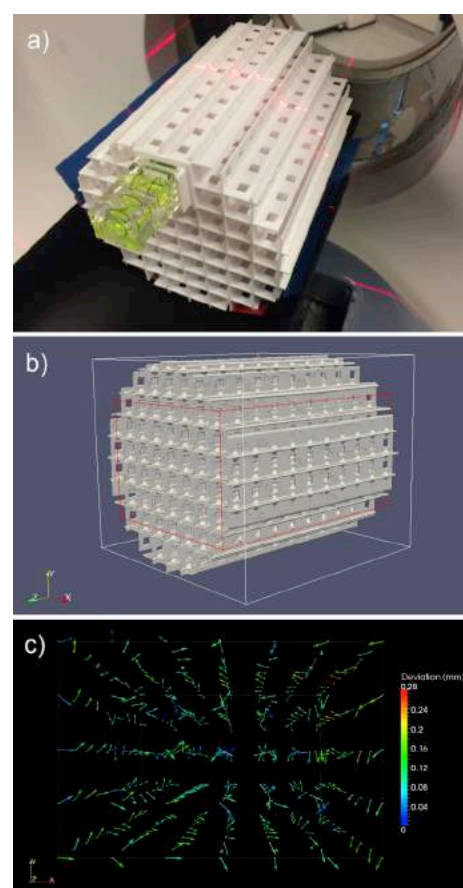


Fig. 1: (a) phantom in position for micro-CT scanning; (b) image processing to segment fiducial beads; and (c) resulting 3D distortion map.

Development and validation of a system for high-frequency vibration of live cells during real-time microscopy

Lorusso, D.^{¶*†‡}, Nikolov, H.N.[†], Chmiel, T.[†], Ochotny, N.M.^{¶‡}, Sims, S.M.^{¶‡}, Dixon, S. J.^{¶‡}, Holdsworth, D.W.^{¶†§±}

[¶]Bone and Joint Institute; ^{*}Collaborative Training Program in Musculoskeletal Health Research; [†]Imaging Research Laboratories; [‡]Robarts Research Institute; [‡]Department of Physiology & Pharmacology; [§]Department of Medical Biophysics; [±]Department of Surgery
Schulich School of Medicine & Dentistry
The University of Western Ontario, London, ON, Canada

Primary Author: Lorusso, D. **Research Supervisor:** Drs. S.J Dixon and D.W. Holdsworth

Introduction: Mechanotransduction is the process by which cells sense – and respond to – the local mechanical environment. This ability to react to external loads and forces is a critical component of mammalian physiology and is essential for normal functioning of our bones, lungs, and blood vessels; yet, the underlying mechanisms are still poorly understood. A form of mechanical stimulation that is commonly implicated in mechanotransduction is acceleration due to vibration. Our goal is to observe the immediate responses of cells to high-frequency oscillatory vibrations. Here, we describe the development and validation of an integrated motion-control system for vibrating live cell cultures at frequencies up to 1000 Hz and accelerations up to 0.5 g, which is compatible with real-time optical microscopy and photometry.

Methods: The motion-control system was mounted on an inverted microscope (Nikon Diaphot) and the moving parts were suspended on a linear air bushing system (NewWay) which was actuated by a voice-coil. Accelerations were measured *via* an on-board calibrated accelerometer (Dytran 7521A1). To ensure vibrations were transferred effectively to the cell culture dish, motion waveforms were imaged with a high-speed camera (Casio Exilim Ex-F1) at 1200 frames per second. MC3T3-E1 osteoblast-like cells were then seeded onto compatible glass-bottom dishes and imaged. In addition, cells were treated with fluorescent calcium dye fura-2 and exposed to vibration during photometry.

Results: During operation between 15 – 1000 Hz and 0.1 – 0.5 g, sinusoidal motion of waveforms were observed from both optical and accelerometer-derived measurements, with displacements ranging from the nanometer to millimeter range. Cultured osteoblast-like cells were vibrated 0.3 g at 45 Hz during photometry and remained adherent and viable.

Conclusions: We have developed, fabricated, and tested a motion-control system capable of – for the first time – delivering physiologically relevant vibrations to live-cells during real-time microscopy and photometry.

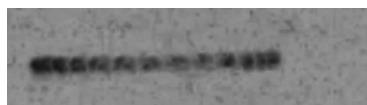


Fig. 1 a Maximum intensity projection of 1 cycle (27 frames) of a marker bead vibrated at 0.3 g and 45 Hz and imaged with a high-speed camera

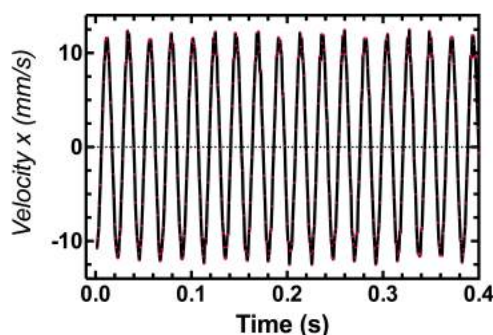


Fig. 2 Velocities of the particle from Fig.1, vibrated at 0.3 g and 45 Hz. Derived from particle tracking of frames captured with a high-speed camera.

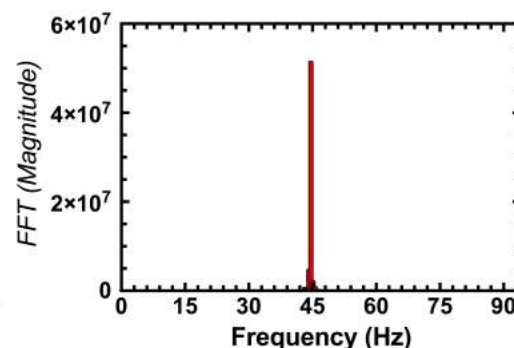


Fig. 3 Fast Fourier Transform of velocities from Fig. 2

Designing and testing a perfusion phantom for validating cerebral blood-flow measurements made with deconvolution techniques

Eric A Wright¹ (primary author), Lynn Keenlside¹, Ting-Yim Lee¹ (supervisor)
Medical Imaging Trial Network of Canada

¹Lawson Imaging, Lawson Health Research Institute, London, Ontario, Canada

Introduction: Time-dependent CT Perfusion (CTP)-based thresholds may be important for guiding selection of the optimal treatment for ischemic stroke patients by identifying the infarcted volume at admission and predicting infarct growth over the therapeutic time window (1). Unfortunately, the lack of standardization between deconvolution-based CTP algorithms from different vendors has made it difficult to clinically implement CTP-based thresholds. Previous studies show that even given the same patient-derived arterial input function (AIF) and tissue time-density curves (TDCs), the quantitative parameter values vary substantially depending on the deconvolution algorithm used (2). As a result, parameter thresholds for brain infarction give significantly different volumes when applied to CTP maps computed with different software packages (3). A recently designed perfusion phantom can evaluate differences in TDCs measured using different scanners and protocols (4), but this does not address the differences in quantitative parameter CBF values due to different deconvolution methods. Therefore, the objective of this work is to design and test a novel perfusion phantom for validating the accuracy of CBF calculations made using different deconvolution algorithms.

Methods: The design of the phantom included an input tube coupled to 32 polyurethane capillary tubes (inner diameter=330 μ m) which are coiled in a random orientation within a Plexiglas chamber to mimic a tissue capillary bed. An arterial input function was calculated using the flow-weighted average of partial volume averaging (PVA) corrected curves from the input to each capillary tube. The tissue density curve was calculated by averaging the curves from ROIs covering the Plexiglas chamber. A program developed in-house was used to deconvolve the tissue density curve and the AIF to give a computed CBF value in units of mL \cdot min⁻¹ \cdot 100g⁻¹. The true perfusion through the phantom is the pump flow rate multiplied by a volume scaling factor (100 divided by volume of ROIs covering Plexiglas chamber) so the units are mL \cdot min⁻¹ \cdot 100g⁻¹. The phantom-derived perfusion values are then compared to the true perfusion values.

Results: For infusion pump flow rates of 5, 10, 15, and 20mL/min, the average true perfusion values were 8.8, 17.4, 26.4, and 35.3 mL \cdot min⁻¹ \cdot 100g⁻¹. The average perfusion values (n=8 in all groups) computed using the AIF and tissue TDC measured with the phantom were 7.3, 15.3, 22.9 and 32 mL \cdot min⁻¹ \cdot 100g⁻¹ respectively. Bland-Altman analysis found an average bias of -2.6 mL \cdot min⁻¹ \cdot 100g⁻¹ between the phantom-derived and true perfusion, the limits of agreement were -5.31 to 0.14 mL \cdot min⁻¹ \cdot 100g⁻¹.

Conclusions: We demonstrated the feasibility of using this perfusion phantom to validate CBF values calculated using different deconvolution techniques. Future directions include testing a wider range of perfusion values and the addition of more deconvolution techniques.

References:[1] d'Este et al. Stroke 2015; 46: 3390-7. [2] Kudo et al. Radiology 2010; 254: 200-209. [3] Fahmi F et al. AJNR 2012; 33: 2074-80. [4] Driscoll et al. Medical Physics 2011; 38: 4866-80.

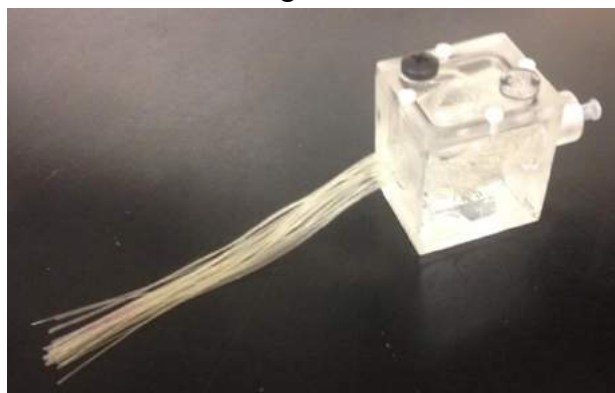


Fig 1: A picture of the perfusion phantom.

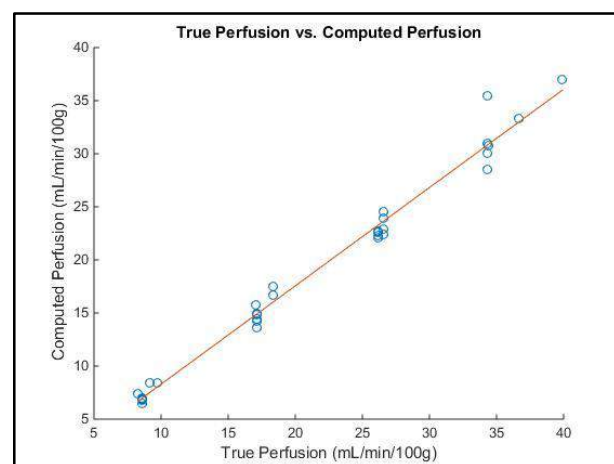


Fig 2: Phantom derived perfusion plotted against true perfusion. The line of best fit is shown in red (slope = 0.93, R² = 0.98).

An Update from the Quantitative Imaging for Personalized Cancer Medicine (QIPCM) Initiative

B. Driscoll³, I. Yeung^{1,2}, C. Coolens^{1,2,3}, H Keller^{1,2}, G. Disney¹, I. Svistoun¹, T. Shek³, J. Publicover³, & D. Jaffray^{1,2,3}

(1) Radiation Medicine Program, Princess Margaret Cancer Center, Toronto, ON

(2) Dept Radiation Oncology, University of Toronto, Toronto, ON

(3) Techna Institute, University Health Network, Toronto, ON

Ontario Institute for Cancer Research – Imaging Translation Program

Introduction: The vision of the Quantitative Imaging for Personalized Cancer Medicine (QIPCM) program is to provide end to end testing and analysis support for clinical trials to achieve improved consistency and reliability in clinical trial data. Over the past year a substantial investment was made upgrading the original QIPCM infrastructure to a robust high performance commercial system capable of supporting an ever expanding number of trials and sites.

Methods: The QIPCM clinical trial data archiving and analysis platform consists of a customizable DICOM anonymizer and secure transport pipelines (RSNAs Clinical Trial Processor, CTP), a dedicated robust virtual desktop infrastructure hosted by VMWare HorizonView, and a dedicated picture archiving and communication system (PACS) for DICOM image storage (DCM4CHE).

At trial activation each participating institution is provided a CTP client customized specifically for the trial and site. These pipelines ensure that all data is anonymized prior to leaving the participating institutions. The CTP client then transmits the data over secure HTTPS connection to the QIPCM CTP receiver. The anonymized patient images received from the remote institutions are held in a secure staging area where they are subjected to a quality assurance review. Images are then sent to the QIPCM PACS where trial based permission controls are enforced.

In addition to the platform infrastructure, QIPCM has built a set of custom image analysis tools. These tools can be made available for use on the virtual desktop infrastructure. Analysis tools include quantitative functional imaging tools (4D kinetic modeling of dynamic contrast enhanced-CT and MR), hypoxic fraction analysis in PET and simple 1D RECIST amongst other standard software such as Matlab and Microsoft Office. Alternatively remote users can choose to utilize their own custom applications on the virtual environment while still making use of the central data storage and powerful remote analysis servers.

Results: Over the past year the QIPCM infrastructure has doubled in size from three to six servers providing computational power for as many as 120 simultaneous virtual desktops. An additional 90 TB storage capacity was allocated to offset the increasing size and complexity of modern imaging intensive clinical trials. VMWare horizon view and Unidesk were installed in an effort to speed up the infrastructure and simplify user creation and desktop management. The platform currently serves 14 internal and 7 multi-center clinical trials spanning 10 hospitals and imaging centers in Canada and the United States.

Conclusions: The newly upgraded QIPCM platform is a fully functional commercial system with robust backup, storage and processing capacity. The system is fully scalable and built to meet the needs of our ever increasing number of trials and image analysis challenges.

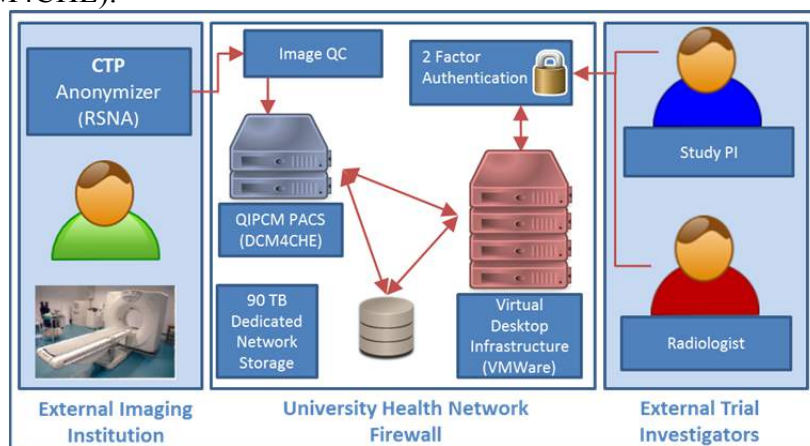


Figure 1 : Graphical representation of multicenter clinical trial data management and analysis setup

| | |
|---------------------------------------|---------------------|
| Current Trials | 21 |
| External Pipelines Established | 17 |
| Patients | 268 |
| Images | 2.33 million |
| Storage / Capacity | 2.1 / 90 TB |

Table 1 : QIPCM Program Key Performance Indicators as of Jan 15 2016

Novel Dual-Echo Planar Imaging Sequence for Hyperpolarized Carbon-13 Magnetic Resonance Imaging Distortion Correction

Benjamin J. Geraghty^{1,2}, Albert P. Chen³, and Charles H. Cunningham^{2,1}

¹Physical Sciences, Sunnybrook Research Institute, Toronto, ON, Canada, ²Dept. of Medical Biophysics, University of Toronto, Toronto, ON, Canada, ³GE Healthcare, Toronto, ON, Canada

INTRODUCTION: Frequency-selective hyperpolarized [¹³C]pyruvate echo-planar imaging (EPI) provides unparalleled acquisition speeds[1], which are essential for metabolic mapping in vivo. Field inhomogeneities can induce distortion in the metabolic maps according to Eq. 1: $y'(r) = y(r) + df(r) / BWpp$, compromising their spatial registration with respect to the underlying anatomy[3]. To address this, we have developed a dual-echo EPI sequence and non-iterative reconstruction that is capable of encoding the field map directly from the ¹³C signals.

METHODS: The dual-echo EPI sequence was implemented by removing every other blip trapezoid in a symmetric EPI readout such that each kx line is traversed twice. The result is two EPI images with opposing readout polarity, separated by an echo time difference of $\Delta TE = 0.892$ ms. The phase of the complex quotient of the dual-echo EPI images produces an estimate $df(r)^*$ in distorted coordinates. To account for echo asymmetry, a fully phase encoded[4] reference scan was acquired on proton.

The final ¹³C field map estimate (figure 1) was used to unwarp the dual-echo EPI images according to Eq. 1. Imaging was performed on a GE MR750 3T MR scanner using a dual tuned T/R ¹H-¹³C rat coil. Sprague-Dawley rat images were obtained in accordance with the local research ethics board. Imaging commenced as 3 mL of 80 mM pre-polarized [¹⁻¹³C]pyruvate solution was injected via tail vein catheter. A centre frequency deviation of -50 Hz was used to induce spatial mis-registration.

RESULTS: Reconstructed metabolic maps were 3X spline interpolated and overlaid on corresponding axial T2-FSE images (figure 2). Corrected images exhibit superior alignment of the signals arising from the aorta and kidneys with respect to the underlying anatomy.

CONCLUSION: The novel acquisition and reconstruction scheme provides tolerance to erroneous frequency variations including B0 inhomogeneities and eddy currents in frequency-selective ¹³C EPI of hyperpolarized compounds. The method is non-iterative, simple to implement, and the degree of apodization is the sole tuning parameter. This parameter was manually adjusted to generate the images in figure 2, and its selection represents a tradeoff between ¹³C phase map SNR and spatial accuracy. The automated selection of this parameter will be investigated in future work.

REFERENCES: [1] Cunningham *et al.* JMR 2008;193:139-146 [2] Jezzard *et al.* MRM 1996;34:65-73 [3] Cunningham *et al.* NMR in BioMed 2014;27:212-218 [4] Chen *et al.* MRM 1999;27:1206-1213

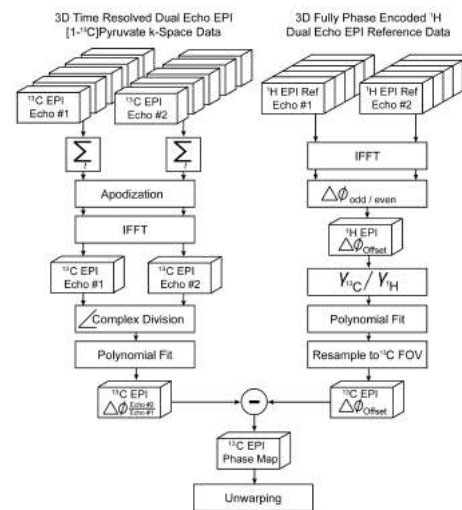


Figure 1: ¹³C Field Mapping Pipeline

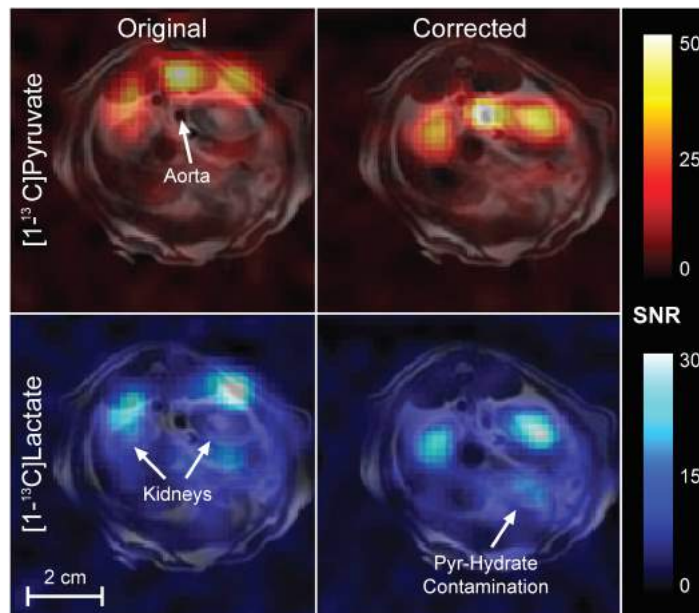


Figure 2: Corrected Metabolic Overlays

Title: Towards assessing therapeutic response of glioblastoma in a rat model of cancer using novel multi-modality imaging.

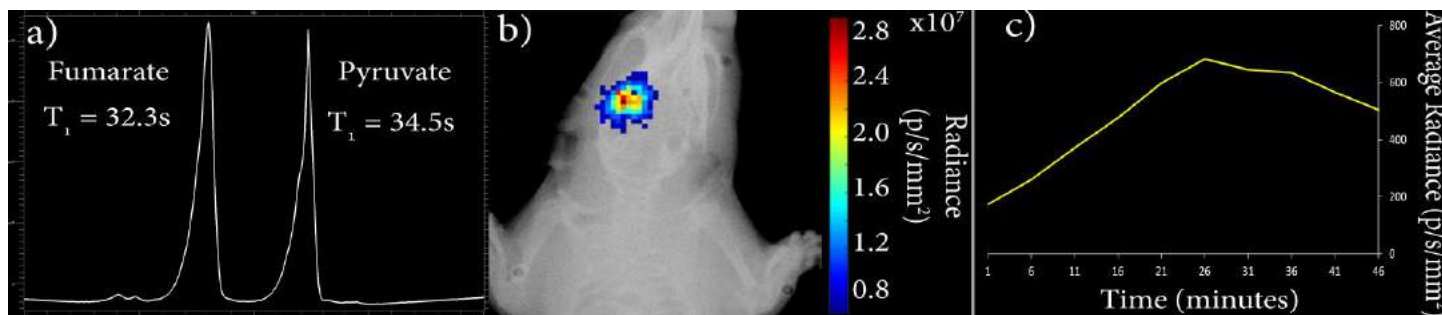
Authors: Trung N.T. Le¹, Heeseung Lim¹, Amanda Hamilton², Katie Parkins¹, Francisco M. Martínez², Timothy J. Scholl^{1,2}, John A. Ronald^{1,2}

Affiliations: 1. Medical Biophysics, Western University, London, ON, Canada.

2. Robarts Research Institute, Western University, London, ON, Canada

Introduction: The current methods to determine tumour response to treatment rely on anatomical information, such as changes in tumour size, and can take weeks to determine if treatment is effective. Probing the biological microenvironment of the tumour will provide an accurate and timely assessment of therapeutic response of tumours which is an ability that will be extremely important in the treatment of cancer. We have transduced C6 rat glioma cells to express luciferase as a novel preclinical model of glioblastoma. Our eventual goal is to compare the assessment of therapeutic response of these tumours to chemo-radiation using hyperpolarized (HP) [$1\text{-}^{13}\text{C}$]pyruvate and [$1,4\text{-}^{13}\text{C}$]fumarate, standard multi-parametric ^1H MRI and bioluminescence imaging (BLI) in a longitudinal animal study.

Methods: 13.2 μL of [$1\text{-}^{13}\text{C}$]pyruvate and 41 μL of [$1,4\text{-}^{13}\text{C}$]fumarate were mixed with OX063 (80 mmol/L), co-polarized by dynamic nuclear polarization (Hypersense, Oxford Instruments) and then buffered to an individual concentration of 40 mmol/L yielding a 5-mL-volume hyperpolarized solution at 37°C. The absolute polarization percentage was measured at 3 Tesla (GE Healthcare Discovery MR750 3.0T) for pyruvate and fumarate immediately after dissolution. A series of ^{13}C spectra were obtained using dynamic free induction decay, chemical shift imaging (FID-CSI) (TR = 3000 ms, BW = 5000 Hz, flip angle = 10°, time steps = 128, number of points = 2048). The spin-lattice relaxation time, T_1 , was calculated using a custom-written script in MATLAB (MathWorks Inc.). One million C6 glioma cells expressing luciferase was surgically implanted into a Wistar rat. Three days after surgery, BL images were obtained after a 1-mL injection of luciferin (30 mg/mL) using an In-Vivo Imaging System FX PRO (Kodak) apparatus.



Results: Figure 1. a) *In vitro* spectrum of co-polarized [$1\text{-}^{13}\text{C}$]pyruvate and [$1,4\text{-}^{13}\text{C}$]fumarate. b) BLI signal obtained 3 days after surgical implantation of one million C6 glioma cells expressing luciferase into the brain of a rat. c) BLI radiance from the implanted tumour measured as a function of time after injection of luciferase.

The values obtained in this study are *preliminary* results. The *in vitro* spectrum demonstrates our ability to co-polarize [$1\text{-}^{13}\text{C}$]pyruvate and [$1,4\text{-}^{13}\text{C}$]fumarate and easily resolve their spectral peaks using chemical shift imaging. T_1 s for pyruvate and fumarate were $34.5 \pm 0.1\text{ s}$ and $32.3 \pm 0.1\text{ s}$ (respectively) while the percentage polarizations (PP) were 6.7% and 7.4%. The earliest BLI signal was obtained on day 3, confirming the presence of viable glioma cells expressing luciferase.

Conclusions: This work establishes the feasibility of using a single injection of co-polarized [$1\text{-}^{13}\text{C}$] pyruvate and [$1,4\text{-}^{13}\text{C}$]fumarate as a probe of tumour metabolism. Initial *in vivo* BLI results demonstrate the ability to image viable C6 glioma cells expressing luciferase in the rat brain. BLI will be useful for non-invasive monitoring of tumour burden and can be used as a reference for HP MR images. Ultimately, we will investigate the use of HP [$1\text{-}^{13}\text{C}$]pyruvate and [$1,4\text{-}^{13}\text{C}$]fumarate to probe changes in tumour hypoxia and cellular necrosis in response to chemo-radiation in this rat model.

Estimating *Ex Vivo* Total and ^{13}C -Lactate Concentration in Rat Tumour using NMR Spectroscopy

Casey Y. Lee^{1,2*}, Justin Y. C. Lau^{1,2}, Albert P. Chen³, Yi-Ping Gu², and Charles H. Cunningham (Supervisor)^{1,2}

¹Medical Biophysics, University of Toronto, Toronto, ON, Canada, ²Physical Sciences, Sunnybrook Research Institute, Toronto, ON, Canada, ³GE Healthcare, Toronto, ON, Canada

Introduction: The accumulation of lactate in tumors has been correlated with poor clinical outcomes (1), suggesting that measuring lactate concentration can potentially be used to assess the risk of metastasis and to monitor response to treatment. Hyperpolarized ^{13}C -substrates, such as $[1-^{13}\text{C}]$ pyruvate, are being actively explored as a tool to image the pyruvate-to-lactate conversion by measuring hyperpolarized ^{13}C lactate and pyruvate signals (2). Since the hyperpolarization decays rapidly ($\sim 60\text{s}$), the fate of the injected ^{13}C -substrates are typically not known outside of this short window. Therefore, we estimate the concentrations of total lactate and $^{13}\text{C}_1$ - and $^{13}\text{C}_3$ -lactate in rat tumors that that has been extracted following $^{13}\text{C}_1$ - and/or $^{13}\text{C}_3$ -pyruvate injection.

Methods: Four Male Rowett nude (RNU) rats (*A – D*, Fig. 1) with subcutaneous xenografts of MDA-MB-231 human breast cancer cell line co-injected with MS1 mouse endothelial cell line were injected with 2ml of pre-polarized 80mM $[1-^{13}\text{C}]$ pyruvate, followed by the injection of 80mM/2ml non-hyperpolarized $[3-^{13}\text{C}]$ pyruvate (approximately 4 min after the initial $[1-^{13}\text{C}]$ pyruvate injection). The tumors were harvested approximately 1 min from the start of $[3-^{13}\text{C}]$ pyruvate injection. Five rats (*E – I*) were injected only with $[1-^{13}\text{C}]$ pyruvate before the extraction while the control rat (*Ctrl*) did not receive any injection prior to the extraction. Metabolites were extracted and re-dissolved in 400 to 450 μl D_2O containing 10mM DMSO for NMR spectroscopic studies. Proton spectra were acquired with 2s water pre-saturation sequence ($\text{TR}=60\text{s}$, 32scans, $\text{sw}=\pm 2500\text{Hz}$) to determine total lactate pool (1.3 ppm), using 10mM DMSO (2.7 ppm) as the internal concentration reference. ^{13}C spectra were acquired using a proton-decoupled (WALTZ-16) sequence (flip angle= 45° , $\text{TR}=5.1\text{s}$, 32768 points, 45052 scans, 10Hz exponential apodization). To enable concentration measurement, a 250mM ^{13}C -urea sample was scanned before each ^{13}C spectra acquisition to compensate for any signal instability. The signal from each peak was determined by calculating the area-under-the-peak. Only the signals with $\text{SNR} > 2$ were considered. ^{13}C -lactate concentrations were determined by comparing lactate signals to signals from 1, 2, 3mM $[3-^{13}\text{C}]$ sodium pyruvate solutions acquired under the same condition. $^{13}\text{C}_1$ -lactate signal was further corrected for using a short TR during the acquisition, assuming an actual T1 of 40s (3). All NMR data were acquired on a 7T NMR spectrometer.

Results and Discussion: Estimated total lactate pool sizes for all rats were within the previously reported lactate concentration range for various human head-and-neck squamous cell carcinoma xenografts (7.3 – 30 $\mu\text{mol/g}$) (1), with an exception of Rat *E* that displayed a higher pool size (39.2 \pm 5.9 $\mu\text{mol/g}$). $^{13}\text{C}_1$ - and $^{13}\text{C}_3$ -lactate (184.2 and 21.8ppm, respectively) were both detectable in all rats (*A – D*) that were injected with both $^{13}\text{C}_1$ - and $^{13}\text{C}_3$ -pyruvate. However, observable levels of $^{13}\text{C}_1$ - and $^{13}\text{C}_3$ -lactate were also found in the control rat at approximately 1% of total lactate pool size, suggesting that there is a detectable level of natural abundance baseline ^{13}C -lactate that should be accounted for in the future analysis. Similarly, $^{13}\text{C}_3$ -lactate was detected in Rat *H*, despite no prior $^{13}\text{C}_3$ -injection. However, both $^{13}\text{C}_1$ - and $^{13}\text{C}_3$ -lactate were not detectable in Rat *E*, despite the highest total lactate pool size. In all the other rats (*E, F, G, I*) that were injected with $^{13}\text{C}_1$ - but not $^{13}\text{C}_3$ -pyruvate, $^{13}\text{C}_1$ -lactate was observed while $^{13}\text{C}_3$ -lactate was not detectable.

Conclusion: A measurable level of $^{13}\text{C}_1$ -lactate remained in rat tumour extracts following the $^{13}\text{C}_1$ -pyruvate injection. Similarly, $^{13}\text{C}_3$ -lactate was detectable in the $^{13}\text{C}_3$ -pyruvate injected rats. Lastly, estimated total lactate pool size in this study agreed with the previously reported values in tumour.

References: (1) Quennet V, et al. *Radiother. Oncol.* 2006;81:130-135. (2) Chen AP, et al. *Magn. Reson. Med.* 2007;58:1099-1106. (3) Harris T, et al. *Proc. Natl. Acad. Sci.* 2009;106:18131-18136.

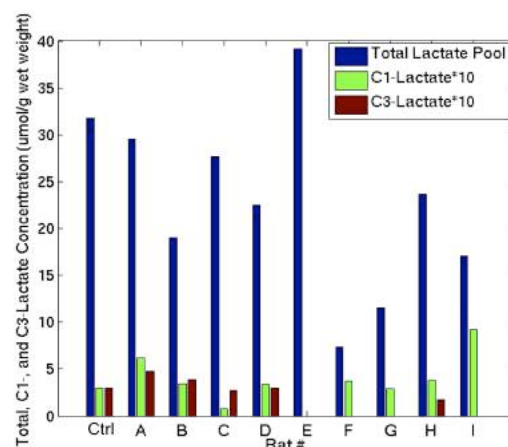


Figure 1. Estimated total lactate pool size, $^{13}\text{C}_1$ - and $^{13}\text{C}_3$ -lactate concentrations for each rat are shown.

Tracer kinetics of histone deacetylase and its metabolites in epigenetic tumors

Fiona Li*, Sung J. Cho, Lihai Yu, Robert H.E. Hudson, Leonard G. Luyt, Michael S. Kovacs, James Koropatnick, Ting-Yim Lee

Ontario Institute for Cancer Research - Smarter Imaging Program
Western University, London, ON

Introduction: Cancer can be caused by both genetic and epigenetic changes. Unlike genetic changes, epigenetic modifications occur without alterations in the DNA sequence and histone deacetylase (HDAC) is a key facilitator. HDACs have been shown to silence tumor suppressor genes leading to the use of HDAC inhibitors (HDACi) to treat cancer where in vivo imaging is required to assess treatment response non-invasively. The tracer 6-(¹⁸F-fluoroacetamido)-1-hexanoic acid (¹⁸F-FAHA) can be used to image HDAC activity^{[1][2]} but it is reduced by HDAC in the tumor and other tissues to the metabolite, ¹⁸F-fluoroacetic acid (¹⁸F-FACE)^[1]. A separate metabolite study is usually required to distinguish these two sources. The aim of this study was to develop a tracer kinetic analysis method capable of dealing with the non-tumoral source without requiring a separate metabolite study to simplify HDAC activity imaging with ¹⁸F-FAHA.

Method: To account for the two sources of metabolite, combined three compartment model (C3CM) was developed which requires a separate metabolite (¹⁸F-FACE) study and is inconvenient clinically. We propose to use the ratio of tumor and normal tissue HDAC activity estimated by single three compartment model (S3CM) as the metabolite corrected tumor HDAC activity. This S3CM method was used to analyze the dynamic ¹⁸F-FAHA PET images of implanted HDAC active tumors on either side of the neck of twenty one immunocompromised mice and non-tumor tissue adjacent to the tumors. The experimental group was divided into three groups: 1) no treatment (n=6) 2) treatment with DMSO (n=8) and 3) treatment with suberoylanilide hydroxamic acid (SAHA, n=7), an HDACi, in DMSO. 40μL of DMSO or SAHA were injected 24 hours before baseline and follow up studies. Follow up studies was done seven days after the baseline studies.

Results: Using known rate constants, tumor time activity curve (TAC) for C3CM was fitted using S3CM to estimate the HDAC activity. A strong correlation was found between the ratio of tumor to non-tumor HDAC activity estimated by S3CM and the true ratio (Fig 1). This result shows that C3CM can be modelled using single three compartment model (S3CM), thereby eliminating need of a separate ¹⁸F-FACE study. Using the S3CM HDAC ratios, the percentage changes of follow up from baseline HDAC activity ratio were compared (Fig 3). The no treatment group had highest positive change and SAHA treated group showed negative change which is in agreement with the PET images (Fig 2). This is expected as SAHA inhibits HDAC activity.

Conclusion: ¹⁸F-FAHA can be used to image treatment response for tumors treated with epigenetic drugs. Similar to standardized uptake value (SUV), commonly used for PET quantification, the HDAC activity in tumor using S3CM model can be normalized by that of normal tissue to account for metabolites. The quantification ability not only eliminates unnecessary biopsies but it can also be utilized to individualize treatment protocol.

References: [1] Yeh et al. *Neuroimage* 2012; 64: 630-639. [2] Mukhopadhyay et al. *J Label Compd Radiopharm* 2006; 49:997-1006

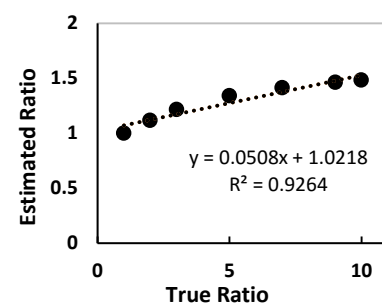


Fig 1: Correlation of true HDAC ratio with that estimated by S3CM

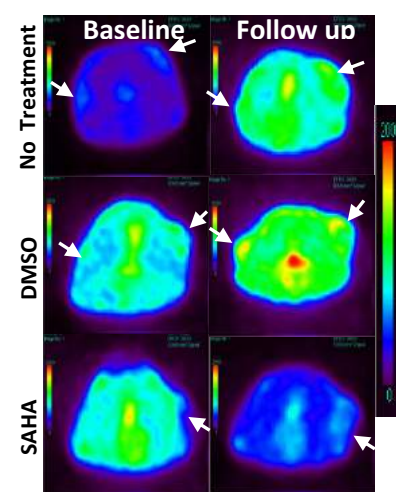


Fig 2: Comparison of PET images of treatment groups at baseline and follow up. White arrows indicate the tumors

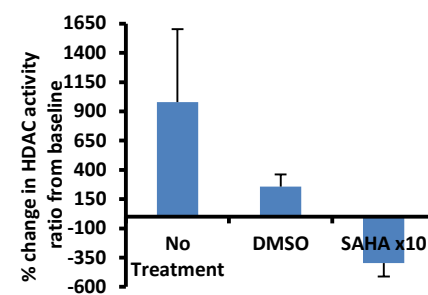


Fig 3: Percentage change of HDAC activity ratio from baseline using S3CM. SAHA group is scaled up by 10 times for better visualization

Monitoring changes in pH gradient using two different magnetic resonance imaging techniques

Heeseung Lim¹, Mohammed Albatany¹, Francisco M. Martinez, Robert Bartha^{1,2}, Timothy J. Scholl^{1,2}

1. Medical Biophysics, Western University, London, ON, Canada.

2. Robarts Research Institute, Western University, London, ON, Canada

Introduction: In tumours, the pH gradient (intracellular pH – extracellular pH) is usually positive and often reversed compared to normal tissue. Given the pharmacokinetics of chemotherapeutic drugs are highly depended on tumour pH, the ability to non-invasively quantify tumour pH is an important aspect of cancer treatment. This study used two magnetic resonance imaging (MRI) techniques to map the intracellular/extracellular pH gradient in a rodent glioma model. The intracellular pH (pHi) was mapped with chemical exchange saturation transfer (CEST) and hyperpolarized ¹³C bicarbonate magnetic resonance spectroscopic imaging (Hyper¹³C) was used to determine regional extracellular pH (pHe).

Methods: 7 Wistar rats were surgically implanted with one million C6 glioma cells in the right caudate nucleus of the brain. pHi and pHe were mapped in the tumour and contralateral brain tissue at day 8, 12 and 15 after implantation. pHi was measured using CEST MRI on a 9.4T small animal MRI scanner (Agilent, Santa Clara, CA). CEST spectra were acquired using a standard fast spin echo (FSE) pulse sequence (TR/TE = 7000/7 ms, ETL = 32, ETE = 7 ms, matrix = 64 × 64, FOV = 40 mm × 40 mm, 2 prescans, slice thickness = 2.0 mm, pre-image saturation pulse = 1.5 μT and 4-s duration). On the same day, extracellular pH was measured using Hyper¹³C bicarbonate on a Discovery MR750 3.0T scanner (GE Healthcare, Waukesha, WI). The animal received a single bolus injection of 150-mM hyperpolarized ¹³C sodium bicarbonate solution through the tail vein and ¹³C spectra of the rat brain were acquired using an optimized 2D FID-CSI sequence (TR = 80 ms, matrix = 8 × 8, FOV = 60 mm × 60 mm, slice thickness = 12.0 mm and BW = 5000Hz).

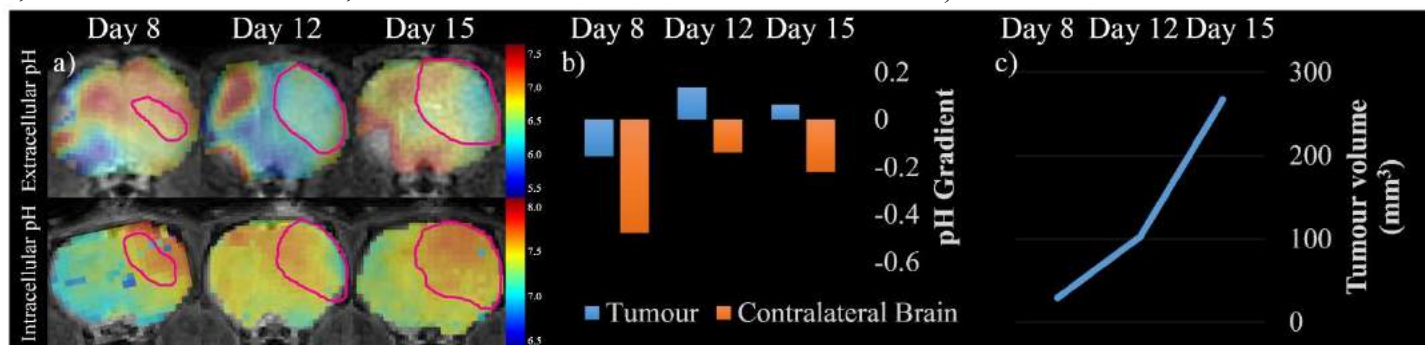


Figure 1. Longitudinal changes in pH for a representative rodent glioma model. a) pHe and pHi maps overlaid on the top of proton rat brain images on days 8, 12 and 15. Tumour is outlined in red b) Longitudinal measurements of the pH gradient in tumour and contralateral brain c) Tumour volume measurements.

Results: Longitudinal measurements of the pH gradient for a representative rodent glioma model for days 8, 12 and 15 after surgery are shown in Figure 1. During tumour growth, the extracellular space within the tumour became more acidic, whereas the intracellular compartment became more alkaline leading to an increase in the pH gradient. Overall, the averaged pH gradient in the tumour changed from -0.01 to 0.28 then 0.09. Conversely the pH gradient of contralateral brain tissue changed from -0.34 to -0.24 then -0.47.

Conclusions: The acid-base balance in the brain is tightly controlled by endogenous buffers such as bicarbonate and phosphate. An alkaline tumour pHi increases the activity of several metabolic enzymes that drive cellular proliferation. In contrast, an acidic tumour pHe is established due to increased lactic acid production and the subsequent active transport of protons out of the cell. In this study, the results showed a consistent agreement of increased pH gradient in tumour compared with the contralateral tissue. Furthermore, the pH gradient of tumour increased during tumour growth. Moreover, the heterogeneity of tumour pH began to increase at later time points as shown in the pH maps of Figure 1. These regional measurements may be useful to assess therapeutic response and predict local areas of treatment resistance. Overall, the intracellular/extracellular pH gradients in this rodent glioma model were non-invasively measured to a precision of ~0.1 pH units at three time points. A large difference in pH gradient was observed between tumour and contralateral brain throughout the growth of the tumours. Since most therapeutic agents are weak acids or bases, *a priori* knowledge of the pH gradient may help guide choice of therapeutic agent. In future work, tumour heterogeneity will be validated using histology.

Clearance of Indocyanine Green by the Liver during Hemodialysis as a Measure of Hepatic Function

R. Marants, E. Stewart, J. Hadway, C. McIntyre, T. Lee

Medical Imaging Trial Network of Canada

Department of Medical Biophysics, Western University, London, Ontario, Canada

Introduction: Hemodialysis (HD) is a medical treatment designed to replace lost kidney function in patients with late-stage kidney disease. HD patients are typically hypervolemic and exhibit congested blood flow among abdominal organs, resulting in higher myocardial demand. During a HD session, a state of temporary hypovolemia is established, causing myocardial demand to decrease and global blood flow to decline. In addition, the liver becomes more vulnerable to the hemodynamic stresses of HD for patients with endotoxemia, increasing the likelihood of hepatic ischemia-reperfusion injury. Therefore, patients are likely to experience reduced global liver perfusion while undergoing standard HD treatment. The goal of this study was to assess how the hemodynamic stresses of HD on liver perfusion affects hepatic function. To accomplish this, pulse dye densitometry (PDD) was used to measure indocyanine green (ICG) clearance by the liver. PPD allows for real-time, non-invasive blood measurements using optical light, while ICG is a synthetic dye that is solely taken up and metabolized by liver cells before being excreted in bile. Clearance of ICG from blood, therefore, reflects liver function.

Methods: ICG clearance was measured in 4 HD patients before, during and after their dialysis sessions using a DDG 3300 unit. The patients were dialyzed using a 2008T Fresenius machine. ICG clearance measurements were done for approximately 15 minutes following a single ICG bolus injection through a peripheral cannula by attaching a finger probe to the patient. ICG clearance from blood was fitted using a two-compartment open model (Figure 1):

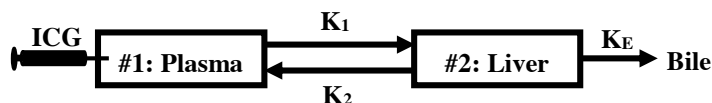


Figure 1: Two-compartment open model for ICG clearance from blood. ICG is injected into plasma (compartment #1) and is taken up by the liver (compartment #2) at a rate of K_1 . Also, ICG is cleared from the liver into the bile at a rate of K_E , which is the quantity of interest. Lastly, backflux of ICG from the liver into the plasma occurs at a rate of K_2 .

$C_{ICG}(t) = C_{ICG}(0) \cdot (Ae^{-\alpha t} + Be^{-\beta t})$, where $C_{ICG}(t)$ is the ICG concentration at time t and $C_{ICG}(0)$ is the ICG concentration at time zero. The clearance of ICG is calculated from the parameters of the biexponential fit as $K_E = Q\alpha\beta / (C_{ICG}(0) \cdot (A\beta + B\alpha))$, where Q is the amount of ICG injected. The biexponential decay fit was only applied to clearance data after the ICG is homogeneously mixed in the plasma compartment (arrow in Figure 2).

Results: The ICG clearance rates for the four patients at different points of their HD treatments are given in Table 1. K_E decreases over the course of the study for patients 1, 3 and 4. Patient 2 was edematous to start and so HD may have decreased the edema, leading to improved liver function.

Table 1: Calculated ICG clearance rate, K_E , values for four patients before, during and after hemodialysis.

*Patient 4 could only dialyze for 3 hours, so ICG clearance was measured 1.5 hours (i.e., halfway) into dialysis.

| Patient | K_E (ml/min) | | | |
|---------|----------------|----------------|-----------------|----------|
| | Before HD | 1 hour into HD | 3 hours into HD | After HD |
| 1 | 493.4 | 416.1 | 290.3 | 317.5 |
| 2 | 78.1 | 99.0 | 84.7 | 94.3 |
| 3 | 92.1 | 77.1 | 77.2 | 65.7 |
| 4 | 751.0 | 541.3* | | 327.5 |

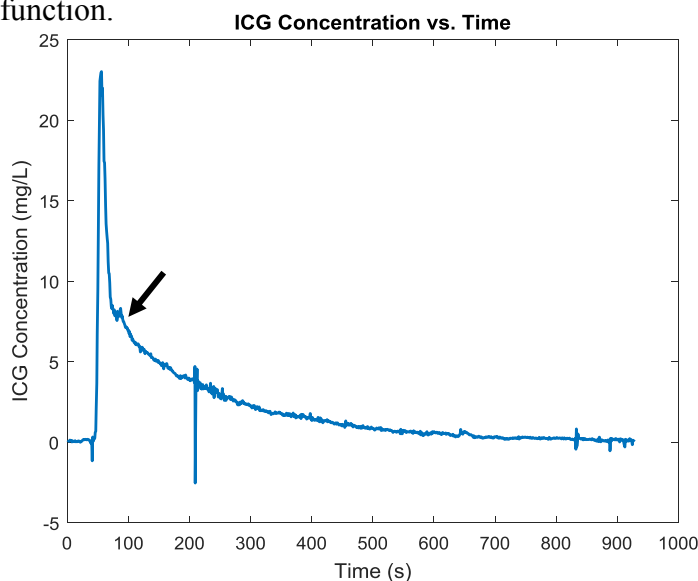


Figure 2: ICG concentration as a function of time. Arrow indicates time when ICG is homogeneously mixed in plasma compartment.

Conclusions: Overall, hemodialysis had the effect of decreasing the clearance rate of ICG by the liver. These results suggest that hepatic function is attenuated due to the hemodynamic stresses of dialysis on liver perfusion.

Numerical Optimization Accuracy & Performance of a Perfusion Kinetic Modeling Algorithm using Volumetric DCE CT

I. Svistoun^{1,2}, C. Coolens^{1,2,3}

¹Ontario Institute for Cancer Research Imaging Translation Program

²Radiation Medicine Program, Princess Margaret Cancer Center, Toronto, Ontario, Canada

³Departments of Radiation Oncology and IBBME, University of Toronto

Introduction: Dynamic-contrast enhanced (DCE) CT imaging is increasingly being used to quantify tissue vascular and functional properties for treatment response assessment by its combination with tracer kinetic modeling. However, clinical kinetic parameter results have been shown to be highly dependent on measurement input and analysis method. Implementing the parameter estimation algorithm involves many design decisions including choice of: data processing sampling rate, continuous-to-discrete system mapping approach and numerical optimization algorithm. As such a simulation framework was designed to investigate the effects of those choices, as well as effects of measured signal aliasing and noise on the accuracy and speed of the parameter estimation.

Methods: A widely-used 2-compartment model (modified Tofts) was chosen which describes the dynamic perfusion properties of a contrast agent using 4 parameters: K_{trans} - transfer from blood plasma into extracellular extra-vascular space, K_{ep} - transfer from extracellular extra-vascular space back to blood plasma, V_b - whole blood volume per unit tissue. To account for separation between injection and measurement site, a time delay τ must be added. The 4 parameter estimation from the measured data requires numerical optimization. Some approaches fit only the first 3 parameters, and require human interaction to estimate the τ . However this introduces operator bias by requiring the operator to visually estimate the delay, and typically does not account for varying τ across the volume, since making hundreds of estimates would be too tedious for a human operator. Therefore for all 4 parameters was used. A test framework was developed where an experimentally derived population-average arterial input function and randomly sampled parameter sets $\{K_{trans}, K_{ep}, V_b, \tau\}$ were used to generate tissue curves. Knowing the ground truth values, 5 numerical optimization algorithms were investigated using multiple starting points from a quazi-random set: sequential quadratic programming (SQP), downhill simplex (Nelder-Mead), pattern search (PS), simulated annealing (SA), and differential evolution (DE). Furthermore, objective function implementation details including: fractional delay filter, discretization approaches – finite impulse response (FIR) and infinite impulse response (IIR) - and varying sampling rates - 1, 10, 20 and 100 Hz - were evaluated to measure their impact on accuracy and speed. DE and Nelder-Mead algorithms were implemented in CUDA to run on a GPU for speed improvement testing since processing even a modest area of 128x128x200 voxels would require days on the CPU.

Results and Conclusions: Nelder-Mead, DE and SQP produced good results on clean and noisy input data outperforming SA and PS in terms of speed and accuracy by a wide margin. Best accuracy achievable under ideal conditions by SA and PS was on average 3.85% and 2.79% overall relative percent error, while Nelder-Mead, DE and SQP could recover original parameters with mean overall relative error of $5.69 \times 10^{-8}\%$, $3.27 \times 10^{-7}\%$, and $8.97 \times 10^{-6}\%$ respectively. When the best algorithms processed a generated data set that matched a typical scanning protocol sampling rate with added white noise ($\sigma = 6HU$) the mean overall relative percent error was found to be 9.61% which represents a lower bound on error when processing this type of noisy data. The continuous Tofts model can be approximated using discrete infinite impulse response (IIR) filter via bi-linear transformation at 1 Hz combined with a fractional delay filter to achieve accuracy results within 1% of the lower bound derived earlier; the average run-time was 5.97 s/voxel on the CPU. In contrast using finite impulse response (FIR) filter discrete approximation required sampling rates of 20Hz (20x the memory) and 24.1 s/voxel to achieve the levels of accuracy near the derived limit. Nelder-Mead and DE were implemented on the GPU for performance reasons and it was found that Nelder-Mead provided the highest performance improvement - 842x (5.59×10^{-3} s/voxel) than its CPU counterpart.

Optimal strategy for quantifying hypoxia from static PET imaging

Edward Taylor¹, Ivan Yeung^{1,2}, Harald Keller^{1,2}, Cristiane Metran-Nascente³, Douglass C. Vines¹, Ur Metser⁴, Neesha C. Dhani³, David Green¹, Michael Milosevic¹, David W. Hedley³, David Jaffray^{1,2,5}

1. Radiation Medicine Program, Princess Margaret Cancer Centre, Toronto, Canada.
2. Department of Radiation Oncology, University of Toronto, Toronto, Ontario, Canada.
3. Division of Medical Oncology and Hematology, Princess Margaret Cancer Centre, Toronto, Canada.
4. Department of Medical Imaging, Princess Margaret Cancer Centre, Toronto, Canada.
5. Techna Institute, University Health Network, Toronto, Ontario, Canada.
Ontario Institute for Cancer Research – Imaging Translation Program

Introduction. PET imaging with F-18-labelled hypoxia-sensitive tracers such as FMISO and FAZA has emerged as a promising non-invasive way of detecting hypoxia in tumours, a condition which correlates negatively with responses to radiation- and chemo-therapy. A key challenge in using *static* PET data to quantify hypoxia is that the tracer uptake in a region of interest (ROI) is sensitive not only to hypoxia, but also to transport properties---perfusion, diffusion, permeability, and blood volume---which vary between voxels and patients. This sensitivity must be reduced before PET imaging becomes the standard for determining hypoxia.

Method. A compartmental model based on a reaction-diffusion equation was used to study FAZA pharmacokinetics. Assuming diffusive equilibrium is achieved rapidly within the ROI, a simple expression

$$C(t) \approx \text{AIF}(t) + K_3 \times \text{AUC}(t) \quad (1)$$

was derived for the time (t) dependent tracer activity C in terms of the arterial input function (AIF), the area under the curve (AUC) for the unbound compartment, and a quantity K_3 which is argued to be proportional to the fraction of space for which the oxygen tension is below ~ 10 mmHg; i.e., hypoxic. Eq. (1) was used to study PET data from 19 patients with pancreatic cancer who were injected with FAZA. Comparing activities in tumour ROIs with values taken from two reference tissues, spinal muscle and blood, the sensitivity of PET imaging to transport inhomogeneities was quantified within the framework of our transport model.

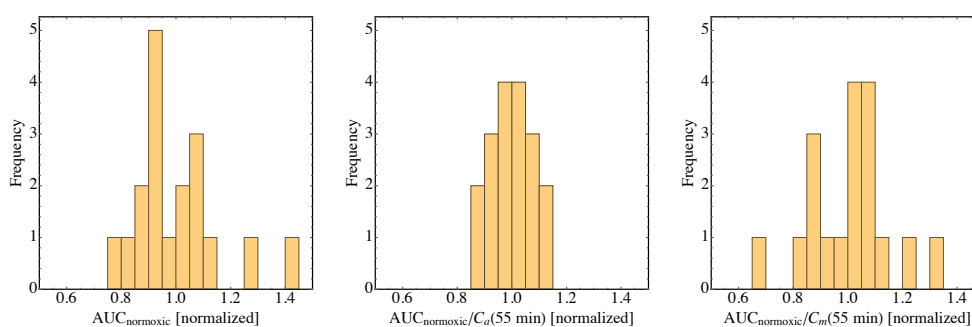


Fig. 1 Normalized AUC for nineteen pancreas tumours

Results. Dividing activity in the ROI by a reference value taken from the patient leads to a reduction in the sensitivity to inter-patient transport inhomogeneities: differences in blood volumes and clearance rates. Because it is poorly perfused, spinal muscle exhibits significant variability in FAZA uptake. In contrast, using blood as a reference leads to a substantial reduction in the sensitivity to transport inhomogeneities, as shown in the middle panel of Fig. 2 where the AUC divided by the AIF—related to hypoxia by Eq. (1)—exhibits a smaller variance than the AUC (left), and the AUC divided by the activity in the spinal muscle (right).

Conclusions. By dividing the measured tracer activity in a region-of-interest contained inside a tumour by a reference value taken from the same patient, PET measurements are sensitive to the presence of hypoxia. The choice of blood as a reference tissue optimizes this sensitivity although our work also delineates the circumstances under which muscle can also reliably be used.

Effects of respiratory gated ^{18}F -FAZA PET-CT on hypoxic fraction in patients and phantom

Douglass C. Vines, Brandon D. Driscoll, Ivan Yeung, Julia Publicover, Alexander Sun, and David A. Jaffray.

(1) Radiation Medicine Program, Princess Margaret Cancer Centre, Toronto, ON

(2) Techna Institute, University Health Network, Toronto, ON

(3) Dept. Radiation Oncology, University of Toronto, Toronto, ON.

Introduction: Respiratory gated (4D) PET has been shown to quantitate radioactivity more accurately in the presence of motion. The purpose of this study was to evaluate the feasibility and potential benefit of using the 4D method in ^{18}F -Fluoroazomycin arabinoside (FAZA-PET) lung imaging with respect to the estimation of hypoxic fraction (HF) in phantom and patient-derived datasets.

Methods: The uptake of FAZA in patient tumor (T) and erector spinae muscle (M) were used to guide the amount of ^{18}F placed into phantom compartments that simulate T and M. The phantom had 3 compartments simulating T, M, and lung and was moved with a known respiratory cycle and amplitude. Attenuation correction (AC) was performed using a helical CT (hCT) for both non-gated and 4D PET data (6 bin). A 4D-CT was also used to reconstruct the matching phase of the 4D PET to create phase-matched AC 4D PET data (PM). PET-CT images of all 6 bins for the phantom were assessed quantitatively for both AC methods by manually placing a 3D volume-of-interest over T and M to measure radioactivity. HF was then estimated according to the method of Mortensen et al, 2012. Using the same methods, and only the primary tumor exhale bin in patients, a study of 9 of the planned 20 patients (non-small cell lung cancer) was performed.

Results: The average FAZA uptake in the 9 patients T (maximum) and M (mean) for exhale PM was 4.9 and 2.2 kBq/ml, respectively. This compared closely to the phantom experiment using 4.2 and 2.1 kBq/ml for simulated T and M. The phantom HF was greater for PM than hCT for all 6 bins, and both 4D PET methods had higher HF than the non-gated method. Patients were divided into 2 groups: motion greater than, or less than 5mm. In patients with motion $> 5\text{mm}$ there appears to be little difference between the NG, hCT, and PM data unlike in the phantom. There may however be differences in the spatial distribution of the hypoxia with the 3 methods

Conclusions: The phantom study demonstrated that 4D PET was both feasible and beneficial with PM having consistently higher values of HF compared to hCT and non-gated data. In the patients 4D PET was feasible, however in the 3 patients with motion, the potential benefit was not as evident as the phantom data. Additional patient datasets with tumor motion are required to determine the usefulness of 4D PET in the context of FAZA lung imaging.

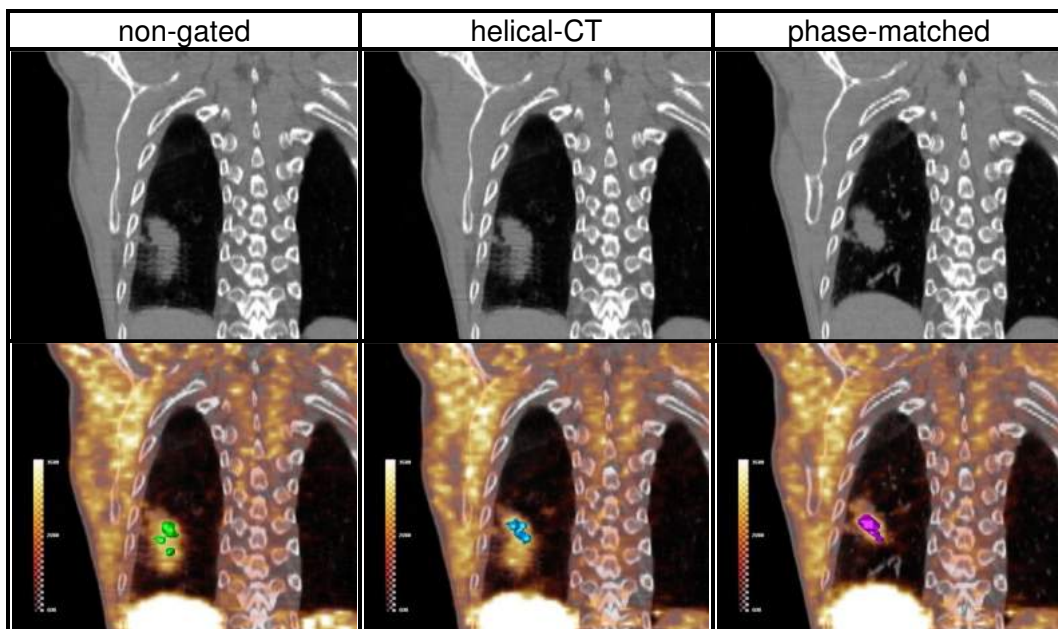


Figure 1

Top row: Helical CT and 4DCT (PM) single coronal slices for each of the 3 methods.

Row 2: PET-CT fused slices with HF displayed in 3D:

non-gated HF = 11.1%

helical CT HF = 14.8%

phase-matched HF = 13.3%

Evaluating the non-small cell lung cancer between pre- and post- radiation therapy

Dae-Myoung Yang^{1,2}, David Palma⁴, and Ting-Yim Lee^{1,2,3} (Supervisor)

¹Department of Medical Biophysics, Western University, London, Ontario, Canada

²Robarts Research Institute, Western University, London, Ontario, Canada

³Lawson Health Research Institute, London Health Sciences Centre, London, Ontario, Canada

⁴Radiation Oncology, London Regional Cancer Program, London, Ontario, Canada

Introduction. Lung cancer is the leading cause of cancer death for both men and women in Canada. Stereotactic ablative radiation therapy (SABR) is a new radiation treatment that delivers high-dose, precise radiation to small tumours. (1) The purpose of this study (MISSILE) is to measure the integration of SABR in non-small cell lung cancer (NSCLC).

Methods. Eight lung cancer patients who have histologically confirmed NSCLC tumour stage T1 or T2a (less than or equal to 5 cm) underwent dynamic contrast enhanced-CT (DCE-CT) and FDG-PET pre- and post-SABR. The post scans were acquired eight weeks after SABR. DCE-CT imaging allows quantitative mapping of blood flow (BF) and blood volume (BV) in the tumours. Since free-breathing was allowed during DCE-CT scanning, breathing motion was minimized by non-rigid image registration (prototype algorithm from GE healthcare) before the BF and BV functional maps were generated with CT Perfusion (GE Healthcare).

Results. DCE-CT images show that following SABR, there was a reduction in tumour size (Figure 1). Moreover, DCE-CT functional maps show that both tumor BF and BV decreased post-SABR (Table 1).

Conclusions. This study demonstrates the effectiveness of SABR in treating NSCLC. DCE-CT showed reduction in tumour size, BF and BV. In future analysis, the metabolic uptake of FDG can be calculated using a hybrid DCE-CT/PET three compartment kinetic model (2).

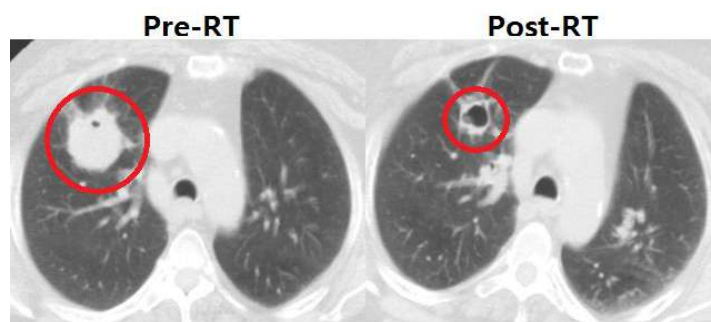


Figure 1. DCE-CT image of a patient pre- and post-SABR study. The tumor (red circle) was in the left lobe of the lung.

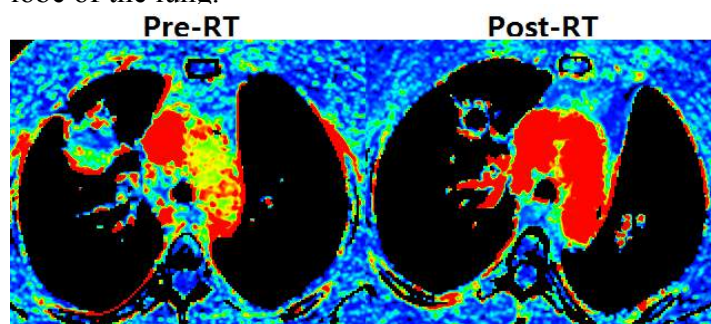


Figure 2. DCE-CT blood flow maps of figure 1.

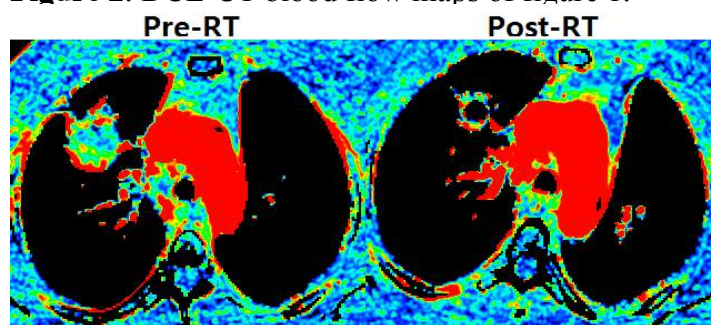


Figure 3. DCE-CT blood volume maps of figure 1.

Table 1. Characteristic of each patient's tumour used in the analysis

| Patient | BF, Pre- (mL/(100g·min)) | BF, Post- (mL/(100g·min)) | BF change (%) | BV, Pre- (mL/100g) | BV, Post- (mL/100g) | BV change (%) |
|---------|-----------------------------|------------------------------|------------------|-----------------------|------------------------|------------------|
| 1 | 189.7 | 118.2 | -37.7 | 15.1 | 5.1 | -66.2 |
| 2 | 164.2 | 79.7 | -51.5 | 15.9 | 12.7 | -20.5 |
| 3 | 173.1 | 142.2 | -17.8 | 9.7 | 7.2 | -25.3 |
| 4 | 190.9 | 27.4 | -85.6 | 20.1 | 1.9 | -90.4 |
| 5 | 308.1 | 146.0 | -52.6 | 14.8 | 10.6 | -28.3 |
| 6 | 243.1 | 190.3 | -21.7 | 16.0 | 11.4 | -28.5 |
| 7 | 105.1 | 86.9 | -17.3 | 9.1 | 5.8 | -36.3 |
| 8 | 550.8 | 220.7 | -59.9 | 28.2 | 12.3 | -56.5 |
| Mean | | | -43.0 | | | -44.0 |

References. [1] Chang *et al.*, *Radiat. Oncol.*, 2012;7:152. [2] Blais *et al.*, *World Congress on Med. Phys. & Biomed. Engi.*, 2015;51:154-157

Effects of the acquisition window length on articular cartilage sodium MR image quality

Alireza Akbari^{1,2}, and Michael D. Noseworthy^{1,2,3}

¹School of Biomedical Engineering, McMaster University, Hamilton, ON, Canada, ²Imaging Research Centre, St Joseph's Healthcare, Hamilton, ON, Canada, ³Electrical and Computer Engineering, McMaster University, Hamilton, ON, Canada

Introduction Sodium magnetic resonance imaging (MRI) is challenging because of the limited signal-to-noise-ratio (SNR). It also suffers from image blurring due to its short biexponential transverse relaxation, T_2 . One way to improve SNR, would be lengthening the acquisition window. SNR is proportional to the square root of the acquisition window, T_{acq} (1). However, the SNR gain would be at the cost of increased image blurring. One sodium MRI application is the assessment of articular cartilage as studies have shown direct correlation between osteoarthritis (OA) severity and articular cartilage sodium content (2-4). Enhancing articular cartilage sodium MR image quality would lead to more accurate sodium quantification and a better assessment of OA severity. The goal of this work was to investigate the balance between sodium image SNR gain and deleterious image blurring when lengthening T_{acq} .

METHODS A density-adapted 3-dimensional projection reconstruction (DA-3DPR) sequence (5) was implemented on a GE MR750 3T (General Electric Healthcare, Milwaukee WI) and home-built 12-rung split design 18cm diameter birdcage transmit/receive RF coil tuned for ^{23}Na (53.311MHz). Sodium DA-3DPR datasets corresponding to $T_{acq} = 4, 8, 12, 16, 20,$ and 25ms were acquired with the following imaging parameters: TE/TR = 0.25/100ms, 11310 projections, isotropic resolution/FOV = 3mm/18cm, and averaging = 2. All images were reconstructed into 60 slices of 540x540 (i.e. 0.3mm in-plane resolution x 3mm thick) using a non-uniform fast Fourier transform (NUFFT) (6). To quantify the effect of readout window length on blurring, the full-width-at-half-maximum (FWHM) of the slice profile across the patellar cartilage was measured for each T_{acq} and SNR was calculated according to Madelin et al. (7).

RESULTS In vivo axial views of the knee with various T_{acq} durations are shown in figure 1. The background noise was noted to markedly decrease as T_{acq} was increased, with only a slight increase in image blurring. The SNR measurement for patellar cartilage is shown in figure 2 for each T_{acq} . The SNR increased considerably with respect to the $T_{acq}=4\text{ms}$ data as indicated by the numbers above each bar. The blurring caused by T_{acq} lengthening in the patellar cartilage is shown in Figure 3. The FWHM as a measure of blurring was observed to slightly broaden by a maximum of 1mm in the articular cartilage as T_{acq} was increased from 4 to 25ms.

CONCLUSIONS Our results indicate that SNR is doubled when T_{acq} is increased from 4 to 25 ms. Image blurring is expected due to short T_2 relaxation (10-30ms) (8); however, the FWHM measurements indicate minimal image blurring. This is in agreement with the measured amount of blurring for a DA-3DPR acquisition scheme (5). This work demonstrates that the benefits of increasing T_{acq} in terms of SNR gain outweighs the minimal adverse effects of blurring on articular cartilage sodium MR image quality using DA-3DPR.

REFERENCES

- Haacke EM, et al. John Wiley and Sons; 1999.
- Lesperance LM, et al. J Orthop Res. 1992;10(30):1-13.
- Reddy R, et al. Magn Reson Med. 1998;39(5):697-701.
- Shapiro EM, et al. Magn Reson Med. 2002; 47(2):284-291.
- Nagel AM, et al. Magn Reson Med. 2009;62(6):1565-1573.
- Fessler J a. J Magn Reson. 2007;188(2):191-195.
- Madelin G, et al. Magn Reson Med. 2012;68(3):841-849.
- Madelin G, et al. Prog Nucl Magn Reson Spectrosc. 2014;79:14-47.

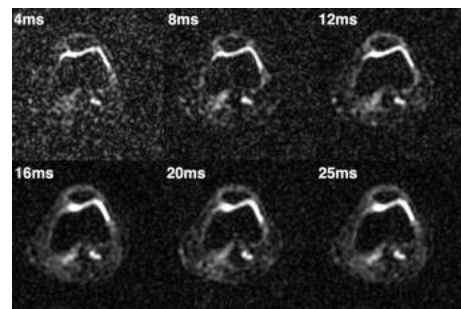


Figure 1. Sodium ^{23}Na images of a healthy human knee obtained with various acquisition window lengths.

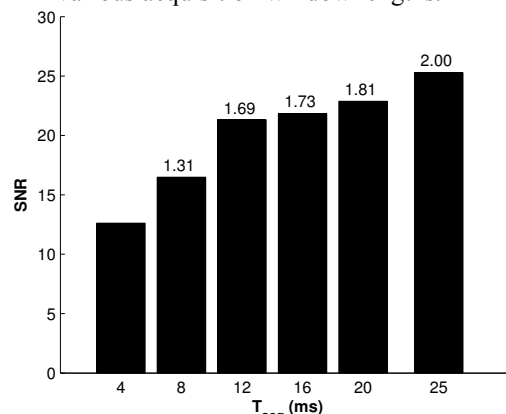


Figure 2. SNR in patellar cartilage from Figure 1 images. The SNR gain relative to $T_{acq} = 4\text{ms}$ is indicated by the number above each bar.

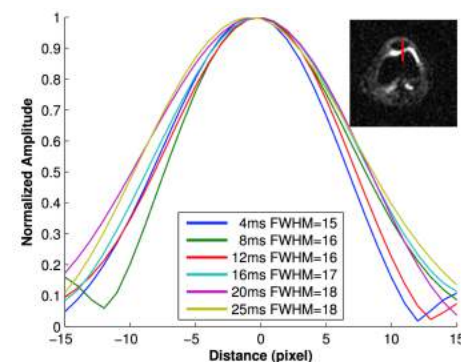


Figure 3. Patellar cartilage slice profiles from Figure 1 images. FWHM as a measure of image blurring in patellar cartilage was calculated for each image. The location of the slice profile is indicated by the orange line drawn in the image at the top-left corner of the figure.

In vivo sodium (^{23}Na) magnetic resonance imaging of human knee using a pseudo-random k-space sampling scheme

Alireza Akbari¹, Konrad Anand², Christopher Anand^{3,4}, and Michael D. Noseworthy^{1,4}

¹School of Biomedical Engineering, McMaster University, Hamilton, Ontario, ²Optimal Computational Algorithms Inc., Ontario, ³Computing and Software, McMaster University, Ontario, ⁴Electrical and Computer Engineering, McMaster University, Ontario

INTRODUCTION: 3-dimensional center-out k-space sampling schemes are at the heart of *in vivo* sodium (^{23}Na) magnetic resonance imaging (MRI) since they offer ultra-short echo times making them ideal for short T2 species such as ^{23}Na . Some of these schemes, such as spectrally weighted twisted projection imaging (TPI)[1], require fewer number of projections in order to fulfil the Nyquist sampling criterion thus leading to shorter scan times. In order to lessen scan time, the number of projections can even be reduced further (i.e. undersampling) at the cost of inducing aliasing artefacts. However, aliasing could be minimized if undersampling is done in a random fashion because it leads to incoherent summation of the aliasing artefacts. This has been the basis for the DURGA sequence using in proton imaging [2]. In this work, we demonstrate the feasibility of pseudo-random k-space sampling (**fig.1**) for *in vivo* ^{23}Na MRI that allows shorter scan times.

METHODS: In order to compare the ability of the pseudo-random scheme in minimizing aliasing artefacts, it was compared to a simulated Cartesian

undersampling scheme. Two sets of 392 trajectories were generated; one with uniformly distributed pseudo-random samples and the other with regularly spaced Cartesian samples. A simulated phantom was sampled and reconstructed using the two sets (**fig.2**). The pseudo-random set was then used to obtain *in vivo* ^{23}Na MR images. Sodium MRI was performed using a GE MR750 3T (General Electric Healthcare, Milwaukee WI) and an in-house-made 16-pole quadrature sodium birdcage coil. The pulse sequence consisted of a single $500\mu\text{s}$ hard pulse, $\text{TE/TR} = 0.46/75$ ms, flip angle = 90° , $\text{NEX} = 32$, 1000 samples per trajectory, sampling rate of $4 \mu\text{s}/\text{sample}$, leading to a total scan time of 16 minutes. The trajectories were designed for a nominal isotropic resolution of 3 mm. Sodium images of a healthy knee were acquired to demonstrate *in vivo* utility.

RESULTS: The effect of under sampling using the two sampling schemes are shown (**fig.2**). Figure 3 demonstrates the *in vivo* sodium knee MR images acquired using pseudo-random sampling scheme.

CONCLUSION: The results indicate that pseudo-random sampling remarkably reduces the aliasing artefacts caused by undersampling. The *in vivo* results confirm the feasibility of this scheme for ^{23}Na MRI. This scheme will help reduce the total scan time through a high sampling-duty cycle with fewer trajectories, while keeping aliasing artefacts minimal due to the randomness of the sampling scheme.

REFERENCES [1] Boada FE, et al. Magn Reson Med. 1997;38(6):1022–8. [2] Curtis AT, Anand CK. Int J Biomed Imaging. 2008;2008.

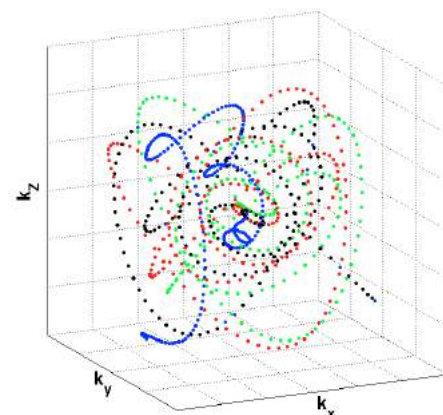


FIG. 1. A subset of pseudo-random 3D k-space trajectories. Each color represents one individual trajectory.

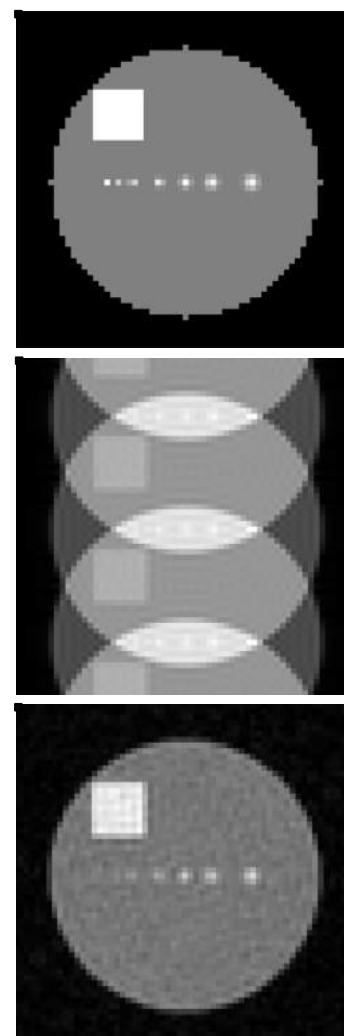


FIG 2. Simulating aliasing artefacts due to undersampling a true image (a). b) Reconstructed image using Cartesian scheme. c) Reconstructed image using

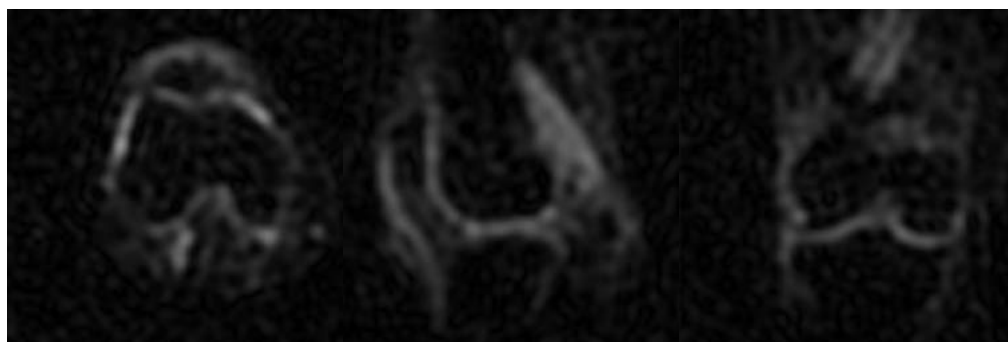


FIG. 3. Axial, sagittal, and coronal views of *in vivo* sodium image of a healthy subject's knee.

Assessing the Effects of Inflammation and Fibrosis using Inert Fluorinated Gas MRI

Marcus J. Couch^{1,2}, Matthew S. Fox^{3,4}, Chris Viel^{1,2}, Gowtham Gajawada^{1,2}, Tao Li^{1,2}, Alexei V. Ouriadov³, and Mitchell S. Albert^{1,2}.

(1) Lakehead University, Thunder Bay, Ontario, Canada. (2) Thunder Bay Regional Research Institute, Thunder Bay, Ontario, Canada. (3) Robarts Research Institute, Western University, London, Ontario, Canada. (4) Department of Medical Biophysics, Western University, London, Ontario, Canada

Introduction: The instillation of lipopolysaccharide (LPS) or bleomycin in rodent lungs has been established as models that mimic inflammation and fibrosis. LPS- and bleomycin-induced lung injury have been previously studied using hyperpolarized (HP) ¹²⁹Xe MRI (1); however, ¹⁹F MRI of the lungs using inert fluorinated gases is emerging as a new and promising alternative. Inert fluorinated gas MRI does not require an expensive polarizer, and the gases are nontoxic, abundant, and inexpensive. In this study, dynamic ¹⁹F MRI was performed in LPS- and bleomycin-instilled rats, and fractional ventilation maps were derived.

Methods: 15 male Sprague Dawley rats (340±31g) were imaged using a 3T Philips Achieva. 5 rats were instilled with a dose of 2.5mg/kg of LPS two days prior to imaging, 6 rats were instilled with a dose of 2.5mg/kg of bleomycin two weeks prior to imaging, and the remaining 4 rats were used as controls. Fractional ventilation maps were obtained using the method of Ouriadov et al. (2). Rats were ventilated in the supine position with a mixture of 80% sulfur hexafluoride (SF₆) and 20% O₂. Breathing was switched to pure O₂ for 9 breaths, and following each breath, a 2D ¹⁹F MR image was acquired during a 10s breath-hold. Washout images were fitted on a pixel-by-pixel basis in order to calculate the fractional ventilation parameter, *r*, defined as the volume of fresh gas entering a volume divided by its end-inspiratory volume.

Results: Figure 1 shows ventilation maps acquired in the axial plane from a control rat, an LPS-instilled rat, and a bleomycin-instilled rat. Bleomycin-instilled rats had a significantly decreased mean *r* value compared to controls (*p*=0.010). For LPS-instilled rats, there was a trend towards decreased *r* values, however, this trend was not statistically significant (*p*=0.56). Figure 2 shows representative fractional ventilation gradients in the anterior/posterior (A/P) direction for each group. Fractional ventilation gradients were significantly different for control rats compared to LPS-instilled rats only (*p*=0.016). Gradients from control rats agreed with expectations, where ventilation was greatest in dependent regions of the lung. Gradients from LPS- and bleomycin-instilled rats had a positive slope, and this result may be explained by changes in lung compliance in dependent lung regions. Histology confirmed the presence of inflammation in LPS-instilled rats and fibrosis in bleomycin-instilled rats.

Conclusions: To our knowledge, fractional ventilation mapping has not been previously performed using ¹⁹F MRI in an animal model of lung disease. This technique has the potential to detect the effects of inflammation and fibrosis using a simple and inexpensive approach that can potentially be translated to humans.

References: [1] Cleveland et al. (2014) NMR Biomed 27:1502-1514. [2] Ouriadov et al. (2015) Magn Reson Med 74: 550–557.

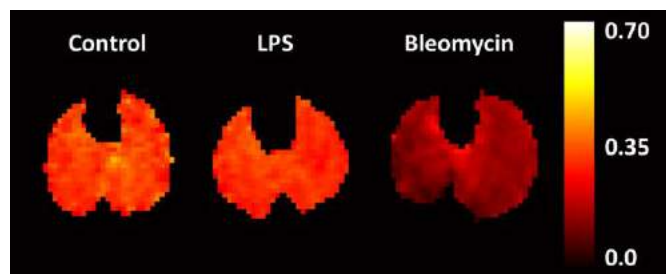


Figure 1: Representative fractional ventilation maps obtained in the axial plane from a control rat, an LPS-instilled rat, and a bleomycin-instilled rat.

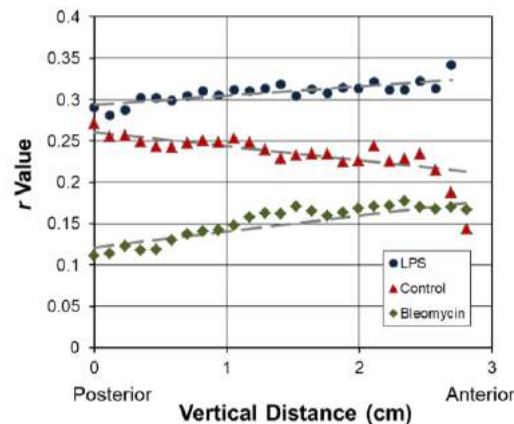


Figure 2: Fractional ventilation gradients calculated in the A/P direction from a control rat, an LPS-instilled rat, and a bleomycin-instilled rat.

Dependence of Signal-to-Noise Ratio on Radiofrequency Coil and Static Magnetic Field Strength for Preclinical Hyperpolarized ^{129}Xe Gas MRI of the Brain

Consortium - Other

Yonni Friedlander, Andrea Kassner and Giles Santyr

Department of Medical Biophysics, University of Toronto, Toronto, Ontario, Canada

Peter Gilgan Centre for Research & Learning, Hospital for Sick Children, Toronto, Ontario, Canada

Introduction: Hyperpolarized (HP) ^{129}Xe MRI is promising for the assessment of brain. One of the major challenges facing HP ^{129}Xe MRI of the brain, is a limited signal-to-noise ratio (SNR) due to low solubility and polarization losses in the blood stream on route to the brain [1]. There are several approaches that are traditionally considered for improving MRI SNR including higher magnetic field strengths, more averaging and improved radiofrequency (RF) coil design. However, it has previously been demonstrated that, because of an inverse proportionality with T_2^* , increasing the field strength has only limited benefits for increasing HP SNR [2]. Furthermore, because the polarization is non-recoverable, increasing the number of averages is not a feasible means for increasing SNR. Therefore, SNR gains from optimal RF coil design are imperative for HP MRI of the brain. In this work, the dependences of HP gas SNR on birdcage coil size and static magnetic field strength are examined theoretically.

Method: SNR calculations were based on a previously established theoretical model for the SNR of a birdcage coil [3][4]. The effects of T_2^* for HP ^{129}Xe of the lung developed by Parra-Robles et al were also included in the calculations [2]. The coil height and leg width were assumed to scale linearly based on the dimensions of a typical rat-sized (radius = 6 cm) coil (Morris Instruments, Ottawa, Canada). The sample size was kept constant with a radius of 1.5 cm to approximate the dimensions of a rat.

Results: Figure 1 shows the SNR improvement as a function of coil radius for three different magnetic field strengths (B_0). It is evident that even a modest reduction in coil size provides a very large improvement in SNR. Furthermore, the SNR dependence on B_0 is largely independent of field strength. Figure 2 shows the phenomenon of decreasing HP ^{129}Xe SNR with increasing B_0 due to the effect of decreasing T_2^* on bandwidth [2]. The field strength where the maximum SNR occurs increases with decreasing coil size. However, the maximum SNR for the 1.7 cm radius coil (1.02 T) is still less than the magnetic field strength found in most commercial clinical MRI systems. The location of the peak is dependent on T_2^* so future studies will develop a model for T_2^* in the brain.

Discussion and Conclusion: Even a slightly oversized coil can greatly reduce the SNR. For example, a 6 cm radius coil has an SNR that is over forty times worse than a 1.7 cm radius coil. The effect shows little dependence on static magnetic field strength so, for all experiments, using an appropriately sized coil can greatly improve the results. If a larger coil size is desired for field uniformity, similar gains could also be realized through the development of transmit-only/receive-only (TO/RO) coil with an appropriately small receive coil [5]. For most practical coil sizes and field strengths, the SNR is inversely proportional to the static magnetic field strength. In order to maximize the limited HP ^{129}Xe signal available in the brain, future experiments should use coils fit as closely as possible to the subject's head, especially at the static magnetic field strengths used for clinical MRI.

Acknowledgements: Funded by NSERC and OGSST-QEII **References:** [1] Li, Haidong et al, NMR in Biomedicine (2016) [2] Parra-Robles, J. et al, Medical Physics 32, (2005), 221-229. [3] Hoult, D.I. and Richards, R.E., Journal of Magnetic Resonance, 24, (1976), 71-85. [4] Hurlston, S.E. et al, Int. J. Imaging Syst. Technol, 8, (1997), 277-284. [5] Doganay, O. et al, Concepts Magn. Reson, 45, (2015), 115-124

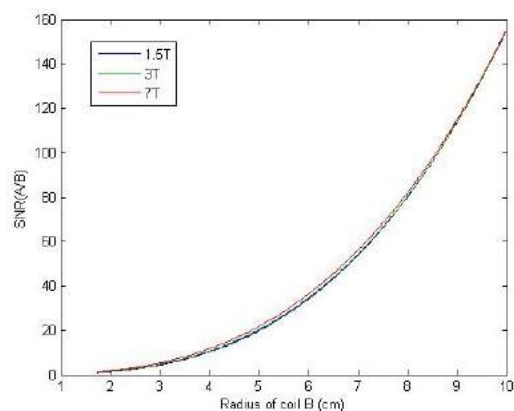


Fig 1: Ratio of SNR for a mouse sized coil ($r = 1.7$ cm) to coils with varying radii.

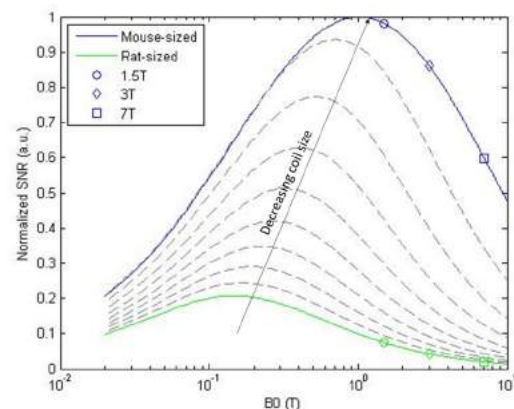


Fig 2: SNR as a function of field strength.

Characterizing the role of stress and Neuropeptide Y in breast cancer metastasis

Kara J^{*1,2}, Hryniewicz J³, Makela A², Foster PJ², Jackson D¹

Ontario Institute for Cancer Research Smarter Imaging Program

1. Department of Medical Biophysics, The University of Western Ontario, London, Ontario

2. Imaging Research Laboratories, Robarts Research Institute, London, Ontario, Canada

3. Department of Biology, The University of Western Ontario, London, Ontario, Canada

Introduction: Studies have demonstrated a correlation between stress and an increased risk of breast cancer. Neuropeptide Y (NPY) expression is up-regulated in chronic stress and is documented to induce proliferation and chemotaxis of 4T1 breast cancer cells via Y5 receptor (Y5R) activation¹. The objective of this study is to identify and characterize the NPY-Y5R as a regulatory system of breast cancer metastasis and recurrence. In this work we compare three breast cancer cell sublines derived from the same mouse mammary fat pad (MFP) tumour, that differ greatly in metastatic potential (67NR, 168FARN, and 4T1). We also compare the highly metastatic 4T1 cell line with a 4T1-Y5R knockdown established in our labs. We are using *in vitro* cell assays, flow cytometry and *in vivo* MRI to investigate the contribution of NPY to the process of metastasis.

Methods: *In vitro assays:* Immunocytochemistry was conducted on 67NR, 168FARN, and 4T1 cells to confirm the presence and localization of Y5R and Western blotting was done to quantify the protein expression of Y5R. An MTS assay was used to investigate the proliferative potential of the breast cancer cell lines induced by NPY (10^{-11} M to 10^{-6} M) and the inhibitive effect of L-152 804 (10^{-4} M), a specific antagonist of Y5R. A 4T1-Y5R knockdown has been established using shRNA and purified with flow cytometry. *In vivo assays:* MRI is underway to assess the developing primary tumour, the presence of metastases in liver, lung and lymph nodes and the presence of iron-retaining metastatic cancer cells. A 3T GE MRI system equipped with a high performance gradient coil insert is being used to acquire whole body mouse images in Balb/c mice implanted orthotopically with each of the cell lines. Cells will be pre-labeled with micron-sized iron particles for cell tracking by MRI.

Results: Immunocytochemistry revealed Y5R expression in 4T1 cells that was predominantly cytoplasmic and Y5R expression in 67NR and 168FARN cells that was nuclear (Fig1). Western blots revealed a significantly greater Y5R expression ($p < 0.05$) in the aggressive 4T1 cell line compared to the 67NR and 168FARN cell lines. Neuropeptide Y had a significant concentration dependent effect ($p < 0.01$) on the proliferation of 4T1, 168FARN and 67NR cells at various concentrations. The Y5R antagonist was able to restore the growth of the cells to the same level as the control in all three cell lines ($p < 0.05$). These results have set the groundwork to proceed to an MRI investigation of tumour growth and metastatic potential of the three cell lines and the 4T1-Y5R knockdown.

Conclusion: Breast cancer lines with a higher metastatic potential express significantly greater Y5R and cytoplasmic localization of the Y5R could support an aggressive phenotype. Neuropeptide Y has the potential to stimulate the proliferation of breast cancer cell lines of various levels of aggression. Y5R antagonists block this stimulatory effect supporting that proliferation is modulated by the NPY-Y5R system. If a direct link can be established between the physiological stress response and breast cancer progression, NPY and its Y5 receptor could be potential therapeutic targets to combat breast cancer metastasis.

References: 1. Medeiros *et al.* Int J Cancer 2012; 131(2): 276-286



Figure 1. DAB immunocytochemistry of Y5R expression of 67NR, 168FARN, and 4T1 cells (top to bottom).

Detecting Hippocampal Changes in Mice on a Diet of 2'-Fucosyllactose Using CEST MRI

Wilfred W. Lam¹, Wendy Oakden¹, Lynsie A. M. Thomason¹, John Bienenstock^{2,3}, Andrew M. Stanisz², Paul Forsythe^{2,3}, and Greg J. Stanisz^{1,4,5}

¹Sunnybrook Research Institute, Toronto, ²St. Joseph's Healthcare Hamilton, Hamilton, ³McMaster University, Hamilton, ⁴University of Toronto, Toronto, ⁵Medical University of Lublin, Lublin, Poland

Consortium Affiliation: Ontario Institute for Cancer Research Smarter Imaging Program

Introduction

2'-fucosyllactose is the most common human milk oligosaccharide and has been shown to improve learning and memory in rodents. Chemical exchange saturation transfer (CEST) is sensitive to dissolved proteins containing ¹H nuclei that exchange with those in water and could potentially detect changes in molecules related to memory.

Methods

One cohort of BALB/c mice were gavaged daily for 28 days with 2'-fucosyllactose ($n = 4$) and a control cohort with lactose ($n = 4$). CEST MRI was performed two weeks after the final gavage. ROIs were manually drawn on the hippocampus and cerebral cortex. A model consisting of a sum of five Lorentzian curves assumed to correspond to dissolved amide, amine, and aliphatic; semi-solid lipid; and water components was fitted to the mean signal of each ROI. The normalized area under each curve was compared using unpaired two-sample t -tests.

Results

Figure 1a shows excellent fits to the hippocampus CEST spectra for representative control and treated animals. The residuals do not show any structure and indicate reasonable and sufficient fits. The normalized areas under the amine and aliphatic peaks (Fig. 1b) show significant differences between cohorts for the hippocampus, but not the cortex, which is expected since several major pathways in the hippocampus exhibit long-term potentiation.

Conclusions

2'-fucosyllactose is a potential therapeutic candidate for disorders of the hippocampus and a further longitudinal study including post-mortem biochemistry assay to increase specificity is warranted.

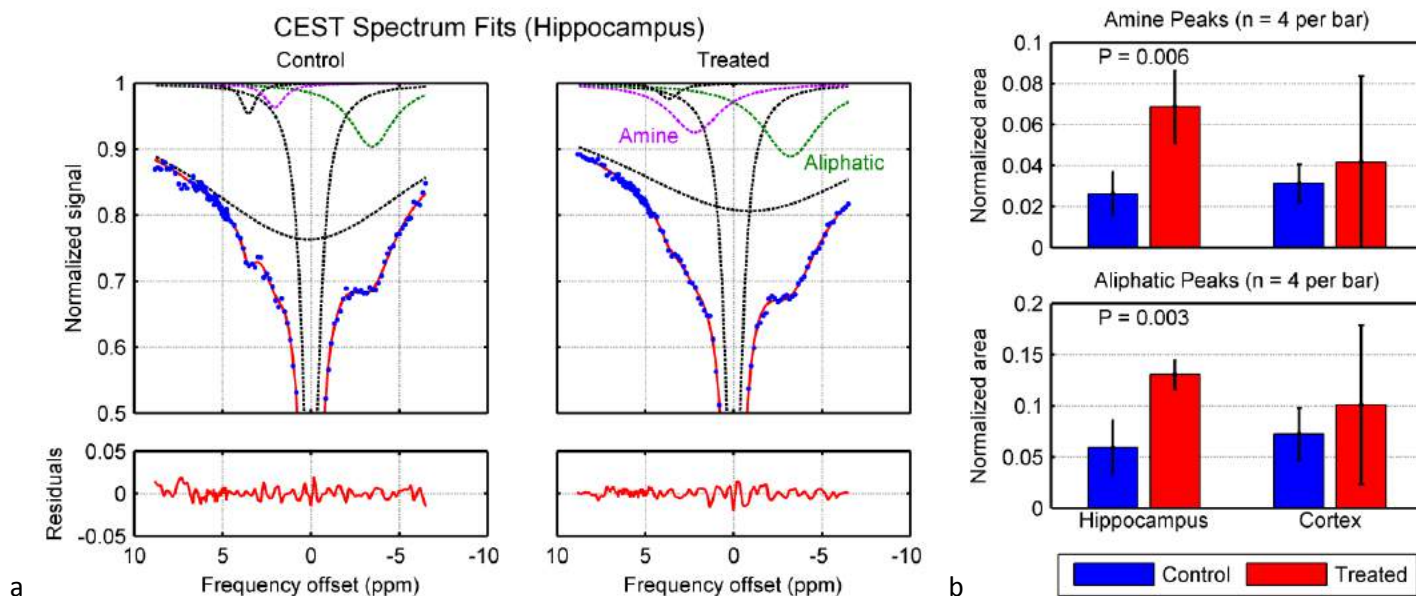


Figure 1. a: CEST spectrum model fits and residuals (solid lines) for data (points) from hippocampus voxels. Model components are shown with dotted lines. b: Normalized mean peak areas and standard deviations for the amine and aliphatic model components.

Acknowledgements

The authors are grateful to Abbott Nutrition for research support.

Dependence of Hyperpolarized ^{129}Xe Lung MRI Morphometry on Diffusion Time, Pressure and Gas Composition

Andras Lindenmaier^{1,2}, Elaine Stirrat², Alexei Ouriadov³, and Giles Santyr^{1,2}

1. Department of Medical Biophysics, University of Toronto, Toronto, ON

2. Peter Gilgan Centre for Research & Learning, The Hospital for Sick Children, Toronto, ON

3. Imaging Research Laboratories, Robarts Research Institute, Western University, London, ON

Introduction: Hyperpolarized ^{129}Xe MRI has been shown to detect microstructural changes in the lung airways associated with various lung pathologies¹. In particular, diffusion-weighted imaging, combined with morphometry, can be used to track microstructural (i.e. alveolar) changes.² For patients suffering from diseases such as cystic fibrosis, chronic obstructive pulmonary disease, emphysema and lung injury, this technique is promising for regional identification of disease and targeting therapy. However, the accuracy of diffusion-weighted MR morphometry depends on several factors pertaining to imaging sequence settings and the administered ^{129}Xe gas composition. In particular, the ^{129}Xe gas self-diffusion coefficient, D_0 , depends on (i) gas composition³, and potentially depends on (ii) the pressure of the gas in the lungs determined by the breath-hold maneuver. Finally, (iii) the diffusion time chosen for the experiments determines the microstructural length scale probed in the lung since the ^{129}Xe atoms diffuse further at longer diffusion times. In this presentation the effects of these three factors on ^{129}Xe MRI morphometry are explored in rat lungs and compared to histology.

Methods: Healthy male Sprague-Dawley rats were imaged using a protocol approved by Western University's Animal Use Subcommittee. The rats were anesthetized, tracheostomized and mechanically ventilated using an MR-compatible ventilator⁴. Following 1, 2 or 4 breaths of ^{129}Xe (effectively changing D_0 in the lungs), MR images of the lungs were acquired in breath-hold fashion using a 2D diffusion-weighted sequence on a 3 T GE MRI system, with FOV = 5x5 cm, matrix size of 64x64, TE = 9.6 ms, TR = 11 ms, BW = 2 kHz and an averaging of 3 images to boost SNR. An insert gradient coil was used to ensure a range of b-values (0, 2.2, 8.9, 20.0, 35.6, 55.6, 80.1, 109.0 s/cm²) at a diffusion time (Δ) of 1.62 ms. Morphometry was performed using a modified Yablonskiy method¹ with D_0 as a fifth parameter in the fitting algorithm. To explore the effect of increasing diffusion time, the experiment was repeated at Δ of 3 and 5 ms, with all other settings unchanged. The extracted morphometric parameter, alveolar diameter (L) was compared to histologically measured alveolar diameter values. For histology, the lungs were embedded in paraffin, cut in 5 μm sections then stained with H&E, imaged on a light microscope at 10x magnification and the mean linear intercept, a common metric for alveolar diameter, was quantified. Finally, in a single rat, the effect of ventilation pressure on morphometry parameters was also explored by ventilating the animal at different peak inspiratory pressures (PIP) ranging from 7-13 cmH₂O.

Results and Discussion: Fig. 1 shows L for increasing breath number (i.e. ^{129}Xe concentration) measured using the conventional and modified Yablonskiy model (variable D_0), as well as L_m obtained from histology. The L value extracted from the modified model is closer to the alveolar diameter estimated from histology, compared to the conventional model. As expected, the diffusion time had an effect on the morphometric parameters extracted as well. At a Δ of 5 ms the distribution of L centers around 96.9 μm , while for Δ of 3 ms and 1.62 ms, it shifts to center around 82.8 μm and 65.7 μm respectively. At shorter Δ L approaches the histological L_m of 60 μm , confirming a shorter diffusion time of 1.6 ms more appropriate for small animals (such as rats) than the clinical standard of 5 ms used in humans. Fig. 2 shows the dependence of L on PIP. As expected L shows an increase with PIP reflecting the expansion of the alveoli. While this effect is much smaller than that due to concentration differences, it may in itself have value for the determination of regional compliance through variation of the measured alveolar diameter as a function of pressure. For future morphometry experiments, all these factors should be considered for best morphometric accuracy and detection of lung microstructural changes due to disease.

References: 1) Yablonskiy, et al. MRM 67, (2012). 2) Ouriadov, et al. MRM e25825 (2015). 3) Lindenmaier, et al. Proc. of ImNO 2015. 4) Couch, et al. MRM 68, (2012). **Acknowledgements:** The authors would like to thank Andrew Wheatley for polarization of ^{129}Xe . We would also like to acknowledge our funding sources: NSERC, CIHR, OPIC, OGS and the Hospital for Sick Children.

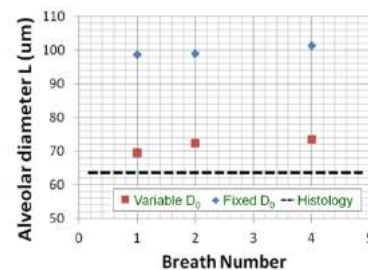


Fig. 1: Variation of the alveolar diameter L as a function of ^{129}Xe breath number with standard Yablonskiy method (blue squares) and when accounting for variable D_0 (red squares). Mean L extracted from histology is also shown.

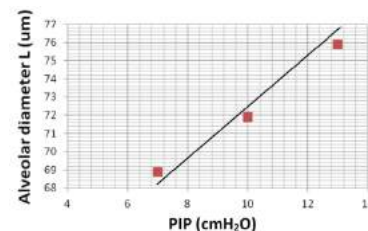


Fig. 2: Alveolar diameter determined from morphometry as a function of peak inspiratory pressure.

Diffusion Tensor Imaging in a Rodent Model of Amyotrophic Lateral Sclerosis

Patrick McCunn*, Alexander Moszczynski, Jason Gopaul, Kathryn Volkening,
Susanne Schmid, Michael J. Strong, Robert Bartha.

Robarts Research Institute, Western University, London Ontario, Canada
Schulich School of Medicine and Dentistry, Western University, London Ontario, Canada

Introduction: Amyotrophic Lateral Sclerosis (ALS) is a devastating neurodegenerative disorder in which patients will progressively lose all muscle control leading to death within 3-5 years from the onset of symptoms. Recent findings show that approximately 50-60% of ALS patients will suffer from a form of cognitive impairment (ALSci) typical of frontotemporal dementia.¹ This project aims to develop a rodent model of ALSci through the use of the tau protein phosphorylated at Threonine 175, an aberrantly phosphorylated protein that has previously been linked to patients suffering from ALSci.¹ Neurodegenerative processes have been associated with loss of white matter integrity reflected in altered water mean diffusivity (MD) and fractional anisotropy (FA) measured by diffusion tensor imaging (DTI). MD is a measure that represents the average distance of diffusion of water molecules, while FA is a relative measure describing the degree of variance of diffusion along different directions (ie. the directionality of diffusion). Generally, FA declines and MD increases in neurodegeneration. We hypothesized that subjects expressing Thr175Asp-tau would show a decrease in FA and an increase in MD as neural degradation consistent with that of ALSci occurs.

Methods: Adult female Sprague Dawley rats (n=40) received bilateral stereotactic inoculations into the hippocampus. Through somatic gene transfer using an EGFP tagged rAAV-9 viral vector, four forms of the tau protein were expressed within the hippocampus: Thr175Asp-tau (pseudophosphorylated tau, n=10), Thr175Ala-tau (n=10), wild-type human tau (n=10) and EGFP only (control n=10). Diffusion tensor imaging was acquired on an Agilent 9.4 Tesla small animal MRI scanner at Robarts Research Institute (TE=36 ms, TR=1s, max b-value=1085 s/mm², 12 directions, FOV=25.6 mm, 192x192 matrix, 20 – 1 mm slices). Scans were performed at 1, 3 and 6 months post-injection. Images were analyzed using the FSL software (5.0.7) to quantify MD and FA (Figure 1) from manually selected ROIs within the hippocampus. Two-tailed t-tests (p<0.05) were used to compare average group values.

Results: There were no significant differences in FA and MD between groups. Further data analysis is ongoing.

Conclusions: We have successfully acquired diffusion tensor imaging data in a rodent model of ALSci and quantified fractional anisotropy and mean diffusivity consistent with previous measurements.² Further studies have begun to improve sensitivity in data analysis; namely the implementation of Tract Based Spatial Statistics (TBSS) in an animal model to allow voxelwise statistical analysis of rodent DTI data.

References: 1. Moszczynski, et al. *Neurobiology of Aging*, 2015, 36, 1590-1599 2. Papp et al. *Neuroimage*, 2014, 97, 374-86

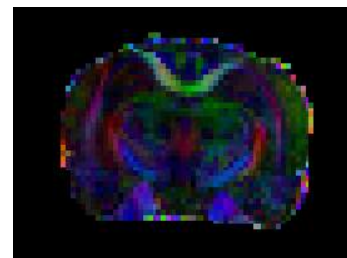


Figure 1: RGB-FA brain map of subject expressing Thr175-tau

Interrogation of neurovascular coupling in an optogenetic mouse model using electrophysiology and two-photon fluorescence microscopy.

James R. Mester^{1,2}, Paolo Bazzigaluppi^{1,2,3}, Peter Carlen^{1,3}, John G. Sled^{1,4}, Bojana Stefanovic^{1,2}

1. University of Toronto 2. Sunnybrook Research Institute 3. Toronto Western Hospital 4. Toronto Centre for Phenogenomics

Introduction: The neurovascular unit is a framework that is used to describe the complex relationship between the cellular and vascular structures in the brain. While it is widely referenced when discussing the mechanisms of brain function, the underlying function of the neurovascular unit is largely not understood. Development of research tools in neuroscience has allowed for more refined approaches to investigate the neurovascular unit, namely optogenetics and two-photon fluorescence microscopy (2PFM). The work described looks to combine optogenetics and 2PFM with electrophysiological recordings to provide a simultaneous readout of neuronal and vascular function during focal neuronal stimulation.

Methods: A transgenic mouse line (thy1-ChR2-YFP, JAX) expressing channelrhodopsin-2 (ChR2) in excitatory pyramidal neurons was selected for these experiments. Mouse physiology was monitored throughout the procedure and experiment. Mice were surgically prepared for imaging with a craniotomy over the somatosensory cortex, and the tail vein was cannulated. 70kDa dextran dye (Texas Red) was injected via the tail vein cannulation for visualization and recording of the vasculature. Imaging and optogenetics stimulation was performed with an FV1000MPE multiphoton microscope (Olympus) and two Ti:Sapphire lasers (Spectra-Physics). Imaging of ChR2-YFP and Texas Red was performed at 960nm. Optogenetic stimulation was done using either 920nm from a Ti:Sapphire laser or 450nm from a fiber-coupled LED. Local field potential (LFP) recordings were made via pipette electrode placed under the pial surface and recorded with a patch clamp amplifier/DAC (HEKA). Optogenetic stimulation was performed at various frequencies and timings (10-50Hz). Vascular recordings were made via raster linescans along direction of flow in blood vessels.

Results: Figure 1 shows vessel flow over time as calculated using previously developed software (Kim et al. 2012). Robust LFP responses are seen in conjunction with the vascular response when recorded simultaneously. Excitation of larger and smaller regions of expressing cells appears to have an effect on both the vascular and neuronal responses.

Conclusions: ChR2-expressing mice were investigated to examine the simultaneous responses of neurons and the vasculature in response to focal optogenetic stimulation. Results indicate that there is a correlative response between the two and that they are spatially and temporally dependent on the means of optogenetic stimulation. Furthering the knowledge of the neurovascular unit is essential for understanding the underlying mechanisms of many CNS disorders and diseases.

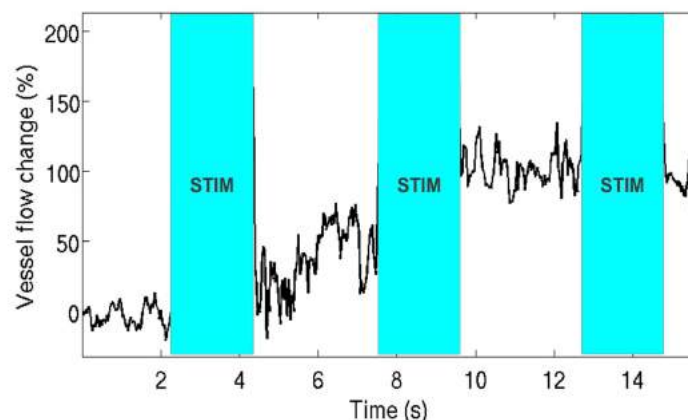


Figure 1: Vessel flow response to LED-fiber optogenetic stimulation. Optical stimulation was delivered at 20Hz at 450nm. Vessel flow calculations were performed using previously developed software (Kim et al. 2012).

Investigating cancer cell dormancy with cellular MRI

Murrell DH^{1,2}, Hamilton AM¹, Foster PJ^{1,2} (supervisor)

Ontario Institute for Cancer Research – Smarter Imaging Program

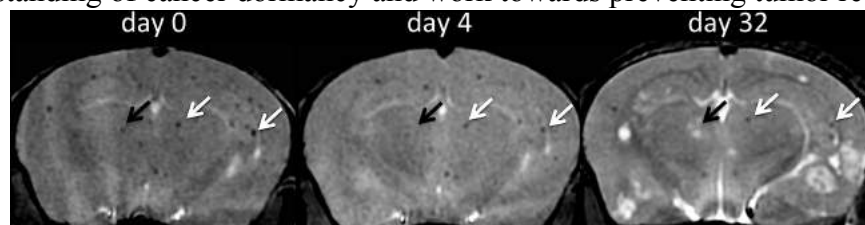
1. *Imaging Research Laboratories, Robarts Research Institute, London ON CAN*
2. *Department of Medical Biophysics, Western University, London ON CAN*

INTRODUCTION: Cell tracking with MRI and iron nanoparticles is commonly used to monitor the fate of implanted cells in disease models. Few studies have employed these methods to study cancer because proliferating cancer cells lose the iron label as they divide. In this research, we demonstrate the ability to use retention of iron nanoparticles by non-proliferative cancer cells, and the resulting MRI signal void, to serve as a marker for cancer cell dormancy. Dormancy is a stage in cancer progression where cancer cells exist in a viable but quiescent state. Most cancer treatments target proliferating cells; therefore, dormant cancer cells may evade treatment and yet retain the capacity to proliferate sometime later, causing recurrence. Our lab has developed technology to track single iron-labeled cells over time [Heyn *et al* (2006) Magn Reson Med]. Here we present studies where this cell tracking technology was applied to investigate the fate of cancer cells *in vivo*.

METHODS: Primary and metastatic brain cancer models were used in this work. Novel glioma cell lines with varying dormancy profiles (U373vIII, TF U373, EV U373) and brain metastatic breast cancer (MDA-MB-231-BR-HER2) cells were labeled *in vitro* with iron oxide nanoparticles then injected intra-cardially into nude mice. A group of brain metastatic breast cancer mice received prophylactic cranial irradiation on day 1 and 2 post-cell injection (PCI, 20Gy/2). MRI was acquired at 3T using 3D bSSFP (resolution: 100x100x200 μ m, scan time=30min) to evaluate signal voids due to iron-labeled cancer cells and tumor development over time. Fractional signal loss (FSL) was measured in a subset of voids that persisted from day 0 to 32. We have previously shown that the FSL, a measure of the contrast due to iron-labeled cells, is related to the iron/voxel and can be used to determine if the amount of iron in voids changes over time. Perls Prussian Blue staining was done on brain sections to confirm the presence of iron-labeled cells in the brain and validate the MRI findings.

RESULTS: Representative images in the figure below illustrate our ability to track cell fate by cellular MRI. Signal voids that represent proliferative cells develop into tumors by endpoint (black arrow). These co-exist with voids that retain iron over time and represent non-proliferative cancer cells (white arrow). Previous studies of the glioma models suggest U373vIII rapidly grows tumors (30-50d) and has no dormant phase; TF U373 has a long latency period with a dormant phase of 70+ days; EV U373 remains dormant for more than 250 days and does not grow tumors. In our study, the number of signal voids declined slowly in U373vIII mice, and voids persisted through day 50 when tumors became evident in 3/6 mice. For TF U373 mice, the number of signal voids declined rapidly between day 0 and 15 and by day 30 no signal voids were detectable; these mice were scanned again on day 70 and neither voids nor tumors were evident. The pattern of void retention was similar in EV U373 mice and these also did not grow tumors by day 70. This suggests that TF and EV U373 cells do not grow brain tumors in this model because cells do not survive and are rapidly cleared; it is not because they remain in the brain as dormant cells. In the 231-BR-HER2 model, most of the signal voids were cleared from the brain over time. The percentage of voids persisting in the brain relative to day 0 was on average 33% on day 4 and 13% on day 32 regardless of PCI treatment, although tumor burden – both in terms of number and volume – was significantly different between the two groups. The average FSL of persisting voids was comparable in both treatment groups and did not change significantly between day 0 and day 32, which indicates that these cells are not proliferating, despite other cells forming tumors. These results suggest that non-proliferative cancer cells persist in the brain, seemingly unaffected, even after PCI treatment has eradicated the tumor burden.

CONCLUSIONS: Here we show longitudinal tracking of non-proliferative cancer cells in two models using cellular MRI. This technique allows us to investigate models thought to have varying dormancy profiles, and to evaluate concurrent treatment responses of tumors and non-proliferative cancer cells. This research is important to improve our understanding of cancer dormancy and work towards preventing tumor recurrence in patients.



The development of a multimodality imaging model to monitor breast cancer metastasis

Katie Parkins*, Amanda M. Hamilton, John A. Ronald, Paula J. Foster
Robarts Research Institute, The University of Western Ontario, London, Ontario, Canada

Introduction: Breast cancer is the second leading cause of cancer related deaths in North America with the majority of deaths due to metastasis¹. Therefore, the clinical need to better understand and prevent metastasis is high. Cellular magnetic resonance imaging (MRI) is an emerging tool that aims to non-invasively visualize and quantify cells in living subjects. This technique uses iron oxide nanoparticles to label specific cells, enhancing their detectability by MRI². The presence of iron in cells causes a distortion in the magnetic field which leads to signal loss in iron-sensitive images². However, cellular MRI has limited ability to differentiate between dead and viable cells. Furthermore, when a cell dies the iron label may be transferred to phagocytic bystander cells leading to a false positive imaging result. Thus, complementary bioluminescence imaging (BLI) can provide a more holistic view of cell fate in living subjects by providing a direct readout of cell viability.

Methods: Human breast carcinoma cells (JIMT1) were transduced with a luciferase reporter gene using a lentiviral vector. Cells were incubated with micron-sized iron particles for 24h; then 175,000 cells/mouse were injected into the left cardiac ventricle of 4-week-old nude mice. Whole body BLI imaging was used to screen mice for successful intracardiac injection on an In Vivo FX PRO. Only mice with bioluminescence detected in the brain proceeded to MRI. On days 0, 8, 21 and 28, mice received 150uL of D-luciferin intraperitoneally and BLI images were captured for up to 30 minutes. 3T MRI was used to image the brain on days 0, 8, 21 and 28. A balanced steady state free precession (bSSFP) imaging pulse sequence was utilized, which has been optimized for iron detection. The volume of each brain metastasis and the number of signal voids were measured from MRI acquired at each timepoint. Bioluminescent signal was expressed as photons per second per square millimeter and was displayed as a signal intensity map. Photon flux was measured at each timepoint and compared to MRI findings.

Results: On day 0, iron labeled cells were visualized as signal voids by MRI, distributed throughout the brain. The number of signal voids in the brain correlated with the brain BLI signal intensity. On day 28, brain metastases appeared as regions of hyperintensity by MRI and BLI signal was detected in the brain and spinal cord (**Figure 1**). Total brain tumour burden measured by MRI showed a strong correlation with BLI signal intensity (**Figure 2**).

Conclusions: Iron-labeled JIMT1 cells were readily detected in the brain and could be tracked to monitor the development of cancer metastasis. Using BLI to complement our current cellular MRI technology, we can screen animals for successful intracardiac injections prior to MRI as well as get a direct measure of cell viability. Furthermore, BLI can be used to track the fate of many different cell populations and will continue to be a valuable tool in monitoring cancer metastasis and treatment response in pre-clinical models of disease.

References: 1. Siegel R, et al. Cancer statistics, 2014. CA: a cancer journal for clinicians 2014, 64(1):9-29. 2. Heyn et al. (2005) MRM (53):312-320.

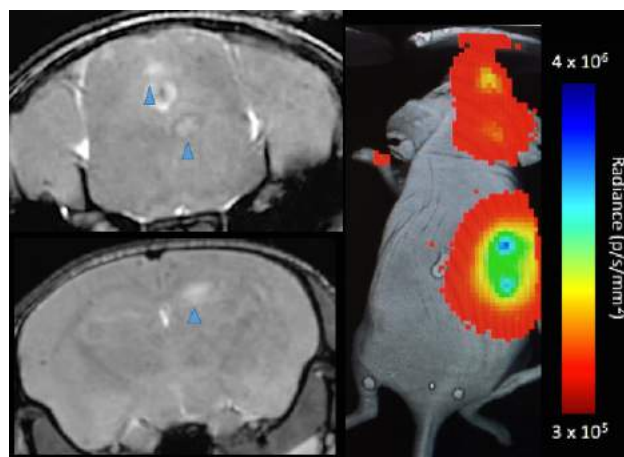


Fig 1: Representative MRI (L) and BLI (R) on day 28 shows metastases detected by MRI (arrowheads) and bioluminescent signal in the brain and spinal cord.

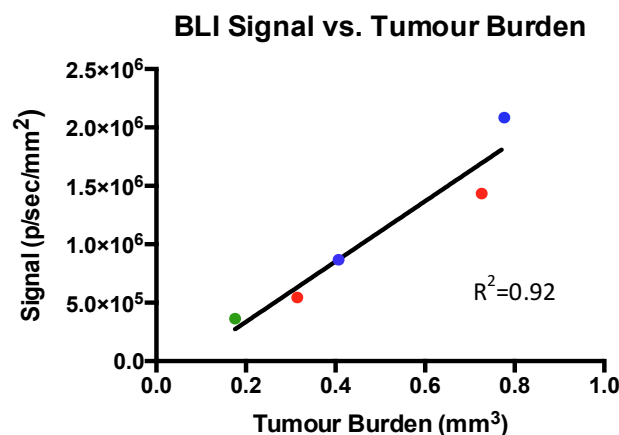


Fig 2: Positive correlation between tumour burden measured with MRI and BLI signal intensity. Data represents 2 mice imaged on day 21 and 28 (blue, red); and 1 mouse imaged only on day 28 (green).

Micro-CT Validation of 3D-Printed Patient-Specific Components

Joseph U. Umoh¹, Hristo N. Nikolov¹, Steven I. Pollmann¹, Jaques S. Milner¹ and David W. Holdsworth^{1,2}

Development of Novel Therapies for Bone and Joint Diseases Consortium

¹Preclinical Imaging Research Centre, Robarts Research Institute,

²Departments of Medical Biophysics and Surgery, Western University, London, ON, Canada

Introduction: Three-dimensional (3D) printing technology helps build prototypes quickly and cost effectively. This concept has been applied in many fields and it is particularly attractive in implementing personalized medicine, where medical products (such as bone plates, cutting guides¹ and bone grafts²) can be produced in a short time and tailored for individual patients. Efforts have been made to analyze the errors in 3D printing, but these studies are often based on measurement of linear dimensions.³ This study presents a micro-CT method for evaluating the surface accuracy of irregular three dimensional-printed (3DP) objects.⁴ The efficacy of this approach was tested on a plastic print of a dental cast, derived from a molded impression. This structure was used to illustrate this technique primarily because of its highly irregular geometry, including small gaps.

Methods: Three-dimensional geometry data of a dental cast were obtained in STL format and used as input for 3D printing. The cast was fabricated by fused-deposition printing in polylactic acid (PLA) thermoplastic, using a commercial 3D printer (Dremel® Idea Builder) with 100 μm layer thickness (Fig. 1a). The fabricated dental cast was then scanned with a commercial micro-CT scanner (eXplore speCZT CT120, GE Healthcare) at 90 kVp and 576 mAs with isotropic spatial resolution of 100 μm ; total scan acquisition time was five minutes. The reconstructed volume was used to derive an isosurface, at a greyscale threshold of -380 HU. To validate the quality of 3D printing, the two STL datasets (*i.e.* prescribed and measured) were analyzed with commercial metrology software (Geomagic Qualify), which co-registered the surfaces and calculated deviations over the entire object.

Results: The STL model datasets aligned to within 0.101 mm, assessed on over 1.4 million surface points. Average surface deviations were +0.061 mm / -0.071 mm, with over 50% of all points within ± 0.06 mm of the expected location (as illustrated by the points shown in green in Fig. 1c). Only 17% of all data points were found to exceed ± 0.1 mm tolerance; these points were shown in deep red or blue in Fig. 1c. The maximum deviation of any point in any direction was 0.196 mm.

Conclusions: Micro-CT imaging represents a rapid and cost-effective technique for routine validation of patient-specific 3D printed plastic components. A complete 3D dataset can be acquired in just under five minutes, with image quality appropriate for surface validation to within ± 100 μm . The image data are inherently 3D, reducing the need for operator intervention. In comparison to optical surface scanning, the entire surface is derived contiguously without specimen repositioning, and it is not necessary to treat the surface in any way to reduce specular reflection. In addition, micro-CT analysis is immune to artifacts that may result from small gaps or re-entrant cavities.

References: [1] Krishnan SP *et al.* A review of rapid prototyped surgical guides for patient-specific total knee replacement. *J Bone Joint Surg Br*; **94**: 1457-1461 (2012). [2] Cohen *et al.* Mandibular reconstruction using 3D printing modeling technology. *Oral and Maxillofacial Surgery*; **108**: 661-666 (2009). [3] Choi and Kim. Clinical application of 3D printing technology in craniofacial plastic surgery. *Archives of Plastic Surgery*; **42**: 267-277 (2015). [4] Teeter M *et al.* How do CAD models compare with reverse engineered manufactured components for use in wear analysis? *Clin Orthop Relat Res*; **470**(7): 1847-1854 (2012).

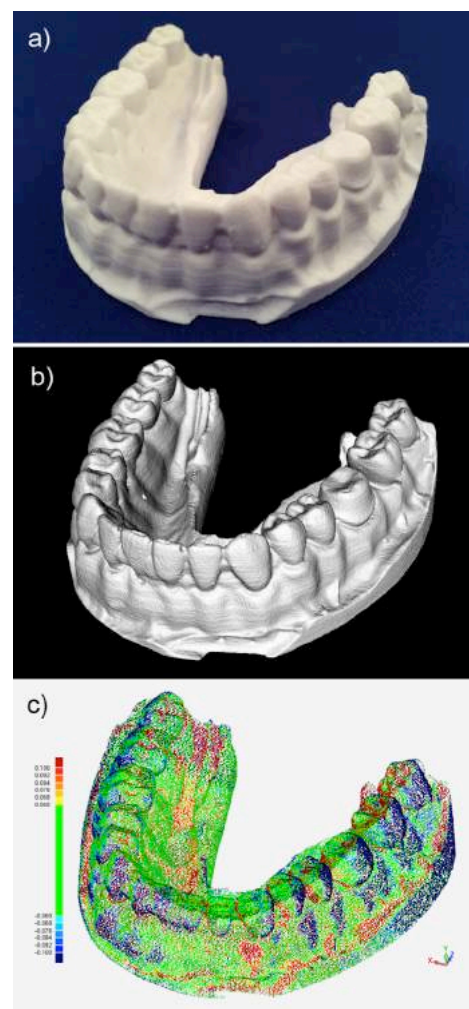


Fig. 1: (a) Photograph of 3D-printed version of dental cast; (b) STL surface, derived from micro-CT image data; and (c) 3D deviation map (mm), comparing prescribed and measured 3D surfaces.

Gas Exchange Quantification using Hyperpolarized ^{129}Xe and a Clinical MRI System

Brandon Zanette^{1,2}, Ozkan Doganay³, Elaine Stirrat¹, Rolf Schulte⁴, and Giles Santyr^{1,2}

¹Peter Gilgan Centre for Research and Learning, The Hospital for Sick Children, Toronto, ON, Canada. ²Department of Medical Biophysics, University of Toronto, Toronto, ON, Canada. ³Department of Oncology, University of Oxford, Oxford, UK. ⁴General Electric Global Research, Munich, Germany.

Consortium – OICR Smarter Imaging Program, Supervisor – Dr. Giles Santyr

Introduction: Magnetic Resonance Imaging (MRI) with the use of hyperpolarized ^{129}Xe has shown promise as a tool for the quantification of gas exchange between the airspaces of the lungs and the capillary blood pool which supplies oxygen to the rest of the body. The large chemical shift ^{129}Xe experiences as it dissolves from alveolar spaces into the surrounding lung tissue (T) and red blood cells (RBCs) allows for the detection of signal from each of these compartments, and the quantification of exchange between them¹. Differences in gas exchange from whole-lung spectroscopy have been reported in previous work using a whole-lung irradiation rat model of Radiation-Induced Lung Injury (RILI)². While this work succeeded in showing the capability of ^{129}Xe MRI to detect RILI as early as two weeks, the whole-lung nature of the study lacked regional information. Recently, a method for directly imaging the dissolved phases of ^{129}Xe in rat lungs has been reported using a Spiral-IDEAL technique³ and a high-performance, small bore animal gradient system. However, this gradient system is not appropriate for clinical translation to much larger human subjects. In this work, we apply Spiral-IDEAL to a cohort of rats using a commercially-available clinical gradient system to

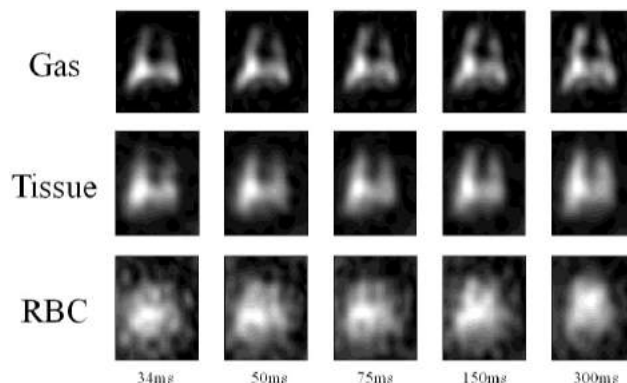


Fig. 1: Representative Spiral-IDEAL coronal rat lung Images of the three phases of ^{129}Xe for five different repetition times (TR).

investigate gas exchange quantification. However, this gradient system is not appropriate for clinical translation to much larger human subjects. In this work, we apply Spiral-IDEAL to a cohort of rats using a commercially-available clinical gradient system to

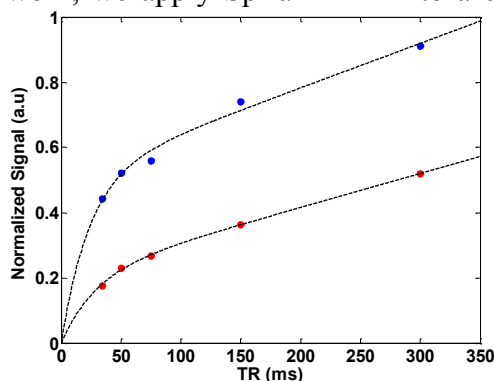


Fig. 2: Tissue (blue) and RBC (red) gas exchange curves. Dashed lines are fits to a theoretical compartmental model⁴.

corresponding to the entire lung were determined from the gas phase images and subsequently applied to the normalized tissue and RBC images. The mean ROI values were fitted as a function of TR to a theoretical model to extract quantitative gas exchange parameters⁴. **Methods:** All rats were imaged following approved protocols. A cohort of age-matched healthy rats (N=7) was used as an animal model. The rats were ventilated with 4 pre-breaths of ^{129}Xe . A Spiral-IDEAL technique was implemented at 1.5T (GEHC) to image all phases of ^{129}Xe in the coronal plane with a 2D projection with an FOV=5×5cm² and Cartesian matrix size=16×16. A frequency-selective RF pulse was centered on the tissue frequency and calibrated to excite the dissolved phases with $\alpha_{T/RBC} \sim 70^\circ$ and the gas phase with $\alpha_G \sim 15^\circ$ ³. The repetition time (TR) was varied between 34, 50, 75, 150, and 300ms to sensitize images to the ^{129}Xe gas exchange between compartments. Images at each time point were averaged from two separate breath-holds. Tissue and RBC images were normalized to gas images between breaths. ROIs

Results: Coronal Spiral-IDEAL lung images from the three ^{129}Xe phases of a representative rat are shown in Fig. 1. Fig. 2 shows gas exchange curves from a single animal. Whole-lung gas transfer times as measured from Fig. 2 were measured to be $\tau_1 = 24\text{ms}$ and $\tau_{RBC} = 29\text{ms}$ for tissue and RBC images respectively, in reasonable agreement with previous work⁵.

Discussion: In this work we were successfully able to image the dissolved phases of ^{129}Xe in rat model using a clinical gradient system and obtain quantitative gas exchange measurements that may be used to detect RILI. In future, the entire cohort of rats will be analyzed regionally and correlated with quantitative histology. The results of this work will aid in the translation of this technique from animals to humans and represents a step towards clinical applicability.

References: 1. Sakai et al., J Magn. Reson. B. (1996). 2. Fox et al., Med. Phys. (2014). 3. Doganay et al., Magn. Reson. Med. (2015). 4. Mansson et al., Magn. Reson. Med. (2003). 5. Doganay et al., Med. Phys. (revisions in progress 2016). **Acknowledgements:** The authors would like to thank the following sources of funding: The Hospital for Sick Children, CIHR, and NSERC. Special thanks to Andras Lindenmaier, Nikhil Kanhere, Yonni Friedlander, and Felipe Morgado.

Performance evaluation of a peripheral cone-beam CT scanner

Rudy Baronette^{1,2,4}, Xunhua Yuan¹, Steven I Pollmann¹, Matthew G Teeter^{2,3}, David W Holdsworth^{1,2,3}

Development of Novel Therapies for Bone and Joint Diseases Consortium

¹Imaging Research Laboratories, Robarts Research Institute

Depts. of Medical Biophysics² and Surgery,³ Schulich School of Medicine & Dentistry

⁴Collaborative Training Program in Musculoskeletal Health, Bone and Joint Institute

Western University, London ON, Canada

Introduction: Weight-bearing imaging of the lower extremity is limited to the supine position by scanner design in conventional clinical CT scanners. Due to recent advances in cone beam computed tomography (CBCT), true 3D weight-bearing CT is now available for clinical evaluations of patients in a health care setting.^{1,2} The Verity CT scanner (Planmed Oy) is a CBCT imaging system that is optimized for imaging upper and lower extremities. The system acquires high-resolution volumetric images of the target and includes a motorized gantry that allows for weight-bearing CBCT imaging of lower extremities. The purpose of this study was to perform a quantitative evaluation for the imaging performance of this peripheral CBCT scanner.

Methods: Performance of the Verity CBCT system (Fig. 1a) was evaluated using both a quality control phantom provided by the manufacturer (80 mm diameter) and a custom-built phantom (15cm diameter). These phantoms were used to assess the noise, resolution, and uniformity, as previously described.³ The manufacturer's phantoms were scanned using predetermined positioning and scan parameters for all performance evaluations. Upon completion of the scan, the performance results are automatically calculated and outputted by the scanner. The custom-built phantom was examined using the same technical factors and image volumes (11cm length, 16 cm diameter), and reconstructed at an isotropic resolution of 0.2mm.

Results: Analysis of the slanted edge image (Fig. 1b) indicated limiting resolution of 1.32 lp/mm, compared with a value of 1.35 lp/mm obtained with the manufacturer's phantom. The noise values were evaluated as the standard deviation within a uniform region, over a range of exposures (Fig. 1c). Minimum standard deviation of 60 HU was observed at the highest exposure setting. The uniformity of the system (calculated as the average difference in signal intensity values between the peripheral and central regions) was 174 HU. Over the central region, the uniformity was observed to be 34 HU (± 6 HU).

Conclusion: The performance evaluation of the peripheral CBCT scanner shows the Verity meets the manufacturer's specifications for the high-resolution scan mode. The analysis of the resolution yielded a limiting spatial resolution exceeding 1.25 lp/mm. The noise characteristics were well within the manufacturer's guidelines, where the HU standard deviation is less than 100 HU. Uniformity performance was excellent over the central region and within the limits of 50 HU set by the manufacturer. The uniformity test displayed a large difference in the average HU from the centre to the periphery, which can be attributed to beam hardening and scatter.

References: **1.** Tuominen, E. K., et al. (2013). "Weight-bearing CT imaging of the lower extremity." *AJR Am J Roentgenol* 200(1): 146-148. **2.** Zbijewski, W.E., Et al. (2011) "A dedicated cone-beam CT system for musculoskeletal extremities imaging: Design, optimization, and initial performance characterization, *Med. Phys* 38(8): 4700-4713. **3.** Du L., et al. (2007) "A quality assurance phantom for the performance evaluation of volumetric micro-CT systems," *Phys. Med. Biol* 52: 7087-7108.

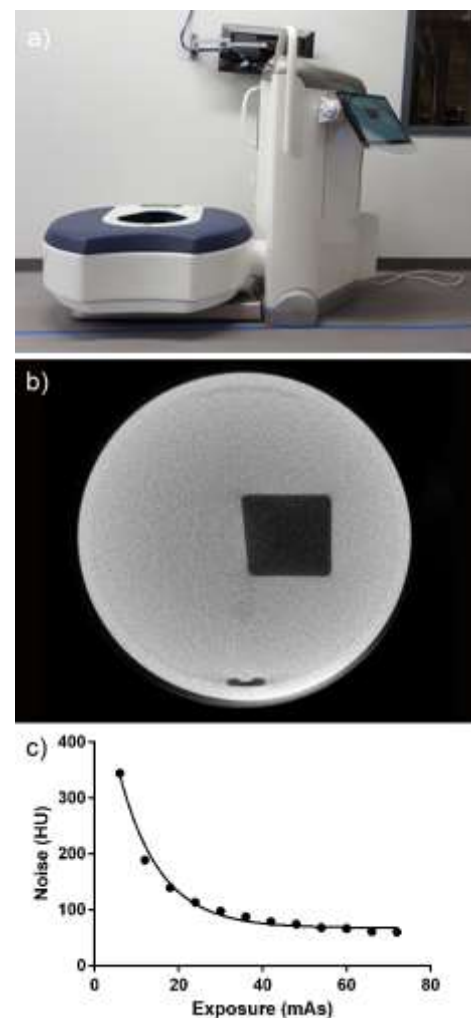


Fig. 1: (a) photo of the Planmed Verity peripheral CT scanner; (b) transverse image of a slanted edge, used to calculate MTF; and (c) noise (SD) in HU vs exposure.

A novel energy-dependent subtraction method for cardiac imaging: Signal and noise analysis

Christiane Sarah Burton, I. A. Cunningham

Oct 1, 2015

Imaging Research Laboratories, Robarts Research Institute, 100 Perth Drive, London, Ontario N6A 5K8, Canada and Department of Medical Biophysics, The University of Western Ontario, London, Ontario N6A 5C1, Canada

Purpose: Cardiovascular diseases (CVD) are currently the leading cause of death worldwide and x-ray angiography is used for 80% of all cases.^{1,2} Digital subtraction angiography (DSA) is a technique that is widely used to enhance the visibility of small vessels and vasculature obscured by overlying bone and lung fields by subtracting a mask and contrast image. However, DSA is generally unsuccessful for imaging the heart, due to the motion that occurs during the several seconds between mask and contrasted images that cause artifacts and can render a study non-diagnostic. We are proposing energy subtraction angiography (ESA) as a method of bringing the benefits of DSA to cardiac imaging without motion artifacts. This method was suggested in the 1970's and it was concluded at the time that image quality with ESA could not compete with that of DSA, and the approach was essentially abandoned.³ However, our work has shown that conclusion was based on limitations of early technology that may be no longer relevant. We show that ESA images can be superior to DSA with careful design of the x-ray system and detectors.

Methods: We developed a theoretical model for iodine signal and noise to form a metric of comparison of image quality between ESA and DSA independent of technology. We used this model to compare the ultimate potential of ESA relative to DSA, and to determine the performance characteristics required to achieve optimal results. Predictions of this model were validated experimentally using a prototype flat-panel x-ray detector system. For ESA low and high applied tube voltages of 50 kVp and 120 kVp (2.5 mmCu), respectively, and for DSA mask and contrast images the applied tube voltage was 80 kVp. Using iodine-specific images of a stepwedge the iodine signal-to-noise ratio (SNR) per entrance exposure was calculated for each iodine mass loading for both ESA and DSA. The scatter-to-primary ratio was measured by varying the air gap between the detector and a 20 cm tank of water while measuring the exposure at each air gap. We incorporate read-noise and scatter into our theoretical model in order to calculate the acceptable read-noise and acceptable scatter-to-primary for ESA and DSA.

Results: The theoretical model showed that in principle; ESA can produce images that are as good as DSA. However, to achieve this, ESA places greater demands on detector performance than DSA in terms of detector quantum efficiency (DQE), read noise, scatter, and speed of detector read out. Our experimental measurements are in excellent agreement with our theoretical calculations. A 500 μm CsI thickness can increase the iodine SNR per root exposure by 15-30% relative to thinner CsI thicknesses in older detector models. Read noise for ESA low and high kV are a factor of 3 and 6 lower than DSA, respectively. The scatter-to-primary (SPR) for the signal component of ESA low and high kV is a factor of 2 and 3 lower than DSA, respectively. For the noise component of ESA low and high kV the SPR is greater than DSA by a factor of 1.5 and 3, respectively, however the acceptable SPR is approximately 0.02-0.03 for greater iodine mass loadings. We show that we can achieve a scatter-to-primary ratio of 0.03-0.04 by increasing the air gap to 30 cm.

Conclusions: With emerging detector technology and x-ray system designs, it is now possible to obtain iodine specific images for ESA with similar image quality to that of DSA. As a consequence, ESA has the potential to be used for background removal in cardiac imaging and other applications, where DSA cannot be used.

References:

¹World Health Organization Geneva. Global status report on noncommunicable diseases, 2015.

²Waters N. M. Ko D. T. Eisenberg J. M. Huyhn T. Rinfret S Knudtson M. L. Ghali W. A. Patel, A. B., Tu J. V. Access to primary percutaneous coronary intervention for segment elevation myocardial infarction in canada: a geographic analysis. *Open medicine*, 4(1):11231131, 2010.

³C. A. Mistretta, M. G. Ort, F. Kelcz, J. R. Cameron, M. P. Siedband, and A. B. Crummy. Absorption edge _uoroscopy using quasi-monoenergetic xray beams. *Invest Radiol*, 6:402_412, 1973.

Fractal Analysis of the brain blood oxygenation level dependent (BOLD) signal of mild traumatic brain injury (mTBI) patients.

Olga Dona¹ and Michael Noseworthy²

¹Biomedical Engineering, McMaster University, Hamilton, Ontario, Canada, ²Electrical and Computer Engineering, McMaster University, Hamilton, Ontario, Canada

Introduction: Mild traumatic brain injury (mTBI) is a common condition that affects many people around the world. While some cases resolve without long-term side effects, others have to live with permanent disabilities such as learning difficulties, behavioral issues, and memory loss [1]. Conventional imaging techniques are unable to detect abnormalities in the brain of mTBI patients that have shown delayed functional response on neuropsychological evaluation. The main objective of this study was to explore a novel analysis approach involving measurement of the temporal fractal nature of the resting state blood oxygen level depending (rsBOLD) signal.

Methods: Fifteen subjects with mTBI (post-concussion symptom scale PCSS= 33.4±24.4) were scanned using a GE MR750 3T MRI and 32-channel RF coil (General Electric Healthcare, Milwaukee, WI). Age-matched (13.5±2.34 y/o) healthy controls were scanned at rest with eyes open (6 from our hospital and 50 downloaded from the ABIDE database [2]). Axial FSPGR 3D images were used to prescribe the rsBOLD (gradient echo EPI, flip angle = 90°, TE/TR = 35/2000ms, 22 cm FOV, 64x64 matrix, 180 temporal points). Motion correction was performed and the anatomical and functional images were aligned and spatially warped to the TT_N27 atlas using AFNI [3]. Fractal analysis, performed over the gray matter, was assessed by calculating the Hurst exponent according to the procedure of Eke *et al* [4]. Statistical analysis used a voxel-based Z-scoring methodology.

Results and Discussion: rsBOLD fMRI is a common method of measuring neural activity in the resting state. It detects regional blood oxygenation changes associated with this activity while providing a balanced spatiotemporal resolution. The time signals acquired are self-similar at various time scales and follow the power law, therefore could be classified as fractals and analyzed using a fractal dimension (FD), considered as an index of complexity. Low FD characterizes less complex signals, which has been associated with pathologies of the brain [5, 6]. A decrease in signal complexity could be associated with lack of adaptability and decreased global connectivity in the brain.

Voxel-based FD was calculated for the every subject in the control group (n=56) to create the mean and standard deviation maps of what would be considered a normal brain for the Z-score analysis. The data was tested for normality using the Kolmogorov-Smirnov test (Figure1a) and Kurtosis and Skewness were also measured (Fig.1b,c). Based on the Kolmogorov-Smirnov test the data was considered normal within the gray matter mask. However, the data was left skewed and leptokurtic (>3) in the center plane of the cerebellum which caused this region to be excluded from the analysis. Z score maps were generated for each mTBI patient.

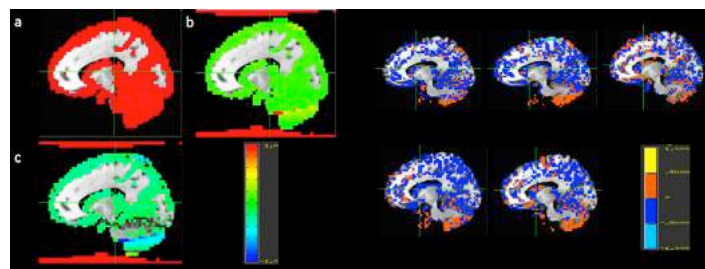


Figure1. a) *h* value for the one-sample Kolmogorov-Smirnov test, b) Kurtosis map and c) Skewness map. Figure2. Z-scoring maps of 5 randomly selected mTBI patients

Conclusions: This preliminary study suggests that the analysis of the fractal dimension of the rsBOLD signal could possibly provide additional information in mTBI. Traditional imaging techniques, mainly based on linear models, are unable to show a clear difference between normal and mTBI patients. It is well known that the brain is best modeled as a complex system [8] and therefore a measure of complexity using FD could provide an additional method to approach this global problem.

References: [1] J.J. Kim *et al.*, *Neu. J Am. Soc. Exp. N.Th.*, vol.8, pp.39-53, 2011. [2] ABIDE. Retrieved 7Jan2016, from http://fcon_1000.projects.nitrc.org/indi/abide/. [3] CoxRW., *AFNI(1996)*, 29(3):162-173, 1996. [4] Eke *et al.* *Eur J Physiol*,(2000) 439:403-415. [5] Goldberger *et al.* *Proc Natl Acad Sci USA* 99 (Suppl):2466–2472. [6] Suckling *et al.* *J Neurosci Methods* 174(2):292–300. [7] *Ann Neurol.* 2011;70(3):374-83. [8] Kannathal, N., S. K. Puthusserypady, *et al.* (2004). *Conf Proc IEEE Eng Med Biol Soc* 1: 604-607.

Radiomics Features Analysis for Tumor Characterization in Pancreatic Ductal Adenocarcinoma

A Eilaghi¹, S. Baig¹, J. Zhang¹, A. Wong³, P. Karanicolas², S. Gallinger², F. Khalvati¹, M. A. Haider¹

¹Medical Imaging, Sunnybrook Research Institute, University of Toronto, Toronto, ON, Canada

²Surgery, Faculty of Medicine, University of Toronto, Toronto, ON, Canada.

³Systems Design Engineering, University of Waterloo, Waterloo, ON, Canada

Introduction: Pancreatic ductal adenocarcinoma cancer (PDAC) is the most common type of pancreatic cancer with the five-year survival of 6% [1]. Contrast enhanced CT is the most common imaging modality to assess PDAC [2]. While the association of tumor heterogeneity defined by radiomics features [2] with survival rate and clinical outcome are shown in many types of carcinomas such as head and neck [3] and lung [4], there is an absolute paucity of information in radiomics feature analysis of PDAC. A CT-derived biomarker of tumour heterogeneity can provide a low cost and minimally invasive approach for prognosis of PDAC. In this exploratory analysis, we hypothesized that radiomics features that describe regional heterogeneity are different in tumorous tissue than the rest of pancreas in PDAC patients.

Methods: Patients who underwent curative surgical resection during 2009-2012 and completed clinical data, pre-operation contrast enhanced CT and one year follow up were included. Cases with an intraductal papillary mucinous neoplasm and those who died within 90 days after surgery were excluded. 9 patients, male ratio = 78% and age = 70.6±6.4 years, were included in this analysis. Whole pancreas gland, normal and tumorous regions were manually contoured by an expert using ProCanVAS, an in-house developed Clinical Decision Support System [5]. Five measures of regional heterogeneity namely: uniformity (Uni.), entropy (Ent.), dissimilarity (Dis.), course irregularity (CI) and structural deviation (SD) were calculated [6]. T-test with unequal variance and Spearman correlation test were used for statistical analysis.

Results: Tumorous tissue showed significantly lower Hounsfield intensity than normal pancreas ($p < 0.001$) in all cases which serves as an internal control for the analysis. Amongst the five studied radiomics features of heterogeneity, uniformity ($p < 0.032$), course irregularity ($p < 0.036$) and structural deviation ($p < 0.024$) were significantly different in tumorous region than the rest of the pancreas gland in all patients as shown in Table 1. A trend toward significance was found in entropy ($p < 0.077$) and dissimilarity ($p < 0.118$). No significant correlation was found across heterogeneity features except between uniformity and structural deviation (correlation coefficient = 0.817 and $p = 0.004$).

Conclusion: Tumorous tissues showed higher heterogeneity compared to normal pancreas tissue despite relatively small sample size. Radiomics features quantify independent aspects of tumor heterogeneity in contrast enhanced CT images of PDAC, which can be used as a predictor for patient outcome.

Table 1. P-values for tumorous tissue vs. normal tissue comparison for each patient (ID).

| ID | Uni. | Ent. | Dis. | CI | SD |
|----|--------|--------|--------|--------|--------|
| 1 | <0.001 | <0.001 | <0.001 | <0.001 | <0.001 |
| 2 | 0.032 | 0.045 | 0.116 | <0.001 | 0.017 |
| 3 | 0.025 | 0.077 | 0.082 | 0.036 | 0.022 |
| 4 | <0.001 | 0.007 | 0.044 | <0.001 | <0.001 |
| 5 | <0.001 | 0.004 | 0.118 | <0.001 | 0.004 |
| 6 | 0.005 | 0.003 | 0.018 | <0.001 | 0.012 |
| 7 | <0.001 | 0.023 | 0.024 | <0.001 | <0.001 |
| 8 | <0.001 | 0.004 | 0.001 | <0.001 | <0.001 |
| 9 | 0.031 | 0.063 | 0.023 | <0.001 | 0.024 |

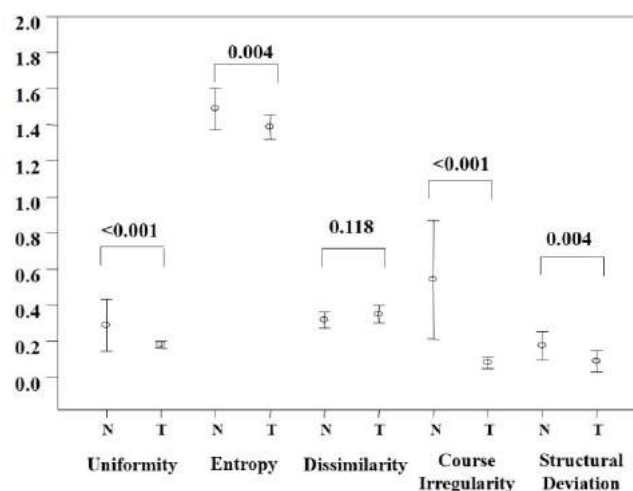


Figure 1. Heterogeneity features for normal (N) and tumorous (T) tissues of a 63 year old male patient (ID=5 in Table 1).

References: [1] R. Siegel, et al. CA Cancer J Clin., 2014, 64:9-29. [2] P. Lambin et al. EJC, 2012, 48(4):441-6. [3] H.J.W.L. Aerts et al. Nat Comm. 2014, 3;5:4006. [4] O. Gevaert et al. Radiology. 2012, 264(2):387-96. [5] F. Khalvati et al. BMC Medical Imaging, 15:27, 2015. [6] A. Cameron, et al. TBME, 2015, doi: 10.1109.

Performance of reduced dose compressed sensing-based sparse view CT myocardial perfusion imaging – a simulation study

¹Esmail Enjilela, ^{1,2}Ting-Yim Lee, ³Jiang Hsieh, ¹Jin Liu and ^{1,2}Aaron So

¹Imaging, Robarts Research Institute, London, Ontario, Canada

²Imaging, Lawson Health Research Institute, London, Ontario, Canada

³CT Engineering, GE Healthcare, Waukesha, Wisconsin, United States

Introduction. In this study, we investigated the effectiveness of compressed sensing (CS) for reconstructing good quality dynamic contrast-enhanced (DCE) CT images from sparsely sampled projections at different noise levels. **Method.** CT myocardial perfusion (MP) imaging was acquired on three pigs (40-60kg) after contrast injection with a GE HD750 scanner using 140kV/80mA/350ms. DCE images were reconstructed using filtered backprojection after the full set of projections (984) for each had been corrected for beam hardening. Synthetic noise that incorporated effect of energy-integrating detector [1] and bowtie beam filtering [2] was added to the projections to simulate 50, 40, 30 and 20 mA. One-third of simulated low-dose projections (328) were used to reconstruct DCE images with CS. MP maps for each DCE image set were generated with CT Perfusion (GE). Mean MP value for lateral, apical, and septal walls were compared between the CS and FBP reconstructions.

Results. It was found that sparse-projection CS reconstruction at all mA levels was able to resolve the same anatomical features as 80 mA full-projection FBP (**Fig. 1**). MP maps derived from each reduced mA (dose) CS sparse-projection DCE image set appeared similar to the 80 mA full-view FBP map (**Fig. 2**). Bland-Altman analyses (**Fig. 3**) showed a slight mean bias of CT MP measurement for all CS protocols compared to standard 80 mA full-view FBP; mean bias of 2.67 mL/min/100g (95% CI 18.37 – 13.04), 5.35 (95% CI 21.51 – 10.81), 6.02 (95% CI 24.34 – 12.29), and 8.77 (95% CI 30.15 – 12.62) for, respectively, 50, 40, 30 and 20 mA. Effective dose of 20 mA 328-view CS was 12 times lower than the standard protocol (0.66 mSv vs. 8 mSv for 8 cm coverage).

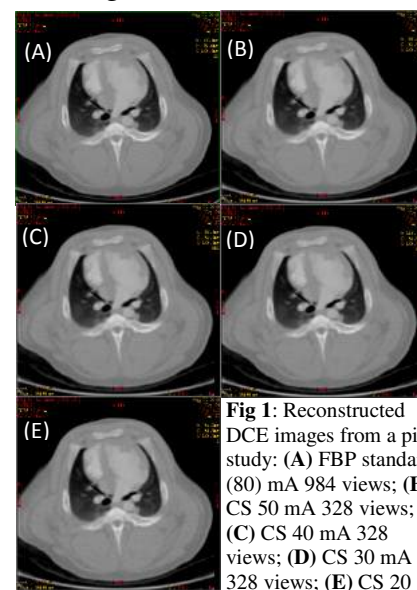


Fig 1: Reconstructed DCE images from a pig study: (A) FBP standard (80) mA 984 views; (B) CS 50 mA 328 views; (C) CS 40 mA 328 views; (D) CS 30 mA 328 views; (E) CS 20

Fig 3: Bland-Altman plots comparing CT myocardial perfusion measurements derived from sparse-projection CS images at (A) 50 mA, (B) 40 mA, (C) 30 mA, (D) 20 mA with those measured from the reference 80 mA full-projection (984) FBP images.

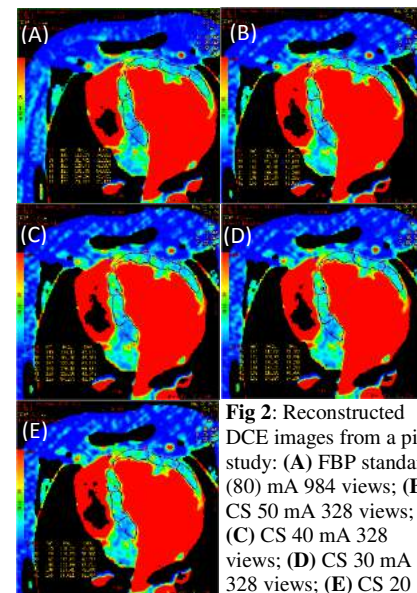
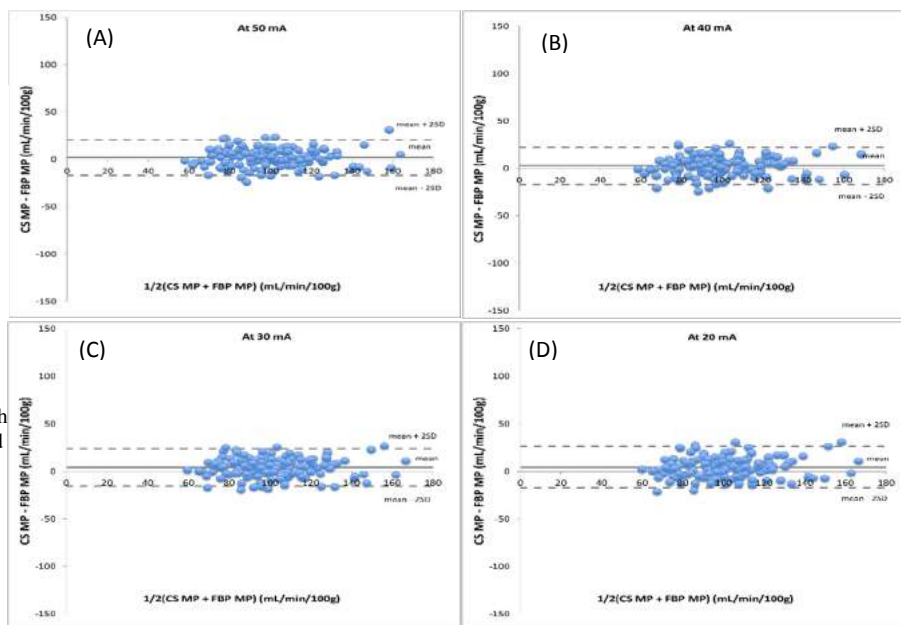


Fig 2: Reconstructed DCE images from a pig study: (A) FBP standard (80) mA 984 views; (B) CS 50 mA 328 views; (C) CS 40 mA 328 views; (D) CS 30 mA 328 views; (E) CS 20

Conclusion. Low mA acquisition coupled with CS sparse-projection reconstruction can minimize the radiation dose while preserving the accuracy of CT MP measurement.

References. [1] Massoumzadeh P. *et al.* Medical Physics 2009;36(1):174-189. [2] Boone J. M. Medical Physics 2010;37(1):40-48

¹⁹Fluorine (¹⁹F) cellular magnetic resonance imaging to monitor *in vivo* therapeutic cell migrationFink, C^{1,2}, Gaudet, J^{1,3}, Foster P^{1,3}, Dekaban, G^{1,2}

OICR Smarter Imaging Program

Molecular Medicine, Robarts Research Institute¹, Departments of Microbiology and Immunology² and Medical Biophysics³, Western University, Canada

Introduction: Cancer immunotherapy is an emerging research area that utilizes one's own immune system to combat cancer. An example involves the *ex vivo* preparation and loading of antigen presenting cells (APC), either in the form of a homogeneous dendritic cell (DC)-based cancer vaccine or heterogeneous APC-based vaccine, with tumor-specific antigen (Ag) to create a cancer vaccine. In order to exert their function as adjuvants in cell-based cancer vaccines, tumor-Ag presenting DC or mixed APC must track to secondary lymphoid organs post injection. Within secondary lymphoid organs such as the lymph node, they interact with T cells to induce tumor Ag-specific T cell proliferation, forming the basis of cancer immunotherapy. Previous research has demonstrated that the quantity of tumor Ag-loaded DC reaching a lymph node is directly proportional to the magnitude of the ensuing tumor Ag-specific immune response. Thus, we propose that ¹⁹F cellular MRI and a ¹⁹F perfluorocarbon cell labeling agent, Cell Sense, can non-invasively track and quantify *in vivo* human APC migration. Therefore, this novel imaging technique can be used as a surrogate marker to assess and improve upon the effectiveness of APC-based cancer vaccines while also assessing their anatomical fate and longevity.

Materials and Methods: Peripheral blood mononuclear cells (PBMC) were obtained from the blood of male volunteers and cultured with the ¹⁹F cell labeling agent, Cell Sense (5.0mg/mL), for 48 hours. Granulocyte macrophage colony-stimulating factor (GM-CSF) was added 24 hours into culture to activate the APC contained within the PBMC mixture. Following culture, Cell Sense-labeled PBMC were injected into the footpads of nude mice. Two days post injection, mice were imaged at 9.4T using ¹⁹F cellular MRI to track and quantify migration to the draining popliteal lymph node. Also, PBMC from prostate cancer patients were isolated and labeled with Cell Sense (5.0mg/mL) overnight under Good Manufacturing Practice conditions (Princess Margaret Hospital, Toronto) and injected subcutaneously into the upper flank of nude mice. ¹⁹F cellular MRI was conducted on day 0 and 2 days post injection to detect and quantify cells at the injection site and observe if migration to secondary lymphoid organs occurred. In each cell culture condition, the phenotype and viability of Cell Sense-labeled PBMC were assessed using flow cytometry and compared to unlabeled controls. Furthermore, a red fluorescent Cell Sense label was used with flow cytometry to qualitatively observe Cell Sense uptake by each cell lineage. This preclinical data was used to submit a clinical trial application such that imaging autologous Cell Sense-labeled PBMC in prostate cancer patients using ¹⁹F cellular MRI can be conducted.

Results: Our laboratory has been able to efficiently label a high percentage (>95%) of human PBMC from both healthy male volunteers and prostate cancer patients with Cell Sense and quantify this labeling using NMR spectroscopy. Human PBMC migration post footpad injection to both the popliteal and inguinal lymph nodes has been detected and quantified in a mouse model using ¹⁹F cellular MRI. GM-CSF treatment of PBMC prior to injection appears to increase the amount of quantifiable migration, which would predict a stronger *in vivo* immune response. Imaging studies using PBMC samples from prostate cancer patients has allowed for detection of ¹⁹F-labeled cells at both the injection site and draining inguinal lymph node. Currently, optimization of this novel imaging technique is being performed while awaiting clinical trial approval to image autologous Cell Sense-labeled PBMC in humans.

Conclusions: Our laboratory is able to track and quantify the migration of human therapeutic cells in mice to secondary lymphoid organs using ¹⁹F cellular MRI and a ¹⁹F-based cell labeling agent, Cell Sense. Future work will focus on correlating quantification of therapeutic cell migration with anti-cancer immune response in order to improve upon the immunogenicity of APC-based cancer vaccine efficacy as well as conducting imaging studies in humans. By doing so, we would be the first in Canada to conduct ¹⁹F cellular MRI in humans.

Quantitative Evaluation of Tumour Associated Macrophages in Breast Cancer Using Fluorine-19 and Iron Based MRI Cell Tracking, AV Makela^{1,2}, JM Gaudet^{1,2} and PJ Foster^{1,2}, Smarter Imaging Consortium
¹Department of Medical Biophysics, Western University, London, ON ²Robarts Research Institute, London, ON

Introduction: Tumour associated macrophages (TAMs) are associated with tumour growth and metastatic spread. Breast tumours can be comprised of up to 50% TAMs and their presence is correlated with a poor outcome. Cell tracking with MRI can be used to image TAMs *in vivo*. Previous studies have shown that iron oxide particles (USPIO) administered intravenously (IV) are taken up by TAMs and that signal loss on MRI corresponds to TAMs identified by histopathology. Quantification of TAMs with iron-based cell tracking is challenging; blooming artifact is present, which causes the signal void area to encompass a larger area than the USPIO. Fluorine-19 (¹⁹F) MRI is being developed to track and quantify cells. A major advantage is the ability to image perfluorocarbon (PFC)-labeled cells with high specificity due to the lack of endogenous fluorine. Most importantly, ¹⁹F MRI is quantitative, since the signal intensity is linearly related to the amount of ¹⁹F present. Therefore, it may be used to quantify the number of ¹⁹F atoms *in vivo*. **Methods:** 4T1 cells were implanted into the inguinal mammary fat pad in female BALB/c mice. Four groups of mice were studied. For Groups 1&2, MRI was performed as soon as tumours were palpable (3 days post implantation (p.i.)). For Groups 3&4, MRI was performed 3 weeks p.i. All images were acquired using a balanced steady state free precession (bSSFP) pulse sequence. *Iron-Based Cell Tracking:* Mice in Groups 1&3 were imaged at 3T pre and 24 hrs post IV injection of a USPIO. Spatial resolution was 200x200x200 μm^3 . *¹⁹F-Based Cell Tracking:* Mice in Groups 2&4 were imaged at 9.4T using a dual-tuned ¹H/¹⁹F birdcage coil, at 48 hrs post IV injection of a red fluorescent PFC. Spatial resolution was 0.5x0.5x1.0 mm^3 . Image data was assessed for regions of signal change within the tumour, corresponding to presence of the label. For Groups 1&3, pre and post iron images were compared to visualize signal loss. For Groups 3&4, the number of ¹⁹F atoms per mm^3 was quantified by relating the detected ¹⁹F signal within the tumour, to the signal generated by a reference tube and dividing by tumour volume. **Results:** *Tumours detected at 3 days p.i. (Fig. 1A&B):* In mice which received USPIO, MRI demonstrates signal loss which encompasses nearly the entire tumor volume. In mice which received PFC, the ¹⁹F signal distribution is similar; however, since ¹⁹F signal is quantifiable, these images reveal higher signal in the central region. *Tumours detected at 3 weeks p.i. (Fig. 1C&D):* Signal loss observed post-iron appears around the periphery of the tumour and spatial distribution corresponds well with iron staining (Fig. 2). ¹⁹F signal is also located around the tumour periphery but appears to occupy less area and may better represent the actual cell distribution since there is no blooming artifact. Quantification (Fig. 3) showed that both cell tracking methods suggest that there is a higher density of TAMs present in tumours at 4 days, with a significant difference ($p < .05$) between the two time points. **Conclusions:** No other cell tracking study has looked at TAMs at such an early time-point during tumour progression. ¹⁹F-based cell tracking may provide a more accurate representation of TAM infiltration when compared to iron-based cell tracking. This is achieved through the ability to quantify ¹⁹F atoms as well as the lack of blooming artifact generated by iron-labeled cells.

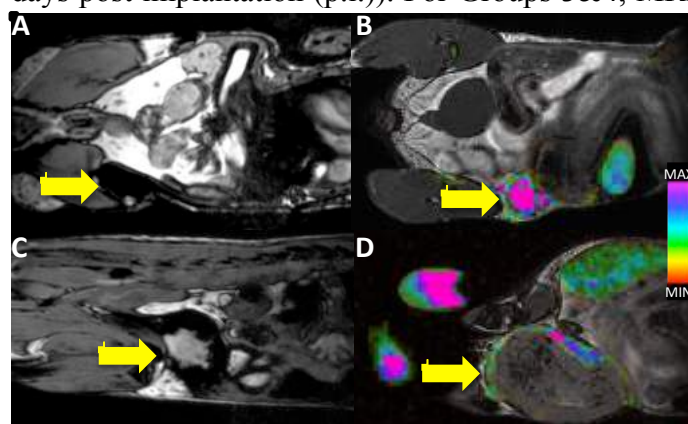


Figure 1: MR images of tumours (yellow arrows) in 4 different mice (A) post iron at 4 days (B) post ¹⁹F at 4 days (C) post iron at 3 weeks and (D) post ¹⁹F at 3 weeks

Tumours detected at 3 days p.i. (Fig. 1A&B): In mice which received USPIO, MRI demonstrates signal loss which encompasses nearly the entire tumor volume. In mice which received PFC, the ¹⁹F signal distribution is similar; however, since ¹⁹F signal is quantifiable, these images reveal higher signal in the central region. *Tumours detected at 3 weeks p.i. (Fig. 1C&D):* Signal loss observed post-iron appears around the periphery of the tumour and spatial distribution corresponds well with iron staining (Fig. 2). ¹⁹F signal is also located around the tumour periphery but appears to occupy less area and may better represent the actual cell distribution since there is no blooming artifact. Quantification (Fig. 3) showed that both cell tracking methods suggest that there is a higher density of TAMs present in tumours at 4 days, with a significant difference ($p < .05$) between the two time points. **Conclusions:** No other cell tracking study has looked at TAMs at such an early time-point during tumour progression. ¹⁹F-based cell tracking may provide a more accurate representation of TAM infiltration when compared to iron-based cell tracking. This is achieved through the ability to quantify ¹⁹F atoms as well as the lack of blooming artifact generated by iron-labeled cells.

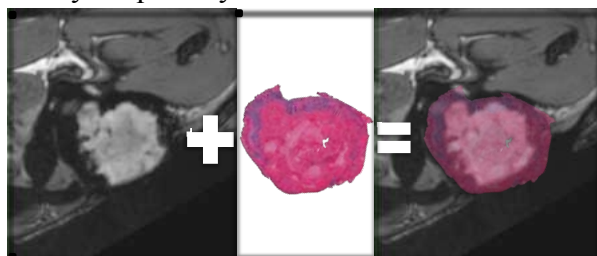


Figure 2: 3 week 4T1 tumour: MRI correlation with histopathology (A) Post-iron MR image, overlaid with (B) whole PPB stained section. (C) Excellent correlation with iron-labeled cell distribution, with blooming artifact present on MR image.

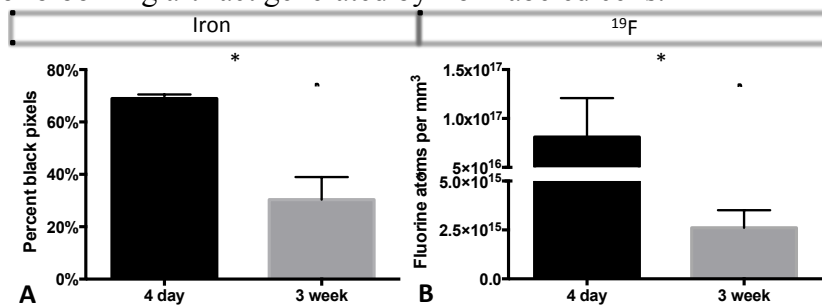


Figure 3: Quantification of (A) Iron and (B) ¹⁹F in tumour volume, suggesting there is a higher TAM content in 4 day vs 3 week time point, $*p < .05$

Deformable Registration of Dynamic Contrast Enhanced Breast MRI: The Influence of Sampling Percent on Enhancement Curves and Computation Time

Matthew Mouawad, Heather Biernaski, Muriel Brackstone, Michael Lock, R. Terry Thompson, Frank S. Prato, Stewart Gaede, Neil Gelman,

Ontario Institute for Cancer Research Imaging Translation Program,

Western University, Lawson Health Research Institute, London Health Sciences Centre, London, ON

Introduction: Dynamic contrast enhanced (DCE) MRI is applied extensively for diagnosis and treatment monitoring of breast cancer. One challenge in analyzing DCE data is that small patient movements can introduce artificial variation in the signal enhancement curves. It has been shown¹ that non-rigid image registration can greatly improve signal enhancement curves but computation time for registration can be long. A parameter that can affect computation time is the percentage of voxels sampled for estimation of the cost function, where larger sampling would lead to longer computation times but theoretically increased registration accuracy, especially for highly spatially varying images such as fat suppressed breast images. The objective of this work was to investigate the relationship between percent sampling and the accuracy of registration, local to the tumor, as assessed by fluctuations in signal enhancement curves.

Methods: Analysis was performed on 3T (Siemens Biograph mMR) images from a patient participating in a REB approved phase II clinical trial². Three-dimensional fat suppressed fast low angle shot images were acquired prior to gadovist injection and at 22 time points following injection. This abstract will focus on the last 14 images which were obtained with higher spatial resolution ($1.0 \times 1.1 \times 2.0$ mm voxels), but lower time resolution than the first eight. Deformable image registration of the affected breast was performed with the 3DSlicer³ software using Mattes mutual information and control point spacing of approximately 3 cm in the transverse plane and 1 cm through-slab. Each post contrast image was registered to the precontrast image, and this was repeated with percent sampling values of 5%, 23%, and 100%. Enhancement curves were generated from five regions of interest (ROI, 6 to 8 voxels) near the tumor edge and center. Second order polynomials were fit to the data using Matlab. The coefficients of variation (CV) of the data about the curve were determined as measures of “smoothness”.

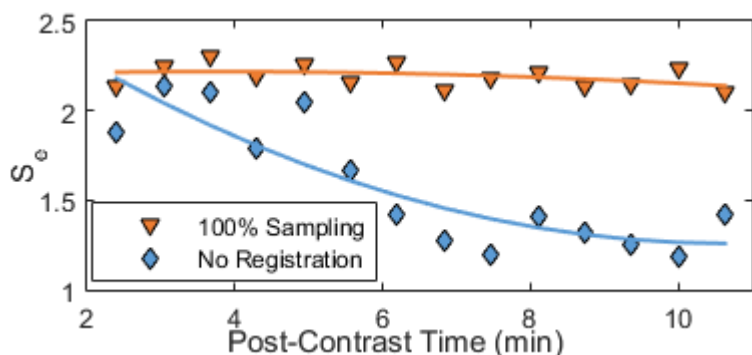


Figure 1 – Signal Enhancement (Se) curve data points for 100% sampling and no registration as well as 2nd order polynomial curve in solid line

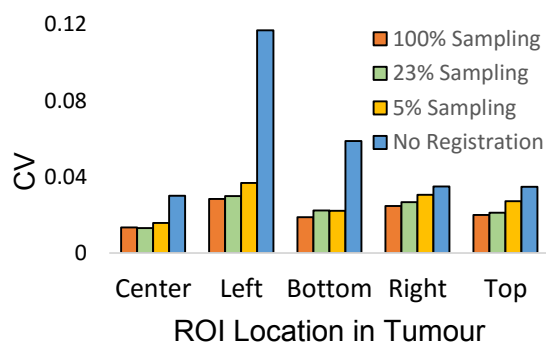


Figure 2 – Coefficient of Variation (CV) for each different sampling percentage in the different ROI locations

Results: Figure 1 shows postcontrast signal values (normalized by precontrast signal), and fitted curves for one ROI near the edge of the tumour for 100% sampling and no registration schemes. Without registration the signal curve shows large fluctuations. Figure 2 shows the CV for three percent sampling values as well as no registration for five ROIs. This demonstrates the large reduction in CVs obtained with image registration depending on ROI location. Higher percent sampling tended to lead to lower CVs but the differences were small, especially considering the longer average computational times (16, 7 and 4 min/image for 100%, 23% and 5% sampling, respectively). The improved tumor alignment after registration was also easily seen visually.

Conclusion: Deformable registration of postcontrast breast DCE images greatly reduces artificial signal variation due to motion. Signal variation appears to decrease with increased sampling but differences are small considering the large increase in computational time.

References: [1] Chebrolu *et al.* Intl. Soc. Mag. Reson. 2015. 23, [2] Guidolin *et al.* J Radiat Oncol 2015;4:423-430, [3] Federov *et al.* Mag. Res. Im. 2012; 30(9):1323-41 (<http://www.slicer.org>) **Acknowledgement:** Breast MRI coil courtesy Siemens healthcare Canada.

***In vivo* Quantitative Fluorescence Imaging Enabled by Spatial Frequency Domain Imaging for Enhanced Glioma Resection**

Mira Sibai^{1,2*}, Israel Veilleux², Frederic Leblond³ and Brian C Wilson^{1,2}

¹ Department of Medical Biophysics, University of Toronto, 101 College Street, Toronto, ON M5G 1L7 Canada

² Princess Margaret Cancer Center/University Health Network, 610 University Avenue, Toronto, ON M5G 2M3 Canada

³ École Polytechnique De Montreal, 2900, boul. Édouard-Montpetit Montréal, Québec H3T 1J4 Canada

Introduction

Intra-operative fluorescence-guided surgery (FGR) enables maximum safe resection of glioma by providing real-time tumor contrast. In its most widely used form, FGR is mediated by the preferential overproduction of the fluorophore protoporphyrin IX (PpIX) in malignant tissue after an oral dose of its precursor 5-Aminolevulinic Acid (ALA) [1]. ALA-PpIX FGR has been shown to significantly increase completeness of tumor resection [2]. However, the subjective visual assessment and the variable intrinsic optical attenuation of tissue limit this technique to reliably delineating only high-grade tumors that display strong fluorescence.

Methods

We have previously shown that quantitative assessment by non-invasive point spectroscopic measurements of the absolute PpIX concentration, [PpIX], in the tissue further improves the accuracy of FGR, extending it also to surgically-curable low-grade glioma [3]. In this approach, diffuse reflectance and fluorescence spectroscopy are used with a light-transport model to decouple the intrinsic optical properties from the fluorescence signal [3]. More recently, we have shown that implementing spatial frequency domain imaging (SFDI) to recover maps of the tissue optical absorption and scattering properties extends the point measurements to wide-field quantitative fluorescence imaging (qFI) [4]. Here, we present first results of this novel technique [4] modified and optimized for preclinical *in vivo* imaging. From SFDI, 2D maps of tissue optical properties are used as inputs to the light transport model that converts the raw hyperspectral fluorescence images to 2D images of [PpIX]. To assess the use of this system during surgery, SFD-enabled qFI has been tested on a rat brain tumor model (RG2) before and after gross tumor resection using 3 different ALA doses. [PpIX] derived by SFD-enabled qFI are compared with [PpIX] derived by the intraoperative probe.

Results

The qFI-derived [PpIX] maps agree within 20% of the [PpIX] values derived by the fiber-optic probe when sampling similar tissue regions *in vivo*.

Conclusions

SFD-enabled qFI is a more accurate imaging modality than state-of-the-art qualitative FGR of gliomas. Importantly, it may represent a more practical extension to the quantitative fiber-optic probe.

Acknowledgments

This work was supported by the National Institutes of Health (US): grant # R01 NS052274. #244217

References

- [1] M. J. Colditz and R. L. Jeffree. *J. Clin. Neurosci.* 19(11), 1471–1474 (2012).
- [2] W. Stummer, U. Pichlmeier, T. Meinel, O. D. Wiestler, F. Zanella, and H. J. Reulen; ALA-Glioma Study Group. *Lancet Oncol.* 7(5), 392–401 (2006).
- [3] P. A. Valdés, A. Kim, F. Leblond, O. M. Conde, B. T. Harris, K. D. Paulsen, B. C. Wilson, and D. W. Roberts. *J. Biomed. Opt.* 16(11), 116007 (2011).
- [4] M. Sibai, I. Veilleux, J.T. Elliott, F. Leblond, and B.C. Wilson. *Opt. Express* 6, 4923-4933 (2015)

Clinical workflow for spinal curvature measurement with portable ultrasoundReza Tabanfar^{a, b}, Christina Yan^a, Michael Kempston^c, Daniel Borschneck^c, Tamas Ungi^a, Gabor Fichtinger^a^aLaboratory for Percutaneous Surgery, School of Computing, Queen's University; ^bSchool of Medicine, Queen's University; ^cDepartment of Surgery, Queen's University

INTRODUCTION: Continual spinal curvature monitoring is essential in making treatment decisions in scoliosis. Monitoring entails radiographic examinations, however repeated ionizing radiation exposure has been shown to increase the risk of cancer later in life. Ultrasound does not emit ionizing radiation and thus is a safer alternative for spinal curvature monitoring. We investigated a clinical sonography protocol and challenges associated with position-tracked ultrasound in spinal curvature measurement in paediatric scoliosis.

METHODS: Lateral ends of transverse processes (TPs) were localized in 3-D space with cross sectional ultrasound snapshots using 3D Slicer software. The transverse process angle (TxA) – the angle between the line joining the midpoint of two opposite TPs and the transverse plane – was determined for each vertebra. Based on the orientation of each vertebra, the overall Cobb angle was determined and compared to the radiographically determined Cobb angle. We tested our methodology on five patients in a local pediatric scoliosis clinic.

RESULTS: Despite correlation between radiographic and ultrasound measurements in phantom studies, we encountered new challenges in the clinical setting, chiefly, differentiating TPs from ribs during landmarking. We observed up to 13° angle variability for a single vertebra and a $9.85^\circ \pm 10.81^\circ$ difference between ultrasound and radiographic Cobb angles for thoracic curvatures. We explored two alternative sonography strategies: (1) landmarking the midpoint of the most medially visible ultrasound snapshot of the TPs (medial TP method) and (2) landmarking the center of two laterally equidistant points from each spinous process (lateral equidistant TP method). Testing on a *healthy volunteer* (14 vertebrae), we observed average TxA values within $3.29^\circ \pm 3.01^\circ$ of expected values for the medial TP method and within $4.80^\circ \pm 4.24^\circ$ for the lateral equidistant TP method. This suggests the medial TP method may yield more accurate Cobb angles; however, further testing is required. We also tested landmark visualization with two machines: the Telemed MicrUs EXT-1H and the Sonix Touch. We found the results to be comparable. Additionally, we were unable to visualize landmarks in the lumbar region where superficial tissue depth was 25-35mm. As a solution, we used a lower frequency transducer with greater penetrative ability. Testing at 5MHz (rather than 10 MHz) on a *healthy volunteer* (11 thoracic and five lumbar vertebrae), we observed average lumbar vertebra angles within $4.03^\circ \pm 3.56^\circ$ of expected values, while we could not evaluate lumbar TxA angles when scanning at 10MHz. When we tested the thoracic region, we observed TxA values within $2.62^\circ \pm 2.56^\circ$ of expected values at 5MHz and angles within $5.29^\circ \pm 4.27^\circ$ at 10MHz. This suggests that scanning at 5MHz, especially in areas with thick soft tissue, might improve accuracy, although more testing is needed. Finally, in volunteers with large Cobb angles (greater than 40° thoracic and 60° lumbar), we observed spinal protrusions, incomplete probe-skin contact, and partial ultrasound images not suitable for landmarking. To mitigate this, we propose using an acoustic standoff pad taped onto the participant's back to create a smooth contour. We tested a 1cm deep standoff pad with a lumbar phantom. The average TxA angle obtained using the pad was found to be within $1.11^\circ \pm 0.61^\circ$ of the TxA angle obtained without using the standoff pad, suggesting this can be a viable strategy to mitigate this challenge.

CONCLUSIONS: Our clinical investigation revealed three main challenges that have not been previously reported in literature on US scoliosis monitoring phantom studies. These include: TP/rib differentiation and accurate anatomical landmarking in the thoracic region, visibility of bony structures in regions with thick soft tissue, and maintaining full probe to skin contact over surface contour protrusions in severe scoliosis. We offer possible solutions to these obstacles. These challenges must be resolved before a clinically practical sonography and angle measurement protocol can be developed for scoliosis monitoring.

Quantification of Vertebral Trabecular Bone Strain Via Feature Based Image Registration

Hoi-Ki Tong^{*1,2}, Michael R Hardisty², and Cari Whyne^{1,2}

Development of Novel Therapies for Bone and Joint Diseases

Institute of Biomaterials & Biomedical Engineering, University of Toronto, Toronto, Ontario, Canada¹

Orthopaedics Biomechanics Laboratory, Sunnybrook Research Institute, Toronto, Ontario, Canada²

Introduction. Strain is a robust indicator of bone failure initiation. Previous work has demonstrated the measurement of vertebral trabecular bone strain through μ CT based image registration using digital volume correlation (DVC) for use in the preclinical studies of the mechanical integrity of bone samples (1, 2). DVC uses a uniform subset image size which results in potentially sub-optimal strain field resolution. Feature based registration uses recognizable feature points that depend on the supplied image for image registration, allowing for a non-uniform strain field resolution that scales with the density of feature points in the image area. This project aims to apply feature based registration to quantify strain in vertebral trabecular bone imaged with μ CT to quantify strain. It is hypothesized that the unique topology of the trabecular structure can be used to extract reliable feature points that can be matched to produce higher resolution strain fields compared to DVC techniques.

Methods. The strain quantification algorithms investigated in this study involve 2 steps. 1) calculating a displacement field from an image of a specimen to an image of a specimen under mechanical load 2) calculating the strain based from the displacement field. Two methods of feature registration, Scale Invariant Feature Transform (SIFT) and Skeletonization, were investigated for calculating the displacement field. The Thin Plate Spline method was compared against a Moving Least Squares Meshless Method for calculating strain from the displacement fields.

To test the algorithm, artificial spatially non-uniform (2% constant compressive strain and 2% linearly varying compressive strain (figure 1)) displacement fields were applied to deform a 2D sagittal μ CT slice of rat tail vertebral trabecular bone.

Results. Initial testing showed that SIFT was unable to reliably perform matching for identified trabecular feature points leading to large errors in the generated strain field. Skeletonization generated a more accurate and precise displacement field. Strain field calculation using Thin Plate Splines was not able to cope with the errors produced by feature matching, whereas the Meshless Methods proved more resilient these errors. Further improvements in strain calculation were found by applying additional smoothing on the initial displacement field using Moving Least Squares prior to strain calculation. Using an ideal 2% linearly increasing strain field, the Skeletonization with Meshless Method approach yielded the best performance, with an accuracy of $-405 \mu\text{strain}$ and a detection limit of $1210 \mu\text{strain}$ at $221 \mu\text{m}$ resolution. A previously reported DVC algorithm yielded a similar detection limit ($1190 \mu\text{strain}$), but with a lower accuracy for the same test ($2370 \mu\text{strain}$) at $770 \mu\text{m}$ resolution (2).

Conclusions. The Skeletonization algorithm combined with the Smoothed Meshless Method calculated strain at a higher resolution, with a similar detection limit, to that of DVC methods. Future improvements to this method include the implementation of subpixel feature point identification and extending the algorithm to 3D. Ultimately, a hybrid feature/DVC registration algorithm may further improve the ability to measure trabecular bone strain using μ CT based image registration.

References. [1] Bay *et al.* Exp Mech 1999; 39:217-226. [2] Hardisty *et al.* J Biomech Eng-T ASME 2009; 13:6.

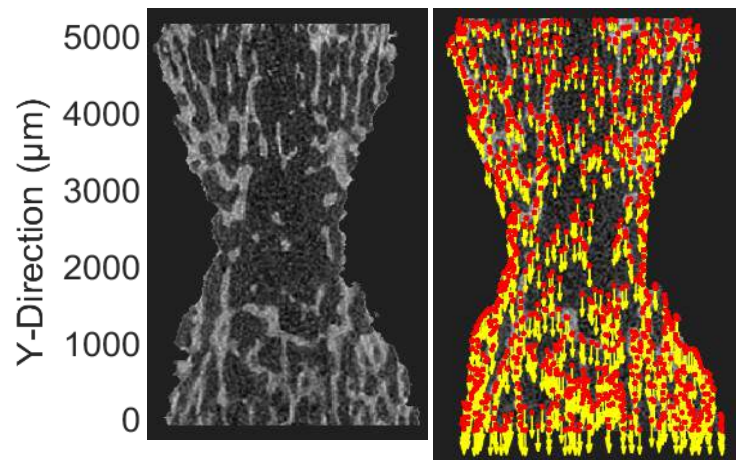


Figure 1: Validation Test: A sagittal μ CT slice of a rat tail vertebra with trabecular network isolated (left), and matched feature points found on the non-deformed image in red along with the resulting displacement vectors, scaled up for visualization, in yellow (right). The displacement field was an artificial 2% linearly increasing strain applied for the purpose of validation of the strain quantification algorithm that used Skeletonization feature identification with Meshless Method strain calculation.

Carotid Atherosclerosis Imaging with Quantitative Susceptibility Mapping

Chaoyue Wang¹, Saifeng Liu, PhD², Sagar Buch², Hyun Seok Choi³, Eo-Jin Hwang³, Zhaoyang Fan⁴, E. Mark Haacke, PhD^{1,2,5,6}

¹School of Biomedical Engineering, McMaster University, Hamilton, ON, Canada, ²MRI Institute for Biomedical Research, Waterloo, ON, Canada, ³Department of Radiology, St. Mary's Hospital, Seoul, Korea, ⁴Department of Radiology, Cedars Sinai Hospital, Los Angeles, California, USA, ⁵Department of Radiology, Wayne State University, Detroit, Michigan, USA, ⁶Biomedical Engineering, Northeastern University, Shenyang, China.

Introduction: Stroke has become one of the leading causes of death and disability worldwide. Carotid atherosclerosis can cause vessel narrowing restricting blood flow to the brain and resulting in stroke.¹ A primary goal of carotid atherosclerosis imaging is to identify different type of plaque, especially high-risk (vulnerable) plaque, this will also have an impact on the choice of treatment for the patient. Quantitative susceptibility mapping (QSM) has been widely used in brain as a method to quantify the tissue susceptibility.² The susceptibility difference between the vessel wall, hemorrhage (or thrombosis), calcium and surrounding tissue makes QSM a powerful tool for characterizing atherosclerosis. The purpose of this study was to develop a new QSM method to detect carotid plaque and recognize vulnerable features.

Methods: *Data acquisition:* Healthy volunteers and patients were imaged on a 3T scanner (MAGNETOM Verio, Siemens Healthcare, Erlangen, Germany) using a five-echo 3D SWI sequence and a 2D TSE black-blood sequence. The imaging parameters for the 3D SWI sequence were: TEs 4.26, 6.68, 9.1, 11.52 13.94 ms, TR=18ms, BW=488 Hz/pixel, voxel size=0.33 x 0.33 x 2 mm³. The imaging parameters for the 2D TSE sequence were TE=59ms, TR=4000ms, FA=160°, BW=407 Hz/pixel, voxel size=0.3 x 0.3 x 2 mm³. *Data processing:* The following steps were performed to generate susceptibility maps using MATLAB: 1) phase unwrapping using the Catalytic Multiecho Phase Unwrapping Scheme (CAMPUS) algorithm; ³ 2) a regional 2D polynomial fitting was performed in the vessel region to remove background field induced by global geometry, air-tissue interfaces and field inhomogeneities;

Results: Healthy volunteer's carotid vessel wall was clearly seen in the susceptibility map (Figure 1). Susceptibility map (Figure 2) indicates there were calcified plaque inside the wall and the geometry agreed with black-blood image (Figure 3). A second example shows a dark region in SWI magnitude image (Figure 4) and susceptibility map (Figure 5) indicates hemorrhage that may represent the advanced stage of vulnerable plaque.

Conclusion: Our preliminary results suggest that a multi-echo SWI approach with regional 2D polynomial fitting method is promising for imaging the carotid vessel wall and atherosclerosis. Further studies to better remove background fields and more clearly represent unaliased data around the plaque should lead to a more robust and easy to use approach clinically. And *ex vivo* histological analysis is necessary to determine the accuracy of this method.

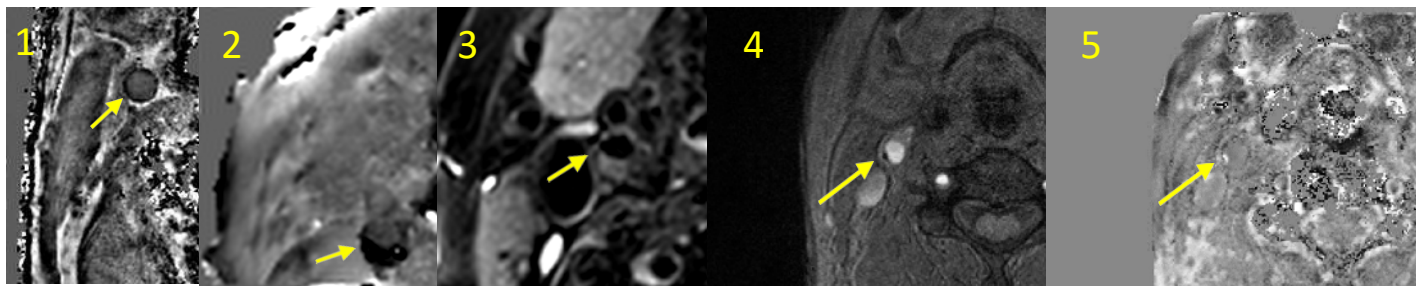


Figure: 1) Healthy carotid artery vessel wall; 2) QSM showing negative susceptibility indicating calcification inside the vessel wall; 3) black blood image showing thickened wall; 4) SWI magnitude image showing the wall and a dark region inside that may represent thrombosis and vulnerable plaque; 5) QSM showing that indeed the dark region is laden with iron.

References: 1. Flaherty, Matthew L., et al. Carotid artery stenosis as a cause of stroke. *Neuroepidemiology* 40.1 (2013): 36-41. 2. Haacke, E.M. et al. Quantitative susceptibility mapping: current status and future directions. *Magn. Reson. Imag.* 33.1 (2015): 1-25. 3. Feng, W. et al. Catalytic multiecho phase unwrapping scheme (CAMPUS) in multiecho gradient echo imaging: Removing phase wraps on a voxel-by-voxel basis. *Magn. Reson. Med.* 70.1 (2013): 117-126.

Radiomics Feature Clusters and Prognostic Signatures Specific for Lung Cancer

Y Zhang¹, A Eilaghi¹, A. Wong², A Oikonomou¹, M. A. Haider¹, F. Khalvati¹

¹Medical Imaging, Sunnybrook Research Institute, University of Toronto, Toronto, ON, Canada

²Systems Design Engineering, University of Waterloo, Waterloo, ON, Canada

Introduction: Radiomics quantifies tumor phenotypes by extracting a large number of quantitative image features. The large number of radiomics features leads to the multiple testing problem, increasing the Type I error rate if not being corrected, or increasing the Type II error rate if being adjusted too conservatively [1]. Consensus clustering (CC) has shown the potential in reducing redundancy of image features and providing efficient radiomics signatures from investigated features [2]. In this work, we used CC technique to identify radiomics feature clusters which yield potential radiomics signature features for lung cancer. We hypothesized that the developed and identified radiomics signature features are associated with clinical outcome in lung cancer patients.

Methods: 159 patients with overall 159 lung tumors, (Female: 79, Male: 80), with mean age 74.67 yrs (52-92), who underwent Stereotactic Body Radiation Therapy (SBRT), were included. Radiomics feature extraction was applied to PET and CT images of staging PET/CT studies [3]. Manual contouring of lesions was performed using ProCanVAS [4]. Through this process, a total number of 96 imaging features were obtained. Cluster building and statistical analysis were performed by R 3.2.2, ConsensusClusterPlus [5], and Survcomp [6] packages, and the cluster medoids (signature features) were selected by choosing the features which have the highest average pairwise correlations within clusters.

Results: From the cumulative distribution function plot of CC, 6 was chosen as the optimal number of clusters. Figure 1 shows the consensus map of the obtained radiomics feature clusters. 5 of those clusters had high cluster consensus (cluster consensus ≥ 0.75), and 1 had moderate consensus ($0.5 \leq$ cluster consensus < 0.75). Also, clusters 1, 3 and 5 showed significant within-cluster correlation and significant association with cancer recurrence, having mean concordance indices (CI) of signature features > 0.5 (Table 1). Our results indicate that a significant correlation exists between identified radiomics feature clusters and cancer recurrence.

Conclusions: Radiomics feature cluster analysis on pre-SBRT CT and PET images showed significant association with recurrence in lung cancer. Also, through trimming 96 features to 6 medoids, consensus clustering showed the potential in reducing the redundancy of lung cancer image features and solving the multiple comparison problems in radiomics analysis.

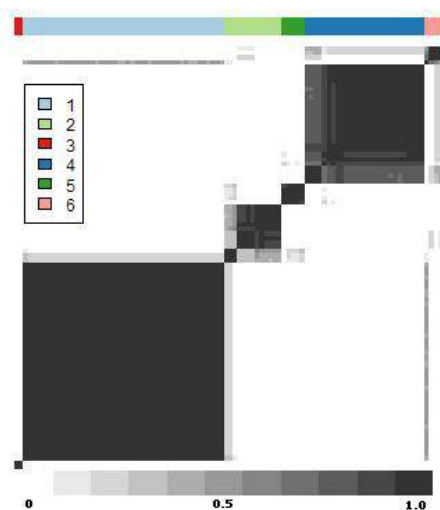


Figure 1. Cluster consensus map of 6 clusters.

| Cluster | Cluster Size | Consensus | Within Cluster Correlation | Correlation P value | Concordance Index |
|---------|--------------|-----------|----------------------------|---------------------|-------------------|
| 1 | 45 | 0.999 | 0.512 | $< 1.0E-50$ | 0.554 |
| 2 | 13 | 0.731 | 0.327 | $< 1.0E-50$ | 0.437 |
| 3 | 2 | 1 | 0.656 | $5.81E-18$ | 0.563 |
| 4 | 27 | 0.912 | 0.356 | $< 1.0E-50$ | 0.437 |
| 5 | 5 | 0.974 | 0.571 | $< 1.0E-50$ | 0.571 |
| 6 | 4 | 0.772 | 0.394 | $1.23E-22$ | 0.450 |

Table 1. Clustering analysis summary.

References:

[1] Kumar et al. Magnetic Resonance Imaging. 30 (2012) 1234–1248 [2] Parmar et al. Nature, Scientific Report, 5:11044 | DOI: 10.1038. [3] Khalvati et al BMC Medical Imaging (2015) 15:27 [4] Oikonomou et al. DOI: 10.1097/RTI.154 Conference: Annual meeting of Society of Thoracic Radiology [5] Wilkerson, et al. Bioinformatics 26, 1572–1573 (2010). [6] Schröder et al. Bioinformatics 27, 3206–3208 (2011).

MagA-derived MR Contrast Persists Despite Cellular Differences in Iron Metabolism

Alizadeh*, K; McGuire, T; Donnelly, S; Liu, L; Thompson, T; Prato, F; Hoffman, L; Gelman, N; Goldhawk, D
Heart Failure: Prevention Through Early Detection Using New Imaging Methods
Imaging Program, Lawson Health Research Institute; Medical Biophysics & Collaborative Graduate Program in
Molecular Imaging, Western University, London, Canada
* Trainee, Supervisor

Introduction: MagA expression in all mammalian cells leads to increases in iron contrast [1]. Nevertheless, iron handling activities vary among cell types and may influence the detection of MagA-derived contrast by magnetic resonance imaging (MRI). For example, there are striking differences in iron uptake and export between MDA-MB-435 melanoma cells and P19 multipotent stem cells, a model of cardiac differentiation. We have expanded our study in these cells and compared their iron-handling properties and magnetic resonance (MR) contrast to that in MDA-MB-231 breast cancer cells and THP-1 monocytes.

Methods: Cells were cultured in the presence and absence of iron supplementation: 250 μ M ferric nitrate / medium. Untransfected parental cells were compared to those expressing MagA, a putative iron transport protein from the AMB-1 species of magnetotactic bacteria [2]. The reversible component of the total transverse relaxation rate, $R2'$ was calculated from the difference between $R2^*$ and $R2$ ($R2' = R2^* - R2$). MRI relaxation rates ($R2^*$, $R2$) were obtained at 3 Tesla (T) using cells mounted in gelatin phantoms [3]. Total cellular iron content was measured by inductively-coupled plasma mass spectrometry and is strongly correlated to $R2'$ [1]. Transferrin receptor and ferroportin levels were detected by Western blot to assess iron uptake and export, respectively.

Results: P19 cells display pronounced iron uptake and export activities unlike MDA-MB-435 cells (Figure 1). Both untransfected and MagA-expressing P19 cells exhibit similar iron uptake when cultured 1 week in the presence of iron supplementation (+Fe). However, within 24 hours after the removal of iron supplement from P19 culture (24h-Fe), active iron export is apparent. Importantly, MagA-expressing cells retain their intracellular stores of iron and $R2'$ contrast (Figure 1) while parental cells do not.

Conclusions: The iron handling activities of P19 cells are quite different than those of MDA-MB-435 and more similar to alternatively activated M2 macrophages with respect to intrinsically high iron import and export functions [4,5]. Whereas MagA expression mainly influences iron uptake in MDA-MB-435, iron export is modulated by the expression of MagA in P19 cells. Apparently, MagA-derived activity in mammalian cells is not appreciably regulated by iron homeostasis.

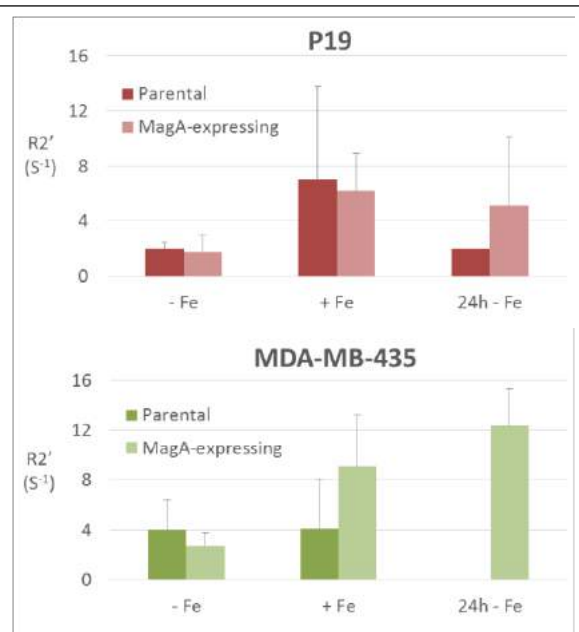


Figure 1. Comparison of $R2'$ transverse relaxation rates in P19 and MDA-MB-435 cells. After 1 week of culture +/- iron-supplemented medium, cells were harvested either immediately (- Fe, + Fe) or after a further 24 hours of culture in non-supplemented medium (24h-Fe). 3T MRI was performed as previously described using multi-echo gradient echo and single echo spin echo sequences to obtain $T2^*$ - and $T2$ -weighted images, respectively [3]. Values are the mean +/- standard deviation where $n = 3$ to 8. For parental P19 at 24h-Fe, $n = 2$. No data is shown for parental MDA-MB-435 at 24h-Fe.

References:

[1] Goldhawk *et al* (2015) *Magnetic Resonance Insights* 8(S1), 9; [2] Goldhawk *et al* (2012) *WIREs Nanomed Nanobiotechnol* 4, 378; [3] Sengupta *et al* (2014) *Frontiers in Microbiol* 5, 29; [4] Corna *et al* (2010) *Haematologica* 95, 1814; [5] Theurl *et al* (2008) *Blood* 111, 2392

Formulation of a GMP Quality Kit for the Preparation of ^{111}In -DTPA-NLS-Trastuzumab Injection: An Auger Electron-Emitting Theranostic Agent for HER2-Positive Breast Cancer
Vanessa A. Prozzo, Conrad Chan and Raymond M. Reilly

Department of Pharmaceutical Sciences, University of Toronto

BACKGROUND: ^{111}In -DTPA-NLS-trastuzumab is routed to the nucleus of HER2-positive breast cancer cells where the Auger electrons emitted by ^{111}In are damaging to DNA yielding potent cell killing in vitro and tumour growth inhibition in vivo in athymic mice. The gamma emissions of ^{111}In permit SPECT imaging to assess the delivery of ^{111}In -DTPA-NLS-trastuzumab to tumours for radioimmunotherapy. Thus, ^{111}In -DTPA-NLS-trastuzumab is a potential theranostic agent for HER2-positive breast cancer. To advance ^{111}In -NLS-trastuzumab to a Phase I/II clinical trial, studies were conducted to develop a kit under GMP conditions to prepare clinical quality ^{111}In -DTPA-NLS-trastuzumab injection. The solubility and tendency of these immunoconjugates (ICs) to aggregate are major challenges in designing these kits.

METHODS: Trastuzumab (Herceptin) was buffer-exchanged into 0.1 M NaHCO_3 , then reacted with a 10- or 15-fold molar excess of benzylisothiocyanate DTPA (bzDTPA). The ICs were then buffer-exchanged by ultrafiltration into 0.1 M NaPO_4 buffer with 0.01% polysorbate-20 (PS-20) to maintain IC solubility and prevent aggregation. Purified DTPA-trastuzumab was modified with maleimide groups for conjugation to nuclear localization sequence (NLS) peptides by reaction with a 5- or 10-fold molar excess of sulfo-SMCC in 0.1 M NaPO_4 buffer with 0.01% PS-20. Following re-purification, the ICs were reacted with a 50-, 60- or 75-fold molar excess of NLS peptides with a terminal thiol group. The DTPA-NLS-trastuzumab ICs were purified and buffer-exchanged into 0.1 M or 0.05 M ammonium acetate (NH_4OAc) buffer with 0.01% PS-20. The final protein concentration was determined by measuring UV absorbance at 280nm, then adjusted to 5.0 mg/mL and 2 mL aliquoted into single vials (kits). The kits were labeled with 111-137 MBq of ^{111}In . Desired specifications were 2-7 DTPA and 5-11 NLS per trastuzumab, >90% labeling efficiency, <5% aggregation assessed by SDS-PAGE and K_a and B_{max} values within $0.1\text{-}2.1 \times 10^7$ L/mol and $0.3\text{-}5 \times 10^6$ HER2/cell respectively.

RESULTS: Six kits (RG001-6) were manufactured. RG001 revealed that addition of PS-20 to the buffers reduced aggregate formation in the kit. RG002 was manufactured using a 10-fold molar excess of bzDTPA, 10-fold SMCC and 50-fold NLS peptides and was formulated in 0.1 M NH_4OAc buffer with 0.01% PS-20. However, aggregation occurred with addition of sulfo-SMCC. In RG003, a 5-fold excess of sulfo-SMCC was used and aggregation was reduced. RG004 was manufactured with a 10-fold excess of bzDTPA, 5-fold SMCC, and 75-fold NLS, and formulated in 0.1 M NH_4OAc buffer with 0.01% PS-20, but aggregation was again noted. In RG005 the NLS reaction ratio was reduced to 60-fold and aggregation was greatly reduced. For RG002-5, DTPA substitution level ranged from 2-4 bzDTPA/trastuzumab, labeling efficiency was $79.5 \pm 0.6\%$, 0-8 NLS per trastuzumab, >5% aggregation, and the K_a and B_{max} were within $0.1\text{-}2.1 \times 10^7$ L/mol and $0.3\text{-}5 \times 10^6$ receptors/cell respectively. In RG006 0.05 M NH_4OAc buffer with 0.01% PS-20 was used for formulation which reduced aggregation to <5%. For RG006 2.6 ± 0.5 DTPA and 10 NLS were conjugated per antibody, the K_a and B_{max} values are 0.1×10^7 L/mol and $0.3\text{-}5 \times 10^6$ HER2/cell respectively but the labeling efficiency was 70.0 %.

CONCLUSION: Careful selection of reaction conditions was required to obtain a kit for preparation of ^{111}In -DTPA-NLS-trastuzumab injection that exhibited a low (<5%) level of IC aggregation. Kits met specifications for DTPA and NLS substitution and exhibited preserved HER2 binding, but further optimization is required to increase the labeling efficiency to >90% for clinical use. This research was supported by a grant from the Canadian Breast Cancer Foundation (Ontario Branch).

Improving the Relaxivity of Non-Gd MRI Contrast Agents: Tuning the Electron Spin of Mn^{III} Porphyrin

Yuanyuan Lyu,^a Henry Tieu,^a Hanlin Liu,^{a,b} Yong Le Zhu,^{a,b} Maryam Abdinejad,^a Meissam Noroozifar,^a Kagan Kerman,^{a,b,c,*} Xiao-an Zhang^{a,b,c,*}

^aDepartment of Physical and Environmental Science, ^bDepartment of Chemistry and ^cDepartment of Biological Sciences, University of Toronto Scarborough, Toronto, Ontario, Canada

Introduction: About 50% clinical MRI scans requires administration of a paramagnetic contrast agent (CA) with unpaired electron (*e*-spin) to improve sensitivity and tissue contrast. Gadolinium based CAs (GBCAs) are the most widely used in clinics, since Gd^{III} has a large number (7) of unpaired electrons.¹ Clinical GBCAs, however, exhibit only moderate contrast enhancement efficiency (measured as *T*₁ relaxivity or *r*₁) which further decreases with increasing magnetic field strength.¹ In addition, GBCAs have been associated with nephrogenic systemic fibrosis (NSF), a severe adverse effect in patients with poor renal function, due to the release of free toxic Gd ions in vivo.² Recently, cases of Gd-deposit in the brain have been increasingly reported in patients with healthy kidneys. To address these limitations, we are developing novel Manganese^{III} porphyrins (MnPs) as non-Gd alternatives.³ MnPs provide advantages such as greater stability, lower toxicity (Mn is a micronutrient), and structural versatility.⁴ More importantly, certain MnPs exhibit anomalously higher *r*₁ than regular GBCAs, particularly at high clinical fields,³ despite the fact that MnP has much less unpaired electrons (4) than GBCA. Here we provide a novel hypothesis to explain this unusual phenomenon and based on this theory, new MnPs with even higher sensitivity have been constructed.

Methods: We propose that a spin-polarization mechanism (SPM) has a significant contribution to the high *r*₁ of MnP. Through a metal-ligand orbital overlap, the porphyrin can donate one electron to Mn^{III}, generating a Mn^{II} and porphyrin radical cation. This excited state configuration has six unpaired electrons instead of four, with five positive spins on Mn^{II} and one negative spin on porphyrin radical. SPM not only increases the effective spin population, but also leads to spin delocalization from the Mn centre to a larger and more accessible area on porphyrin ring. Both effects will enhance the hyperfine coupling interaction between electron spins and water ¹H nuclei, thus improving *r*₁. To test this hypothesis, we synthesized a series of new MnPs, derivatized from MnTPPS, by introducing different functional groups, which either promote or prohibit the SPM (Fig 1A). The difference in electron donating ability of these new porphyrins were examined with electrochemistry and UV-vis spectroscopy. DFT calculation is pursued on spin configuration. The field-dependent *r*₁ values were obtained as the nuclear magnetic resonance dispersion (NMRD) profiles, using a fast field cycling NMR relaxometer coupled with a cryogen-free superconducting magnet (HTS-110), covering fields from 0 to 3 tesla.

Results: All new MnPs and apo-porphyrins intermediates were synthesized with multiple steps, purified and characterized with HPLC, NMR, ESI-MS and UV-vis spectroscopies. Cyclic voltammetry plots confirmed that introducing an electron-rich group, NH₂, increases the electron-donating tendency of porphyrin ligand to form a cation radical. Vice versa, an electron-withdrawing group, NO₂, decreases this tendency. The electron donating effect also facilitates the ligand-metal electron transfer, as verified by UV-vis spectra of different MnPs. DFT calculations of spin density and delocalization is under investigation. Finally, the NMRD profiles demonstrated that MnP with NH₂ exhibits higher *r*₁ than MnTPPS, and the analog with NO₂ shows lowest *r*₁, in a good agreement with our hypothesis (Fig 1B). We have further demonstrated that *cis* isomer of MnP with two NH₂ groups, shows higher *r*₁ than the *trans*-analog, consistent with the prediction.

Conclusions: A spin-polarization mechanism was proposed for the first time to rationalize anomalously high *r*₁ of MnPs. This novel mechanism offers a unique approach to further optimize the *r*₁ of MnPs, providing the next generation Gd-free CAs with high sensitivity at high clinical fields.

References: [1] *Chem. Rev.* **1987**, 87, 901; [2] *Radiol. Clin. North Am.* **2009**, 47, 827. [3] *J. Med. Chem.* **2014**, 57(2), 516. [4] *J. Biol. Inorg. Chem.* **2014**, 19, 229

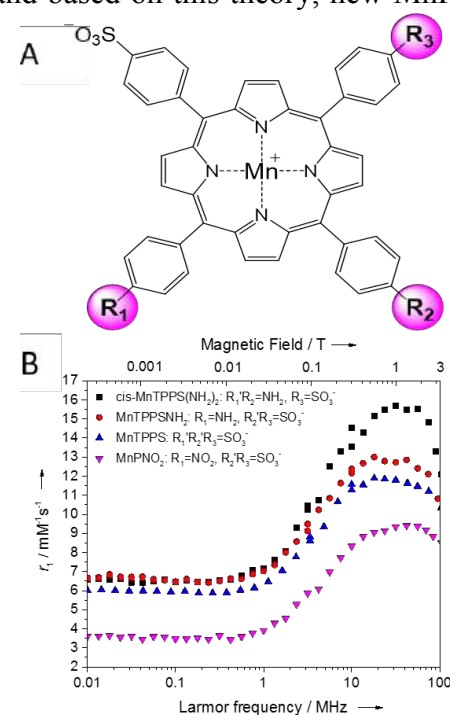


Figure 1: a) Structures of MnP derivatives. b) Selected NMRD profiles

Contrast Optimization for Prostate Cancer Tumours *in vivo* at 3T

Christopher Brian Abraham^{1,2} Boguslaw Tomanek^{2,3} Laura Curiel^{1,2}

¹Thunder Bay Regional Research Institute, ON, ²Lakehead University, Thunder Bay, ON, ³University of Alberta, Department of Oncology, Edmonton, AB, Canada

Introduction: Magnetic Resonance Imaging (MRI) has high spatial resolution and the best soft tissue contrast among *in vivo* imaging modalities. However, contrast to noise ratio (CNR) of cancerous tissues is often insufficient for accurate diagnosis. These tissues are very difficult to identify when using standard T₁ or T₂-weighted MRI, in particular when normal and diseased tissues have similar relaxation times, such as prostate tumours.¹ This poor differentiation between healthy and malignant tissue, often leads to overtreatment degrading future quality of life of cancer patients. To rectify this problem contrast agents are used. However multiple applications can lead to unknown side effects. Therefore the purpose of this work was to find out the optimal TE using a spin-echo pulse sequence that provides the maximum CNR for prostate cancer at 3T.

Methods: Signal for spin echo sequences (SE) with sufficiently long TR is defined by Eq. (1). We used this equation to calculate the CNR between two tissues as a function of TE and obtained a maximum by taking the derivative of CNR with respect to TE that resulted in Eq. (2).³

$$S_i = \kappa_i \rho_i e^{-\left(\frac{TE}{T_2^i}\right)} \quad (1) \quad TE^{max} = \frac{T_2^1 T_2^2}{T_2^2 - T_2^1} \ln\left(\frac{\kappa_1 \rho_1 T_2^2}{\kappa_2 \rho_2 T_2^1}\right) \quad (2)$$

Where κ_1 , κ_2 are the proportionality constants, ρ_1 , ρ_2 are the spin densities, T_1^1 , T_1^2 and T_2^1 , T_2^2 are the longitudinal and transversal relaxation times of sample 1 and 2 respectively; TR is the repetition time and TE is the echo time.

***In vitro* Experiments:** Molday ION Rhodamine Carboxyl (MIRB) was diluted to prepare nine samples in de-ionized water in 5-mm NMR tubes (T₂ values of samples in ms: 618, 323, 232, 169, 109, 86, 75, 47, 21). A MESE sequence was used with an 8-channel head coil (32 echoes, $\Delta TE = 20$ ms, TR = 5000ms, FOV = 100 mm x 100 mm, 3 mm slice thickness, 224 x matrix, NEX = 4).

***In vivo* Experiments:** 5×10^6 LNcaP cells suspended in 100 μ L of PBS were subcutaneously injected in the flank of 8 male athymic nude mice (Charles River). Data was acquired using a MESE sequence using an 8-channel sense wrist. (30 echoes, $\Delta TE = 8$ ms, TR = 1396ms, FOV = 240 mm x 240 mm, 3 mm slice thickness, 156 x 156 matrix, NEX = 4) For CNR calculations *in vivo*, κ values for each sample were approximated by extrapolating (1) to TE=0 from the MESE images.²

Results: Figure 1a and 1b show images at 2 different TEs showing the increased CNR by using the ideal TE. Figure 1c shows CNR as a function of TE for the different regions of interests used for CNR calculations. Max CNR for the example shown in figure 1 between muscle and prostate tumour tissue was found to occur at a TE of 56ms and was predicted to occur at a TE of 55.2ms a difference of 1.43%. Figure 2a shows a spin echo image at a TE of 40ms for *in vitro* samples. Figure 2b shows the CNR between different sample pairs as a function of TE. The mean correlation value between experimental and theoretical data for *in vitro* was $r = 0.998 \pm 0.002$ and $r = .991 \pm 0.005$ for *in vivo* and therefore correlates to theory. By using eq. 2 we were able to obtain a TE at which the max CNR between 2 samples was achieved within .1% \pm .4% for *in vitro* data of the maximum CNR observed in experiments.

Conclusions: It was possible to maximize prostate tumours CNR by selecting TE for SE pulse sequences based on theoretical predictions using Eq. (2). The implications of this work would allow MR users to optimize pulse sequence parameters to ensure they are getting the highest CNR possible

References: [1] Barentsz et al. (2012). ESUR Prostate MR Guidelines 2012. Eur Radiol, 746-757. [2] Tofts, P. (2003). Proton Density of Tissue Water. Quantitative MRI of the Brain. [3] Brown et al. (2014) *Magnetic Resonance Imaging: Physical Principles and Sequence Design*.

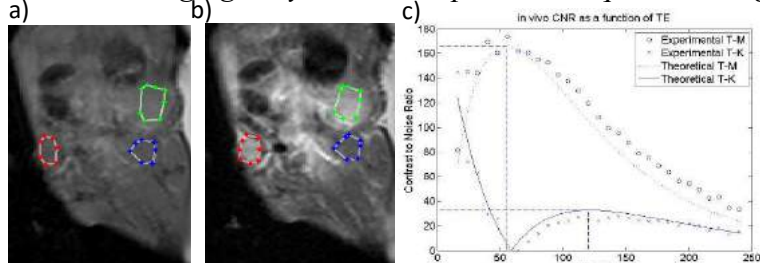


Figure 1-a),b) *in vivo* MR image showing region of interests used for CNR calculations tumour, muscle, and kidney as red, blue and green respectively. Images show highest CNR between TEs (TE=16ms, TE=56ms) c) CNR as a function of TE for *in vivo* data for different tissues as labeled. T,M,K represent the tumour, muscle, kidney respectively

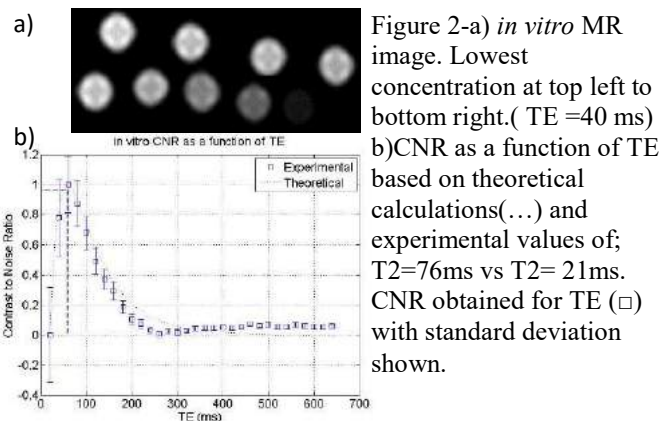


Figure 2-a) *in vitro* MR image. Lowest concentration at top left to bottom right. (TE = 40ms) b) CNR as a function of TE based on theoretical calculations (...) and experimental values of; T₂=76ms vs T₂=21ms. CNR obtained for TE (□) with standard deviation shown.

Validation of 3D Slicer Based Gel Dosimetry Analysis

K.M. Alexander¹, C. Pinter², G. Fichtinger², L.J. Schreiner^{1,3}

(1) Department of Physics, Queen's University, Kingston, Ontario. (2) School of Computing, Queen's University, Kingston, Ontario. (3) Medical Physics Department, Cancer Centre of Southeastern Ontario, Kingston, Ontario.

Introduction: In recent years, three-dimensional (3D) conformal radiation therapy techniques have advanced dramatically. Due to the complexity of these treatments, quality assurance for clinical processes, treatment units, and patient specific treatments is required to confirm that the radiation dose is delivered accurately and precisely. Three-dimensional radiation dosimetry tools, such as gel dosimeters, have been shown to be promising tools for measurement and verification of radiation dose deliveries. However, adoption of gel dosimetry in routine clinical processes has been challenging; the data collection, processing, and analysis needed to get meaningful results is laborious and time intensive. In this work, we present the validation of new software that executes the elaborate workflow needed to analyze a gel dosimeter.

Methods: In our clinic, gel dosimeter analysis was initially performed using the Computational Environment for Radiotherapy (CERR) package for Matlab (MathWorks, Natick, MA), coupled with custom Matlab scripts. To reduce analysis time and to produce a more robust analysis system, the gel dosimeter analysis workflow has been implemented in 3D Slicer (www.slicer.org) by developing a custom software extension. A toolbox of features tailored to radiation therapy called SlicerRT (www.slicerrt.org) allows for loading of DICOM-RT data, manipulation of structures, computation and display of dose-volume histograms, dose volume comparisons, and dose distribution visualization. Building on these pre-existing tools, we have developed a simple user interface which easily guides the user through the complete gel dosimetry workflow. In order to validate the developed gel dosimetry extension, each step of the extension has been analytically compared to the previous analysis method using Matlab and CERR. In this work, we present some of the validation and benchmarking of the registration step, dose calibration step, and gamma dose comparison step by comparing gel dosimeter analysis using the developed 3D Slicer gel dosimetry tool to the results obtained using the older Matlab and CERR analysis method.

Results: When compared to analysis performed using CERR and Matlab, the gel dosimetry analysis extension in 3D Slicer reduces analysis time from several hours to a matter of 5-10 minutes. The registration step in 3D Slicer is more robust and user friendly, eliminating tedious manual transformations in Matlab. The calibration step was found to have high reproducibility and precision (variation in dose sensitivity determination within 0.6% across multiple users). This is promising as it implies that multiple users can easily achieve similar calibration results. Results from the gamma dose comparison tool in SlicerRT align perfectly with results when using our in-house gamma algorithm. The behaviour of the SlicerRT comparison with respect to changes in noise, resolution, and the role of the reference and evaluated dose distributions were consistent with previous findings.

Conclusions: Preliminary results show that the 3D Slicer gel dosimetry workflow yields the same results as the former analysis method using Matlab, while substantially reducing the processing time and lowering the chance of user error. The increased efficiency of gel dosimetry analysis using 3D Slicer makes 3D dosimetry more clinically accessible.

Acknowledgements: This work was in part funded by OCAIRO, with additional funding by CIHR (MOP115101).

Coded Hemodynamic Imaging for Non-Contact Detection of Abnormal Blood Pulse Waveforms

Robert Amelard, David A Clausi, Alexander Wong

Department of Systems Design Engineering, University of Waterloo, Waterloo, ON, Canada

Introduction. Early detection of arrhythmias is a crucial step towards developing an effective treatment plan. However, early arrhythmia detection often relies on symptom-driven investigation, and may require expensive medical procedures. Recent developments in photoplethysmographic imaging (PPGI) have enabled long-distance non-contact monitoring of the blood pulse waveform [1]. Through easy and safe non-contact imaging, this technology can support early detection and prevention of cardiovascular diseases. Although recent results have been promising for this non-contact system, little work has been done to validate PPGI technology for detecting cardiovascular abnormalities. In this study, we present a first step towards using PPGI for detecting arrhythmias in the blood pulse waveform in order to generate interest for using PPGI to assess early onset of arrhythmias.

Methods. We used the Coded Hemodynamic Imaging (CHI) PPGI system [2]. CHI monitors a patient's blood flow at multiple arterial points simultaneously and without direct contact with the skin. The setup comprised a near-infrared (NIR) sensitive camera, a coded tungsten-halogen light source, and signal processing software. An 850-1000 nm NIR optical bandpass filter was mounted in front of the lens to collect data in the NIR optical window for increased tissue penetration. The light emitted from the coded light source is spatially coded using a diffuser to achieve uniformity. The intensity values were converted to absorption values using a Beer-Lambert law formulation. An ideal bandpass filter (0.5–3.5 Hz) was used to produce the blood pulse waveform signal. The discrete Fourier transform was used for frequency domain analysis. This study was approved by a University of Waterloo Research Ethics Committee.

Results. For validation purposes, a finger photoplethysmography (PPG) cuff was worn to provide the ground-truth signal that would be attained with a single-point contact-based device. The participant assumed a resting position on a bed, and the CHI system was mounted over the bed facing down. Figure 1 shows the temporal and frequency plots of the extracted blood pulse waveform using the CHI system (top, red) and finger PPG (top, blue), and their associated power spectral density (bottom). During the recording duration, the CHI signal shows that the patient experienced two arrhythmias (at approximately 3 s and 11 s), consistent with the ground-truth reading. In the frequency domain, the CHI spectral power peaks matched those of the PPG peaks, thus enabling frequency domain processing using non-contact technology.

Conclusions. Arrhythmias were detected in the blood pulse waveform generated by CHI. Accurate PPGI power spectral density responses can allow for frequency domain analysis using existing techniques developed for detecting cardiovascular abnormalities. These results show promise for non-contact monitoring of the blood pulse waveform to help detect arrhythmias earlier, leading to more effective and timely treatment plans.

Acknowledgements. This work was supported by NSERC, AGE-WELL NCE Inc., Canada Research Chairs Program, and the Ontario Ministry of Research and Innovation.

References. [1] Amelard et al., "Feasibility of long-distance heart rate monitoring using transmittance photoplethysmographic imaging (PPGI)," *Sci. Rep.*, 5:14637, (2015).
[2] Amelard et al., "A portable plug-and-play imaging system for physiological monitoring," *Vis. Lett.*, 1, VL121, 2015.

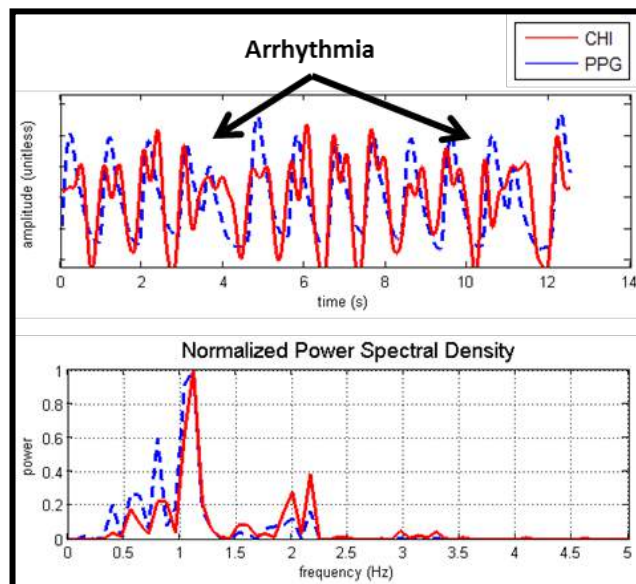


Figure 1: Non-contact assessment of abnormal blood pulse waveforms using Coded Hemodynamic Imaging (CHI) (red) compared to the ground truth (blue). CHI is able to elucidate arrhythmias, and the frequency domain peaks are consistent

Cyclic Continuous Max-Flow for MRI Phase Processing

John SH Baxter*, Zahra Hosseini, Maria Drangova, and Terry M Peters

Robarts Research Institute, The University of Western Ontario, London, Ontario, Canada

Introduction: Changes in magnetic susceptibility of tissues produce small changes in the phase information acquired by magnetic resonance imaging which are often discarded in clinic but can be used through post-processing techniques such as susceptibility weighted imaging. [1] A crucial aspect of this technique is the separation of phase deviations caused by natural contrast in the underlying anatomy (such as the presence of veins and increased iron concentration) from the smoothly varying background phase caused by deviations in the main magnetic field and tissue-air interfaces. Because phase is inherently non-linear, having a cyclic topology, linearization is often used in order to employ traditional linear image processing operations. This linearization occurs either through processing the complex image as in homodyne filtering [2] or phase unwrapping [3], which may be computationally expensive or susceptible to error. Our objective is to develop a fast and robust phase-processing technique that avoids linearization altogether.

Methods: Cyclic continuous max-flow (CCMF) uses the inherent topology of phase in the processing pipeline. This allows it to minimize the energy:

$$\min_{\theta(x)} \int_{\Omega} (D_{\theta(x)}(x) + S_{\theta(x)}(x)|\nabla\theta(x)|)dx \quad (1)$$

associated with a probabilistic model representing the smoothly varying background phase. This is solved for using a primal-dual optimization approach shown in Figure 1. The anatomy of interest is visualized by subtracting the estimated background phase from the observed phase.

```

 $\forall x, \theta, u_{\theta}(x) = 1/2\pi ;$ 
while not converged do
   $\forall(x, \theta), q_{\theta}(x) \leftarrow \text{Proj}_{|q_{\theta}(x)| \leq S_{\theta}(x)} (q_{\theta} + \tau \nabla (\text{div } q_{\theta}(x) + p_{\theta}(x) - p_S(x) - u_{\theta}(x)/c));$ 
   $\forall(x, \theta), p_{\theta}(x) \leftarrow \min\{D_{\theta}(x), p_S(x) - \text{div } q_{\theta}(x) + u_{\theta}(x)/c\};$ 
   $p_S(x) \leftarrow \frac{1}{2\pi} (1/c + \int_{-\pi}^{\pi} (p_{\theta}(x) + \text{div } q_{\theta}(x) - u_{\theta}(x)/c) d\theta);$ 
   $\forall(x, \theta), u_{\theta}(x) \leftarrow u_{\theta}(x) - c (\text{div } q_{\theta}(x) - p_S(x) + p_{\theta}(x));$ 
end

```

Figure 1: Algorithm used for minimizing the energy expressed in Eq. (1) using the indicator function $u_{\theta}(x)$

CCMF was applied in a channel-by-channel basis (Figure 2) and compared to two common post-processing techniques: phase unwrapped high-pass filtering (PUHPF) and homodyne high-pass filtering (HHPF)

Results: CCMF performs comparably to PUHPF in terms of artifact removal near the sinuses while performing comparably to HHPF in terms of computational efficiency. CCMF shows increased robustness compared to HHPF while having increased contrast compared to PUHPF.

Conclusions: We have successfully shown that by using the inherent topology of phase, higher quality MRI phase processing can be accomplished in a relatively short amount of time through variational optimization.

References: [1] Haacke, et al. , Magn. Res. Med., 2004; 612-618. [2] Noll, Nishimura & Macovski, IEEE TMI., 1991; 154-163. [3] Liu & Drangova, Magn. Res. Med., 2012 1303-16.

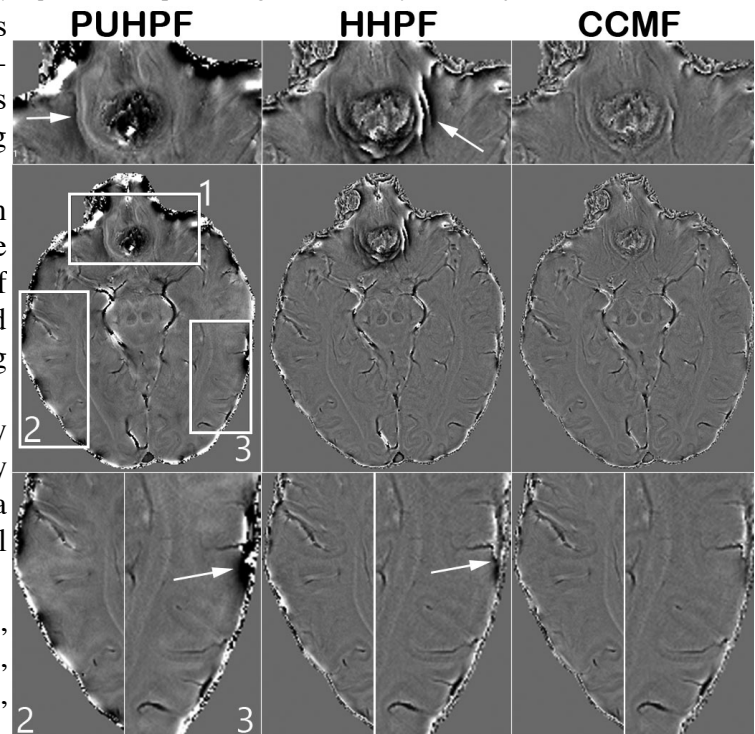


Figure 2: Channel-combined high-pass images

A Unified Reconstruction Framework for Compensated Magnetic Resonance Imaging

A. Boroomand¹, E. Li¹, M.J Shafiee¹, F. Khalvati², M.A. Haider² and A. Wong¹

¹Dept. of Systems Design Engineering, University of Waterloo, Waterloo, Ontario, Canada

²Dept. of Medical Imaging, University of Toronto, Toronto, Ontario, Canada

Introduction. Image quality is an important issue in all different forms of magnetic resonance imaging (MRI). The overall quality of MR images is highly affected by different factors, such as aberrations related to intrinsic characteristics of the MR scanner, magnetic field variations (leading to bias field), and inherent MR noise. Such factors can limit the overall quality of MR images, which can negatively impact analysis and interpretation of MR images. Therefore, a computational mechanism for compensating such factors jointly is highly desired and can facilitate for more accurate clinical analysis and interpretation. Motivated by this, we propose a unified framework for compensated magnetic resonance imaging (CMRI) that accounts for major factors related to MR image quality to improve the overall quality of MR images in a joint fashion. Such a framework can enable a higher quality MRI that aids radiologists for an easier interpretation and better diagnosis of different diseases.

Methods. The proposed unified CMRI framework aims to produce high quality MR images by jointly compensating for different factors that can degrade MR image quality including 1) aberrations related to intrinsic properties of the MR scanner, 2) magnetic field variations (bias field), and 3) MR noise. These factors are jointly modeled using a nonlinear MR measurement formation model that relates the MR measurements to the desired CMRI image. A calibration procedure using a phantom (here, a CIRCS Model 053 prostate phantom) is performed to learn the parameters of the formation model. The CMR image is then produced by solving an inverse problem, where the goal is to obtain the CMRI image given the MR measurements and the formation model. The solution of the inverse problem was formulated within a Maximum A Posteriori (MAP) framework that incorporates the formation model with learned parameters, as well as a novel stochastically fully connected conditional random field (SFCRF) model [1], which consists of a unary term aimed at enforcing measurement fidelity, and a pairwise term that enforces prior constraints on all possible voxel interactions within the MRI image. As such, this unified formulation allows for the estimation of the desired CMRI image given the MR measurements such that the aforementioned factors affecting MR image quality are compensated for, along with additional constraints to preserve signal fidelity. Finally, a gradient descent algorithm was utilized to solve the designed inverse problem and produce the desired CMR image.

Results. The proposed CMRI framework was used to compute CMR images from T2w MR and DWI image measurements, as shown in (Fig 1- a,b). All measurements were acquired using a 1.5T MR scanner at Sunnybrook Health Sciences Center Toronto, Canada and according to the institutional research ethics board. As the results in Fig. 1 (c, d) show, bias field effects are greatly reduced (as marked with red arrows) in the produced CMR images such that there is significant improvement in delineation of prostate gland from surrounding tissue. Furthermore, the CMR images can better exhibit tissue details and fine structures due to the ability of the proposed CMRI framework in compensating for aberrations related to the intrinsic properties of the MR scanner. Finally, the overall contrast of the CMR images is improved compared to the baseline MR measurements. This resulted in better visualization of different fine structures and details of prostate tissues in the CMR images as seen in Fig. 1 (c, d).

Conclusions. We developed a computational imaging framework for CMRI that can be integrated in to any type of MR scanner and it reconstructs high quality CMR images with an overall better visualization of different tissue structures.

Acknowledgments. This research is funded by NSERC, Canada Research Chairs program, Ontario Ministry of Research and Innovation, and OICR.

References:

M.J. Shafiee, et al. "Efficient bayesian inference using fully connected conditional random fields with stochastic cliques." ICIP 2014.

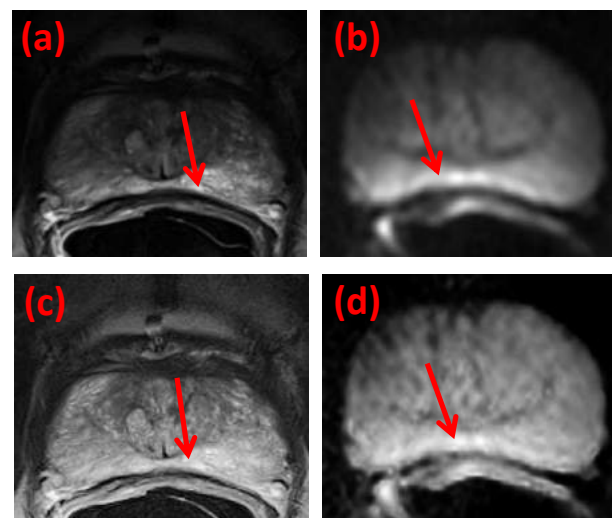


Figure 1: (a) T2w prostate MR image, (b) DWI prostate MR image. (c and d) computed CMR images using proposed CMRI framework for MR images in (a) and (b).

Accuracy of Melanoma Classification using Dermal Radiomic Sequences

Daniel S. Cho^a, David. A. Clausi^a, Alexander Wong^a

^aVision and Image Processing Lab, Systems Design Engineering, The University of Waterloo, Waterloo, ON

Introduction: Melanoma is a type of skin cancer and around 7000 Canadian has been diagnosed as invasive melanoma each year [1]. Melanoma originates from melanocytes, which are responsible for making melanin. Unlike other types of skin cancer, Melanoma has high mortality rates because as it develops, it moves further down into blood stream, and causes metastasis. Therefore, early detection of this cancer is the key for better prognosis, but the conventional approach still depends on the naked eye and the expertise of dermatologists and family physicians. While most computer-aided approaches for melanoma diagnosis focus on quantifying the appearance of melanomic lesions using mathematical formulations (i.e. asymmetry, color variation, and border irregularity), radiomics has emerged as a new cancer diagnostic tool. Radiomics utilizes image analysis and feature extraction techniques on medical images for better screening results. For dermal radiomic sequences have been previously proposed in [2], in this study, we investigate how these features perform on diagnosing malignant melanoma compared to the state-of-the-art computer-aided skin features.

Methods: Given a skin lesion image, the proposed dermal radiomic sequences were generated based on the underneath skin physiological biomarkers. As aforementioned, melanoma originates from melanocytes, and thus concentrations of melanin can serve as excellent biomarkers for melanoma diagnosis. Via non-linear random forest regression model, the concentrations of two different types of melanin (eumelanin, and pheomelanin) as well as the one of hemoglobin were acquired. Based on these biomarkers, 306 dermal radiomic sequences were generated [2]. The state-of-the-art techniques used mathematical formulations to quantify 17, 14, and 25 features for asymmetry, border irregularity, and color variation of the lesion, respectively. The experiment was conducted with a benchmark dataset consisting of 206 dermatological images, which is composed of 119 benign, and 87 malignant cases. For validation test, 10-fold cross validation was conducted using simple Bayesian classification.

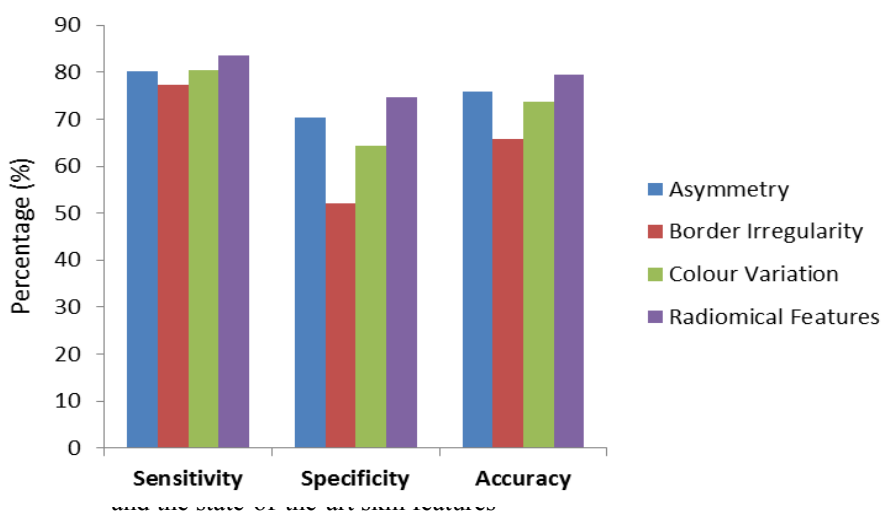
Results: Results in Fig. 1 shows that the proposed radiomic sequences outperformed over the state-of-the-art feature sets in sensitivity, specific and accuracy. While all of feature sets showed an excellent sensitivity of diagnosing melanoma, the proposed features showed the superior performance on specificity and accuracy. We believe that the results can be further improved by combining and optimizing all of the proposed radiomic sequences and the existing feature sets.

Conclusion: In this work, the melanoma classification was conducted with newly proposed radiomic sequences. The validation with the proposed features showed the promising results on accuracy, and consequently, classification using the proposed model with the existing ones will aid dermatologists and clinicians for better melanoma screening results.

Acknowledgement: This work was funded from Agfa Healthcare, the Natural Sciences and Engineering Research Council of Canada, the Canada Research Chairs program, and the Ontario Ministry of Research and Innovation

[1] Canadian Cancer Society's Advisory Committee on Cancer Statistics. (2015). Canadian Cancer Statistics 2015. Toronto, ON: Canadian Cancer Society.

[2] Cho, D., Clausi, D. and Wong, A., 2015. Dermal Radiomics for Melanoma Screening. Vision Letters, 1(1).



In vitro study of the effects of vessel stiffening on carotid artery hemodynamics using particle image velocimetry

Amanda L. DiCarlo*¹ and Tamie L. Poepping^{1,2}

¹Department of Physics & Astronomy and ²Department of Medical Biophysics, University of Western Ontario, London, Ontario, Canada

Introduction: Atherosclerosis – a thickening or hardening of blood vessels – often occurs at bifurcations or stenosis and is a common risk factor for ischemic stroke. Reduction in arterial compliance – a measure of the elasticity of blood vessels – typically manifests with aging, diabetes, hypertension, and other associated risk factors for cardiovascular disease. Both local compliance (i.e. atherosclerotic plaque) as well as changes in systemic arterial stiffness (i.e. arteriosclerosis) can alter the shape of the pulsatile flow-rate and pressure waveforms. The carotid artery bifurcation is a primary site of atherosclerosis. Subsequently, local hemodynamics are affected by the changes in vessel structure and waveforms, and resulting disturbed flow conditions can promote further plaque development and encourage plaque rupture. Here we investigated how local hemodynamic patterns may be affected by either a reduction in local compliance or changes in systemic compliance using particle image velocimetry (PIV), an optical technique for studying fluid dynamics with high temporal and spatial resolution, in conjunction with an in vitro flow facility.

Methods: An in-vitro flow loop was constructed for the experiment, incorporating a positive displacement pump to produce an appropriate flow-rate waveform. Two optically transparent silicone phantoms were employed with identical vessel geometry, a 50% eccentric stenosis of the internal carotid artery (ICA), but different compliance as a result of vessel wall thickness. Downstream flow resistors were used to mimic a physiological outlet flow division, but also included a compliant tubing component, whose length (30cm, 15cm, or no compliant tubing) was adjusted to mimic the effect of reduction in downstream or global compliance when the pump-generated waveform remained unchanged. Electromagnetic flowmeters and pressure catheter ports were connected at the inlets and outlets allowing flow and pressure to be measured. A refractive-index matched blood mimicking fluid was used for PIV measurement. Data were collected using a stereoscopic, time resolved, PIV system. Velocity maps were phase-averaged and flow disturbances were quantified by calculating the variances of velocity, denoted turbulence intensity (TI).

Results: Inlet common carotid artery (CCA) flow waveforms measured for the compliant and rigid phantoms were similar, however a higher maximum TI was observed in the rigid model (i.e. lower compliance). A reduction in downstream compliance resulted in a reduction in the pulsatility index of the CCA inlet waveform, contributing to a reduction in TI along with lower jet velocities (see figure); this is consistent with in vivo observations of ageing¹ and previously shown via lumped parameter modeling.²

Conclusion: Both local and downstream compliance were shown to effect flow and TI in carotid artery models.

References:

- [1] Hoi et al. (2010) *Physiol Meas* 31:291-302
- [2] Onaizah. (2015). M.Sc Thesis, University of Western Ontario, London.

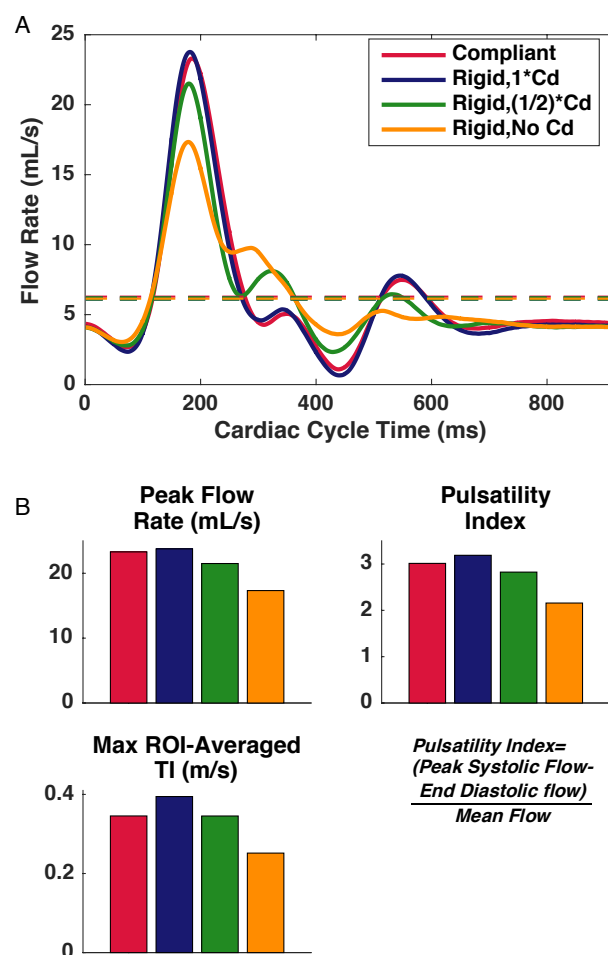


Fig.1 A. Flow waveforms measured at CCA inlet as well as mean flow rate (~6.0mL/s for all cases), B. Comparison of peak systolic flow rate, pulsatility index of CCA inlet flow waveform, and max observed TI averaged over a downstream region of interest in the ICA. (Flow components for each case indicated by legend in A: Compliant/Rigid refers to phantom type, Cd = downstream compliant tubing)

Subject-specific patch-based denoising for contrast-enhanced cardiac MR images

Lorraine Ma¹, Mehran Ebrahimi¹, and Mihaela Pop^{2,3}

Corresponding Author: mehran.ebrahimi@uoit.ca

¹ Faculty of Science, University of Ontario Institute of Technology, 2000 Simcoe Street North, Oshawa, ON, Canada, L1H 7K4

² Imaging Research, Sunnybrook Research Institute, 2075 Bayview Avenue, Toronto, ON, Canada, M4N 3M5

³ Department of Medical Biophysics, University of Toronto, Toronto, Ontario, Canada

Introduction

Many patch-based techniques in imaging, e.g., Non-local (NL) means denoising, require tuning parameters to yield optimal results. In real-world applications, e.g., denoising of MR images, ground truth is generally not available and the process of choosing an appropriate set of parameters is a challenge. Recently, Zhu et al. (*) proposed a method to define an image quality measure, called Q, that does not require the ground truth.

We evaluate the effect of various parameters of the NL-means denoising on this quality metric Q. Our experiments are based on the late-gadolinium enhancement (LGE) cardiac MR images that are inherently noisy. Our described exhaustive evaluation approach can be used in tuning parameters of patch-based schemes. Even in the case that an estimation of optimal parameters is provided using another existing approach, our described method can be used as a secondary validation step. Our preliminary results suggest that denoising parameters should be case-specific rather than generic.

Methods

Late-gadolinium enhanced (LGE) MR data was obtained in two pigs with chronic myocardial infarction on a 1.5T GE scanner using a 5-inch surface coil. Images were acquired using a conventional 2D fast gradient echo (FGRE) pulse sequence approximately 15-20 minutes following Gd-based intravenous injection. Two such datasets were denoised using the method introduced by Coupe et al. Denoising experiments were performed with patch size fixed at 3x3, search radii of 3, 6, and 9 and patch sizes used for measuring Q of 8 and 16. The quality of the denoised images was measured with Q, the image quality measure proposed by Zhu et al.

Results

Values of Q were measured for two sets of data where the search radius was varied between 3, 6, and 9 and the size of patches in measuring Q was 8 and 16. Figures are excluded due to size restrictions of this abstract.

Conclusions

We performed a set of patch-based denoising experiments on LGE MR data and assessed the quality of each output image without ground truth. We measured the peak of the plotted Q curves over a number of different parameters.

The exhaustive method described in this abstract can be used in tuning parameters of patch-based schemes. Even in the case that an estimation of optimal parameters is provided using another existing approach, our described approach can be used as a secondary validation step.

Our preliminary results suggest that denoising parameters should be case-specific rather than generic. Our experiments demonstrated the feasibility of using this denoising method for cardiac LGE and optimization on a subject-specific fashion.

(*) **Reference:** Xiang Zhu and Peyman Milanfar, Automatic parameter selection for denoising algorithms using a no-reference measure of image content, IEEE Trans. Image Processing, 19(12):3116–3132, 2010.

Single-Click Lung Nodule Contouring Method Using a Hierarchical Conditional Random Field (HCRF)

Shahid A. Haider^{*1}, Audrey G. Chung¹, Mohammed Javad Shafiee¹, Herman Grewal¹, Farzad Khalvati², Anastasia Oikonomou², Masoom A. Haider², and Alexander Wong¹

¹: Vision and Image Processing Research Group, University of Waterloo, Waterloo, Ontario, Canada

²: Medical Imaging, University of Toronto and Sunnybrook Research Institute, Toronto, Ontario, Canada
Consortia: Ontario Institute for Cancer Research - Smarter Imaging Program

Introduction: Lung cancer is the second most common cancer in the United States, with an estimated 224,210 new cases of lung cancer and 159,210 deaths in 2014. Accounting for 27% of cancer deaths, lung cancer is the deadliest form of cancer [1]; however, if caught early enough, the 5-year survival rate is 49% [2]. To assess the size and development of a cancerous nodule, radiologists contour the nodule on CT images using free hand trace or point-polygon methods. While accurate, these manual contouring methods are extremely time-consuming. Semi-automatic methods, like intelligent scissors and region growing, have been used to decrease the time required to contour a nodule, but fail when presented with noisy data or irregularly shaped nodules. We propose a single-click method for lung nodule contouring via a hierarchical conditional random field (HCRF) model designed to contour high frequency edges and nodules with textural uncertainties.

Method: The HCRF is formulated with two-stages. The first stage uses a set of statistical textural features as observations, and labels of inside or outside the contour as the state. Using the state estimate of the first stage as the initial state estimate, the second stage uses the CT intensity measurements as the observations, and the state being estimated is a label of inside contour or outside contour. The estimates are solved as a Maximum A Posteriori problem using the Gibbs energy formulation. The unary term is trained via leave-one-patient-out using features from the radiologist's contours, and the pairwise term in the formulation is the Ising model.

To demonstrate the accuracy of our proposed method for lung nodule contouring, we used 27 contoured lung nodules studies from Sunnybrook Health Sciences Centre and compared the accuracy of the proposed method with intelligent scissors and region growing techniques. Consisting of detached nodules, the studies were contoured by a radiologist via the point-polygon method, and the semi-automatic contours were generated using the point-polygon contour as reference.

Results: Using the point-polygon contour as ground truth, we evaluated the performance of the proposed method (HCRF), region growing (RG), and intelligent scissors (IS) using sensitivity, specificity, accuracy, Dice, and Jaccard metrics. These metrics were averaged over all 27 studies. The table below shows that HCRF was capable of performing similarly or better than IS and RG across all categories.

| Algorithm | Sensitivity | Specificity | Accuracy | Dice | Jaccard |
|-----------|--------------|--------------|--------------|--------------|--------------|
| HCRF | 0.961 | 1.000 | 1.000 | 0.928 | 0.867 |
| RG | 0.919 | 0.917 | 0.917 | 0.791 | 0.737 |
| IS | 0.914 | 1.000 | 1.000 | 0.906 | 0.830 |

Conclusions: The single-click, hierarchical conditional random field method (HCRF) presented in this abstract achieved the highest performance across all metrics, demonstrating the potential of this method for fast and accurate lung cancer nodule contouring.

Acknowledgements: We would like to thank the Natural Sciences and Engineering Research Council of Canada (NSERC), the Canada Research Chairs Program, and the Ontario Ministry of Research and Innovation for their sponsorship of this research.

References:

- [1] Rebecca Siegel *et al.*, *CA: a cancer journal for clinicians*, vol. 64, no. 1, pp. 9–29, 2014.
- [2] Vei Mah *et al.*, *Cancer research*, vol. 67, no. 21, pp. 10484–10490, 2007.

Automatic Prostate Cancer Mapping on Digital Histopathology Imaging

W. Han^{1,6}, E. Gibson^{5,7,8}, M. Gaed^{5,6}, J. A. Gomez², M. Moussa², J. L. Chin^{3,4}, S. Pautler^{3,4}, A. D. Ward^{1,4,6}

Depts. of 1. Medical Biophysics, 2. Pathology, 3. Surgery, 4. Oncology, 5. Robarts Research Institute, Western University, 6. Lawson Health Research Institute, London, Ontario, Canada, 7. Centre for Medical Image Computing, University College London, UK, 8. Radiology, Radboud University Medical Centre, Netherlands OICR Smarter Imaging Program; Research Supervisor: Aaron Ward

Introduction: The prognosis of prostate cancer of a patient is known to be related to the stage and Gleason grades of the tumours observed in the resected specimen [1]. This information is challenging to report quantitatively and subject to inter-observer variability [2]. To enable fully quantitative pathology reporting including a visual cancer map on the tissues, our objectives are (1) to develop an automatic system labeling tissue components (e.g. nuclei, stroma, etc), and (2) to use labeled tissue component distributions and texture features to automatically classify fields of view (FOVs) within the image as cancerous or non-cancerous.

Methods: We acquired digital images of hæmatoxylin and eosin (H&E)-stained whole-mount histology sections from surgical pathology specimens from 10 patients at 20X (0.5 µm/pixel) using an Aperio Scanscope. Color deconvolution was used to isolate the different stains, and quadtree decomposition on the hæmatoxylin channel yielded a fast segmentation of the image into nearly isointense subregions not smaller than the typical size of a nucleus. A trained classifier labeled each subregion with one of three tissue components: nucleus, lumen, or stroma. We calculated the proportions of different tissue components within fields of view (FOVs) of a specified size, and used machine learning methods to classify each FOV as cancerous or non-cancerous. The experiment was conducted using leave one patient out cross validation with 100 repetitions at different FOV sizes. For comparison, the experiment was repeated with the addition of 19 texture features describing the spatial arrangement of different tissue components.

Results: Fig. 1 shows the performance of the system for a range of FOV sizes. Interestingly, varying the FOV size adjusts the compromise between the false-positive rate (FPR) and false-negative rate (FNR). We selected the 240×240 µm FOV for further analysis because its low FNR is valuable to our application. Fig. 2 shows that adding texture features capturing the spatial arrangement of tissue provided a substantial reduction in error rate, FPR, and FNR. This came at the expense of additional computation time (15 hours per image using an unoptimized Matlab implementation).

Conclusion: A machine learning classifier can be trained to identify prostate cancer within small FOVs of digital histology images with high sensitivity, using features measuring image texture and tissue component proportions. This yields label maps throughout the image that delineate cancerous regions, supporting the eventual development of a fully quantitative and visual pathology report. Our ongoing work includes accelerating texture feature computation and automating the grading of foci.

References:

- [1] L. Egevad et al, *Mod Pathol* 24(1), 1–5, 2011.
 [2] T. H. van der Kwast et al, *Mod Pathol* 24(1), 16–25, 2011.

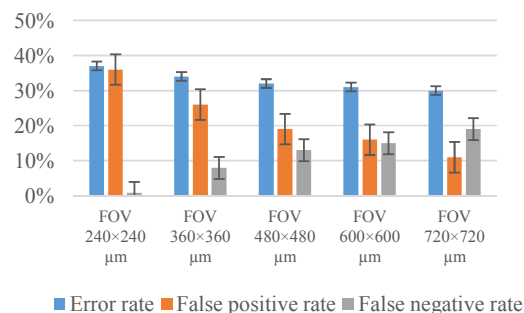


Fig. 1: Performance at different FOV sizes.

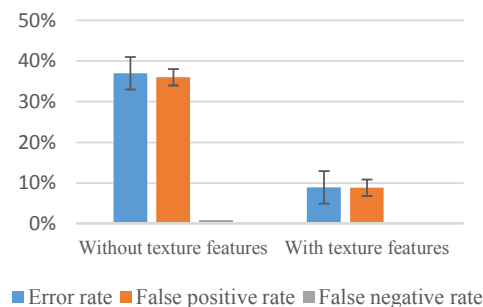


Fig. 2: Performance gain from use of texture features with 240 × 240 µm FOV.

Large scale segmentation free analysis of 3D microscopy data

Santosh Hariharan¹, Philipp Mergenthaler² and David W. Andrews¹

Affiliations:

¹ Biology Platform, Sunnybrook Research Institute, University of Toronto, ON, Canada;

² Dept. of Neurology, University of Charite, Berlin, Germany

Supervisor: David W. Andrews

Introduction

With the advancement of high-content/high-throughput automated microscopy techniques, it has become simpler to acquire large sets of images for multiple different conditions very quickly. Currently most cell culture image data sets are acquired in single planes (2D). However, for some cell types even traditional cell cultures present as three dimensional structures and thus there is a need to acquire images in three dimensions (3D). Yet, analyzing large sets of 3D image data requires expertise and is computationally intensive. Typically, the first step of automated microscopy image analysis requires segmenting individual cells. However, for 3D data this step is computationally intensive, time consuming and requires expert technical knowledge. Additionally, there typically is a need for an appropriate marker for used only for cell segmentation.

Methods

With these limitations in view, we have developed a fast, segmentation free strategy to analyze 3D microscopy images. The algorithm works by first estimating the background and computing a set of local hierarchical image features without the need to segment individual cells. Briefly pixels are assigned to pixel categories obtained from a set of sample images. 3D Neighborhood pixels are then grouped together to form super-voxels and assigned to super-voxel categories identified using histograms of pixel categories within the super-voxel. The process of grouping and categorization is then repeated on super-voxels to obtain mega-voxels and mega-voxel categories. Finally an image is defined by the histogram of mega-voxel categories. These features are then used to visualize the image data and train a random forests classifier.

Results

Using this approach, we analyzed a 3D spinning disk microscopy data set of cultured embryonic mouse brain cortical neurons exposed to excitotoxic stress. Excitotoxicity is one of the mechanisms contributing to acute neurodegeneration after different insults to the brain, including stroke, traumatic brain injury and epileptic seizures. Our preliminary results using NMDA-receptor antagonists as controls suggest that, indeed, segmentation-free image analysis and calculating local features in 3D enables accurate classification of this image data set. Thus, this tool can be used for microscopy-based mechanistic studies as well as in imaging-based drug discovery projects.

Conclusion

With our 3D features we are able to achieve accurate classification without the need for individual cell segmentation. Although we have tested this approach using neuronal cultures as a model, it can readily be used to analyze any 2D or 3D image data sets.

Preservation of details and contrast in 7 T local frequency shift maps by processing channel phase data prior to combination

Z. Hosseini,¹ J. Liu,² and M. Drangova^{2,3}

¹Biomedical Engineering Graduate Program, ²Imaging Research Laboratories, Robarts Research Institute, ³Department of Medical Biophysics, University of Western Ontario, London, Ontario, Canada

Consortium affiliation: Other. Supervisor: M. Drangova

Introduction: Extracting local frequency shift (LFS) maps from data acquired with multi-channel coils requires care to remove channel-dependent effects, background contribution and phase wraps. To combine the multi-echo multichannel phase data, the channel-dependent phase term can be eliminated by subtracting the first echo image from the subsequent images and then performing complex summation through all the channels.¹ To remove background contribution and phase wraps, a homodyne² high pass filter (HHPF) can then be used to generate an echo-specific LFS map, which is obtained post channel combination (post-CC). A recently published inter-echo variance (IEV) channel combination technique³ processes the individual channel phase data and uses the inter-echo variance of LFS maps over echoes as a weighting factor for channel combination. Thereby, the IEV generates LFS prior to channel combination (pre-CC). In this study we compare the post-CC and the pre-CC approaches implemented using two optimized processing pipelines.

Methods: Imaging: Two healthy volunteers were scanned with a six-echo, GRE sequence at 7-T using a 16-channel Tx/Rx head coil (TR/TE/echo spacing/flip angle 40/3.7/4.1 ms/13°, GRAPPA R=2). **Post-processing: post-CC:** To optimize the HHPF, the filter size was varied between 10 to 90 percent of the field of view (FOV). **pre-CC:** The channel data were unwrapped⁴ and subsequently high-pass filtered with a Gaussian filter⁵ (GHPF) for background field removal. The processed channel data were then combined using the IEV channel combination technique;² the GHPF size was varied from 1 to 50 mm. **Analysis:** Five veins were selected in each of four regions in the two sets of LFS maps. Line profiles were drawn across the veins. Contrast was defined as the absolute difference between minimum pixel intensity on the line profile (the vessel signal) and the mean value of pixels coinciding with the tails of the line divided by average of the two signals. Contrast curves were used for the identification of an optimal filter size for HHPF and GHPF. Contrast in the optimized LFS maps was subsequently compared to evaluate the performance of each processing pipeline (Wilcoxon test).

Results: Analysis of the filter sizes showed that consistent optimal contrast was achieved in images processed with a filter size of 30% FOV for HHPF and 7 mm for GHPF. Images obtained from the pre-CC pipeline preserved the details of the phase image more consistently throughout the brain volume for both volunteers. Figures 1 and 2 show the intermediate images in each pipeline; the details seen in the raw channel data are preserved in the pre-CC pipeline images (Fig. 1b-d) but are lost in the post-CC channel combined LFS map (Fig. 2a-b). Contrast analysis showed higher contrast in the LFS maps obtained from pre-CC pipeline ($[mean \pm SEM] 4.3 \pm 1.1$ vs. 3.8 ± 1.6 , $p = 0.0003$). **Conclusion:** LFS maps generated from the pre-CC pipeline have higher contrast and preserve the detail measured in the raw channel phase images.

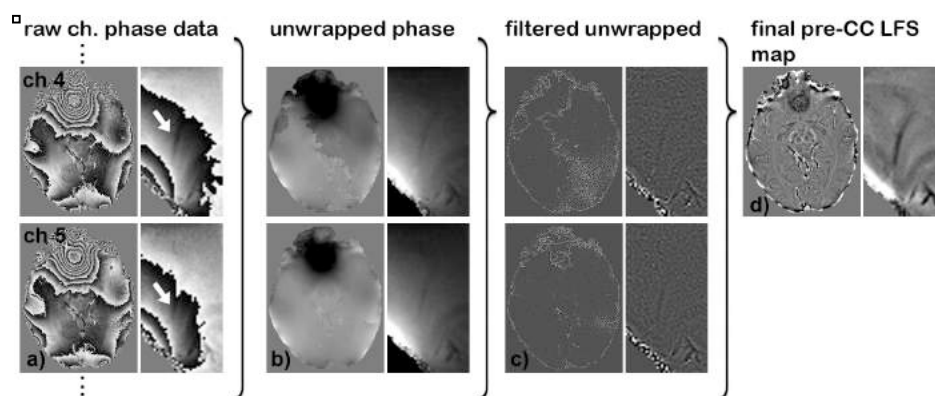


Fig. 1: Flow diagram of pre-CC pipeline illustrated using a representative image slice: Raw channel phase data (a) are unwrapped (b) and filtered (c). The processed channel data are then combined using IEV. Vessel seen on the raw channel data appears on the intermediate

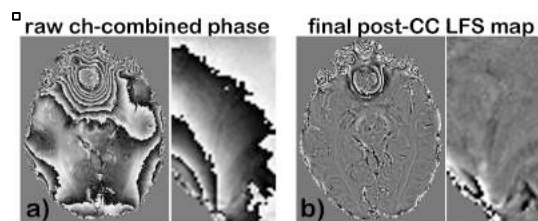


Fig. 2: Flow diagram of post-CC pipeline illustrating channel combined image (a) and the final processed LFS map (b) corresponding to the same slice as in Fig. 1. Vein clearly seen on the channel data is lost due to signal cancellation in the channel combination process.

REFERENCES: [1] Bernstrin et al., MRM, 1994, 32:330-334. [2] Noll & Nishimura, IEEE TMI., 1991, 10:154-163. [3] Liu & Drangova, MRM, 2014, 73:1654-61. [4] Liu et al., MRM, 2012, 68:1303-16. [5] Rauscher et al., JMRI, 2008, 26:1145-1151.

Seamless Reconstruction of Preview Images in Digital Pathology

Mahdi S. Hosseini,^{a,b*} Dongwoon Lee,^b Frank Yang,^b Savvas Damaskinos,^b Konstantino N. Plataniotis^a

^aThe Edward S. Rogers Sr. Department of ECE, University of Toronto, Toronto, ON M5S 3G4, Canada

^bHuron Digital Pathology, 550 Parkside Drive, Waterloo, Canada, N2L 5V4

*Mahdi S. Hosseini, E-mail: mahdi.hosseini@mail.utoronto.ca

Introduction. Whole slide imaging scanners in digital pathology (DP) use high resolution imaging optics to acquire submicron resolution images of organ tissues on glass-slides. Prior to such scan, a low resolution preview image of the whole mount tissue slide ($\geq 50\text{mm} \times 75 \text{ mm}$) is required to guide the scanner to find regions of interest (ROI) including tissue, label, barcode on each slide. The preview image is usually obtained by stitching together several tiles of multiple cameras within the imaging system. The reconstructed images contain artefacts caused by non-uniform illumination on the tile borders and aberrations due to the optical arrangement, which cause discontinuities in the image and degrade the image quality, see Figure.1(a). The objective is to correct the corresponding distortion/shading effects to result in a seamless high quality image.

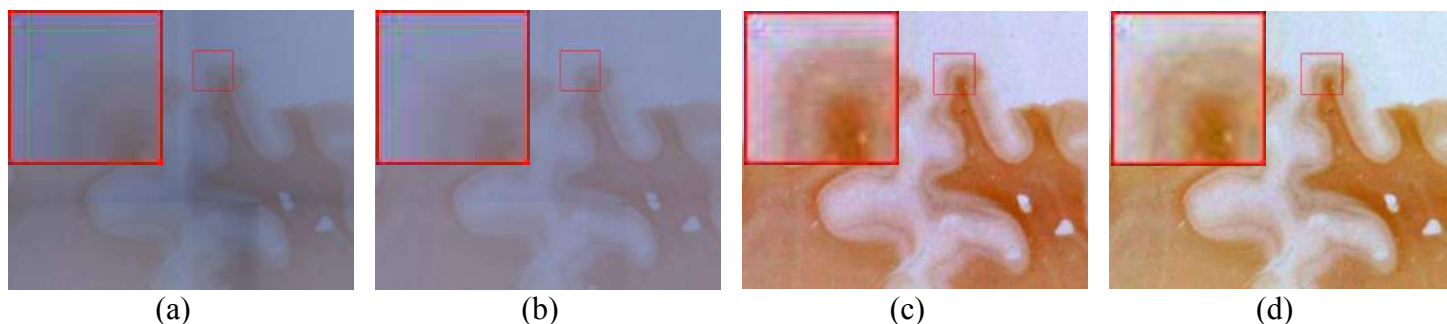


Figure. 1. (a) Raw stitching, (b) Flat-field correction, (c) Harker method [3], (d) Proposed method

Methods. Multiple image tiles T_i are provided from different sections of each slide to cover the whole FOV. Here, the subscript i indicates the section index from FOV. For instance, here four different tiles are considered to construct the whole image $F = \begin{bmatrix} T_1 & T_3 \\ T_2 & T_4 \end{bmatrix}$. In fact, this form of construction is the raw stitching without any correction, see Figure.1(a). Two cameras are used to cover upper (T_1, T_3) and bottom (T_2, T_4) tiles, respectively. Flat-field correction is performed on each tile to cancel the vignetting effect of both cameras by replacing every tile $T_i \leftarrow (T_i - C_D) \odot G$, where C_D is dark camera image and $G = 1/(C_F - C_D)$ is the gain factor obtained by flat-fielded camera image C_F , see Figure.1(b) for correction. Next, the gradient of each tile is calculated and stitched together to form the FOV gradient field $\bar{\nabla}F = \begin{bmatrix} \nabla T_1 & \nabla T_3 \\ \nabla T_2 & \nabla T_4 \end{bmatrix}$. The benefit of such gradient stitching is the bias/smooth illumination discrepancy will be mostly canceled in the gradient field while coherent transitions are maintained on the tile borders. The final step is to reconstruct the image I from the stitched gradients $\bar{\nabla}I$ by means of quadratic minimization formulation i.e. $\tilde{F} = \min_I \|\nabla I - \bar{\nabla}I\|_2^2$. The pseudoinverse representation to this formulation is obtained using the Sylvester equation i.e. $[D \otimes I + I \otimes D] \text{vec}(F) = \text{vec}(\bar{\nabla}_x F \cdot D + D^T \cdot \bar{\nabla}_y F)$, where D is the numerical difference convolution matrix and vec is the lexicographical ordering operator. The numerical solution is followed by Hessenberg matrix reduction and Schur decomposition algorithm [1]. For design of the derivative matrix D we have used the high accuracy method in [2].

Results and Concluding Remarks. The reconstructed images are shown in Figure.1(c)-(d) using Harker method [3] and our proposed approach respectively. The numerical difference scheme used in [3] high frequency magnitudes are not encoded accurately resulting in ripple artefacts and inaccurate color recovery. Our design shown in Figure 1(d) is robust through detecting relevant information in highband frequency and preserving better color features.

References.[1] G. H. Golub, S. Nash, and C. V. Loan. "A Hessenberg-Schur method for the problem $AX + XB = C$." *Aut. Cont., IEEE Trans.* 24.6 (1979): 909-913. [2] M.S. Hosseini and K. N. Plataniotis, "Explicit Finite Differentiation in Image Processing," under review, *Image Proc., IEEE Trans.*, submitted in Sept 2015. [3] M. Harker, and P O'Leary. "Regularized reconstruction of a surface from its measured gradient field." *J. of Math. Imaging and Vision* 51.1 (2015): 46-70.

Quality Assessment in Digital Pathology Images

Keyvan Kasiri*, Hicham Sekkati, David A Clausi
 Vision & Image Processing (VIP) Research Group, Systems Design Engineering
 University of Waterloo, Waterloo, Ontario, Canada

Introduction: An important role in pathology is interpreting and examining tissue and cell images at a high resolution. The microscope has historically been the only available instrumentation to provide live images at high resolutions. Nowadays, whole-slide-imaging (WSI) provides the process of scanning and digitization of the whole microscopic glass into digital images. The quality of captured image is satisfactory to a pathologist if it is identical to the image view through a real microscope image. Focusing is a simple task for a trained microscope user; however, for automated systems to provide high quality visual representation of an image of a pathology slide is challenging. Therefore, a quality assessment framework is desired to automatically identify the in-focus and out-of-focus regions and score the quality of the captured pathology tissue image based on the percentage of focused regions [1].

Methods: The proposed framework aims to automatically assess the quality and score digital pathology images. The image quality, which is mainly defined by sharpness, contrast, and colors, is related to image resolution and focus [2]. Pathology slide images are evaluated by assessing the amount of blurriness of the image, and identifying in-focus and out-of-focus areas. Focus is measured in a patch-based paradigm based on histogram range of each color channel. The focus measurement is calibrated in a reduced-reference quality assessment framework using a number of reference points. Reference points, which are identified by the instrument, provide prior information about the focusing and help to locally constrain the focus scale. The overall score can be deduced based on the percentage of tissues that are in an acceptable range of focus.

Results: The proposed framework is used to assess the quality of digital pathology images acquired at resolution $0.25\mu\text{m}$ using the TissueScope scanner at the Huron Digital Pathology Inc. The result of focus measurements are validated by the staff at Huron. Figure 1 illustrates images of a pathology tissue, captured in approximately 0.1 of the original resolution, in different focus levels along with the focus measurement results. The tissue images are shown in Fig 1 (a)-(c) and the results are given in Fig. 1(d)-(f), where the blue and the green colors respectively stand for the lowest and the highest values of the measurement. As is shown, the averaged normalized measurement Avg is increasing as the sharpness of the image increases. Focus measurement for an $11.22 \times 18.02 \text{mm}^2$ whole-slide scan is shown in Fig 2. The distribution of the reference points used to calibrate the measurement is shown in Fig. 2(a) and the result of the focus measurement is given in Fig. 2(b).

Conclusions: We developed an assessment approach to automatically evaluate the quality of the digital pathology images by defining a focus measure. The proposed framework took advantage of locality and information captured from the reference points to calibrate the focus measurement.

Acknowledgements: This research is funded by Natural Sciences and Engineering Research Council (NSERC) of Canada and is undertaken in collaboration with the Huron Digital Pathology Inc.

References: [1] R. Redondo, et al. "Autofocus evaluation for brightfield microscopy pathology." *J biomedical optics* (17), 2012. [2] W. Huang, et al. "Evaluation of focus measures in multi-focus image fusion." *Pattern Recognition Lett.* (28), 2007.

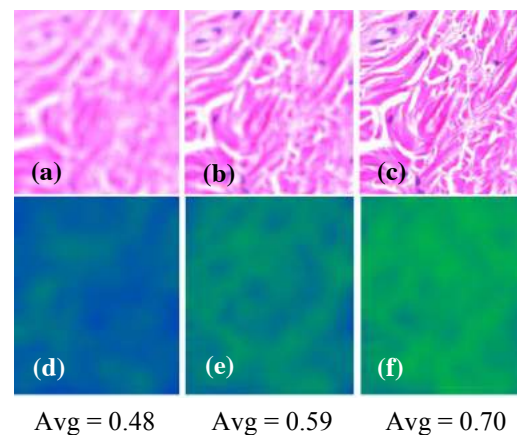


Figure 1. Focus measurement for a region in different focus levels.

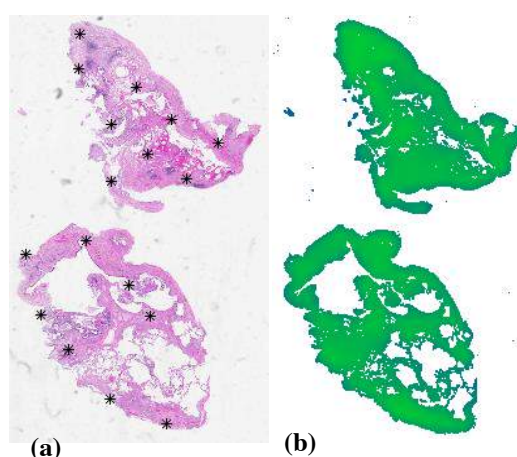


Figure 2. Whole-slide scan, (a) Distribution of the reference points, (b) Focus measurement

Cross Modality Label Fusion in Multi-Atlas Segmentation of Brain MRI

Keyvan Kasiri*, Paul Fieguth, David A Clausi

Vision & Image Processing (VIP) Research Group, Systems Design Engineering
University of Waterloo, Waterloo, Ontario, Canada

Introduction: Magnetic resonance imaging (MRI) of the brain is a widely used imaging technique for studying the human brain and for the diagnosis of neurological disorders. Quantitative studies and interpretation of brain MR images rely on the accurate segmentation of brain scans, where a reference model provided by an *atlas* offers prior information about the brain's anatomy to help simplify the labeling of brain scans. However, the segmentation will be problematic if the atlas and the target image are not accurately aligned. Furthermore a single deformation cannot represent the range of anatomical variations present in a whole population of potential target cases. Recent *multi-atlas* based approaches provide highly accurate segmentations by propagating manual delineations from a group of atlases and combining the atlas labels. *Label fusion*, which is the key challenge associated with the multi-atlas approach, commonly relies on the *similarity* between the intensity values of the atlases and target scan, where the definition of similarity may frequently be problematic in those cases where the atlases and target scan are obtained via different sensor types or acquisition protocols.

Methods: The proposed framework aims to find a tissue label map associated with the target image by combining labels from the already registered atlases to the target image. Based on an inference from the maximum-a-posteriori estimation framework, the prior probability that relates the atlas labels to the target image can be interpreted as image similarity. Traditional label fusion methods take the image-intensity into account as a criterion to approximate the similarity and to determine the contribution of each atlas in the final segmentation. Instead, we propose to measure similarity based on structural features that can represent images from different modes with almost the same representation. The overall block-diagram of the proposed label fusion framework is described in Fig. 1, in which the atlas labels are weighted based on approximating the similarity of each atlas and the target image. The similarity is locally measured by calculating the mutual information between structural features extracted from the atlas and the target image. The structural features combine a scale-dependent over-complete Log-Gabor complex wavelet transform with edge information.

Results: The proposed framework was tested on simulated data, a set of 3D brain MR scans from BrainWeb [1], and real data from LONI [2], on T1, T2, and PD modes. The segmentation approach is performed first with a PD and then a T2 image as the target image, while the atlas database is in T1 mode. Table 1 shows the comparison of the proposed *Seg* method with the conventional majority voting (MV) [3] expressed with the average Dice coefficient.

Conclusions: A cross-modality label fusion framework is proposed based on measuring the similarity of local structural features in a patch-based paradigm and weighting the atlases. Unlike traditional label fusion approaches, the weighting approach does not rely on the image-intensity comparison to segment a target scan.

References:

- [1] BrainWeb simulated brain database, <http://www.bic.mni.mcgill.ca/brainweb/>.
[2] The UCLA laboratory of Neuro Imaging (LONI), <http://www.loni.ucla.edu/>.
[3] R A Heckemann, et al. "Automatic anatomical brain MRI segmentation ...," *NeuroImage* (33), 2006.

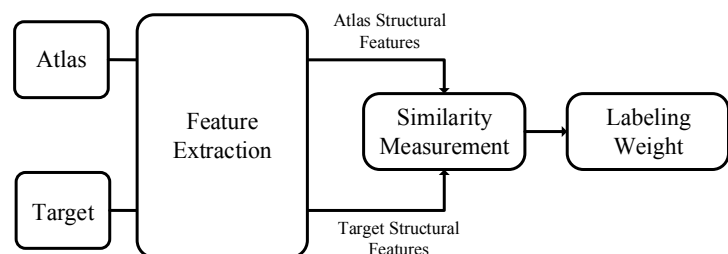


Table 1. Segmentation results in average dice coefficients.

| Case 1: PD mode as the target image | | | |
|-------------------------------------|----------|----------|----------|
| Tissue | WM | GM | CSF |
| Seg | 89.3±0.2 | 90.1±0.3 | 83.4±0.6 |
| MV | 85.6±0.4 | 85.4±0.5 | 77.6±1.3 |
| Case 2: T2 mode as the target image | | | |
| Seg | 81.4±0.6 | 79.2±0.3 | 62.6±0.7 |
| MV | 79.8±0.9 | 76.9±0.7 | 58.3±1.9 |

Fig. 1. Local weighted labeling for cross-modal multi-atlas segmentation based on measuring similarity of structural features.

Noise in parallel MRI: how to determine whether single-coil assumptions still hold (they don't)

Jesse Knight*, Alan R. Moody**, April Khademi*

Canadian Atherosclerosis Imaging Network (CAIN)

*Image Analysis in Medicine Laboratory (IAMLAB), School of Engineering, University of Guelph

**Department of Medical Imaging, University of Toronto

Introduction. Single coil MR image noise is typically modelled as an additive field which is assumed (i) to have a Gaussian or Rician PDF, (ii) to be stationary, and (iii) to be spatially uncorrelated [1, 2]. Importantly, these three assumptions underpin many of the popular image analysis tools, including the SPM and FSL segmentation tools [3, 4]. However, parallel MRI (PMRI) image noise has been shown to possibly contradict each of these assumptions, meaning the use of methods designed for single coil images on PMRI images may be invalid [2, 5]. While there have been efforts to model PMRI noise, they are almost always theoretical, entail per-scan coil sensitivity profiles, or require access to proprietary reconstruction algorithms. It is therefore prudent to explore image noise empirically; specifically, we describe a framework to consider each of the three classical assumptions separately, in order to determine whether single coil analysis algorithms can be employed.

Methods. First, image slices are subdivided into patches, and only patches completely within a background mask are considered (Figure 1). To test for stationarity, each patch is compared with all other patches using a 2-sample KS test. This tests the hypothesis that the data in both patches come from the same distribution, but makes no assumptions about that distribution. Next, the data in each patch are tested to determine if they follow a known distribution. For each distribution, the parameters are estimated using maximum likelihood; then a KS Test is used to test the hypothesis that the patch data are indeed from the optimally fit distribution. Finally, an extension of Mantel's Test, the 2D Spatial Correlation Test (2DSCT), has been shown to indicate spatial correlation without making any assumptions data distribution [5]. The test computes a measure of correlation between graylevel difference and spatial distance for pixels in a patch, and compares this with statistics from randomly permuted versions of the same patch.

Results. The analysis framework described was demonstrated on 12 PMRI FLAIR volumes, with patch sizes of $56 \times 56 \times 1$ used throughout. The results of the noise tests indicate that the classical assumptions are invalid for this image set (Table 1). The images demonstrate significant nonstationarity: 96% of patch-to-patch comparisons rejected the hypothesis of equal distributions. Similarly, patch data appeared to rarely conform to common distributions, with the most consistently plausible function being the Weibull; yet this only agrees with about 10% of tested patches. Finally, 88% of the patches showed evidence spatial correlation using the 2DSCT.

Conclusions. Assumptions of stationarity, common PDF distributions, and spatial uncorrelation have been incorporated into many MRI analysis algorithms. However, PMRI images have been shown to have noise fields which violate these assumptions, potentially rendering a large number of models, like Gaussian mixtures, obsolete. Here we present an exploratory noise analysis framework capable of identifying when these assumptions are violated, and demonstrate the results on 12 PMRI FLAIR images.

References. [1] P. Thunberg and P. Zetterberg. *Mag Reson Imaging* 2007; 25: 1089-1094. [2] O. Dietrich *et al.* *Mag Reson Imaging* 2008; 26: 754-762. [3] J. Ashburner and K. J. Friston. *Neuroimage* 2005; 26(3): 839-851. [4] Y. Zhang, M. Brady and S. Smith. *IEEE Trans Med Imag* 2001;20(1): 45-57. [5] A. Khademi *et al.* *Digit Signal Process*, 2009; 1-6.

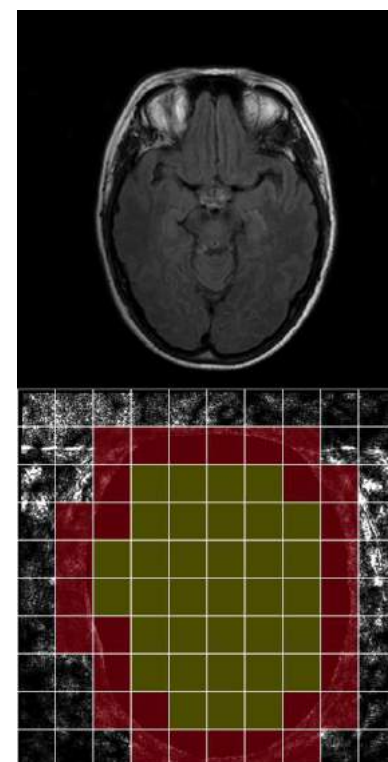


Figure 1: Original PMRI image and patched background signal. Un-coloured patches are completely background and used for testing; red patches contain noise signal not tested; yellow patches are completely head signal.

Table 1: Summary of test results: percentages of patch tests for which the hypotheses of single-coil or classical assumptions could not be rejected.

| | Mean | SD |
|------------------|------|-----|
| # Tested Patches | 2240 | 240 |
| % Stationarity | 4.3 | 2.1 |
| % Gaussian | 0.1 | 0.3 |
| % Rician | 0.5 | 0.3 |
| PDF Match | 0.3 | 0.3 |
| % Rayleigh | 10.4 | 3.5 |
| % Weibull | 12.2 | 2.3 |
| % Uncorrelated | | |

Discovery Radiomics for Lung Cancer Classification

D. Kumar, M. J. Shafiee, A. G. Chung, F. Khalvati*, M.A. Haider* & A. Wong

Systems Design Engineering, University of Waterloo, Waterloo, ON, Canada

*Medical Imaging, Sunnybrook Research Institute, University of Toronto, ON, Canada

Introduction: Lung cancer is the leading cause for cancer related deaths. As such, there is an urgent need for a streamlined process that can allow radiologists to provide diagnosis with greater efficiency and accuracy. A powerful tool to do this is radiomics, where the wealth of quantitative imaging features is derived from imaging data for characterizing tumour phenotype and for quantitative diagnosis. In this study, we take the idea of radiomics one step further by introducing the concept of discovery radiomics for lung cancer classification using CT imaging data. Rather than using pre-defined, hand-crafted feature models as with current radiomics-driven methods, we discover custom radiomic sequencers that can generate radiomic sequences consisting of abstract imaging-based features tailored for characterizing lung tumour phenotype.

Method: To realize the concept of discovery radiomics for lung cancer detection in this study, we introduce a deep convolutional radiomic sequencer that is discovered using a deep convolutional neural network (three convolution layers of 3x3 with {20, 50, 500} receptive fields, one fully connected layer with 5000 neurons and softmax loss layer). First, using the wealth of CT imaging data, radiologist annotations, and diagnostic results for past patients available in a medical imaging archive, a custom radiomic sequencer is discovered for generating radiomic sequences composed of abstract, quantitative imaging-based features that characterize tumour phenotype. Once we obtain the discovered radiomic sequencer, we can apply the discovered sequencer to any new patient case to extract radiomic sequences tailored for lung cancer characterization and detection.

Experiments and Results: To create the input data for discovering the radiomics sequencer (DRS), we first extract the lung CT scans from the LIDC-IDRI [1] dataset for 93 patients for which diagnostic data (malignant or benign) is available. From each individual scan, we extracted the lesion based on the provided radiologists annotations of the lesion (i.e., it is annotated by four radiologists at most) in the particular CT scan image. We then perform data augmentation process to obtain an enriched dataset containing 42,340 lung lesions (29,956 of malignant and 22,384 benign). For evaluation purposes, we divide the dataset into two parts: 90% is used for discovering a custom radiomic sequencer, and 10% is used for testing classification performance using the discovered radiomic sequencer. We further divide the 90% into two parts: 80% for training and 10% as a validation set for validating the training process. A binary decision tree classifier is used to perform 10 fold cross validation. The results of the proposed method (DRS) and comparison with state-of-the-art method (DARS) [2] which uses 5 layer stacked autoencoder, is shown in Fig 1. The DRS produced a sensitivity, specificity and accuracy of 79.06, 76.11 & 77.52 as compared to 83.14, 20.18 & 75.01 obtained by DARS [2].

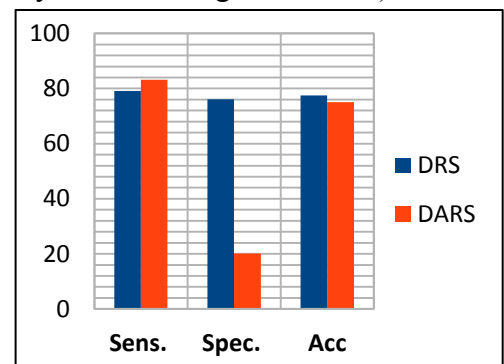


Fig.1 Comparison of lung nodule classification results (avg.) obtained using DRS and DARS [2]

Conclusion: The proposed discovery radiomics framework can be a low cost, fast and repeatable way of producing quantitative characterizations of tumour phenotype that has the potential to speed up the screening and diagnosis process while improving consistency and accuracy.

Acknowledgement: This research has been supported by OICR, NSERC, Canada Research Chairs program & Ministry of Research & Innovation, ON.

Reference: [1] The Cancer Imaging Archive Team. Data From LIDC-IDRI. doi:10.7937/K9/TCIA.2015.LO9QL9SX

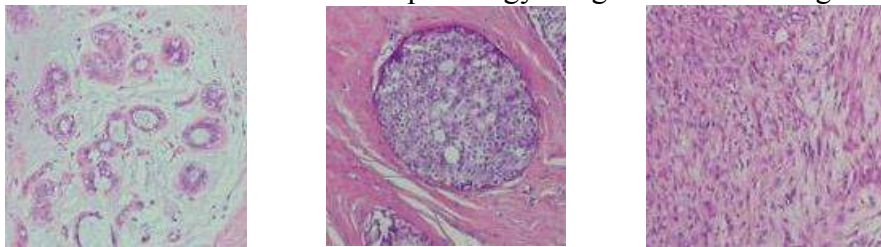
[2] Kumar *et al.* Lung nodule classification using deep features in ct image. CRV, pg 133–138, 2015.

Toward breast cancer histopathology image diagnosis using local color binary patterns

Xingyu Li*, and Konstantinos N. Plataniotis

Multimedia Lab, The Edward S. Rogers Department of Electrical and Computer Engineering
University of Toronto, 10 King's College Road, Toronto, Canada

Introduction. Breast cancer is the most common female cancer in the world. Generally, breast cancer, either “in-situ” or “invasive”, has different characteristics from normal breast tissue. In specify, in the normal case, a group of healthy cells are placed along ducts’ walls; However in the “in-situ” breast cancer, carcinoma cells fill the ducts, developing further to the “invasive” cancer where malignant cells spread into nearby tissues. In breast cancer diagnosis via histopathology images, Hematoxylin and Eosin (H&E) are usually used to stain biopsy samples for visibility enhancement. In H&E stained images, Hemaxotylin stains nuclei in cells blue/purple, and Eosin stains cytoplasm and connective tissues pink. Hence, color distribution, or color variation, in an image actually reveals the spatial organization of cells. Figures bellow show examples of an H&E stained normal sample, an in-situ breast cancer and an invasive histopathology images from left to right.



In image analysis, image textures describe the spatial distribution and local variation of image intensities or colors. Since color distribution patterns in H&E stained histopathology images are important information source for malignant cell distributions, this paper innovates the use of the powerful texture descriptor, local color binary pattern (LCBP) proposed in [1], in breast cancer diagnosis scenario.

Methods. In an H&E stained breast biopsy image, thanks to the chemical staining, color textures reveal the nuclei spatial structures in an image. Hence, for each H&E stained image, LCBP features are extracted. Let $I=[i_1, i_2, i_3]$ represent an RGB image, where the three components represent the red, green, and blue components respectively. According to [1], LCBP consists of 4 local binary patterns (LBP), among which one is computed from color norm $R=||I||=(i_1^2+i_2^2+i_3^2)^{0.5}$, and the other three LBPs are estimated from ratios of pixel values within color channel pairs $\gamma^{(n,m)}=\arctan[i_n/(i_m+\epsilon)]$ for $n<m, n=1,2,3$ and $m=2,3$. Consequently, 4 indexed images are generated, which are color norm image R , and color angular images $\gamma^{(1,2)}, \gamma^{(1,3)}, \gamma^{(2,3)}$. For each of these indexed images, LBP operator with 8-pixel circular neighbourhood is applied, resulting in a 256-length histogram. Then the obtained 4 histogram is concatenated, forming a long feature vector LCBP.

To evaluate the discriminative power of the LCBP pattern in breast cancer histopathology images, the LCBP feature is fed into a classification pipeline, where the feature is first processed by PCA to reduce the feature dimension and then passed to a linear classifier. In this study, we use a breast cancer image set published in 2015 [2] which contains 361 H&E stained breast cancer sample images. Since the image set contains 119 normal tissue images, and 242 in-situ or invasive breast cancer images, we maintain this prevalence in the 10-fold cross-validation experiment. To quantitatively evaluate the performance of LCBP, the classification precision, sensitivity, specificity, and accuracy are summarized based on 10 10-fold cross validation results.

Results. The classification performance on the breast cancer histopathology images is reported as follows: precision= 0.8407 ± 0.076 , sensitivity= 0.7748 ± 0.078 , specificity= 0.8905 ± 0.071 , accuracy= 0.8751 ± 0.0382 . It is noteworthy that the average classification accuracy outperforms the diagnosis accuracy 0.823 reported in [2].

Conclusions. Motivated by the observation that color distribution conveys the information of nuclei spatial organization in an H&E stained breast histopathology image, we innovate the use of LCBP to describe the nuclei distribution characteristics. Our experiment suggests that LCBP is effective for breast cancer diagnosis. Future work will focus on whether LCBP is discriminative for in-situ and invasive breast cancer classification.

References. [1] Lee et al, “Local color vector binary patterns from multichannel face images for face recognition,” IEEE Trans. Image Process., vol. 21, no. 4, pp. 2347 – 2353, Apr. 2012. [2] S.H. Bhandari, “A bad of features approach for malignancy detection in breast histopathology images”, IEEE ICIP, 2015.

Imaging scar with two-point bipolar Dixon MRI

Junmin Liu,¹ Dana Peters,² and Maria Drangova^{1,3}

¹Imaging Research Laboratories, Robarts Research Institute, Western University, London, Ontario, Canada

²Department of Diagnostic Radiology, Yale Medical School, New Haven, Connecticut, USA

³Dept. of Medical Biophysics, Schulich School of Medicine & Dentistry, Western University, London, Canada

Consortium: Cardiac Arrhythmia Network of Canada; **Supervisor:** Maria Drangova

Introduction. The late gadolinium enhancement (LGE) technique has become the clinical gold standard for imaging scar, where the short-inversion-time inversion recovery (STIR) imaging technique is sometimes used for fat-suppression. However, the STIR technique is sensitive to B0 and B1 inhomogeneity. Recently, several publications have suggested the use of the Dixon technique as a replacement to STIR and have demonstrated that uniform fat-suppression is achieved in the water-only image over the entire field of view, while the fat-only image provides additional diagnostic information. Before accepting cardiac Dixon-based LGE as clinically feasible, an optimized pulse sequence and a robust fat-water separation algorithm should be identified, thereby representing an area of research interest. Two-point bipolar (b-2pt) acquisition seems to be the most feasible for high-resolution (~1mm) LGE (1). However, the fat/water separation algorithm needs to be improved. This work aims to extend the multi-echo B0-NICE technique (2) to accommodate acquisitions (B0-NICEbd), resulting in improved robustness of fat-suppressed LGE.

Method. The B0NICE method generates an initial B0 map from a “pseudo in-phase” data set, followed by correcting the phase errors using both phase and magnitude information. Specifically, the B0-NICE method fits the multi-echo data to a multi-peak fat model for generating the magnitude-based fat/water masks and performs phase unwrapping to map B0. Adapting the B0-NICE technique to accommodate bipolar readout gradients (*i.e.* B0-NICEbd) faces additional challenges: 1) fitting to a multi-peak model is no longer feasible; 2) the phase errors due to the bipolar acquisition must be removed prior to B0 mapping; and 3) phase unwrapping can be challenging when processing the low SNR b-2pt data sets, combined with signal-loss along the fat-water boundaries. The B0-NICEbd technique is summarized in the flowchart of Fig. 1. The method was tested on cardiac images of nine atrial fibrillation (AF) patients and the results are compared to those obtained with the well-established phasor-based region-growing algorithm (3). Acquisition parameters can be found in a reference (1).

Results. Representative results of the B0-NICEbd fat/water separation are shown in Fig. 2, where Fig. 2a shows the final B0 map and the corresponding water- and fat-only images are shown in Fig. 2b and 2c respectively. For comparison, Fig. 2d and 2e show the results obtained using the phasor-based region-growing technique. Fat-water swaps are observable in the region identified by the box. Importantly, a fat/water swap is also observed in the pericardial fat region indicated by the arrows. Such swaps are not present in the B0-NICEbd processed images of Fig. 2b and 2c.

Conclusion. The B0-NICEbd unwrapping-based 2pt bipolar Dixon approach yields robust B0 and fat/water maps that are automatically calculated, with no user intervention. The combination of the rapid acquisition afforded by the use of bipolar gradients and the B0-NICEbd technique promises to be clinically feasible.

References. 1. Shaw et.al., JMRI 2014;40(1):119-125.; 2. Liu and Drangova, MRM 2015;74(4):1177-1188; 3. Ma, 2004;52(2):415-419.

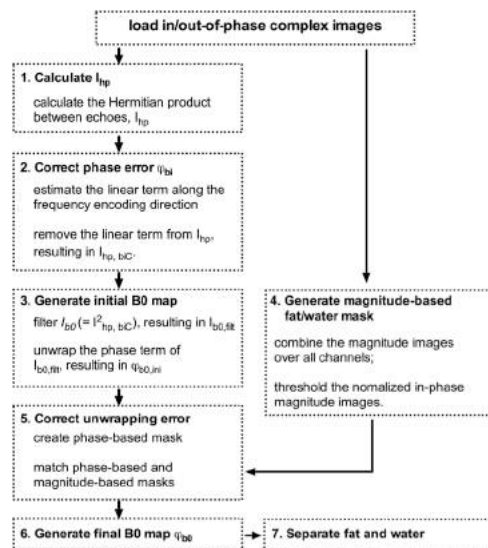


Fig. 1. The B0NICEbd technique.

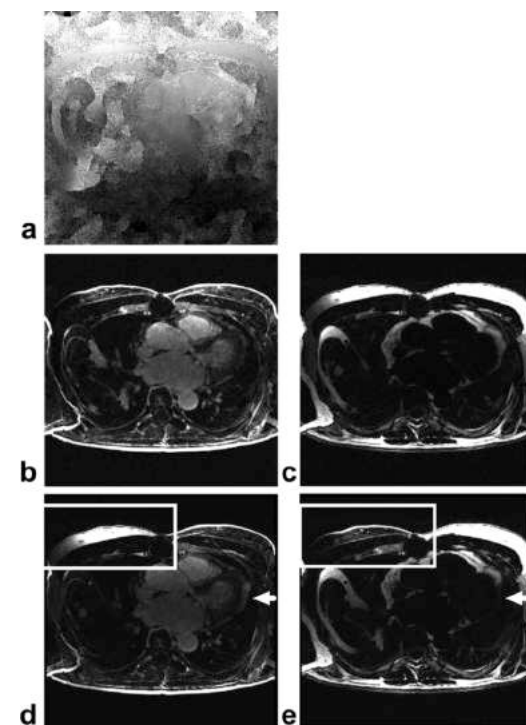


Fig. 2. Final deblurred B0 map (a); B0-NICEbd generated water-only (b) and fat-only (c) images; phasor-based region-growing algorithm generated water-only (d) and fat-only (e) images. Arrows in (d) and (e) indicate the fat-water swaps identified in the pericardium.

Web-application Based Ultrasound Bone Segmentation Evaluation

Matthew Lougheed, Gabor Fichtinger, Tamas Ungi

Laboratory for Percutaneous Surgery, Queen's University, Kingston, Ontario, Canada

INTRODUCTION: Currently bony structures are most commonly visualized using X-ray. This modality provides clear images of the bone, but drawbacks of X-ray-based techniques include exposing patients to ionizing radiation and the cost of hardware. Ultrasound (US) imaging is a safe and inexpensive alternative that has promise in overcoming the noted drawbacks of X-ray imaging. Ultrasound images contain large amounts of image artifacts which increase the difficulty of interpreting an image however, making automatic segmentation difficult. Due to this nature of US imaging, as well as the diverse set of anatomical features imaged, a variety of algorithms have been developed for bone segmentation. These algorithms see different levels of performance due to the particular heuristics used in each method. Algorithm evaluations are often based on manually segmented ground truths, but are performed using different US images as well as different metrics making objective comparison of published methods impossible. Additionally, source code for algorithms is often not easily obtainable for analysis and use. This creates difficulties in determining which algorithm is appropriate for a particular task. More accurate comparison of algorithms requires segmentations to be performed on the same US image and evaluated with the same metrics. To facilitate this goal, we have explored a web-application based approach to bone segmentation evaluation which provides the ability to acquire and share datasets as well as evaluate segmentations.

METHODS: Four main components were required for the application: users, datasets, algorithms, and results. Users of the application can create dataset objects which consist of the US image and ground-truth images required for evaluation. These dataset objects can then be downloaded by other users to test segmentation algorithms. Users can also create algorithm objects, which provide an outline of the developed method and, if desired, the source code. Results contain computed metrics of a segmentation evaluation and are connected to a particular dataset and algorithm object. A user downloads a dataset object, runs their segmentation algorithm, and uploads the segmentation while specifying the algorithm object to create a result. Three metrics were implemented for the web application to compute, Hausdorff, Dice coefficient, and true positive / false negative metrics as described in [1]. Uploaded segmentations are evaluated using C++ scripts which use ITK to compute the desired metrics.

RESULTS: A web application was developed using Ruby on Rails which enables US datasets to be uploaded and downloaded by users, provides information on developed algorithms, and evaluates segmentations. Access to multiple datasets is beneficial in algorithm development to validate segmentation robustness. Developers can download a dataset, run their segmentation algorithm on the image, and upload the segmented result to the application to be evaluated. The ability to compute metrics by the web application eliminates the need of individuals to implement the evaluation code separately. The computed metrics can be chosen to be shown public, displaying the algorithms performance on a particular dataset. These results provide a direct way to compare algorithms on a particular dataset.

CONCLUSIONS: By consolidating US images, algorithms, and metric computations in a web-application, users can easily view algorithms and compare their performance against various US images. Developers avoid the need to write evaluation code and can discover algorithms aligned with their interest while end users can find an appropriate algorithm efficiently. The web-application focussed on bone segmentation in ultrasound but can be easily applied to other forms of segmentation.

REFERENCES: [1] Lougheed, M., Fichtinger, G., & Ungi, T. (2015, March). Evaluation metrics for bone segmentation in ultrasound. In *SPIE Medical Imaging* (pp. 941516-941516). International Society for Optics and Photonics.

Automatic pipeline of lesion classification on breast 3D MRI data

YingLi Lu², Hongbo Wu¹, Cristina Gallego-Ortiz¹, Sharmila Balasingham², Anne Martel^{1,2}

¹Medical Biophysics, University of Toronto

²Physical Sciences, Sunnybrook Research Institute

Introduction: The automatic classification of benign and malignant lesions on breast magnetic resonance imaging (MRI) data has the potential to improve the positive predictive value of screening and to improve the radiologists workflow. We have developed a fully automatic pipeline computer-assisted diagnosis system for breast lesion detection and classification. Robust image processing/analysis and machine learning algorithms were developed in Python and R and then an efficient pipeline was implemented in C++. This abstract describes the system.

Methods: The proposed pipeline includes 8 steps: **Step 1**, extract the requisite sequences/series 3D volume data from 2D DICOM files, and convert it 3D formats(mha, mhd, NIFTI, MINC etc.); **step 2**, affine registration between the non-fat suppressed volume and pre-contrast fat suppressed volume using Elastix[1]. **Step 3**, motion correction of post-contrast volumes using optical-flow [2]. **Step 4**: breast segmentation of the baseline volume based on random forest[3]. **Step 5**, lesion detection using deep learning[4]. **Step 6**, vessel removal based on shape measures. **step 7**, lesion classification based on random forest[5]. **step 8**: using different colors to discriminate benign and malignant lesions, and overlay detected lesions on the maximum intensity projections of the subtraction image.

Results: One representative example of running the pipeline is illustrated. We extracted the baseline volume (T1 weighted MR image sequences acquired without fat suppression), 5 post-contrast volumes from 1415 DICOM files retrieved from the PACS server. The dimension of the 3d volume is 512x512x84. Representative results are show in Fig.1. The computing time(Intel Xeon 3.5 GHz processor) of each step is show in Table. 1.

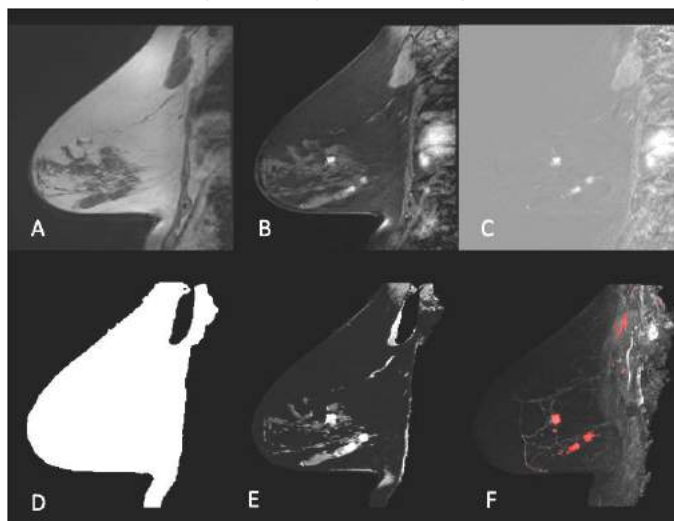


Fig. 1. Representative results. A: non-fat suppressed image(registered), B: 1st post-contrast image, C: subtraction image(1st post-contrast - pre-contrast), D: breast mask, E: lesion probability map, F: lesion(red) after vessel removal, and overlaid on MIP image.

Table. 1. Computing time

| | Step1 | Step2 | Step3 | Step4 | Step5 | Step6 |
|--------------------------|-------|-------|-------|-------|-------|-------|
| Computing time (seconds) | 15 | 18 | 59 | 160 | 16 | 2.5 |

Discussion and Conclusions: An automatic pipeline for lesion classification on breast 3D MRI data has been described. The initial results tested on a small datasets indicate that it will streamline the research and clinical processing. The use of ITK, VTK and OpenCV libraries greatly simplified the conversion from Python to C++. Future work will focus on GPU acceleration and development of a graphical user interface.

Acknowledgements: This work was funded by OICR Smarter Imaging Program and Federal Economic Development Agency for Southern Ontario.

References

1. Klein, Stefan, et al. "Elastix: a toolbox for intensity-based medical image registration." *Medical Imaging, IEEE Transactions on* 29.1 (2010): 196-205.
2. Martel, A. L., et al. "Evaluating an optical-flow-based registration algorithm for contrast-enhanced magnetic resonance imaging of the breast." *Physics in Medicine and Biology* 52.13 (2007): 3803.
3. Martel, A.L. et al. "Breast segmentation in MRI using Poisson surface reconstruction initialized with random forest edge detection " *Proc. SPIE* 2015, 9784-464.
4. Hongbo Wu, et al. "Deep Artificial Neural Network Approach to Automated Lesion Segmentation in Breast DCE-MRI", *Proc. MICCAI-BIA* 2015, 73-80
5. Gallego-Ortiz, Cristina, et al. "Improving the accuracy of computer-aided diagnosis (CAD) for breast MRI by differentiating between mass and nonmass lesions". *Radiology*. ISSN 0033-8419 (In Press)

Apodized Aperture Pixel Design: A novel x-ray detector with higher detective quantum efficiency and reduced aliasing

Tomi Nano, Terenz Escartin, and Ian A. Cunningham
Western University, Robarts Research Institute, London ON

Primary author: Tomi Nano
Consortium affiliation: Ontario Institute for Cancer Research – Imaging Translation Program
Research supervisor: Dr. Ian A. Cunningham

ABSTRACT

Introduction: X-ray-based imaging is the mainstay of medical imaging facilities around the world and an essential part of modern medicine. However, exposure to radiation also carries a small risk of creating new cancers so it is imperative that x-ray systems be designed to produce the best possible images for minimal acceptable exposures. The ability to improve visualization of structural information in digital radiography, without increasing radiation exposures, requires improved image quality at high spatial frequencies. Image quality in radiology is quantified by the detective quantum efficiency (DQE) of the detector as a function of spatial frequency. We present a method of increasing DQE at high spatial frequencies by improving the modulation transfer function (MTF) and reducing spatial aliasing.

Methods: The Apodized Aperture Pixel (AAP) design uses a detector with micro-elements to synthesize desired pixels. A cascaded system analysis (CSA) considering different x-ray detector characteristics such as x-ray interactions, electronic readout-noise, and pixel size is used for comparison of the theoretical MTF, noise power spectrum (NPS), and DQE. Using a clinical system to demonstrate AAP and conventional images, we show experimental comparisons of the MTF, NPS, and DQE.

Results: Compared to conventional detectors, the MTF was improved by 50% and the DQE by 100% at the sampling cutoff frequency for the AAP design. This resulted in improved image contrast and signal-to-noise ratio at high frequencies for a given pixel size. AAP images showed a greater visual impact of fine image content due to the improved contrast and reduced aliasing.

Conclusion: An improvement in high-frequency DQE is significant because it means that our ability to visualize small structures and fine detail will be improved by the same factor. The enhanced visualization of fine detail and small structures is important for early cancer diagnosis. Additionally, this provides the basis for the development of a novel x-ray detector with improved image quality at current exposures or conventional image quality at lower patient exposures.

Single Slice US-MRI Registration for Neurosurgical MRI-Guided US

Utsav Pardasani*, John S.H. Baxter, Terry M. Peters, Ali R. Khan
 Roberts Research Institute, London, Ontario, Canada;
 Western University, London, Ontario Canada

1. INTRODUCTION

Image-based ultrasound to magnetic resonance image (US-MRI) registration can be an invaluable tool in image-guided neuronavigation systems. State-of-the-art commercial and research systems utilize image-based registration to assist in functions such as brain-shift correction, image fusion, and probe calibration.

Since traditional US-MRI registration uses reconstructed US volumes or a series of tracked US slices, the functionality of this approach can be compromised by the limitations of optical or magnetic tracking systems in the neurosurgical operating room. These drawbacks include ergonomic issues, line-of-sight/magnetic interference, and maintenance of the sterile field. For a “universal” system that would work with any given ultrasound machine, these issues are compounded with the challenge of instrumenting the probe without permanent modification and calibrating the probe face to the tracking tool.

To address these challenges, this paper explores the feasibility of a real-time US-MRI volume registration in a small virtual craniotomy site using a single slice.

2. METHODS

We employ the Linear Correlation of Linear Combination (LC2) similarity metric as well as our own faster variant on data from the Brain Images for Tumour Evaluation (BITE) dataset as a PyCUDA enabled Python module in Slicer. Our experiments attempt to recover the pose in both 3 degrees-of-freedom (DOF) and 6DOF. When searching in 6DOF for the ultrasound pose, we employ expert-identified landmarks in the BITE database to validate our algorithm’s results.

3. RESULTS

Our initial results are positive, and our algorithm can consistently place the ultrasound probe pose close to optical tracking. (See Figure 1 and 2) We shall show quantitative results from our metric evaluation.

4. CONCLUSION

TBD

5. ACKNOWLEDGEMENTS

The authors are grateful for funding support from the Canadian Institute for Health Research (CIHR), National Sciences and Engineering Research Council (NSERC), the Ontario Graduate Scholarship program (OGS), and Synaptive Medical Inc. We are also grateful for the valuable discussions with Dr. Jonathan C. Lau and Adam Rankin.

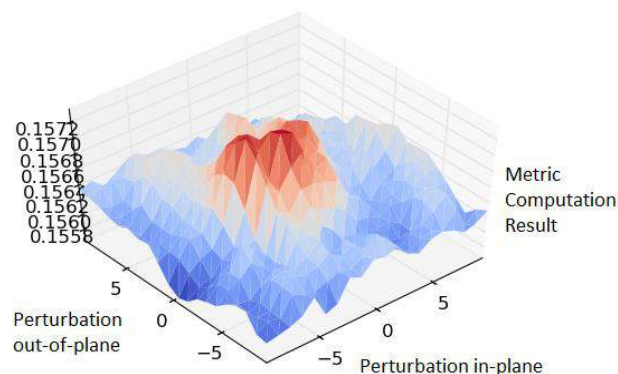
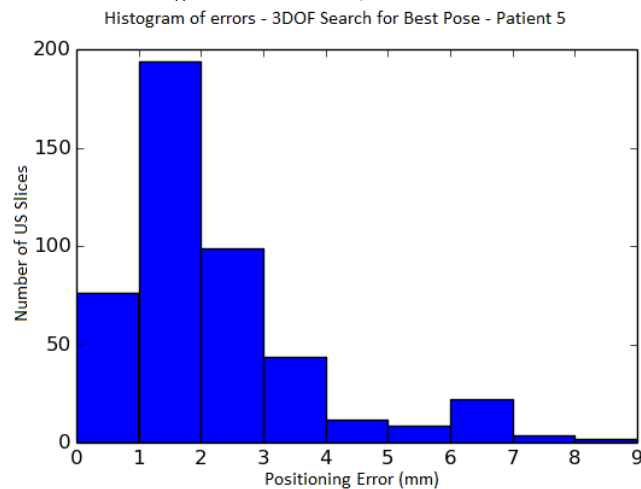


Figure 1 (top) – Objective function sampling with LC2 similarity metric measuring the similarity between a given US slice and MRI slice, perturbing the provided optically tracked US probe pose in two directions. Figure 2 (below) Histogram of errors for US slice placement in Patient 5 of the BITE dataset using the LC2 similarity metric.



Method for global thresholding in Metal Artifact Reduction (MAR)

I. Petrov,¹ D. Holdsworth,^{1,2} and M. Drangova^{1,2}

¹Imaging Research Laboratories, Robarts Research Institute, ²Department of Medical Biophysics, University of Western Ontario, London, Ontario, Canada

Consortium: *Imaging for Cardiovascular Device Intervention* Supervisor: M. Drangova

Introduction: It is well known that image quality in computed tomography (CT) is degraded by the presence of dense materials. Dense objects cause heavy artifacts that radiated out of the dense objects, often affecting large areas of the image. Methods for metal artifact reduction (MAR) have been proposed and most involve the correction of the values corresponding to the dense object in the raw projection images (*i.e.* sinogram space);¹ projection data corresponding to the dense object are replaced with smooth, interpolated “corrected” values. However, the MAR methods are very sensitive to the selection of the threshold value that identifies metal in the projection images. The present work addresses this issue and proposes a new technique for accurate segmentation of the reconstructed volumes into two classes and correcting the high-density metal class.

Methods: For each reconstructed volume, the dynamic range of the gray scale values is divided into fifty equal steps (i) and each step is used as a threshold for selecting the high density “metal” to be corrected. At each threshold, all values below the threshold are set to zero, the ratio (N_i/N_0) of pixels above the threshold (N_i) to the total number of pixels (N_0) is calculated, as is the total entropy² ($S_i = -\sum p_k \log_2(p_k)$) of the thresholded image. The difference between the normalized entropy (S_i/S_0) and $Prob_i$ is calculated and the value of i at which $S_i/S_0 \sim N_i/N_0$ is identified (Fig. 1b, arrow). For all values above this level, $Prob_i$ is fitted to a decaying exponential ($b \cdot e^{-a \cdot i}$) Fig. 1c. The global threshold – to be used as the threshold identifying the dense metal components – is selected as the gray value corresponding to the first minimum of the residuals between the fit and $Prob_i$. Standard MAR methods can then be applied. In this study we implemented the “in-paint” method³ to identify the “metal” voxels in the images and subsequently to correct the projection images through interpolation.

The method was evaluated on images of several metal objects obtained using an O-arm cone-beam CT scanner. Results of implantable cardioverter-defibrillator (ICD) leads placed in agar are presented. Images were acquired in SD mode (391 views in 13 s; 120 kVp, 25 mA). Raw projections were reconstructed using the Feldkamp algorithm⁴ then binned $2 \times 2 \times 2$ for identification of the threshold. For quantitative comparison, the contrast to noise ratio (CNR)⁵ between the agar and the surrounding air was calculated.

Results and Discussion: CT images of the ICD leads before and after MAR correction are shown in Fig. 2. Visibly, there were fewer streaks in the corrected volume and a dramatic improvement in the line profile through the artifact region is seen in Fig. 2c. CNR was up to 8 times higher in the corrected image. Similar results were obtained while correcting scans with numerous metal rods.

The presented method successfully identified an appropriate threshold for separating CT images into low and high-density classes prior to the application of a MAR algorithm. For very large, dense objects (over 2 cm in diameter, results not shown), while an appropriate threshold was identified the MAR algorithm based in the “in-paint” function suffered from its limited ability to recover the correct values in the projection images. Combining the presented threshold identification technique with *a priori* knowledge of the scanned object promises to yield further improvement in metal artifact correction.

REFERENCES: [1] Wagenaar D, et al., 2015, PLoS ONE 10(6). [2] Gonzalez, R.C., et al., Prentice Hall, 2003. [3] Garcia D., 2010, Comput Stat Data Anal; 54(4):1167-1178. [4] Fessler JA, IRT. [5] Michetti J, et al., Conf Proc IEEE Eng Med Biol Soc, 2015:7905-8.

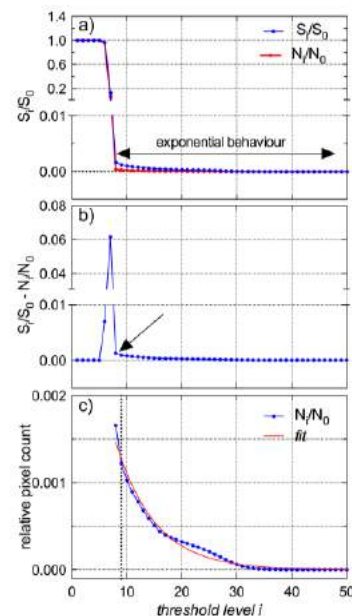


Fig. 1 Intermediate steps of threshold identification.

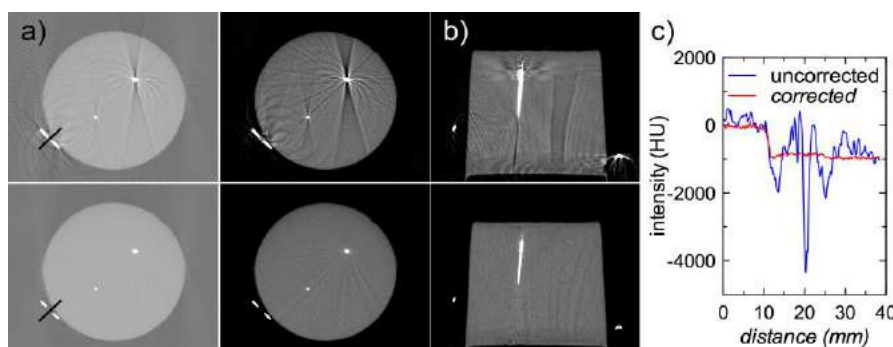


Fig. 2 Uncorrected (top) and corrected (bottom) images of the ICD leads. a) transaxial view at two different window/level settings; b) multi-planar reformatted image through a lead. c) corrected and uncorrected line profiles through the black line in a).

Validation of the prostate segmentation on MRI: manual vs computer-assisted methods

Maysam Shahedi^{123*}, Derek W. Cool³⁴, Cesare Romagnoli³⁴, Glenn S. Bauman¹⁵⁶, Matthew Bastian-Jordan⁴, George Rodrigues¹⁵, Belal Ahmad¹⁵, Michael Lock¹⁵, Aaron Fenster^{2346†}, and Aaron D. Ward^{1256†}

(*Primary author, †Co-supervisors)

OICR Smarter Imaging Program

¹London Regional Cancer Program; ²Graduate Program in Biomedical Engineering, ³Robarts Research Institute,

⁴Department of Medical Imaging, ⁵Department of Oncology, ⁶Department of Medical Biophysics, Western University, London, Ontario, Canada

Introduction: Three-dimensional (3D) segmentation of the prostate on medical imaging is useful for prostate cancer (PCa) diagnosis and therapy guidance. However, manual segmentation of the prostate is laborious, time-consuming and subject to inter-observer variability. The focus of this study was on (1) accuracy, reproducibility and procedure time measurement for prostate segmentation on T2-weighted (T2w) endorectal (ER) magnetic resonance (MR) imaging (MRI); and (2) assessment of the potential of a computer-assisted segmentation to be translated to clinical practice for PCa management.

Methods: We collected 42 ER MR images from patients with biopsy-confirmed PCa. Prostate border delineation was manually performed by one observer on all 42 images and by two other observers on a subset of 10 images. We used mean absolute distance (MAD), Dice similarity coefficient (DSC), recall rate, precision rate, and volume difference (ΔV) as a complementary boundary-, region- and volume-based error metric set to measure different types of segmentation errors. We applied this evaluation for expert manual segmentation as well as semi-automatic and automatic segmentation approaches before and after manual editing by expert physicians. Physicians were instructed to edit the segmentations to their satisfaction for use in clinical procedures, as would be done with any prostate segmentation technique integrated into the clinical workflow. We recorded the time needed for user interaction to initialize the semi-automatic algorithm, algorithm execution, and manual editing where applicable.

Results: On 42 images, comparing to a single-observer manual segmentation reference, the measured errors for semi-automatic and automatic algorithms on the whole prostate gland were, respectively, MAD of 2.0 mm and 3.2 mm; DSC of 82% and 71%; recall of 77% and 69%; precision of 88% and 76%; and ΔV of -4.6 cm³ and -3.6 cm³. These results compared favourably with observed difference between manual segmentation and a simultaneous truth and performance level estimation (STAPLE) [1] reference for a subset of 10 images (whole gland differences as high as MAD = 3.1 mm, DSC = 78%, recall = 66%, precision = 77%, and ΔV = 15.5 cm³). For each 3D image, the SA algorithm required about 30 seconds, on average, to be initialized. Using an unoptimized Matlab research platform on a single CPU core, the average execution times for the semi-automatic and automatic 3D segmentation algorithms were 85 sec and 54 sec, respectively. We also measured average editing times of 330 and 390 seconds for the semi-automatic and automatic segmentation results, respectively, whereas, on average, an expert spent 564 seconds manually segmenting an image and 210 seconds editing manual segmentations performed by another expert. Table 1 shows editing times recorded for different segmentation labels. We showed higher consistency and lower accuracy of semi-automatic segmentation prior to manual editing compared to manual segmentation. However, we observed improved accuracy and consistency after editing the semi-automatic segmentation. Figure 1 shows the results for one metric (MAD).

Conclusions: The main conclusions of this study were that (1) the accuracies of the computer-assisted approaches were within the range of observed variability in manual prostate segmentation performed by experts, (2) manual editing of semi-automated and automated segmentation approaches improved the accuracy and inter-operator variability, (3) the recorded procedure time for prostate segmentation was reduced using computer-assisted segmentation approaches followed by manual editing compared to fully manual segmentation, and (4) starting the manual segmentation from an initial computer-assisted segmentation label could reduce final segmentation variability.

References: [1] Warfield *et al.*, IEEE TMI 2004; **23**, 903-921.

Table 1. User manual interaction time for ready to use prostate segmentation in T2w MRI.

| Segmentation labels | User interaction time |
|-----------------------------------|-----------------------|
| Manual | 213 ± 90 sec |
| Semi-automatic | 328 ± 126 sec |
| Semi-automatic + user interaction | 351 ± 128 sec |
| Automatic | 393 ± 146 sec |

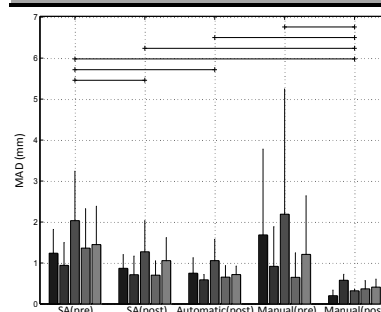


Figure 1. Inter-operator variability pre- and/or post-manual editing. Each bar shows the average MAD value for one image across five operators. ($p < 0.05$).

Scattering Wavelet Representation of fMRI BOLD data

Saurabh B Shaw¹, Michael D Noseworthy^{1,2}

¹School of Biomedical Engineering, and ²Electrical and Computer Engineering, McMaster University, Hamilton, Ontario, Canada

Introduction: Functional Magnetic Resonance Imaging (fMRI) is widely used to probe activity of the brain under various functional loads. Traditionally, the recorded haemodynamic response of the BOLD signal is compared to the expected HRF signature using a generalized linear model (GLM) to identify active brain regions. The expected HRF is very hard to estimate for complex tasks such as memory or spatial localization tasks. Multivariate methods are then typically used to identify active regions of the brain. One such novel multivariate tool is the Scattering Wavelet transform (ScWT). This abstract aims to explore this technique in the context of fMRI data analysis.

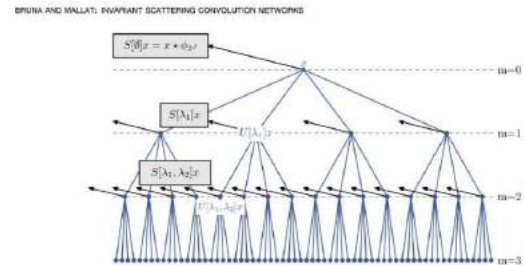


Figure 1 - Scattering Wavelet tree. The levels are represented by m . At each level, there are j paths created.

Methods: The Scattering Wavelet Transform (ScWT) is a wavelet-based tool, which is invariant to finite group actions such as translations or rotations, making it an ideal candidate for motion contaminated fMRI datasets. The ScWT was implemented as a convolution network (Fig. 1), where the signal (x) is recursively convolved with wavelet filter banks (φ & λ). The repeated convolution gives a matrix of scattering coefficients representing interference of the signal with the wavelets. A GE MR750 3T MRI and 32 channel RF coil (General Electric Healthcare, Milwaukee, WI) was used for data acquisition. Axial fSPGR 3D images were used to prescribe a bilateral motor finger activation fMRI task (gradient echo EPI, FA=90°, TE/TR=35/2000ms, 64x64 matrix, 31 continuous 4.5 mm slices, 180 temporal points). BOLD data was motion corrected using AFNI and the ScatNet MATLAB Toolbox (<http://www.di.ens.fr/data/software/scatnet>) was modified and implemented to compute scattering coefficients from BOLD data. A unique set of scattering coefficients were computed for the BOLD time series at each voxel. These were compared with the GLM results, computed using AFNI.

Results: The GLM showed bilateral activation of the primary motor cortex. ScWT analysis showed a consistent scattergram differences between the activated & quiescent voxels (Fig 2). Activated voxels showed lower levels of ScWT coefficients, especially around the low-scales and very high-scales.

Discussion: This study shows that ScWT can be successfully used to predict activated voxels from their BOLD time series for a simple task. ScWT coefficients mathematically signify a Lie group. Hence, other actions constituting noise can be modeled as a Lie group and added to the convolutional network. This will result in the coefficients becoming invariant to the noise thereby creating a robust descriptor of the BOLD data. Further investigation is required to quantify its efficacy in identifying active regions in a more complex task.

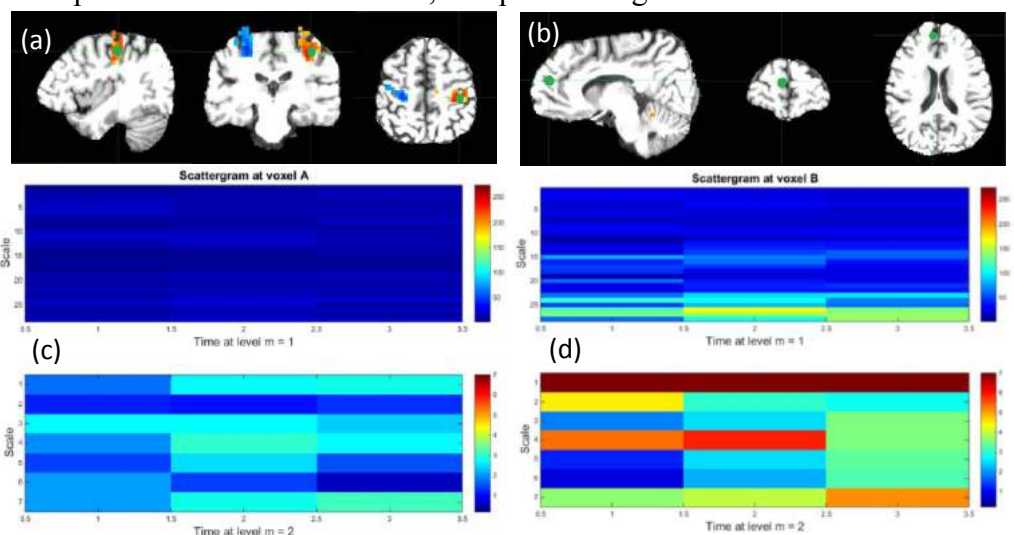


Figure 2 – An active voxel A & an inactive voxel B, as determined by GLM analysis, is shown in (a) & (b) respectively. (c) & (d) Scattergram of voxels A & B. The first image row of a scattergram displays first order scattering coefficients ($m = 1$) in a time-scale representation i.e. lower frequencies are at the bottom with increasing frequency towards the top. The second row corresponds to second order scattering coefficients ($m = 2$) at a finer scale representing higher frequencies.

References: [1] Mallat S (2012) *Comm Pure and Appl Math* 65.10:1331-1398. [2] Bruna J, Mallat S (2013). *IEEE Trans Pattern Ans Mach Intell* 35.8:1872-1886.

Cartan frames for characterizing myofiber geometry in pig hearts from diffusion tensor imaging (DTI)

Heart Failure: Prevention Through Early Detection Using New Imaging Methods

Damien Goblot* (primary author), Mihaela Pop[^] and Kaleem Siddiqi* (research supervisor)

*School of Computer Science, McGill University; [^]Dept. Medical Biophysics, Sunnybrook, Univ. of Toronto

INTRODUCTION: Myofiber geometry plays a critical role in the electro-mechanical function of the heart. Imaging modalities that can assess myofiber integrity are thus of interest for disease prevention and early detection of pathology. Recent results point to a minimal surface organization, as corroborated by fits to diffusion tensor (DT) images of *ex vivo* mammalian hearts [1,2]. It has also been shown that chronic infarcts have a higher apparent diffusion coefficient (ADC) due to an increase in extracellular space [3] and a decreased fractional anisotropy (FA) [4] due to a build up of collagen in the scar. However, less is known about the manner in which infarcts affect fiber geometry. To examine this we apply Cartan frame fitting methods and assess fitting errors to local (orthonormal) frames fit to DT images of porcine hearts. We hypothesize that infarcted regions are more likely to lead to higher errors of fit due to a breakdown in fiber anisotropy.

METHODS: Diffusion imaging of 2 healthy and 4 infarcted pig hearts was performed *ex vivo* at a sub-millimetric voxel size on a 1.5T GE SignaExite scanner, using 7 directions for diffusion gradients [3]. We performed a local voxel-wise DT reconstruction and then used the unit direction of the first principal eigen vector (the local fiber orientation) as the first axis \mathbf{f}_1 of a local Cartesian coordinate frame. The heart wall normal was then estimated at each voxel within the left ventricle (LV) and the axis \mathbf{f}_3 was taken to be the unit vector in the direction of the component of the heart wall normal orthogonal to \mathbf{f}_1 . The third axis \mathbf{f}_2 was constructed as the cross product of \mathbf{f}_1 and \mathbf{f}_3 . We then used the Cartan frame fitting methods of [1] to compute the 9 1-form parameters \mathbf{c}_{ijk} at each voxel. The term \mathbf{c}_{ijk} describes the local amount of turning of frame \mathbf{i} towards frame \mathbf{j} for a step in the direction of frame \mathbf{k} . The fits minimized an energy modeled as the angular error between the fiber orientations measured from diffusion data in a neighborhood of each voxel and the orientation given by the rotations of \mathbf{f}_1 at that voxel by the computed 1-form fits. We then computed the histograms of the 1-forms as well as the local error of fit, to compare an infarcted pig heart with a healthy one.

RESULTS: Fig. 1a illustrates the scalar ADC map in an axial slice of an infarcted pig heart. The infarct region exhibits a degree of incoherence in fiber orientation, as suggested by the visualization of fiber directions \mathbf{f}_1 in Fig. 1b. In [1,2] the 1-form parameter \mathbf{c}_{123} is key since it describes the rate at which fibers turn in a transmural penetration from outer wall to inner wall. The histogram of \mathbf{c}_{123} over the LV wall of an infarcted pig heart in Fig. 1c (top) follows a trend similar to that observed for healthy mammalian hearts in [1,2] (mean $\mathbf{c}_{123} = -0.053$ radians/voxel or -3.04 degrees/voxel), but with a high error of fit, shown in Fig. 1c (bottom). In contrast, the histograms for a healthy pig heart in Fig. 1d reveal a doubling of the transmural turning rate (mean $\mathbf{c}_{123} = -0.101$ radians/voxel or -5.79 degree/voxel), and lower errors of fit, favouring our hypothesis.

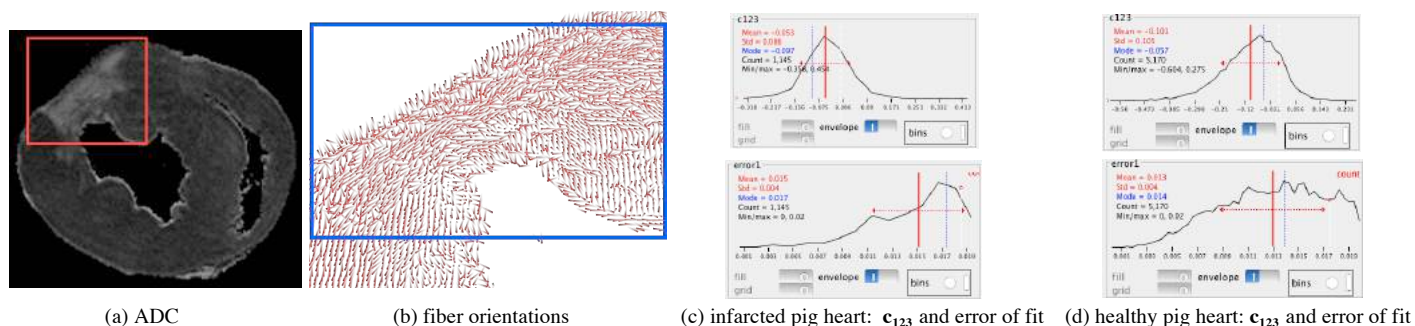


Figure 1: (a) The ADC map shows a region of increased apparent diffusion in the infarct area (red rectangle); (b) fiber orientations \mathbf{f}_1 obtained as the first principal eigen vector of the diffusion tensor for a region including the infarct; (c) histograms of the 1-form parameter \mathbf{c}_{123} (top) and of errors of fit (bottom) for this infarcted heart; and (d) the same histograms for a healthy pig heart. The other 1-form parameters are close to zero, except those that describe the local curvature of the heart wall.

CONCLUSIONS: Cartan frame analysis allows us to assess the integrity of the geometry of fibers in the presence of myocardial infarcts. In future work we plan to extend this analysis to a larger database of hearts.

References: [1] Savadjiev *et al.* PNAS:109(24):9248-9253, 2012. [2] Piuze *et al.* PAMI:37(12):2492-2504, 2015. [3] Pop *et al.* PMB:58(15):5009-5028, 2013. [4] Wallenburg *et al.*, J. Innov. Opt. Health Sci.:3(109), 2010.

Computer-Assisted Prostate Cancer Characterization on Multi-Parametric MRI

D. Soetemans^{1,7}, G. S. Bauman⁵, E. Gibson^{1,2,8,9}, M. Gaed^{2,3}, J. A. Gomez³, M. Moussa³,
J. L. Chin^{4,5}, S. Pautler^{4,5}, A. D. Ward^{6,5,7}

OICR Smarter Imaging Program; Research Supervisor: Aaron Ward

Ontario Institute for Cancer Research Smarter Imaging Program

1. Biomedical Engineering Graduate Program, 2. Robarts Research Institute, Depts. of

3. Pathology, 4. Surgery, 5. Oncology, 6. Medical Biophysics, Western University,

7. Lawson Health Research Institute, London, Ontario, Canada,

8. Centre for Medical Image Computing, University College London, London, UK,

9. Department of Radiology, Radboud University Medical Centre, Nijmegen, Netherlands

Purpose. Prostate cancer (PCa) is the second leading cause of cancer related death among men in North America¹. PCa localization suffers from large inter-radiologist variability². Suspicious regions can be characterized as malignant or benign by computer models using machine learning algorithms, which can improve radiologist performance, especially for novices³. However, most current models are validated using histology obtained from biopsies that are preferentially guided toward suspicious regions identified on multiparametric magnetic resonance imaging (mpMRI). Such validation is impacted by sparse and spatially-biased sampling, and biopsy localization uncertainty. Widespread clinical implementation of computer-assisted PCa lesion characterization remains elusive; *critically needed is a model that is validated against a histologic reference standard that is densely-sampled in an unbiased fashion*. We address this using our technique for highly accurate fusion of mpMRI with whole-mount digitized histology of the surgical specimen (Fig. 1)³. We present a preliminary model for computer-assisted characterization of PCa characterization, validated with whole-mount histology.

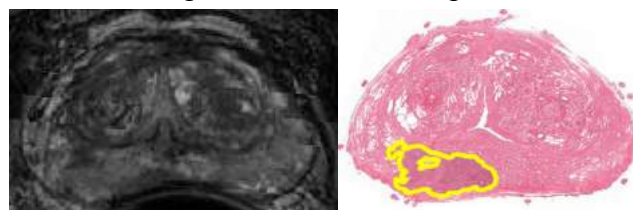


Figure 1: Registered T2W MRI and histology showing tumour location

Methods. We obtained pre-surgical mpMRI (T2-weighted and diffusion-weighted) from 22 patients who underwent radical prostatectomy. Spatial T2W signal variation due to endorectal coil sensitivity was mitigated using the N4ITK image bias correction algorithm⁴. These images were accurately registered to digitized histology images of the specimen obtained post-surgery³. Malignant and benign regions contoured and graded on histology were mapped onto mpMRI. First and second order texture features (44 in total) were extracted from mpMRI within these regions, and feature selection was performed using a t-test filter. Malignant-vs-benign classification performance was measured using 5-fold cross-validation for three classifiers: support vector machines (SVM), k-nearest neighbours (KNN) and random forest (RF).

| Table 1: Classification Performance (mean±std) | | | |
|--|-----------|-----------|-----------|
| Classifiers | SVM | KNN | RF |
| PZ MCR | 0.27±0.10 | 0.27±0.16 | 0.21±0.11 |
| CZ MCR | 0.22±0.10 | 0.26±0.05 | 0.24±0.08 |
| PZ AUC | 0.62±0.19 | 0.57±0.26 | 0.60±0.22 |
| CZ AUC | 0.69±0.15 | 0.61±0.13 | 0.62±0.16 |

Results. Table 1 shows the misclassification rate (MCR) and area under the receiver operating characteristic curve (AUC) for detection of cancer within the peripheral zone (PZ) and central zone (CZ). A two-factor ANOVA was performed across classifiers and between the PZ and CZ. No statistically significant differences ($\alpha=0.05$) were found.

Conclusions. A computer model can characterize suspicious regions as malignant or benign using 1st and 2nd order texture features on prostate mpMRI with similar performance within the PZ and the more challenging CZ using surgical pathology for validation. After further improvement and validation, this approach has the potential to serve as a second observer to improve physician performance in identifying threatening lesions and recommending personalized prostate cancer treatment.

References. [1] Siegel, R. L. et al, *A Cancer Journal for Clinicians*, 65: 5–29, 2015. [2] Salarian M. et al, *SPIE Medical Imaging* 9041, 2014. [3] Hambrook T. et al, *Radiology* 266 (2):521-530, 2013. [4] Gibson E. et al, *J Magn Reson Imaging* 36(6), 1402–1412, 2012. [5] Tustison N. and, Gee J, *The Insight Journal* January–June 2009, <http://hdl.handle.net/10380/3053>.

Max-tree\Watershed Combination for Medical Image Segmentation

Roberto Souza,^{1,2} Leticia Rittner,¹ Richard Frayne,² Roberto Lotufo¹

¹School of Electrical and Computer Engineering, University of Campinas, Campinas, Brazil

²Calgary Image Processing and Analysis Centre (CIPAC), Foothills Medical Centre, Calgary, Canada

Purpose: Present a segmentation methodology that combines the max-tree¹ and its shape information with the watershed transform².

Introduction: The watershed transform is a fast segmentation technique that, given a set of markers, partitions an image. It has been widely used in medical segmentation problems. Its major drawbacks are that it does not consider shape, and it is very sensitive to the choice of markers. The max-tree² (Fig. 1) is a hierarchical image representation based on threshold decomposition. Loosely speaking, applying a threshold (t) to an image ($f \geq t$) generates a “black and white” image, where each “white island” in this binary image is called a connected component (CC). CCs have a hierarchical property that allows building the max-tree – a tree where each CC is a node. The max-tree construction is based on image intensities, but size and shape attributes can be computed from its nodes, allowing for more complex analysis. Both the max-tree construction and attributes extraction can be computed efficiently^{3,4}.

Methodology: The size and shape information of the image structures provided by the max-tree were used to select robust markers for the watershed transform. The selection of the max-tree nodes is problem oriented and is very suitable for medical image problems, since average sizes and shapes of the structures of interest are known, and can be used to select the appropriate max-tree nodes as markers.

Applications: The first application of the methodology proposed consists in the brain extraction problem, and can be seen as an improvement of the method proposed by Hahn and Peitgen⁵. The max-tree of the brain image (Fig. 1) is computed, and, for each node, the area attribute is computed, *i.e.*, area of the CC represented by the node. The brain and the skull are the two largest structures in the image, so the markers are chosen as the two nodes with largest areas immediately after a max-tree bifurcation (Fig. 2a). The quality of the markers is high and the brain shape is noticeable in the marker image. The watershed transform is applied using these markers, resulting in the final brain segmentation (Fig. 2b). The total processing time to process this brain image, which is 256×256 pixels, on a four-core virtual machine running in the Intel Xeon X5675 server with clock of 3.06 GHz was of 0.10 seconds. The second application consists in the segmentation of the carotid artery wall (Fig. 3). The carotid artery is expected to have a circular shape, and its range of area values are known, therefore the criteria used to choose the marker nodes were area and circularity attributes. The total processing time to process the carotid image, which is 512×512 pixels was of 0.17 seconds. These applications are shown in 2D for illustration purposes, the methodology is readily applicable in 3D. A web-based interactive application of the methodology presented is available at: <http://adessowiki.fee.unicamp.br/adesso/wiki/code/view/>.

Conclusion: A segmentation methodology that profits from the size and shape information contained in the max-tree, the power of the watershed, and the a priori knowledge of medical structures sizes and shapes was presented. Two important medical segmentation applications were illustrated.

References: [1] Salembier et al. IEEE Transactions on Image Processing, 1998. [2] Couprie et al. IEEE Transactions on Pattern Analysis and Machine Intelligence, 2011. [3] Carline and Géraud. IEEE Transactions on Image Processing, 2014. [4] Xu et al. ISMM, 2015. [5] Hahn and Peitgen. MICCAI, 2000.

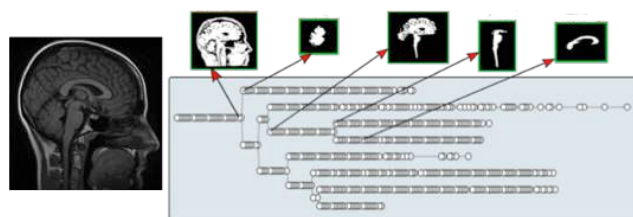


Fig. 1 Brain MR slice (left) and its max-tree representation (right). Each node represents a CC at a different threshold.

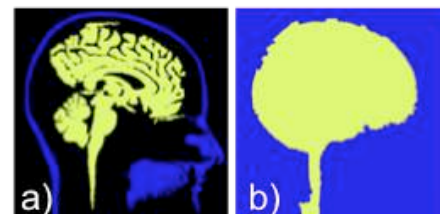


Fig. 2 (a) Max-tree markers and (b) watershed result.

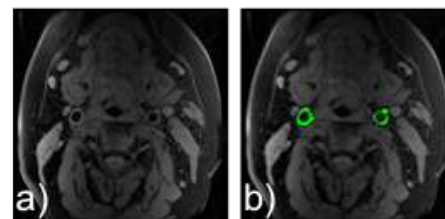


Fig. 3 (a) Carotid image and (b) segmentation result.

Virtual electrophysiological study using T1 mapping techniques improves sensitivity in predicting adverse arrhythmic events in post-infarction patients

Eranga Ukwatta^{1,4}, Plamen Nikolov^{3,4}, Tasnim Vira¹, Natalia Trayanova^{3,4},
Graham Wright^{1,2}

¹Sunnybrook Research Institute, Sunnybrook Health Science Centre, Toronto, ON, Canada

²Department of Medical Biophysics, University of Toronto, Toronto, ON, Canada

³Biomedical Engineering, Johns Hopkins University, Baltimore, MD, USA

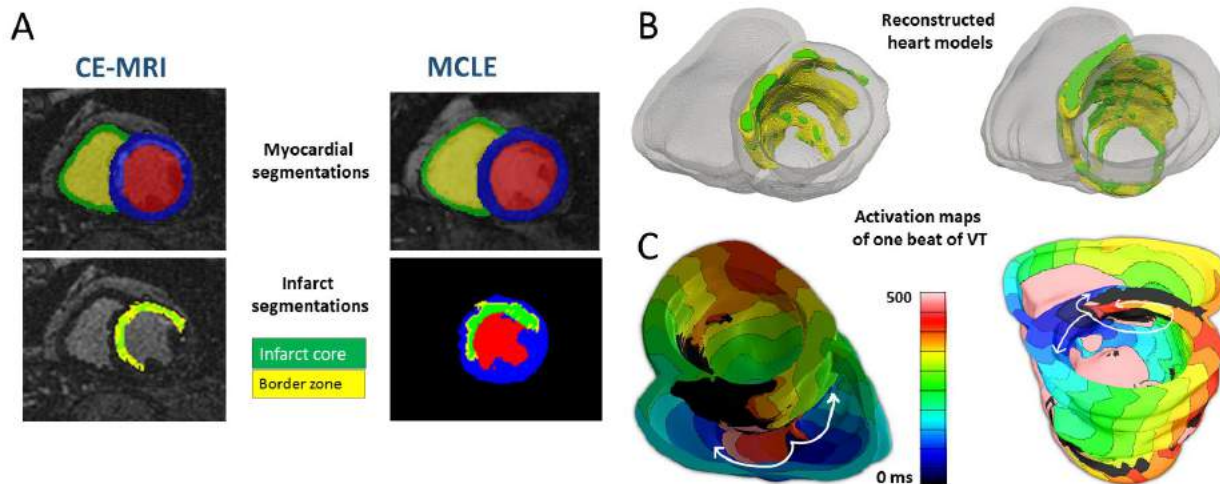
⁴Institute of Computational Medicine, Johns Hopkins University, Baltimore, MD, USA

Background Myocardial infarct (MI)-based indices determined by contrast enhanced (CE) MRI have been widely investigated in stratifying patients suitable for Implantable cardioverter-defibrillator (ICD) implantation to complement less sensitive Left ventricular ejection fraction (LVEF) measures. In comparison to CE-MRI, T1 mapping techniques, such as multi contrast late enhancement (MCLE), have provided more quantitative and reproducible estimates of MI regions. The goal of this study was to evaluate, retrospectively, patient-specific heart computer models built from T1 mapping to predict patient risk for post-MI ventricular tachycardia (VT).

Methods 21 patients (age 63 ± 10 yrs, 85% men, average LVEF $26.3 \pm 10.7\%$) with MI underwent CE-MRI and T1 mapping prior to ICD implantation and were followed up for 6-46 months. Myocardium and MI regions were segmented (Fig. A) from CE MRI and MCLE images using semi-automated image processing software specialized for each technique. Patient-specific computer heart models were built (Fig. B) separately for each technique by incorporating the corresponding MI segmentations, and were probed by simulating delivery of a programmed stimulation at 2 sites on the right ventricle. The methods were tested for accuracy by comparing simulated inducibility of VT (Fig. C) in virtual heart models to ICD therapy in patients.

Results Nine patients had at least one appropriate ICD therapy for ventricular arrhythmias at follow-up. Comparing CE-MRI and MCLE, the virtual heart models built using the latter yielded higher sensitivity (66.7% vs 77.8%) and specificity (77.8% vs 91.7%) in predicting appropriate ICD therapy.

Conclusions T1 mapping techniques, as compared to conventional CE-MRI, may be more accurate in estimating the MI structure and hence may be more sensitive in predicting patient risk for post-MI VT.



Prediction of the spatial distribution of deformable image registration error in lung 4DCT's

Jason Vickress¹, John Morgan³, Rob Barnett^{1,2,3}, Jerry Battista^{1,2,3}, Slav Yartsev^{1,2,3}

Departments of ¹Medical Biophysics and ²Oncology, Western University and

³London Regional Cancer Program, London Health Sciences Centre, London, Ontario

Introduction: Deformable Image Registration (DIR) is currently being introduced into image-guided radiation therapy to model the daily anatomical deformation and indicate when plan adaptation is required. This tool has worked well in diagnostic image registration applications but has not been tested for quantitative applications to dose evaluation and accumulation. The efficacy of DIR has been the subject of much scrutiny, particularly in the application of industry-protected “black box” algorithms. Many studies assign a single DIR error value (e.g. 2 mm) across an entire image volume, without considering the heterogeneous distribution of DIR error. In this study we investigate methods to predict the spatial DIR error throughout a 3D volume.

Methods: DIR evaluation was performed on 10 thoracic 4DCT images. The 4DCT studies contained images at different points of respiration at 10% intervals and each image set also included 300 manually acquired landmark pairs from dir-labs [1], matching homologous points between the 0% and 50% respiratory phases. Deformable image registration was performed using two algorithms: MIM (MIM Software) and Pinnacle (Phillips). Pointwise DIR error was calculated for each landmark pair, comparing the distance between final landmark position and the DIR-predicted location. Four different methods were tested to approximate pointwise DIR error: Inverse Consistency Error (ICE), Transitivity Error (TE), Distance Discordance Metric (DDM) and Normalized Cross Correlation (NCC). ICE, TE and DDM are measures of the deformation vector field consistency, while NCC measures the similarity between the volumes surrounding the two registered points. Regional DIR error was measured using the DICE similarity coefficient between deformed and original contours ($DICE_D$) of the left and right lungs for the thoracic images. Prediction of regional DIR error was assessed using the DICE coefficient between contours of non-deformed 0% and 50% images ($DICE_O$). Regional DIR error prediction was evaluated using the correlation between $DICE_O$ and the measurement of DIR error ($DICE_D$). The four methods predicting the pointwise DIR error were evaluated using Pearson correlation and a receiver operator characteristic (ROC) curves for predicting an error greater than 2 mm.

Results: The mean overall deformation was 8.5 mm (0 to 30.6 mm) for the 4DCT images across 3000 landmarks. Average overall deformation accuracy for the 4DCT thorax images was 3.5 mm (± 5.5 mm) and 3.7 mm (± 4.4 mm) for MIM and Pinnacle, respectively. The R^2 values from the Pearson correlation for predicting pointwise DIR error using ICE, TE, DDM and NCC across all landmarks are shown in Table 1. For regional error prediction the correlation between $DICE_O$ and $DICE_D$ was shown to be 0.787 and 0.813 for the complete lung contour, using MIM and Pinnacle respectively as shown in Figure 1.

Conclusions: Finding metrics that correlate with DIR error is challenging. We have shown that ICE, TE, DDM and NCC metrics can predict pointwise DIR error accurately in thoracic 4DCT images. Regional DIR error was shown to strongly correlate with the degree of differences between similar structures of images registered with DIR. The next step is to better characterize the DIR error within different regions of an image and determine impact on dose accumulation across multiple radiotherapy fractions.

References: [1] Castillo R, Castillo E, Guerra R, et al. A framework for evaluation of deformable image registration spatial accuracy using large landmark point sets. *Phys Med Biol* 2009;54:1849-1870.

Table 1: Pearson correlation values for Pointwise prediction of DIR error

| Algorithm | Pearson Correlation (R^2) | | AUC | |
|-----------|-------------------------------|----------|-------|----------|
| | MIM | Pinnacle | MIM | Pinnacle |
| ICE | 0.581 | 0.521 | 0.853 | 0.737 |
| TE | 0.610 | 0.768 | 0.843 | 0.772 |
| DDM | 0.840 | 0.840 | 0.877 | 0.808 |
| NCC | 0.573 | 0.483 | 0.888 | 0.827 |

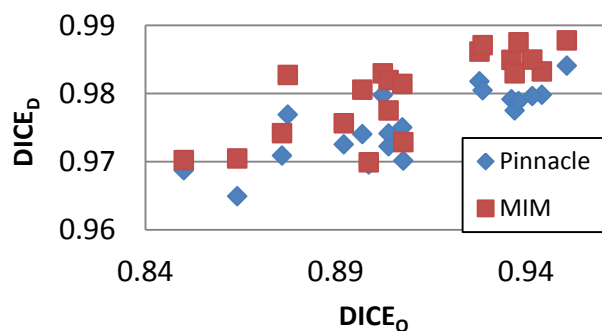


Figure 1. Correlation between contour overlap before ($DICE_O$) and after ($DICE_D$) DIR.

Automated 3D morphometry of the vasculature derived from whole-slide digital histology

Yiwen Xu¹, J. Geoffrey Pickering^{*1,2}, Zengxuan Nong², Aaron Ward^{*1,3} * Supervisors

Ontario Institute for Cancer Research - Smarter Imaging Program

1. Dept. of Medical Biophysics, 2. Robarts Research Institute, 3. Dept. of Oncology, Western University

Introduction: Properties of the microvasculature that contribute to tissue perfusion can be assessed using immunohistochemistry on 2D histology sections. The smooth muscle components of the vessel walls are responsible for the control of the vessel lumen caliber; the smooth muscle dilates and constricts to allow for changes in tissue perfusion. Vessel wall abnormalities can cause vascular disease and organ failure, which is generally assessed in 2D on select fields of view. However, the vasculature is inherently 3D and the ability to measure and visualize the vessel wall components in 3D will aid in detecting focal pathologies. Our objectives were (1) to develop a method for 3D measurement and visualization of microvasculature in 3D on whole slide histology, (2) to compare the normal and regenerated post-ischemia mouse hind limb microvasculature, and (3) to compare the 2D and 3D vessel morphology measures.

Materials and Methods: Vessels were stained for smooth muscle using 3,3'-Diaminobenzidine (DAB) immunostain and the nuclei with hematoxylin for both normal ($n = 6$ mice) and regenerated vasculature ($n = 5$ mice). 2D vessel segmentations were reconstructed into 3D using a nucleus landmark based registration (Fig. 1). [1] A surface was fit to the reconstructed vessel contours using the marching cubes algorithm. [2] Measures of vessel wall area, thickness and perimeter were performed in 2D on the tissue sections and in 3D from the vessel surfaces.

Results/Discussion: No substantial bias was found in the 2D measurements relative to 3D, but larger differences were observed for individual vessels oriented non-orthogonally to the plane of sectioning. A larger value of area, perimeter, and vessel wall thickness was found in the normal vasculature as compared to the regenerated vasculature, for both the 2D and 3D measurements ($p < 0.01$). The measures were found to be non-normally distributed ($p < 0.05$); thus, the median, confidence interval, and interquartile range (IQR) were reported (Table 1). To illustrate, local distribution differences between the 2D and 3D vessel wall thickness measurements are shown in Fig. 2 for one sample vessel. Aggregated 2D measurements are sufficient for identifying morphological differences between groups of mice; however, one must interpret individual 2D measurements with caution if the vessel centerline direction is unknown.

Conclusion: Visualization of 3D measurements permits the detection of localized vessel morphology aberrations that are not revealed by 2D measurements. With vascular measure visualization methodologies in 3D, we are now capable of locating focal pathologies on a whole slide level using 3D histology reconstruction.

Table 1: 3D and 2D measures of normal and regenerated vasculature

| Value | Median | Normal ($n = 1220$) | | | Regenerated ($n = 2194$) | | | |
|--------------------------------|--------|-----------------------|--------|--------|----------------------------|--------|--------|--------|
| | | CI | IQR | Median | CI | IQR | | |
| 3D Area (μm^2) | 184.21 | 170.45 | 194.75 | 230.05 | 107.28 | 102.03 | 112.91 | 162.42 |
| 3D Perimeter (μm) | 33.07 | 31.29 | 34.69 | 37.79 | 25.08 | 24.18 | 26.07 | 28.24 |
| 3D Thickness (μm) | 3.72 | 3.58 | 3.77 | 2.43 | 3.07 | 3.02 | 3.18 | 2.15 |
| 2D Area (μm^2) | 173.29 | 161.40 | 183.59 | 214.35 | 96.00 | 91.43 | 102.54 | 142.79 |
| 2D Perimeter (μm) | 43.70 | 41.09 | 46.55 | 46.46 | 31.11 | 30.14 | 32.68 | 39.76 |
| 2D Thickness (μm) | 3.16 | 3.05 | 3.25 | 1.66 | 2.69 | 2.61 | 2.70 | 1.34 |

[1] Xu, Y, et al. PloS one 10.5 (2015): e0126817.

[2] Lorensen, WE., et al. ACM siggraph computer graphics. Vol. 21. No. 4. ACM, 1987.

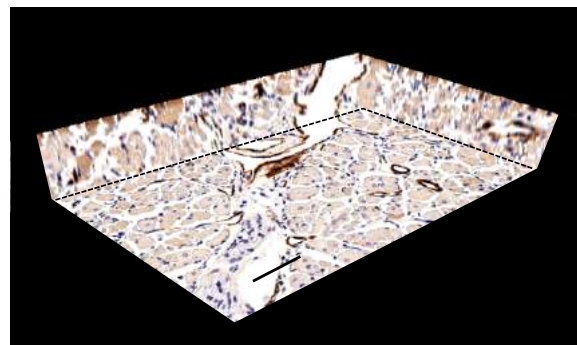


Fig. 1: 3D reconstruction of serial histology sections of regenerated mouse TA post-femoral artery excision, immunostained for smooth muscle α -actin. Scale bar 50 μm .

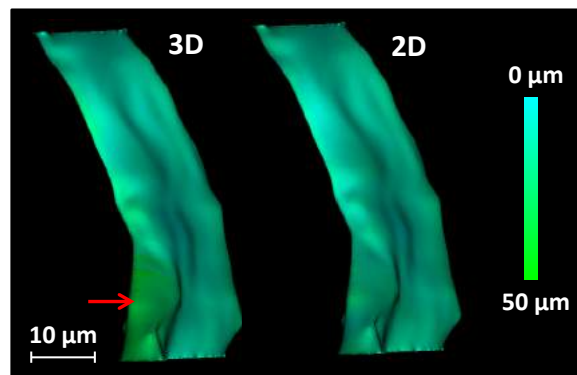


Fig. 2: 3D renderings of normal vessel wall thickness measurements (colour scale) obtained from the 3D vessel surface, compared to thickness measurements obtained from 2D sections.

Evaluating rigid and deformable registration of brain images before and after temporal lobectomy

Yujun Zeng, Jonathan Lau, Ali Khan, Terry Peters

Robarts Research Institute, University of Western Ontario, London, Ontario, Canada

Introduction: Anterior temporal lobectomy (ATL) is one of the effective treatments to control medically intractable temporal lobe epilepsy. However, one of the potential complications of ATL is a visual field cut, which can occur in about 50-100% of the patients. Using pre- and post-operative images to evaluate white matter integrity may help us understand how ATL surgery can affect optic tract and surrounding white matters, thus enable to plan more tailored surgical approaches. An important first step in this evaluation is to register post-operative images to pre-operative ones.

Method: We obtained magnetic resonance imaging (3T MRI) from 5 patients (11 images in total, follow-up at 2 different time for one case) before and after surgery. Rigid and deformable (BSpline) registration was conducted using 3D Slicer to register post-operative images to pre-operative ones. A mask of the brain excluding the resection zone was generated semi-automatically and used to constrain the deformable registration. We placed 95 fiducials on corresponding anatomical landmarks in each image. Fiducials were comprised of 5 midline (anterior commissure - post commissure [AC-PC] line), 30 peri-lesional, 30 ipsilateral to resection, and 30 contralateral to resection. These were further categorized by lobe and classified as either peri-ventricular or peri-cortical. Fiducial distances between pre-operative and post-operative registered images were obtained to evaluate the accuracy of the registration. Wilcoxon matched-pairs signed rank test was employed to compare rigid and deformable registration for different lobes and hemispheres.

Results: Registration was performed with checkerboard comparisons shown in Figure 1. A total of 570 fiducials were acquired from 11 images. Mean fiducial distances are shown in Figure 2. No significant difference was identified between the rigid and deformable registrations ($p=0.66$) with all the fiducials. Mean fiducial distances of rigid on ipsilateral hemisphere and AC-PC line was higher than that of deformable registration ($p=0.02$ and $p=0.0001$, respectively). These two registrations showed no significant difference in peri-lesional part ($p=0.17$) and contralateral hemisphere ($p=0.07$). For different lobes, no significant difference was identified of all the lobes ($p=0.28$ for frontal lobe, $p=0.89$ for temporal lobe, $p=0.82$ for parietal lobe and $p=0.48$ for occipital lobe). But the fiducial distances of rigid registration on peri-ventricular cortex is significantly higher than that of deformable registration ($p<0.0001$).

Conclusion: Both rigid and deformation are effective methods to register post-operative images to pre-operative ones. Deformable registration works better than rigid registration in ipsilateral hemisphere of the lesion, AC-PC line and peri-ventricular cortex, while in other hemisphere or lobes of brain, these two registration methods show no significant differences.

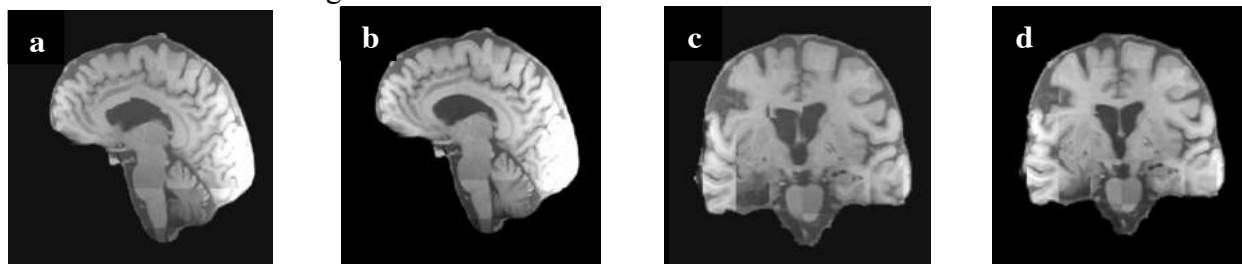


Figure 1. Checkerboard of pre- and post-operative images after rigid (a, c) and deformable registration (b, d)

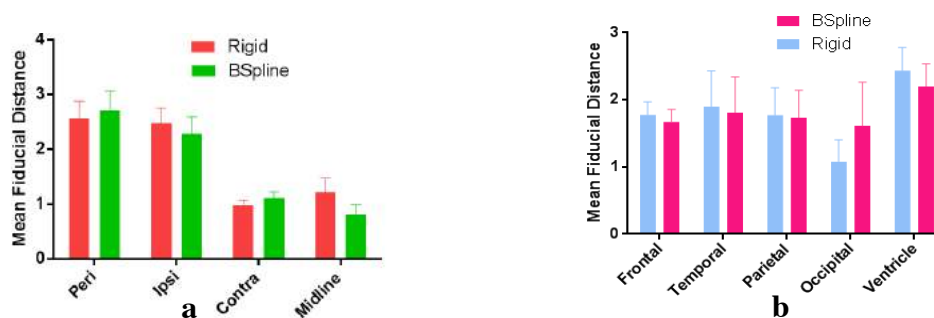


Figure 2. Mean fiducial distance of different hemispheres (a) and lobes (b)

Presenter Index

Listed by last name of presenter with talk or poster number and abstract page.

| | | | |
|-------------------------------|--------------|---------------------------------|---------|
| Abraham, Christopher | 188 | Driscoll, Brandon | 148 |
| Adair, David | 103 | Dufort, Paul | 71 |
| Akbari, Alireza | 47, 159, 160 | Ebrahimi, Mehran | 195 |
| Albatany, Mohammed..... | 126, 127 | Eilaghi, Armin | 175 |
| Alexander, Kevin..... | 189 | El-Sherif, Omar | 122 |
| Alsaden, Noor..... | 39 | Elkerton, Sachi..... | 80 |
| Amelard, Robert..... | 190 | Engler, Steven..... | 104 |
| Ameri, Golafsoun | 78 | Enjilela, Esmaeil..... | 50, 176 |
| Araya, Yonathan | 61 | Escartin, Terenz..... | 140 |
| Arkhangorodsky, Michelle..... | 34 | Faraz, Azharhosein | 105 |
| Arnott, Stephen..... | 44 | Farha, Georges | 133 |
| Baronette, Rudy | 172 | Fazel Bakhsheshi, Mohammad..... | 141 |
| Batchelor, Connor | 128 | Fink, Corby..... | 177 |
| Baum, Zachary..... | 132 | Forward, Sarah | 142 |
| Baxter, John..... | 191 | Foster, Paula..... | 40 |
| Beera, Kiran..... | 120 | Friedlander, Yonni | 162 |
| Blokker, Alexandra | 139 | Gaudet, Jeff | 57, 123 |
| Boroomand, Ameneh | 192 | Gelman, Daniel..... | 143 |
| Burton, Christiane | 173 | Geraghty, Benjamin..... | 149 |
| Chisholm, Alexander | 75 | Gholampourkashi, Sara | 134 |
| Cho, Daniel | 193 | Gillies, Derek | 33 |
| Chuang, Audrey..... | 91 | Goldhawk, Donna..... | 185 |
| Cocker, Myra | 45 | Gribble, Adam | 60 |
| Coolens, Catherine | 121 | Haider, Shahid | 196 |
| Couch, Marcus..... | 161 | Han, Wenchao..... | 197 |
| Cruje, Charmainne..... | 53 | Hariharan, Santosh..... | 198 |
| Daly, Michael..... | 38 | Harish, Vinyas..... | 31, 106 |
| deKemp, Robert | 48 | Hess, Margaret..... | 144 |
| Dekker, Kurtis..... | 86 | Holden, Matthew | 107 |
| Desmond, Kimberly..... | 73 | Holdsworth, David..... | 74, 145 |
| DiCarlo, Amanda | 194 | Hosseini, Mahdi..... | 200 |
| Dona, Olga..... | 174 | Hosseini, Zahra | 199 |

| | | | |
|---------------------------|----------|--------------------------|-----|
| Hrinivich, William | 89 | MacFarlane, Michael..... | 137 |
| Hughes, Alec..... | 36 | MacNeil, Kyle..... | 113 |
| Ibrahim, Amani..... | 76 | Makela, Ashley | 178 |
| Inoue, Jiro..... | 78 | Marants, Raanan | 154 |
| Jaffray, David..... | 30 | Martin, Peter..... | 114 |
| Jayarathne, Uditha | 108 | Mattonen, Sarah | 69 |
| Jechel, Christopher..... | 135 | McCunn, Patrick | 166 |
| Johnson, Patricia | 90 | McKee, Trevor | 93 |
| Joo, Lewis | 46 | McNabb, Evan | 81 |
| K Saeid, Ali..... | 136 | Mester, James | 167 |
| Kara, Jenna | 163 | Michael, Justin..... | 115 |
| Karami, Elham | 109 | Morgado, Felipe | 59 |
| Kasiri, Keyvan | 201, 202 | Mouawad, Matthew..... | 179 |
| Kazemzadeh, Farnoud | 87 | Murrell, Donna | 168 |
| Khalvati, Farzad | 37 | Nahlawi, Layan | 116 |
| Kishimoto, Jessica..... | 110 | Nano, Tomi..... | 209 |
| Knight, Jesse | 203 | Oppermann, Sina..... | 56 |
| Krahn, Philippa | 67 | Overchuk, Marta | 55 |
| Kumar, Devinder | 204 | Paish, Adam..... | 54 |
| Lam, Wilfred..... | 164 | Pardasani, Utsav..... | 210 |
| Lau, Justin..... | 62 | Parkins, Katie..... | 169 |
| Lausch, Anthony..... | 72 | Petrov, Ivailo | 211 |
| Le, Trung..... | 150 | Pinter, Csaba | 92 |
| Lee, Casey..... | 151 | Pop, Mihaela | 65 |
| Li, Fiona | 152 | Prozzo, Vanessa..... | 186 |
| Li, Tao | 129 | Rankin, Adam | 117 |
| Li, Xingyu | 205 | Reiche, Brittany | 35 |
| Lim, Patrick..... | 153 | Renaud, Jennifer | 79 |
| Lindenmaier, Andras | 165 | Rodgers, Jessica..... | 118 |
| Liu, Hanlin..... | 49 | Santos, Marc..... | 70 |
| Liu, Junmin | 63, 206 | Schranz, Amy | 43 |
| Lorusso, Daniel | 146 | Shahedi, Maysam | 212 |
| Lougheed, Matt..... | 207 | Shaikh, Noor | 66 |
| Lu, YingLi..... | 208 | Shaw, Saurabh..... | 213 |
| Lugez, Elodie..... | 85 | Sibai, Mira | 180 |
| MacDonald, Matthew | 111, 112 | Siddiqi, Kaleem..... | 214 |

| | | | |
|-----------------------------|----------|-------------------------|-----|
| Sivanesan, Sinthu | 77 | Umoh, Joseph..... | 170 |
| Skanes, Allan | 64 | Ungi, Tamas..... | 32 |
| Soetemans, Derek | 215 | Vaughan, Thomas..... | 119 |
| Souza, Roberto | 216 | Vickress, Jason..... | 218 |
| Spencer Noakes, Leigh | 124 | Vines, Douglass | 157 |
| Stapleton, Shawn | 42 | Wang, Chaoyue | 183 |
| Sunderland, Kyle..... | 138 | Wang, Dan..... | 41 |
| Svistoun, Igor..... | 155 | Wilk, Benjamin | 51 |
| Tabanfar, Reza..... | 181 | Wright, Eric..... | 147 |
| Tao, Ashley | 82 | Xhaferllari, Ilma | 83 |
| Tavallaei, Mohammad..... | 88 | Xu, Yiwen..... | 219 |
| Taylor, Edward | 156 | Yan, Christina | 125 |
| Thiessen, Jonathan..... | 84 | Yang, Dae-Myoung | 158 |
| Tieu, Henry | 187 | Yeung, Ivan | 131 |
| Tong, Hoi-Ki..... | 182 | Zanette, Brandon | 171 |
| Tsang, Adrian..... | 58 | Zeng, Yujun..... | 220 |
| Tse, Justin | 52 | Zhang, Yucheng | 184 |
| Ukwatta, Eranga | 130, 217 | | |

2016 ImNO Annual Meeting would like to thank you for attending, and acknowledge its supporting consortia and all sponsors.

We invite you to attend the 15th ImNO Annual Meeting in 23-24 March 2017 at the DoubleTree Hilton in London, Ontario.

